Forschungszentrum Karlsruhe
in der Helmholtz-Gemeinschaft

Wissenschaftliche Berichte
FZKA 7481

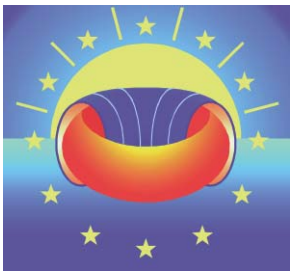

Nuclear Fusion Programme Annual Report of the Association Forschungszentrum Karlsruhe / EURATOM

January 2008 – December 2008

Programm Kernfusion

Juli 2009

Forschungszentrum Karlsruhe

in der Helmholtz-Gemeinschaft

Wissenschaftliche Berichte

FZKA 7481

Nuclear Fusion Programme
Annual Report of the
Association Forschungszentrum Karlsruhe/
EURATOM
January 2008 – December 2008

compiled by I. Pleli
Programm Kernfusion

Forschungszentrum Karlsruhe GmbH, Karlsruhe
2009

This work, supported partially by the European Communities under the contract of Association between EURATOM and Forschungszentrum Karlsruhe, was carried out partially within the framework of the European Fusion Development Agreement. The views and opinions expressed herein do not necessarily reflect those of the European Commission.

Forschungszentrum Karlsruhe GmbH
Postfach 3640, 76021 Karlsruhe

Mitglied der Hermann von Helmholtz-Gemeinschaft
Deutscher Forschungszentren (HGF)

ISSN 0947-8620

urn:nbn:de:0005-074810

Introduction

The worldwide energy consumption is mainly covered by fossil energy sources. Their environmental impact, to a certain extent already visible, requires in the long term new ways of energy supply. In addition the worldwide energy demand will substantially increase in the course of this century in particular in populous countries such as China and India. Nuclear fusion offers an option of an environmental benign energy source with favourable safety features and almost unlimited fuel resources.

Nuclear fusion research is aiming to generate the physical and technical basis of a fusion power station which, similar to the sun, gains energy from the fusion of light atoms. In order to attain ignition of the plasma, the fuel, a mixture of deuterium/tritium (isotopes of hydrogen), must be confined by strong magnetic fields and heated up to more than 100 million degrees.

The construction of the experimental reactor ITER in Cadarache/France in the framewok of a worldwide project marks the next big step on the way to a fusion power station. For the first time a fusion power of 500 Mega Watt will be generated by a long burning plasma and applied technologies will undergo extended tests.

In the framework of the European Fusion Programme the Association FZK-EURATOM is developing key technologies in the areas of superconducting magnets, microwave heating systems (Electron-Cyclotron-Resonance-Heating, ECRH), the deuterium-tritium fuel cycle, He-cooled breeding blankets, a He-cooled divertor and structural materials as well as refractory metals for high heat flux applications including a major participation in the international IFMIF project. Furthermore investigations on plasma wall interactions and core and divertor modelling are carried out and a global plasma model is being developed.

The results from experimental activities such as the tests of high temperature superconducting current leads in the test facility TOSKA, the quasi-stationary gyrotron operation and the operation of fuel cycle subsystems and components with deuterium-tritium have already been utilised for the design work for ITER.

With the construction of ITER new challenges have to be mastered by the EURATOM-Associations. While up to now concepts for components and systems have been developed and their functionality has been tested in laboratory scale or semi-technical scale, now plant components have to be constructed for fabrication by the industry and their integration into the plant has to be supported. In order to effectively deploy personal and financial resources consortia of European Association Laboratories have been formed which will bear the responsibility for the realisation of components and systems in accordance with the procurement packages of ITER. The Association FZK-EURATOM is leading a consortium for the construction of the European test blanket module (TBM) systems. In addition the Association FZK-EURATOM is also involved in other consortia such as construction of the upper port plug ECRH microwave launcher, the fuel cycle and the development and procurement of gyrotrons providing microwaves of 170 GHz and 2 MW output power for ITER. Furthermore the already existing co-operation with industrial companies is being intensified.

The design and construction of ITER components and subsystems need to be supported by experiments such as prototype testing, validation of scale up factors and additional R&D. For this purpose a helium loop HELOKA is being constructed which not only serves for experimental investigations of the TBM, but also as a pilot loop in view of the loops to be installed in ITER for the cooling of test blanket modules.

The demonstration power station DEMO constitutes the next step beyond ITER which is supposed to be planned after some years of ITER operation. In the framework of a European DEMO study the Association FZK-EURATOM is developing the so-called multi-module blan-

ket concept which promises reduced plant shutdown times during remotely controlled exchange of blankets and thus contributes to an increased plant availability.

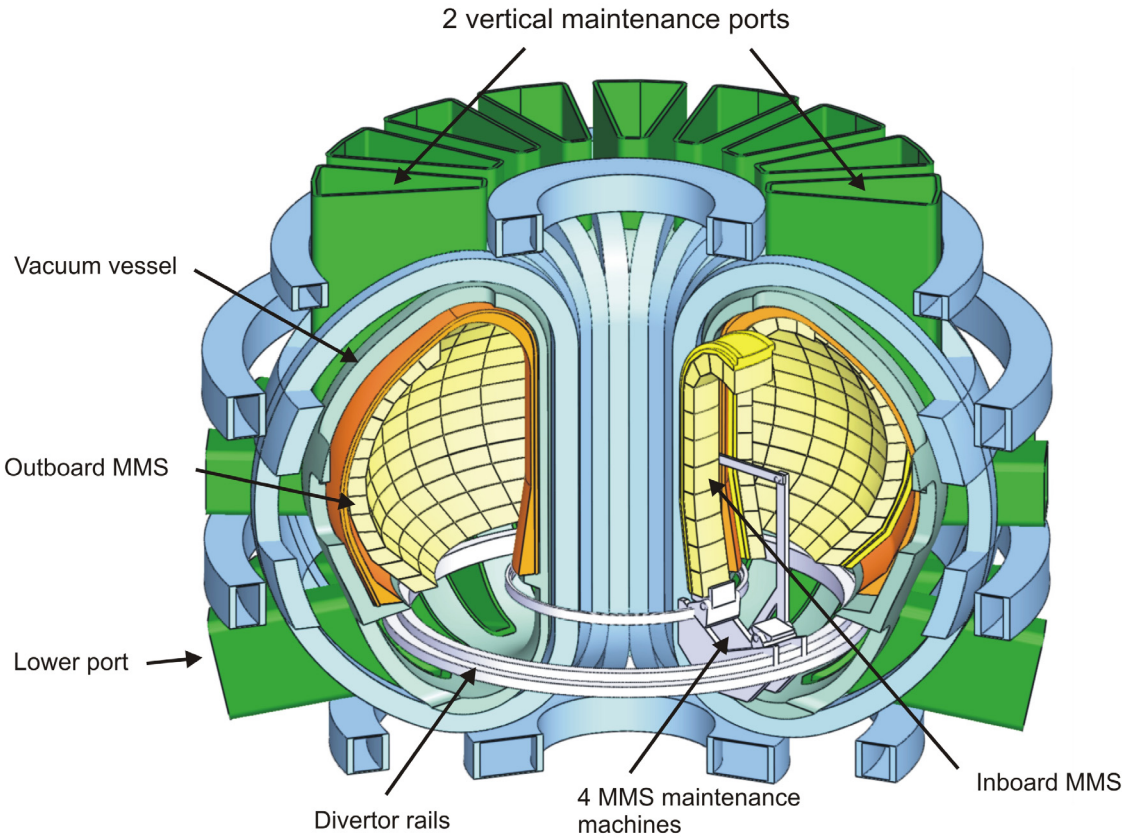

Remotely controlled exchange of blanket modules according to the MMS concept.

Furthermore a helium cooled divertor for DEMO is under development.

About 230 professionals and technicians are involved in the fusion programme of the Association FZK-EURATOM with additional support of technical departments.

Progress from January 2008 to December 2008 is reported here. More information is available from the programme management and from the responsible scientists. The website www.fzk.de/fusion offers further access to the fusion activities of FZK.

Contents Page

Introduction

Plasma Edge 1

TW6-TPP-DAMTRAN WP08-PWI-04 Modelling of ITER Plasma Components Damage and Consequences for Plasma Evolution following ELMs and Disruptions, and Melt/dust Erosion 3

TW6-TPP-DAMTRAN WP08-ITM-TFL2 and WP08-PWI-09 Modelling of ITER Plasma Components Damage and Consequences for Plasma Evolution following ELMs and Disruptions and ITER inter-ELM Scenario Periods Modelling 8

Divertor and Core Plasma Modelling for ITER 14

Heating and Current Drive - Physics 23

EFDA/06-1406 (TW6-TPHE-ECHULB4) and TW6-TPHE-ECHULA Design and Analysis of the Upper Launcher for the ITER-ECH&CD System Analysis and Testing of the Upper Launcher for the ITER ECH&CD System 25

Project funded by the Ministry for Education and Research (BMBF): Exploring Be related Manufacturing Technolgies for the Realisation of a Test Stand for the ITER ECH Upper Launcher 29

Heating and Current Drive – Diagnostics 33

EFDA/06-1446 (TW6-TPDS-DIADES9) Diagnostic Design for ITER: Bolometry (Engineering Analysis for Bolometer Cameras) 35

Vessel/In-Vessel 37

EFDA/07-1704-1624 (TW6-TVV-LEAKD2) Leak Localisation for In-vessel Components 39

Magnet Structure and Integration 43

EFDA/07-1704-1604 (TW6-TMSM-CRYOGT) Materials Cryogenic Testing 45

Current Leads for Wendelstein 7-X and JT-60SA 50

EFDA/06-1522 (TW6-TMSC-COILMO) Definition of Procedures for Coil Electrical Testing and PF Transient Analysis 56

New Quench Detection System for Fusion Magnets 59

Development of HTS-Roebel-cables 66

TOSKA Refurbishment and Preparation for Coil Testing 69

Cryogenic Infrastructure 71

Breeding Blanket 75

TW5-TTB-001 Construction of the High Pressure Helium Loop (HELOKA-HP/TBM) for Testing of Test Blanket Modules (TBMs) 77

TTBB-001 Helium Cooled: TBM Design, Integration and Analysis 79

TW5-TTBB-001 D 2 Detailed Design of Sub-components and Prototypical Mock-ups for the HCPB TBM Qualification 79

TW5-TTBB-001 D 8 Detailed HCPB TBM Development Work Plan and First Technical Specification Document 81

Page

	TW5-TTBB-001 D 9	Experimental Verification of Pebbles Filling in the HCPB TBM	85
	TW5-TTBB-001 D 10	Manufacturing and Testing of a FW Channel Mock-up for Experimental Investigation of Heat Transfer with He at 80 bars and Reference Cooling Conditions. Comparison with Numerical Modeling	86
	TW6-TTBB-001 D 3	HCPB TBM Design and Integration Analysis	92
TTBB-003	Helium Cooled: Out of Pile Testing		95
	TW5-TTBB-003 D 1	Manufacturing and Testing of Mock-ups for Investigation of Coolant Flow in the Manifold System of HCPB TBM (GRICAMAN Experiments)	95
Helium Cooled Pebble Bed: Breeder and Neutron Multiplier Materials Development of Beryllium and Beryllium Alloy Pebble Beds with Improved Tritium Release Characteristics – Part 1			97
Helium Cooled Pebble Bed: Breeder and Neutron Multiplier Materials Development of Beryllium and Beryllium Alloy Pebble Beds with Improved Tritium Release Characteristics – Part 2 -			103
Modelling of Pebbles and Pebble Beds Modelling of Pebble Beds has been carried by Means of Continuum Mechanics and Discrete Element Method (DEM)			106
Activation of Lithium Orthosilicate Breeder Materials			108
TTBC-006	Helium-Cooled Lithium Lead: Magneto-Hydrodynamics and Liquid Metal Materials		114
	TW5-TTBC-006 D 1	MHD Experiments in a Mock-up Relevant for a Helium Cooled Lead Lithium Test Blanket Module for ITER	114
Materials Development – Structural Materials			119
EFDA/05-1244 (TW4-TTMS-RedAct)	Investigation of Options to Reduce Critical Elements in Low Activation Ferritic/ Martensitic Steels		121
EFDA/06-1520 (TW6-TTB-EUROFER)	Support and Follow-up of the EFDA/06-1903 Art. 7 Contract for Procurement of EUROFER for the TBM Fabrication Technology Trials and Mock-ups		123
TTMS-001	Irradiation Performance		125
	TW2-TTMS-001b D 5	Tensile, Charpy and Fatigue Specimen Testing after Neutron Irradiation up to 15 dpa in the Range of 250°C – 450°C, Completion of the Irradiation and Post-irradiation Examination	125
	TW2-TTMS-001b D 9	Fast Reactor Irradiation up to 30 dpa, at 340°C of Tensile, Charpy and LCF RAF/M Specimens, Completion of the PIE	130
	TW5-TTMS-001 D 10	Mechanical Post Irradiation Examinations of FZK-Specimens Irradiated in the ARBOR-2 Experiment in the BOR 60 Reactor	132
	TW5-TTMS-001 D 4	Tomographic Atomic Probe Analysis of EUROFER Materials Irradiated in the ARBOR Irradiation Campaign	135
	TW6-TTMS-001 D 5	Studies of the Effect of Implanted He on Mechanical Properties of EUROFER in the T-range 300 – 500°C	138
TTMS-004	Qualification Fabrication Processes		140
	TW6-TTMS-004 D 1+2	Improve Design Limits of Welded Components through Improved Post Weld Heat Treatments, Qualification and Improvement of Welded and Diffusion Bonded Joints	140

Page

TTMS-005 Rules for Design, Fabrication and Inspection ... 146

TW2-TTMS-005b D 4 Creep-fatigue Lifetime Prediction Rules for Irradiated EUROFER ... 146

TW5-TTMS-005 D 5 High Temperature Fracture Mechanical (creep-fatigue) Rules: Formulation and Implementation ... 148

TW5-TTMS-005 D 6 Define and Perform Accompanying Experiments to D 5 (e.g. creep crack growth at 550°C) ... 149

TW6-TTMS-005 D 4 Experimental Verification and Validation of Newly Implemented HT Creep-fatigue Rules ... 151

TW6-TTMS-005 D 5 Qualification of NDT (non-destructive detection techniques) for Evaluation of Limits of Detectable Cracks ... 155

TTMS-006 High Performance Steels ... 156

TW5-TTMS-006 D 5 Nano Composited Ferritic Steels for HT Application: Identification of Promising Candidate Allow Compositions and Respective Fabrication Routes According to the Outcome of the 2004 Study. Production of Different Laboratory Batches (14%Cr) ... 156

TTMS-007 Modelisation of Irradiation Effects ... 161

TW6-TTMS-007 D 10 Elaboration of a Critical Review of the Physical Metallurgy of EUROFER Alloying Elements and Impurities, Heat-treatment/Phases/Microstructure, Phase Stability, and Segregation ... 161

Corrosion Resistance of Bare and Coated EUROFER in Liquid PbLi ... 164

Materials Development – Advanced Materials ... 173

TTMA-002 Divertor and Plasma Facing Materials ... 175

TW6-TTMA-002 D 6 Fundamental Studies on Mechanical Properties of W-alloys ... 175

TW5-TTMA-002 D 6 Mechanical Testing of Irradiated W Tungsten Samples ... 180

PM Production and PIM of Tungsten and Tungsten Alloys ... 182

TW6-TTMA-002 D 8 Production of Small Laboratory Scale Batches of Improved Materials for Characterization ... 185

Electrochemical Machining (ECM) of Tungsten and Tungsten Alloys ... 188

Materials Development – Nuclear Data ... 195

EFDA/07-1704-1626 (TW6-TTMN-001B) Nuclear Data: EFF/EAF Data File Upgrade, Processing and Benchmark Analyses ... 197

EFDA/07-1704-1631 (TW6-TTMN-002B) Nuclear Data: Benchmark Experiments to Validate EFF/EAF Data ... 206

Materials Development – IFMIF ... 217

International Fusion Materials Irradiation Facility (IFMIF) Test Cell ... 219

Helium Gas Loop (HELOKA-LP): Procurement and Installation ... 224

International Fusion Materials Irradiation Facility – Engineering Validation Engineering Design Activities (IFMIF-EVEDA)
Study of the Effect of Tungsten Plates on Material Irradiation Conditions in the Medium Flux Test Module (MFTM) ... 226

Page

Fuel Cycle – Vacuum Pumping 231

TW5-TTFF-VP 58 Upgrade of TIMO 233

EFDA/07-1704-1567 (TW6-TTFF-VP 79) Definition of Detailed TIMO-2 Test Programme for the ITER Prototype Torus Cryopump 237

EFDA/07-1704-1546 (TW6-TTFF-VP 73) Supply of CATIA Manufacturing Drawings for the ITER Prototype Torus Cryopump 240

TW5-TTFF-VP 57 ITERVAC Validation Test 241

EFDA/06-1498 (TW6-TTFF-VP 68) Conductance Modelling of ITER Divertor and Torus Pumping Duct 246

EFDA/07-1704-1566 (TW6-TTFF-VP 78) ITER Torus Cryopump Mechanical and Thermal EM Load Study 249

TW6-TTFF-VP 53 Tritium Test of Ferrofluidic Cartridge Seals for Roots Roughing Pump 253

EFDA/07-1704-1568 (TW6-TTFF-LD 71) Risk Analysis Tool for ITER Operations from Vacuum Leaks 256

EFDA/07-1704-1547 (TW6-TTFF-VP 72) Study of the Effects of ITER off-normal and Mitigation Events on Torus and Cryostat Cryopumps 259

EFDA/07-1704-1618 (TW6-TTFF-VP 75-1) DNB Cryopump Initial Design Study 263

Fuel Cycle – Tritium Plant 267

TW4-TTFD-TR 41 and TW4-TTFD-TR 43 Experimental Investigation of Undesired Side-reactions in PERMCAT and Comparison of Batch and Continuous Operation Modes for the Impurity Processing Stage of the Tokamak Exhaust Processing System 269

TW4-TTFD-TR 44 Inactive Tests of Selected SDS Control Loop Performance under Typical ITER Operating Conditions 275

TW6-TTFD-TR 64 Endurance Tests of Water Detritiation System 276

TW6-TTFD-TR 56 Isotope Separation Tests for Evaluation of Column Packing Options 278

TW6-TTFD-TR 63 Testing of Isotope Separation System (ISS) with the WDS 280

EFDA/06-1510 (TW6-TTFD-TPI 55) Update of ITER-ISS-WDS Process Design – 1 282

EFDA/06-1514 (TW6-TTFD-TR 65) Development and Customization of CATIA V5 for Tritium Plant Systems 284

EFDA/06-1512 (TW6-TTFD-TR 66) Design Study of ITER HVAC/LAC, Depression Systems, ADS/VDS and Safety Tritium Monitoring – 1 286

EFDA/07-1704-1550 (TW6-TTFD-TR 69) ITER Design Review 2008 WG7 (Tritium) FZK input (TLK part) 288

Safety Analysis and Environmental Impact 291

EFDA/07-1704-1592 (TW6-TSS-SEA 4.5a) Experiments and Calculations for Demonstration of Inert Gas Injection Feasibility 293

EFDA/07-1704-1575 (TW6-TSS-SEA 5.4) Magnet Busbar Arc – Development of an ITER-representative Model and Supporting Validation Experiments 299

Doses to the Public and Validation of UFOTRI 303

Page

DEMO Conceptual Studies 305

TRP-001 PPCS He-cooled Divertor Concepts 307

TW6-TRP-001 D 2 Manufacturing of Medium Scale Mock-ups – First Tests 307

TRP-002 DEMO Physics Studies 314

TW6-TRP-002 D 3 Development of an Improved Treatment of Plasma Radiation for Medium- and High-Z Impurities 314

TRP-005 Neutronic Analysis, Model Generation and Neutronic Design Analyses 316

TW6-TRP-005 D 1a Model Generation and Neutronic Design Analyses for the European DEMO Conceptual Study 316

EFDA/06-1454 (TW6-TRP-007) DEMO Conceptual Design – FZK Contribution - Design Conflicts arising between different Tasks for DEMO Conceptual Studies for In-vessel Integration 320

TRP-012 Optimisation of a Fusion Power Plants for the Production of Hydrogen 324

TW6-TRP-012 D 1b Optimisation of a 'Start-up' Scenario where the Power is less than 100 MW 324

TW6-TRP-012 D 2 Assessment of the Impact of a Fusion Power Plant for H_2 Production on Internal Components 326

JET Technology 331

JW5-FT-5.20 Shutdown Dose Rate at JET Tokamak – Code Benchmark 333

JW2-FT-2.4/ JW5-FT 2.24 Tritium Inventories of Spent Cryopanels and Waste Conditioning/ Characterisation of ITER relevant Cryosorption Panels after Tritium Operation at JET 335

Heating Systems Technology Project 337

EFDA/06-1502 (TW6-THHN-NBD1) Design Activities for the first ITER HNB Injector 339

EFDA/05-1352 (TW5-THHN-MONRF) Monitoring the EU/RF Collaborative Tasks on the First ITER NB Injector and the ITER NB Test Facility 343

EFDA/07-1704-1583 (TW6-THHE-CCGDS5) European Development of a Gyrotron for ITER: Design and Analysis, and Support to the Industrial Contracts

D 1: Design of an improved RF optical system for the refurbished gyrotron and support to the experiments on the FZK pre-prototype 348

D 2a: Preliminary design of a 170 GHz, 1 MW, CW cylindrical cavity gyrotron as fallback solution 354

Physics 359

ECR Heating and Current Drive – Step-Tunable Gyrotron Development 361

Design Studies towards to a 170 GHz 4 MW coaxial Gyrotron 365

Microwave Heating for Wendelstein 7-X 367

Underlying Technology 375

Operation of the Fusion Materials Laboratory 377

Page

Goal Oriented Training Programme 379

WP08-GOD-EUROBREED (FU07-CT-2008-00047)
Goal Oriented Training Programme “Breeding Blanket Developments for Fusion Reactors” 381

WP08-GOT-TRI-TOFFY (FU07-CT-2008-00047)
Goal Oriented Training Programme “Tritium Technologies for the Fusion Fuel Cycle” 383

Appendix I FZK Departments Contributing to the Fusion Programme 385

Appendix II Fusion Programme Management Staff 387

Appendix III Glossary 389

Plasma Edge

TW6-TPP-DAMTRAN
WP08-PWI-04
Modelling of ITER Plasma Component Damage and Consequences for Plasma Evolution following ELMs and Disruptions, and Melt/dust Erosion

Introduction

In the future tokamak ITER, the plasma edge localized modes (ELMs) may result in vaporization erosion at the divertor and first wall surfaces. Another kind of ITER wall erosion is surface melting of metallic targets (beryllium and tungsten) caused by transient loads. For modelling the melt motion damage, the incompressible fluid dynamics code MEMOS was applied. The new calculations with MEMOS, including bulk heat transport and surface melt motion, are described and compared with recent experiments at the plasma gun QSPA-T of TRINITI.

Tungsten is a reference material for the ITER divertor armour, except for the separatrix strike point armoured with CFC. This substantiates the investigation of tungsten damage resistance under transient heat loads. Investigations of tungsten dust production have been performed using the thermomechanic code PEGASUS. First comparisons with experimental observations for the dust production in the JUDITH and in the QSPA-T facilities have been done.

Simulations of melt motion damages using the code MEMOS

Previous three-dimensional MEMOS simulations for the melt erosion of the tungsten macrobrush after single ELM loads with 0.5 ms time duration have shown that melting of the frontal and lateral brush edges starts at Q > 0.45 MJ/m^2 whereas the melting of the top brush surface starts at Q > 1 MJ/m^2, which agrees well with the melting thresholds obtained in the QSPA-T experiments. The calculations revealed a significant damage to brush edges caused by the interaction of impacting plasma with the lateral surfaces. The MEMOS simulations demonstrated that for heat loads Q < 1.6 MJ/m^2, evaporation is mainly responsible for the W mass losses (average evaporation of 0.06 μm per shot calculated for Q = 1.6 MJ/m^2 is comparable with the experimental results). The calculated magnitude of melt erosion depends linearly on the tangential pressure of impacting plasma at the surface. For example, for Q = 1.5 MJ/m^2, after each shot the surface roughness along a single brush increases by 0.2 μm at 0.05 MPa (which is the expected plasma pressure of ITER ELMs) and by 1.5 μm at 0.4 MPa (the pressure measured at QSPA-T). Thus, with the repetitive transient loads anticipated in ITER, the PFC lifetime can significantly decrease: e.g., 0.2 μm×10^3 ELMs = 0.2 mm.

The Lorentz (**J**x**B**) force resulting from the current density J = 1 MA/m^2, crossing a target in a strong magnetic field (B = 5 T), corresponds to the pressure gradient 5 MPa/m. For a tungsten target under plasma load, this is one order of magnitude less than the typical pressure gradient at the surface and thus it can be neglected. Furthermore, such an order of magnitude of **J** is expected at loads of ~10 MJ/m^2. Therefore, for ITER ELM loads the J×B force is not important even for strong ELMs (the ELMs with plasma shield, which for the reference pulse duration of 0.5 ms occurs at Q > 2.5 - 3 MJ/m^2). Thus, the plasma pressure gradient is the main driving force. In the case of ELMs without vapour shield (Q < 1.6 - 1.8 MJ/m^2), the direct momentum transfer from the impacting plasma stream becomes the main driving force.

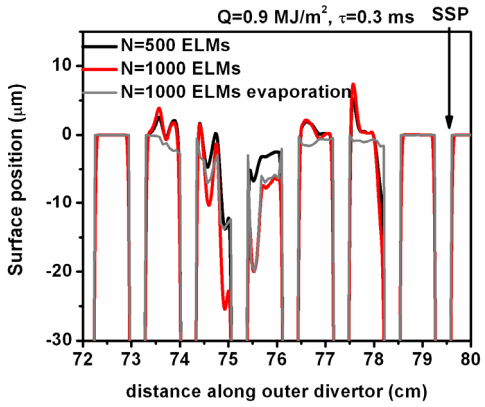

Fig. 1: Erosion of the outer divertor W- brush armour under ITER-like repetitive transients.

Further numerical simulations with MEMOS for W targets were focused on damage estimations after repetitive heat loads. The damages to W-macrobrush targets that underwent multiple ELM- and disruption-like loads at the plasma gun QSPA-T, as it is anticipated for ITER transients, were investigated calculating the changes of surface roughness after every load pulse in the subsequent erosion evolution. These numerical simulations demonstrated that the erosion monotonically increases with the number of pulses. The surface roughness is proportional to the pulse number. This is shown in Fig.1 for moderate ELMs with an average heat load of Q_a = 0.9 MJ/m^2 and a corresponding peak heat load of Q_{max} = 2 MJ/m^2 (for the reference pulse duration τ_R = 0.5 ms and the vapour shield as calculated by the code FOREV). The brush roughness after the repetitive transient loads is proportional to the energy load. For Q_a = 0.9 MJ/m^2 and after 10^3 ELMs, the surface roughness reached 30 μm (see Fig. 1). For Q_a = 1.8 MJ/m^2 (Q_{max} = 4.2 MJ/m^2, τ_R = 0.5), the surface roughness reached 60 μm.

The MEMOS simulations for a W macrobrush also showed that, if the separatrix strike point (SSP) moves along the divertor target during a transient, such random movements can decrease significantly the melt erosion and the vaporization erosion in comparison with those calculated assuming a fixed SSP position. This effect becomes significant as soon as the mean amplitude of the SSP motion exceeds the full width of the area where significant roughness is produced by a single transient event. This effect is shown in Fig. 2 for disruption-like loads. After 100 disruptions with Q = 6 MJ/m^2 and a load duration time τ = 2 ms, the effect is small: the depth of the crater caused by melting is about 0.8 mm, while for a single event the crater depth is about ~10 μm, and thus it would be about 1 mm after 100 equal disruptions. However, for a series of 100 large energy load disruptions with Q = 15 MJ/m^2 and τ = 5 ms, the effect becomes significant: a deep crater of about 1.5 mm and a mountain near the crater edge of 1.5 mm appear (Fig. 2), while for a single event the crater depth is about 35 μm (3.5 mm after 100 disruptions).

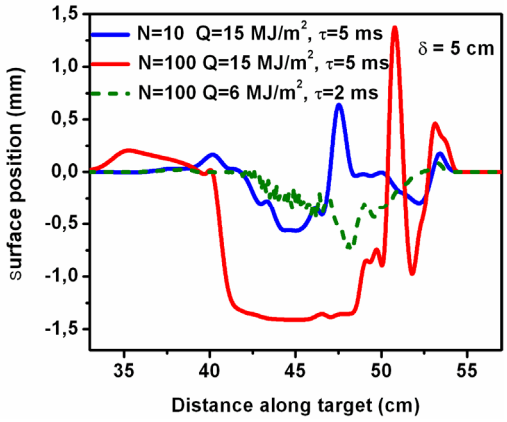

Fig. 2: Distribution of the erosion along the outer divertor after 10 and 100 disruptions, SSP motion within δ=5 cm.

In the case of a thermal quench disruption, the influence of the **J**x**B** forces along the macrobrush surface (associated with the current flow perpendicular to the surface) on the W melt layer acceleration is found to be negligible for J < 4 MA/m^2 and a toroidal magnetic field with B ~ 5T. However, the **J**x**B** forces perpendicular to the surface (caused by the eddy currents induced by the flattening of the current profile during the thermal quench and the poloidal magnetic field) produce significant splashing due to the Rayleigh-Taylor (RT) instability. During the thermal quench, at SSP J ~0.1 MA/m^{-2} is estimated. This is more than an order of magnitude larger than the RT instability threshold J_{th} = ~4 kA/m^2 obtained for the typical poloidal field of 0.5 T at the SSP.

The Kelvin-Helmholtz (KH) instability is also found to be an important mechanism of droplet formation under ITER transient loads. The calculated threshold for the droplet ejection predicted by the KH-instability for QSPA-T conditions is Q = 1.3 MJ/m^2, the expected droplet sizes lie in the range of 20 - 50 μm, and droplet velocities are in the range of 4 – 6 m/s. These values agree reasonably well with experimental data both for perpendicular plasma impact on a flat W target and for inclined plasma impact on the W macrobrush. MEMOS simulations carried out for similar energy loads for plasma conditions as expected during ITER ELMs (i.e., a factor of 10 lower pressure compared to that of QSPA-T) showed that neither the plasma pressure nor the Lorentz forces can accelerate the molten layer to the level required for the onset of KH-instability. This allows the conclusion that during ELMs, no

splashing by droplets due to the KH instability is expected in ITER. For ITER disruptions this problem should be investigated.

The RT instability at the edges of the macrobrushes can cause the extension of the melt layer to the next brush, thus producing bridges between brushes as it was found in the QSPA-T experiments. An analysis shows that at a high melt layer velocity V_m > 1 m/s, sharp macrobrush edges lead to a fast growth of the RT-waves and the droplet ejection occurs at the edges with a typical droplet size r < 100 μm. At lower velocities, the RT instability leads to the formation of bridges between the neighbouring brushes. For ITER, due to the lower plasma pressure and low Lorentz forces, the expected velocities of the molten layer are small and cannot produce strong droplet formation by the RT-instability. In the simulation of the W-brush armour after 1000 pulses and an energy of 0.9 MJm^{-2} neither bridging nor droplet ejection take place.

Dust production from W surface

Experiments on tungsten in plasma guns and electron beam facilities have proven an intense crack formation, melt droplet splashing and dust production. The droplet splashing occurs under severe heat loads typical of ITER ELMs, where surface melting takes place. Dust production due to brittle destruction is important in the case of smaller ELMs. The reason for cracking of any material close to the surface heated by severe heat loads is the thermostress produced in the sample due to the temperature gradient. A steep temperature gradient is generated, and the faster heating rate the stronger the gradient. It seems that cracking and dust production are absent in the stationary regime and occur under off normal events only.

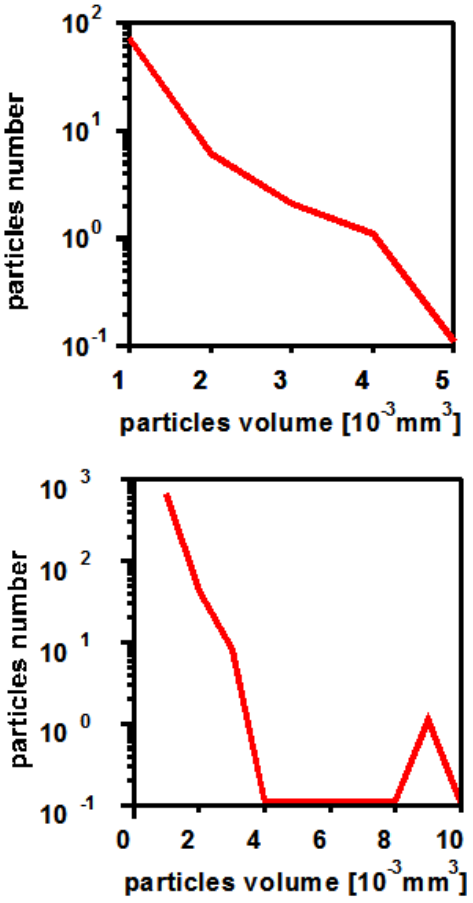

Fig. 3: Two examples of tungsten dust production simulation under an ELM-like surface heat load. Shown is particle size distribution for W-dust generated in a thin pre-surface layer.

Tungsten droplets might be generated in the case of extremely high plasma loads corresponding to ITER disruptions. The droplets are produced due to the KH-instability in a thick molten layer at the tungsten surface under the action of the plasma stream flowing along the free surface of the melt. The mechanism of dust generation from W-droplets is extremely effective. The numbers of W-dust particles from droplets are much larger than of those produced by brittle destruction. The brittle destruction of W is the main mechanism for dust production in the case of smaller heat loads. If the ELM load is not high enough to melt the W-surface, the dust is produced due to cracking under thermostress. The thermostress in this case arises due to plastic deformations during heating to temperatures close to, but lower than, the melting temperature. Then, in the course of fast cooling following the ELM induced heating, the thermostress at the heated surface produces cracks, and closing the cracks splits off the dust particles. A similar mechanism for dust production occurs if the heating is sufficient for melting the W-surface, but not enough for generating the KH-instability in the molten layer. The tensile stress developed in the thin resolidified W-layer produces larger cracks and larger amounts of dust than in cases without melting.

Observation of W dust production was reported recently in experiments on the electron beam facility JUDITH. The dust particles have been produced in an experiment with an energy deposition of 0.88 MJ/m^2. This heating produces a thin melt layer (the melting threshold is 0.71 MJ/m^2).

First simulations of W dust production with PEGASUS have been done using the same parameters as those used for simulations of the crack network with two different scales of tungsten cracking under ELM-like surface heating. Two examples of the dust particles distribution obtained in this simulation are shown in Fig. 3. In the simulation, the dust particles consist mainly of very few, 1 to 4, numerical cells, except very few particles up to 9 cells size. Thus dust particles with sizes exceeding 10 μm are practically absent in the simulation.

Simply increasing the cell number in the simulations would need too large computation time. Now, a rough estimation for the W-dust production under ELMs of 0.5 ms duration has been obtained, producing a melt layer of 15 μm at the W-surface. In the PEGASUS calculation carried out so far, the dust production rate was ~10^2 dust particles per ELM, with sizes from 10x10x10 μm^3 to 10x10x30 μm^3 from a sample of ~10 mm^2 surface area.

The particle size distribution after an ELM-like heat load of 1 MJm^{-2} and 0.5 ms duration can be approximated as $N(r) = N_0 \times \exp(-\alpha r + 10)$, where N is the number of particle of the size r (in μm) emitted from 1 m^2, and the constants $N_0 = 7.7 \times 10^6$ m^{-2}, $\alpha \sim 1$.

Conclusions

The code MEMOS has been developed further and now allows the simulation of sequential multiple transient loads on ITER PFCs. The upgraded code is applied for the simulation of melt damages to the W armour caused by different types of multiple ELMs and disruption loads. The numerical simulations demonstrated that at the stochastic motion of the SSP along the target surface, the total erosion (melt motion and vaporization) can significantly decrease in comparison with that of a fixed SSP.

In the current dust simulation, the very rough resolution is not sufficient to obtain realistic dust parameters . The simulations should be repeated with finer resolution. This is the aim of further investigations.

Staff:

B.N. Bazylev
I.S. Landman
S.E. Pestchanyi

Literature:

[1] B. Bazylev, G. Janeschitz, I. Landman, S. Pestchanyi, A. Loarte, G. Federici, M. Merola, A. Zhitlukhin, V. Podkovyrov, N. Klimov, J. Linke, T. Hirai, Experimental validation of 3D simulations of tungsten melt erosion under ITER-like transient loads. PSI-18, P1-87, to be publ. JNM.

[2] N. Klimov, V. Podkovyrov, A. Zhitlukhin, D. Kovalenko, B. Azylev, G. Janeschitz, I. Landman, S. Pestchanyi, G. Federici, A. Loarte, M. Merola, J. Linke, T. Hirai, J.Compan, Experimental study of PFCs erosion under ITER-like transient loads at plasma gun facility QSPA, PSI-18, I-04, to be publ. JNM.

[3] B. Bazylev, Y. Igitkhanov, G. Janeschitz, I. Landman, Simulation of hot-spot formation at ITER vessel surface during multiple transient events, 35th European Physical Society Conference on Plasma Physics, Hersonissos, Crete, Greece, June 9-13, 2008, P1.015, Conf. Proc., CD Vol. 32D.

[4] B. Bazylev, G. Janeschitz, I. Landman, S. Pestchanyi, A. Loarte, G. Federici, M. Merola, A. Zhitlukhin, V. Podkovyrov, N. Klimov, V. Safronov, J. Linke, T. Hirai, I. Garkusha, V. Makhlay, Simulations of material damage to divertor and first wall armour under ITER transient loads by modelling and experiments, 22nd IAEA

Fusion Energy Conference, Geneve, Swiss Confederation, October 13-18, 2008, IT/P6-10, Conf. Proc., To be issued on CD.

[5] B. Bazylev, G. Janeschitz, I. Landman, A. Loarte, V. Podkovyrov, N. Klimov, V. Safronov, Experimental and theoretical investigation of droplet emission from tungsten melt layer, 25th Symp. Fus. Techn., Rostock, Germany, Sept. 15-19, 2008, Invited talk, for publ. Fusion Engineering and Design.

[6] B. Bazylev, G. Janeschitz, I. Landman, S. Pestchanyi, A. Loarte, Erosion simulation of first wall beryllium armour under ITER transient heat loads, 13th International Conference on Fusion Reactor Materials, Nice, France, December 10-14, 2007, to be publ. JNM.

TW6-TPP-DAMTRAN
WP08-ITM-TFL2 and WP08-PWI-09
Modelling of ITER Plasma Component Damage and Consequences for Plasma Evolution following ELMs and Disruptions and ITER inter-ELM Scenario Periods Modelling

Introduction

In the future tokamak ITER, the plasma edge localized modes (ELMs) may result in vaporization erosion at the divertor CFC and tungsten surfaces. In the periods between the ELMs, the main erosion mechanism is sputtering. The eroded species such as carbon, tungsten and beryllium contaminate the scrape-off layer (SOL) and then the confined core plasma. The contamination deteriorates the reactor performance, decreasing the fusion energy gain, or can even lead to disruptions of the confinement.

The FZK computer modelling aimed at the tolerable ELM frequency in the H–mode of ITER operation is carried out using the two-dimensional (2D) MHD codes FOREV and TOKES that describe the core and SOL plasmas. In these codes the surface processes such as the sputtering and the vaporization at the wall surfaces and the back propagation of eroded species into the core is simulated. Below, the latest applications of FOREV, that was validated against the new experiments at the plasma gun MK-200UG (TRINITI, Troitsk, Russia) and further improved implementing an analytical model for a vapour shield in front of the target, and the development of TOKES, that acquired advanced ion population- and radiation transport models and performed for first time simulations for SOL, are described.

Experiments at MK-200 UG and FOREV validation

The plasma gun MK-200UG reproduces the energy flux, impact ion energy, plasma density and pressure of ITER ELMs, but has 10 times smaller time duration. As result, the vaporization threshold pulse energy density q_{vap} and the threshold of vapour shield q_{vs} are a factor of 3 lower than that after the ELMs. The CFC NB31 was tested under heat fluxes of varying magnitude. The samples have a flat rectangular shape with a face surface of 2.5×2.5 cm^2 and 1 cm thickness. To measure the absorbed energy, the targets are equipped with thermocouples. The surface temperature T_s is measured by means of a pyrometer with 0.1 μs time resolution. For the analyses of the evaporated carbon, visible (4000-7000A) and EUV (10-400A) spectrometers with space resolution of 0.1 cm were applied.

For the evaluation of realistic CFC thermal conductivity, λ, the threshold of CFC vaporisation, has been measured and then the FOREV value of λ was adjusted, to achieve the measured vaporization threshold in the simulation for the MK-200UG configuration. In the experiment, a weak evaporation occurs already at $q \sim 0.15$ MJ/m^2 ($T_s \approx 3600$ K) and intense evaporation starts at $q \approx 0.2$ MJ/m^2 ($T_s \approx 4000$ K). With further increase of q, T_s remains unaltered, which indicates that $q_{vap} \approx 0.2$ MJ/m^2. At $q = 0.2 – 0.3$ MJ/m^2, the carbon plasma consists of $C^{+1} – C^{+5}$ ions reaching the temperature 10 – 30 eV. The density of C near the surface is $n_C = 2\times10^{23}$ m^{-3}, and C propagates along the magnetic field with a velocity $1–2\times10^4$ m/s and $n_C > 10^{21}$m^{-3}. Two series of experiments have been performed, one with a narrow target letting the plasma stream of 5 cm diameter bypass it, and another with a wide target covering whole plasma stream. In the first case the vapour shield gets thin, which increased the vapour shield threshold for approximately four times.

The code FOREV models the processes on the time scale of 1 ms assuming a CFC wall. It calculates the vapour shield that develops in front of the ITER divertor surface, protecting it after strong ELMs and during the disruptions, and also the following propagation of eroded ionized carbon into the SOL and the edge of the confined plasma. Using the MK-200UG re-

sults for the experiments with the wide target, FOREV validation for the carbon plasma parameters has been done.

The carbon density of the vapour shield in front of the target has been measured at one moment in time. Comparison of the space distribution of electron density for the measured and the simulated plasma shield densities illustrated in Fig. 1 showed good agreement. The vapour shield densities at a distance of 1 cm from the surface, measured and calculated for various power heat loads, are also in a reasonable agreement, as it is seen from the right panel of Fig. 1.

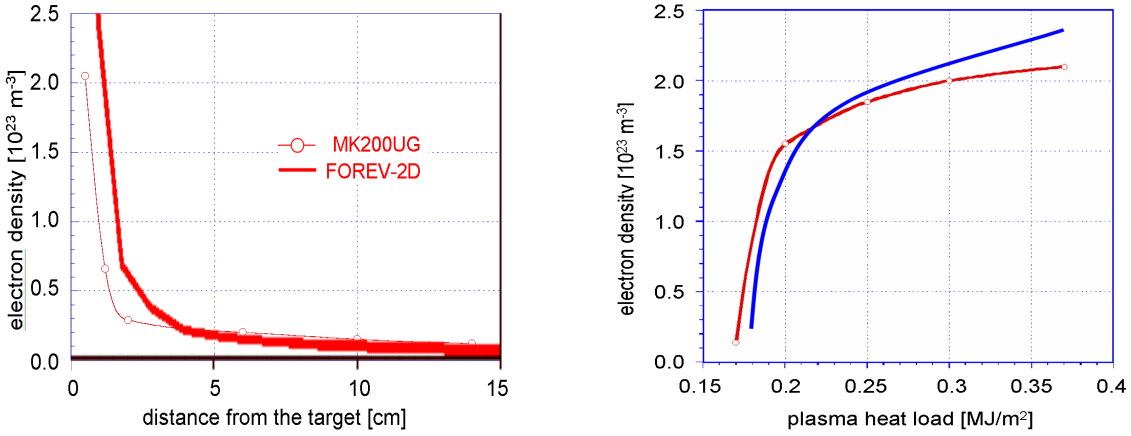

Fig. 1: Comparison of measured and simulated space distribution of the electron density in front of the CFC target at 10-15 μs. q = 0.3 MJ/m^2, λ = 0.35λ$_{ref}$ shown in the left panel and the density at 1 cm distance from the target versus plasma heat load.

As in these experiments such measurements have not been done at different times, for a rough estimation of the correlation between the measurements and the simulations at different times, one can use the measurements where the integral of the electron density over the pulse time has been obtained at different distances from the target surface. Fig. 2 shows the measured dependence of the time-integrated electron density on the distance from the target in comparison with the simulated spatial dependences. It is quite difficult to estimate the details of these measurements, but a comparison between them and the calculations at several moments in time may shows that there are no large differences between densities calculated by FOREV and the MK-200UG densities.

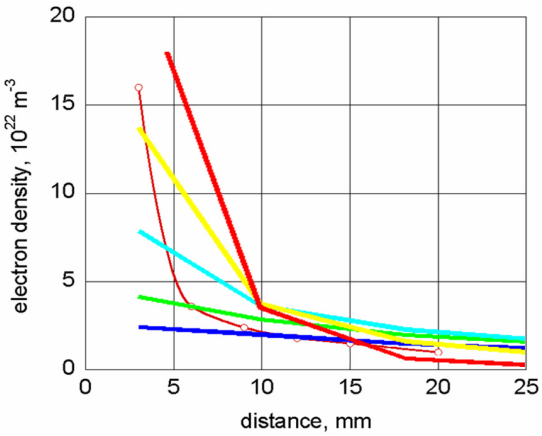

Fig. 2: The experimental curve (marked by the circles) corresponds to the time integral over whole pulse of 0.8 MJ/m^2 total heat load. The simulated curves correspond to the time moments 6, 12, 25, 31 and 38 μs.

Analytical model of the carbon vapour shield for the code FOREV

Earlier FOREV simulations for ITER ELMs have revealed that the vaporization at the divertor plate can be described in a simplified way, which considerably saves CPU time. This model uses the result that the plasma shield temperature is not sensitive of the heating flux. The full simulations for ELMs with the shielding showed that after the vaporization onset followed by a short transition period, the vaporization rate r_{vap} becomes almost constant during 0.15 - 0.2 ms, and r_{vap} depends only on the heat flux increase rate $\dot{G}$ of the ELM. Pre-surface carbon plasma density and temperature becomes also approximately independent of time, which can be seen from Fig. 3.

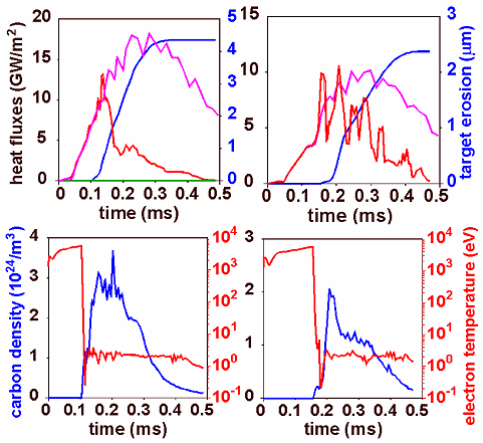

Fig. 3: Upper panels show the time dependences for the heat flux to the divertor armour with (magenta curve) and without (red) the shielding and for the erosion (blue) for the ELMs of the peak heat loads of 3.1 MJ/m^2, and 1.5 MJ/m^2. The average heat loads are 1.84 MJ/m^2 and 0.84 MJ/m^2. The lower panels show calculated time dependences for the vapour shield plasma temperature and density close to the target.

As a result, the maximum vaporization depth h_{vap} after, e.g. one ELM of τ = 0.5 ms duration saturates at increasing $\dot{G}$ at $h_{vap} \approx 6.5$ μm. The vaporization area increases with increasing $\dot{G}$, therefore the vaporized amount N_{vap} does not saturate. The following analytical formula fits well the calculated dependence of r_{vap} on $\dot{G}$:

$$r_{vap}\left[\mathrm{atom}/m^2 s\right] = 1.5\cdot 10^{27}\ln\left(\dot{G}/\dot{G}_0\right)$$

$$\dot{G} \geq \dot{G}, \dot{G}0 = 0.15\times 10^5\ \mathrm{GW/m^2/s}$$

For example, at the ELM deposition energy of 1.8 MJ/m^2, which needs $\dot{G} = 0.27\times 10^5$ GW/m^2/s and τ = 0.5 ms, the evaporated amount is: $N_{vap} = 0.88\times 10^{23}$ m^{-2}.

TOKES development for integrated simulations of ITER

The code TOKES was recently developed for integrated simulation on the discharge time scale (10^3 s), however permitting multiple ELMs. In this code, the magnetic field can evolve together with the confined plasma, because the currents are recalculated after each time step. The poloidal field coils automatically control the plasma shape. The fluids are ionized plasma species from hydrogen isotopes to tungsten of different charge states, and bound electron excitation states. The detailed species description in the confinement region allowed the implementation of a corona model including ionization equilibrium. The SOL transport is implemented based on a guiding centre model for ions.

The TOKES model for ion populations N_{mzk} and radiation transport is newly implemented, with m being the isotope index from H, D, T to W, z the charge state and k the index of bound electron levels. The N_{mzk} are calculated along with T_e and transition rates among the levels of energies E_{mzk}. The photon absorptions and emissions are described in terms of opacities, which are emission coefficients β and absorption coefficients κ' that include spontaneous and induced radiation. The database of TOKES contains also the oscillator strengths $f_{mzkk'}$ and the transition frequencies $\nu_{mzkk'}$ for resonance excitations, and ν_{mzk} for the ionization of atoms and ions by electron and photon collisions, which was collected using diverse sources and approximations. The ground state ionization potentials $I_{nz} = E_{m,z+1,0} - E_{m,z,0}$ (with n the chemical number of isotope m) are available for all m and z, but only the frequencies of the transitions from ground state to excited states of neutral atoms (z = 0) are usually known. Therefore, for ions (z > 0) some scaling laws on the ratios $I_{n+z,z}/I_{n0}$ are applied along the isoelectronic sequences n–z = const. The complexity of atomic data prevents in reality direct multi-species self-consistent radiation transport simulations; therefore in TOKES the data is reduced and approximated grouping the energy levels.

This radiation-population model is developed so far only for the confined plasma. The radiation losses from the SOL are not yet implemented. As to the plasma dumped from the pedestal into the SOL across the separatrix, it is still represented by fully ionized ions and their energies. To the latter, the electron thermal energy multiplied by the ion mean charge state and the internal energy of the plasma ions are added. Thus, an ion m impacting on the wall brings the full energy that consists of a) the contribution of electrons, which the ion gains in reality when crossing the electric sheath in front of the wall, and b) the recombination contribution (because the internal energy of ions would be released at the wall surface heating it).

The ionization and the charge-exchange processes in the SOL are also simulated preliminary, attributing to the SOL plasma the temperature according to the ion energies, which allowed estimations of recycling of dumped plasma at high temperature, T_{edge} which is the separatrix temperature. Over the whole vessel, the conservation of the particle number for each kind m, energy and momentum is observed.

With the new models three benchmark calculations of a full ITER H-mode ELM-free discharge have been performed for auxiliary heating by a 1 MeV deuterium beam of 80, 96 and 144 MW power, respectively, and fuelling by pellets simulated by homogeneously spreading 1 eV D-atoms over the confinement region. The plasma shape was fixed. The simulations demonstrated that, with 80 MW heating, the discharge terminated after 33 s because of increasing radiation losses. Fig. 4 demonstrates the evolution of the radiation power and the edge temperature T_{edge}. The main radiation losses are due to bremsstrahlung. In the end phase, the beam is mainly stopped at the plasma periphery and therefore cannot prevent the radiation collapse. For 96 and 144 MW heating, after about 20 s a steady state is reached.

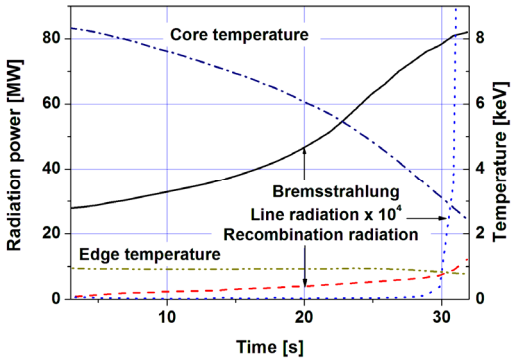

Fig. 4: Radiation losses and plasma temperatures obtained with TOKES, 80 MW heating.

Table 1: Calculated steady state parameters of deuterium species.

BP MW	B MW	R MW	L W	n_D 10^{20} m^{-3}	T_{core} keV	T_{edge} keV	$\Gamma_{SOL/D}$ 10^{20} s^{-1}	$\Delta\Gamma_{SOL/D}$ 10^{20} s^{-1}
96	21	4.7	11	1.1	10.5	1.07	103	0.12
144	8.5	0.31	3	0.65	18.5	1.54	103	0.06

Table 1 shows some results of the steady state discharges. BP is the beam power. Bremsstrahlung (B) always dominates over recombination (R)- and line (L) radiation. n_D and T_{core} are averaged over plasma volume. The edge temperature is above 1 keV, which causes substantial impurity influxes by sputtering. The role of the SOL in stopping of lost D-ions is small: their inflow (Γ_{SOL}) is much larger than the atom outflow to the wall after charge-exchange collisions with SOL neutrals ($\Delta\Gamma_{SOL}$). Thus, in the current TOKES calculations almost all dumped plasma freely reaches the divertor plates.

Calculation of the poloidal field in TOKES

Besides the plasma issues, in TOKES the poloidal field (PF) in the entire vessel is essential, because it determines at each time step the shape of confined plasma. The PF is described with the poloidal magnetic flux $w(\mathbf{p})$, where the point $\mathbf{p} = (r,z)$, with r and z major cylindrical coordinates. The function $w(\mathbf{p})$ has its maximum at the plasma centre.

The PF coil currents I_n are obtained using the plasma currents I_i. It is to note that if I_n was fixed but I_i not, then due to the evolution of the plasma shape, the plasma boundary can touch the wall in a few time steps, which is not acceptable. Therefore, to keep the plasma off the wall, a dynamical updating of I_n is done in TOKES.

The following control scheme is implemented: 1) the positions $\mathbf{p}_{x0}$ and $\mathbf{p}_{x1}$ of two x-points are fixed as expected in ITER (see Fig. 5); 2) the confined plasma is bounded by the separatrix magnetic surface $w(\mathbf{p}) = w_{x0} \equiv w(\mathbf{p}_{x0})$; 3) another separatrix $w(\mathbf{p}) = w_{x1} \equiv w(\mathbf{p}_{x1})$ is located outside the plasma and a small difference $\Delta w = w_{x0} - w_{x1}$ is fixed; 4) some fixed positions $\mathbf{p}_{cj}$ for several points near the vessel surface are chosen where the plasma would touch the wall most probably; 5) the point $\mathbf{p}_{cjmax}$ of maximum value of $w(\mathbf{p}_{cj})$ obtained with the available I_i and previous I_n is used for calculation of new I_n from the condition $w(\mathbf{p}_{imax}) = w_{x1}$. Based on

these constraints, the code calculates I_n, which allows keeping the outer separatrix $w(\mathbf{p}) = w_{x1}$ near the wall and therefore the plasma at some distance from the wall.

Here the evaluation by TOKES of the currents In at a total plasma current of 15 MA is demonstrated, assuming the plasma conductivity $\sigma(w)$ to be linearly dependent on w (the bootstrap current is ignored). At fixed $\mathbf{p}_{xm}$, $\mathbf{p}_{cj}$ and $\mathbf{P}_n$, the ratio $h = \sigma(w_{max})/\sigma(w_{x0})$ determines the plasma currents, magnetic field and plasma shape completely. In Fig. 5 the calculated plasma configurations at different plasma current profiles are shown. As demonstrated in these calculations, the separatrix that crosses the x-point x_0 is always located not appropriately in the outer divertor leg. Therefore, an additional PF coil near the divertor leg is necessary for the required shift of SSP.

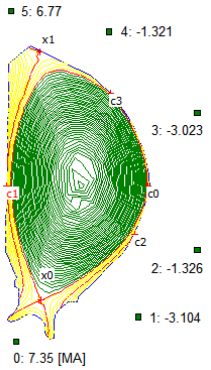

Fig. 5a: h = 4.13

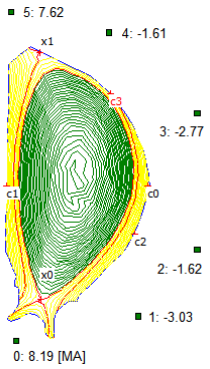

Fig. 5b: h = 1

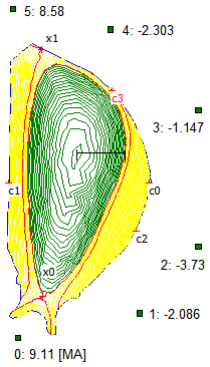

Fig. 5c: h = 0.39

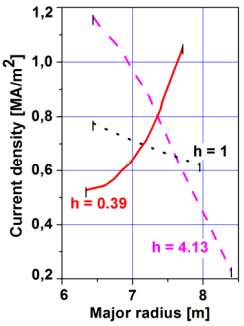

Fig. 5d: Currents

Conclusions

The analysis of earlier simulations with the code FOREV for widely varying transient loads that cause vaporization at the CFC surface and a plasma shield revealed some common features of the plasma wall interaction, namely that the shielding can be described in terms of the increase rate of impacting heat flux. The full radiation transport simulations implemented in the code TOKES with all kinds of radiation, and the preliminary SOL model of TOKES are significant design steps. By this, the code acquired major features necessary for 2D integrated tokamak modelling. The numerical approach considered combines hydrodynamic and kinetic descriptions of plasma and neutrals that includes recycling in the SOL. The results obtained provide useful benchmarks for tokamak simulations, but more work is needed for further development of the codes in order to reach reliable integrated modelling including plasma and surface aspects.

Staff:

B.N. Bazylev
I.S. Landman
S.E. Pestchanyi

Literature:

[1] S. Pestchanyi, I. Landman, Experimental verification of FOREV-2D simulations for the plasma shield, PSI-18, P1-97, to be publ. JNM.

[2] I.S. Landman, G. Janeschitz, Modelling of SOL transport and radiation losses for ITER with the integrated tokamak code TOKES, PSI-18, P1-98, to be publ. JNM.

[3] S. Pestchanyi, I. Landman, Simplified model for carbon plasma production by ELMs in ITER, EPS-35, P4.014, Conf. Proc., CD Vol. 32D.

[4] I.S. Landman, G. Janeschitz, Calculation of poloidal magnetic field in tokamak code TOKES, EPS-35, P5.057, Conf. Proc., CD Vol. 32D.

[5] S.E. Pestchanyi, V.M. Safronov, I.S. Landman, G. Janeschitz, A. Loarte, Y. Igitkhanov, B.N. Bazylev, Integrated modelling of ITER plasma dynamics and wall processes following type I ELMs and consequences for tokamak operation, 22nd IAEA Fusion Energy Conference, Geneve, Swiss Confederation, October 13-18, 2008, IT/P6-11, Conf. Proc., To be issued on CD.

[6] S. Pestchanyi, ITER divertor armour issues: lifetime, safety and influence on its performance, Intern. Conf./ School on Plasma Phys. Contr. Fusion, Alushta, Ukraine, Sept. 22-27, 2008, Invited talk, to be publ. in Ukrainian Journal on Plasma Physics.

[7] I.S. Landman, G. Janeschitz, Modelling of radiation impact on ITER beryllium wall, 13th International Conference on Fusion Reactor Materials, Nice, France, December 10-14, 2007, to be publ. JNM.

Divertor and Core Plasma Modelling for ITER

Introduction

The goal of the core and divertor plasma modelling program is the development, improvement, and application to ITER of a set of modelling codes which describe the ITER plasma from the core to the divertor plates in a coherent way so as to permit a consistent prediction of ITER plasma operating modes, operating windows, performance, and scenarios. Two codes are used for this purpose: the 2D coupled fluid-Monte Carlo code B2-EIRENE for two-dimensional modelling of the ITER divertor and scrape-off layer, and the ICPS model incorporated into the 1D ASTRA transport code for one-dimensional modelling of the ITER core and pedestal. The two codes communicate via scaling laws derived for the separatrix parameters from stand-alone runs of the codes. ITER performance modelling can be carried out only with such a consistent plasma model. Our model has been developed in the framework of a quadripartite collaboration (FZ Karlsruhe, ITER International team, Hydro-Québec, Varennes, Québec, Canada, and INRS-EMT, Varennes, Québec, Canada), as described in previous Annual Reports. The evolving model is described there and in [1] and references therein. Results obtained in this calendar year have been reported at the PSI, EPS and IAEA conferences 2008 and are detailed in [2] through [6]. Related EFDA Tasks are discussed in [7], [8]. Preliminary discussions were held at FZK to explore augmentation of the TOKES model (this Annual report) and potential future implementation of key elements of the ICPS model in TOKES.

Divertor Plasma Modelling

In the course of the year, parallel processing has been implemented by the developers of the EIRENE code and the ITER team, reducing the time necessary for convergence and thus enabling DEMO calculations with the nonlinear neutral model. These will be reported in a subsequent Annual Report.

<u>Neon seeding of ITER</u>

To prepare a study of ITER carbon-less operation at a later stage and to perform calculations to prepare for the DEMO calculations to follow, seed impurities (neon) were added to the edge plasma of ITER, and density scans performed at varying neon concentrations. Although detachment occurs at the same pressure, the maximum temperature in the inner divertor increases as neon increases, while the radiation in the inner divertor (but not overall) decreases. With neon, the peak power load now occurs on the inner divertor rather than on the outer as with carbon.

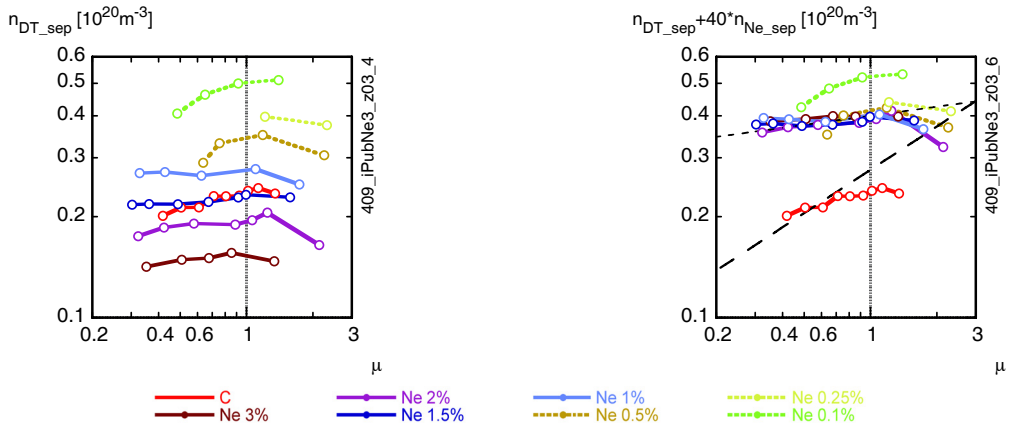

Fig. 1: DT density n_{DT_sep} (a, left) and combined density $n_{DT\_sep} + 40 n_{Ne\_sep}$ (b, right), at the separatrix versus μ (see [6]).

The scaling of the peak power is similar to that for the outer target with carbon, but the numerical value is 30% lower and independent of c_{Ne} in this range. (Differences in flux expansion, divertor plate angle, and divertor length also play a role). Strikingly, with neon the DT density varies strongly with c_{Ne} at given throughput (i.e. the same normalised neutral pressure), Fig. 1. As c_{Ne} increases the power available for DT dissociation, ionisation, and excitation decreases and n_{DT} decreases. To a very good approximation (Fig. 1), for the neon cases compared to carbon, the sum $n_{\mathrm{DT\_sep}} + 40\, n_{\mathrm{Ne\_sep}}$ depends on normalised pressure μ but is almost independent of c_{Ne} for $c_{\mathrm{Ne}} \geq 0.01$. Since neon is almost completely ionised at the separatrix, and the total ionisation energy required to attain this state is about 100 times that of DT per atom, the decrease of deuterium density occurs because less power is available for DT ionisation. The electron density also decreases, and this in turn is responsible for the fact that the radiated power is almost invariant with c_{Ne} for $0.01 < c_{\mathrm{Ne}} < 0.03$.

Scaling relations developed from these edge/divertor simulations have been used as boundary conditions for the core plasma in ITER core modelling below. It is hoped that their extrapolation, benchmarked and modified by analysis of the relatively small number of DEMO runs under way when they become available, will lead to a consistent picture for DEMO and allow completion of the related EFDA Tasks [7] [8]. Further work on updating the scaling is found in [3].

Assessment of ITER divertor modifications

In the course of the ITER design review it was found that the divertor dome as originally designed imposed excessive requirements on the accuracy of the plasma position control system because it strongly constrained the allowable positions of the magnetic separatrix. The key features of the modified geometry are the lowering of the divertor dome and the reduction of its size, Fig. 2. The inner target is moved outwards and tilted somewhat less with respect to the magnetic surfaces in order to accommodate a wider range of ITER plasma equilibria with flatter current profiles in the core (minimum l_i of 0.6 vs. original 0.85), along with other detailed variations [1], [4].The final geometry at present is F57.

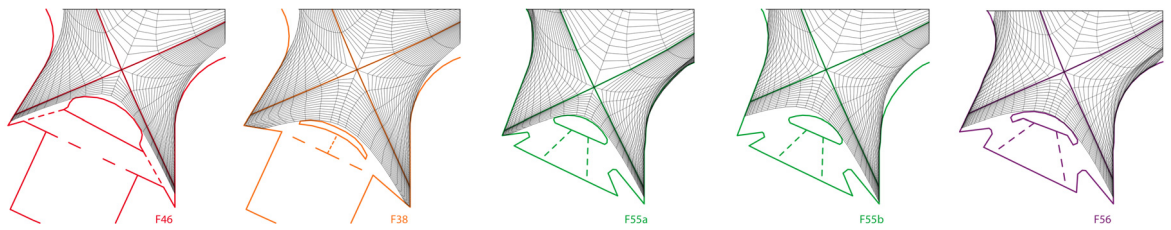

Fig. 2: Dome geometry, left to the right: F46 – the original geometry [3]; F38– an intermediate geometry with reduced dome; F55 – shifted modified dome and inner target, flat current equilibrium l_i = 0.63; the same F55 with the old reference plasma equilibrium; F56 – the final position of the dome and inner target, equilibrium with l_i=0.7; F57– the reflector plates in the final position. Dashed lines show partially transparent structures giving access to the pump ducts. From [4].

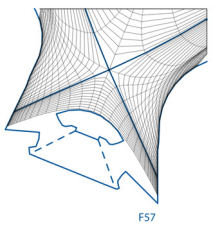

Some effects of the dome modifications are shown in Fig. 3, where different parameters characterizing the divertor performance are plotted against the normalised neutral pressure in the divertor, μ (full inner divertor detachment is at $\mu = 1$, the normalisation factor is 0.7, 0.5, and 0.45 for the flat-current case, F56, and F57, respectively, relative to the former reference F46). The peak power loading for the old reference equilibrium with l_i = 0.85 (dashed lines) decreases progressively as the dome size decreases from F46 through F38 to F55. (For the latter case, the power load, usually maximum on the outer divertor, actually peaks

on the inner divertor.). For the plasma equilibrium consistent with flatter current profiles, the divertor asymmetry increases for the modified geometries F55 and F56, and the resulting peak power load (solid lines in Fig. 3a) is similar to the former reference F46. The DT ion density at the separatrix increases but remains low and the neutral particle influx across the separatrix remains small, ≤ 20 Pa-m^3/s so that extra core fuelling is still required. The conditions for helium removal become worse by a factor 2-3 for the modified divertor (higher separatrix density, Fig. 3b, and slightly lower neutral influx, Fig. 3c, for the low- l_i case and F56; higher influx and density for the old reference equilibrium and F55).

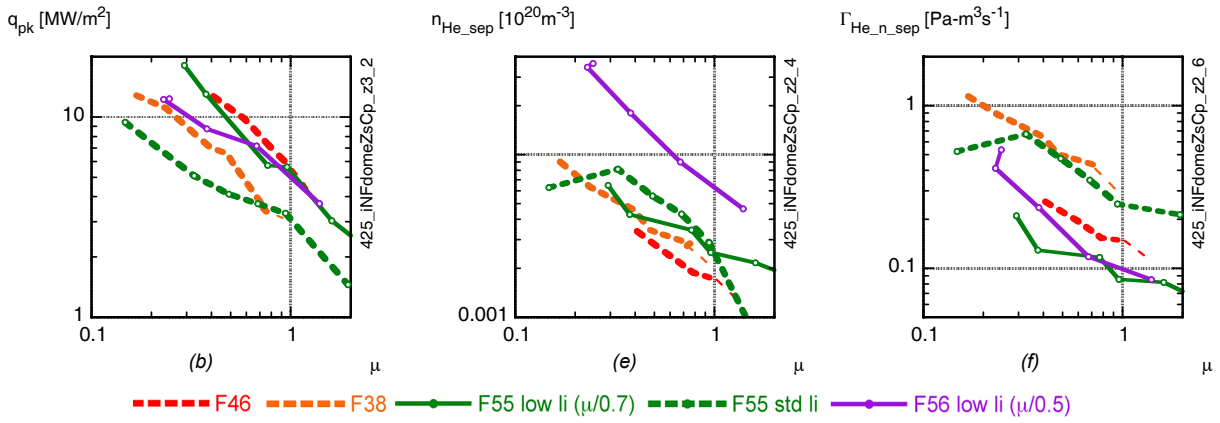

Fig. 3: Modelling results vs. normalized neutral pressure under the dome, μ, for the geometries: (a) peak power loading of the targets; (b) average helium ion density at the separatrix; (c) helium neutral influx to the core. Dashed lines: old reference equilibrium; solid lines: low-l_i (see text) From [4].

Nevertheless, the He levels remain low, so that integrated modelling such as described below indicates that this increase of the helium does not modify the ITER operating window significantly.

Initial results for the current divertor geometry F57 (not shown) indicate only minor changes from F56. The proposed divertor modification thus fits the qualitative picture developed previously: a reduction of the dome renders the divertor more in-out symmetric, which is beneficial for the peak power loading on the targets but somewhat detrimental for helium removal. Moreover, the new divertor offers some degree of detachment asymmetry control by changing the position of the separatrix strike point at the inner target. The influence of widening the gaps in the divertor cassettes has also been studied [4] but space precludes its discussion here.

Core Plasma Modelling

Validation against experiment

In recent simulations, the pressure obtained at the pedestal top in the simulations has been compared with that predicted by the scaling formula of Sugihara (Fig. 4, see [2] for full details), and found to agree to better than 30% for JET with MMM and GLF transport models. The pedestal pressures simulated for ITER lie within 15% of the scaled values.

Operating window for ITER and DEMO

As introduced in the previous Annual Report and [1], [2] and references therein, the operating window of ITER is determined from mutually consistent core-edge-divertor modelling. The plasma density and auxiliary heating power are systematically varied, specifying that the peak power load on the divertor plate cannot exceed a given value, and the plasma parameters determined at each of these operating points. The operating window is delimited by: low Q (e.g.Q=5 –yellow line), maximum available heating power (=73 MW, green), edge density

limit (throughput limit for partial detachment =90% of edge density limit, dashed blue curve), maximum alpha power at given beam power (low temperature limit at high density - dark blue line), and the LH transition at low power (red line), and is the coloured region inside all these limits (Fig. 5a).When mapped to the plane Q versus alpha particle power (Fig. 5b), ITER performance, described by the maximum P_α attained and by the corresponding Q, is obtained from the width and height of the operating window.

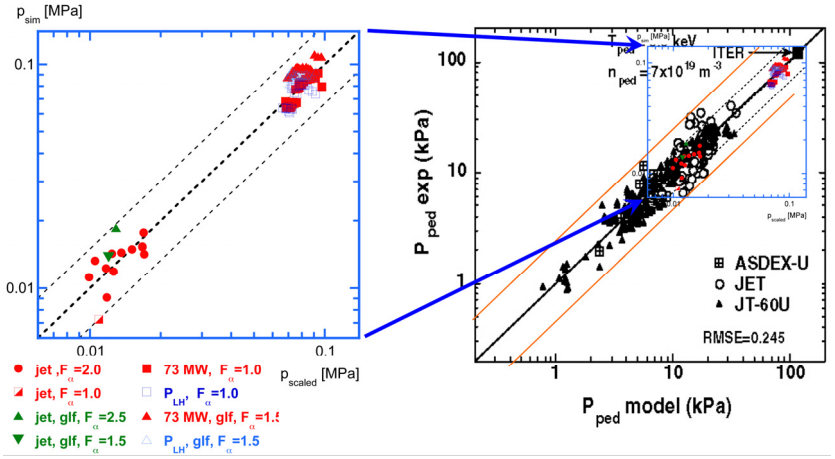

Fig. 4: Pressure at pedestal top obtained in the simulations plotted versus scaling law of Sugihara et al. Thin dashed lines indicate 30% deviation from scaling law. From [2].

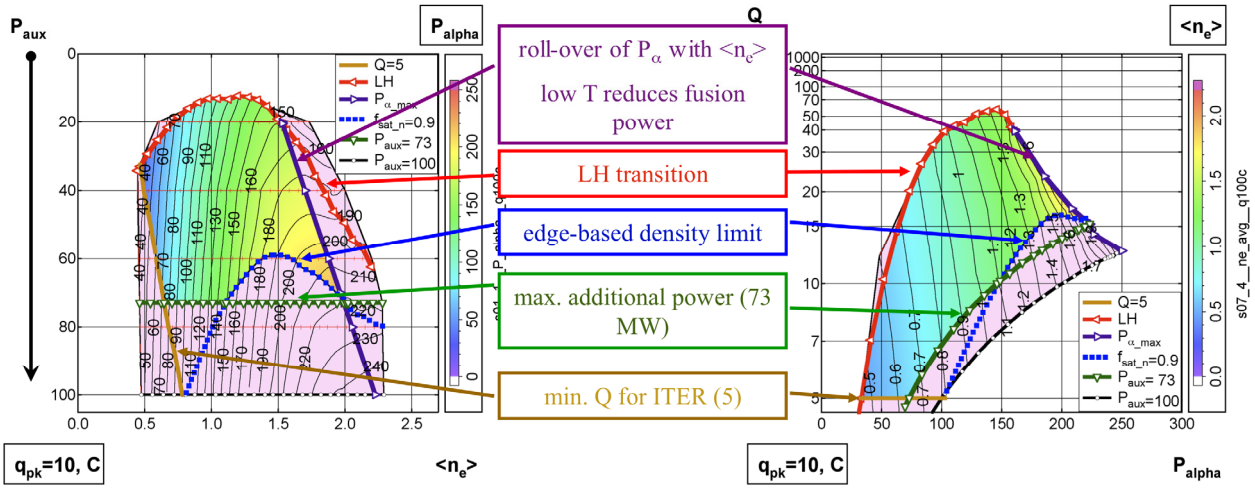

Fig. 5: Alpha particle power, a) in the plane beam power (reversed scale) vs. average electron density, b) Q vs. alpha power for peak, for power per unit area to the divertor plates of 10 MW/m^2, carbon walls.

Since DEMO operations are to be reactor-like, different limits apply. Enough alpha particle power is always available so that the LH back-transition is irrelevant for DEMO. Furthermore, the ion temperature always remains sufficiently high so that the limit on maximum alpha particle power at high density, resulting from the degradation of the fusion cross-section, is not encountered for DEMO. However, economic considerations will impose a lower limit on Q, say 20 or higher, and controllability an upper limit, say 50. Other limits include desired maximum and minimum values of fusion power, and the edge-based density limit as for ITER. Fig. 6 illustrates the DEMO operating window for the reactor-relevant case with low toroidal momentum input. Gas puffing is provided in addition to the core fuelling, so as to keep the peak power at the divertor plate at or below 7.8 MW/m^2 to allow for helium cooling in DEMO.

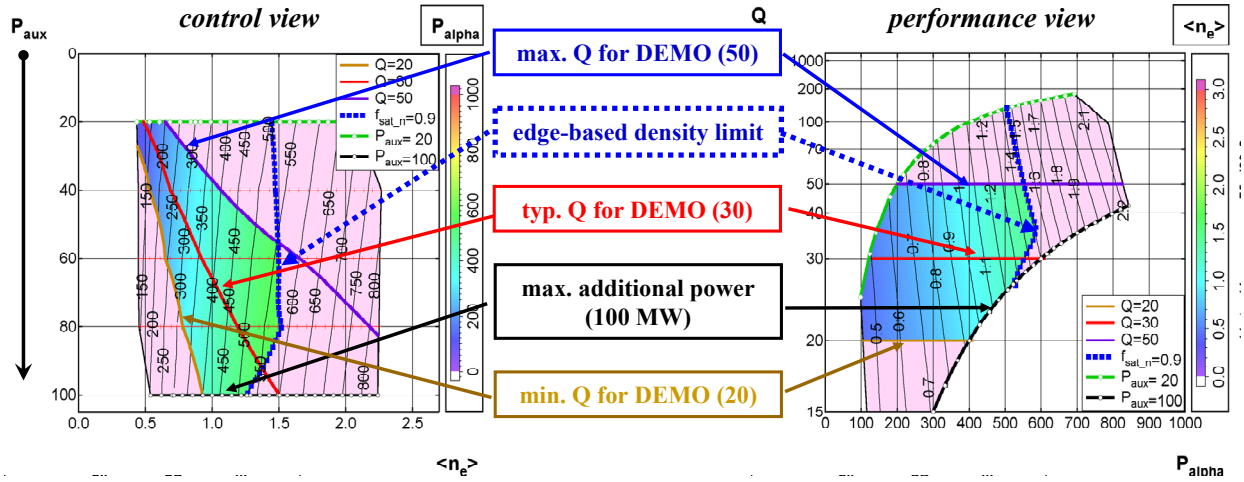

Fig. 6: DEMO operating window in the P_{aux}-n_e (left) and in the Q-P_{alpha} (right) planes. The limits relevant for reactor-like operation are indicated.

ITER operating window - parameter variations

For ITER, operation windows have been examined to evaluate the impact of different transport, magnetic field, variation in DT and helium pumping (not discussed here, see [1], [2]), as well as by neon seeding and variation of the peak divertor power load. As to neon seeding of ITER, the scaling relations described above have been used to determine the operating window, Fig. 7. Despite the 30% lower q_{pk} with neon (Sec. 2), the operating window is reduced both in Q and alpha power at $q_{pk}=10$, where the edge density limit does not play a strong role. When a more stringent condition, $q_{pk}=5$, is specified and very strong gas puffing would be required, the edge density limit strongly constricts the operating window at high alpha power, and neon seeding then increases the operating window in alpha power (but not in Q since neon core radiation reduces the SOL power and the LH transition margin). The transition to carbon-free divertor operation with low seeding has not yet been fully explored. The effect of varying the specified peak divertor power load (without neon seeding) is seen in Fig. 7b. To maintain 5 and 7.5 $\mathrm{MW/m^2}$, respectively, much higher throughput at the same Q and P_{alpha} would be required than the standard case at 10 $\mathrm{MW/m^2}$ if the edge density limit were not encountered first. For higher $q_{\mathrm{pk}}=15$ $\mathrm{MW/m^2}$ and at high values of Q, no gas puff is necessary. Therefore, lower peak divertor power loads lead to a stronger constraint by the edge density limit and therefore a smaller operating window in alpha power but not in Q.

ITER long pulse operation in ELMy H-mode

Long-pulse operation is especially important for the ITER testing mission for which desired neutron wall load is ≥ 0.5 MW/m^2, i.e. ~100 MW alpha power. The burn duration and fluence per discharge constitute reasonable performance indicators. For the estimated burn flux of 39 volt-seconds at 15 MA plasma current, the resulting burn duration and fluence per discharge are shown in Fig. 8 for the on-axis heated discharge. At the desired average neutron wall load corresponding to 100 MW alpha power and Q=7 (73 MW auxiliary power), the desired total neutron fluence for the testing mission is 0.3 MWa/m^2 (total integrated fluence 7.6x10^6 GJ), requiring ~23000 pulses at full current without current drive. With current drive, both pulse duration and fluence per discharge increase appreciably to ~1400 s and 500 GJ with near-axis (not shown) and to ~2000 s and 800 GJ with off-axis current drive (Fig. 9). The maxima are attained somewhere along the trajectory composed of minimum Q, maximum additional power, and maximum allowed density (yellow, green, and blue lines of Fig. 8).

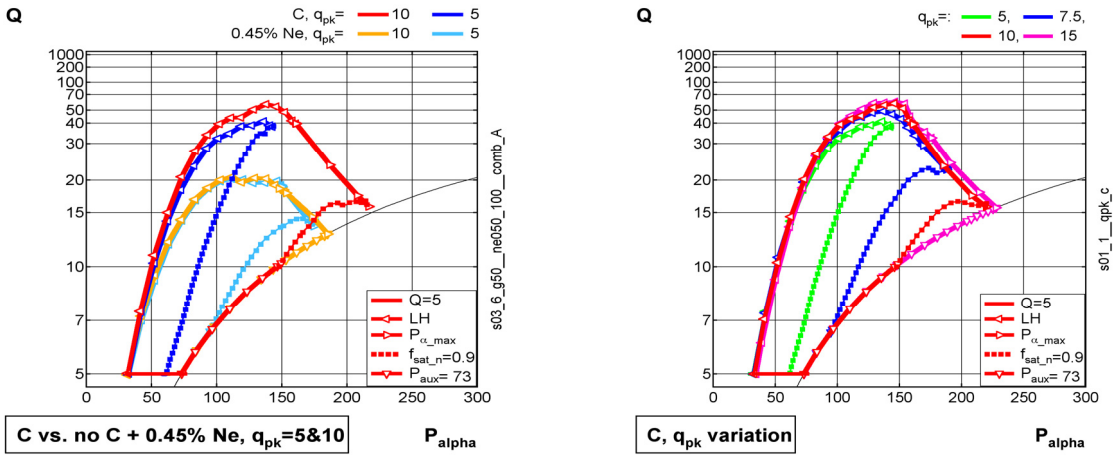

Fig. 7: ITER operating diagram in Q - P_{alpha} plane (limits as in Fig. 5) a) for peak power $q_{pk} = 5$ and 10 with carbon walls and with carbon-free walls with neon density $n_{Ne\_sep}/\langle n_e \rangle = 0.45\%$ b) limiting q_{pk} of 5, 7.5, 10, 15 $\mathrm{MW/m^2}$ without impurity seeding. From [2].

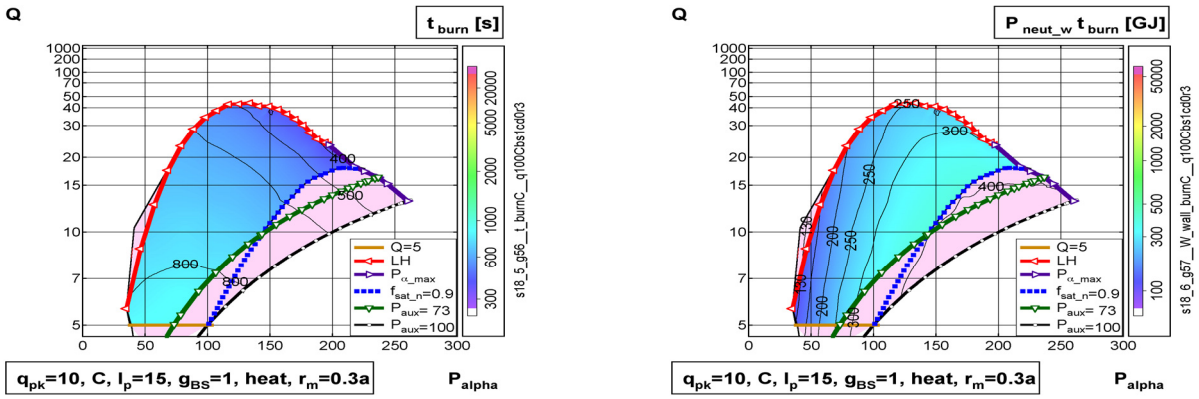

Fig. 8: Operating space for ITER in ELMy H-mode at 15 MA with near-axis heating: burn duration and total fluence per discharge for 39 Vs available for burn. From [5].

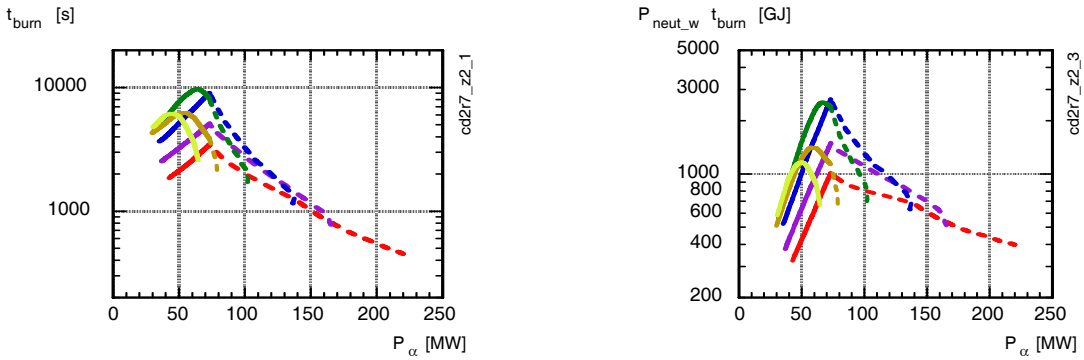

Fig. 9: Burn time and fluence along trajectory (see text) with off-axis current drive for different plasma currents: 15 (red), 14 (purple), 13 (blue), 12 (green), 11.5 (brown), and 11 (yellow) MA. From [5].

If the current is reduced to provide more volt-seconds for the flat-top (~16.5 Vs per MA), the performance can be augmented. On Fig. 9 for off-axis current drive, burn duration and fluence are seen to increase with a moderate decrease in plasma current, and peak for all currents at or just below the alpha power of 73 MW. At the desired alpha power of 100 MW, the 13 MA case exhibits the best performance with 3200s and 1300 GJ, and the 14 MA case is almost equivalent. The entire testing mission would then require approximately 5900 such

pulses. Note that the best performance for the testing mission is well below the Greenwald density. The maximum non-inductive current is 75 %,i.e. far from steady-state.

DEMO long pulse operation in ELMy H-mode - preliminary results

Fig. 10 illustrates the reactor-relevant performance of a DEMO reactor in ELMy H-mode operation without impurity seeding (carbon is assumed as the intrinsic impurity for these initial calculations). The parameters are shown at constant Q and varying fusion power, assuming 100 Vs available for burn at 21 MA plasma current. For near-axis current drive, at Q=30, a burn time of 5000s or more is obtained for a large range of alpha power (220 - 550 MW, i.e. fusion power 1100 - 2750 MW), indicating appreciable flexibility for reactor-like operation.

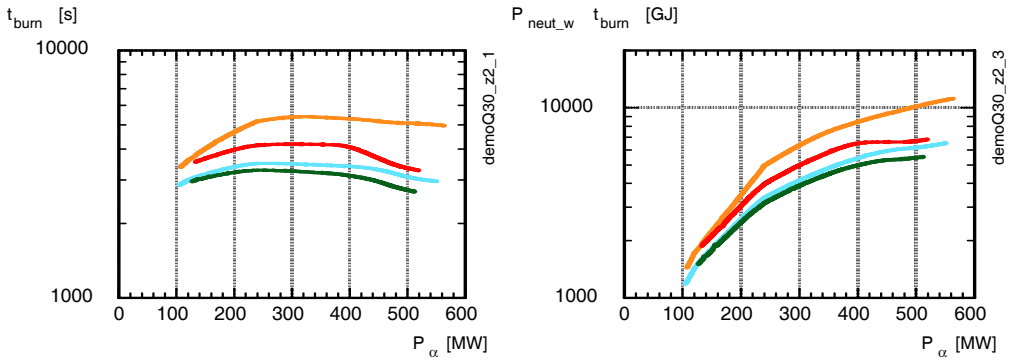

Fig. 10: Burn time and fluence at Q=30 for DEMO at 21 MA. Near-axis (turquoise) and off-axis heating (green), and near-axis (orange) and off-axis (red) current drive.

Perspectives

- In two-dimensional modelling of the ITER scrape-off and divertor plasma with walls having realistic carbon erosion-deposition, improvement of the parameter scaling determined from ITER and DEMO modelling, continuation of the study of variations of ITER geometry with the nonlinear neutral model, further application of the code with both linear and nonlinear neutral models to a highly radiating prototypical DEMO plasma, and continuation of studies including seeded impurities in the edge plasma for ITER and application to DEMO.
- In one-dimensional modelling of the plasma core, the work will concentrate on integration of scaling advances from the two-dimensional modelling, integration of scaling results for carbon-free plasmas without impurity seeding once they become available, variation of the impurity model for present experiments once validated data on impurity transport becomes available, modelling of impurity-seeded operation of ITER, initial development of the model toward hybrid operation with a view to modelling hybrid operation for DEMO.
- Other simulation work necessary to be determined with FZK, for example simulations of hydrogen and helium plasmas to assess ITER start-up possibilities.

Staff:

H. D. Pacher (INRS-EMT, Varennes, Québec, Canada)
G. W. Pacher (Hydro-Québec, Varennes, Québec, Canada)
G. Janeschitz
I. Landman
S. Pestchanyi, with the collaboration of G. Pereverzev (IPP Garching)
A.S. Kukushkin (ITER Organization

Literature:

[1] Pacher H.D., Pacher G.W., in collaboration with ITER IT Garching, FZ Karlsruhe, Max-Planck-Institut für Plasmaphysik Garching, EFDA CSU Garching, "Divertor and core plasma modelling for ITER - Final Report June 2008", INRS Energie, Mat. et Télécom. Report, INRS-EMT-043-0608, June, 2008

[2] Pacher, G.W., Pacher, H.D., Janeschitz, G., Kukushkin, A.S., "ITER operation window determined from mutually consistent core–SOL–divertor simulations: definition and application", Nucl. Fusion 48 (2008) 105003 (26pp).

[3] Pacher, H.D., Kukushkin, A.S., Pacher, G.W., Kotov, V., Janeschitz, G., Reiter, D., Coster, D.P., "Impurity seeding and scaling of edge parameters in ITER", presented at 18th Int. Conf. on Plasma-Surface Interactions, Toledo, Spain (2008), accepted for publication in J. Nucl. Mat. (2009)

[4] Kukushkin, A.S., Pacher, H.D. ,Loarte, A., Komarov, V., Kotov, V., Merola, M., Pacher, G.W., Reiter, D. "Analysis of Performance of the Optimized Divertor in ITER", Proc. 22nd IAEA Fusion Energy Conference (2008)

[5] Pacher G.W., Pacher H.D., Janeschitz G., Kukushkin A.S., "Operation Window with Mutually Consistent Core SOL Divertor Conditions in ELMy H-Mode: Prospects for Long Pulse Operation in ITER and DEMO", Proc. 22nd IAEA Fusion Energy Conference (2008)

[6] Kukushkin, A.S., Pacher, H.D., Komarov, V., Merola, M., Kotov, V., Reiter, D., Pacher, G.W., Physics Analysis of Divertor Modifications in ITER", Proc. 35th EPS Conf. on Plasma Physics (2008)

[7] Pacher G.W., Pacher H.D., Kukushkin A.S., Janeschitz G., "ITER operating window with varying divertor constraints", Proc. 35th EPS Conf. on Plasma Physics (2008)

[8] Pacher H.D., Pacher G.W., "Task TW6-TRP-002.D3 D3 - Development of an improved treatment of plasma radiation for medium- and high-Z impurities", this Annual Report

[9] Pacher H.D., Pacher G.W., "Task TW6-TRP-012.D1b, D 1b - Optimisation of a ‘start-up’ scenario where the power is less than 100MW", this Annual Report

Heating and Current Drive – Physics

EFDA/06-1406 (TW6-TPHE-ECHULB4)
Design and Analysis of the Upper Launcher and Port Plug for the ITER ECH&CD System

and

TW6-TPHE-ECHULA
Analysis and Testing of the Upper Launcher for the ITER ECH&CD System

Introduction

The Electron Cyclotron Resonance Heating System (ECRH) for ITER uses high power diamond window assemblies with parts of metallic and nonmetallic components. These components, being part of the primary vacuum boundary, have the function of containing the products of the nuclear reactions as the primary tritium barrier. On the base of Finite Element Modelling (FEM), a special window prototype has been designed and manufactured in collaboration with JAEA (Japan). EU is responsible for the ECRH „Upper Launcher“ in ITER, while Japan is responsible for the equatorial launcher. The goal is to realize a common torus window concept for both launcher types. The low power tests for the diamond window assemblies have been performed at FZK, the high power tests at the 1 MW / 170 GHz gyrotron facility in Japan.

Within the framework of the preparation for ITER, the investigation of technology on bench-scale for the assembly and the test of launcher components has been started as a central topic. Therefore, specimens for the First Wall Panel (FWP) have been manufactured and successfully tested.

Activities and results

Fabrication and characterization of ITER torus window assemblies

The low dielectric loss diamond window (70DB1, manufacturer: Element Six), brazed to copper cuffs, is integrated into a metallic housing with the cooling circuit (indirect cooling) separated from the diamond disk. On the plasma side, a valve is introduced near the disk to provide a test section for vacuum monitoring (potential detection mode for cracks in the window) and/or vacuum separation of a failed window unit. In Figure 1, the reference design for the torus window unit is shown. The special configuration of the Γ-shaped welding area forms the connection to the corrugated waveguide with an inner diameter of 63.5 mm. After brazing a maximum curvature of about 20 μm can be observed in the center of the disk.

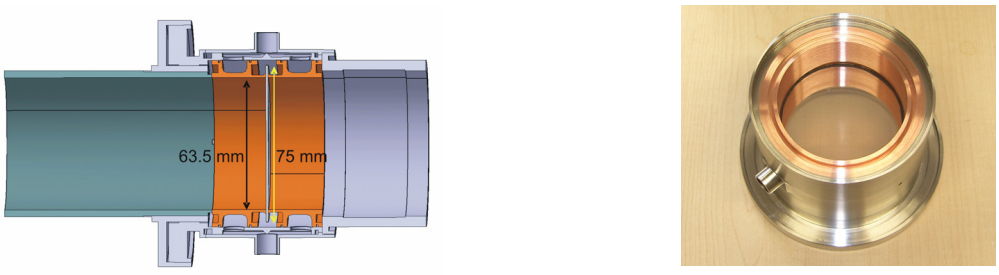

Fig. 1: CAD design and photograph of the CVD diamond torus window unit with the CVD diamond disk separating the torus vacuum section from the dedicated transmission line section. The red section is formed by a copper cuff with two symmetric cooling chambers separated from a vacuum segment at the outer diamond edge. The left part is the torus side, the right part the transmission line side.

At FZK, a dedicated measurement facility (Fabry-Perot resonator) is available for the characterization of the losses. The loss qualification is made by open resonator setups which consist of a spherical mirror and a planar mirror or two spherical mirrors. The resonance fre-

quency and the quality factor of the loaded resonator, together with the quality factor of the empty (unloaded) resonator, yields the dissipative part of the complex dielectric permittivity. The characteristic quantity for the qualification is the loss tangent tanδ, which is the ratio of the dissipative imaginary and real part. The distribution of the dielectric loss over the bare disk is parameterized with a hemispherical measurement setup in terms of the onset (D10), median (D50) and terminal (D90) distribution parameters, which indicate the occurrence of dielectric loss tangent values up to the given parameter within the 10%(D10), 50%(D50) and 90%(D90) fraction of the inspected area (Figure 2).

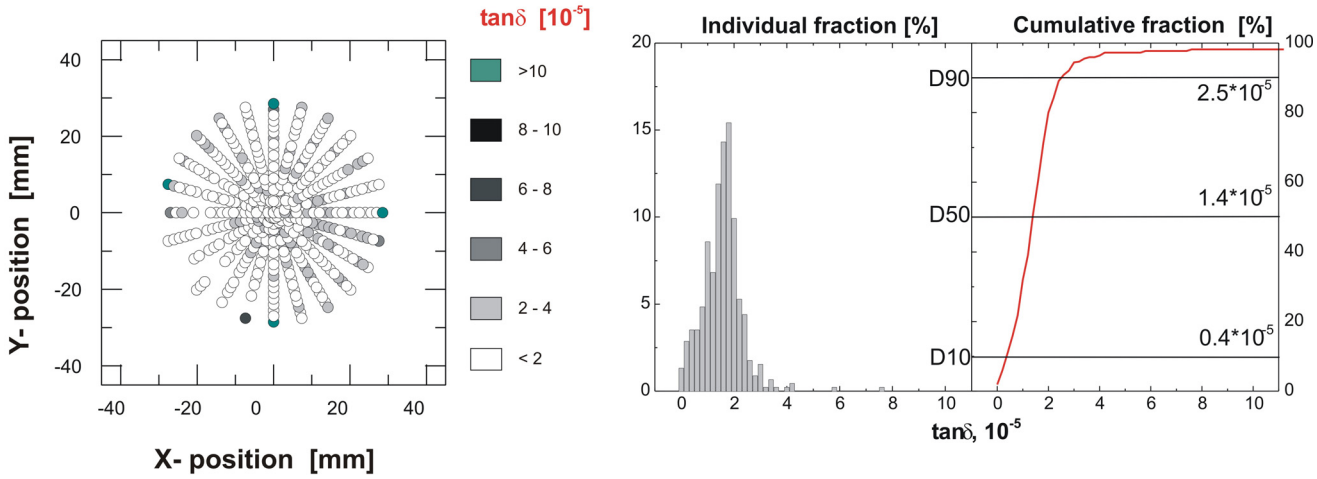

Fig. 2: Dielectric loss mapping of the bare CVD diamond window disk 70DB1 (Manufacturer: Element Six) measured at a frequency of 100.71 GHz. The diameter of the diamond disk is 75 mm, the thickness 1.114 mm and the dielectric constant 5.67. The length of the resonator was 116.54 mm.

The evaluation of the loss tangent in a symmetric spherical resonator setup with two spherical mirrors with a resonator length of 334 mm at the resonant frequency of 170 GHz shows a very low effective loss in the centre of the bare disk with $\tan\delta = 0.9 \times 10^{-5}$. In this configuration, also complete window assemblies can be measured. So, for the loss tangent in the brazed diamond disk a value of of 3.4×10^{-5} was found, respectively.

High power tests of diamond torus window assemblies for ITER

For the high power experiments, the diamond window assembly is connected to a transmission line separated by a gate valve (GV), as shown in Figure 3. The small waveguide volume between the valve and the diamond disk is evacuated by a turbo molecular vacuum pump (TMP). The opposite window site is in air to allow a line of sight for a video (VTR) and an IR camera to observe light spots and to measure the temperature distribution over the whole diamond area. An additional fiber/photomultiplier scope is used for arc detection and interlock purposes. After the free air transit, the RF power is dissipated in a load with a pre-attenuator part.

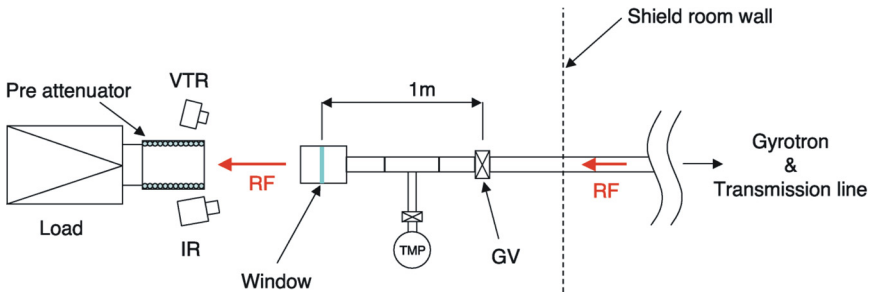

Fig. 3: Setup for CVD diamond window testing at 170 GHz/1MW gyrotron at JAEA.

Short and long pulse measurements have been performed for different levels of microwave power. Figure 4 shows two characteristic long pulse temperature measurements. The temperatures measured at the positions A, B and C go to saturation after several seconds. The temperature maxima increase with the applied microwave power. From the colour distribution of the IR image it is obvious that the beam profile is not Gaussian. This effect causes a non-radial-symmetric distribution of temperature and electrical field strength over the diamond area. Reasons for this undesired effect are mode mixing and the influence of several mitre-bends in the waveguide between the matching optical unit (MOU) and the window.

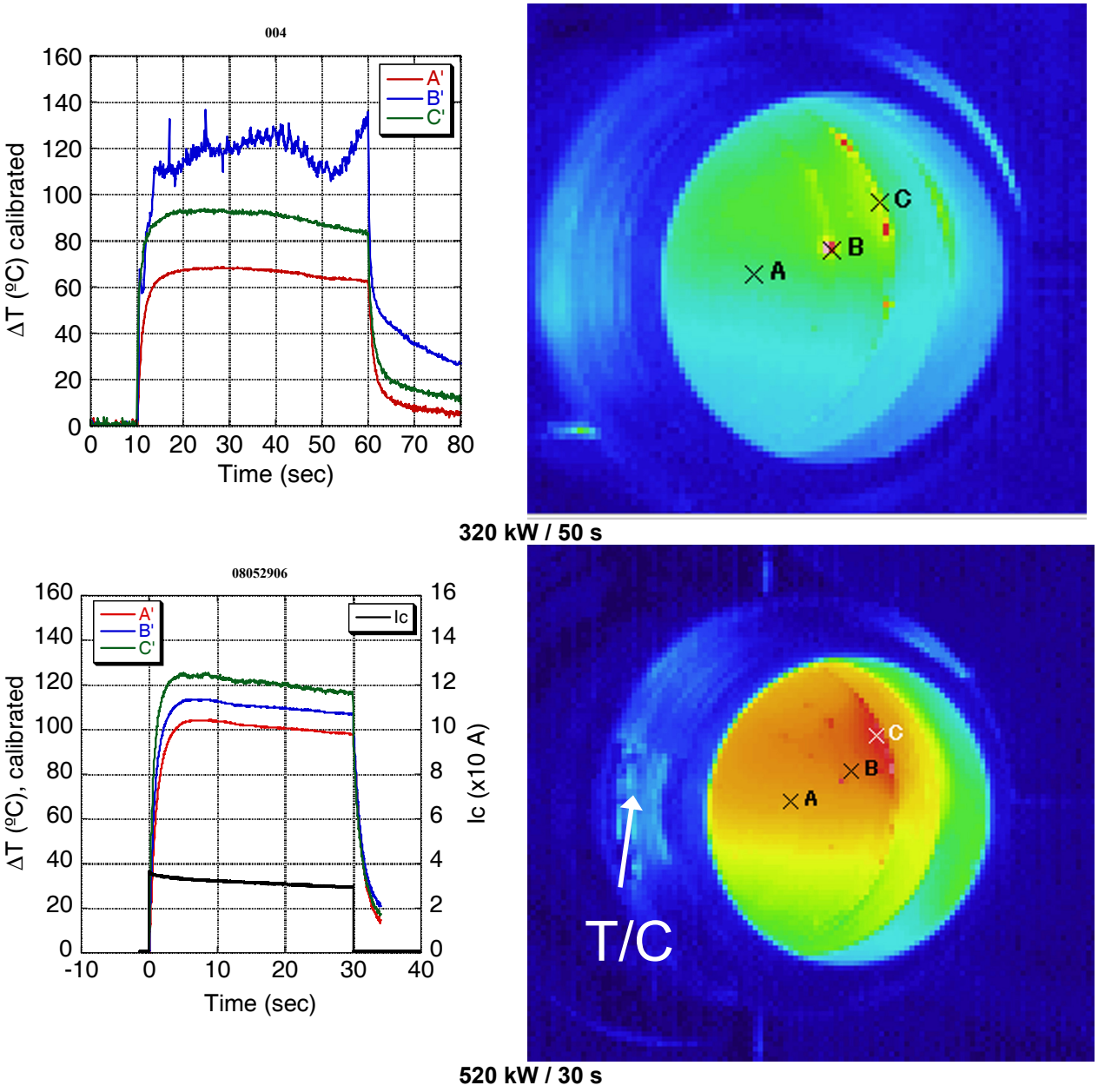

Fig. 4: Temperature-time dependence of a CVD window unit for different microwave power. After ca. 5 s, the temperatures go to saturation.

The existence of non-Gaussian modes is responsible for the excitation of high order parasitic oscillations in small gaps in the housing of the window unit, resulting in additional losses in the metallic window parts (thermocouple T/C in Fig. 4). No Arcing effects have been observed.

Staff:

R. Heidinger
A. Meier
T. A. Scherer
P. Späh
D. Strauß

Literature:

[1] T. A. Scherer, R. Heidinger, A. Meier, K. Sakamoto, T. Takahashi, K. Kajiwara, M. Henderson, R. Chavan, „Design aspects and RF characterization of ITER-RF-CVD-Diamond windows“, 15th Joint Workshop on Electron Cyclotron Emission and Electron Cyclotron Resonance Heating, EC-15, Yosemite (CA), USA, Proceedings, 09. March – 14. March 2008.

[2] D. Strauss, R. Heidinger, G. Hailfinger, K. Kleefeldt, A. Meier, T. Scherer, P. Spaeh, A. Vaccaro, „Plasma disruptions in ITER and the ECH upper port plug design“, Conf. Abstracts, ICOPS 2008, 16-19 June 2008, Karlsruhe, 1C3, 2008 IEEE, p. 120.

[3] R. Heidinger, S. Cirant, R. Chavan, M. De Baar, B. Elzendoorn, G. Gantenbein, M. Henderson, K. Kleefeldt, W. Leonhardt, A. Meier, D. Mellein, G. Saibene, T. Scherer, P. Spaeh, D. Strauss, A. Vaccaro, H. Zohm, (IMF-1 FZK, IFP, CNR, CRPP, EPFL, FOM, EFDA, MPI, IPP), “Design and testing of the ECH upper port plug for ITER”, Conf. Abstracts, ICOPS 2008, 16-19 June 2008, Karlsruhe, 1C4, 2008 IEEE, p. 121.

[4] V. V. Parshin, A. L. Vikharev (IAP Nizhny Novgorod), R. Heidinger, A. Meier, T. Scherer (IMF-1 FZK), B. M. Garin (IRE Moscow), J. M. Dutta (DOPhysics NC Centr. Univ.), “Material aspects of high power microwave windows”, Conf. Abstracts, ICOPS 2008, 16-19 June 2008, Karlsruhe, 3B1, 2008 IEEE, p. 224.

[5] T. A. Scherer, R. Heidinger, A. Meier (IMF-1 FZK), K. Takahashi, K. Kajiwara, K. Sakamoto (JAEA, Naka, Japan), „Microwave testing of a CVD diamond torus window prototype for ITER“ Conf. Abstracts, ICOPS 2008, 16-19 June 2008, Karlsruhe, 3B2, 2008 IEEE, p. 225.

[6] R. Heidinger, M. Henderson, Th. Scherer, D. Strauss, K. Takahashi, “Design and Prototype Testing of ITER ECH Upper Launcher Components“, 7th Internat. Workshop “Strong Microwaves: Sources and Applications”, Nizhny Novgorod, SMSA-2008, 27.07-02.08.2008.

[7] T. A. Scherer, R. Heidinger, A. Meier, D. Strauss, (FZK); K. Takahashi, K. Kajiwara, K. Sakamoto, (JAEA), „Experimental and theoretical thermal analysis of CVD diamond window units fort he ITER upper launcher“, IRMMW-THZ 2008, 33rd Intern. Conf. on Infrared, Millimeter, and Terahertz waves, CALTECH/NASA-JPL, Pasadena, CA, Sept. 15th -19th 2008, USA.

[8] T. A. Scherer, R. Heidinger, A. Meier, D. Strauss, (FZK); K. Takahashi, K. Kajiwara, K. Sakamoto, (JAEA), „Experimental and theoretical thermal analysis of CVD diamond window assemblies“, Workshop on RF Heating Technology of Fusion Plasmas 2008, US-EU-JPN RF Heating Technology Workshop, General Atomics, San Diego, CA/USA, Sept. 10th -12th 2008, USA.

[9] R. Heidinger, R. Bertizzolo, A. Bruschi, R. Chavan, S. Cirant, A. Collazos, M. de Baar, B. Elzendoorn, D. Farina, U. Fischer, J. Gafert, F. Gandini, G. Gantenbein, A. Goede, T. Goodman, G. Hailfinger, M. Henderson, W. Kasparek, K. Kleefeldt, J.-D. Landis, A. Meier, A. Moro, P. Platania, E. Poli, G. Ramponi, G. Saibene, F. Sanchez, O. Sauter, T. Scherer, A. Serikov, H. Shidara, C. Sozzi, P. Spaeh, D. Strauss, V. S. Udintsev, A. Vaccaro, H. Zohm, C. Zucca, (FZK, CRPP, CNR-ENEA, FOM, MPI-IPP, ITER, IPF, F4E, Tsukuba Univ.), “Conceptual design of the ECH upper launcher system for ITER”, 25th Symposium on Fusion Technology SOFT, 15th -19th Sept. 2008, Rostock, Germany.

Project funded by the Ministry for Education and Research (BMBF):

"Erkundung von Beryllium-bezogenen Fertigungsverfahren für die Implementierung eines Versuchsstandes für den ECH Upper Launcher in ITER" – "Exploring Be related manufacturing technologies for the realisation of a test stand for the ITER ECH Upper Launcher"

Reference: 03FUS0005 „Vorbereitungen für ITER und Broader Approach"

Prototype studies for the First Wall (Blanket Shield Module)

Laboratory scale technology investigations for the assembly and the test of launcher components

In the framework of the BMBF contract: „Erkundung von Beryllium-bezogenen Fertigungs-Verfahren für die Implementierung eines Versuchsstandes für den ECH Upper Launcher in ITER" sample tests have been performed at the Köppern company (Hattingen, Germany) for the purpose to develop the joining technology for the Blanket-Shield-Module (BSM) including the First Wall Panel (FWP) by using the Hot Isostatic Pressing technology (HIP).

The following test series have been performed with FWP samples (100 mm x 100 mm; material: SS 316 L or 316 LN, thickness 20 mm) without a Be-layer:

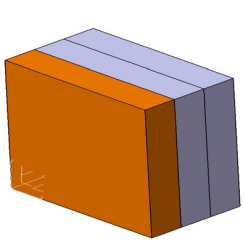

a) CuCrZr –SS

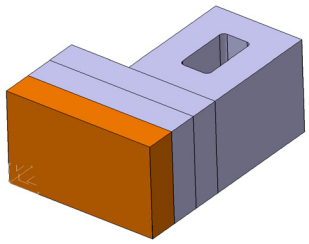

b) CuCrZr–SS double wall

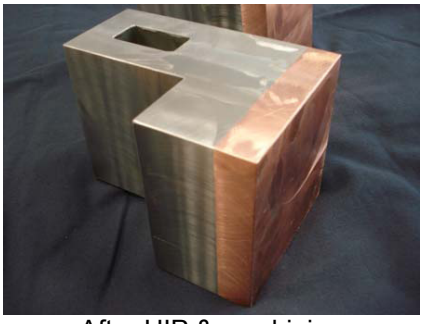

After HIP & machining

Prior to HIP-process

After HIP-process

Prior to HIP-process

Fig. 1: FWP without Beryllium.

The joining quality has been investigated by non destructive X-ray and ultrasonic testing; destructive testing was done after preparation of tensile specimens. After the HIP process, some samples passed a solution annealing process. In result,,the annealed samples showed an an increased σ_{max} = 230 MPa as compared to the samples not annealed (σ_{max} = 190 MPa). The annealing temperature was about 1000°C. Figure 3 shows two linescans covering the diffusion bonded zone of the CuCrZr/SS joint. As expected, there are gradients of Fe, Cu and – less steep– of Ni. Furthermore, the bonding zone apparently gets enriched with Cr at the SS side.

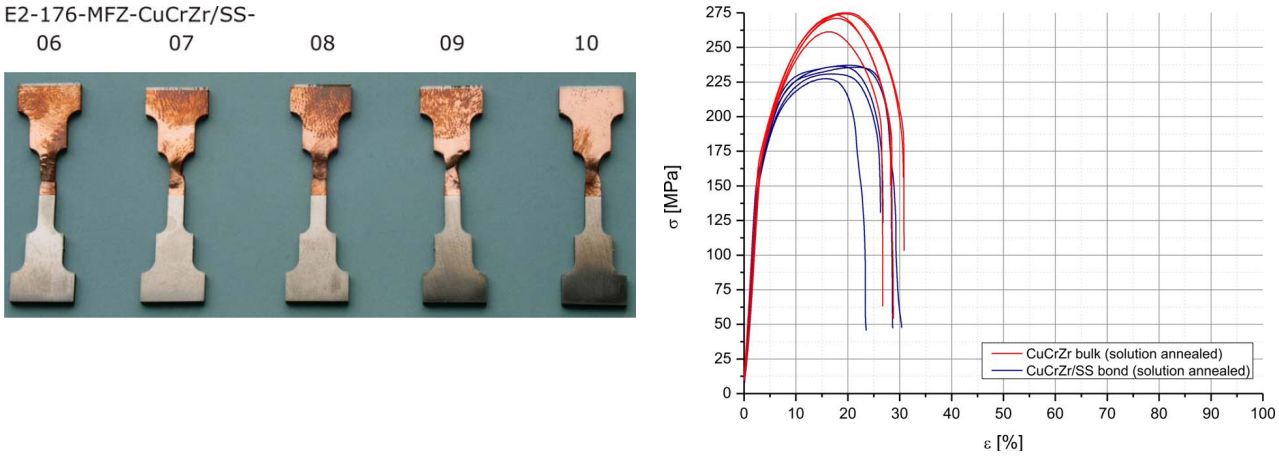

Fig. 2: Tensile specimens CuCrZr/SS after solution annealing.

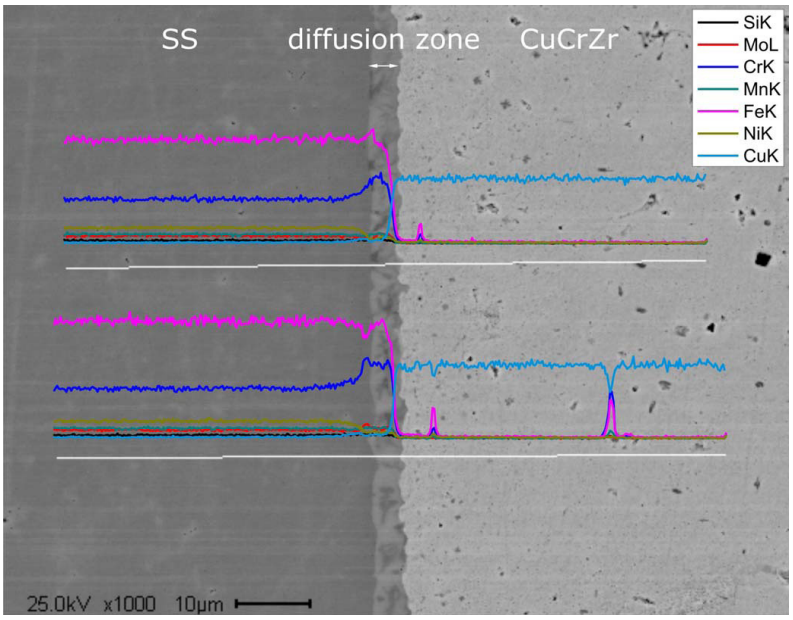

Fig. 3: Line profile of SS/CuCrZr-joint after HIP-process.

Scaling up of FWP to BSM size

In a further study together with the British company AMEC (Knutsford), a concept for the arrangement of the Be-tiles on the FWP was developed. Figure 4 shows two possible variants. The colored trapezoid array is the preferable configuration because of the stability of the edge tiles.

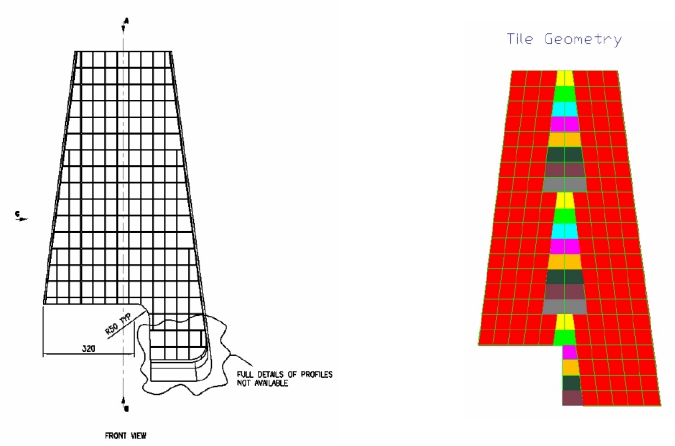

Fig. 4: Beryllium-tiles arrangement for the FWP.

Staff:

R. Heidinger
A. Meier
T.A. Scherer
P. Späh
D. Strauss

Heating and Current Drive – Diagnostics

EFDA/06-1446 (TW6-TPDS-DIADES9)
Diagnostic Design for ITER: Bolometry (Engineering Analysis for Bolometer Cameras)

Deliverable 5.3
Neutronics analyses of the ITER bolometer system

The objective of Task Deliverable 5.3 of TW6-TPDS-DIADES9 was to contribute to the development of the project plan for the procurement package related to the bolometer and pressure-gauge diagnostic and the advancement of the design in critical areas.

The objective of the work performed by FZK was to contribute to the conceptual engineering analysis and feasibility study of the bolometer camera integration in the divertor and behind the blanket by evaluating nuclear heat loads using existing information on the nuclear environment in ITER.

The related neutronics analyses were based on three-dimensional Monte Carlo calculations using the MCNP code and a global 40 degree torus sector model of ITER. MCNP models of the bolometers were generated automatically by conversion from the CAD (CATIA) models, provided by the Max Planck Institute for Plasma Physics (IPP) Garching, using the McCad interface programme previously developed at FZK. The converted models were integrated into the MCNP torus sector model of ITER. The state-of-art nuclear data library FENDL-2.1, developed for nuclear fusion applications, has been applied in the MCNP calculations. Nuclear heating was calculated on the basis of the nominal ITER fusion power of 500 MW. The results were obtained for a set of volume segments to provide information about the spatial distribution inside the mini-cameras.

Two representative locations for the bolometer mini-cameras have been selected for the nuclear analyses. The first location is behind the inner baffle of the divertor cassette (Fig. 1), the second one at the inboard vacuum vessel behind the blanket module. In the latter case, 2 different bolometer types (T-301 and T-302) have been compared to assess the effect of different collimator designs on the results for two different detectors (reference and measurement), Fig. 2.

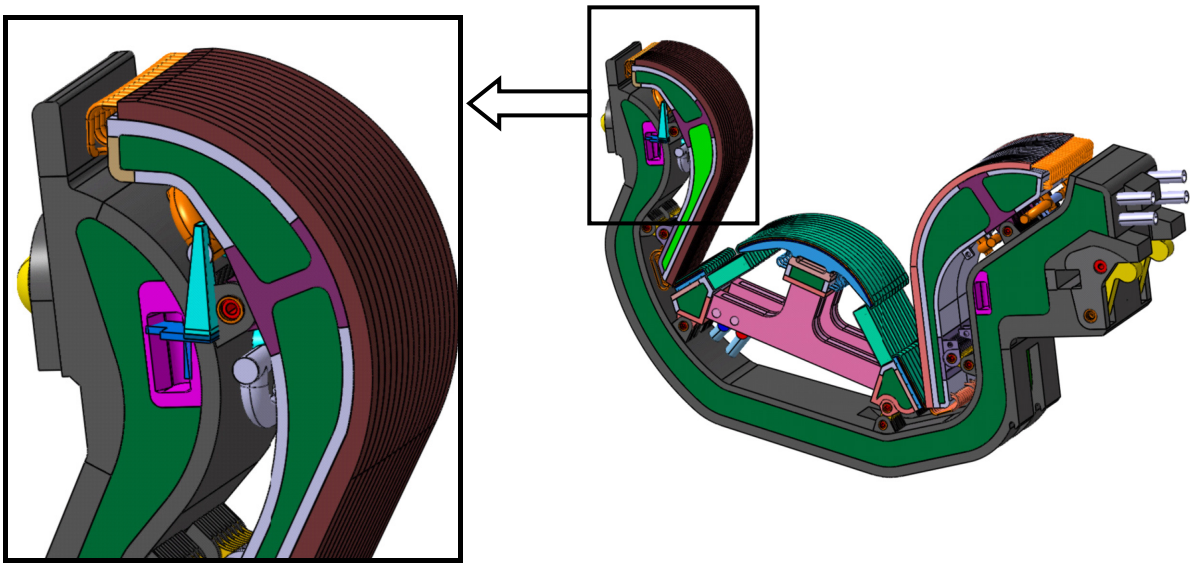

Fig. 1: ITER divertor cassette with bolometer integrated behind the inner baffle (CATIA model).

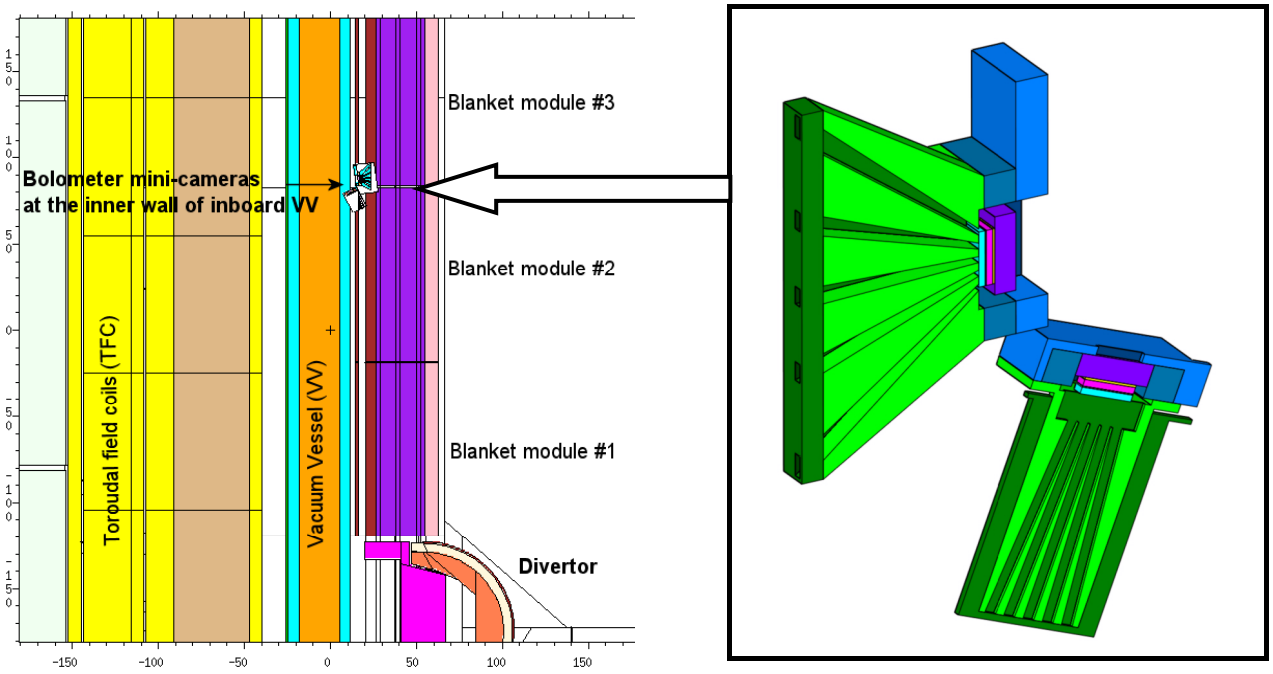

Fig. 2: Bolometer mini-cameras types T-301, T-302 (CATIA model, right figure) integrated at the inner wall of the inboard vacuum vessel (VV) (MCNP model, vertical cut, left figure).

Detailed distributions of the nuclear heat density have been calculated for all bolometer parts. For both bolometer positions, the nuclear heat density in the steel frame is around 0.7 to 1.0 W/cm^3. The contribution by photons is about 90% or more due to the secondary photons originating from the massive steel shielding. The differences in the nuclear responses in the reference and measurement detectors of the two bolometer camera types have been studied by point-detector simulations. The line-of-sight to the plasma depends on the location of the mini-camera as well as on the respective collimator design. In the case of the symmetric collimator of T-301 with full line-of-sight, the 2 point-detector results differ only by statistical fluctuations. In the case of the T-302 with asymmetric collimator, the reference detector has no full line-of-sight to the plasma chamber. Accordingly, the neutron flux is about 5% lower as compared to the measurement line. On the contrary, due to the massive shielding around the reference detector, the secondary photon flux is increased by around 26%. The overall nuclear heating is dominated, as explained above, by the photon contribution.

All results have been collected in form of tabular data and have been provided to the designers to be used as appendices of the final report.

Staff:

U. Fischer
A. Serikov
S. Stickel
H. Tsige-Tamirat

Vessel/In-Vessel

EFDA/07-1704-1624 (TW6-TVV-LEAKD2)
Leak Localisation for In-vessel Components

Background and objectives

Plasma performance depends to a large extent on the impurity concentration within the plasma. Experience from systems with water cooled components in fusion devices shows that components can be expected to develop leaks during operation, often in unexpected places. The demands on leak localisation are unique in ITER because of the level of leak detection required combined with the environment in which the detection has to be performed. Where space and practicality allow for it, vulnerable components will be provided with monitored interspaces like bellows or windows, but for in-vessel components this is not the case.

The ITER leak detection and localisation strategy should be performed in several stages: firstly, determine the leaking type of the water cooling system (PHTS); then identify the leaking loop; further on, identify the leaking component; finally assess the size of the leak in order to take a decision of the urgency for component replacement or in-situ repair. However, since most of the components have very complicated design, it may be unpractical (and nearly impossible) to pinpoint the exact leak location in-situ. Therefore it is suggested to remove the faulty component and repair it in hot cell. Apart of a front leak, the possibility to locate a leaky component with a “hidden” leak is equally very important. The goal of the leak detection strategy is therefore to guarantee that the leak rate inside the primary vacuum boundary, in operating conditions, shall not exceed 10^{-7} Pa·m^3/s. Nevertheless, the sensitivity for leak detection for each individual component during operation should be better than 10^{-8} Pa·m^3/s. On the other hand the leak localisation system should have less sensitive tools too, which would allow the localisation of a large leak significantly faster than a small one.

ITER constraints

There are 7 primary heat transfer system (PHTS) loops:

- 3 loops for the primary first wall and blanket PHTS,
- 1 loop for the divertor and limiter PHTS,
- 2 loops for the vacuum vessel PHTS, and
- 1 loop for the neutral beam injector PHTS.

With regard to tracer addition theoretically it is possible to use 7 different tracers for leak localisation. The valves can separate eight blanket modules and one divertor cassette, one limiter or port plug.

As every in-vessel component is typically distanced from the neighboring one with a ~1 cm gap, the leaking water should be considered in two types of location: on the plasma facing surface – the vapour is streaming to the plasma; and “hidden” leaks – the vapour distributes in the voids behind the modules and partly exits to the plasma through the gaps around the leaky module, partly exits to the plasma through the other gaps, and partly goes directly to the cryopump. The distribution strongly depends on the individual geometry and leaky point. E.g. a hidden leak in the divertor cassette would likely fully go to a vacuum pumping duct.

Leak localisation methods can be divided into two groups: methods that require venting of the machine; and vacuum methods, when the localisation succeeds without draining the cooling circuits and without venting the torus. All methods have been thoroughly revised in the final report of this task. The techniques which can be used to isolate to the required level over the leak range 10^{-7} Pa·m^3/s to 10^{2} Pa·m^3/s (equivalent He) do not require any in-vessel

access, which is an essential requirement in view of ITER activation, contrary to most other fusion machines.

Spectroscopic method

Based on the review of leak localisation techniques elaborated in the first stage of this task, focus in 2008 was given on the spectroscopic method. The basic idea is to scan the first wall by the wide angle viewing system (which is anyway foreseen for plasma monitoring and covers 90% of the surface) during a plasma or glow discharge and look in the spectrum for typical emission lines coming from the water vapour excitation. The existing viewing system is working best in the infrared spectrum. It was theoretically shown, that during plasma operation an infrared line of neutral oxygen can be detected for a leak of 10^{-6} Pa·m^3/s within few m^2.

However, with account of impurities background the most clearly detectable band is hydroxyl, which emits an UV light (wavelength 309 nm). The suitability of that signal for leak localisation purposes has already been demonstrated [1], see Fig. 1. A conservative assessment of the achievable resolution by the hydroxyl line emission under glow discharge excitement conditions showed 10^{-8} Pa·m^3/s at a spatial area of 10x10 cm². But the reference ITER optical system is tuned for the infrared spectrum, while for ultraviolet light its transmission would be very small.

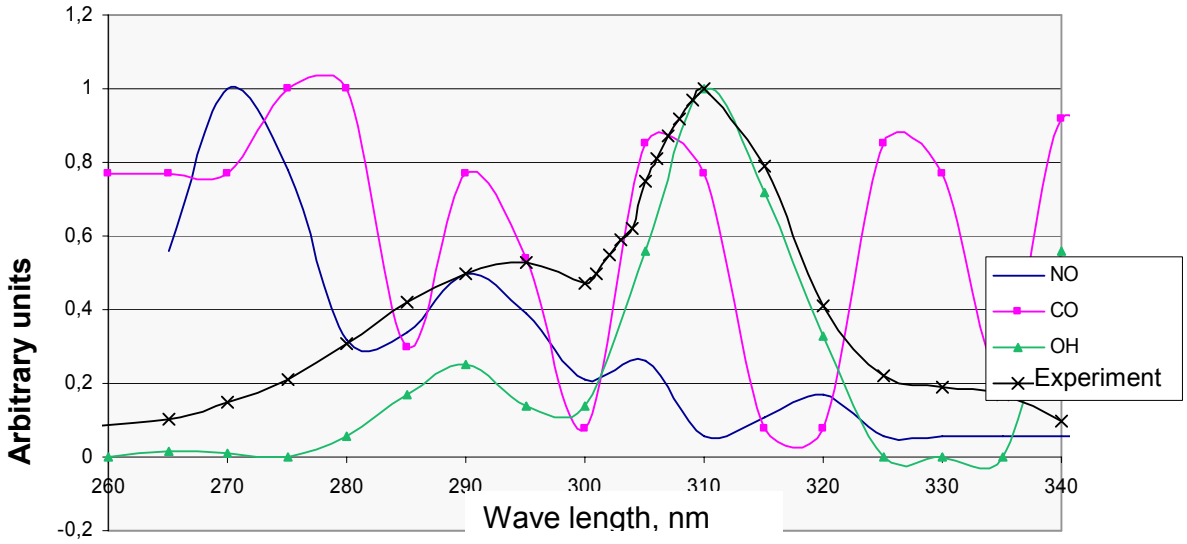

Fig. 1.: Reconstruction of the relative intensity distribution for NO, CO and OH bands from the measured integral curve.

One other alternative is to use the Kitagawa band of the H_2O excitation (570-700 nm). The line is less intense and the background will be more difficult to clear, thus one should assume up to three orders of magnitude sensitivity reduction, in comparison with the hydroxyl option. Using this method during micro-wave (ECR or ICR) discharges would gain these three orders of magnitude due to higher fast electron concentration in proximity to the first wall.

Altogether, optical spectroscopy is considered to be a very promising method for ITER [2]. Hence, future activities should be concentrated on the possible modification of the ITER wide angle viewing system in order to improve its transmission in the ultraviolet spectrum and to equip it with corresponding spectrometer systems. As well “blind spots” on the plasma facing surface for the ITER viewing system should be localised in order to analyse the leak pinpointing by indirect viewing of the neighbouring areas.

Staff:

A. Antipenkov

Literature:

[1] A. Antipenkov, O. Afonin, I. Vizgalov, V. Kurnaev, V. Kolesnikov, Water micro-leaks detection in ITER torus, Questions of Atomic Science and Engineering, Moscow, 2006, issue 3, 46-55 (in Russian)

[2] D. Abramenko, O. Afonin, A. Antipenkov, V. Kolesnikov, V. Kurnaev, I. Vizgalov, Spectroscopic method for water vacuum leak pin-pointing in ITER torus, SOFT 2008, Rostock, Germany.

Magnet Structure and Integration

EFDA/07-1704-1604 (TW6-TMSM-CRYOGT)
Materials Cryogenic Testing

Background and objectives

Since the magnet windings and structures of ITER require materials and welded joints with high mechanical properties to withstand the large electromechanical loads during charge-up of the machine and the operational pulses the mechanical testing of these materials at cryogenic temperatures is indispensable. The following investigations shall be carried out as necessary at the facilities and with the equipment available at the cryogenic laboratory of Forschungszentrum Karlsruhe (CryoMaK):

- Fatigue life tests on the chosen structural materials
- Cryogenic mechanical characterization of structural materials and welds according to the task progress
- Tensile strength and fatigue properties tests for the selected candidate structural materials at cryogenic temperature (4 - 7 K)
- Thermal expansion and thermal conductivity measurements of the structural and non-structural materials at the cryogenic temperature range.

Tests of aged and compacted TF-conduit material

Regarding the TF-magnet, the conduit material 316LN was not tested yet in the final condition compacted and aged. Therefore several samples were prepared representing different compaction steps, followed by a temperature aging process comparable to the heat treatment of the TF-conductor.

Specimens were machined by EDM to obtain flat standard tensile specimens to examine the mechanical behaviour of the compacted and aged samples. In Fig. 1 the samples and machined specimens are shown. Table 1 summarizes the results obtained from the stress strain curves of Fig. 2.

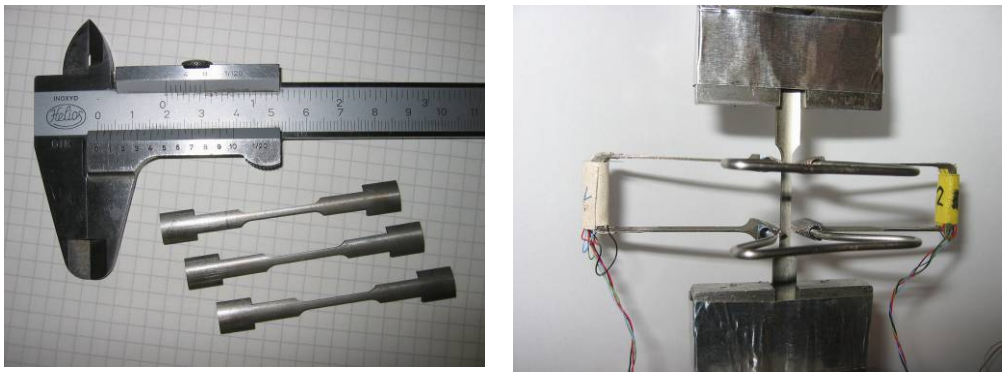

Fig. 1: Machined flat specimens for tensile testing and mounted sample for test.

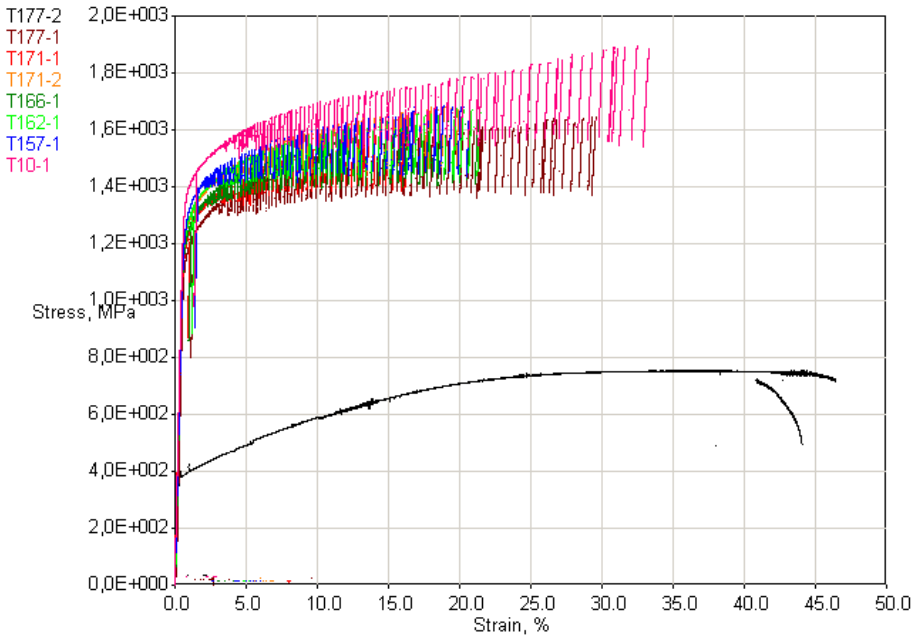

Fig. 2: Stress-strain curve of the different specimens tested at RT and 7 K.

Table 1: Results obtained from the stress strain curves of Fig. 2; possible error for stress values +/-1.5% due to small size of flat specimen and area determination.

Filename	Temperature	Young's Modulus	Yield Strength	Ultimate Tensile Strength	Uniform Elongation	Total Elongation	Compaction
-	K	GPa	MPa	MPa	%	%	%
T177-2	295	195.3	381	755	44.0	49.7	0
T177-1	7	205.2	1159	1647	29.3	29.6	0
T177-3	4	204.1	1099	1518	21.4	21.4	0
T177-4	4	197.1	1134	1527	21.3	21.3	0
T171-1	7	194.7	1188	1598	16.1	16.3	~4
T171-2	7	217.5	1232	1680	18.9	19.9	~4
T171-3	4	204.9	985	1509	22.7	22.7	~4
T171-4	4	196.8	1095	1483	21.3	21.3	~4
T166-1	7	196.2	1205	1638	20.7	21.3	~7
T162-1	7	212.1	1225	1673	19.8	21.5	~9
T162-2	4	194.0	1201	1566	22.8	22.8	~9
T162-3	4	202.0	1129	1562	20.9	20.9	~9
T157-1	7	209.0	1270	1685	18.9	20.7	~12
T10-1	7	212.9	1357	1894	32.5	33.3	prestrain 10%

Tensile tests of conduit material for the European Dipole EDIPO Project

Due to the larger compaction and deformation of the conduit material for the EDIPO conductor, the material shows a large spring back effect during winding of the coil leading to complications to keep the coil shape. To examine the material properties of the conduit, flat specimens were machined from the compacted tube and also the empty conduit was tested under tensile load. In Fig. 3 the samples and machined specimens are shown.

As can be seen in Fig. 4 the conduit sample reaches higher stress values, due to the fact, that also the deformed corners attribute to the overall mechanical performance. T12-3 with weld shows almost the same results as T12-2, but the total elongation is reduced and the failure occurs within the weld. The results from the tensile tests can be found in Tables 2 and 3.

Fig. 3: Conductor samples and machined flat specimens after test.

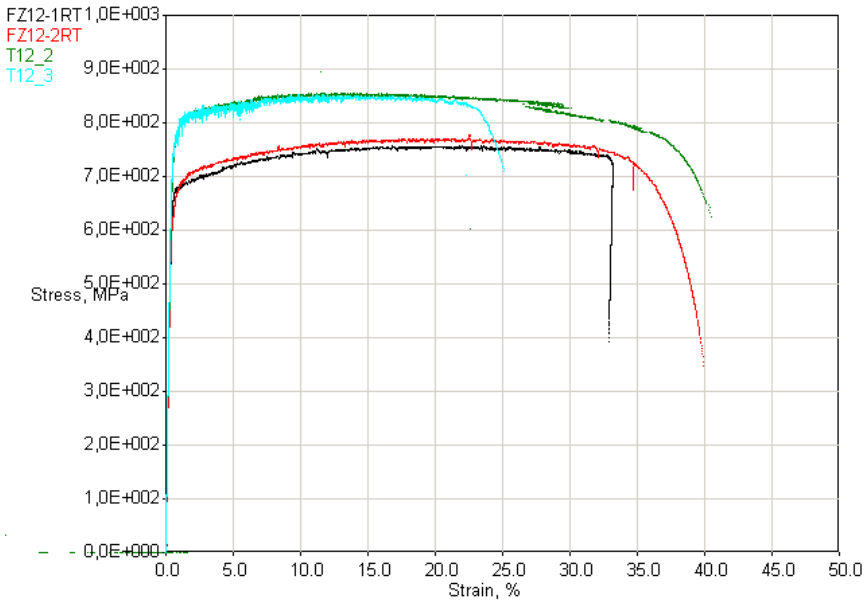

Fig: 4: Stress strain diagram of flat specimens and empty conduit.

Table 2: Results of flat specimens extracted by EDM from the tube (see Figure 3).

Filename	Temperature	Young's Modulus	Yield Strength	Ultimate Tensile Strength	Uniform Elongation	Total Elongation
-	K	GPa	MPa	MPa	%	%
FZ12-1	295	181.8	653	757	22.0	33.2
FZ12-2	295	173.2	630	778	22.5	39.9

Table 3: Results of empty tube without conductor inside. T12-2 pure tube, T 12-3 tube with weld(*). Compare with figure 3.

Filename	Temperature	Young's Modulus	Yield Strength	Ultimate Tensile Strength	Uniform Elongation	Total Elongation	Area
-	K	GPa	MPa	MPa	%	%	mm²
T12-2	295	184.4	741	895	11.5	40.5	75.78
T12-3*	295	188.8	751	853	11.7	25.1	75.78

Push-through experiment on 3x3 CICC array for the European Dipole EDIPO Project

To test the insulation material in shear mode of a 3x3 cable in conduit array, the push-through technique was used to compare the results with former experiments. The measurement was done under compression using a pushing steel plate adjusted to the middle sc-CICC and a counter mask (see Fig. 5). From each of the two samples, using glass fabric with and without size material, three different specimens were cut with the height of 15 mm, 20 mm, and 25 mm. The specimens were cooled down force free to 4.2 K and initially loaded during the measurement.

In Table 4 the achieved maximum load is listed and with the measured outer steel area of the conductor the shear strength is obtained. The results are similar to the one obtained in former experiments.

From this it seems that the specimens using glass fabric with size material achieve higher shear strength values compared to the specimens using desized glass fabric. However, due to the low number of specimens (three with different height) the result has to be handled carefully. Moreover, this kind of test is not ideal to measure the real shear strength possible for the insulation material. Therefore bending experiments will be done on especially machined specimens.

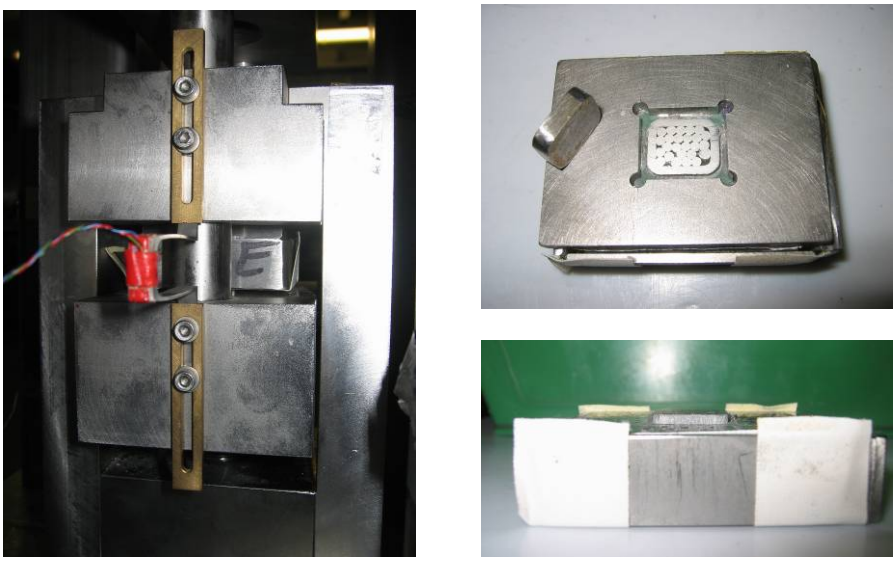

Fig. 5: Setup for the push through experiment.

Table 4: Results of the push-through experiment.

Filename	Temperature	Max. Load	Area d x c*	Shear-Strength
-	K	kN	mm²	MPa
Glass fabric **with** size material (“nicht entschlichtet”)				
NE-15	4	33.87	15 x 52.6	42.9
NE-20	4	37.37	20 x 52.6	35.5
NE-25	4	70.86	25 x 52.6	53.8
Glass fabric **without** size material (“entschlichtet”)				
E-15	4	17.89	15 x 52.6	22.6
E-20	4	32.20	20 x 52.6	30.6
E-25	4	33.62	25 x 52.6	25.5
* height d and measured circumference c of sc-CICC steel tube				

Shear tests of insulation of the TF pancake structure

To test the shear strength of the insulation material used for the TF pancake structure a mock-up was provided by EFDA (see Fig. 6). Special specimens will be machined to test the shear strength under bending.

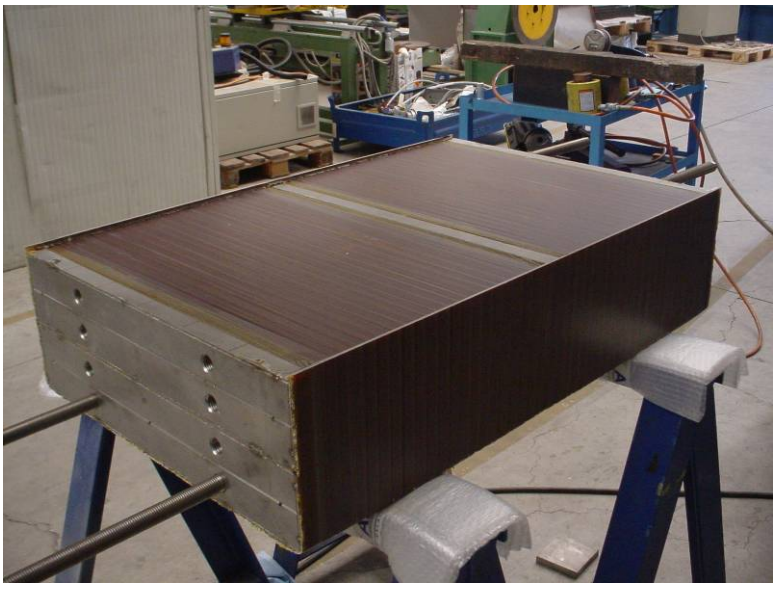

Fig. 6: Picture of the TF pancake mock-up for shear tests on the insulation.

Staff:

A. Ehrlich
K.-P. Weiss
S. Westenfelder

Current Leads for Wendelstein 7-X and JT-60SA

Introduction

Current leads are a component of a superconducting magnet system where currently commercialized HTS (high temperature superconducting) material can be used because the external field is usually well below 0.5 T. The potential of HTS current leads can be exemplified by the ITER HTS current lead demonstrator which has been developed and built by Forschungszentrum Karlsruhe in collaboration with the Centre Recherches en Physique des Plasmas, Switzerland in the frame of an EU Fusion Technology task.

In the meantime, other fusion devices under operation or construction like EAST (China), W7-X (Germany) and JT-60SA (Japan) plan to use HTS current leads. Forschungszentrum Karlsruhe has taken over the responsibility for the design, construction and testing of the HTS-CL for two fusion experiments, i.e. the stellarator W7-X and the satellite tokamak JT-60SA.

Critical design parameters which influence strongly the performance are:

- Cold end contact resistance between the HTS elements and the copper cold end connection which determines the cold end heat load at operation current.
- Warm end contact resistance between the HTS elements and the heat exchanger which determines the 50 K He mass flow rate.
- Efficiency of the heat exchanger which determines the 50 K He mass flow rate and the length of the heat exchanger.
- Temperature margin of the HTS elements which is related to the current sharing temperature at operation conditions and determines the performance of the current lead in case of LOFA and quench.

Current Leads for Wendelstein 7-X

The stellarator W7-X presently under construction at the Greifswald branch of the Max-Planck-Institute for Plasma Physics (IPP) consists of 50 non-planar and 20 planar coils with a maximum conductor current of 17.6 kA. Forschungszentrum Karlsruhe will deliver the current leads for the magnet system. In total 14 current leads are required (maximum design current I_{max} = 18.2 kA, nominal current I_{nom} = 14 kA). The main parameters of the current leads are summarized in Table 1.

Table 1: Main parameters of W7-X current leads.

Parameter	Value
Number of current circuits of non-planar/planar coils	5/2 (10 coils in series each)
Number of current leads	14
Maximum design current	18.2 kA
Nominal current	14 kA
Max. voltage to ground (test voltage)	±13 kV
Orientation	cold end at top
Overall length	2500 mm
Max. diameter	200 mm
Basic operation schedule	steady state for 4-5 days

Four main requirements of the W7-X machine dominate the design of the current leads:

1. Mounting in upside-down position, i.e., the cold end of the current lead is at the top and the warm end at the bottom side. In conventional leads this may give rise to cooling problems, because the large He density gradient between 4.5 K and room temperature (factor 500) can lead to free convection flow in the opposite direction to the forced convection flow. This would increase the He mass flow rate and the necessary cooling

power drastically. The use of conduction-cooled HTS material between 4.5 K and 60 K has the consequence that the He in the heat exchanger has to cover only the temperature range between 50 K (the inlet temperature) and room temperature. This will drastically reduce the free convection process because the density gradient between 50 K and room temperature is now only 6 instead of 500 for conventional designs using no HTS material. The penalty is the higher cost for the current leads due to the expensive HTS material.

2. The necessity of using low-Co stainless steel material and the limitation of the amount of silver. Due to the design of W7-X, the current leads are located inside the biological shield, very close to the magnet system. Therefore, neutron activation has to be considered and as far as possible, Co and Ag should be avoided. However, because Bi-2223 is Ag-sheathed, silver cannot be avoided in the design of the HTS current lead.
3. The location of the current leads very close to the magnets results in a rather high magnetic stray field. Due to the strong field dependence of the critical current especially at higher temperatures, a much higher amount of HTS material is needed.
4. Paschen tightness and relatively large high test voltage of 13 kV of the current lead and its instrumentation has to be assured.

The design of the binary current lead for W7-X follows the same principles as that of the 70 kA ITER demo current lead mentioned above. It consists of a HTS part covering the temperature range between 4.5 K and 60 K and a conventional heat exchanger in the range of 60 K to room temperature. The HTS part is cooled by heat conduction from the 4.5 K end whereas the heat exchanger is cooled with 50 K helium. The HTS material used in the current leads is Bi-2223/AgAu tape. As AMSC has stopped the production of first-generation HTS wires in 2006, a material qualification programme was started and different suppliers have been asked to provide samples of single tapes and stacks soldered from several single tapes for electrical, thermal and mechanical testing. At the end of the qualification programme, Bi-2223/AgAu tapes with critical currents >110 A (at 77 K and in self field) became industrially available. Soldered stacks can also be made in industry.

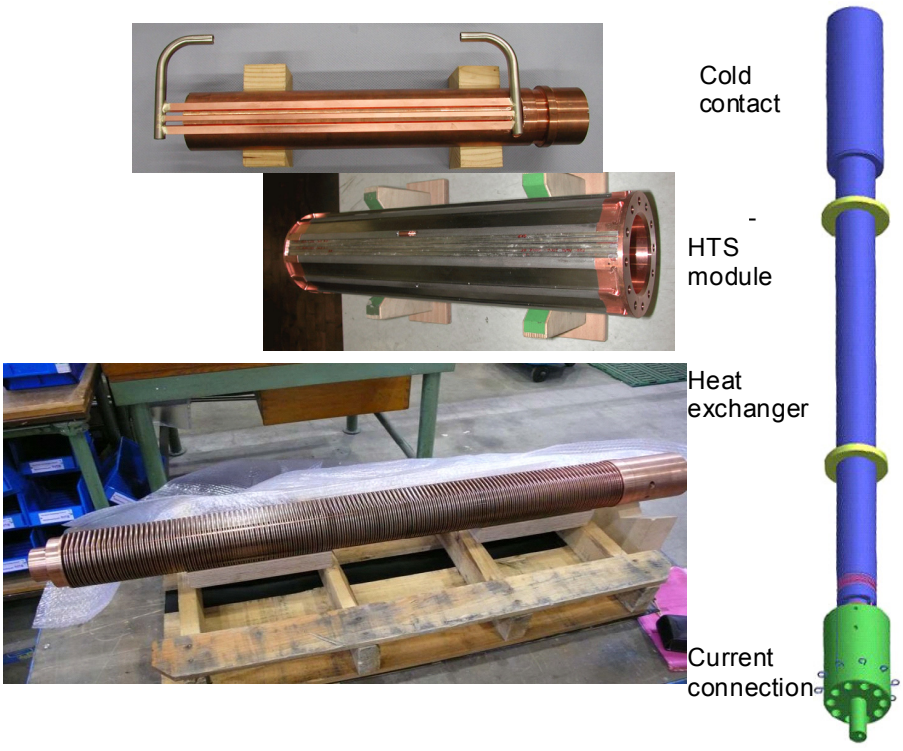

Fig. 1: W7-X current lead: schematic drawing and mock-ups of the cold contact end, HTS module and heat exchanger.

Fig. 1 shows an example of the HTS current lead as well as an example the mock-ups of the cold contact copper end including the cooling piping, the HTS module carrier made from stainless steel to reduce heat conduction, and the copper heat exchanger including the room temperature head.

The high-voltage requirement of W7-X requested a special design of the electrical insulation system. Earlier designs (e.g., for the ITER demo current lead) used a concentric electrical insulation tube around the pressure vessel of the current lead together with the use of stagnant helium as insulating gas. However, such a solution causes high thermal losses: Stagnant helium around the current lead causes thermal acoustic oscillations driven by the heat flow in the room temperature region of the lead. So a different approach was chosen for the current leads currently under design and construction at FZK: The electrical insulation will be directly performed on the outer surface of the current lead pressure vessel by a solid insulation and a G10 flange will be integrated to serve as a connection part to the vacuum vessel of the facility. First tests have shown encouraging high-voltage insulation performance and satisfactory mechanical strength according to the original W7-X requirements.

Fig. 2 shows a picture of the HV-insulation mock-up. The insulated region is covered with conductive paint (black) to provide a definite ground potential.

Fig. 2: HV-insulation mock-up - left: glas/G10 insulation, right: mock-up covered with conductive paint.

Beginning of 2008 IPP has made a design change regarding the mechanical loads acting on the G10 flanges resulting in an increase of the loads up to a factor of eight. Thus it is necessary to re-investigate the mechanical strength; therefore a mock-up has been built in the FZK workshop and insulated by industry (BNG) using the technology developed at that company in the frame of the W7-X coil production. Presently the mock-up is being tested under relevant HV conditions and will be then provided to IPP for further investigations; for this purpose IPP has selected a company who will do the mechanical testing at room temperature and at LN2 temperature taking into account the mechanical loads (3-dimensional forces and moments) given by W7-X. Thus the responsibility for a safe operation in W7-X will not be taken by FZK anymore but has moved to IPP. Due to strong time constraints IPP decided to proceed with the prototype current lead design and manufacturing and investigate the mechanical load issue in parallel to solve it for the series current leads.

The project status is as follows:

- The design of the prototype current leads is completed and agreed with IPP, except for the Paschen tight HV-insulation which is still under investigation.

- The manufacturing and assembly of the various components (cold end contact, HTS module, heat exchanger) is in the qualification stage by mock-ups which have been built and are being used to examine all manufacturing details. Due to the refurbishment work of TOSKA for testing the W7-X non-planar coils, the personal resources for the qualification work was not available over a longer time period in 2008 leading to a significant delay. The qualification work has been continued in October 2008.
- The production of the required materials and semi-finished products, i.e. HTS stacks, copper bars, stainless steel tubes, bellows, piping etc. is underway or already completed and available.
- The present planning assumes the completion of the two prototype current leads in summer 2009 and the completion of the assembly of the test setup until end of 2009.

Current Leads for JT-60SA

In the frame of the Broader Approach Agreement between Japan and the EU and concomitantly to the ITER project, a satellite tokamak project called JT-60SA has been agreed. The magnet system of JT-60SA consists of 18 toroidal field coils (25.7 kA), 4 central solenoid modules (20 kA) and 7 poloidal field coils (20 kA). Following the commitment of the German Government to the EU, FZK shall design, construct and test the current leads. In total 6 leads for a maximum current of 26 kA and 20 leads with a maximum current of 20 kA, mounted in vertical, upright position are required. The plasma and basic parameters of JT-60SA are defined by Japanese and EU Satellite Tokamak Working Groups considering its mission. The main parameters of the current leads are summarized in Table 2.

Table 2: Main parameters of JT-60SA current leads

Parameter	TF	CS/PF
Number of current circuits	3	4/6
Number of current leads	6	8/12
Maximum current	25.7 kA	20 kA
Max. voltage to ground (test voltage)	±7 kV	±21 kV
Orientation	vertical	vertical

Again the current leads will be of the binary type, the HTS part covering the range between 4.5 K and 60 K while the heat exchanger should cover the range between 60 K and room temperature and be cooled by 50 K He. Part of the results of the qualification programme of the current leads for W7-X can also be used for the leads of JT-60SA. This is especially valid for the HTS material and the electrical insulation.

Two prototype leads will be tested in CuLTKa, which is a special test facility currently under construction in FZK using JT-60SA-relevant conditions. After the prototype tests 26 current leads will be built in industry with final acceptance test of all leads in CuLTKa.

The status is as follows:

- Presently the procurement arrangement for the HTS current leads for JT-60SA is being prepared by JT-60SA EU home team.
- The detailed design will be done after completion of the design of the current leads for W7-X. Two prototype leads will be tested in CuLTKa using JT-60SA-relevant conditions. Afterwards 26 current leads will be built in industry whereas the final acceptance test of all leads will be done in CuLTKa.
- The notification of approval of the German government for the financing of the design work, prototype testing, the preparation of the test facility and the ordering of the materials and semi-finished components has been sent to FZK. The order for the HTS stacks has been prepared.

Construction of the test facility CuLTKa

For the test of the W7-X and JT-60SA current leads the Current Lead Test Facility Karlsruhe (CuLTKa) has to be newly built and commissioned. There is a severe time constraint for the completion because it has to be ready for the test of the prototype current leads for W7-X as well as for JT-60SA. Afterwards, the final acceptance test of 14 series current leads for W7-X to be built in industry will be done in CuLTKa in 2011-2012. Afterwards the acceptance test of 26 series current leads for JT-60SA will follow in 2013-2014.

CuLTKa will be built in the hall 406/1 of ITP and consists of a control part and a testing part. The control part will provide the cryogenic conditions like 4.5 K helium and 20 - 80 K helium with appropriate mass flow rates whereas the testing part will be the test bed for the current leads and the control unit for these tests.

Fig. 3 shows a CAD view of the actual planning stage of CuLTKa. Special care has to be taken for the test cryostats which have to be able to provide the test bed for the W7-X current leads to be installed up-side down as well as for the JT-60SA current leads to be installed in the normal vertical condition. Both conditions have to match the geometrical boundary conditions of the infrastructure (i.e. hall 406, He and current supply etc.). One further issue is the feeding of the current from the 30 kA power supply located in the adjacent TOSKA hall 406/2 to the test bed.

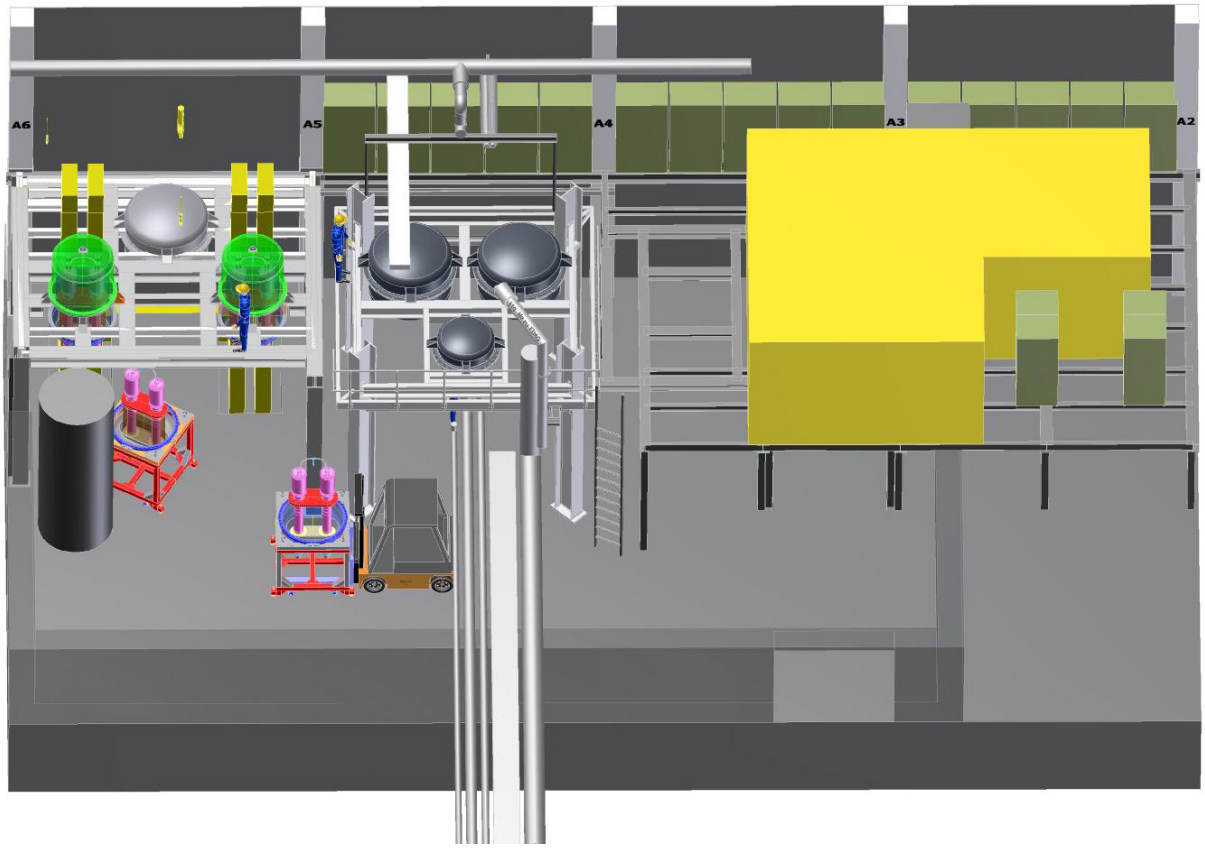

Fig. 3: CAD drawing of CuLTKa.

Staff:

W.H. Fietz
R. Heller
A. Kienzler
T. Vogel

Literature:

[1] R. Lietzow, R. Heller, H. Neumann, "Performance of heat exchanger models in upside-down orientation for the use in HTS current leads for W7-X", Advances in Cryogenic Engineering: Transactions of the Cryogenic Engineering Conference - CEC, Vol. 53 (2008) 1243-1250

[2] M. Schwarz, K.P. Weiss, R. Heller, W.H. Fietz, "Thermal conductivity of BSCCO tapes for current lead applications", ADVANCES IN CRYOGENIC ENGINEERING MATERIALS: Transactions of the International Cryogenic Materials Conference - ICMC, Vol. 54 (2008) 455-450

[3] R. Heller, W.H. Fietz, P. Keller, S. Schlachter, M. Schwarz, K.P. Weiss, "Electrical, mechanical and thermal characterisation of Bi-2223/AgAu material for use in HTS current leads for W7-X", IEEE Trans. on Appl. Supercond., 18 (2) (2008), 1443-1446

[4] A. Pizzuto, P. Bayetti, A. Cucchiaro, P. Decool, A. Dellacorte, A. Di Zenobio, J.L. Duchateau, W.H. Fietz, R. Heller, M. Kikuchi, K. Kizu, L. Muzzi, C. Portafaix, F. Rondeaux, L. Semerao, S. Turtu, K. Verger, Y. Yoshida, L. Zani, "JT-60SA toroidal magnet system", IEEE Trans. on Appl. Supercond., 18 (2) (2008), 505-508

[5] W.H. Fietz, R. Heller, A. Kienzler, R. Lietzow, " High Temperature Superconductor Current Leads for WENDELSTEIN 7-X and JT-60SA", 2008 Applied Superconductivity Conference, Chicago, IL, accepted for publication in IEEE Trans. on Appl. Supercond.

[6] P. Keller, M. Schwarz, K.P. Weiss, R. Heller, A. Jung, A. Aubele, "Electromechanical and Thermal Characterization of Stacked Bi-2223 Tapes at Cryogenic Temperature", 2008 Applied Superconductivity Conference, Chicago, IL, accepted for publication in IEEE Trans. on Appl. Supercond.

[7] W.H. Fietz, R. Heller, A. Kienzler, R. Lietzow, "Status of HTS Current Leads for WENDELSTEIN 7-X and JT-60SA", presented at 25th SOFT, Rostock, Germany, submitted for publication in FED

[8] M. Schwarz, K.P. Weiss, R., W.H. Fietz, "Thermal conductivity measurement of HTS tapes and stacks for current lead applications", ", presented at 25th SOFT, Rostock, Germany, submitted for publication in FED

EFDA/06-1522 (TW6-TMSC-COILMO)
Definition of Procedures for Coil Electrical Testing and PF Transient Analysis

Introduction

Large superconducting coils operate with high current densities in the conductors. In case of a quench in superconducting windings the coils have to be discharged to avoid the damage of the coils. The fast discharge can lead to oscillations within the coil and to a non-linear voltage distribution between the windings and thus to high voltage stress on different kinds of coil insulation, e. g. conductor, layer and ground insulation. Further the resonance frequency of the coils was expected to be in the frequency rage near to the operation frequency of the coil AC/DC converter. This means that high voltage stress during the normal operation conditions can also occur. Additionally the consideration of CS coil modules is also necessary to ensure accurate investigations of the ITER PF coil system because of the magnetic coupling between the CS and PF coils. For detailed analysis the PF 3 and PF 6 coils were selected, because PF 3 has the largest main radius of the PF coils (12 m) and PF 6 the largest number of turns (432).

Strategy on Calculation of Voltage Stress on Large Superconducting Coils

The calculations of the voltage stress within the PF 3 and PF 6 coils were started with calculations in a Finite Element Method (FEM) programme and are continued by calculations in a network programme. The flow chart of the calculation strategy is shown in Fig. 1. With the given geometry and materials the FEM-model of the coil was established. The values for frequency depending inductances were calculated with the FEM programme. The frequency independent capacitances were calculated with formulas for parallel plate and cylinder capacitors. The calculated values were taken into a network model of the coil as lumped elements. The calculations with the network models were separated in frequency and time domain. In the frequency domain the resonance frequency of the coil was calculated, which gives the first benchmark on the electrical behaviour of the coil for different transient voltage excitations like they appear during the fast discharge. The detailed calculations of the voltage stress on different kinds of insulation within the coils in time domain are started.

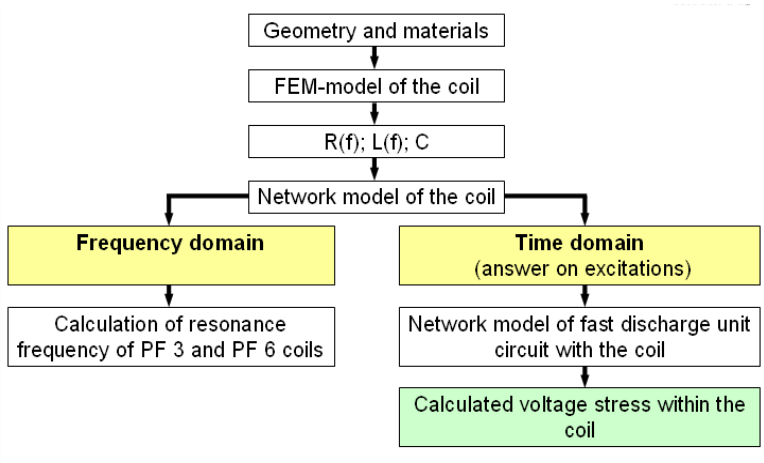

Fig. 1: Calculation strategy of voltage stress within the coil.

Finite Element Methods Calculations

The Finite Element Method (FEM) calculations were initiated with the calculation of the self and mutual inductances of the complete coil system with a simplified model of the coils, which is shown in Fig. 2. The calculations of the complete coil system include also simplified models of the CS coils due to the magnetic coupling between the CS and PF coils. The CS and PF coils have rotational symmetry, which allows establishing two dimensional FEM models of the coil system. The inductances of the superconducting coils which will be used for ITER have a strong frequency dependence. It is caused by eddy currents which will be induced in the conducting parts close to the coils. Thus the magnetic coupling between the coils for frequencies higher than 10 kHz can be neglected.

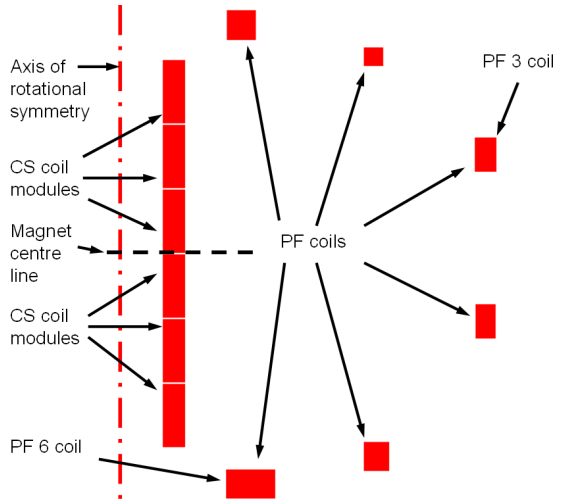

Fig. 2: Simplified FEM model of coil system.

The inductances of the coils in the simplified FEM model of the coil system were calculated for DC operation because of the magnetic coupling between the CS and PF coils at low frequencies. The calculated values for self inductances for all CS coils were 0.78 H. The self inductances for PF coils vary between 0.41 H and 2.01 H depending on the coil diameter and the number of turns. The mutual inductances in CS PF coil system have values between 4 mH and 0.45 H.

The calculated results for DC coupling in CS PF coil system will be used in network calculations in time domain to analyse the influence of the magnetic coupling between the coils during the fast discharge, the normal operation and a failure scenario, e. g. short circuit to the ground. The self inductances can also be used to compare the inductance of the PF 3 and PF 6 coils calculated with detailed FEM models of these coils.

The first step for the calculation of the voltage distribution within one specific coil is the establishing of a detailed FEM model and the calculation of inductances for every conductor of this coil. The detailed procedure of calculation will be shown on the example of PF 6 coil. Fig. 3 shows a part of the detailed FEM model of the PF 6 coil consisting of 2 X 4 conductors. The complete detailed FEM model of the PF 6 coil consists of 16 conductor layers, which are called pancakes. Each pancake consists of 27 conductors. Two pancakes are summarized to one double pancake, thus the PF 6 coil consists of 8 double pancakes. The total number of conductors in the PF 6 coil amounts to 432. Due to the relatively simple geometry between conductors the capacitances were calculated by formulas for parallel-plate and cylinder capacitances.

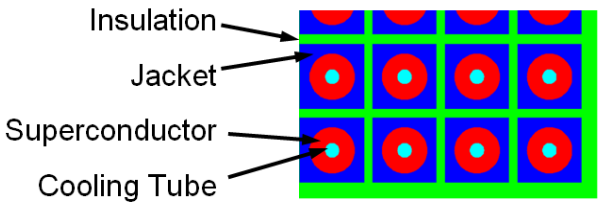

Fig. 3: Part of the detailed FEM model of PF 6 coil.

The calculated values for self inductance of a conductor and the mutual inductances to all other conductors were summarized to the cumulative DC inductance of the conductor. The cumulative DC inductance of the conductors of PF 6 coil varies from 3.29 mH to 5.5 mH, depending on the location of the conductor in the coil. The total DC inductance of the PF 6 is calculated by summarizing all the cumulative DC inductances of the conductors of one coil. The total DC inductance of the PF 6 coil calculated by detailed model is 2.06 H which fits well to 2.01 H, which is the calculated total DC inductance of PF 6 coil with the simplified coil model. The calculated values for capacitances between the conductors and from conductor to ground vary from 5.8 nF to 9 nF.

Network Calculations in Frequency Domain

The detailed network models of PF 3 and PF 6 coils were established with calculated values for inductances and capacitances. Fig. 4 shows a part of the detailed network model of PF 6 coil. Every turn of the coil is established as an RL circuit. All capacitors between the conductors, between the layers and on the outer layers of the coil to the ground are included into the detailed network model of the coil. To simulate the superconductivity of the coil conductors the resistances were set to 1 pΩ. The resonance frequency of the PF 3 coil was calculated to be 20.6 kHz and for PF 6 coil to be 28.6 kHz.

Furthermore, the influence of instrumentation cables on the resonance frequency of the coils was analysed. The instrumentation cables were taken into the detailed network model of the coil as additional capacitances with values from 13 nF to 20 nF, which were placed on the connections between the double pancakes of the coil. The resonance frequency of the PF 3 and PF 6 coils with instrumentation cables were calculated to be 17 kHz respectively 22.9 kHz. This calculations show that instrumentation cables have strong influence on the resonance frequencies of the superconducting coils and move the resonance frequencies to lower values.

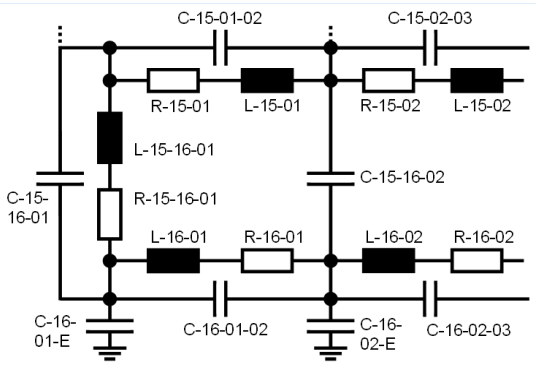

Fig. 4: Detailed network model of PF 6 coil.

Conclusions

The calculation on transient electrical behaviour of PF coils is an important part of the high voltage insulation co-ordination of the PF coils. The simplified and detailed FEM and network models of the CS PF coil system respectively PF 3 and PF 6 coils were established to calculate the voltage stress during transient electrical excitations of the coils. As the first calculation results the resonance frequencies of PF 3 and PF 6 coils were calculated. Furthermore, the influence of the instrumentation cables on the resonance frequencies of the coils was investigated. The consideration of instrumentation cables in the network model decreases the resonance frequency of the coils. The network model of the complete coil system will be established and the influence of the coupling between CS and PF coils will be analysed.

Staff:

W. H. Fietz
S. Fink
A. Winkler

New Quench Detection System for Fusion Magnets

Introduction / general objectives

Based on a contract with Max Planck-Institute of Plasma Physics / IPP Greifswald the FZK (Institute of data processing and elektronics - IPE) started to develop a new Quench Detection System (QDS) at the end of 2005. With the objective of an universal operation at W7-X planar and non-planar coils (differential mode) as well as a simple application on bus-bars (non differential mode) combined with special requirements concerning HV-compatibility it was necessary to create a complete new design of compact quench detection electronics.

Fig. 1: Quench Detector UNIQD IPE 3410 (sealed / unsealed).

Requirements to the new Quench Detection System at W7-X (extraction) [1]*:*

- Isolation Voltage min. 13 kV (permanently), 17 KV (1 min) against GND
- 500V / 1000V Input voltage capability (Input-Chan. to HV-GND / Inp.-Chan. to Inp.-Chan.)
- Input-Delay < 500 µs (10% to 90%)
- 2 MB On-Board quench event record buffer (10 sec. @ 100KS/sec, 12 Bit resolution)
- Ultra Low Power / Rugged Long-Life Design
- Magnetic stray field capability of min. 30mT
- Fail-Safe and redundant design of electronics combined with internal self diagnostics
- Stand-alone safety operation / remote parameterisation
- Strictly 20KV-optical isolation of all communication-interfaces / inputs / outputs
- Vibration and shock compliance according to ETS 300 019-2-4
- EMC according to EN 55022 and EN 55024
- Development and manufacturing according to EN ISO 9001 (Quality management)

Basic conditions of the Quench Detection System at W7-X (parallel operation of up to 560 QD-Units) required new digital and “screwless” operation techniques compared to earlier versions of existing quench detectors [1]. Additionally special coil circuitries to the QD-Units at W7-X need a higher degree of QD-input balancing possibilities in differential mode than used in former applications.

Based on latest FPGA-technology (Altera® Cyclone II) the IPE designed a new scalable modular Quench Detection System consisting of:

- Single QD-Unit modules (Fig. 1)
- Q-Detector racks with communication backplanes (supplying of 8 QD-Units)
- QD-switching cabinet consisting of 9 QD-racks (max. amount of 72 QD-Unit per cabinet) with integrated real time system [2] for quench event logging

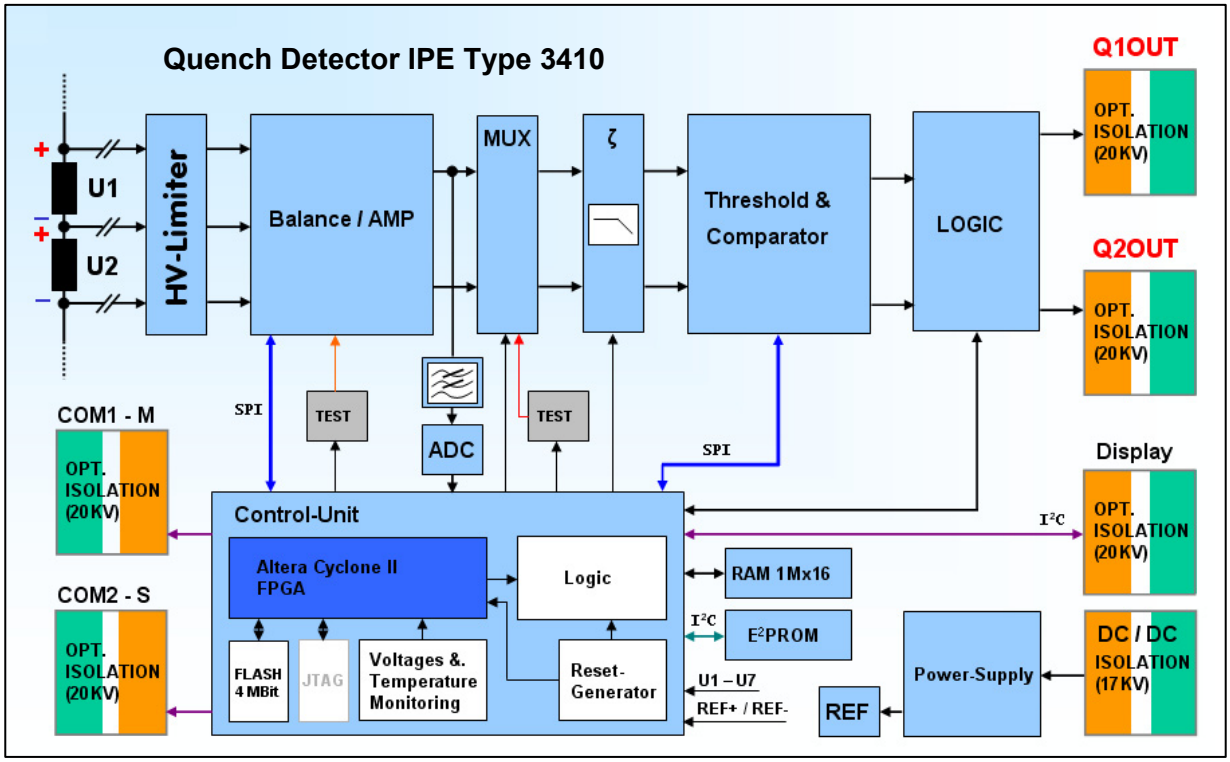

Fig. 2: Simplified schematic of IPE Quench Detector Type 3410.

Fig. 3: Quench Detection switching cabinet delivered to IPP/ Greifswald by FZKin November 2007 including:

- 72 linked QD-Units (via optical isolated high-speed RS 485 dual bus system)
- Integrated real time quench event logging system (discrete connec-tions to all 72 QD-Units)
- Additional optical separators (Ether-net, con-trol bus´s, auxiliary inputs / outputs)
- Optical isolated QD-Outputs for emergency cut out (wired-or)
  (2 straight quench event signals to PLC-connection)
- 24V DC-UPS (provided by IPP)
- Heat exchanger
- Cable conduit (QD-HV-conductors)
- Diagnostic interfaces

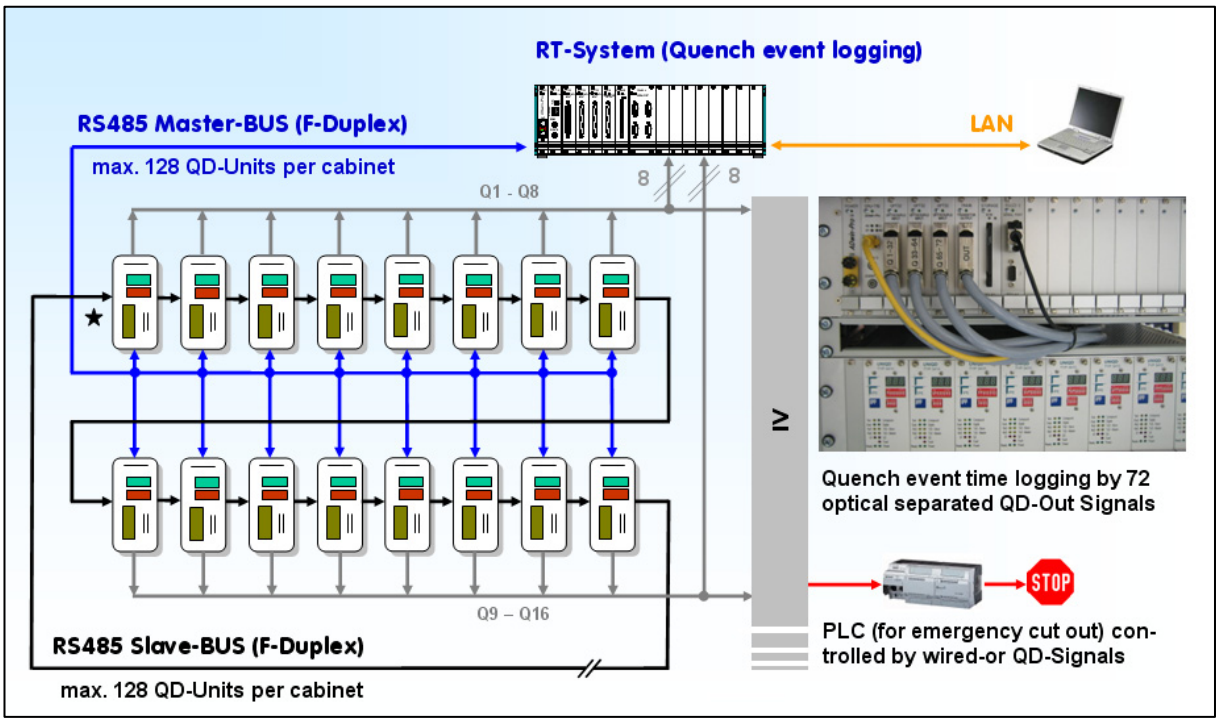

Fig. 4: Quench event time logging by real time system (ADWin®-System, Fabr. Jäger)

Logging of quench events is accomplished by using an additional real time signal collection system [2]. For this purpose it is necessary to connect all QD-Units (QDOUT of the QD-Unit) in parallel to a real time system (Fig. 4). The real time system creates individual time stamps according to accrued quench events. Quench identification itself and therefore QDOUT-signal generation of the QD-Unit depends on its individual parameterisation. Time resolution of quench events in this topology is fast (Res. < 1 µs) and independent of internal Q-Detector timing. No time initialization of (all) detectors is required. The disadvantages of the mentioned topology is caused by an expensive real time systems and proprietary pro-gramming.

Objectives of the task in 2008:

1. **Substitution of real time signal collection system by software based quench event logging**
2. **Assembling of new Quench Detection equipment at TOSKA facilities**

Several considerations with respect to general charges to hardware components, maintenance and effort of developing software at different platforms caused a decision, to change the existing quench event logging system based on the real time system.

Overview of developed software components at the end of 2007:

(1) FPGA-software of quench dectector unit (VHDL)

(2) Proprietary evaluation and programming / processing module for the QDU´s (Labview ®)

(3) RT-System quench event logging software (ADWin® Basic language)

(4) GUI to ensure download of RT-system code and remote operation / parameter download to the QDU´s (Labview ®)

(5) Windows®-based software “QVision” for QDU´s data management, visualisation and operating diagnostics, calibration of QD-Units (Visual Studio®)

To simplify maintenance process and to ensure required long-term availability of quench detection software operating at W7-X on future operating systems an alternative kind of quench event logging has been developed at FZK (IPE) since the beginning of 2008.

The ADWin® real time signal collection system was replaced by an rugged low cost industrial personal computer (embedded PC) running on Windows® XP Professional or Windows® XP Embedded. The available at IPE developed Software “QVision” has been highly expanded by Multitasking / Multithreading capability and completed by a special software mechanism to generate quench event time schedules by reading and interpreting the QD-Unit´s internal quench event record buffer (QRAM). Due to this method only 2 instead of 4 software platforms have to be maintained. Furthermore installation / wiring of the QD-system is well simplified.

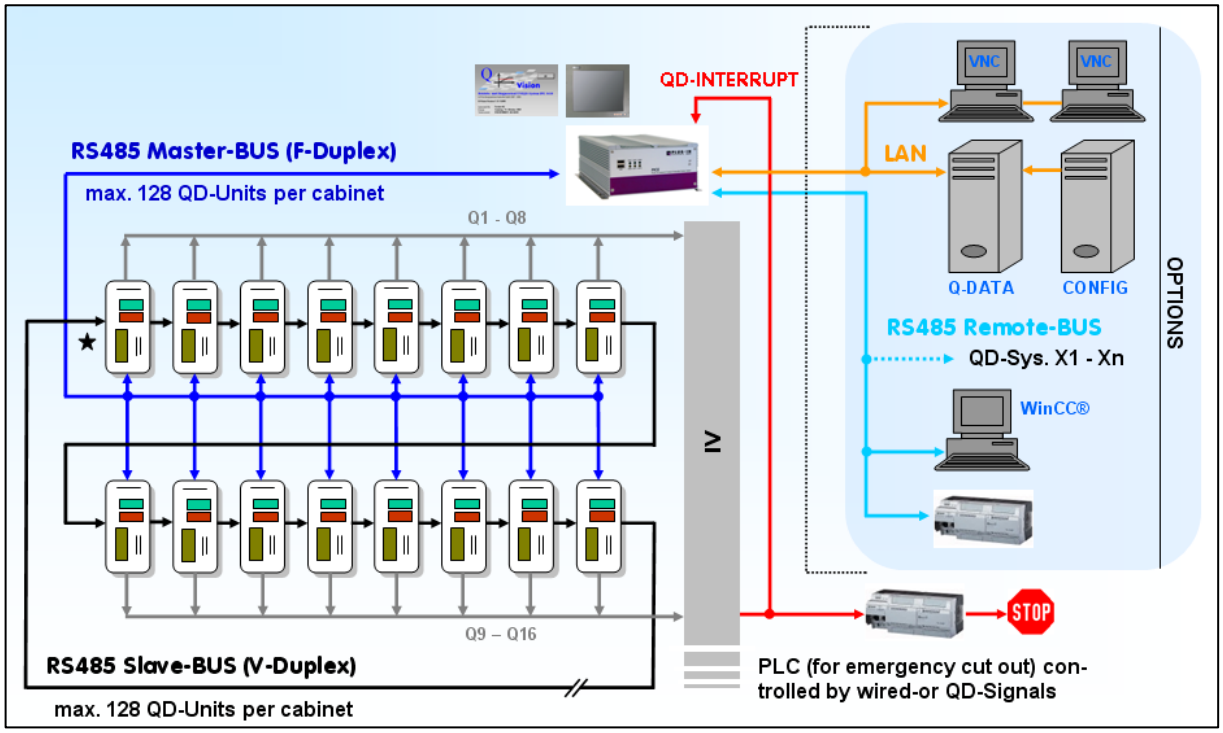

Fig. 5: Quench event base time logging by embedded PC-system (hardware interrupt).

At this topology (Fig. 5) one single timebase-recording is triggered by hardware interrupt actuated by the *first* Quench event (all QDOUT-signals are wired-or). Accuracy of time base recording depends on operating system (approx. 16 ms @ WIN XP or 1 ms @ WIN Vista). Quench event table generating (at multiple quench events) is arranged by reading out the QRAM record buffer of all installed and activated QD-Units. By sorting and interpreting the recorded data the software calculates a quench event table in chronological order. Temporal resolution of the chronological order only depends on sampling rate of the ADC in the QD-Unit. At used sampling rate of 100 ks/sec temporal resolution is 10µs.

Along with this smart method of quench event calculating by software many additional possibilities by using standard Windows® -platforms are opened and implemented in QVision-Software, for example:

- Networking via LAN / Ethernet (remote operation of the QD-System)
- Saving of QRAM-data to any mounted drives (data collection and storage)
- Direct visualisation of voltage gradients online by integrated viewer (simple balancing procedure)

- Additional remote control possibility of QD-System through embedded PC by external interface / instance

Further advantages along with the usage of an embedded PC is the possibility to use a standard NTP as time server or to improve time base accuracy by GPS time logging (no additional software-engineering needed).

New Quench Detection equipment installed at TOSKA facilities

A new Quench Detection System manufactured bei FZK - IPE based on previous described technology (by embedded PC supervised QD-system) was installed in spring 2008 at TOSKA test-facilities at FZK.

Fig. 6: Quench Detection system at TOSKA consisting of:

- 24 linked QD-Units (via optical isolated high-speed RS 485 dual bus system)
- Integrated embedded PC for parameterisation and supervising operation of QD-System
- Additional optical separated remote interface for QD-data recording at emergency cut out triggered by separate instances (e.g. cryostat)
- Optical isolated QD-Outputs for emergency cut out (wired-or)
  (1 straight quench event signal to PLC-connection)
- 24V DC-Power-Supply / 230 VAC UPS
- Diagnostic interfaces
- Data base connection by Ethernet (LAN) with continuous ADC-data recording (all channels)
- Integrated QD-operation environment software *QVision Professional* (latest Version)

The Quench Detection System at TOSKA is equipped with the latest Version of the integrated operation and diagnostics tool *QVision Pro* developed at FZK - IPE. Version 2.0 includes a new comprehensive supervising operation of the QD-system.

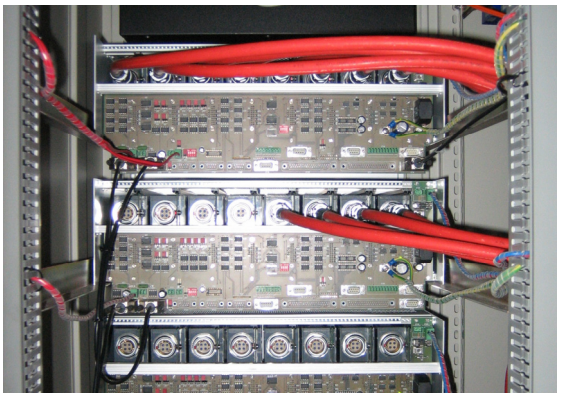

Fig. 7: Connection of HV-QD-signal leads (red) by special HV-Plug (Fabr. Lemo) inside the cabinet.

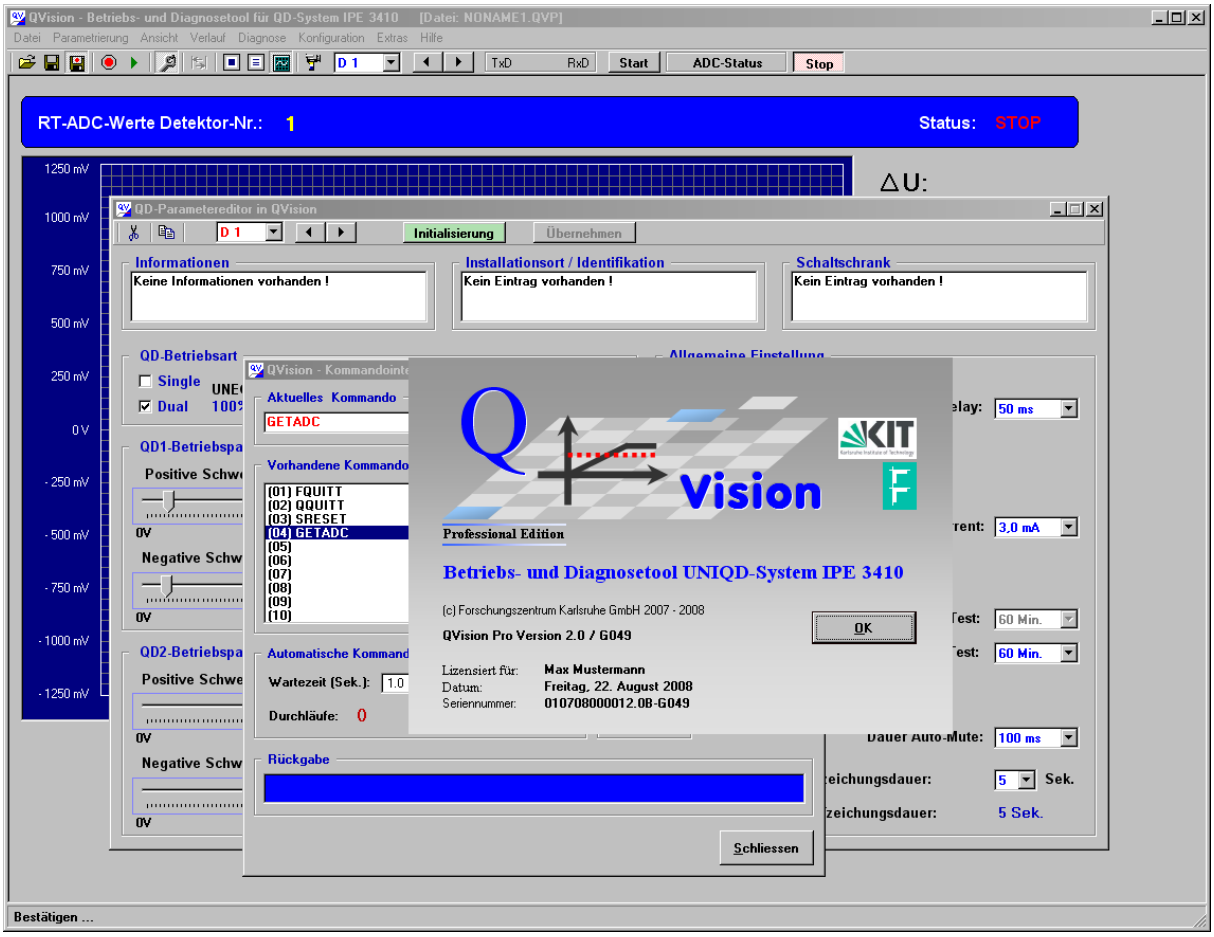

Fig. 8: Integrated Windows® operation tool "*QVision*".

QVision is a universal - all in one - multitasking software package that includes (extraction):

- Data management of up to 128 QD-Units
- QD-Unit calibration tool
- Parameter viewer / editor (e.g. balancing combined with integr. online QD-signal viewer)
- Command interpreter (for test and evaluation purposes)

- QD-Unit operation analysis and diagnostics
- QRAM viewer / QRAM reader with data export possibility (several export filters)
- Supervising monitor

The supervising monitor includes an automatic quench event and error logging of the QD-system, supervision of QD-Unit operation, read-out and back-up of all QRAM´s after quench event and calculation / generation of quench event time schedules. Along supervision operation continuous data recording is selectable (data base loader to Microsoft SQL is available).

Test of QD-system at CEA / Saclay - Results / Outlook

Until 08/2008 a total amount of 160 QD-Units have been manufactured by FZK. A subset of the QD-System Type IPE 3410 has been successfully tested by IPP / Greifswald in November 2008 at the superconducting W7-X Coils in Saclay (test facilities of CEA).

Along proofing different balancing procedures at constant current slope with di/dt = 50A/sec (I_{max} = 17KA) the test at CEA / Saclay was completed successfully by intended quench event generation through temperature raising inside the cryostat. No complaints regarding hardware or software-functionality of the QD-system are known after test at present. All test procedures have been performed at planar and non-planar W7-X coils.

The described Quench Detection System developed by FZK could be a guideline for the Quench Detection System at ITER. There are few different requirements particularly with regard to high voltage potential separation (min. 34 KV at ITER). Limiting factors at FZK-QD-Unit is primarily based at QD-lead´s HV-Plug (max. 18KV) and the DC/DC-Converter used in the detectors built-in power supply. General design of QDU electronics should be able to withstand high voltage potential separation in the range up to 50 KV without changes.

Staff:

A. Bacher
H. Demattio
A. Ebersoldt
K. Petry
S. Stricker
D. Tcherniakhovski

Literature:

[1] D. Birus et al., Development of Quench Detection System for W7-X, Fusion Engineering and Design 82 (2007) 1400 - 1405

[2] Jäger GmbH, ADWin Pro Messwerterfassungssystem, Produktbeschreibung Lorsch 2006

Development of HTS-Roebel-cables

Roebel-cables **A**ssembled from **C**oated **C**onductors (**RACC**) were introduced by FZK as high current low AC conductors for application in windings and magnets. This concept is the only so far for the second generation (2G) High Temperature Superconductors (HTS), which provides the necessary features as segmentation of the superconductor into different percolation paths (strands) which are in addition transposed along the conductor. Goal of the R&D work is to establish a reliable preparation method, to test the potential of current carrying capability of this concept, to learn about the cable details and to investigate possibilities to implement this cable design to larger cables which are suited for fusion magnets.

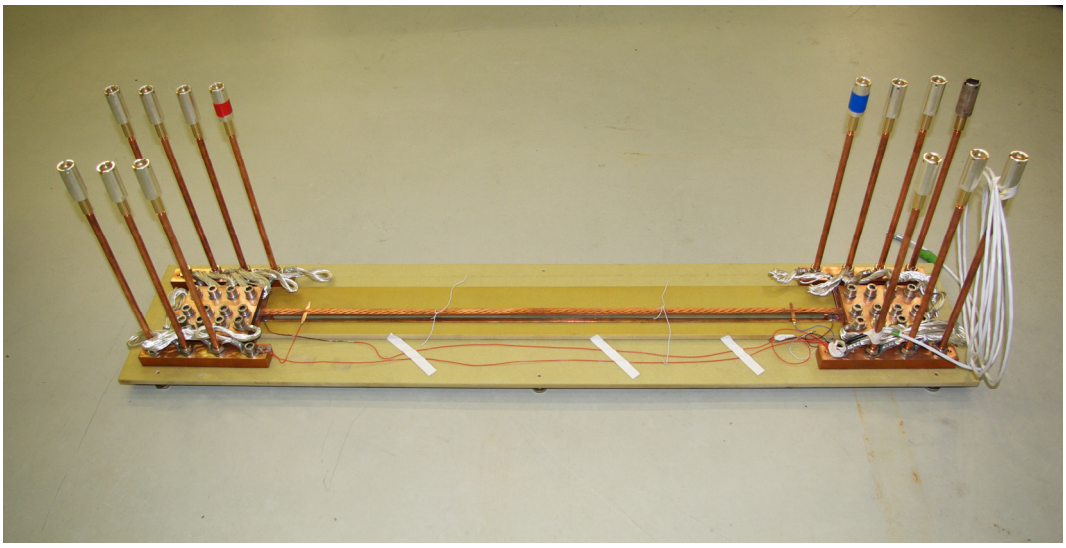

Fig. 1: 2.6 kA RACC-cable with 1.1 m length mounted in the test rig.

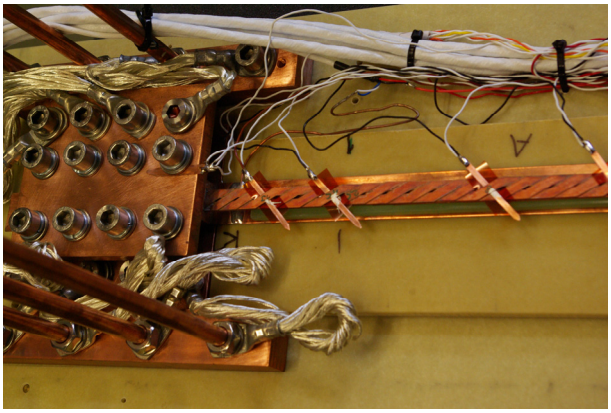

Fig. 2: Current feed-in section of the RACC cable.

Status of the work was a RACC-cable with 1 kA transport current in self field and 0.36 m lengths produced from commercial SuperPower CC material. The behaviour of the cable under excitation was excellent and stable. The preparation method, in particular the punching step, could be qualified as a very precise technique suitable for automatic long length production. The challenge of this reporting period was primary to prove a way for an upgrade of the transport current and the sample length. The sample should serve to investigate current distribution effects and the conditions for the current feed-in. The solution for the upgraded design was the increase of assembled CC. applying 3 tapes in each of 15 strands. The transposition width of the 15 strands was the same, 19 cm, and the cable length of 1.1 m allowed 6 transposition lengths (see Figs. 1 and 2). The characterisation of the cable was performed by monitoring the cable current on 3 strands over several transposition lengths and over the both feed-in sections.

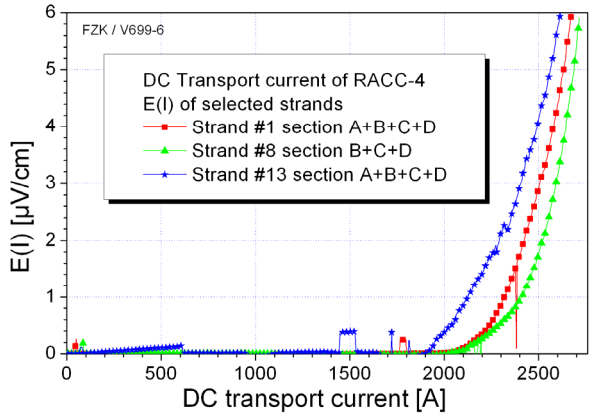

Fig. 3: Critical current measurement on three strands (spikes and steps come from movements in the cable (Lorentz Forces).

A transport current of 2628 A was measured (5 V/cm) reproducibly (see Fig. 3) at 77 K. Measurements of the current in different transposition sections showed very different behaviour, indicating effects of current redistribution (Fig. 4). This is an indication that a moderate strand coupling is desirable for a future technical cable to assist current redistribution effects. Strand coupling effects and the related influence on the AC losses was investigated on smaller RACC cables. The characterisation of the current feed-in showed that the contact length of half a transposition length is too short to serve for a good current percolation. Modelling the self field effect could explain the quite high current degradation of 60% (Fig. 5). The field anisotropy is expected to reduce in windings and the self field induced current reduction will become smaller. The self field model could also in this cable explain the measured current as is shown in Fig. 6 with the load line and the expected cable current of 6727 A without self field degradation.

Summarizing the results, the current upgrade of the RACC cable was very successful. Since the new concept allows a further increase of the number of CC's applied in the cable and a longer transposition length, a further large increase of the transport current is possible. It is planned to demonstrate this in a new cable. The developed RACC concept represent the 5 kA class cable at 77 K and the 10 kA class cables at 65 K operation temperatures. Technical investigations and modifications will be continued on the existing cables. Investigations on small cables of 4 mm width will start. The RACC cable technique is planned to be used as the fundamental module for future cable concepts for fusion magnets (DEMO) with > 20 K operation current.

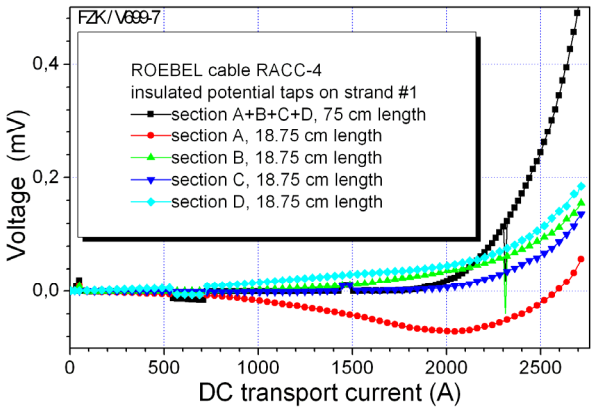

Fig. 4: Current measurement in 4 sequential transposition sections of one strand, showing inhomogeneous current distribution in the cable.

Staff:

W. Goldacker
A. Drechsler
R. Heller
A. Kudymow
A. Kling
C. Schmidt
S. Terzieva

Literature:

[1] W.Goldacker, A.Frank, A.Kudymov, R.Heller, S.Terzieva, A.Kling, C.Schmidt, "improvement of superconducting properties in ROEBEL assembled coated conductors (RACC)", Appl.Superc.Conf. ASC 19th-22nd.Aug.2008, sub.to Procc. Adv. Appl. Superc.

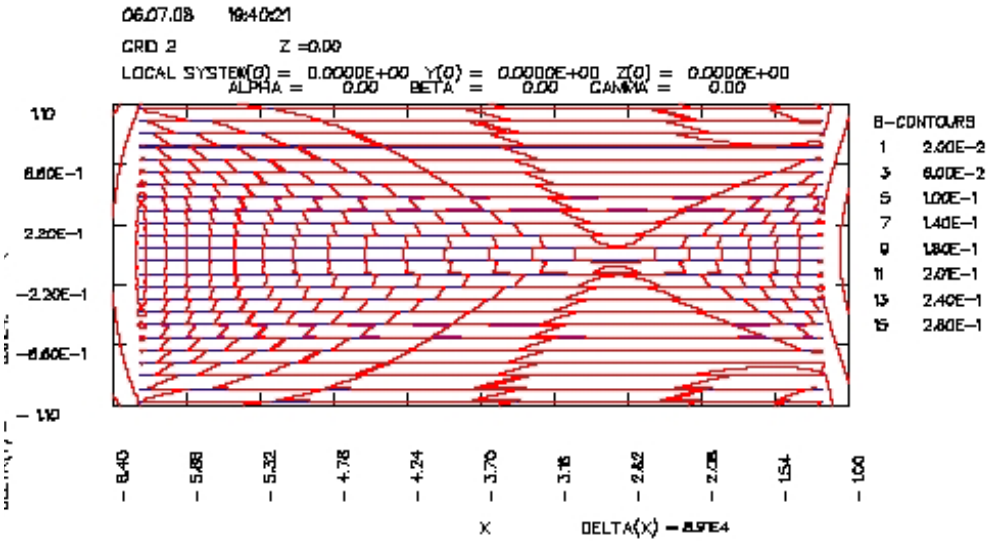

Fig. 5: Self field pattern from modelling in one cable side.

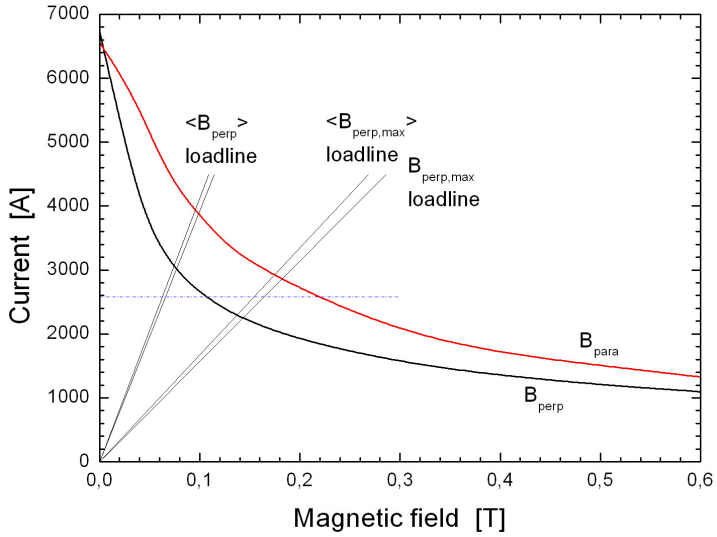

Fig. 6: Expected cable current without self field effect and load lines (details see ref. 1), the measured cable current is indicated by a horizontal line.

TOSKA Refurbishment and Preparation for Coil Testing

TOSKA was refurbished in 2007/2008 as a back up for W7-X coil testing in the case that the coil test facility in Saclay would have severe problems. The TOSKA system was adapted to cool down three W7-X coils in parallel with a complete revision of the cryogenic system. A complex pipe system was installed with multiple valves, capillaries, venturies and all necessary sensors. The complex cryogenic system is now prepared to host three coils with a new developed process measuring and control system. A new data acquisition and quench detection system was built up to cover three coils. The current supply was equipped with fast current switches and a special current distribution to power the three coils individually using four 30 kA current leads. The system is online and ready to host coils.

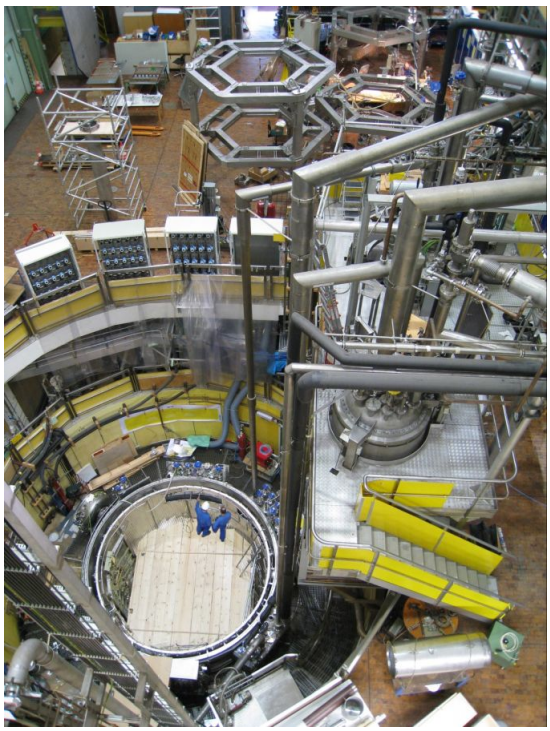

Overview of TOSKA facility during preparation for W7-X coil testing

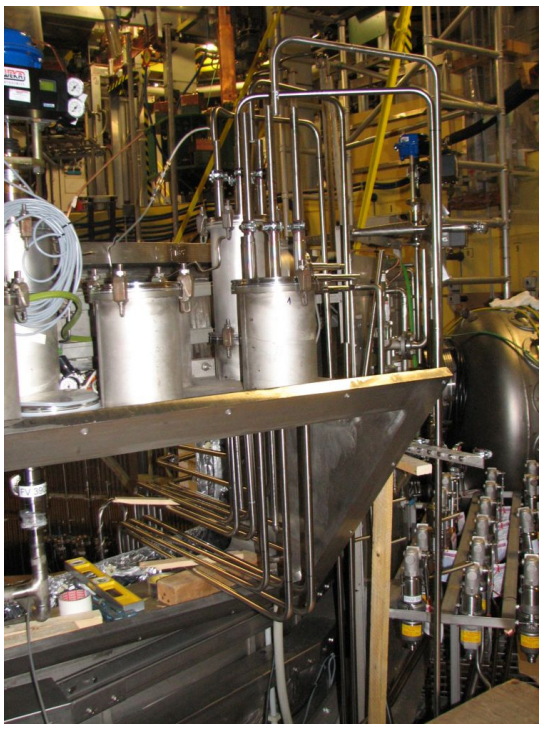

Complex cryo infrastructure was installed to host three coils in cryostat B300.

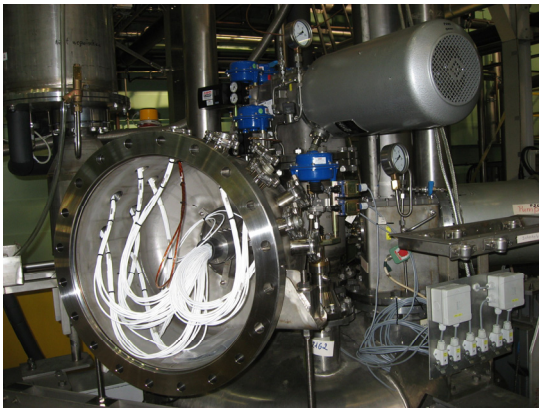

Sensor feedthrough from control cryostat B250

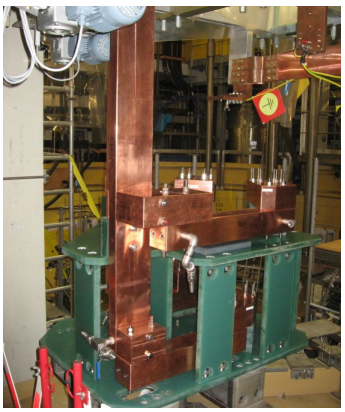

Current distribution system to load three coils individually with 19 kA

Staff:

M.S. Darweschsad
G. Dittrich
W.H. Fietz
S. Fink
U. Fuhrmann
B. Ganninger
M. Gehrlein
R. Heger
M. Heiduk
H. Lahn
C. Lange
V. Leibbrand
R. Lietzow
I. Meyer
T. Möhring
R. Müller
R. Rotondo
U. Saller
E. Specht
M. Süßer
V. Zwecker

Cryogenic Infrastructure

Introduction

The cryogenic infrastructure of the Institute for Technical Physics (ITP) supplies different experiments within the ITP and other institutes of the Forschungszentrum Karlsruhe, which are working for the Fusion Programme with refrigeration power or liquid helium. Such experiments in the ITP are tests of superconductive components in the TOSKA facility, experiments for the ITER-cryopump in TIMO, and mechanical material tests in different cryostats equipped with traction engines.

For these experiments the cryogenic infrastructure comprises among other things:

- A 2 kW-refrigerator at 4.4 K with a liquefaction rate of 21 g/s (equivalent to 600 litres/h), see Fig. 1.
- A 300 W-refrigerator at 1.8 K with a liquefaction rate of 5 g/s (equivalent to 145 litres/h), see Fig. 2.

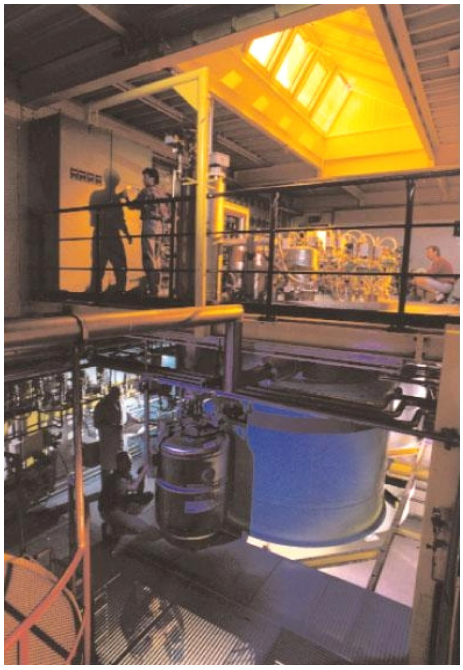

Fig. 1: Valvebox and Coldbox of the 2 kW- refrigerator.

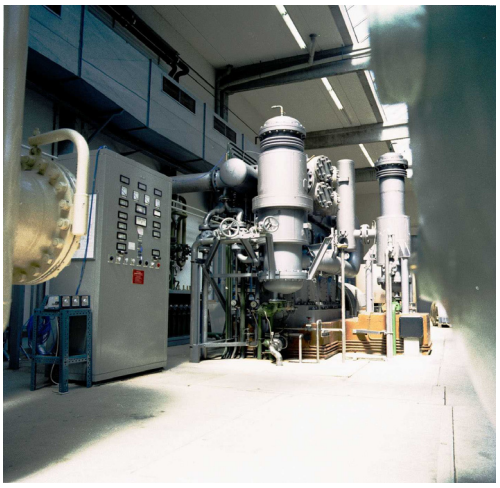

Fig. 2: Helium dry-running compressor of the 300 W-refrigerator.

- A high pressure helium purifier working at 200 bar with a continuous purification mass flow of 14 g/s and a discontinuous purification mass flow of 28 g/s. The residual impurity content is lower than 1 ppm.
- Three recovery compressors with a pressure increase from one to 200 bar and a maximum mass flow of 26 g/s or 527 standard cubic meter respectively.
- A helium storage system consisting of:
  - stationary liquid helium vessels with a capacity of 15,000 litres or 1,875 kg respectively
  - storage tanks for impure helium with a capacity of 1,075 kg
  - storage tanks for pure helium with a capacity of 1,275 kg

The whole storage system has consequently a capacity of 4,225 kg or 23,985 standard cubic meter respectively, see Fig. 3.

- A liquid nitrogen storage vessel with a capacity of 32,650 litres for the supply of all experiments and a filling station to distribute liquid nitrogen in transport vessels.

Fig. 3: Helium storage system.

The cryogenic infrastructure is controlled by a state-of-the-art control system based on PCS7 and WinCC. The operation of the components can be done in two control rooms or via clients installed directly at the experiments.

A team of five operators, three engineers and one academic staff member is responsible for maintenance, repair, upgrading and extension of the cryogenic infrastructure for new or changed experiments.

Additional tasks are the supervision of peripheral installations such as

- energy distribution system
- re-cooling water unit
- compressed-air distribution system.

Also, maintenance, repair, upgrading and extension of the

- vacuum systems
- different safety devices like oxygen monitors

are tasks of this group.

Beyond these regularly routine works this report is focused on selected extension projects, as well as giving an overview of the cryogenic supply activities for fusion projects.

Selected maintenance and extension works

<u>300 W (1.8 K) refrigerator</u>

The following selected maintenance and extension work at the 300 W-refrigerator were done in 2008:

- Installation of new valve-positioners
- Installation and tests of a new cooling aggregate for improved oil removal
- Reorganization of PCS7/WinCC-Server within a new cabinet. In addition a new programmic PC was installed in the cabinet to allow on-site changes.
- Implementation of a new data concentrator based on PCS7. In addition this new data concentrator was connected to the TIMO control system, also based on PCS7. For this the software was installed and successfully tested. Also a gateway between the Teleperm system and the PCS7 ethernet bus-system was implemented, see Fig. 6.
- Repair of the cold valve for the 5,000 litres vessel of the refrigerator.
- Revision of the compressor, see Fig. 4.

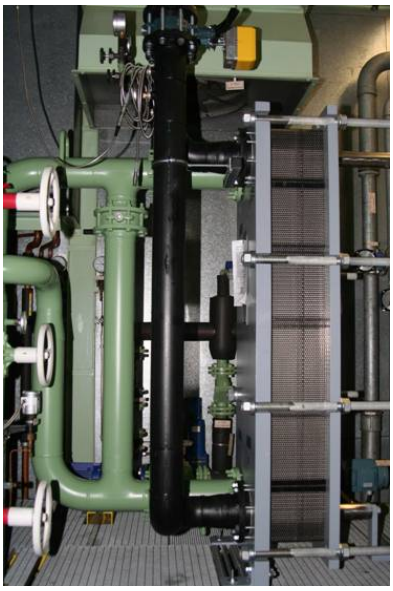

Fig. 4: Driving mechanisms of the helium dry-running compressor of the 300 W-refrigerator.

Fig. 5: New connection of the water cooling for the 2 kW-refrigerator to the water re-cooling unit.

2 kW (4.4 K) refrigerator

The following selected maintenance and extension works at the 2 kW-refrigerator were done in 2008:

- Connection of the water cooling to the water re-cooling plant, see Fig. 5.
- Reorganization of PCS7/WinCC-Server within a new cabinet. In addition a new programmic PC was installed in the cabinet to allow on-site changes.
- Change and improvement of the relays for the pressure monitoring, see Fig. 6.
- Change and repair of a ventilator for the cooling water unit.

a) b) c) d)

Fig. 6: a) PCS7 / WinCC Server of 300 W-refrigerator within a new cabinet;
b) new programmic PC within the cabinet to allow on-site changes;
c) new data concentrator based on PCS7;
d) PCS7 / WinCC Server of 2 kW-refrigerator within a new cabinet

He-recovery and purification system

The following selected maintenance and extension works at the He-recovery and purification system were done in 2008:

- Implementation and test of a new WinCC panel for the purifier.
- Implementation of new temperature sensors in one He-compressor.
- Improvements of the new sound cover by implementation of:
  - lamps
  - automatic exhaust air control
  - pluggable connections for an easier assembly and disassembly of the sound cover
  - flow meter for the chemical sewage water
  - ultrasonic measuring transducer for the gasometer

Miscellaneous

- Modifications on some oxygen sensors.
- Reorganisation and extension of the complete control system.
- Integration of some parts of the TOSKA in the control system of the cryogenic infrastructure.

Cryogenic supply for the Fusion Programme

The different experiments for the Fusion Programme in ITP are supplied with circa 14,000 litres liquid helium or 10,000 standard cubic meter. In addition the refrigerators ran nearly 270 hours in 2008 for the supply of refrigeration power.

For comparison, the average consumption for such experiments in the period between 2001 and 2007 is about 27,400 litres liquid helium or 19,500 standard cubic meter respectively and 2,400 hours of refrigeration power. So in 2008 we had a significantly lower consumption than the years before. This decreased consumption was caused by the time consuming structural reconstruction work for new experiments in TOSKA and TIMO which also resulted in modifications of the cryogenic infrastructure.

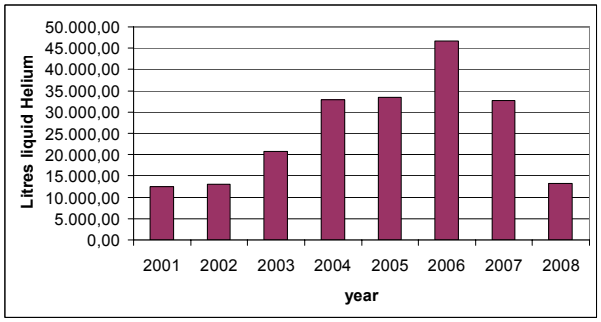

Fig. 7: Liquid helium supply between 2001 und 2008.

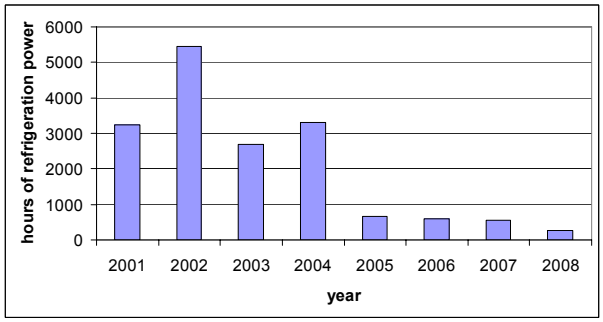

Fig. 8: Hours of refrigeration power between 2001 und 2008.

Staff:

A. Baumgärtner
S. Bobien
M. Duelli
H. Neumann
B. König
K. Metzger
E. Ternig
D. Wetzel
H. Zimmermann

Breeding Blanket

TW5-TTB-001
Construction of the High Pressure Helium Loop (HELOKA-HP/TBM) for Testing of Test Blanket Modules (TBMs)

The objective of this task is to construct the HELOKA-HP/TBM loop as presented and agreed in the “EFDA HELOKA Assessment Report” in a renovated building of FZK comprising the purchase of loop components and supply systems, acceptance tests at the manufacturer’s site, installation, commissioning and acceptance tests.

In 2008 substantial progress has been achieved in the following areas:

The water cooling system of the experimental hall (building 660) was completely revised. New equipment such as a complete instrumentation, new motors, new water distribution, a water quality management system, a test section for heaters including thyristor power equipment, new valves and more was installed and put into operation. The data acquisition and control system (DACS) for the water cooling system was installed and put into operation. This system is the basis for further HELOKA DACS systems such as the helium cycle control unit and the TBM data acquisition system.

Fig. 1: HELOKA support structure.

Further more the support structure for the helium loop was completed (Fig. 1). The calculation and layout of the piping system was completed and the technical documents for the technical inspection authority were finalized. The pipes were ordered, supplied and sent to a specific company to perform the bending processes according to the technical documents.

A number of key components were supplied and tested in regard on helium leak tightness at FZK site: helium heater, helium cooler, helium control valves, filter unit and others. Further equipment was ordered, e.g. instrumentation such as flow meters.

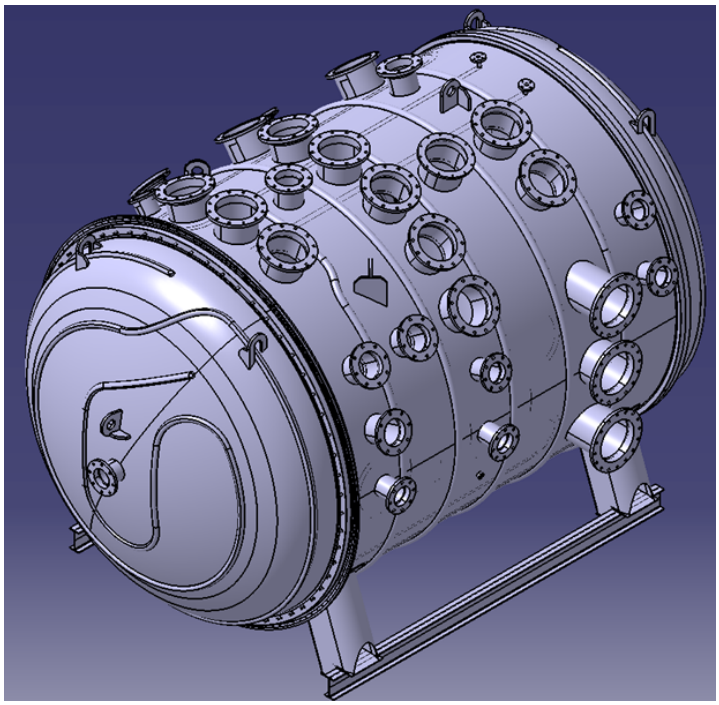

Fig. 2: Design of the vacuum vessel.

In addition, the test section was specified and the detailed design of the vacuum vessel was finalized (Fig. 2). Further work was performed to develop the internal structures in the test vessel such as support frames and heat shields.

Staff:

S. Berberich
B.-E. Ghidersa
T. Ihli
A. Jianu
Ch. Klein
E. Magnani
V. Marchese
G. Messemer
G. Porempovics
N. Prothmann
J. Rey
E. Stratmanns
V. Szabó
K. Tian
A. Von der Weth

TTBB-001
Helium Cooled: TBM Design, Integration and Analysis

TW5-TTBB-001 D 2
Detailed Deign of Sub-components and Prototypical Mock-ups for the HCPB TBM Qualification

Subtask c) Prototypical mock up

In the frame of this task a prototypical mock up of the HCPB (Helium Cooled Pebble Bed) TBM (Test Blanket Module) has been designed. This mock up is based on the latest design of the HCPB TBM in vertical arrangement but it is limited to 2 breeder cells in toroidal and 3 breeder cells in poloidal direction. The dimensions of the breeder cells are full size. The design is corresponding to the vertical TBM arrangement. The manufacturing technology is based on the processes and technology suggested for the assembly of the real full scale TBM. The prototypical TBM mock up is designed for installation in a test facility (e.g. HELOKA) to be tested under ITER relevant conditions (8 MPa; 300°C inlet temperature). To simulate the surface heating as well as the volumetric heating the MU will be equipped with heater devices which will be integrated in the MU in detail in the next step of the design. Figure 1 shows a cross section through the TBM MU box (breeder unit not included) indicating the compartment for the 6 breeder cells. Figure 2 indicates the main outer dimensions of the prototypical 6 cell mock up of the TBM.

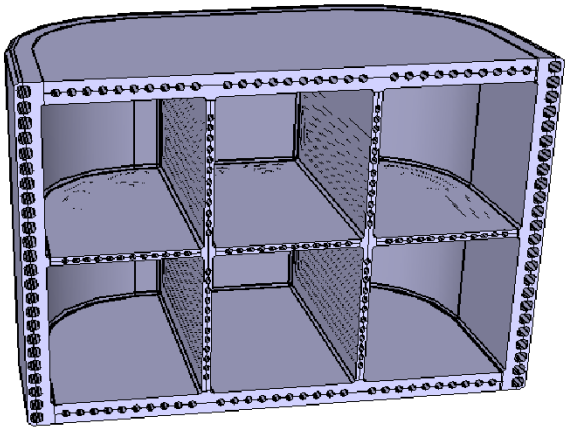

Fig. 1: Cross section of the 6 cell mock up.

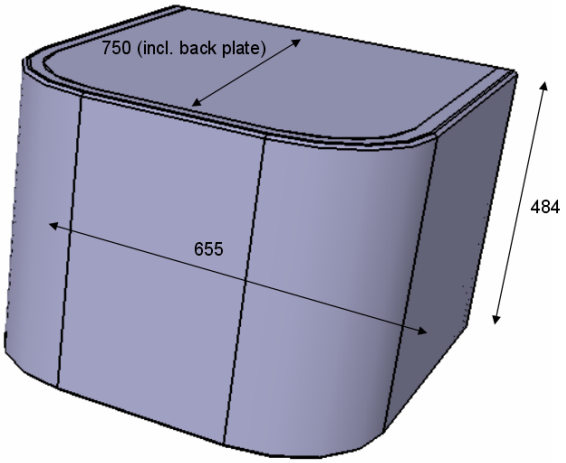

Fig. 2: Outer dimensions of the 6 cell mock up.

Subtask d) Manufacturing mock up

In the frame of this activity a mock up has been designed to demonstrate relevant TBM manufacturing and assembly processes which are currently available. The TBM box designed for accommodation of two breeder chambers consists of a first wall with the dimensions of 500 mm x 800 mm manufactured by HIPping. The feasibility of this sub-component has already been demonstrated in 2007. The first wall will be bended (90°) and connected to the caps, one vertical and one horizontal grid plate. The grid plates are represented by solid plates only including dummy cooling channels close to the welding environment to simulate realistic welding conditions. A dummy breeding unit back plate as well as a simplified manifold structure will be added to include all kinds of TBM relevant welding processes. After manufacturing the mock up will be used for destructive material tests. Figure 3 shows the integral MU and Figure 4 indicates a cross section through the mock up.

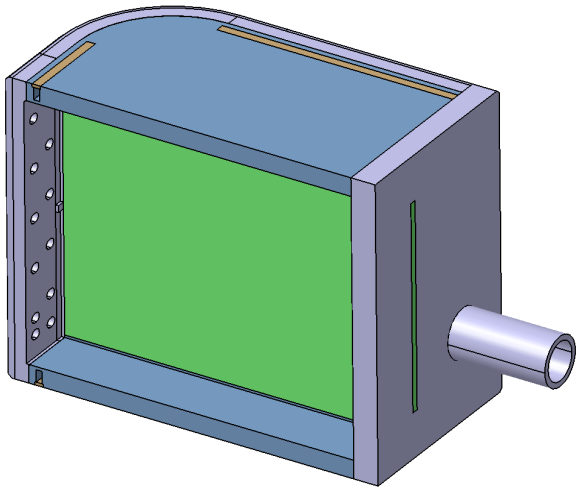

Fig. 3: Manufacturing mock up.

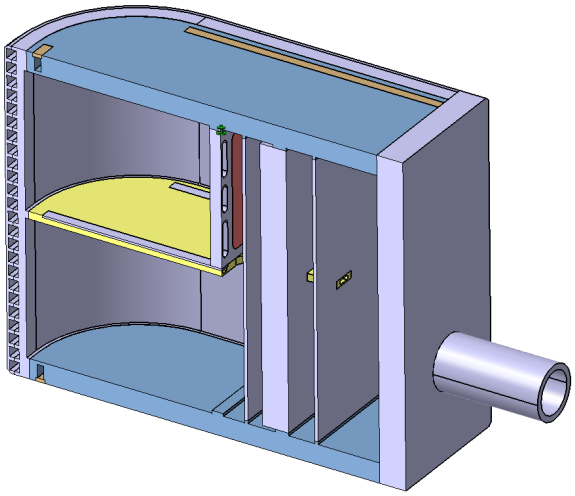

Fig. 4: Cross section through the mock up.

Staff:

O. Bitz
F. Cismondi
M. Lux
H. Neuberger
J. Rey

TW5-TTBB-001 D 8
Detailed HCPB TBM Development Work Plan and First Technical Specification Document

Objective

The objective of this task is to contribute together with the EFDA management to the preparation of the task breakdown, the work plan and the technical specification document for the HCPB TBM.

Results in 2008: Technical Specification of the HCPB System

Technical specifications have been defined for the HCPB TBM System. The reference design will be described in the following; it is based on the assumption that one equatorial port of ITER is available for testing the two TBMs based on the concepts supported by the EU (HCPB and HCLL, respectively). In particular the HCPB blanket concept [1] for DEMO and the future fusion power plant has been developed starting from the nineties under the leadership of the Forschungszentrum Karlsruhe. A vertical configuration (i.e. the two TBMs are hosted in the Port side by side) has been selected as common solution for the HCLL and HCPB concept as compromise among the respective testing needs. The two concepts have been standardised to an external dimension of the box of 484 mm (toroidal) x 1660 mm (poloidal) x ~700 mm (radial).

The design of the HCPB TBMs had a constant evolution in the last years; these steps are documented in a series of papers of FZK for the HCPB TBM, presented during the major fusion conferences [2, 3, 4]. With the decision of adopting a common vertical configuration, the two TBM designs are converging to a very similar architecture of the box. Main feature of this new common design is the use of a U-shaped FW with channels in poloidal-radial direction. A detailed description of the FW design and an assessment of the relevant thermo-hydraulics performances for the HCPB TBM are reported in [4]. For the design of the breeder zone and of the manifolds the adopted solution was already presented in previous papers [4].

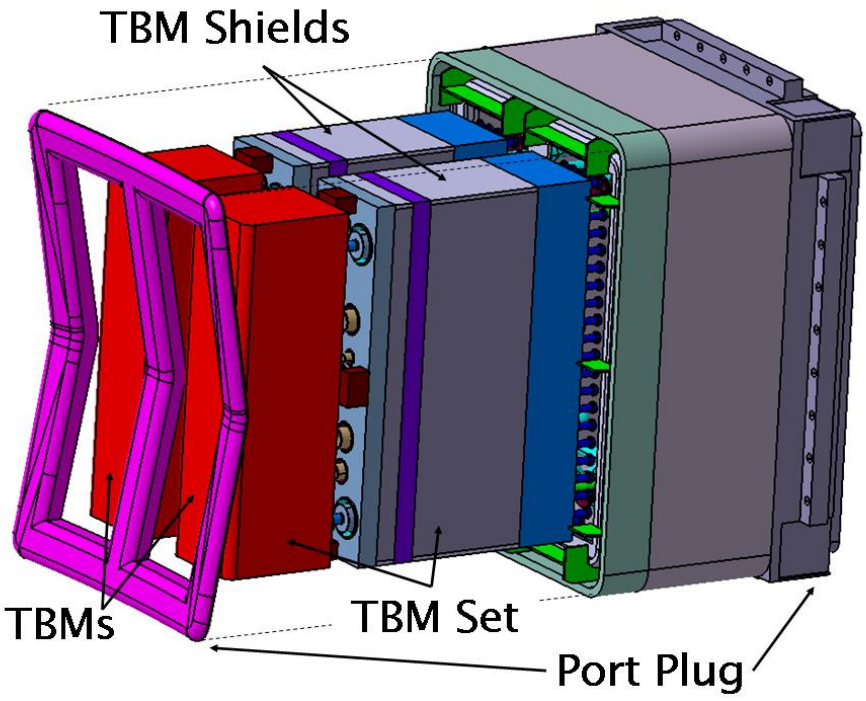

Fig. 1: View of the 2 TBM Assemblies mounted inside the TBM Port Plug Frame in vertical configuration. Part of the side walls of the frame have been removed to allow the view of the TBM Assemblies.

The TBMs back wall features a series of pipe connections necessary for the cooling and tritium extraction. In the HCPB system the tritium is extracted by the solid materials by means of a He flow; a low pressure purge flow is pumped into the pebble beds and the outlet flow containing tritium is sent directly to a dedicate equipment that provides the removal of T from the He carrier, the T accountancy and finally the H isotopes (and impurities) transfer to the ITER Fuel Cycle. The present version of this system, whose main components are located in the tritium building, has been designed by ENEA and is described in [5].

The integration of the two EU TBMs in the Port Plug follows a design suggestion of ITER in which an assembly (later referred as “TBM Set”) constituted by the TBM itself and a water cooled shield (see Figure 1) is inserted by means of a bolted flange in a PP frame. This configuration allows an independent exchange of the 2 TBM Sets in the ITER Hot Cell. Each TBM Set can be manufactured/assembled as a block in the workshop and delivered to ITER where it can be mounted into the Port Plug; after the testing in ITER the TBM Set can be removed from the Port Plug frame and the frame reused in a later test campaign [6, 7, 8].

The TBM connecting pipes are routed through the TBM shields, the equatorial port extension, the cryostat boundary and the Bio-shield Plug to reach the Port Cell (PC) behind. From there the main He coolant pipes and the tritium lines continue in the ITER building to reach the areas dedicated for the helium cooling and processing equipments.

In addition the port cell area should accommodate a variety of TBM system subcomponents. In particular the following systems have been identified: 1) some components of both helium coolant systems (HCSs) like valves and piping for the control of the flow and the insulation of the TBMs; 2) the PbLi loop (component that appears only in the HCLL concept), including the T-extractor; 3) few components of the tritium extraction system; 4) measurement equipments.

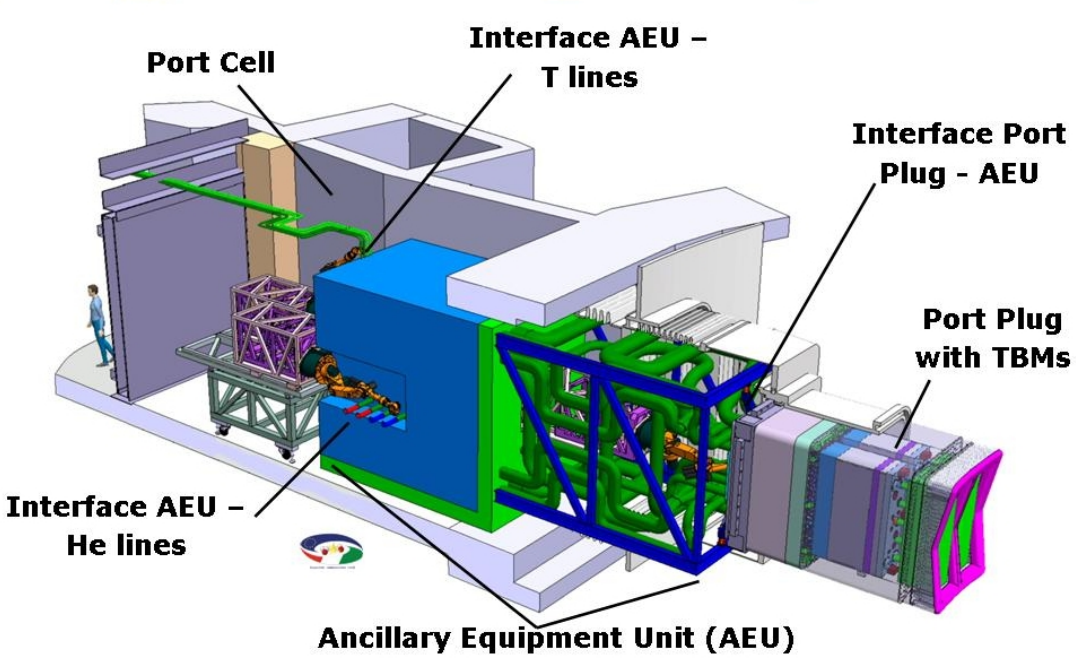

Fig. 2: Proposal of arrangement of the Port Cell area based on the AEU concept.

An arrangement design for the PC area has been proposed by FZK and HAS; according to this design all these sub-components will be arranged into one unique assembly, the Ancillary Equipment Unit (AEU). This system is illustrated in Figure 2 and a detailed description of the proposal can be found in [7, 8]. The proposal includes the integration of remote handling equipment that should be used for the cutting and re-welding of the pipes at the PP boundary; this interface zone is located in the port extension inside the Bio-shield, where the hu-

man access is difficult due to the pipe lay-out and to the irradiation level after neutron operation. The main advantage of the AEU concept is the limitation of interfaces required for disconnection and removal of the AEU to access the port plug for TBM exchange in the frame of ITER maintenance shutdowns.

The ITER Hot Cell should be used for several operations related to the TBM systems: the replacement of the TBM from/to the PP (as already described above), the refurbishment of the AEU and the dismounting of the TBM Set before the TBMs shipping in casks for their transport outside ITER. Furthermore, it serves for the storage of irradiated components like Port Plug or dummy TBMs that would have necessitated to be used in substitution of damaged TBMs. Dedicate equipment (in remote handling) and procedures should be developed for performing the above mentioned operations.

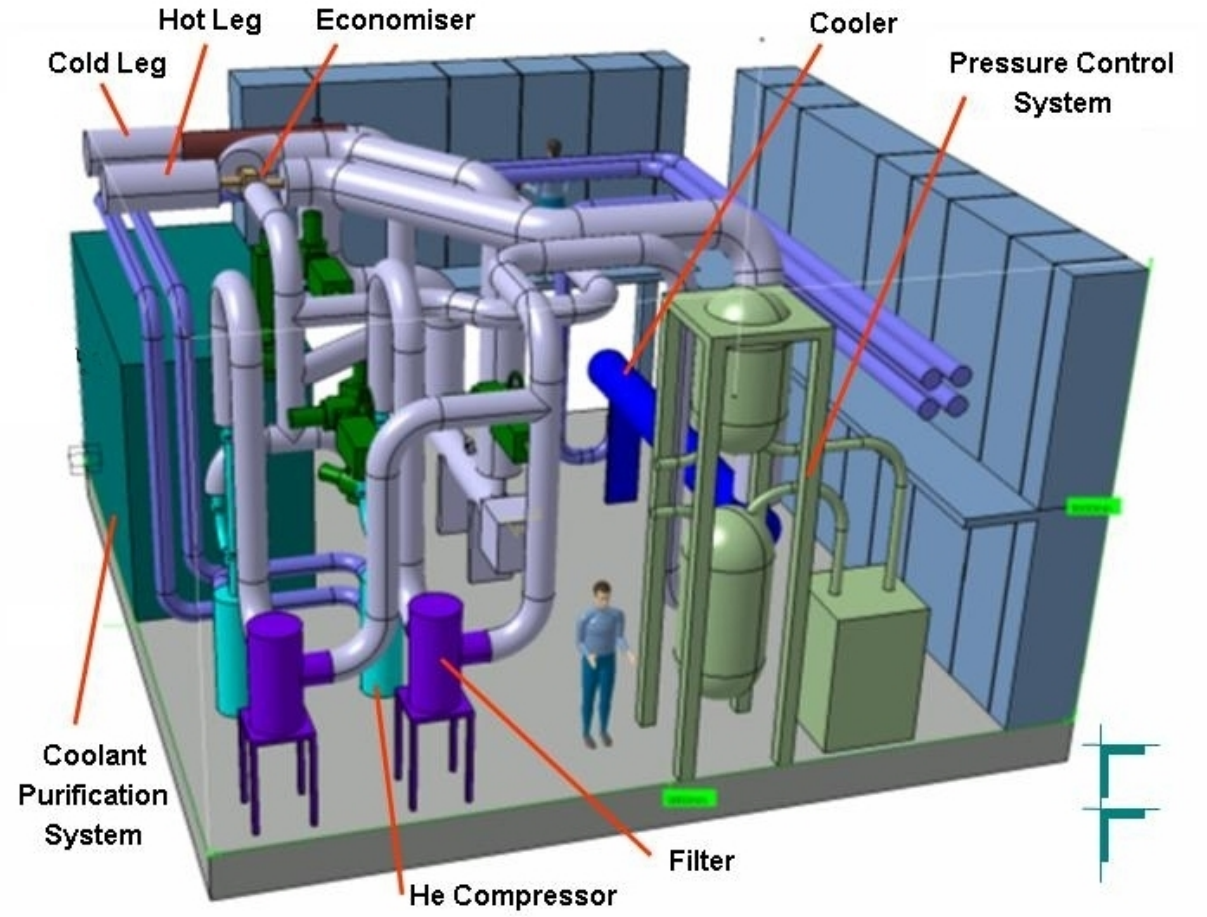

Fig. 3: View of a HCS designed to be located in the Level 3 or 4 of the Tritium Building.

Two independent HCSs are necessary to operate both TBMs. Each one of them has been designed for a max He mass flow of about 1.3 kg/s and a nominal pressure of 8 MPa. The HCS can support the TBMs with Helium at inlet temperature of 300°C and can withstand a maximum outlet temperature of 500°C (see FZK design proposal in [9]). Locations for the main components of the Helium system have been identified at level 3 and 4 of the tritium building (see Figure 3). The interface with the heat rejection system of ITER is realised with a cooler that can extract the power produced in each TBM (about 1 MW) during the fusion pulses.

It is necessary to establish typical CODAC functions for the TBM Systems (control monitoring, operational scheduling and operational plan) fitting general ITER CODAC architecture. As known instrumentation and control in ITER is distributed in three tiers (CODAC, Interlocks

and Safety) and two layers (central system and networks, local TBS as plant system). The definition of this system is only at the beginning. The next goals are to establish: 1) the characteristics of monitoring signal to be processed and the integration of TBS phase experimental testing data acquisition system within CODAC, 2) the structure of the TBS and subsystems control elements according to interlock and safety systems reacts demands; 3) scheme of communications between TBS Plant Control/TBM CODAC Network and operational requests, between TBS interlocks and central interlock networks and systems, TBS safety and central safety.

Status of the work

The final report will be finalised in 2009.

Staff:

L.V. Boccaccini

Literature:

[1] L.V. Boccaccini, L. Giancarli, G. Janeschitz, S. Hermsmeyer, Y. Poitevin, A. Cardella et al., Materials and design of the European DEMO blankets, Journal of Nuclear Materials 329-333 (2004) 148-155.

[2] J.-F. Salavy, G. Aiello, P. Aubert, L.V. Boccaccini, M. Daichendt, G. De Dinechin et al., Ferritic-Martensitic Steel Test Blanket Modules: status and future needs for design criteria requirements and fabrication validation, Journal of Nuclear Materials, in press.

[3] M. Lux, T. Ihli, J. Rey, H. Neuberger, C. Polixa, Helium-cooled Pebble Bed Test Blanket Module: alternative design and fabrication routes, Fusion Engineering and Design 83 (2008) 1249–1252.

[4] F. Cismondi, S. Kecskés, M. Ilic, G. Légrádi, B. Kiss, O. Bitz et al., Design update, thermal and fluid dynamic analyses of the EU-HCPB TBM in vertical arrangement, Fusion Engineering and Design, in press.

[5] I. Ricapito, A. Ciampichetti, P. Agostini, G. Benamati, Tritium Processing Systems for the Helium Cooled Pebble Bed Test Blanket Module, Fusion Engineering and Design 83 (2008) 1461–1465.

[6] H. Neuberger, L.V. Boccaccini, T. Ihli, R. Roccella, A. Tesini, O. Bede, Design of the integration interface between the EU HCPB TBM and the ITER TBM Port Plug including operations for connection, Fusion Engineering and Design 83 (2008) 1861–1864.

[7] O. Bede, I.G. Kiss, H. Neuberger, A. Piros, J. Recski, Test Blanket Module maintenance operations between Port Plug and Ancillary Equipment Unit in ITER, Fusion Engineering and Design 83 (2008) 1865–1869.

[8] S. Madeleine, A. Saille, J.-P. Martins, J.-F. Salavy, N. Jonquères, G. Rampal et al., Engineering studies for integration of the TBM Systems inside an ITER Equatorial Port Plug, Fusion Engineering and Design, in press.

[9] H. Neuberger, X. Jin, L.V. Boccaccini, B.E. Ghidersa, R. Meyder, Helium Loop for the HCPB Test Blanket Module, Fusion Engineering and Design 82 (2007) 2288–2293.

TW5-TTBB-001 D 9
Experimental Verification of Pebbles Filling in the HCPB TBM

In the frame of this task strategies have been developed and experimentally investigated to fill the pebble beds of the HCPB-TBM after manufacturing of the TBM box. The filling procedures have been simulated by using a full scale mock-up of the breeding unit made by Plexiglas. Parameters of the filling process have been varied to optimize the procedure of filling of the pebble beds. Conclusions have been drawn with regard to the latest design of the HCPB-TBM BU as well as changes in the filling strategy (e.g. performing the PWHT of the TBM box with breeding ceramic material already inserted). Summarizing the results of this experiment it can be concluded that the filling of the HCPB-TBM breeding unit has been demonstrated successfully. Figure 1 shows the experimental equipment used for this study. Figure 2 shows the improvement of the package density due to optimization of the package process.

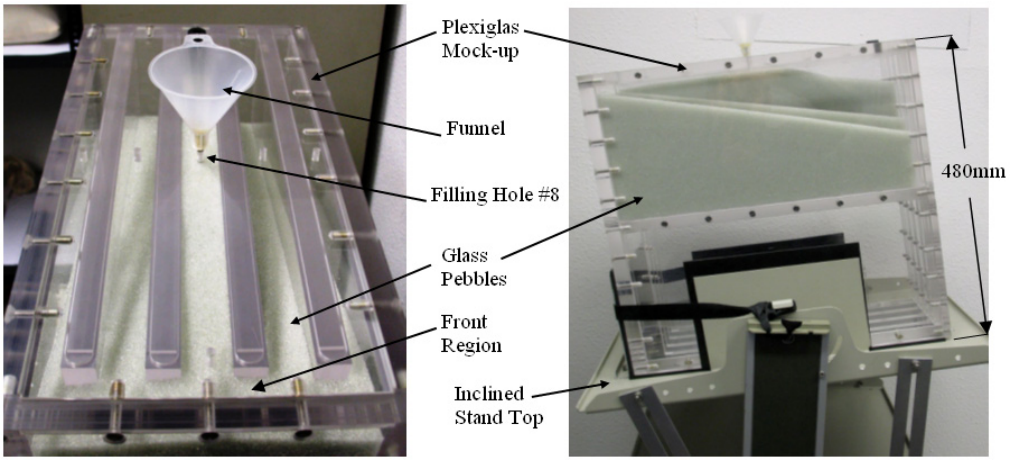

Fig. 1: Experimental facility.

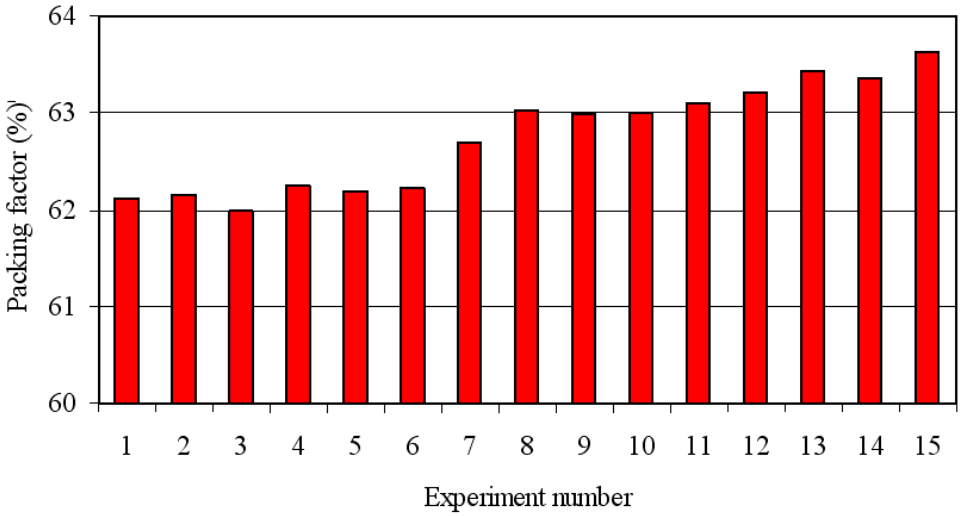

Fig. 2: Package densities.

Staff:

A. Abou-Sena

Literature:

[1] Experimental investigation on the possible techniques of pebbles packing for the HCPB test blanket module, Ali Abou-Sena, Heiko Neuberger, and Thomas Ihli, FZK-EURATOM, Forschungszentrum Karlsruhe, D-76021 Karlsruhe, Germany; SOFT 25

TW5-TTBB-001 D 10
Manufacturing and Testing of a FW Channel Mock-up for Experimental Investigation of Heat Transfer with He at 80 bars and Reference Cooling Conditions. Comparison with Numerical Modelling

Introduction

The HETRA experiment has been motivated by corresponding three-dimensional (3D) numerical analyses which revealed significant effects of the asymmetrical heat loads on the cooling of the first wall. These analyses have shown that the heat transfer coefficient in the first wall is ~15% lower than predicted by one-dimensional heat transfer evaluations based on Dittus-Boelter-like correlations and that satisfactory cooling of the first wall can be achieved only with hydraulically rough channels. The verification of the methods developed is going to be done on the basis of the results of the HETRA experimental campaign. A single first wall channel will be tested in a Helium cycle at 8MPa, while the surface heat load will be represented by a set of electrical heaters. The goal of the experiment is to verify results of 3D computational analysis through: (i) detailed temperature measurements in the structure of the first wall and (ii) measurements of pressure losses in the first wall channel.

Layout of the HETRA experimental facility

The main components of the HETRA experimental facility are presented in Figure 1. The facility involves one U sweep of the first wall channel made of original steel EUROFER. Relevant parameters of the helium coolant (pressure of 8MPa, temperature from RT to 573K and mass flow rate of 0.1kg/s) are provided by connection of the HETRA test section to the HEBLO facility by two side channels shown in Figure 1. As the purpose of the side channels is to provide developed flow conditions at the entrance of the heated section, their flow cross-section is identical to the one of the first wall - square 14.3x14.3mm with rounded corners (radius of 4mm).

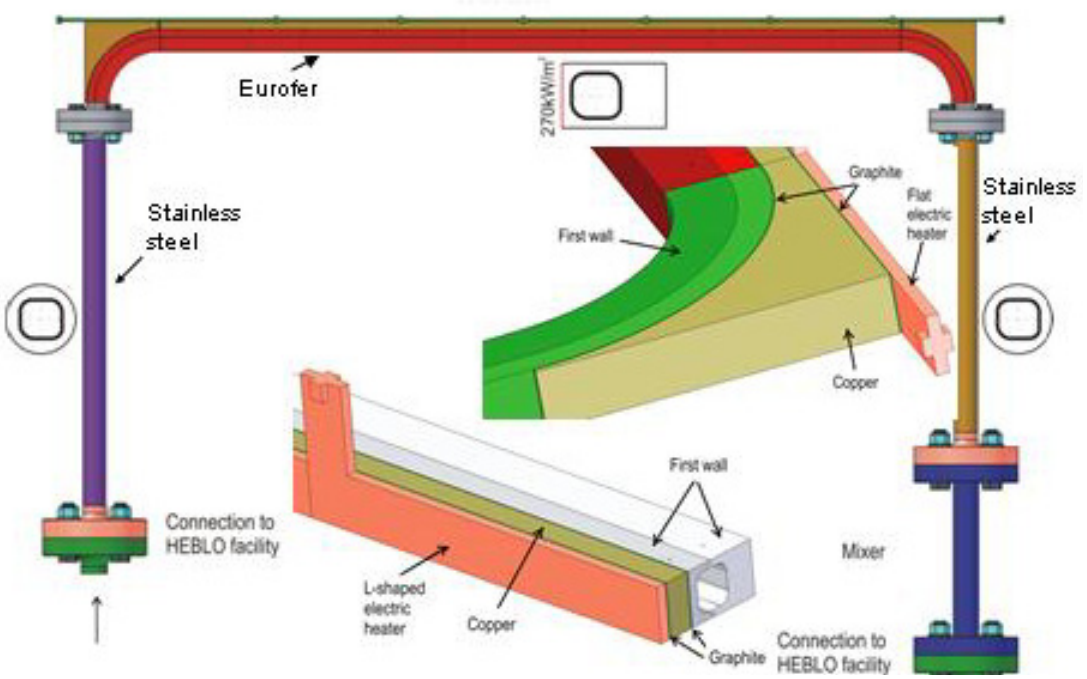

Fig. 1: Main parts of HETRA experimental facility. Inserts present arrangement of heaters at straight channels section and at channel bends.

The HETRA section to be heated involves two channel bends and a long straight section which simulates the plasma adjacent part of the first wall. This section will be heated only on one side, the representing plasma facing side. The heating of the back side of the first wall which in TBM comes from breeding units is in HETRA experiments neglected due to its multiple lower magnitude. The heat flux of 270kW/m^2 at the plasma facing side of the first wall is simulated by a set of 8 flat ceramic heaters. Inserts in Figure 1 show the heater arrangement at the HETRA heated section. To ensure uniform heat flux and to diminish effects of imperfect thermal contact, the gap between the heaters and the first wall, will be bridged by two thin graphite layers (thickness of 0.5mm) between which a 10mm layer of copper is placed. Since the results of numerical simulations showed that one-sided heating causes significant temperature gradients over the channel cross-section, at the exit of the outlet side channel a mixer is placed, which should provide a uniform helium temperature, i.e. avoid incorrect determination of the fluid bulk temperature.

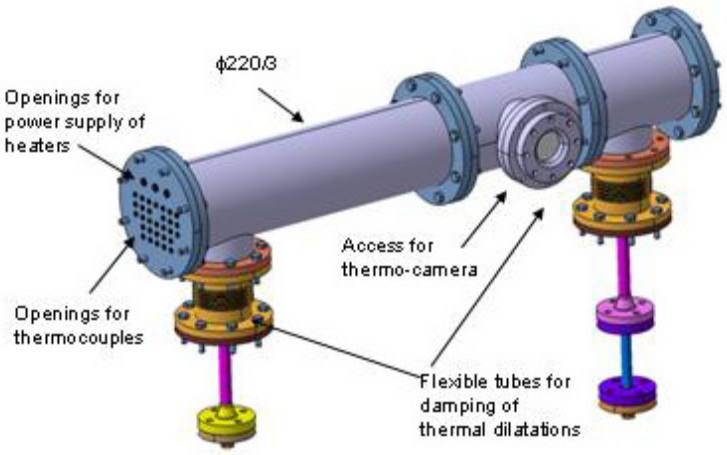

Fig. 2: Vacuum tube for isolation of the heated HETRA section.

The heated HETRA section will be thermally isolated applying the vacuum tube as presented in Figure 2. The advantage of a vacuum tube to a former design with classical thermal isolation is that an access for the thermo-camera can be made and in that way the surface temperature on three channel surfaces (which are not covered by heaters) can be recorded.

Fabrication of HETRA main parts

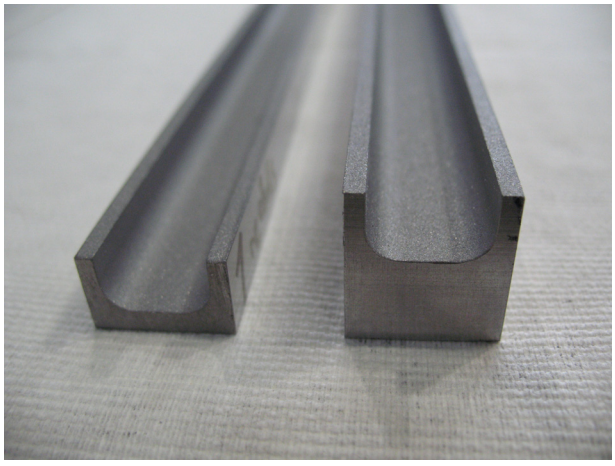

Fig. 3: Two parts of the heated straight channel section after fabrication of surface roughness: left- plasma facing part, right- BU facing part.

The channel has been divided into the following parts for the fabrication: inlet side part, outlet side part, two bends and the straight section. As the side parts are not relevant for heat transfer, they are fabricated by erosion of the channel cross-section in stainless steel cylinders with diameter of 30 mm. The wall cross-section of channel bends and the straight channel section is chosen to be relevant of the TBM first wall - a rectangle 19.3x30mm. The straight section is made by milling of channel halves in EUROFER (see Figure 3). To fabricate channel bends, channel halves are fabricated by turning into two rings (see Figure 4). The rings will be cut to produce 90^0 bends. The channel halves of both straight sections and channel bends will be connected by Electron beam welding (EB). EB welding will also be applied to connect the channel bends with the straight section. The probe with electron beam welding has already been performed and satisfactory weld properties are obtained: the welding seam does not penetrate the channel, measured hardness values are below the allowed values and fine grained structure is obtained.

The heated channel section will be connected to side channels with flanges (corresponding flange pair is presented in Figure 5). The flow cross section of flanges is the same as the one of the channel, so that no flow disturbances are induced at locations where the heated and not heated HETRA parts are connected. The flanges are from stainless steel and welded to corresponding channel parts. Use of flanges enables replacement of the heated section, i.e. use of HETRA facility for eventual future tests in which different roughness heights/types will be examined.

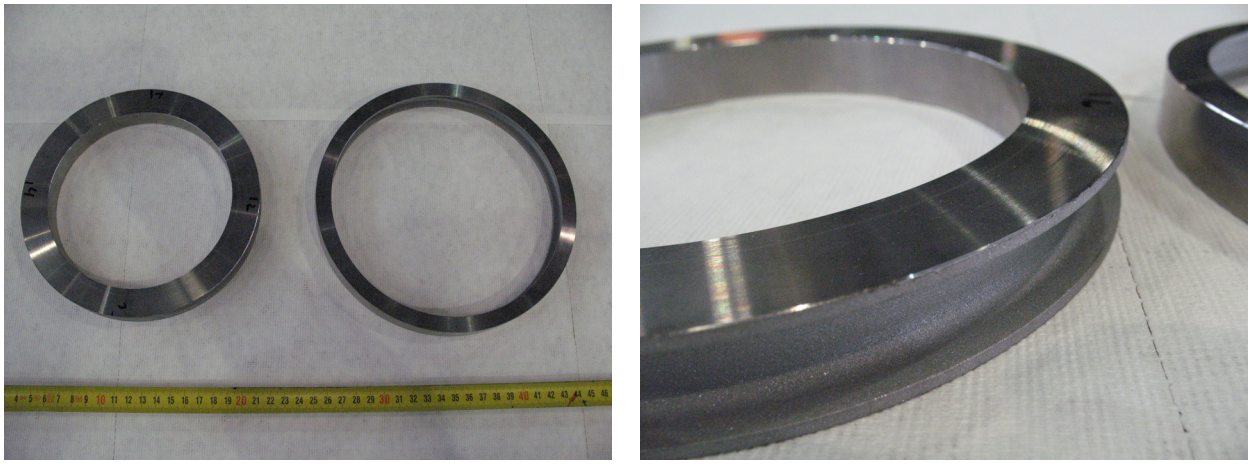

Fig. 4: Rings with turned channel halves which will be cut in 900 pieces and then welded to form channel bends. Surface roughness is also fabricated on these surfaces.

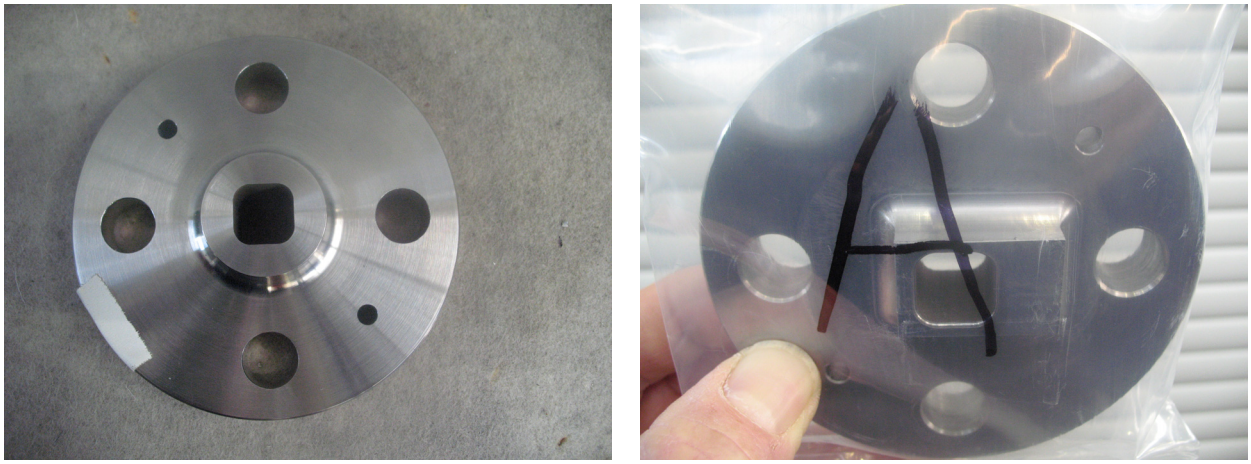

Fig. 5: Flanges to be welded on side (inlet/outlet) section (left) and on heated section (right).

The preliminary numerical simulations have shown that the reliable cooling of the first wall can be done only with hydraulically rough channel walls with the absolute roughness height of 20 μm. In relation to that, the channel walls of heated HETRA section have been roughened. The fabrication of the surface roughness was especially demanding. After numerous pretests it turned out that the best results are obtained with jets of chiselled glass particles 300-600 μm. The control measurements of fabricated wall roughness were done on several locations at the straight section and on channel bends (see Figure 6 and Figure 7). It turned out that the roughness in the range of 18-22 μm could be obtained at the front (heated side) and back walls and a roughness of 12-19 μm on side walls. This situation is caused by different angle of the particle jet in two cases. The roughness height could not be measured at rounded channel surfaces.

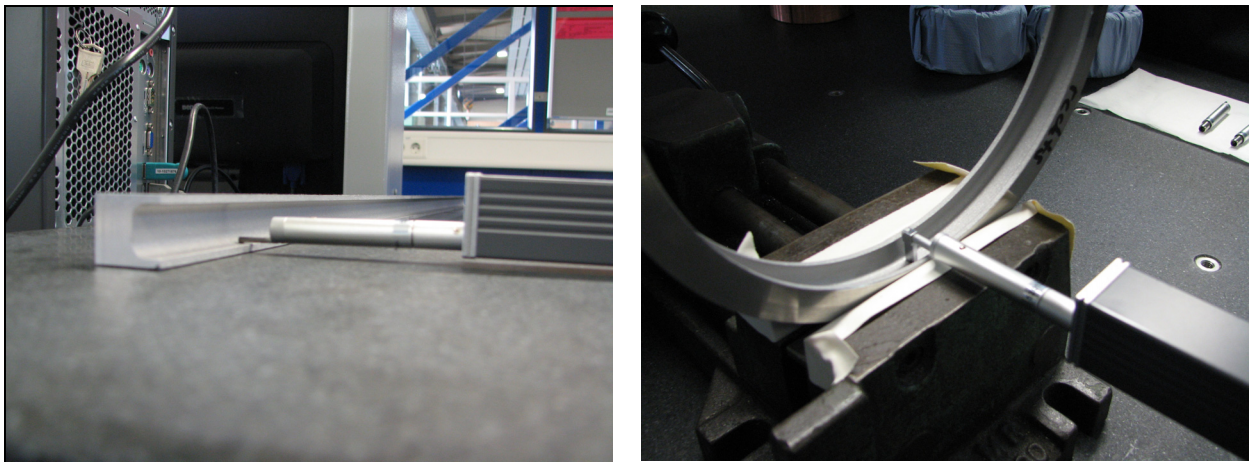

Fig. 6: Measurements of surface roughness at channel surface: side of straight section (left) and outside surface of channel bend (right).

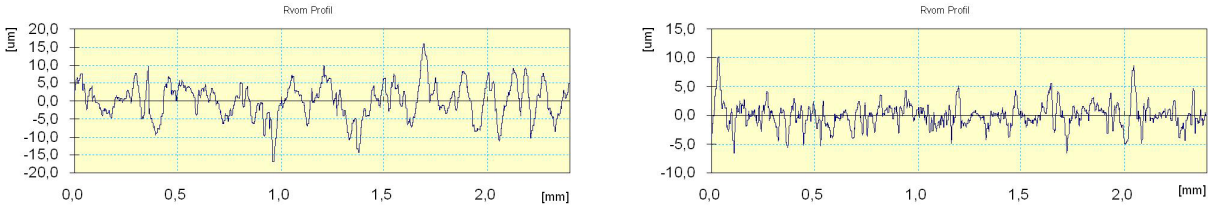

Fig. 7: Measured roughness profiles. Examples are given for the plasma facing surface (left) and the side channel surface (right) in the middle of the straight section.

Definition of measuring positions in HETRA experimental facility

Planned measuring positions for the HETRA experiment are presented in Figure 8. Pressure loses will be determined through differential pressure measurements between relevant locations at the inlet (position p_1) and the outlet (position p_2) side channel. At the inlet to the HETRA section the absolute pressure will be measured (position p_a). Helium bulk temperature will be measured at the inlet (position T_{f1}) and after the mixer (position T_{f2}). For each heater the temperature (denoted as $T_{heaters}$) and power (denoted as $Q_{heaters}$) will be measured.

As the temperature measurements within the flow stream in the heated domain would significantly disturb the fluid stream due to high coolant velocities, the computational results will be verified only via experimentally determined steel temperatures. For that purpose 6 sets of temperature measurements will be performed along the heated section (denoted as I-VI in Figure 8). The measuring planes are positioned in the middle of the heating elements to avoid the effects of the discrete heaters. The measurements will be done applying thermocouples with diameter of 0.5mm. The thermocouples will be inserted orthogonally to the heat flux (from bottom/top side of heated section) in order to minimize temperature gradients along the thermocouple cable. The pattern of thermocouples within one measuring plane is arranged so to obtain temperature data along three constant z coordinates, i.e. corresponding temperature gradients along four lines (see insert in Figure 8). As the temperature gradients in the front (heated) channel wall are very strong, it is planned to place three thermocouples for each measuring line in this domain. In the back (not heated) wall only two thermocouples along a measuring line are foreseen. Therefore, within each set the temperature of the steel wall could be measured at 10 positions.

However, as it is not clear if the holes for the thermocouples which are concentrated at a narrow region of the wall will disturb the heat flow, a HETRA pre-experiment has been designed where these effects will be examined. Figure 9 presents how the pre-experiment is arranged. A 3.5mm thick EUROFER plate is heated in the same way as the heated HETRA section. Within this plate three different thermocouple patterns are foreseen: one as in Figure

8 and two with reduced number of thermocouples. The isolation is applied on all sides but one side left (see Figure 9). The Temperature of this side will be recorded with a thermo-camera and in this way eventual disturbances of heat flow will be noticed.

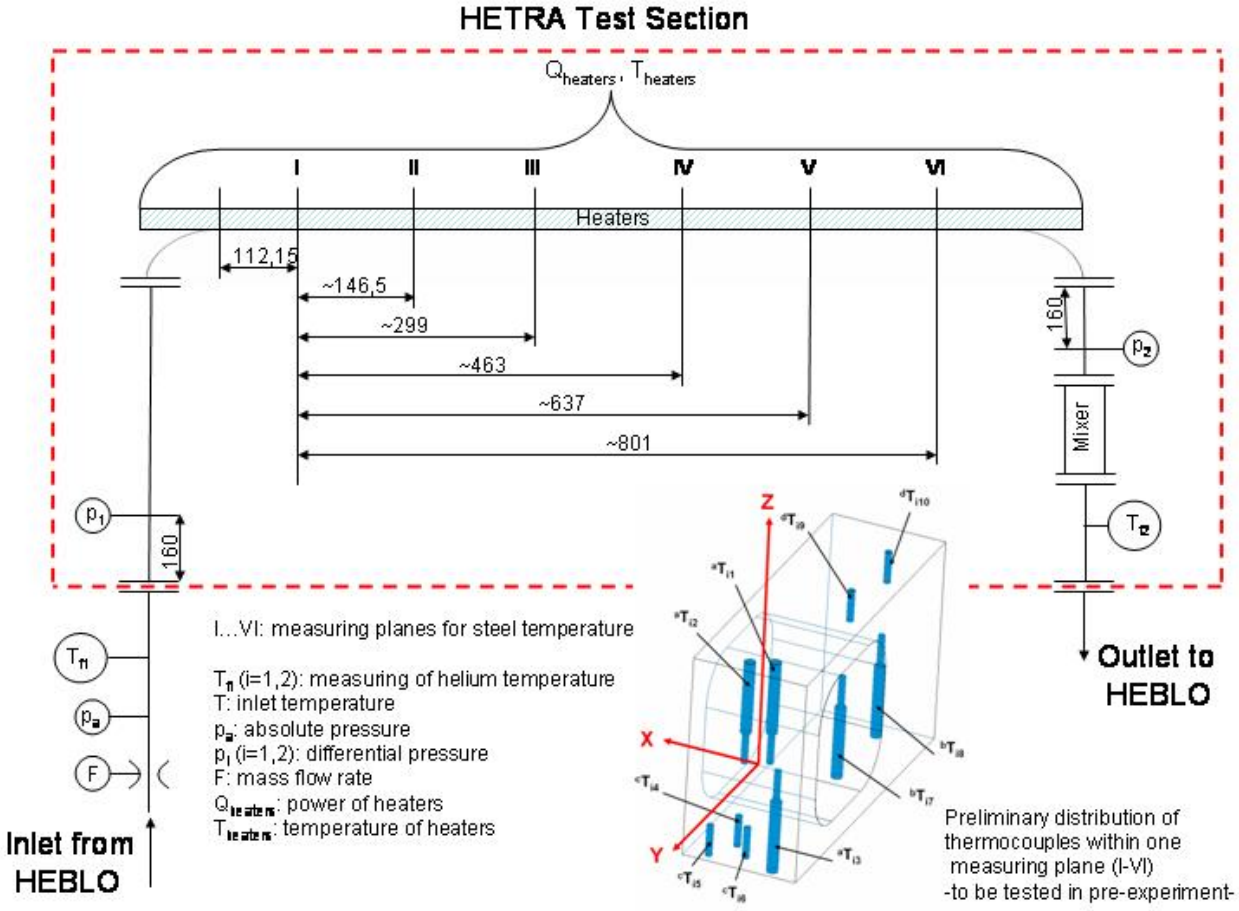

Fig. 8: HETRA measuring plan. Insert represent desired pattern of thermocouples within one of the measuring planes I-VI.

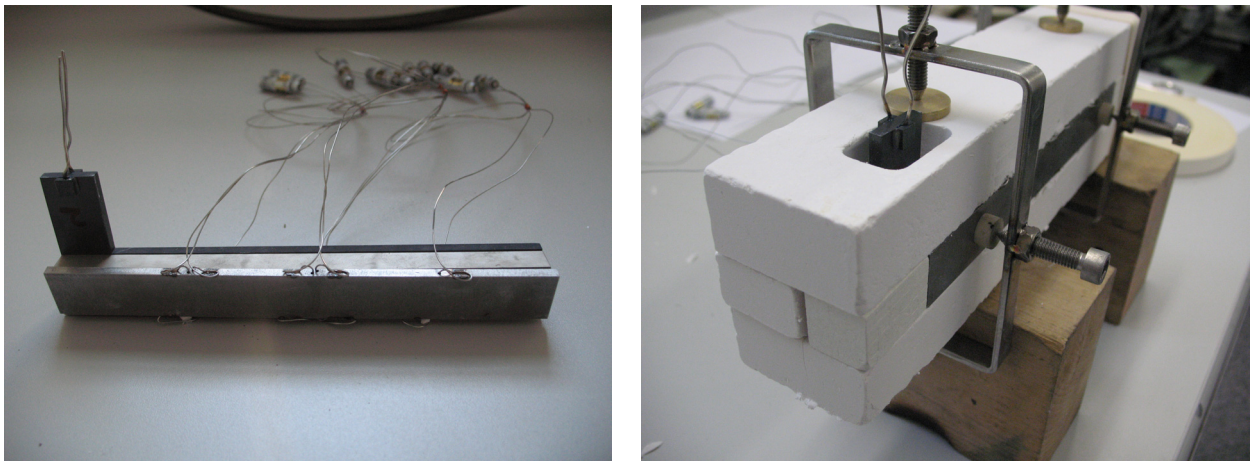

Fig. 9: HETRA pre-experimental mock-up for testing effects of thermocouple locations on temperature distribution in plasma facing channel wall.

Conclusions

The HETRA facility has been designed for the verification of numerically found effects of asymmetrical heating on the cooling of the first wall. The investigations will be performed for a portion of the first wall containing one U sweep of the cooling channel. The tests will be

done in a Helium cycle at 80 bars. The heat load of 270kW/m^2 on the surface representing plasma facing side of the first wall will be achieved by a set of electrical heaters. The numerical results will be verified through comparison with detailed temperature measurements in the steel structure. Most of the HETRA components are fabricated. The first tests are expected in spring of 2009.

Staff:

T. Ihli
M. Ilic
B. Kiss
G. Messemer
K. Zinn

TW6-TTBB-001 D 3
HCPB TBM Design and Integration Analysis

The objective of the task is the continuation of the engineering design work on the HCPB TBM System. In particular the updating of the TBM design, the production of detailed drawings of the TBM, the mechanical integration of the instrumentation, the definition of maintenance sequences, and design and integration of the Helium Cooling System (HCS).

Subtask a) TBM update acc. to frame design

The scope of this task was originally limited to the impacts on the TBM design due to the change of the outer dimensions according to the re-definition of the frame dimensions (agreed in the TBWG-17 in Cadarache). The TBM dimensions changed from 1270 mm x 740 mm (TBM ref 1.0) to 1208 mm x 710 mm (TBM ref 1.1). The radial dimension of 750 mm (including attachment plate) for the HCPB-TBM remained unchanged. The first wall analysis originally required in this deliverable was focused on a horizontal arrangement of the TBM first wall, corresponding to the port plug frame dimensions update. Additionally the cross section area of the cooling channels had to be changed from rectangular to square shape with regard to manufacturing technology related reasons (HIP). By the end of 2007 it has been decided by the HCPB-TBM team that also a change of the HCPB-TBM design from a horizontal into a vertical arrangement will be taken into account.

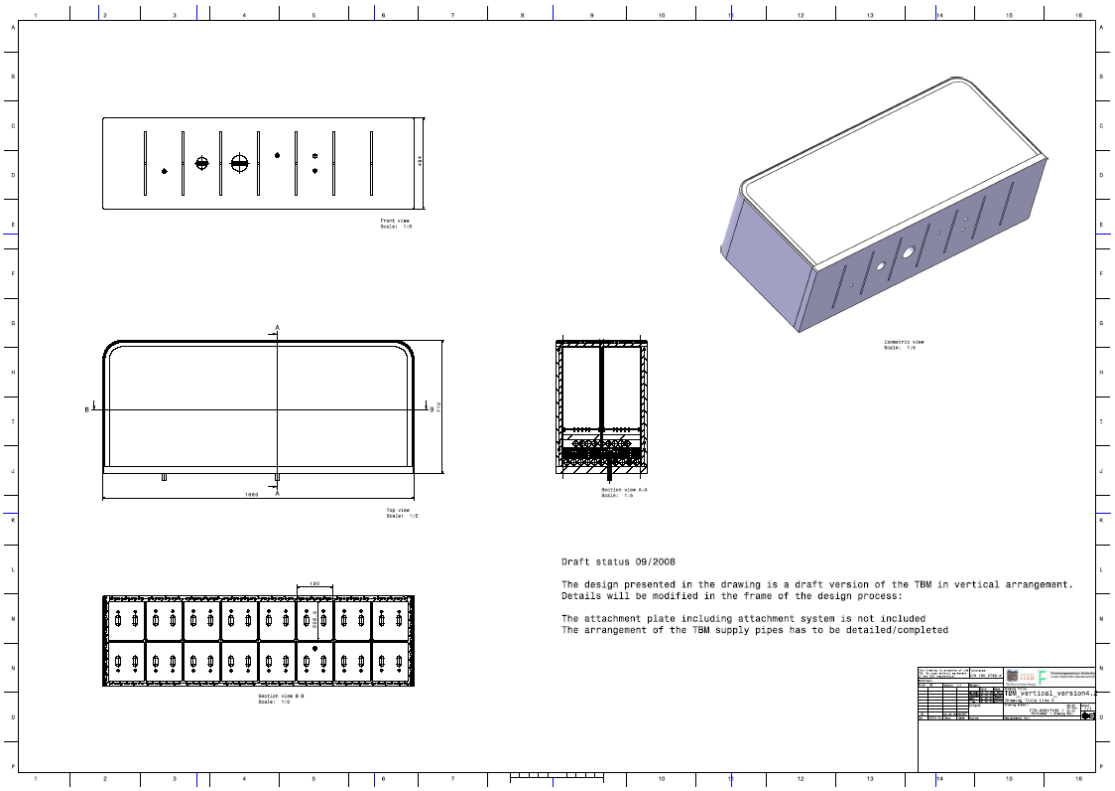

Fig. 1: Preliminary design of the HCPB TBM in vertical arrangement.

The sub-deliverable includes the following analysis/data:

- CAD design of TBM ref. 1.1 (horizontal)
- Preliminary design of the HCPB TBM (vertical), see figure 1
- Update of correction values for thermo-hydraulic FE calculations
- Preliminary HCPB TBM First Wall thermal analysis, see figure 2
- Preliminary Breeding Unit analysis update, see figure 3
- Preliminary structural analysis update of the TBM first wall

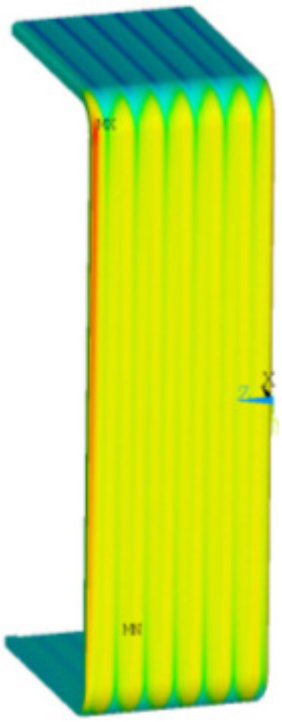

Fig. 2: Preliminary TBM FW thermal analysis.

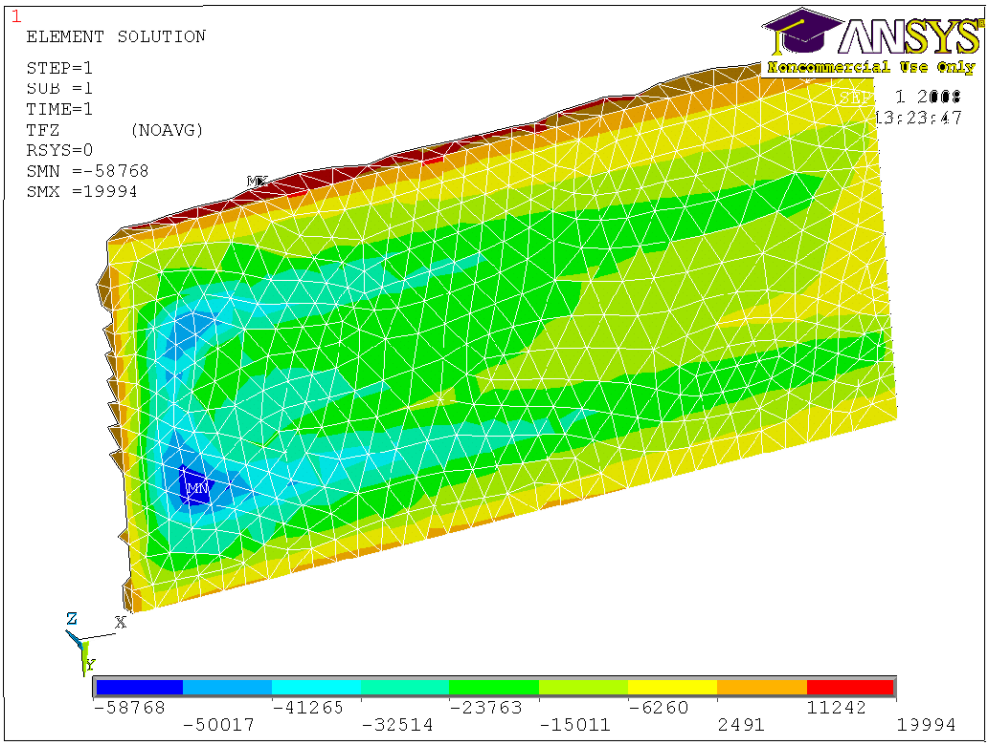

Fig. 3: Heat flux profile: pebble bed → vertical grid.

Subtask b) Support to fabrication R&D + sub component testing

The design of the TBM from a manufacturing point of view is presented in the frame of this report where sub-component fabrication as well as the TBM assembly by welding is taken into account. Dimensional tolerances of components and acceptance criteria for joint are specified with focus on the TBM first wall. The impact of dimensional tolerances of the first wall cover layer has been investigated. The sensitivity of the first wall maximum temperature and maximum stress due to the pressure inside the first wall cooling channel has been investigated dependent on the cover layer thickness in a parametric study. It can be concluded that a deviation of the dimension of the first wall cover layer (nominal dimension = 3.5 mm) of +/- 0.3 mm does not cause significant changes of the operational parameters. Additionally the sensitivity of the first wall temperature to deviations of the mass flow in a separate cooling channel has been analyzed. Figure 4 shows the model used for the parametric studies.

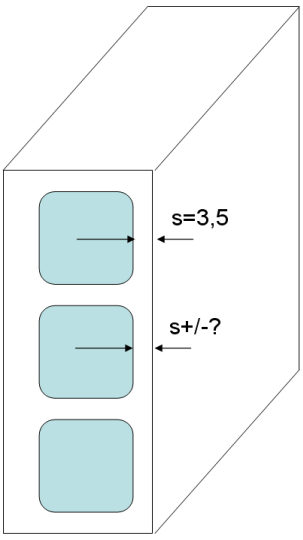

Fig. 4: Analysis model.

The assembly strategy for the TBM has been investigated more detailed in the frame of this study with focus on the welding processes. In the frame of this task a catalogue has been developed indicating type, number, location and dimensions of each TBM assembly welding. Fig.5 shows a matrix of the connections required in between the TBM sub-components.

	FW	Cap	BP	GD hor.	GD vert.	MF 1	MF 2	MF 3	MF 4	MF 5	BA (rad.)	BA (pol.)
FW												
Cap	4											
BP	13	18										
GD hor.	2	5	19									
GD vert.	3			1								
MF 1	6	6		7	14							
MF 2	8	8		9	15							
MF 3	6	6		11	16							
MF 4	6	6		7								
MF 5	6	6		7								
BA (rad.)			20						17	17		
BA (pol.)	11			11				10			12	

Fig. 5: TBM assembly-matrix.

Subtask c) Mechanical integration of instrumentation (particular EM-TBM)

This activity continues the work already started with task TW5-TTBB-001-D1b. Instrumentation and monitoring systems (that are being developed in other tasks) will be integrated in the EM-design. In particular the impact on the reference design will be analysed, the necessary modifications will be implemented and the compatibility with the integral TM system including remote handling systems in ITER will be checked. This report on the task also takes into account the results of the EU/RF collaborative task on the Development of diagnostic systems for the electromagnetic TBMs, part 1 and 2 on Development of Conceptual Design of the Electromagnetic -and Mechanical Monitoring System EMMS (FZK monitoring task TW6-TTB-RFMON-D1) and describes the impact on the TBM design by applying the results of the Efremov reports concerning EMMS. It can be summarized that the general concept for integration of EM-diagnostic as well as TBM standard diagnostic is advanced up to a point where diagnostic experts should be considered to evaluate the state of the art of diagnostic systems as well as for additional equipment such as cables and feedthroughs. If available suitable diagnostic equipment should be selected from the market and development needs should be identified. Details concerning the boundary conditions of the procedures for installation of sensors into the TBM should be checked with regard to feasibility and compatibility with the TBM application. This work should be supported by the design of facilities to test TBM diagnostic equipment under TBM relevant conditions.

Staff:

F. Cismondi
S. Kecskés
M. Lux,
H. Neuberger
J. Rey

Literature:

[1] F. Cismondi, M. Ilic, H. Neuberger, J. Rey, A. von der Weth, O., L. Boccaccini, and T. Ihli, Design update and thermo-mechanical analysis of the EU-HCPB TBM in vertical arrangement; 25th Symposium on Fusion Technology, 15-19 September 2008, Rostock, Germany

[2] J. Rey, A. von der Weth, S. Kecskés, H. Neuberger, M. Ilic, O. Bitz, L.V. Boccaccini, T. Ihli, Design update and mock-up test strategy for the validation of the EU-HCPB-TBM concept; 25th Symposium on Fusion Technology, 15-19 September 2008, Rostock, Germany

TTBB-003
Helium Cooled: Out of Pile Testing

TW5-TTBB-003 D 1
Manufacturing and Testing of Mock-ups for Investigation of Coolant Flow in the Manifold System of HCPB TBM (GRICAMAN Experiments)

The objective of GRICAMAN experiments is to contribute to the out-of-pile testing of HCPB TBM. The envisaged activity focuses on out-of-pile testing of a look-alike mock-up of the TBM manifold system, in particular to the optimization of the coolant flow.

The flow distribution in a TBM coolant system is quite complex. The coolant, helium at 8MPa and 300^{0}C enters the manifold 1 with a mass flow rate of 1.2kg/s, from where it is distributed into coolant channels of the first wall (FW channels). The outflow from FW channels is collected in the manifold 2 where one part (0.578kg/s) flows through by-pass pipes out of the system, and the rest is distributed among stiffening grids (14 horizontal and 8 vertical) and two caps. The mass flow rate through each grid/cap channel is specified. The outflow from grids and caps is collected in manifold 3 and from there uniformly distributed among 16 breeding units. The outflow of BU's is led into the manifold 4 from where it, finally, leaves TBM. In order to find out whether such a flow distribution can take place, GRICAMAN (GRIdCApsMANifolds) experiments are proposed. The main goals of the experiments are:

1. to investigate whether the mass flow distribution in the manifold 2 among the caps and stiffening grid channels corresponds to the designed one,
2. to investigate whether individual stiffening grid and cap channels are supplied with designed portion of coolant flow and
3. to investigate whether the mass flow distribution among breeding units is uniform.

The design of GRICAMAN mock-up has been completed at the end of 2007 and fabrication of the components, assembling the facility and testing has been planned to be completed in 2008. However, at the end of 2007 the horizontal HCPB TBM design, on which the Gricaman arrangement was based, has been abandoned and replaced by the vertical HCPB TBM design. In relation to this, the Gricaman domain has to be newly defined in order to represent realistically the flow distribution in manifold system of the vertical HCPB TBM. Figure 1 shows the domain of the vertical TBM that has to be investigated in the GRICAMAN experiments.

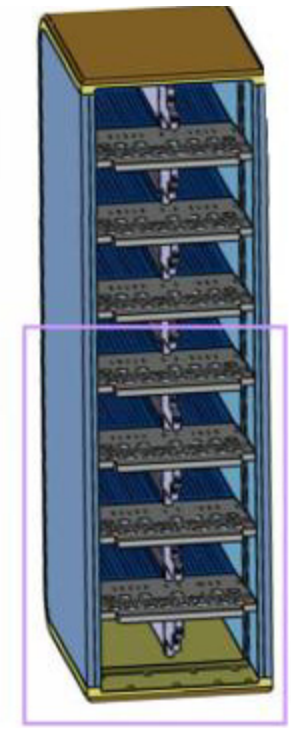

Fig. 1: Design of vertical HCPB TBM with domain to be investigated in GRICAMAN experiments.

Due to the change to the vertical orientation of HCPB TBM, its arrangement is more similar to the HCLL TBM. Therefore, testing of flow distribution for both TBMs manifolds within one common facility, namely GRICAMAN, seems to be possible. Nevertheless specific adjustment of interfaces and measuring equipment will be necessary.

In relation to the aforementioned status of the vertical TBM design the development of the CAD design for the new Gricaman as well as the corresponding numerical model are in progress but not yet finalized. The activity of Gricaman was frozen till July 2008 when the first CAD version of TBM in vertical arrangement was available. Since then we started the CAD design for the arrangement of auxiliary systems (flow supply and outflow components) and the planning of the manifold boxes.

Staff:

T. Ihli
M. Ilic
T. Kuhn

Helium Cooled Pebble Bed: Breeder and Neutron Multiplier Materials

Development of Beryllium and Beryllium Alloy Pebble Beds with Improved Tritium Release Characteristics – Part 1

Introduction

At present Beryllium is under planning for use as a plasma facing material in ITER and as neutron multiplier in the TBM ITER and DEMO blanket [1,2]. In DEMO the beryllium will be exposed to high dose neutron irradiation that will lead to strong radiation damage. Some beryllium alloys especially titanium beryllides ($Be_{12}Ti$) are considered to be one of advanced materials for neutron multiplier in future fusion reactor [3, 4]. This seems to be a reasonable way in order to overcome some of the possible disadvantages of existing beryllium grades in form of pebbles. The most important relevant properties of beryllium materials for neutron multiplier application like tritium and helium release, radiation embrittlement, swelling, thermal conductivity and radiation-thermal creep at blanket operating temperatures must be investigated on full scale. But firstly it is necessary to investigate some relevant properties of advanced beryllium grades and beryllium-based alloys ($Be_{12}Ti$) on a laboratory scale. For example this can be done in a tritium release experiment with preliminary loaded tritium into beryllium pebbles and titanium beryllide samples.

The irradiation of several types of beryllium pebbles and also titanium beryllide samples produced by NGK, Japan; Bochvar Institute, Russia and FZK was finished in 2007 in the HFR, Petten, Netherlands. The irradiation was carried out at 425-750ºC up to 3000 appm ^4He accumulation [5] in the frame of the HIDOBE benchmark irradiation program.

Under neutron irradiation the beryllium pebbles and titanium beryllide microstructure undergoes evolution. Post irradiation examination of beryllium microstructure with use of metallography, SEM and especially TEM leads to the understanding of radiation damage nature and allows providing the data for the development of advanced modeling of the tritium release and the swelling of irradiated beryllium materials.

Start of SEM/TEM analyses on irradiated and as received samples

The start of TEM analyses on irradiated samples was in 2008 not possible because the transportation of the HIDOBE-1 irradiated beryllium samples from NRG, Petten was delayed. However TEM examinations of six beryllium grades by Brush Wellman Inc., USA production were carried out [6]. The ultimate strength depends sensitively on the beryllium oxide (BeO) content, at least between 0.35 and 1.81 wt.% for all beryllium grades investigated.. Regarding total elongation, beryllium grades have the best plasticity properties in the range of 0.6-0.7 wt.% of BeO. However, beryllium grades with minimum and maximum BeO contents have smaller values of total relative elongation.

Fig. 1 (a) presents TEM micrographs of I-220H beryllium grade which includes 1.81 wt.% BeO. It is clearly visible that beryllium has a grain structure with the grain size varying from 0.5 µm to 5 µm. The grains show a different crystallographic orientation. The investigation shows the presence of numerous BeO particles in the sample. The particles often decorate the grain boundaries however numerous faceted particles were detected inside grains. Fig. 1 (b) presents the S-65H grade with content of BeO 0.65 wt%. The particles have often hexagonal form. The size of the BeO particles varied from few tens of nanometers to 500 nm. The particles which are located on the grain boundaries have normally the size down to 50 nm. Fig. 1 (c) presents S-200F beryllium grade with 1.18 wt%. BeO content. The numerous large BeO particles are located mainly on grain boundaries. Analogous situation takes place in the O-30H (0.35 wt.%.BeO) beryllium grade (Fig. 1 (d)) where particles are located also on grain boundaries. All beryllium grades have particles of two types – bigger particles with the hexagonal form and fine inclusions having, under existing magnification, not defined shapes.

The definite correlation between amount and morphology of the BeO particles in microstructure on TEM pictures and ultimate strength or total elongation as a result of mechanical test are not established.

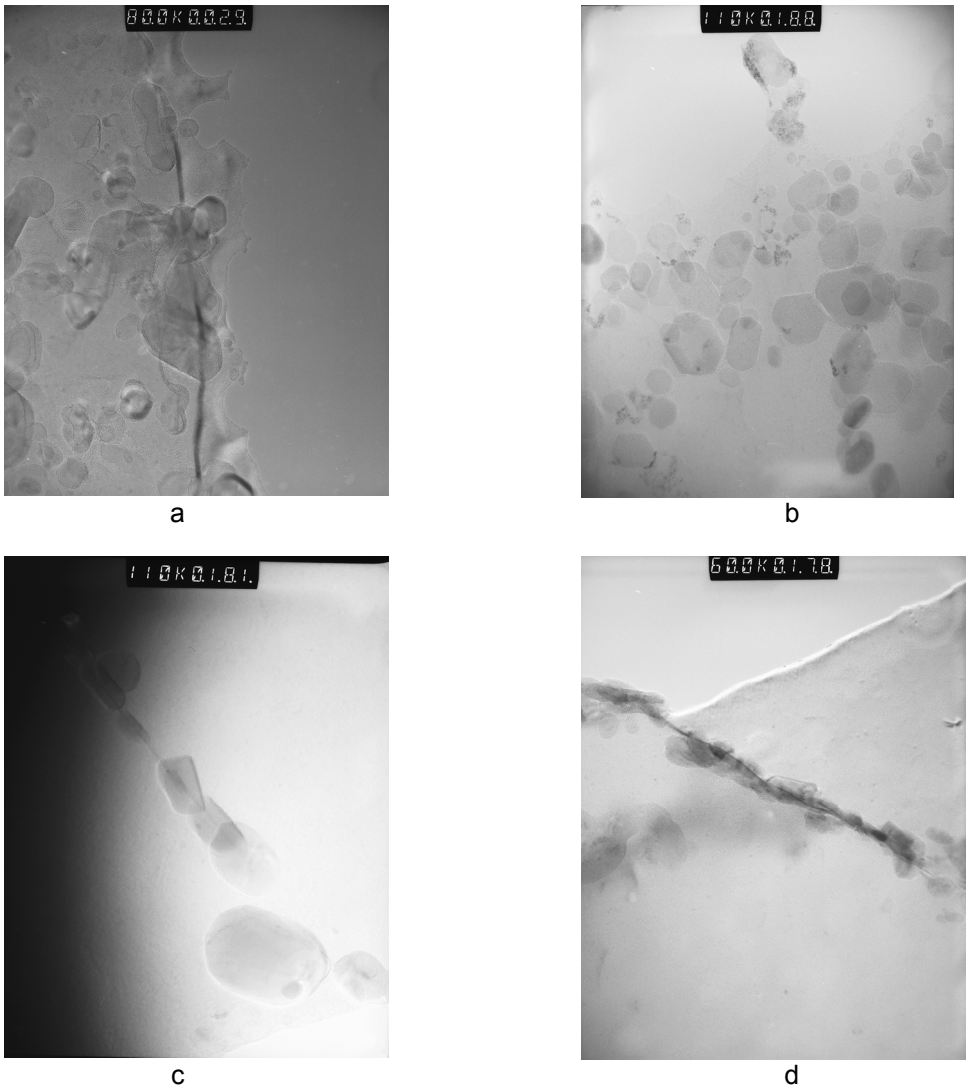

Fig. 1: TEM investigation of I-220H (a), S-65H (b), S-200F (c), O-30H (d) beryllium grades.

This investigation was carried out using a CM30 electron microscope. Since October 2008 the assembling of a modern electron microscope Tecnai is in process. This microscope provides Dispersive X-Ray (EDX) and Electron Energy Loss Spectroscopy (EELS). The analytical investigations can be performed in Scanning TEM (STEM) regime using a High Angle Annular Dark Field (HAADF) detector. This new electron microscope will present the possibility to examine the irradiated beryllium pebbles and titanium beryllide samples with high scientific level.

Start of thermal desorption of hydrogen and helium isotopes from irradiated samples

For the same reason of a delay of transportation of the HIDOBE-1 irradiated beryllium samples from NRG to FZK, it was impossible to realize the thermal desorption experiments on irradiated beryllium samples. Therefore a tritium release experiment on 12 beryllium samples with preliminary loaded tritium was performed. Tritium was loaded to samples in a special facility at temperature of 850 °C and pressure of 4 bar for 6 hours in helium with 50 appm ^{3}H (tritium). Two heating conditions for the tritium release measurement were used – the stepped heating with step parameters of 50°C, 0.5 h up to 1100°C and the permanent heat-

ing with rate of 6-7°C/min also up to 1100°C. The activity of the released tritium has been measured using a proportional counter. The measured activity has been depicted by two different curves: one curve shows a release rate in Bq/g*sec and another depicts the cumulative amount in Bq. The third curve reflects the changes in temperature during the experiment. Thus, each gas release experiment is represented by three curves reflecting ramping of temperature, current and integrated gas release.

The following specimens have been investigated: (i) beryllium pebbles with 1 mm diameter by NGK, Japan, (ii) beryllium pebbles with 2 mm diameter by Brush Wellman Inc., USA, and (iii) titanium beryllides with coarse and fine grains, produced at FZK in cooperation with GORAIEB facilities. The results of tritium release measurements from pebbles by NGK production are shown in the Fig. 2 (stepped (Fig. 2 (a)) and permanent (Fig. 2 (b)) heating) and from titanium beryllide, as melted in the Fig. 3 (stepped (Fig. 3 (a)) and permanent (Fig. 3 (b)) heating).

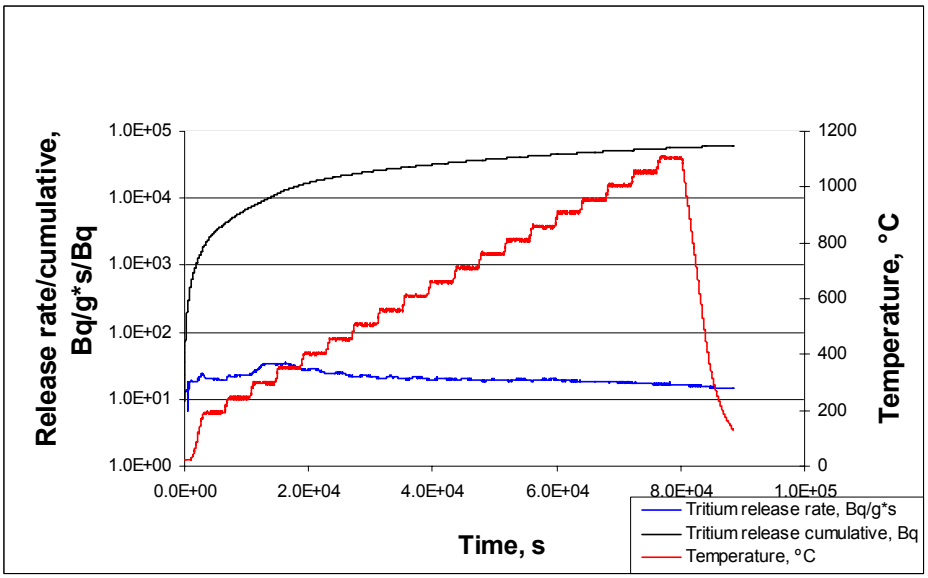

a

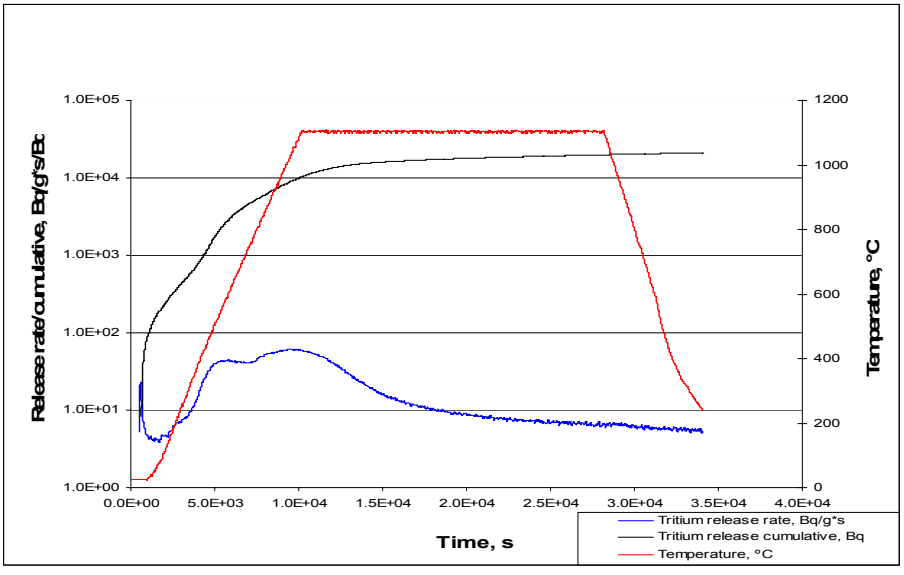

b

Fig. 2: Tritium release rate and tritium release cumulative for 1 mm beryllium pebbles by NGK production at stepped (a) and permanent (b) heating.

The main results of the tritium release experiment were as follows:

1. Three peaks of accelerated tritium release show up. The first peak is at 150-200°C, the second peak is at 400-600°C, and the third peak is at 750-1100 ° C. Probably the first peak is caused by surface defects that lead to the release of tritium atoms at low temperature. The second peak can be caused by internal surfaces such as grain boundaries, second phase boundaries, dislocations. The release from these structural traps began at middle temperatures. And the third peak can be caused by disintegration of beryllium hydroxide. It is formed by reaction of tritium with beryllium oxide layer placed on a surface of beryllium sample during loading of tritium to sample.
2. The pebbles with 2 mm diameter by BW production have higher release rate compared with the 1 mm pebbles by the NGK production one. The obvious reason is the higher fraction of open porosity on the surface of the American pebbles.
3. The maximal tritium release rate is from $Be_{12}Ti$, as melted state, the minimal rate is from $Be_{12}Ti$ with coarse grains. The microstructure examination shows that some dependence of tritium release rate on grain size and kind and morphology of second phases (beryllium oxide particles) in beryllium exists.

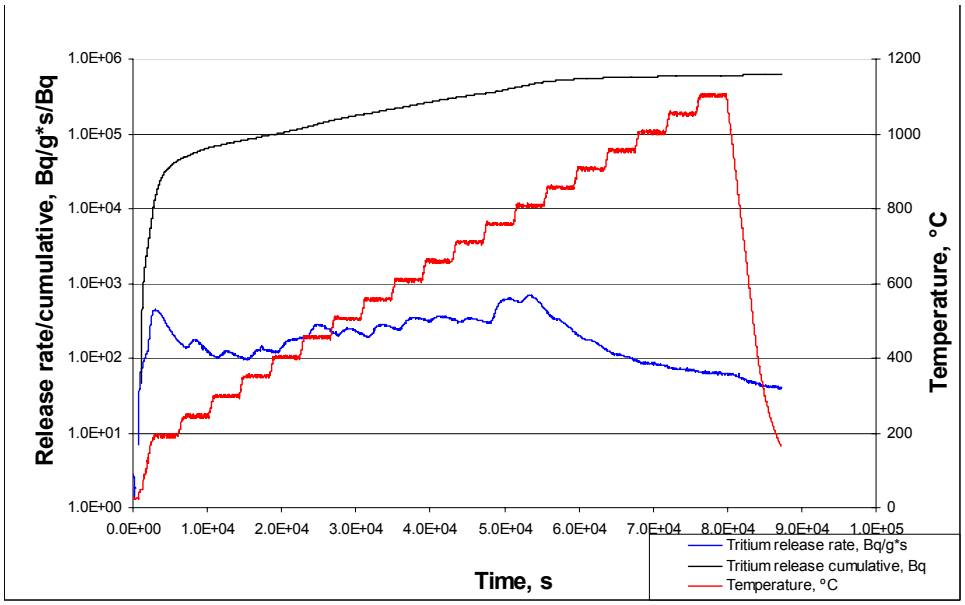

a

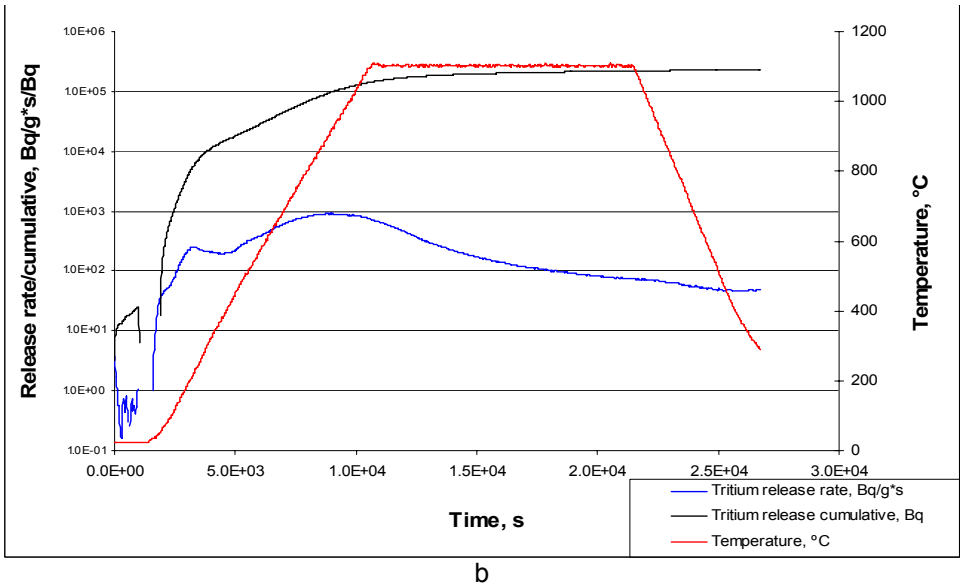

b

Fig. 3: Tritium release rate and tritium release cumulative for titanium beryllide as melted state by FZK production at stepped (a) and permanent (b) heating.

Start of swelling and micro hardness measurements

The start of swelling and micro hardness measurements couldn't be realized in 2008 because of the delay of the transportation of the HIDOBE-1 irradiated beryllium samples from NRG, Petten to FZK. But it is possible to estimate the swelling of irradiated beryllium pebbles from HIDOBE-1 using the experimental results received on examination of irradiated fragments from the SM reactor beryllium blocks (Fig. 4) [7-10]. It is necessary to understand that there is a serious restriction on the annealing temperature value after low temperature irradiation of beryllium, which is expressed in a sharp swelling increase with rising of the annealing temperature. Tritium release is specifically pronounced at the annealing temperatures of 800°C, when the swelling value can reach of 20-25 %. Such substantial growth of beryllium volume can lead to problems with operation of beryllium blocks in a nuclear reactor. The HIDOBE-1 beryllium pebbles had the irradiation temperature up to 750°C therefore the size of pebbles can be increased to 6-8%. The increase of pebble diameter into pebble bed must lead to increase of contact stresses between pebbles.

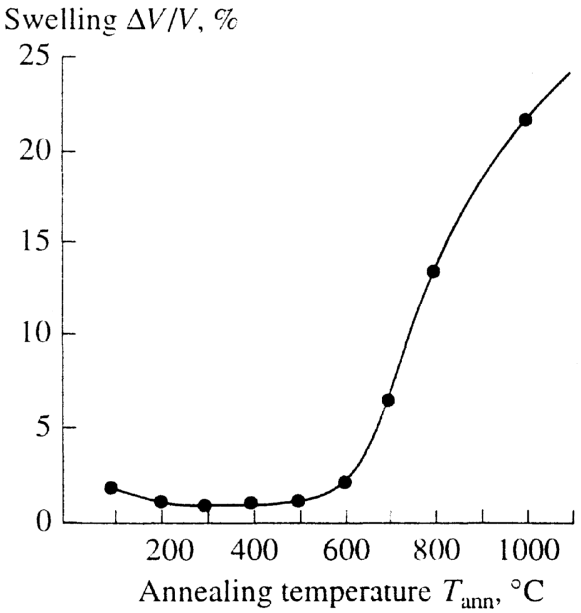

Fig. 4: Swelling of beryllium irradiated at 70°C to 3000 appm ^{4}He after annealing during 1 h.

Conclusions and Future Prospective

TEM examination of six advanced beryllium grades by Brush Wellman Inc., USA production in the received state was carried out. The investigation shows the presence of numerous beryllium oxide particles by hexagonal form which are distributed on grain boundaries and also inside grains. Tritium release experiment on twelve beryllium and titanium beryllide samples with preliminary loaded tritium were performed. The maximal tritium release rate was from $Be_{12}Ti$, as melted state, the minimal rate was from $Be_{12}Ti$ with coarse grains. The microstructure examination shows that the tritium release rate depends on grain size and kind and morphology of beryllium oxide particles.

At 2009 the beginning and finish of PIE of the HIDOBE-1 irradiated beryllium pebbles and titanium beryllide samples will be carried out by all available experimental methods at FZK. Tritium release and microstructural examination of low temperature high dose irradiated beryllium fragments of the BR2 reactor matrix will be made with annealing at high temperatures. The purpose of this experiment is to receive new data for advanced modelling of the tritium release and the swelling of beryllium. The new beryllium materials including beryllides will be examined by SEM and TEM methods.

Staff:

V. Chakin
P. Kurinskiy
A. Möslang
and Goraieb Versuchstechnik

Literature:

[1] V. Chakin, A. Möslang, M. Svyatkin, A. Posevin, P. Vladimirov and R. Latypov, Beryllium application for fission and fusion, Proceeding of the 1st International Symposium on Material Testing Reactors, JAEA-Oarai, Japan, July 16-17, 2008, to be published.

[2] K. Tsuchiya, G. Longhurst, V. Chakin, I. Tazhibayeva, F. Druyts, C. Dorn and H. Kawamura, Problems and Future Plan on Material Development of Beryllium, Proceeding of the 1st International Symposium on Material Testing Reactors, JAEA-Oarai, Japan, July 16-17, 2008, to be published.

[3] P. Kurinskiy, V. Chakin, A. Möslang, R. Rolli, A.A. Goraieb, H. Harsch, E.A. Alves and N. Franco, Characterization of titanium beryllide with different microstructure, Proceeding of the 25th Symposium on Fusion Technology, Rostock, Germany, September 15-19, 2008, to be published in Fusion Engineering and Design.

[4] A. Möslang, V. Chakin and P. Kurinskiy, Beryllium activity at FZK, International Meeting on PIE of the HIDOBE-1, NRG, Petten, the Netherlands, August 19-20, 2008.

[5] V. Chakin, R. Rolli and A. Möslang, The PIE possibilities for the HIDOBE-1 irradiated beryllium samples at FZK, International Meeting on PIE of the HIDOBE-1, NRG, Petten, the Netherlands, August 19-20, 2008.

[6] V. Chakin, M. Klimenkov, A. Möslang, P. Kurinskiy, R. Rolli, L. Ryczek, C. Dorn, E. Vidal, G. Shuster and A. Markovsky, Microstructural examination of advanced beryllium grades for fusion application, Proceeding of the 25th Symposium on Fusion Technology, Rostock, Germany, September 15-19, 2008, to be published in Fusion Engineering and Design.

[7] V. Chakin, A. Posevin, R. Latypov, M. Svyatkin, A. Izhutov, A. Petelin, Radiation damage of beryllium as reflector and moderator of the SM and MIR research reactors, Proceeding of the 8th IEA International Workschop on Beryllium Technology, Lisbon, Portugal, December 5-7, 2007, to be published.

[8] V. Chakin, A. Posevin, A. Obukhov and P. Silantyev, Radiation growth of beryllium, Proceeding of the 13th International Conference on Fusion Reactor Materials, Nice, France, December 10-14, 2007, to be published in Journal of Nuclear Materials.

[9] V. Chakin, Recycling of radioactive beryllium waste, Work Meeting on Radioactive Beryllium Waste, SCK●CEN, Mol, Belgium, April 1-3, 2008.

[10] V. Chakin, A. Zakharov, A. Shimansky, A. Posevin and A. Möslang, Radioactive beryllium waste in fusion: storage or recycling? Proceeding of the 25th Symposium on Fusion Technology, Rostock, Germany, September 15-19, 2008, to be published in Fusion Engineering and Design.

Helium Cooled Pebble Bed: Breeder and Neutron Multiplier Materials

Development of Beryllium and Beryllium Alloy Pebble Beds with Improved Tritium Release Characteristics – Part 2

Introduction

Beryllium and its alloys are needed in large quantities for the construction of the fusion reactor ITER and its successor DEMO as breeding and structural materials. The handling of beryllium has to take place in glove boxes which must be run under negative pressure and inert gas atmosphere.

$Be_{12}Ti$ is one of the alternative materials for use as a neutron multiplier in the breeding blanket of fusion reactor. It has a number of advantages compared to pure Be (smaller swelling under neutron irradiation, smaller reactivity with stainless steel, water steam and air at elevated temperatures), so that $Be_{12}Ti$ becomes interesting for use in EU-HCPB blanket.

GVT (Campus Company at FZK) is allowed to handle Be-based materials up to 1000 kg in a newly built Beryllium Laboratory and is involved in the design of a $Be_{12}Ti$ pebble production facility in cooperation with FZK.

Schematic Plan of Beryllium Laboratory

Within the reporting period, the Beryllium Laboratory was refitted into a highly secure lab in cooperation with the relevant authorities. The total area of the laboratory is 70 m^2 and it consists of:

- Hot Zone Area (45 m^2) which stays constantly under 20 Pa (0,2 mbar) negative pressure. The whole volume of this area is pumped through with a frequency of 10 room volumes per hour (approx. 150 m^3/hour).
- Control Room, which is separated from Hot Zone Area by a transparent Plexiglas window, allows remote controlling of some processes.
- Air Lock room will be used for a staff entrance into Hot Zone Area.
- Storage room provides material transport and its storage.
- Engine Room is equipped with pumping systems and filters needed for safety operating of the laboratory.

Figure 1 depicts, schematically, a lay-out of beryllium handling laboratory.

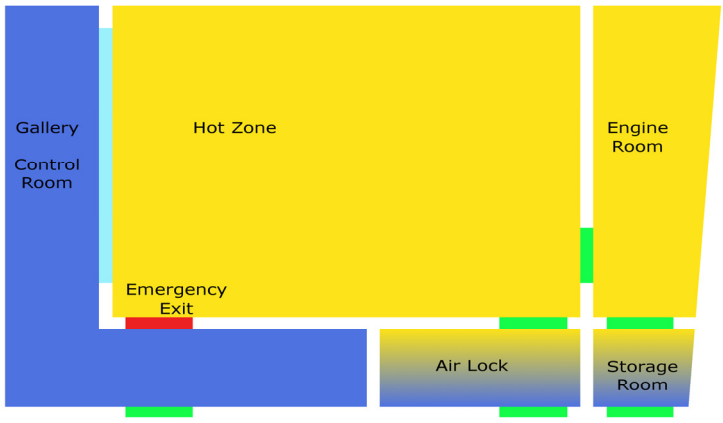

Fig. 1: Lay-out of Beryllium Laboratory.

Design of the facility for $Be_{12}Ti$ pebble production

The facility for fabrication of metallic pebbles has been designed and built by the Company Goraieb Versuchstechnik (GVT) which works in close cooperation with IMF-I/MW, FZK. It was placed into Hot Zone Area and then connected to a gas- and electric supply systems. An automatic welding device made by Company Merkle Schweisstechnik GmbH is used for melting of metallic wire (or stab) in a glove-box. A general view of the glove-box in the Hot Zone Area is shown in Fig. 2.

Fig. 3 shows a wire fixed between two electrodes. By changing the parameters of an electric current and a distance between electrodes, one can adjust a stable arc which melts down a metallic wire. Pebbles, disrupted by an electric arc, fall down from the end of a wire and solidify with a very high cooling rate. Encouraging test results were obtained by melting of a copper wire having 2 mm diameter, although some adjustment of working parameters is still needed for optimization of a diameter distribution of fabricated metallic pebbles.

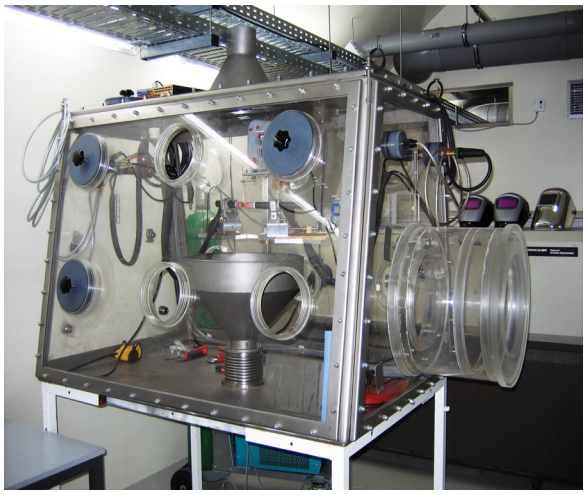

Fig. 2: General view of a melting facility in a glove-box.

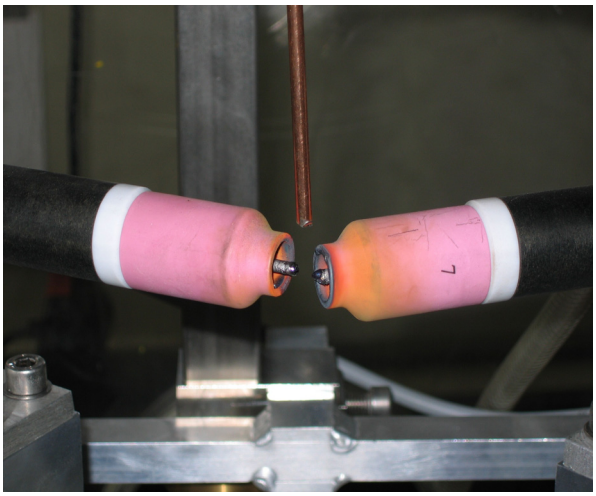

Fig. 3: Metallic wire fixed between two electrodes.

One should note that the diameter of a wire or cross-sectional diagonal of a stab can not exceed 4 mm. This size is restricted by parameters of an electric current and, secondly, it is important to melt the whole volume of a wire (or stab) end, avoiding unstable location of an electric arc contact with material which leads to formation of non-spherical particles.

The construction of $Be_{12}Ti$ pebble fabrication facility foresees also an onward movement of a “target” by a motor. This technical decision favours the droplets of a melted material to disrupt in the same time intervals. Also this facility is supplied with necessary adjusting devices to fix a position of a “target”. Fig. 4 shows a schematic draft of the melting facility.

Be-Ti rods fabricated at FZK by methods of powder metallurgy in the previous years could be used as “targets” in this process. Some additional mechanical treatment will be needed in this case in order to achieve necessary geometric sizes of a specimen to be melted.

Conclusions and Future Prospective

The facility for Be12Ti pebble production was designed and put into a glove-box which is placed in the Hot Zone Area. Preliminary tests on copper wire have shown the possibility of pebble production in diameter range of 0.5-2 mm. Some process parameter adjustment is needed for a stable running of an electric arc.

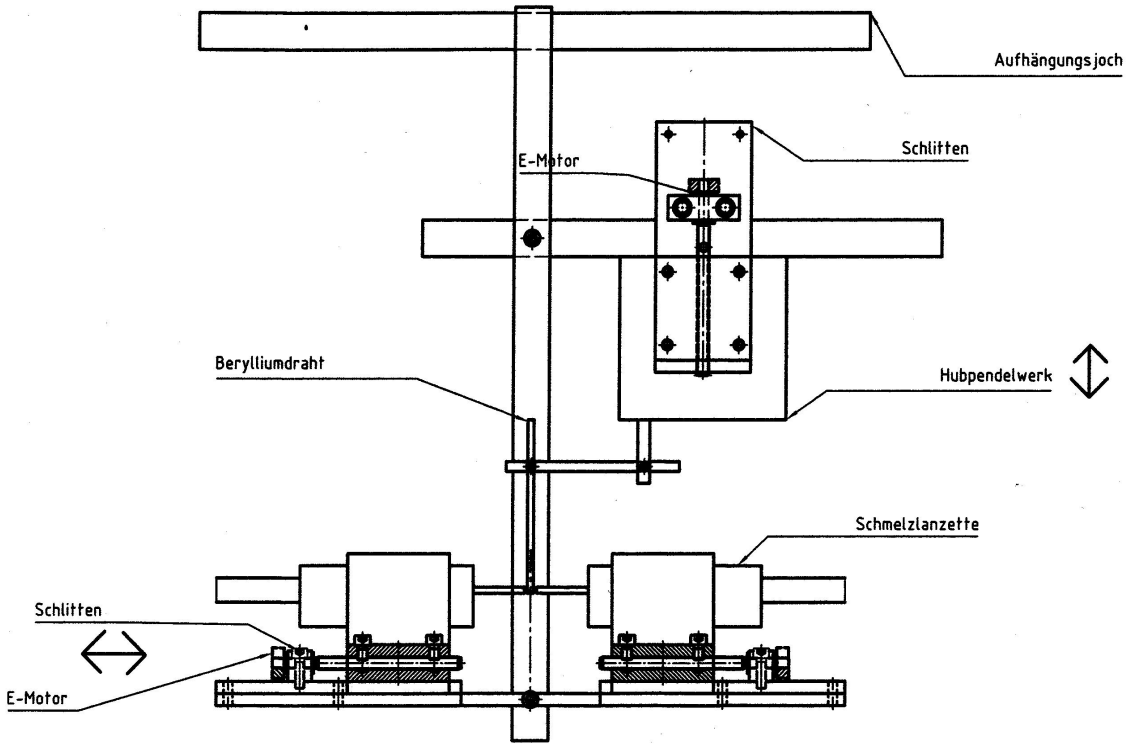

Fig. 4: Schematic draft of the melting facility for Be12Ti pebble fabrication.

Main aims of the next year are:

- Finishing of the preparation works in Beryllium Laboratory and putting it in operation;
- Performing of arc-melting tests on Be-Ti target;
- Tritium release experiments and characterisation of microstructure of fabricated specimens.

Staff:

P. Kurinskiy
A. Möslang
and Goraieb Versuchstechnik

Literature:

[1] P. Kurinskiy, A. Moeslang, A. Weisenburger, A.A. Goraieb, H.Harsch, “Characterisation of titanium beryllides”, Proceedings of 8th International Workshop on Beryllium Technology; 4-6 December 2007, Lisbon, Portugal (to be published);

[2] P. Kurinskiy, V. Chakin, A. Moeslang, R. Rolli, A.A. Goraieb, H. Harsch, E. Alves, N. Franco, “Characterisation of titanium beryllides with different microstructure”, Proceedings of 25th Symposium on Fusion Technology, 15-19 September 2008, Rostock, Germany (accepted for publishing).

Modelling of Pebbles and Pebble Beds

Modelling of Pebble Beds has been carried by Means of Continuum Mechanics and Discrete Element Method (DEM).

Development of DEM code

A discrete element simulation scheme for pebble beds in fusion blankets is being developed. Each individual pebble is considered as one element obeying equilibrium conditions under contact forces. It is possible to investigate by this method the rearrangement of particles and the overall behaviour of an assembly under the action of the macroscopic compressive stresses.

The simulation of uniaxial compression tests of Li_4SiO_4 pebble beds shows that the initial packing factor plays an important role in the mechanical response to the external excitation. A macroscopic irreversible deformation of pebble beds has been observed for assemblies with only elastic particles, suggesting that the rearrangement of particles is an important mechanism for macroscopic irreversibility. For different external loading levels and samples, the normalized force distributions are the same in the view of statistics. Furthermore, the average coordination number, as well as the average and maximum normal contact forces, is obtained as a function of the macroscopic hydrostatic pressure. This investigation gives not only a basic understanding of the response of pebble beds, but also the possibility to characterize the pebbles in a microscopic way. The discrete element method provides promising solutions for pebble bed related problems, such as the quantitative analysis of the crush probability, and moreover the yield surface of pebble beds.

Fig. 1 shows a typical visualization of a DEM simulation, including the inter-particle contact forces and elastic potential energy induced by contacting with neighbouring pebbles.

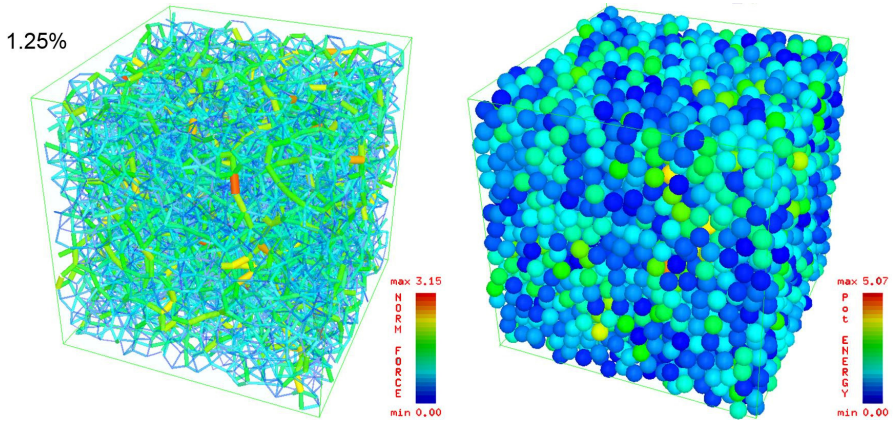

Fig. 1: Visualization of DEM simulation results: left, inter-particle force chain (unit: *N*); right, elastic potential energy (unit: $10^{-6}J$).

The scattering of strength of Li_4SiO_4 pebbles

The objective of this investigation is to study the crush probability of pebbles in HCPB blankets. First, the crush behaviour of single pebbles should be identified. It is appropriate to use probabilistic method to describe the strength due to data scattering.

Crush load tests of single pebbles were performed at the Fusion material laboratory (FML), IMF II. The diameters of the pebbles in the experiments vary over a range from 0.5 *mm* to 0.56 *mm*. The strength of the pebbles is depicted in terms of crush probability over crush

force under different test conditions (Fig. 2). The scattering of the strength is significant. However, the Weibull distribution can describe such distributions. The pebbles are crushed by a BK7 plate which is a relatively soft optical glass. From this, we try to derive the strength distribution when the pebbles are crushed by neighboring pebbles, which is the real case in HCPB and which is difficult to be carried in an experiment. To this end, the Weibull parameters are derived from the experiment data together with the simulated stress distribution. Then, the contact strength in terms of crush force is assessable. The software STAU is also used which is based on multiaxial Weibull theory.

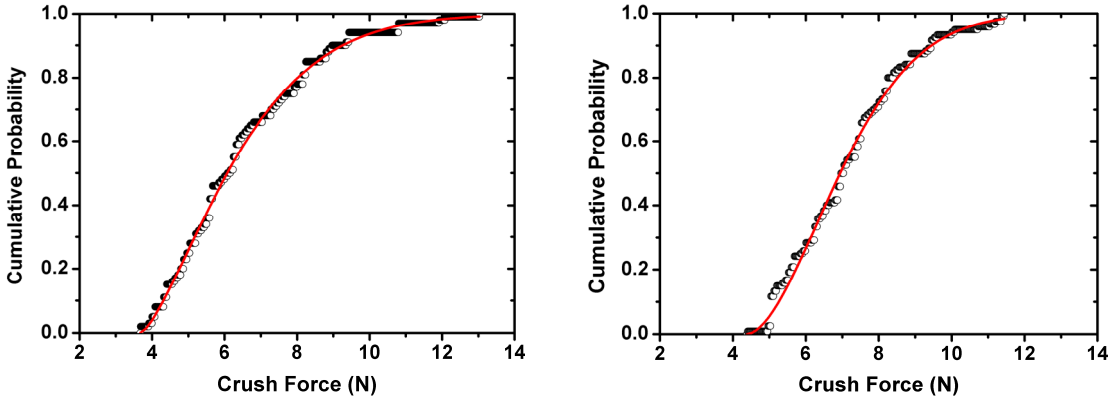

Fig. 2: Cumulative probability distribution of Li_4SiO_4 pebbles. (Left) Dried at 300°C; (Right) Un-dried. Red lines are the fitting curve with Weibull distribution.

The influence of coordination number

The contact strength of pebbles is derived in a uniaxial loading test (N_C=2). The influence of coordination number should be taken into account. We found an analytical solution of the stress distribution inside a pebble subject to compression by neighbouring pebbles. In this method, the pebbles are assumed to have perfect sphericity. Both uniformly distributed contact pressure and Hertzian contact pressure are adopted, respectively. A displacement potential is used together with the Fourier-Associated Legendre expansion for boundary conditions to obtain the stress distribution. From the analytical solution, it has been found that if volume fracture dominates, the influence of N_C is significant.

Staff:

M. Kamlah
Y. Gan
S. Zhao

Literature:

[1] Y. Gan and M. Kamlah (2007) Identification of material parameters of a thermo-mechanical model for pebble beds in fusion blankets. *Fusion Engineering and Design* **82**(2): 189-206.

Activation of Lithium Orthosilicate Breeder Materials

The fabrication of lithium orthosilicate (OSi) pebbles by melt-spraying enables a facile reprocessing of irradiated material by direct remelting [1]. However, the necessary waiting period for the reprocessing is determined by the long-term activation of the material under irradiation that is dominated by the impurities. The activation characteristics for the current composition of lithium orthosilicate pebbles were assessed on the basis of three-dimensional activation calculations for a fusion power reactor. The calculations were used to identify critical amounts of impurities and were compared to the results of a hypothetical, pure material without impurities, as well as to a calculated Li-6 enriched OSi composition [2].

The activation of the different OSi materials was calculated for a thin front layer in the central outboard blanket module of a fusion power reactor based on the HCPB blanket concept, i.e. the material was considered to be subjected to the highest radiation level over one full power year. The assumed fusion power amounts to 3300 MW. The neutron spectrum was calculated by a 3D Monte Carlo calculation with the MCNP5 code in a 175 energy group structure. The total flux calculated by MCNP is at $8.86 \cdot 10^{14}$ n/s·cm^2. The activation calculations were performed with the FISPACT inventory code using EAF-2007 activation data and the neutron flux spectrum provided by the MCNP calculation.

The contact dose rates (CDR) depending on time after shutdown were assessed for a hypothetical, pure OSi without impurities, for the current OSi pebble composition, as well as for a calculated composition of Li-6 OSi, based on the analysis of a 95.4% enriched Li-6 metal and a very pure silica powder [1]. For better comparison, the activation of former OSi pebbles with the composition given in [3] was recalculated for the irradiation conditions mentioned above. These OSi pebbles exhibited critical impurities of 4 µg/g Co and 60 µg/g Al. By using different raw materials, these impurities have been lowered to less than 1 µg/g Co and 30 µg/g Al for the current OSi pebbles. The most significant difference, however, is due to the fact that Pt-impurities were not considered in the former composition. For the current OSi pebbles platinum impurities of about 90 µg/g were measured that originate from the crucible used in the melt-spraying process.

Figure 1 displays the CDR versus time after shutdown for pure OSi, which mainly results from the production of Al-28, Na-24, Be-7, and Al-26. Due to the activity of Be-7, the recycling limit for remote handling (10 mSv/h) and the hands-on limit (10 µSv/h) are reached after <1 and <4 years, respectively. For the current OSi pebbles these limits are achieved after significantly longer times (Fig. 2). While there is no considerable difference in the activation during the first day (~$3 \cdot 10^{-3}$ years), the activation for up to 50 years is dominated by Co-60 originating from the assumed 1 µg/g Co-59 in the OSi pebbles, which is the determination limit in the current chemical analysis. The recycling limit is therefore only reached after nearly 40 years. After this time the CDR is dominated by Pt-193 that is responsible for reaching the hands-on limit after almost 400 years.

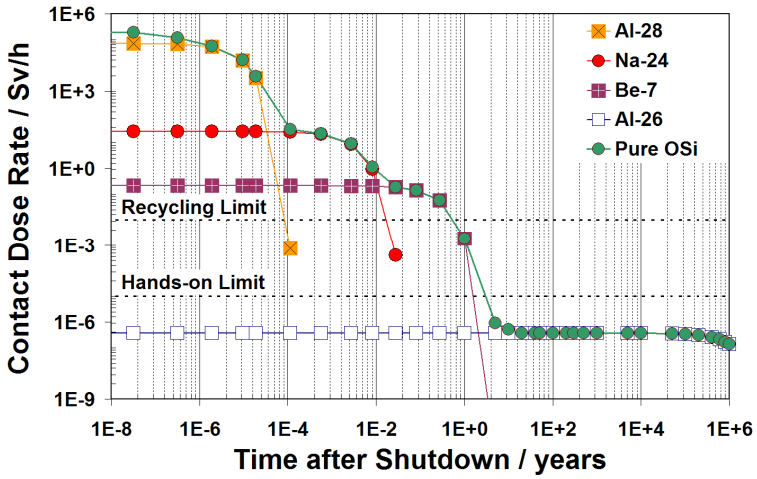

Fig. 1: Contact dose rate versus time after shutdown of pure OSi without impurities, and the main contributors Al-28, Na-24, Be-7, and Al-26 (from top to bottom).

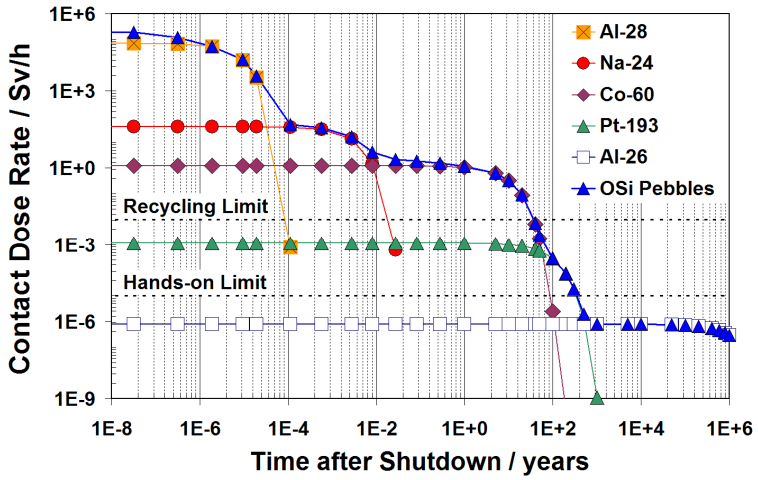

Fig. 2: Contact dose rate versus time after shutdown of current OSi pebbles, and the main contributors Al-28, Na-24, Co-60, Pt-193, and Al-26 (from top to bottom).

In Figure 3 the CDR of pure OSi and OSi pebbles are compared to the results gained for Li-6 OSi and the recalculated former OSi pebbles [3]. In the time up to 1 day the activation is dominated by Na-24. As the matrix effect of Na-24 is about 58%, due to the activation of Si-28, and only 42% of its activation is caused by Na-impurities, the higher Na-content in Li-6 OSi has no considerable influence on the total CDR. Additionally, Na-24 originates from Al-27, so that the lower Al-content in Li-6 OSi somewhat compensates the effect of the higher amount of Na-impurities.

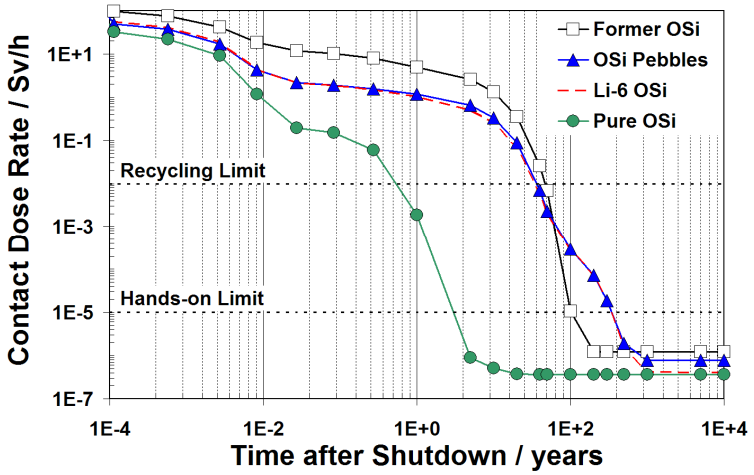

Fig. 3: Comparison of contact dose rates of former and current OSi pebbles, of Li-6 OSi, and of pure OSi.

The slightly lower Co-content in Li-6 OSi also has no significant effect on the CDR, and the waiting period for remote handling is barely changed compared to the current OSi pebbles. The hands-on limit is also reached after the same time, as the same Pt-content was assumed for Li-6 OSi. The activity of Al-26, dominant at very long times, depends besides the matrix effect also on the Al-content in the material. The CDR of Li-6 OSi at times >10^3 years is therefore smaller than in case of the current OSi pebbles, but both are well below the hands-on limit. The CDR of the former OSi material displays a different behaviour. Because of the higher Co-content of 4 µg/g, the limit for remote recycling is only reached after about 50 years. As Pt-impurities were not considered in the former composition, the limit for hands-on recycling is “apparently” reached after shorter times of 100 years. The higher amount of Al-impurities leads in this case to a notably higher activation at times >200 years that is yet below the hands-on limit.

The activation of OSi is strongly influenced by impurities. Compared to former OSi pebbles, the reduced amount of Co in the current OSi pebbles leads to a decrease of the waiting period for remote recycling from 50 to less than 40 years. It has to be emphasized, however, that 1 µg/g Co is the determination limit in the current chemical analysis by ICP-OES. That also means that no definitive statement can be made for the waiting period for remote recycling, and the current limit of detection may lead to an overestimation of activity. The reduced Al-content results in a lower activation at times >10^3 years, but as for both materials the value is below the hands-on limit, no significant improvement for the recycling is accomplished. The activation of the calculated Li-6 enriched OSi exhibits no relevant differences to the current OSi pebbles. The most significant result of the study is the activation of OSi by – formerly neglected – Pt-impurities. It was shown that due to these impurities the waiting period

for hands-on recycling is considerably increased from about 100 to almost 400 years. The study reveals that the activation of breeder materials is very sensitive to the smallest amounts of impurities. For reliable statements on the waiting period for recycling, the impurities of the raw materials and all possible contaminations by processing or handling have very carefully to be considered.

Present calculations focus on the change of activation as well as of the chemical composition after multiple steps of irradiation and subsequent reprocessing. In the considered scenario, lithium orthosilicate pebbles were assumed to be irradiated in a fusion power reactor over three full power years. In order to compensate the burn-up of Li-6, a remelting of the pebbles was supposed to take place after a waiting period of not more than ten years, in which the hands-on limit or at least the remote-handling was reached. The averaged contact dose rates of the ceramic breeder inventory and the change of the isotopic composition were calculated for 15 cycles of irradiation and remelting. The results demonstrated that it seems to be possible to recycle the OSi pebbles by a simple remelting over a long period without a need for a wet-chemical recycling step to extract any impurities.

Thermal Conductivity of Sintered Lithium Orthosilicate Compacts

The design of solid breeder blankets is strongly affected by the low values of thermal conductivity and density of ceramic breeder pebble beds. A significant rise of both quantities would enhance the thermal performance and lead to an increased tritium breeding ratio. In order to improve these quantities sintered lithium orthosilicate compacts were considered as alternative breeder materials [4]. Ceramic compacts with different densities were made from different pretreated OSi pebble material. Crushed material or large OSi pebbles were dry pressed and subsequently sintered at different temperatures. Furthermore, samples of low density cellular ceramics were also prepared by infiltration of polymer foams with ceramic slurry. OSi pebbles and the microstructure at fracture surfaces of sintered compact with densities ranging from 23 to 89% TD are shown in figure 4.

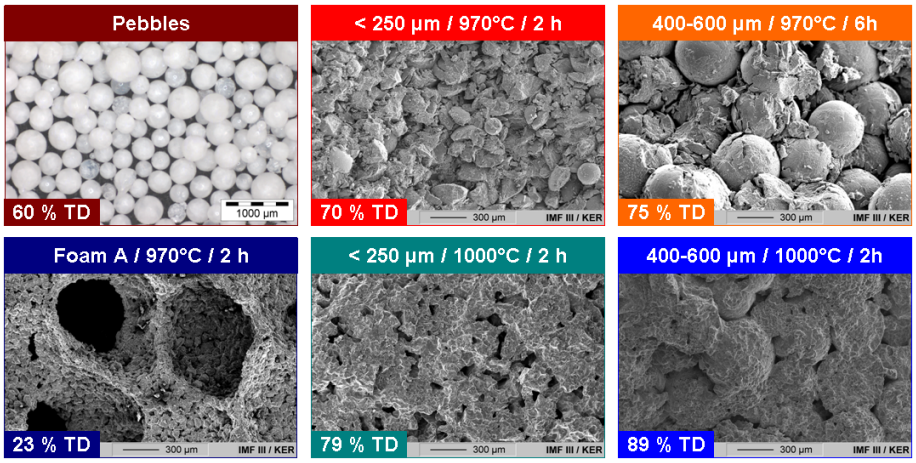

Fig. 4: SEM images of pebbles and fracture surfaces of porous sintered compacts.

The thermal diffusivity of cylindrical ceramic pellets was determined by the heat pulse method using a laser flash device at temperatures between 25 and 750 °C in helium atmosphere, ceramic foams were measured in argon. A pebble bed characteristic sample was also investigated in order to check the measurement accuracy in comparison with previous results. The thermal conductivity λ was evaluated from the thermal diffusivity α, the measured OSi specific heat capacity c_p and the OSi density ρ as a function of temperature according to $\lambda(T) = \alpha(T)\ \rho(T)\ c_p(T)$.

The results shown in figure 5 demonstrate that the thermal conductivity is not only affected by the sample density but by the microstructure and the pore structure as well. The highest values of thermal conductivity were determined for samples made of large particles, followed by the samples made of crushed powder. In each case the sample with the higher density – resulting from a higher sintering temperature - exhibits the higher thermal conductivity. While for most dense sample (89% TD) thermal conductivity values of more than 2 W/m K were obtained, the lowest values (0.5 W/m K at 600 °C) belong to foam with a density of 23% TD. For the low density foams, the contribution of the gas to the effective thermal transport may be larger compared to the other samples, which also leads to a different temperature dependence of the thermal conductivity, i.e. the value increases with rising temperature.

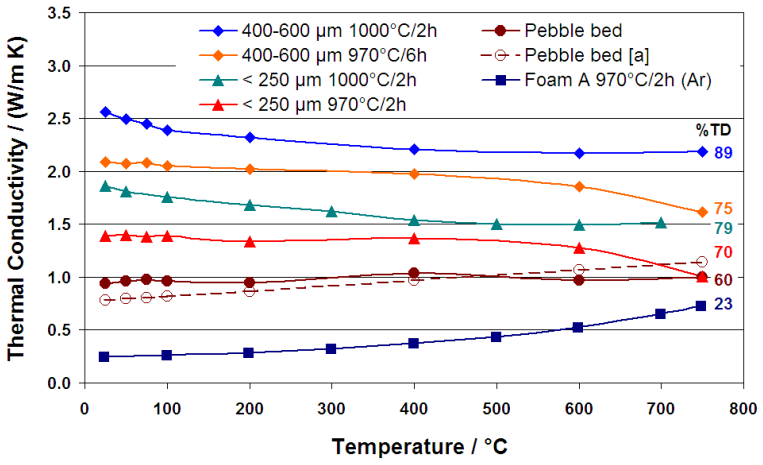

Fig. 5: Thermal conductivity of pebble beds and porous samples. The colours refer to the samples in fig. 4 ([a] Reimann & Hermsmeyer, Fus. Eng. Des. 61-62 (2002) 345-351).

The results show that the thermal conductivity is affected by the density as well as by the microstructure of the ceramic samples. Therefore, variations in the manufacturing procedure have a clear impact on the thermal conductivity of sintered lithium orthosilicate plates. Compared to OSi pebble beds, the sintered bodies consisting of relatively large particles have thermal conductivities up to two times higher. The OSi density also increases remarkably by up to 30%. These two improvements have a large impact on the blanket design: A larger thickness of breeder zones can be realized which reduces the inventory of the structural material. This leads to an increased breeding ratio which enables blanket designs with a smaller radial thickness or a reduced beryllium inventory. The open porosity in sintered plates consisting of large particles should be favourable for tritium removal. Presently the pressure drop of these samples is investigated in order to prove a sufficient flow of the purge gas.

Out-of-Pile Tritium Release from Current Lithium Orthosilicate Pebbles

Out-of-pile annealing tests were performed using lithium orthosilicate pebbles irradiated in the Kyoto university research reactor [5]. Moreover, the effect of the deposition of palladium in the lithium orthosilicate pebbles on the behaviour of tritium release was investigated [6]. Therefore palladium was deposited by the incipient wet impregnation method before irradiation. In the out-of-pile experiments the temperature was increased with 5 K/min up to 900 °C using a sweep gas of 0.1% H_2/N_2 with a flow rate of 100 ml/min. Subsequently the samples were held at 900 °C for 3 hours. During this time the sweep gas was mixed with 1% H_2O/N_2 to gain a sweep gas of (0.05% H_2 + 0.5% H_2O)/N_2 with a flow rate of 200 ml/min to ensure the release of all the tritium in the breeder material. The concentrations of tritium were traced with two ionization chambers for the separate measurement of different chemical forms of tritium. The total tritium concentration (molecular form of tritium and tritiated water vapour, HT and HTO) was measured with the first ionization chamber. Then the gas was introduced to a water bubbler, which removes tritiated water vapour from the process gas. After this procedure, the gas was again introduced to the second ionization chamber, which makes it possible to measure only the concentration of molecular form of tritium (HT).

Figure 6 shows the result of out-of-pile annealing tests with OSi pebbles irradiated for 6 min in the thermal reactor and with a 0.1% H_2/N_2 sweep gas [5]. In this figure, the change in the total tritium concentration (denoted as HT+HTO) in the outlet stream of the reactor and the change in the concentration of molecular form of tritium (denoted as HT) are shown. The dotted line shows the change in the reactor temperature. The main tritium release started at approximately 200 °C. The release curve appears to have two major peaks at temperatures of 310 and 450 °C. At higher temperatures tritium was gradually released with increasing temperature. The change in the concentration of molecular form of tritium (denoted as HT) indicates that almost no molecular form of tritium was released. Thus, it can be said that almost all the tritium bred in the OSi pebble was released as tritiated water vapour. This result suggests that the isotope exchange reaction on the Li_4SiO_4 sample surface is quite slow. Even after the reactor temperature reached 900 °C, the tritium was continuously released. When the sweep gas was replaced by (0.05% H_2 + 0.5% $H_2O)/N_2$, tritium release was once enhanced and the tritium release still continued for 3 h. However, compared to former investigated OSi pebbles [7], the tritium release performance of the current OSi pebbles fabricated from LiOH and SiO_2 was considerably improved as larger amounts of tritium were released at lower temperatures.

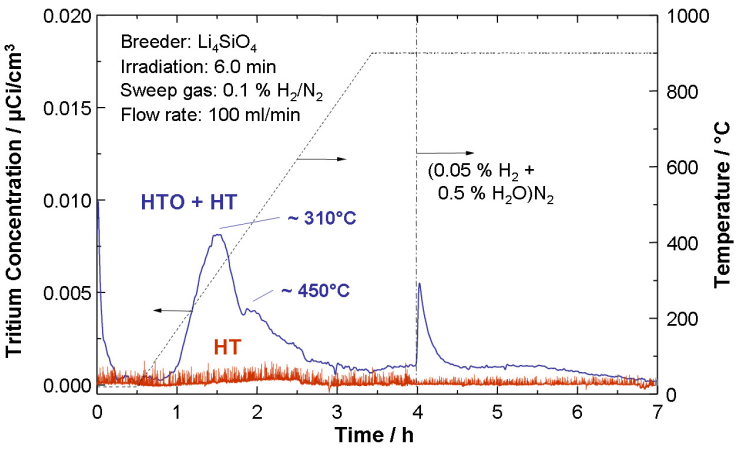

Fig. 6: Out-of-pile annealing experiment of irradiated Li_4SiO_4 pebbles.

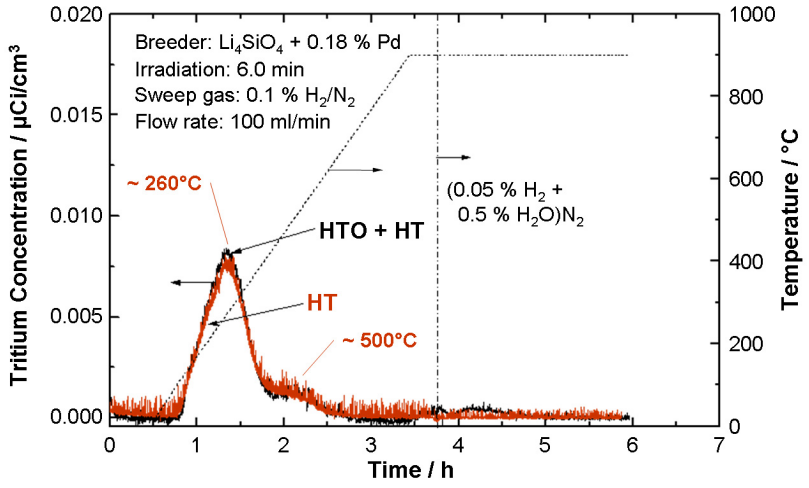

Fig. 7: Out-of-pile annealing experiment of irradiated Li_4SiO_4 pebbles with 0.18% Pd.

Figure 7 shows the result of out-of-pile annealing tests with the Li_4SiO_4 pebble deposited with 0.18 wt.% of Pd, which was irradiated for 6 min in the thermal reactor [6]. The main tritium release started at approximately 100 °C. The release curve appears to have one major peak at a temperature of about 260 °C. These results suggest that the tritium was released at lower temperatures in comparison to Li_4SiO_4 with no catalyst. Figure 7 also indicates that almost all the tritium was released as HT. This result suggests that the isotope exchange reaction on the surface of the Li_4SiO_4 pebble was substantially promoted and the release rate of tritium as the molecular form was enhanced by the deposition of palladium.

The experimental results indicate that almost all tritium was released as tritiated water vapour from the untreated lithium orthosilicate pebbles. In contrast, it was found that tritium was released as HT from the lithium orthosilicate pebbles deposited with palladium at lower temperatures. Therefore, it can be said that the deposition of catalytic metal in the lithium orthosilicate pebble is effective to improve the tritium release from the breeder. Yet it should be

considered that a deposition of palladium would significantly increase the activation of OSi pebbles under irradiation.

Staff:

C. Adelhelm
B. Dörzapf
U. Fischer
S. Herber
U. Kaufmann
R. Knitter
B. Löbbecke
C. Odemer
M. Offermann
M. Rohde
B. Wagner

Literature:

[1] R. Knitter, B. Löbbecke, Reprocessing of lithium orthosilicate breeder material by remelting, J. Nucl. Mater. 361 (2007) 104-111.

[2] R. Knitter, U. Fischer, S. Herber, C. Adelhelm, Reduction of impurities and activation of lithium orthosilicate breeder materials, to be published in J. Nucl. Mater.

[3] U. Fischer, H. Tsige-Tamirat, Activation characteristics of a solid breeder blanket for fusion power demonstration reactor, J. Nucl. Mater. 307-311 (2002) 798-802.

[4] B. Löbbecke, R. Knitter, M. Rohde, J. Reimann, Thermal conductivity of sintered lithium orthosilicate compacts, to be published in J. Nucl. Mater.

[5] K. Munakata, T. Shinozaki, K. Inoue, S. Kajii, Y. Shinozaki, R. Knitter, N. Bekris, T. Fujii, H. Yamana, K. Okuno, Tritium release from lithium silicate pebbles produced from lithium hydroxide, Fus. Eng. Des. (2008), doi:10.1016/j.fusengdes.2008.05.039.

[6] K. Munakata, T. Shinozaki, K. Inoue, S. Kajii, Y. Shinozaki, T. Takeishi, R. Knitter, N. Bekris, T. Fujii, H. Yamana, K. Okuno, Tritium release from lithium orthosilicate pebbles deposited with palladium, to be published in J. Nucl. Mater.

[7] K. Munakata, Y. Yokoyama, A. Koga, N. Nakashima, S. Beloglazov, T. Takeishi, M. Nishikawa, R.-D. Penzhorn, K. Kawamoto, H. Moriyama, Y. Morimoto, K. Okuno, Effect of catalytic metals on tritium release from ceramic breeder materials, J. Nucl. Mater. 307-311 (2002) 1451-1455.

TTBC-006
Helium-Cooled Lithium Lead: Magneto-Hydrodynamics and Liquid Metal Materials

TW5-TTBC-006 D 1
MHD Experiments in a Mock-up Relevant for a Helium Cooled Lead Lithium Test Blanket Module for ITER

Experimental and theoretical investigations of magnetohydrodynamic (MHD) flows in a scaled mock-up of a Helium-Cooled Lead Lithium (HCLL) Test Blanket Module (TBM) for ITER have been performed to get insight into the complex physics that governs the flow of the electrically conducting breeding material PbLi, while it is slowly circulated through the module placed in the strong plasma-confining magnetic field. The blanket module is subdivided into a number of rectangular boxes called the Breeder Units (BUs), which are arranged in poloidal columns. In the present mock-up design each breeder unit contains five *radial-toroidal* cooling plates that subdivide each box into six slender ducts. The MHD interaction between the moving electrically conducting fluid and the magnetic field influences the flow distribution and determines the pressure drop in the TBM. Moreover, since all the walls are electrically conducting, currents induced in one breeder unit may cross common walls towards neighboring fluid domains creating a strong electromagnetic coupling among all breeder units and sub-channels. An overview about liquid metal blankets with focus on the present helium cooled TBM has been given in [1], a detailed description about electromagnetic flow coupling in the TBM can be found in [2],[3], the experimental results are described in [4].

The MHD mock-up has been fabricated and installed into the liquid metal NaK loop of the MEKKA laboratory at the Forschungszentrum Karlsruhe [5]. In this loop flow rates up to 25 m^3/h and pressure heads up to 9 bar can be realized. The test section is placed in a strong homogeneous magnetic field $\mathbf{B} = B\hat{\mathbf{z}}$ that can reach values up to B=2.1 T. Experiments are performed for different values of the magnetic induction and flow rate, denoted by the nondimensional Hartmann and Reynolds numbers,

$$Ha = LB\sqrt{\frac{\sigma}{\rho\nu}} \quad \text{and} \quad Re = \frac{v_0 L}{\nu}, \tag{1}$$

respectively. Here, L stands for the Hartmann length of the breeder units as shown in Figure 1 and v_0 represents the average velocity in one breeder unit. The variables σ, ρ and ν denote electric conductivity, density and kinematic viscosity of the liquid metal. The test blanket modules in ITER are operated at Hartmann numbers Ha > 104 and Reynolds numbers Re < 500. In the present experiment flows at 500 < Ha ≤ 5000 and 150 < Re < 16000 have been investigated with the aim to extract the relevant scaling laws that allow a physically correct extrapolation of results to reactor conditions.

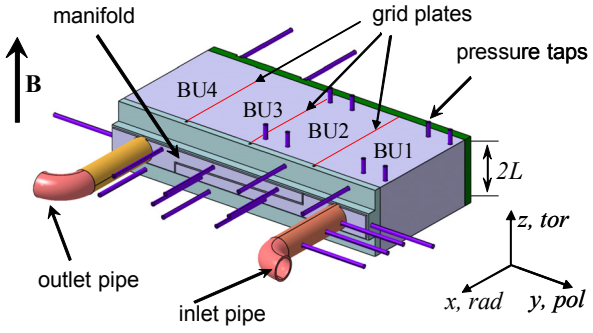

Fig. 1: Test section consisting of 4 BUs, manifolds, inlet and outlet pipes. Pressure differences are measured at 27 pressure taps.

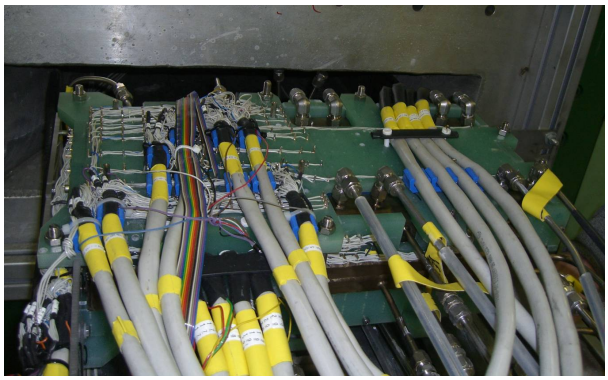

Fig. 2: Instrumented test section in front of the magnet. Insulating plates carry 600 sensors for measuring the distribution of surface potential.

A major concern for the operation of a HCLL TBM is the MHD pressure head that is necessary to drive the liquid breeder at a required flow rate. For that reason the pressure distribution on the surface of the module was recorded at 27 pressure taps (Figure 1) along typical flow paths, as indicated in Figure 3, for various Hartmann and Reynolds numbers. A characteristic result is shown in Figure 4. Here the nondimensional pressure distribution (pressure scaled by $\sigma v0LB^2$) is shown along the length of individual flow paths, starting from the entrance pipe (AB) and inlet manifold (BC), through breeder units (DE and FG) and exit manifold (HI). The major pressure drop occurs in the feeding and draining pipes and along the manifolds since in these elements the velocity is the highest. Along the breeder units instead the pressure drop is almost negligible as estimated in [6].

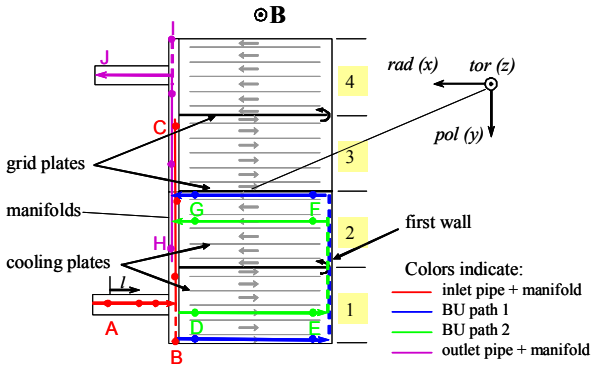

Fig. 3: Sketch of flow paths in the mock-up: (AC) entrance pipe and manifold, (DE and FG) breeder units, (HI) exit manifold.

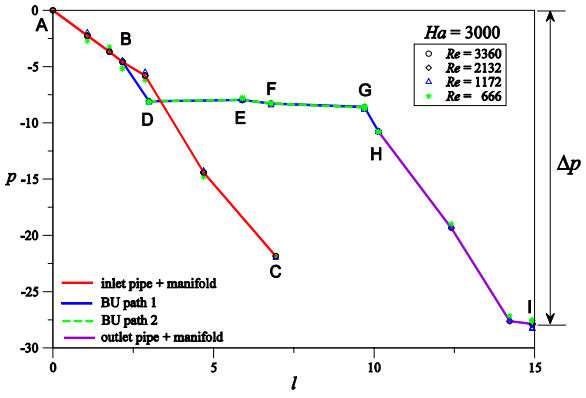

Fig. 4: Pressure distribution along typical flow paths for Ha=3000 and different Reynolds numbers.

Another quantity measured during the experiments is the electric potential recorded on the surface of the test section. Its distribution gives essential information about the flow pattern inside the mock-up. It can be shown that the velocity components in a plane perpendicular to the applied magnetic field are related to the potential ϕ as $u \approx -B^{-1}\partial\phi/\partial y$, $v \approx B^{-1}\partial\phi/\partial x$, i.e. in a uniform magnetic field the potential ϕ serves as approximate hydrodynamic streamfunction of the flow. Isolines or contours of ϕ, as shown for example on the top

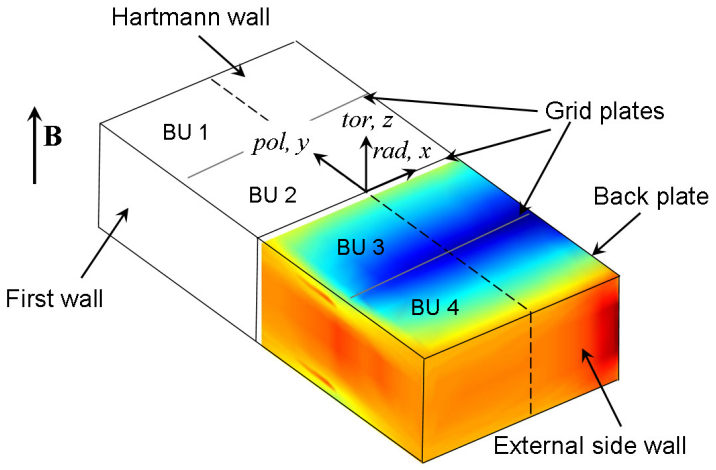

Fig. 5: Colored contours of measured surface potential on BU3 and BU4 indicate the flow distribution in the two breeder units for Ha=3000, N=1325.

wall of the test section in Figure 5, represent the streamlines of the considered MHD flow. The displayed experimental result has been obtained for a strong magnetic field corresponding to a Hartmann number of Ha=3000. Further results have been published in [7].

More quantitative values for potential distribution across 4 BUs, measured in the middle of the module at x=0, can be seen from Figure 6. We observe an almost linear variation of the nondimensional potential ϕ (potential scaled by v_0LB) within each breeder unit. A comparison with numerical simulations [3] confirms the quality of the measurements, supports and validates the assumptions used for simulations and the numerical methods.

As mentioned above the potential gradient $\partial\phi/\partial y$ can be directly related to the velocity component u so that the potential difference between two internal cooling plates at distance Δy gives the flow rate or average velocity in the considered subchannel. Results for nondimensional average velocity $\bar{u}$ (velocity scaled by v_0) are displayed in Figure 7 for a constant Hartmann number Ha=3000 and various Reynolds numbers. We observe a flow towards the first wall (negative velocity) in breeder units BU1 and BU3 and a flow towards the back plate in BU2 and BU4 as expected from the design. The flow distribution becomes more uniform for lower flow rates like those foreseen in blanket applications, where the Reynolds numbers are small. A detailed study showing the influence of the magnetic field strength and flow rate can be found in [4].

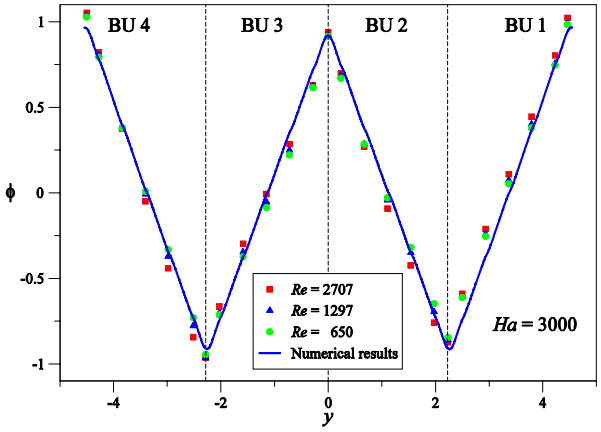

Fig. 6: Variation of potential on the upper wall of the module at x=0 for Ha=3000.

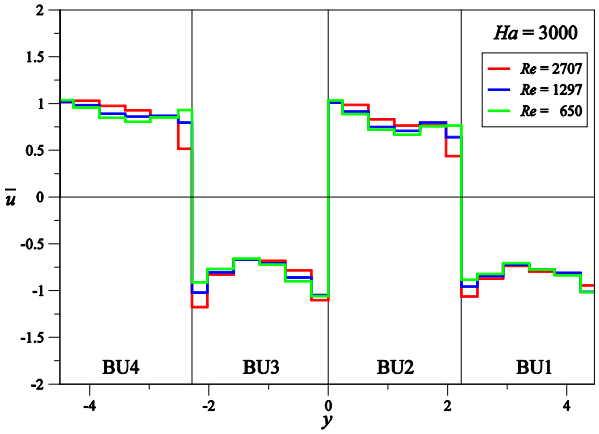

Fig. 7: Variation of average velocity in four breeder units of the module at x=0 for Ha=3000.

Further suggested investigations

In the present experiment walls and cooling plates, containing helium channels in the proposed blanket concept, have been manufactured as solid walls. Helium channels have been taken into account by adjusting the wall thickness to reach electric conductance comparable to that in the original design. Future studies will address these issues, related to the non-homogeneous wall conductance due to the presence of helium channels, which have been identified in [9],[10]. Moreover, the current database will be extended to account also for flows in non-uniform magnetic fields.

Influence of sensors on MHD flows

In liquid metal duct flows exposed to an external magnetic field, data for local velocity may be obtained from measurements of electric potential gradients. They are recorded by Liquid-metal Electromagnetic Velocity Instruments (LEVI), also known as conduction anemometers, which are moved across the channel. They consist of a number of fine sensing wires, placed at defined reciprocal distance, insulated except at the tips. A four-wire probe is shown in Figure 8. If electric currents are sufficiently small, the potential gradient signals can be directly interpreted as a measure for velocity components perpendicular to the magnetic field. In-

stead if 3D currents are present the LEVI readings may become inaccurate. The presence of the probe itself may introduce perturbations to the flow since internal shear layers develop along the magnetic field lines tangent to the shaft and body of the probe. Experiments [11] show asymmetry in the distribution of the measured transverse potential gradient and its underestimation compared to the one expected from flow rate measurements.

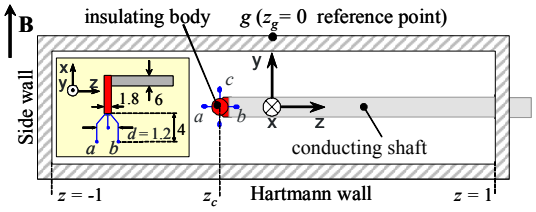

Fig. 8: Sketch of a LEVI in a rectangular duct.

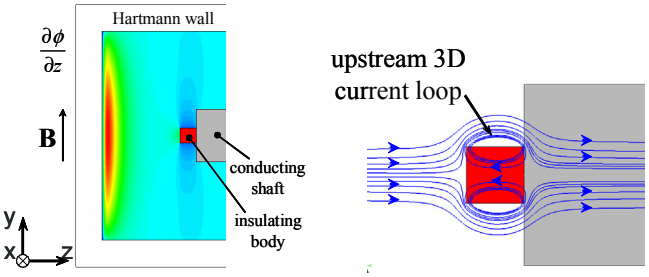

Fig: 9: Numerical results of a MHD flow around a probe. a) contours of electric potential, b) streamlines of 3D recirculating currents.

A numerical analysis of 3D MHD flows around a probe in a rectangular duct has been performed to study the influence of the instrument on the readings. The numerical results (Figure 9) indicate, as a possible reason for the observed experimental deviations, the occurrence of 3D disturbances in the vicinity of the probe caused by circulating currents and internal parallel layers produced by the instrument. Calculations confirm that probes can give reliable data for potential and its gradient after careful calibration. See references [11]-[13].

Staff:

L. Bühler
H.-J. Brinkmann
S. Horanyi
C. Mistrangelo
K. Starke

Literature:

[1] L. Bühler, 2008 Evolution of Liquid Metal Blankets and Requirements for Magnetohydrodynamic Predictions, Proceedings of XXVI UIT Heat Transfer Conference, Palermo.

[2] C. Mistrangelo, L. Bühler, 2008, Electric flow coupling in the HCLL blanket concept, Fusion Engineering & Design, accepted.

[3] C. Mistrangelo, 2008, Magnetohydrodynamic flow in a mock-up of a HCLL blanket. Part I numerical analysis, Technical report FZKA 7312, Forschungszentrum Karlsruhe.

[4] L. Bühler, H.-J. Brinkmann, S. Horanyi, K. Starke, 2008, Magnetohydrodynamic flow in a mock-up of a HCLL blanket. Part II Experiments, Technical report FZKA 7424, Forschungszentrum Karlsruhe.

[5] K. Starke, L. Bühler, S. Horanyi, 2007, Experimental investigations of liquid-metal MHD flows in a mock-up of a HCLL blanket (poster), 8th International Symposium on Fusion Nuclear Technology (ISFNT-8).

[6] L. Bühler, L. Giancarli, 2005, Magnetohydrodynamic flow in the European HCLL blanket concept, Technical report FZKA 7069, Forschungszentrum Karlsruhe.

[7] K. Starke, L. Bühler, S. Horanyi, 2008, Experimental investigations of liquid-metal MHD flows in a mock-up of a helium cooled lead-lithium test blanket for ITER, Proceedings of 7th PAMIR International Conference on Fundamental and Applied MHD, Giens.

[8] K. Starke, L. Bühler, S. Horanyi, 2008, Experimental MHD-flow analyses in a mock-up of a test blanket module for the ITER, 25th Symposium on Fusion Technology (SOFT), Rostock.

[9] C. Mistrangelo, L. Bühler, 2008, Influence of helium cooling channels on liquid metal magnetohydrodynamic flows in the HCLL blanket, 25th Symposium on Fusion Technology (SOFT), Rostock.

[10] C. Mistrangelo, 2008, Effects of cooling channels on magnetohydrodynamic flows in liquid metal blankets, Technical report FZKA 7443, Forschungszentrum Karlsruhe.

[11] L. Bühler, S. Horanyi, C. Mistrangelo, Interpretation of LEVI velocity signals in 3D MHD flows, Fusion Engineering & Design, 2008, accepted.

[12] C. Mistrangelo, L. Bühler, 2008, Perturbations of MHD flows caused by the presence of an electric potential probe, Proceedings of 7th PAMIR International Conference on Fundamental and Applied MHD, Giens.

[13] C. Mistrangelo, L. Bühler, 2008, Disturbances produced by an electric potential probe on MHD flows in rectangular ducts, Technical report FZKA 7415, Forschungszentrum Karlsruhe.

Materials Development
Structural Materials

EFDA/05-1244 (TW4-TTMS-RedAct)
Investigation of Options to Reduce Critical Elements in Low Activation Ferritic/ Martensitic Steels

In the last few years considerable improvement has been made in the definition and fabrication of ‘reduced activation’ ferritic-martensitic steels (RAFM). Two batches of a 9CrWVTa-steel called EUROFER 97-1 and EUROFER 97-2, respectively, including 10 heats were produced by Boehler in 1999 and by SaarSchmiede in 2003. A third batch of about 11 tons is currently being produced. The activities have demonstrated that RAFM steels can be successfully produced at industrial scale. The steels, nominally according to the same specification, actually differ in the detailed contents of minor alloying elements and of impurities. All met the goal of an overall low content of those elements which have a detrimental effect on the long-term activation behaviour. Thereby, a remarkable step is achieved towards the final goal of the production of ‘low activation’ steels for the use in a DEMO (demonstration reactor).

Studies for further reduction of impurities need to be launched as a generic property of RAFM steels.

The objectives of this task are

- To identify a number of critical elements that should be further reduced for the EUROFER 97 technical specification and to which level.
- To assess in cooperation with steel producers the technical feasibility.
- To define the specifications of a new heat (or a series of heats) to be produced.
- To determine in cooperation with the steel producers the uncertainty range in the concentrations of the various elements (alloying elements and impurities) in the heat.
- To determine the different and likely increasing costs of the heats with reduced impurity levels.
- To analyse by different laboratories (i.e. the steel producers and qualified EU/EFDA associations) and different methods, the chemical composition of the material produced up to now and from the new melts.

In order to qualify laboratories well in advance a Round Robin should be organized where a ‘blind test’ of a laboratory heat is going to be analysed for a list of critical elements specified in advance.

Status of work

A comparison of the chemical composition as specified in the technical specification for EUROFER 97-1 and EUROFER 97-2 and the results achieved in the industrial production of the different products has been performed and the reasons for deviations from the specifications have been analysed.

A web-based version of the FISPACT 2005 code has been implemented and numerous calculations with varied compositions of EUROFER have been performed to check the influence of different radiologically undesired elements [1] (Nb, Mo, Al, Ni, Cu, Co) on the activation behaviour of the steel. The calculations showed that only EUROFER 97-1, passing the Low Level Waste activation level after about 100 years, can be regarded as reduced activation material. EUROFER 97-2 needs about 30,000 years to fall below this limit. The main originator for this behaviour is Niobium, the content of which is 5 times higher for EUROFER 97-2 than for EUROFER 97-1. Calculations for EUROFER 97-2 with a systematic variation of the Nb content and unchanged contents of the other alloying elements showed, that the Nb content should be well below 10 ppm to assure “low level waste” properties.

On the basis of the above mentioned calculations trial heats can be specified. Input for a separate Art. 7 contract for the cooperation with steel manufacturers has been given. A call for tender has been launched and a manufacturer, experienced in the production of RAFM steels, was selected as industrial partner for the production of trial heats and performance of the above mentioned study. In the course of this study the different pathways on which the above mentioned detrimental elements come into the final RAFM steel product were analysed. These findings were used in the production of the new 11 ton EUROFER 97-3 heat and led to a considerable reduction of the Nb content.

In preparation of the Round Robin experiment for the chemical analysis of the undesired detrimental elements, material of former and also the latest production has been selected. This material underwent analytical homogeneity tests to assure, that the chemical composition does not vary locally. Six different industrial and research laboratories affirmed their participation in this Round Robin experiment. The results are expected for mid of the year 2009.

Staff:

R. Lindau
C. Adelhelm
T. Kaiser

Literature:

[1] Lindau, R.; Möslang, A.; Rieth, M.; Klimiankou, M.; Materna-Morris, E.; Alamo, A.; Tavassoli, A.-A. F.;. Cayron, C; Lancha, A.-M.; Fernandez, P.; Baluc, N.; Schäublin, R.; Diegele, E.; Filacchioni, E.; G.Rensman, J.-W.; v.d. Schaaf, B.; Lucon, E.; Dietz, W.; Present Development Status of EUROFER and ODS-EUROFER for Application in Blanket Concepts, Fusion Engineering and Design, 75-79 (2005) p.989-996

[2] S. Kelzenberg; Berechnung und experimentelle Verifizierung von Materialaktivierungen in D-T Fusionreaktoren, Dr.-Thesis, FZKA Report 5836 (November 1996) p. 48.

[3] Lucon, E.; Benoit, P.; Jacquet, P.; Diegele, E.; Lässer, R.; Alamo, A.; Coppola, R.; Gillemot, F.; Jung, P.; Lind, A.; Messoloras, S.; Novosad, P.; Lindau, R.; Preininger, D.; Klimiankou, M.; Petersen, C.; Rieth, M.; Materna-Morris, E.; Schneider, H.C.; Rensman, J.W.; van der Schaaf, B.; Singh, B.K.; Spätig, P.; The European effort towards the development of a DEMO structural material: irradiation behaviour of the European reference RAFM steel EUROFER. Fusion Engineering and Design 81(2006) S.917-23

EFDA/06-1520 (TW6-TTB-EUROFER)
Support and Follow-up of the EFDA/06-1903 Art. 7 Contract for Procurement of EUROFER for the TBM Fabrication Technology Trials and Mock-ups

The main objective of this task is to support the EFDA Art. 7 contract 06-1903 for the procurement of app. 11 tonnes of EUROFER 97 RAFM steel in various semi-finished product forms. This material shall be used for fabrication technology trials and to build various components and mock-ups of Test Blanket Modules (TBM). An additional goal is to check the reproducibility of properties compared to two batches of EUROFER 97 available from the previous fabrications and to assess the achievable limits of reduction of detrimental impurities like Nb, Mo, Ni, Cu, Al, Co.

In order to follow-up the EUROFER fabrication process, meetings (including kick-off and acceptance meetings) with the steel manufacturer have to be organised. If necessary, intermediate meetings to resolve questions arising during the fabrication, in particular the problems arising during rolling of thick plates (which have not been produced so far) must be organised.

The outcome of the meetings has to be reported to EFDA and a final technical report describing EUROFER fabrication process details and results of the performed tests and controls has to be prepared.

Status of work

After a Europe-wide call for tender for the production of about 11 tonnes of EUROFER 97 RAFM steel in various product forms (see table 1) Saarschmiede was assigned for the production according to the technical specification, which is close to the specification for the recent production of EUROFER 97-2. Table 2 gives the specified chemical composition of the material to be produced. After signature of the contract by the partners, a kick-off meeting took place in November 2007 where the critical issues for the production were discussed.

Table 1: Dimensions and quantity of semi-finished products.

Semi-finished product	Thickness	Area	Length	Mass	Total Mass
	mm	m^2	mm	kg	kg
Plates *)	1	14		109	
	8	5		312	
	10	5		390	
	12	14		1310	
	16	15		1872	
	20	4		624	
	25	10		1950	
	32	10		2496	
	35	3		819	
	48	1		374	
					10256
Forging/billet	100 x 100 mm^2		3000	234	
					234
					10490

*) All plates 1000 x 2000 mm

Table 2: Specified chemical composition.

Element	Min. Value (wt%)	Max. Value (wt%)	Remarks
Carbon	0.090	0.120	Target 0.11
Manganese	0.20	0.60	Target 0.4
Phosphorus		0.005	
Sulphur		0.005	
Silicon		0.050	
Nickel		0.01	ALAP
Chromium	8.50	9.50	Target 9.0
Molybdenum		0.005	ALAP
Vanadium	0.15	0.25	
Tantalum	0.10	0.14	Target 0.12
Tungsten	1.0	1.2	Target 1.1
Titanium		0.02	
Copper		0.01	ALAP
Niobium		0.005	ALAP
Aluminium		0.01	ALAP
Nitrogen	0.015	0.045	Target 0.030
Boron		0.002	ALAP
Cobalt		0.01	ALAP
As+Sn+Sb+Zr		0.05	Target
Oxygen		0.01	

Before the rolling of the billets to plates, a technical meeting with the subcontractor for rolling, Böhler Bleche in Austria, took place in June 2008. In this meeting specific problems concerning the rolling procedure of the thicker plates (t>25 mm) where discussed in order to ensure overall homogenous properties.

Outlook

The production is finished and the products have been tested according to the specification. The delivery of plates ex works can take place after acceptance by EFDA/F4E.

Staff:

R. Lindau

TTMS-001
Irradiation Performance

TW2-TTMS-001b D 5
Tensile, Charpy and Fatigue Specimen Testing after Neutron Irradiation up to 15 dpa in the Range of 250 °C - 450 °C, Completion of the Irradiation and Post-irradiation Examination

Objectives

In the HFR IIb SPICE-T irradiation program the emphasis is put on the investigation of irradiation induced embrittlement and hardening in the newly developed RAFM steel EUROFER 97 and a first alloy EUROFER 97 ODS HIP. EUROFER belongs to the category of 8-10%Cr-WTaV steels which are a successful material for the nuclear use in a wide temperature range. Such advanced martensitic steels are leading candidates for fusion structural components. They are interesting due to their resistance to void swelling, and good balance of different physical und mechanical properties. However, a critical effect of low temperature irradiation-induced hardening and embrittlement occurs in the range of 250 – 350 °C. In this context, different RAFM alloys were irradiated but with a matter of particular interest in the EUROFER 97 alloys, table 1.

Table 1: Chemical composition of EUROFER97 given in wt.%.

Alloying Elements	**C**	**Si**	**Mn**	**Cr**	**Mo**	**Ni**	**Al**	**Nb**	**Ti**	**V**	**W**	**N**	**Ta**
	0.12	0.04	0.48	8.91	<0.001	0.02	0.009	0.0017	0.001	0.2	1.08	0.02	0.14

EUROFER 97 was irradiated in two conditions; as received (980 °C 0.5 h + 760 °C 1.5 h), and as received and heat treated (1040 °C 0.5 h + 760 °C 1.5 h). The advantage of the additional heat treatment was to get a homogenous grain size (∅ 22 μm) and reduction of internal stresses. The ODS version, EUROFER ODS HIP with 0.5 wt.% Y_2O_3, was the prime ODS test of EUROFER 97 alloy without any optimization or heat treatment.

Work Performed in Previous Reporting Periods

A special wrapper, with irradiation capsules accommodating tensile, small Charpy and miniaturized fatigue specimens, was inserted in the central part of the reactor core of HFR. The irradiation was set to 250, 300, 350, 400, and 450 °C. The cumulative neutron fluence E>0.1 MeV m^{-2} was 22.85 x 10^{25}. The neutron irradiation was carried out in 771 FPD up to nominal dose of ~15 dpa. The experimental obtained damage levels for monitor set positions in the specimen holder varied between 13.4 to 18.1 dpa. Neutronic calculations have shown that the volume-average displacement dose of all specimens was ~16.3 dpa for stainless steel, table 2.

Table 2: Evaluation of operation temperature and material damage data in specimen holder 330-01 (SPICE-T).

Target temperature in °C	**250**	**300**	**350**	**400**	**450**
Temperature deviation in °C	241-269	288-302	338-349	379-389	429-435
Damage dose in N_{dpa}	13.4	14.6	16.2	17.2	18.1

Irradiation Effect on Mechanical Properties of EUROFER97
Results of impact and tensile tests

After the irradiation, the specimens were transported to the Hot Cell facility of the FML (Fusion Material Laboratory) to perform the post-irradiation examinations tests.

First series of impact tests were performed and detailed reported by Gaganidze et. al.. An example of the most important data as USE, DBTT, and LSE of EUROFER 97 is shown table 3, a comparison of as received and heat treated (HT) material. There was no influence to the USE, but a clear improvement could be observed after irradiation. The heat treated irradiated EUROFER 97 could achieve a better DBTT than the as received state.

Table 3: USE and DBTT of EUROFER97 as rec. and EUROFER97 HT.

Material conditions	EUROFER 97 as rec. USE in J	EUROFER 97 HT USE in J	EUROFER 97 as rec. DBTT in °C	EUROFER 97 HT DBTT in °C
Unirradiated	9.84	9.84	-81	-91
16.3 dpa at 250 °C	8.21	8.51	109	58

Impact testing of EUROFER ODS HIP with 0.5 wt.% Y_2O_3 did not yet show any satisfying results after impact tests. But it is important to affirm, this material was the first ODS test of EUROFER 97 alloy without any optimization or heat treatment.

All irradiated tensile specimens were tested fully instrumented with a tensile velocity of 0.1 mm/min in the temperature range 250 – 450 °C. Unirradiated specimens were tested only at 20, 300 and 450 °C. Yield strength $R_{p0.2}$ and total elongation A_g of EUROFER 97 are compared with the internationally investigated alloy F82H mod. and shown in figure 1 and 2. Data of EUROFER ODS HIP are illustrated separately in figure 3 and 4.

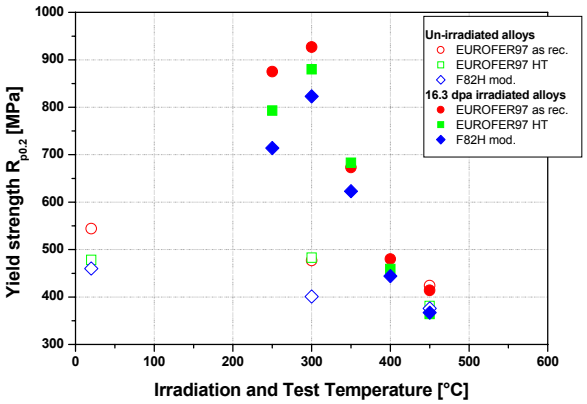

Fig. 1: Yield strength $R_{p0.2}$ of EUROFER97 and F82H mod.

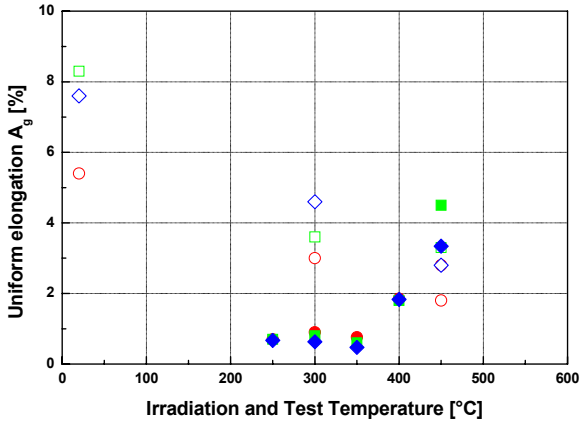

Fig. 2: Total elongation A_g of EUROFER 97 and F82H mod.

Yield strength $R_{p0.2}$ render the strengthening effect at lower irradiation temperatures <400 °C, which is combined with a reduction of material deformation, shown by A_g. The data of EUROFER 97 are slightly higher than that of F82H mod.. The heat treatment of EUROFER 97 showed small advantages during the tests, too. The deformation capacity of EUROFER 97 ODS HIP is better than in the steel alloys and can be proved by the comparison of the stress/strain diagrams of figure 5. The typical drop of irradiated RAFM steels after the highest stress could not be observed in the EUROFER 97 ODS HIP alloy.

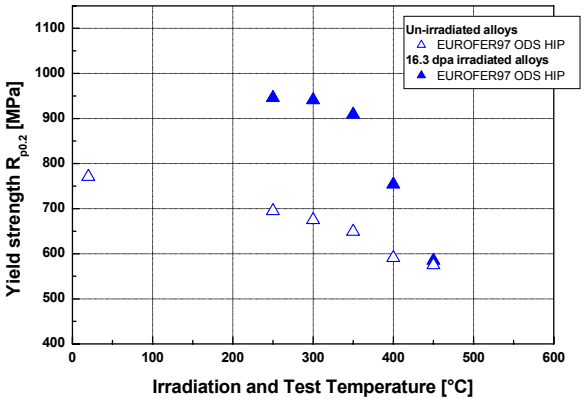

Fig. 3: Yield strength $R_{p0.2}$ of EUROFER 97 ODS HIP.

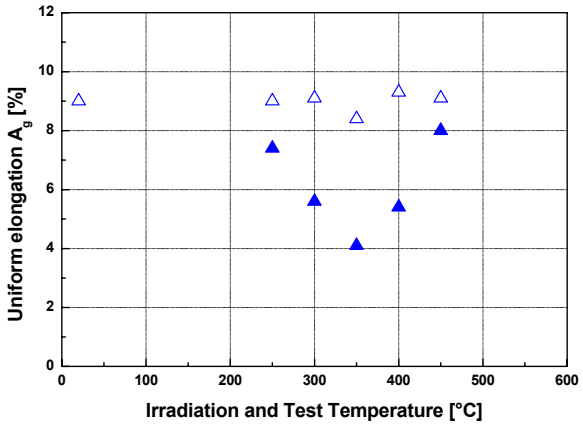

Fig. 4: Total elongation A_g of EUROFER 97 ODS HIP.

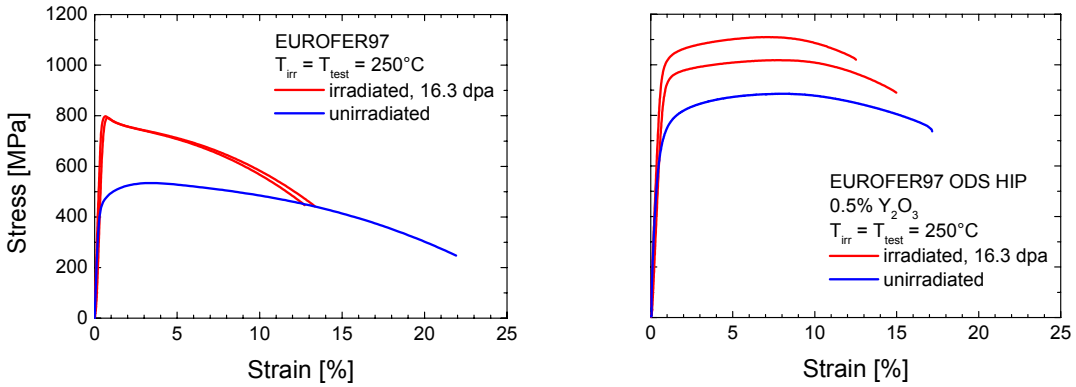

Fig. 5: Stress/strain curves of EUROFER 97 and EUROFER 97 ODS HIP.

Strain controlled isothermal fatigue experiments $T_{test} = T_{irr} = 250$ °C

The fatigue tests have shown a pronounced irradiation hardening below about 350-400 °C at lower strain ranges, figure 6. This severe irradiation hardening was also observed during fatigue testing in the stress strain hysteresis loops. Due to the pronounced irradiation hardening of the irradiated specimens, the plastic strain amplitude is much smaller. However, it is important to note that a smaller plastic strain amplitude does not automatically end up with better N_f values. An irradiation assisted fatigue live increase has been observed also earlier by other investigators, although the effect was not as pronounced. A scientific explanation for the irradiation assisted N_f-increase

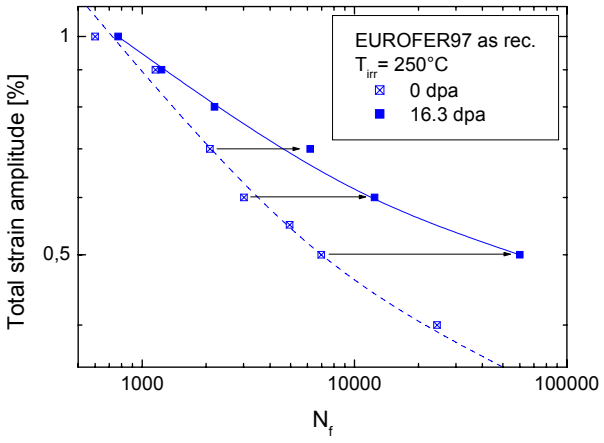

Fig. 6: Effect of low temperature irradiation on fatigue lifetime Nf at Tirr = Ttest = 250 °C.

has not been given in earlier studies. Most of the authors gave the reduced plastic strain amplitude as reason for the N_f-increase, which, however, is likely only empirically based.

Based on this report and on the experience coming from other material classes, the authors have good reason to attribute the enormous lifetime extension to the homogeneous distribution of stable irradiation induced defects on the slip plane that retard significantly the cyclic motion of dislocations and the related fatigue micro crack initiation and propagation. A more detailed study will follow later.

$T_{test} = T_{irr} = 450$ °C

In contrast to the low temperature results, no obvious effect of irradiation on fatigue life can be derived above about 400 °C, as figure 7 shows. The dashed and solid lines in this figure are only a guide for the eye, but even this guide may end up in a single line for all specimens, if the lifetime (~35 000 cycles) of the unirradiated specimen at $\Delta\varepsilon_t$ = 0.35% is attributed to the fatigue endurance limit. There is, in agreement with the tensile tests, no irradiation hardening visible, neither in the hysteresis loops nor in the total stress and plastic strain amplitudes. It is therefore important to note that within the statistical uncertainties the unirradiated and irradiated specimens show practically no difference in the hysteresis loops, the cyclic softening and related plastic stain evolution. Consequently, the data points (except of that of the one at $\Delta\varepsilon_t$ = 0.35%) in figure 7 might be attributed to the statistical scatter.

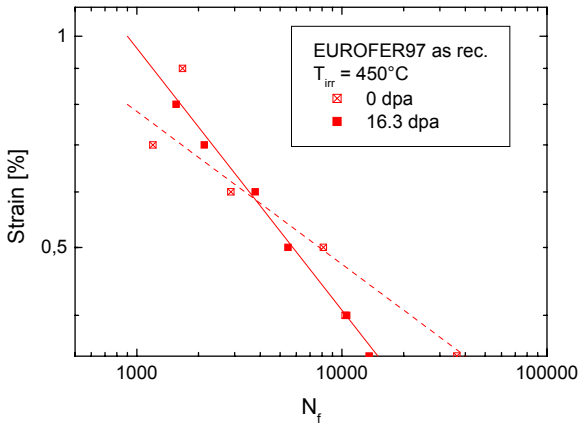

Fig. 7: Effect of low temperature irradiation on fatigue lifetime N_f at $T_{irr} = T_{test} = 450$ °C.

These results observed in EUROFER 97 have also implications for the designers: if this fatigue behaviour is also confirmed at damage levels much higher as 15-16 dpa and if it is valid also for fusion relevant He/dpa ratios, the designers can use the results of unirradiated specimens as they would represent also the irradiation behaviour.

Conclusions

- The expected strengthening at lower temperatures at 250 – 300 °C irradiation and test temperature were confirmed.
- The hardening and strengthening in the test alloys were generated by dislocation loops, α`-precipitates, and to a less extend be He.
- The thermally induced recovery and the hardening effect of dislocation loops and α`-precipitates was dissolved, which was observed by TEM in specimens of irradiation temperature > 400 °C.
- The comparison of tensile and impact findings showed that the effect of He on tensile properties with static load is nearly negligible, but for the dynamic load low levels of He are recognizable by an increase of DBTT.
- A pronounced fatigue lifetime extension of up to almost one order of magnitude has been observed after neutron irradiation to 16.3 dpa at $T_{irr} = T_{test} = 250$ °C at lower total strain amplitudes, but no irradiation effects at all on fatigue properties at $T_{irr} = T_{test} = 450$ °C.

- This impressive increase of fatigue life after 250 °C irradiation is attributed to the almost homogeneous distribution of stable irradiation induced defects on the slip plane that retard significantly the cyclic motion of dislocations and the related fatigue micro crack initiation and propagation.

Staff:

J. Aktaa
B. Dafferner
J. Ehrmann
E. Gaganidze
M. Holzer
S. Lautensack
E. Materna-Morris
A. Möslang
H. Ries
R. Rolli
H.-C. Schneider

Literature:

[1] E. Materna-Morris, A. Möslang, R. Rolli, H.-C., Schneider: Effect of Helium on Tensile Properties and Microstructure in 9%Cr-WVTa-Steel after Neutron Irradiation up to 15 dpa between 250 and 450 °C. ICFRM-13, Nice, France, 2007. Accepted at J. of Nucl. Mat..

[2] Gaganidze, E., Dafferner, B., Ries, H., Rolli, R., Schneider, H.-C., Aktaa, J.: Irradiation Programme HFR Phase IIb – SPICE. Impact testing on up to 16.3 dpa irradiated RAFM steels. FZKA 7371, April 2008.

[3] E. Materna-Morris, R. Lindau and A. Möslang: Development of Low-Activation Martensitic 8-10%Cr-Steels for Nuclear Applications. Materials Science and Engineering (MSE) : Congress and Exhibition on Advanced Materials and Processes, Nürnberg, September 1-4, 2008.

[4] Gaganidze, E.; Aktaa, J.; Schneider, H.C.; Petersen, C.; Povstyanko, A.; Prokhorov, V.; Fedoseev, A.; Makarov, O.; Materna-Morris, E. Mechanical properties of RAFM steels after high dose neutron irradiation. Ulyanovsk State University, 3.April 2008, Russia.

[5] E. Gaganidze, C. Petersen and J. Aktaa, "Helium Embrittlement of RAFM Steels", Proceedings of the 13th International Conference on Fusion Reactor Materials, December 10-14, 2007, Nice, France. Accepted at J. of Nucl. Mat..

[6] E. Materna-Morris; A. Möslang; H.-C. Schneider; R. Rolli: Microstructure and tensile properties in reduced activation 8-9% Cr steels at fusion relevant He/dpa ratios, dpa rates and irradiation temperatures. 22nd IAEA Fusion Energy Conference, 13-18 October 2008, Geneva, Swiss.

[7] E. Materna-Morris, R. Lindau and A. Möslang: Werkstoffentwicklung auf Basis der 8 bis 10%Cr-Stähle für die Fusionstechnologie. VDEh FVW/FVHT (Forschungsvereinigung Warmfeste Stähle/Forschungsvereinigung Hochtemperaturwerkstoffe), 31. Vortragsveranstaltung am 28. November 2008, Düsseldorf.

[8] E. Gaganidze, J. Aktaa, The effects of helium on the embrittlement and hardening of boron doped EUROFER97 steels, Fusion Engineering and Design 83 (2008) 1498–1502

TW2-TTMS-001b D 9
Fast Reactor Irradiation up to 30 dpa, at 340°C of Tensile, Charpy and LCF RAF/M Specimens, Completion of the PIE

Objectives

In an energy generating fusion reactor structural materials will be exposed to very high levels of irradiation damage of about 100 dpa. Due to the fact, that fast reactor irradiation facilities in Europe are not available anymore, a co-operation with the Russian institution SSC RF RIAR has been implemented. The irradiation project is named “ARBOR 1“ (Latin for tree). Impact, tensile and low cycle fatigue specimens of Reduced Activation Ferritic/Martensitic steels, e.g. EUROFER 97, F82H mod., OPTIFER IVc, EUROFER 97 with different boron contents and ODS-EUROFER 97 have been irradiated in a fast neutron flux (> 0.1 MeV) of $1.8*10^{19}$ $n.m^{-2}$ at a temperature less than 340°C up to ~ 30 dpa. Mechanical PIE including impact, tensile and LCF tests of the different materials is terminated at SSC RF RIAR.

Specimens of ARBOR 1 for transport to FZK

For a detailed analysis of the implication of irradiation damage on mechanical properties a sophisticated microstructural analysis of the damaged specimens is necessary, therefore a series of deformed and undeformed specimens of different materials (Table 1) was selected for transport to the Fusion Materials Laboratory (FML) of FZK (Fig. 1).

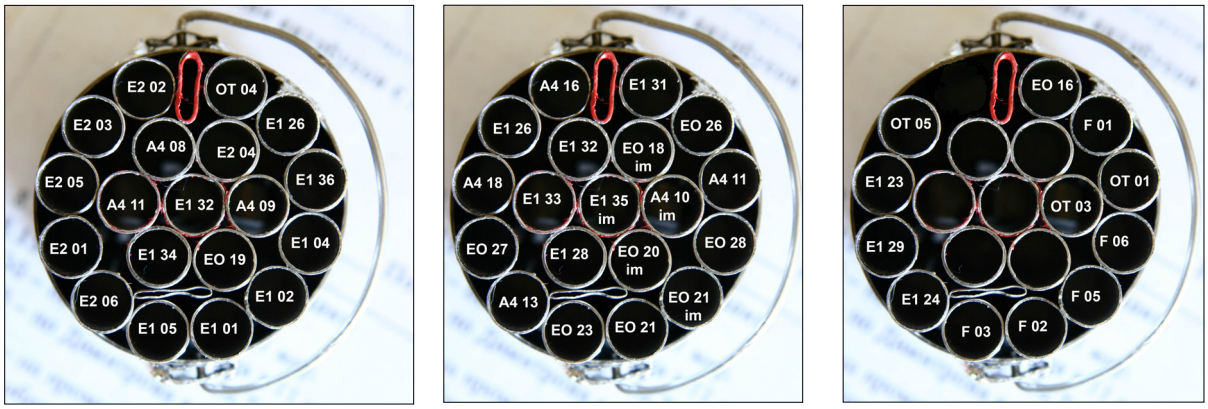

Fig. 1: Container chart (loading position of the specimens).

The transport was performed during spring 2008 and the specimens are now ready for microstructural analysis in the FML of FZK.

Staff:

C. Petersen
H.-C. Schneider

Literature:

[1] C. Petersen, A. Povstyanko, V. Prokhorov, A. Fedoseev,O. Makarov and M. Walter: “Tensile and Low Cycle Fatigue Properties of different Ferritic/Martensitic Steels after the Fast Reactor Irradiation “ARBOR 1””, to be published as special edition of Journal of Nuclear Materials of ICFRM-13, 9.-14.12,2007, Nice, France

Table 1: Selection of irradiated specimens from ARBOR 1.

Material	Quantity of samples *)	Sample type	Sample numbers	Comments
EUROF 1	2,5	KLST	One half of E 1 01 - E 1 05,	Charpy samples
EUROF 1	2,5	FZK-type	One half of E 1 15 - E 1 17, one full of E 1 18	Tensile/Fatigue samples
EUROF 2	4	KLST	One half of E 2 01 - E 2 06, one full of E 2 08	Charpy samples
EUROF 2	2,5	FZK-type	One half of E 2 15 - E 2 17, one full of E 2 18	Tensile/Fatigue samples
F82 H mod.	4	KLST	One half of F 01 - F 06, one full of F 07	Charpy samples
F82 H mod.	1,5	FZK-type	One half of F 10 - F 12	Tensile/Fatigue samples
OPTIFER IVa	3	KLST	One half of OT 01 and OT 03 - OT 05, one full of OT 07	Charpy samples
OPTIFER IVa	2,5	FZK-type	One half of OT 06 - OT 08, one full of OT 09	Tensile/Fatigue samples
ADS 2	3	KLST	Three full of A 2 13 – A 2 15	Charpy samples
ADS 2	2,5	FZK-type	One half of A 2 09 - A 2 11, one full of A 2 12	Tensile/Fatigue samples
ADS 3	3	KLST	Three full of A 3 13 – A 3 15	Charpy samples
ADS 3	2,5	FZK-type	One half of A 3 09 - A 3 11, one full of A 3 12	Tensile/Fatigue samples
ADS 4	3	KLST	Three full of A 4 05 – A 4 07	Charpy samples
ADS 4	1,5	FZK-type	One half of A 4 01 - A 4 03	Tensile/Fatigue samples
EUROFER-ODS HIP (0.5% Y_2O_3)	3	KLST	Three full of E O 05 – E O 07	Charpy samples
EUROFER-ODS HIP (0.5% Y_2O_3)	2,5	FZK-type	One half of E O 10, E O 12, E O 15 and one full of E O 17	Tensile/Fatigue samples

TW5-TTMS-001 D 10
Mechanical Post Irradiation Examinations of FZK-Specimens Irradiated in the ARBOR-2 Experiment in the BOR 60 Reactor

Objectives

In an energy generating fusion reactor structural materials will be exposed to very high levels of irradiation damage of about 100 dpa. Due to the fact, that fast reactor irradiation facilities in Europe are not available anymore, a co-operation with the Russian institution: SSC RF RIAR, has been implemented. “ARBOR-2“ is the succeeding experiment after ARBOR-1 from FZK and ALTAIR from CEA, to reach irradiation damages up to 70 till 80 dpa.

PIE of ARBOR 2

Impact test results of 12 to 70 dpa irradiation damaged RAF/M steels are available. From Fig. 1 the appearance of the impact behavior can be depicted. At 12 dpa OPTIFER XI and OPTIFER XII have a DBTT of 90°C and EURODShip thermal treated of 140°C. Whereas diffusion welded EUROFER 97 reaches a DBTT of 150°C and an USE of 4 J.

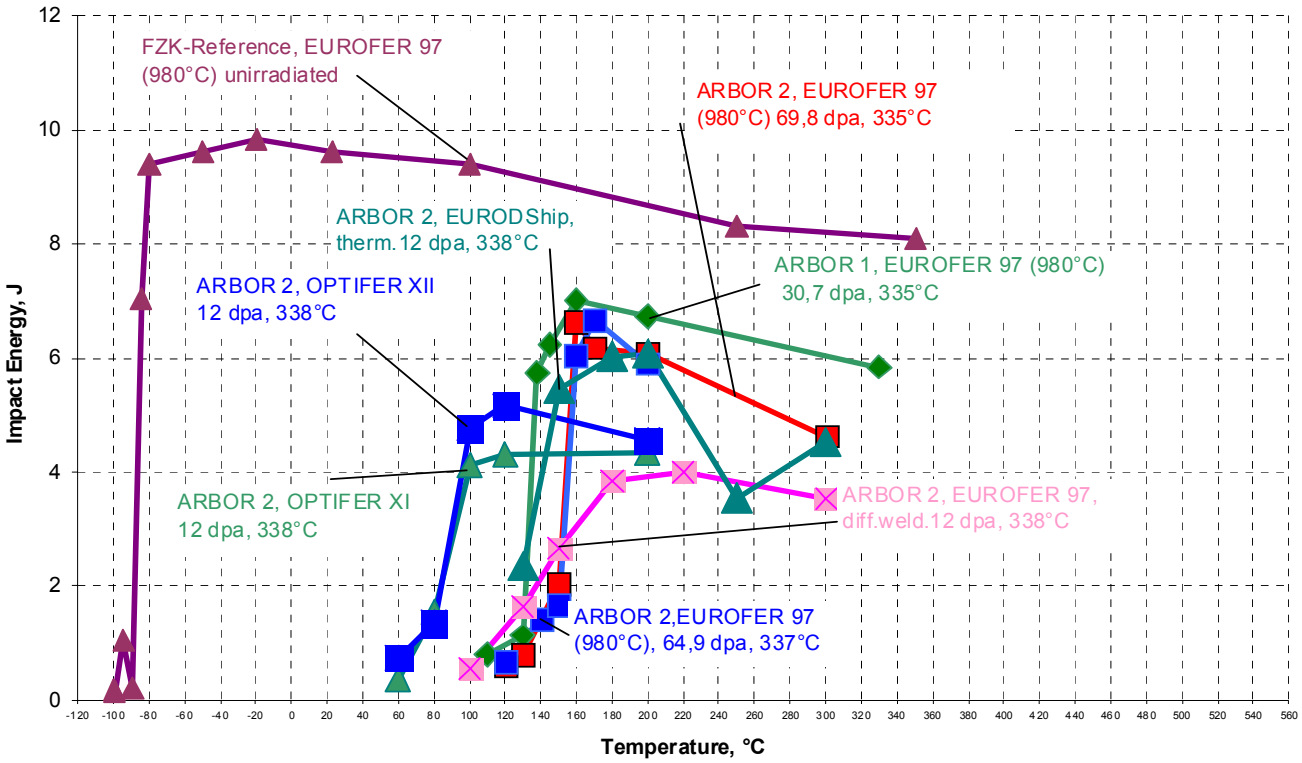

Fig. 1: Comparison of different materials under various ARBOR 1 and 2 irradiation conditions (indications: irradiation conditions and irradiation temperature).

The tensile tests are performed with a tensile and LCF testing facility of INSTRON-DOLI 1362 type, equipped with a 100 KN load cell, a high temperature furnace and a strain measurement system, installed in the K-12 hot cell of the SSC RF RIAR.

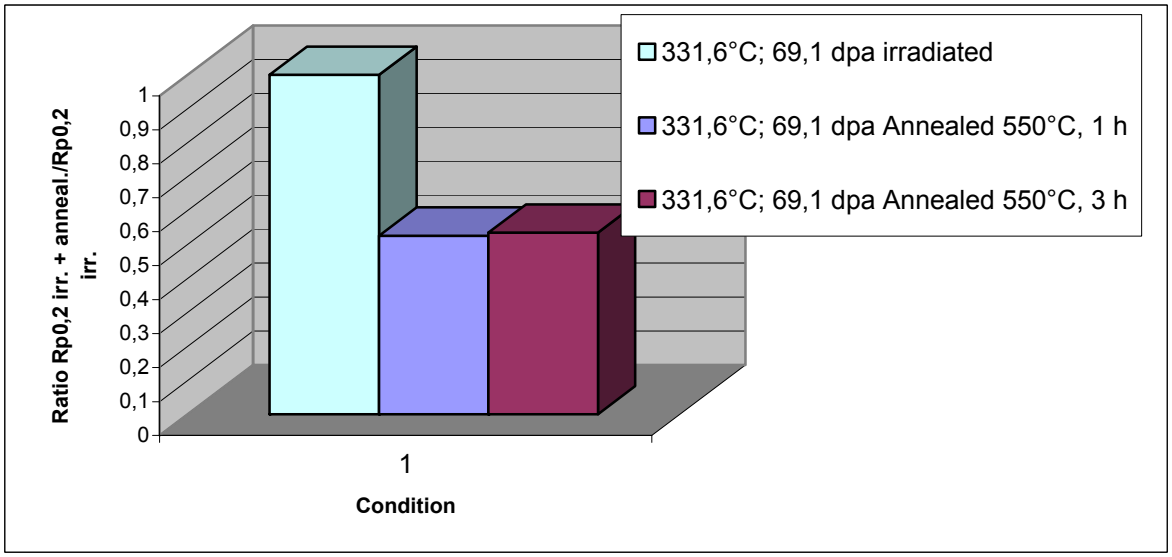

Fig. 2: Time dependence of the post irradiation annealing of EUROFER 97 (980°C) as the ratio of the yield stress $R_{p0,2}$.

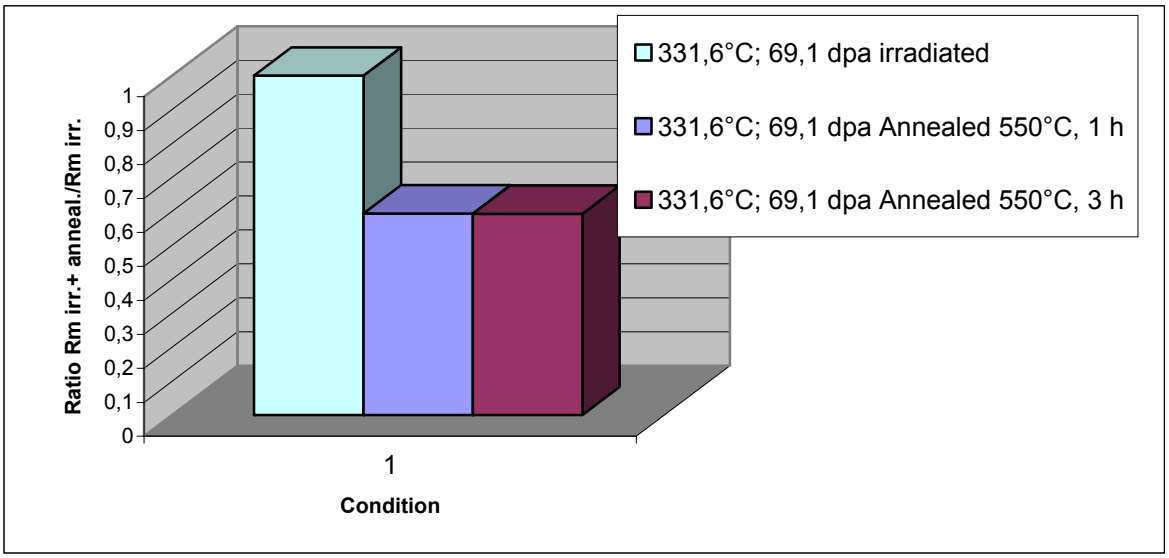

Fig. 3: Time dependence of the post irradiation annealing of EUROFER 97 (980°C) as the ratio of the ultimate tensile strength R_m.

Most of the tensile test on the different RAF/M materials are performed and will be reported in an intermediate report.

The post irradiation annealing behavior of EUROFER 97 (980°C) has been studied in more detail, mainly in respect to the time needed for recovery. Recently only annealing times of 3 hours at the annealing temperature of 550°C have been realized. But with an additional experiment it could be demonstrated now, that even after 1 hour the full recovery of EUROFER 97 was accomplished, as can be seen from Figs. 2 and 3 for the the yield stress $R_{p0,2}$ and the ultimate tensile strength R_m ,respectively.

Staff:

U. Bürkle
E. Gaganidze
M. Klotz
C. Petersen

Literature:

[1] E. Gaganidze, H.-C. Schneider, C. Petersen, J. Aktaa, A. Povstyanko, V. Prokhorov, R. Lindau, E. Materna-Morris, A. Möslang, E. Diegele, R. Lässer, B. van der Schaaf, E. Lucon, “Mechanical Properties of Reduced Activation Ferritic/Martensitic Steels after High Dose Neutron Irradiation”, presented at 22nd IAEA Fusion Energy Conference, 13-18 October 2008, Geneva, Switzerland

TW5-TTMS-001 D 4
Tomographic Atomic Probe Analysis of EUROFER Material Irradiated in the ARBOR Irradiation Campaign

Introduction

The aim of this task is to investigate atomic scale microstructure of EUROFER steel before and after irradiation. The ECOTAP (Energy Compensated Optical Tomographic Atom Probe) which is able to reconstruct atom positions within investigated sample seems to be appropriate for this task. This report contains the data for non-irradiated EUROFER1 ADS2, ADS3, ADS4, EUROPODShip 0.5%Y2O3) steels.

Method

The principle of three dimensional atomic probe (3DAP) is based on evaporation of surface atoms induced by strong electric field pulses. Some fraction of the evaporated and ionized atoms (usually ~50%) fly to a detector where they are registered and their final position is fixed. Their initial position in the lattice can be recalculated using known electric field distribution. Analysis of the measured time of flight of each atom from the tip of the probe to the detector provides information on the charge to mass ratio, which is usually sufficient to determine uniquely the nature of evaporated chemical species.

The necessity of high electric field requires preparation of the samples in form of very thin needles with a sharp tip with a radius of ~10-50 nm. Samples were first cut into 10-mm long sticks with a cross-section of 0.3x0.3 mm using electro-erosion cutting in water. This technique does not induce strains and overheating above 100 °C thus preserving material microstructure as opposed to mechanical cutting.

The sticks were necked by anodic etching in electrolyte. The diameter and shape of specimen tip were controlled using transmission electron microscope.

Results

Samples without ODS particles

In case of ADS2, ADS3, ADS4 samples no impurity segregation was observed. Lower impurity concentrations in comparison with those obtained by chemical analysis could be due to solutes segregations at the grain boundaries or dislocations outside the investigated volume. The obtained spatial distributions are similar for all three kinds of the specimens. It is worth noticing that a significant increase of Cr, B and other elements concentration at dislocations and, as a result, matrix depletion were also confirmed in several publications.

Samples with ODS particles

EUROPODShip (EUROF 1+ 0.5%Y2O3) specimens were prepared and investigated by the same methods. It was noticed that if dark areas, which are supposed to be oxide particles, were observed on TEM images, early break of the specimens took place during the atom probing process due to heterogeneity of particle-matrix interface.

The mass spectrum interpretation reveals evaporation of molecular ions like YO and VO. This finding confirms the strong binding between these pairs of elements.

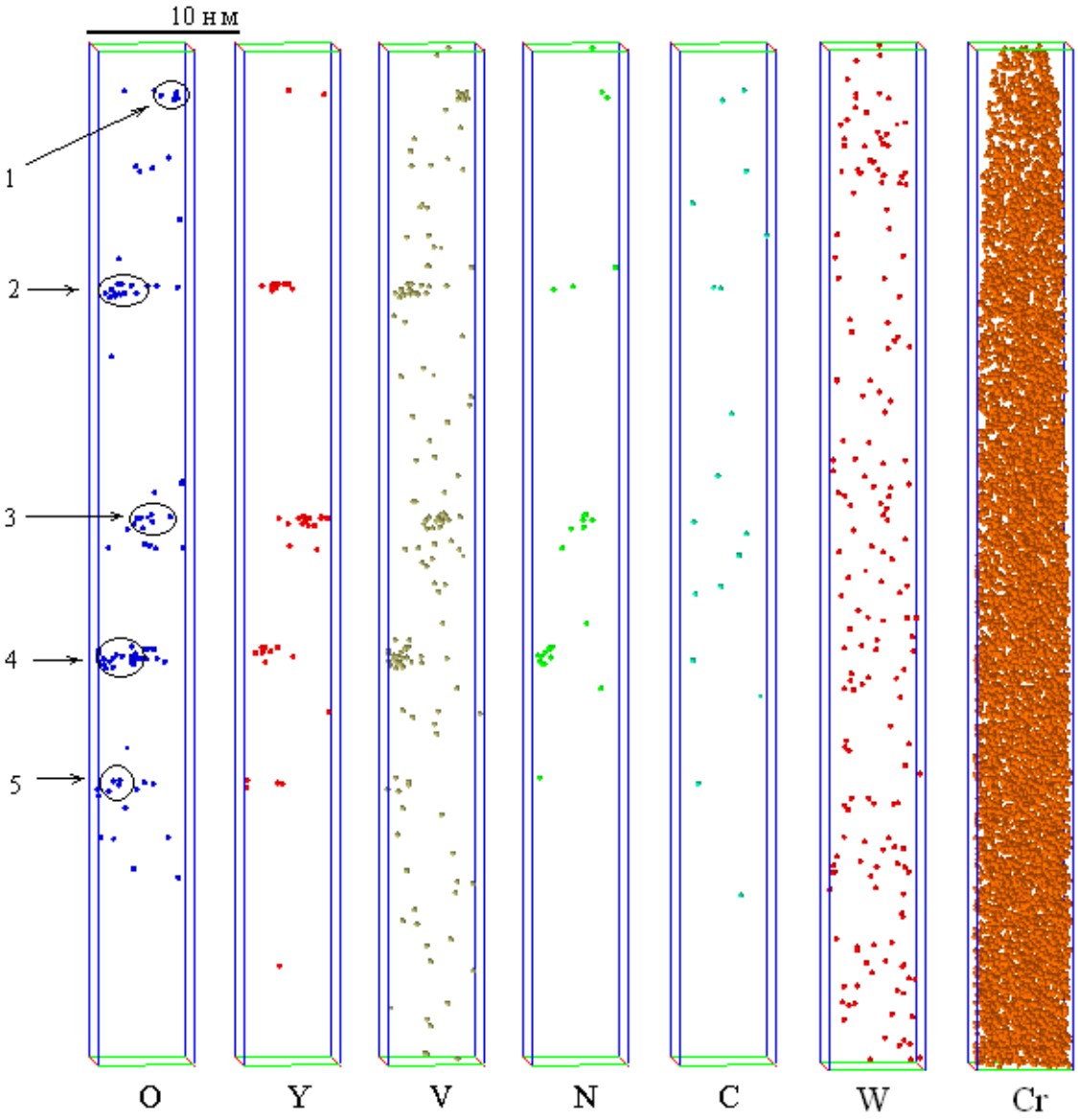

Fig. 1: Example of small solute clusters in unirradiated ODS EUROFER.

Recently the post processing procedures of atom probe data were significantly improved. As a result, a substantial part of events that were previously considered as noise is now identified. Previously, we studied unirradiated EUROFER and EURODShip 0.5%Y2O3) specimens. Those tomographic atom probe investigations of(EUROF 1 EURODShip specimens revealed two types of structure. The first one has more or less uniform solutes distribution in the volume. However, it was in those specimens where clusters of characteristic size 3x3x3 nm^3 were found. Increased concentrations of such elements as Y, Cr, C, Mn, Ni, V, O, S, Cu, Si were found in these clusters. The second type is characterized by layers of increased impurity concentration. These layers have a characteristic thickness of 2 nm and are positioned perpendicular to the long axis of the cylinder of which the specimen was made. The spacing between the layers can be varied from 2 to 30 nm in the same specimen. The concentrations of Y, V, O, N, C, Cu, S and Ta in the layers were found to be several times higher than the average concentrations in the volume under investigation.

In the present work a new data processing that influences mass resolution was applied. The better geometrical model that includes second order aberrations allows increasing the mass resolution from ~200 to more than 600. Moreover, malfunction of a detector system was found and the post-processing program was corrected so that multi-hit events can be extracted from TAP data and doubled peaks that decrease the mass resolution have been

merged. Using advanced post-processing procedures allowed to determine concentrations of solute elements more precisely. They are very effective for elements with low concentration such as C, N, Cu, P.

With the new post processing procedure it is possible to resolve crystallographic plains, which appear to be nearly perpendicular to the needle axis. In this work we have processed the data sets obtained previously by improved methods (see Figure 2).

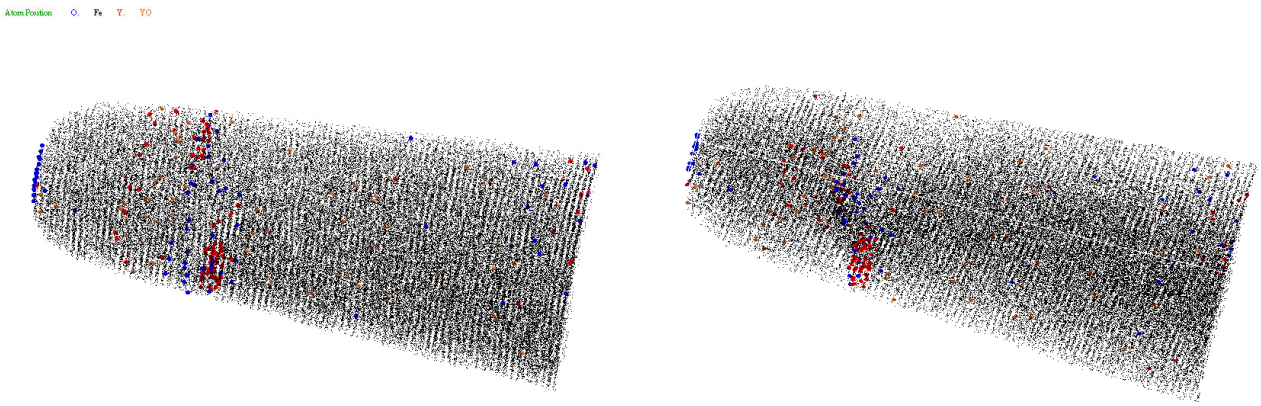

Fig. 2: Atom maps of investigated volume with clearly visible atomic planes after improved data processing.

Conclusions

Tomography atomic probe experiments were performed on non irradiated samples of EUROFER steel with and without ODS particles. Samples without ODS have shown no segregation patterns, while two types of segregations were found in presence of ODS. The first type of segregation is a spherical region of about 3 nm in diameter with local impurity concentration increase. This type might correspond to the early stages of ODS particle formation. The second type of segregation pattern is a layer with a thickness of about 1 nm. Physical origin of this type of segregation is not quite clear presently.

Staff:

A. Möslang
P. Vladimirov
S.V. Rogozhkin and
A.G Zaluzhnyi (Institute for Theoretical and Experimental Physics, Moscow, Russia)

TW6-TTMS-001 D 5
Studies of the Effect of Implanted He on Mechanical Properties of EUROFER in the T-range 300 - 500°C

Introduction

It is well known that Helium can considerably contribute to low temperature irradiation embrittlement (below ~400 °C) and dislocation channeling in bcc steels. On the other hand, ODS steels have shown recently very favorable tensile properties with significant work hardening capability even after substantial neutron irradiation (30 dpa). In addition it is expected that another favorable behavior of RAFM-ODS steels is the capability of ODS particles to act as very effective trapping centers for migrating helium, thus suppressing substantially helium bubbles formation at lath and grain boundaries or the surface of larger $M_{23}C_6$ precipitates. As a consequence, nano-dispersed ODS particles should greatly retard the helium embrittlement.

It is foreseen to irradiate tensile samples made of EUROFER and EUROFER-ODS with 60 MeV alpha particles, thus implanting 1000 appm helium very homogenously in the deformation volume. The irradiation temperature will vary between 300 and 550 °C. The post irradiation examinations include instrumented tensile tests at $T_{test} = T_{irr}$ and detailed microstructural analyses with TEMs to analyze the helium and defect morphology and their interaction with ODS particles. The results would also be a major input for the validation of modeling of the kinetics of atomic helium and He_nVac_m-Clusters and their interaction with dislocations and with nanodispersed ODS particles.

Experimental

A new target system for helium implantation experiments was developed. The target system is placed inside a hermetic cube, which is situated at the end of an ion beam guide and separated from the guide vacuum by a window (see Fig. 1).

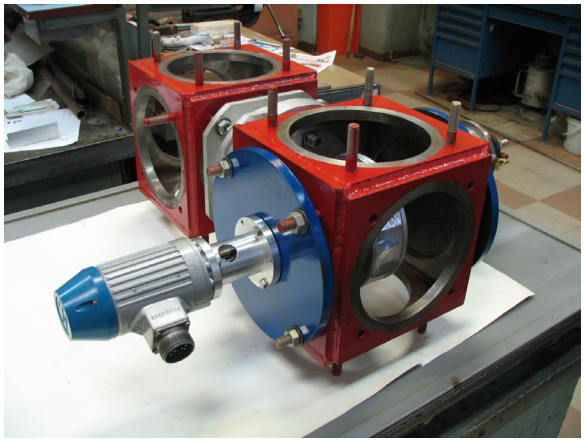

Fig. 1: Target system with step-wise electromotor for rotation of degrader wheel.

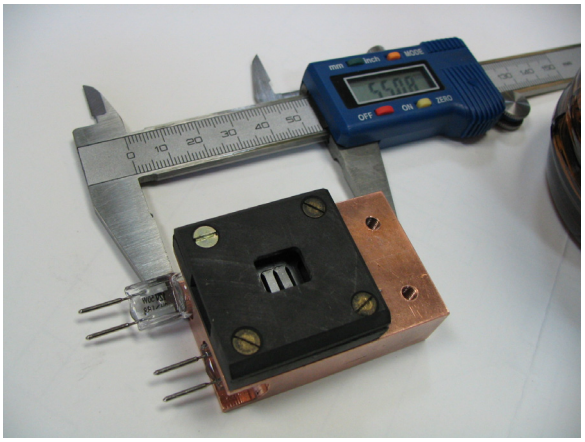

Fig. 2: Graphite box with samples mounted on the copper cooling block. The samples are seen through the hole on the front side of the box. Halogen heater and thermocouple connection are on the left side.

An additional split 4-sector diaphragm for precise adjustment of the ion beam position with respect to implanted samples is positioned at the window inside the target system. The samples are mounted inside a graphite box (see Fig. 2), which is cooled by helium. The box contains a hole on the beam side. Thermocouples for measuring the sample temperatures are wired through the rear side of the box. The back side is connected with a copper block with two halogen heaters. There is another thermocouple for controlling the temperature of the block. The position of the whole target system can be adjusted in the vertical direction or the target can be completely shifted out of the beam footprint.

An energy degrader is used for obtaining more homogeneous helium spatial distributions in the implanted specimens. It is designed as a cylinder with a set of degrading foils. The degrader rotation is synchronized with the ion beam pulses of the cyclotron.

Conclusions

A new target system for getting of irradiation conditions for uniform saturation of EUROFER and EUROFER-ODS samples with helium atoms was developed and manufactured. Numerical calculations of radiation damage profiles and implanted helium concentrations in irradiated ODS samples after rotating the degrader with aluminum foils for energy intervals of helium ions (in the interval of energies of helium ions from 0 to 60 MeV) for the choice of best irradiation conditions were performed. A dedicated helium cooling system for irradiated samples was developed. Some tests on the cyclotron for the choice of the best irradiation conditions (current of helium ions for the heating of samples by helium beam and cooling of samples by helium gas at some pressure) for getting of an irradiation regime at fixed irradiation temperatures: T = 300 °C and T = 550 °C were performed. The irradiation of samples by helium ions on the RRC KI cyclotron according to the task schedule will be started soon.

Staff:

A. Möslang
P. Vladimirov
A. Ryazanov (Kurchatov Institute, Moscow)

TTMS-004
Qualification Fabrication Processes

TW6-TTMS-004 D 1 + D 2
Improve Design Limits of Welded Components through Improved Post Weld Heat Treatments, Qualification and Improvement of Welded and Diffusion Bonded Joints

Overview

According to the current design for the European Helium Cooled Pebble Bed (HCPB) ITER Test Blanket Module (TBM) there are basically six subcomponents which have to be fabricated and assembled: first wall, caps, stiffening grid, breeding units, back plates/manifolds, and attachment system. The main technologies needed for blanket fabrication are joining of parts (particularly production of plates with internal cooling channels and welding at inaccessible component areas) and applying suitable post weld heat treatments. Both steps together are the key technologies that determine the mechanical strength of the blanket, the ductile-to-brittle transition temperature (DBTT) which is important under neutron irradiation, and the potential for a compact design. While it is certain that the structural material will be EUROFER, most joining technologies and/or procedures have still to be developed, adapted, or qualified.

The designated welding techniques may be divided into two groups: diffusion or solid phase welding, and fusion welding, whereas the first is either performed in a hot isostatic press (HIP) or in a uniaxial hydraulic press, both after different specific joint preparations. Fusion welding may be performed either by electron beam (EB), laser beam, hybrid MIG/laser, or by tungsten inert gas (gas tungsten arc) welding with filler wire.

The general objective is to support the fabrication development in the blanket areas and to improve the reliability of the materials and joints according to the TBM design. The joint quality produced by a low pressure HIP diffusion bonding process has to be investigated with respect to prior surface state conditions (D1). The quality assessment of fusion welds will be continued with special emphasis on 40 mm thick welds and their post-weld heat treatments (PWHT) within D2.

Initial Status D1 (Diffusion Weld Parameter Study)

For the characterization and evaluation of diffusion welding technologies for the fabrication of first wall components a large number of weld samples and some small mock-ups have been fabricated using different milling tools and parameters. Within this initial programme the effect of the surface fabrication process on the diffusion weld quality was studied. It could be seen that basically all industrial standard milling tools are suitable for the surface fabrication. In some cases, however, a specific chip removal leads to porous surfaces and, hence, to remaining cavities in the weld interface which deteriorate the Charpy properties significantly.

Another study concerned the effect of heat treatments on the surface milling process. Here a solution to the chip removal problem was given by hardening the surfaces.

Finally the effect of a second HIP step was tested on defective welds. A rather beneficial effect of such a high pressure cycle could be demonstrated. All cavities vanished and there was no detectable weld line. That is, the second HIP step can be applied, so to say, as repair or back-up solution. In any case, it could and should be performed as a security measure.

The ongoing activity was then to examine the influence of surface contamination and cleaning which are both relevant issues for a production route within an industrial environment.

Initial Status D2 (Deep EB Weld Development)

To develop a weld process for joining the 40 mm thick upper and lower caps to the first wall was in the focus of this study. Since EB welds have led to best results in our previous studies on 5 mm thick plates, we started with the development of an appropriate EB weld fabrication process on 40 mm thick EUROFER bars. As a first result it could be demonstrated that with properly adjusted parameters the EB beam produces a rather straight and equally narrow fusion zone. There was just a small heat affected zone (HAZ) and first microstructure examinations have revealed a low defect density of bubbles and micro-cracks. Unfortunately, the fusion zone was littered with δ-ferrite formations which reduce the strength of the joint.

Due to the chemical composition of EUROFER, δ-ferrite transforms usually into austenite (at temperatures above 1300 °C) and then into martensite (below 385°C) during cooling. But in the case of this first EB weld, quenching was so fast that a significant amount of δ-ferrite remained. Therefore, a second try included tempering the bars before welding to about 500 °C to prevent quenching with too high cooling rates. The good news was that δ-ferrite formation was suppressed as intended. But at the same time many bubbles formed in the weld centre with rather large diameters in the millimetre range.

The goal of ongoing activities was then to vary the weld parameters in order to prevent both, formation of δ-ferrite and of bubbles.

Progress D1 (Diffusion Weld Parameter Study)

In contrast to laboratory conditions, industrial fabrication procedures are usually far from ideal with respect to cleanliness and chronology of the single production steps. Both are oriented on efficiency and utilization. Since for diffusion welding clean surfaces are obligatory, there might be a discrepancy between optimum joining and commercial fabrication of such relatively large parts such as TBMs. Surface contamination includes two principally different effects which may act as diffusion barriers and, hence, deteriorate the weld properties. Evidently, one is oxidation. This applies especially to chromium steels, where the corrosion resistance is caused by thin Cr_2O_3 surface layers, which in turn suppress diffusion. The other effect literally results from dirt. In commercial fabrication facilities this typically follows from contact with oil and coolants (or dust, wrapping, etc.). That is, before diffusion welding, the surfaces have to be cleaned. But then, there might either remain traces of the cleaning agents or of the dirt or of both. However, such remnants could react locally with the surface during the HIP process and also act as diffusion barrier.

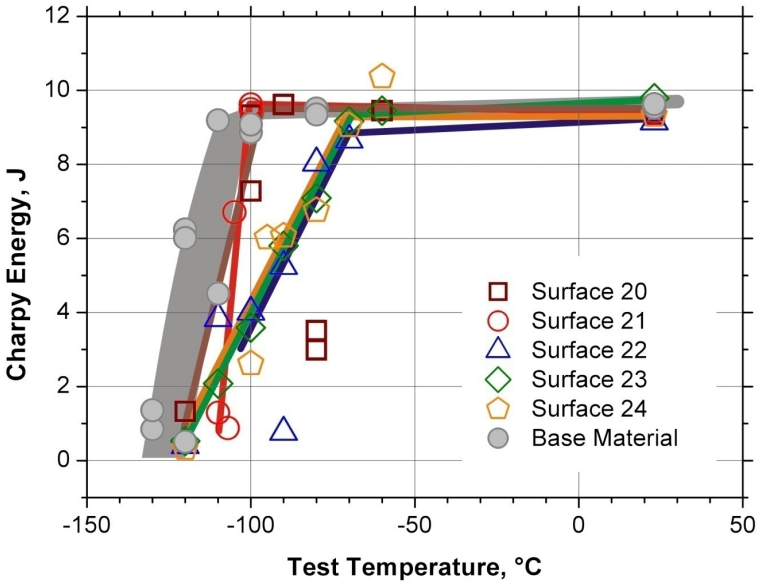

Fig. 1: Charpy test results of the samples with different oxidation periods prior to diffusion welding at 25 MPa, 1150 °C for 2 hours and after post weld heat treatment of 980 °C/0.5 h + 760 °C/2 h. Oxidation times at 70% relative humidity: 20-0 h, 21-24 h, 22-48 h, 23-72 h, 24-14 days.

During a real TBM production the weld surfaces will always be exposed to air for more or less extended periods and hence form more or less distinct oxide layers. This effect was studied by the first test series (see table 1, sample no. 20-24). A reference sample (in this

context no. 20) was fabricated for comparison. It was immediately sealed vacuum tight by an EB-weld after milling. Four other samples have been put in a humidor with a constant relative humidity of 70% for 24 hours, 48 hours, 72 hours, and for 14 days (no. 21-24) prior to sealing in the EB-weld chamber. Finally, the samples were put in a HIP for two hours at a pressure of 25 MPa – and unfortunately (at least at a first glance) at a temperature of 1150 °C which was a mistake of the HIP company (Bodycote, Haag-Winden, Germany). Thereafter, the standard post weld heat treatment has been applied before the fabrication of the Charpy specimens. The results are plotted in Fig. 1. Before going into details, it is striking that all oxidation conditions led to the same upper shelf energies and that DBTT is shifted by only 30 °C in the worst case. This had to be caused by the elevated HIP temperature (1150 °C) because it is well known that diffusion welding in the range around 1050 °C is very sensitive to oxide layers.

Table 1: Preparation and fabrication details of the surface contamination study.

Sample No.	Surface treatment/preparation/condition
20	***Reference Sample*** • *Reference surface*: as surface no. 11 (s. HIP-Test-Samples-I: Cutter Ø63 mm Knifehead, 90° Plates, 6 Teeth, Sandvik 1025 R390-11T3 04M-PM, VC=130, fz=0.05, S=660, ap=0.15, F=198), *dry milled* • then ***immediately*** put into vacuum chamber and EB-welded for vacuum tightness
21	• *Reference surface, dry milled* • ***24 hours*** *in humidor* (70% rel. humidity) • then EB-welded (vacuum tight)
22	• *Reference surface, dry milled* • ***48 hours*** *in humidor* (70% rel. humidity) • then EB-welded (vacuum tight)
23	• *Reference surface, dry milled* • ***72 hours*** *in humidor* (70% rel. humidity) • then EB-welded (vacuum tight)
24	• *Reference surface, dry milled* • ***14 days*** *in humidor* (70% rel. humidity) • then EB-welded (vacuum tight)
25	• *Reference surface, dry milled* • *Surface sealed with WD40 (spray oil)* • ***14 days*** *in humidor* (70% rel. humidity) • *Cleaning with isopropanol in ultrasonic bath and drying with wipes* • then EB-welded (vacuum tight)
26	• *Reference surface, dry milled* • *Surface sealed with WD40 (spray oil)* • ***14 days*** *in humidor* (70% rel. humidity) • *Cleaning with soap* • then EB-welded (vacuum tight)
28	• *Reference surface milled with coolant (industrial standard)* • *Drying with wipes* • then EB-welded (vacuum tight)
29	• *Reference surface milled with coolant (industrial standard)* • *Cleaning with isopropanol in ultrasonic bath and drying with wipes* • then EB-welded (vacuum tight)

Anyway, a significant difference between the different oxidation periods is still recognizable: It seems that up to 24 hours oxide formation does not much deteriorate the diffusion bond.

On the other hand, after 48 hours there is a deterioration of DBTT, but it is not further impaired by extended oxidation periods up to 14 days. However, there are two outliers in the test results of the reference surface (no. 20) – both at -80 °C – which cannot be explained (and maybe also for surface no. 22 at -90 °C). Therefore, the presented conclusion should better be treated as a tendency and not stressed too much. On the other hand, it should be a reliable conclusion to state that down to test temperatures of at least -70 °C there is no brittle fracture in all welds.

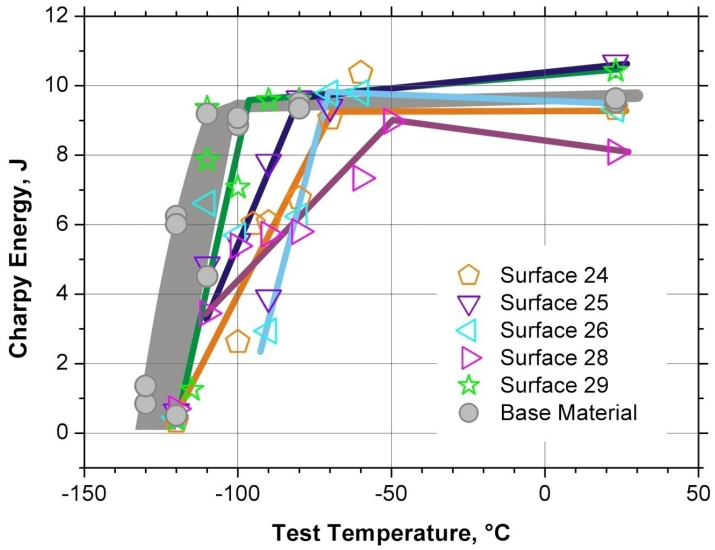

Fig. 2: Charpy test results of samples with different cleaning and contamination treatments prior to diffusion welding at 25 MPa, 1150 °C for 2 hours and after post weld heat treatment of 980 °C/0.5 h + 760 °C/2 h. 24-14 days oxidation on air, 25-surface sprayed with oil/14 days oxidation on air/cleaning with isopropanol, 26-25-surface sprayed with oil/14 days oxidation on air/cleaning with soap, 28-milling with coolant/surface just wiped, 29-milling with coolant/cleaning with isopropanol.

The effect of oxidation protection by using spray oil has been studied on two further samples. The surfaces of the first sample (no. 25) have been cleaned with isopropanol after 14 days rest in air with a relative humidity of 70 %. The other sample (no. 26) has been cleaned with usual soap after 14 days oxidation. Sample no. 24 from the previous study has been used as a reference. The results are plotted in Fig. 2. As can be seen, oiling the surfaces reduces the negative oxidation effect. But only isopropanol removes the oil without residues. Cleaning with soap leads to the same (or slightly worse) results compared to unprotected oxidation (there is scattering which makes a definite assessment difficult).

Finally, the influence of milling with coolant (as is standard for industrial production processes) on the weld quality was studied by two additional samples. One sample was just wiped dry after milling (no. 28). The other was cleaned with isopropanol (no. 29). Figure 2 shows that using coolant has no effect on the diffusion weld process, if the coolant is removed with isopropanol. Without cleaning (that is just drying the surfaces with wipes) the weld is clearly deteriorated. In this study too, the high HIP temperature of 1150 °C led to the same upper shelf energies for all samples (except for no. 28). Also DBTT was on an acceptable level in all cases.

The micrographs of all weld interfaces show large grain sizes of the austenitic phase which is due to the high HIP temperature. But also, the weld line is not detectable in all welds which is the reason for the good toughness (high upper shelf energies) of these diffusion welds. As an example, the micrograph of sample 28 is shown in Fig. 3. The microstructure images of the other samples are looking similar.

Progress D2 (Deep EB Weld Development)

After the first try with EB welding a preheated sample, a third weld was produced with a slightly decreased welding current and with a lower preheating temperature. Again, the exact temperature could only be estimated because the preheating treatment was performed by the electron beam (in a defocused mode). But also this lower welding temperature led to severe bubble formation as is shown in Fig. 4.

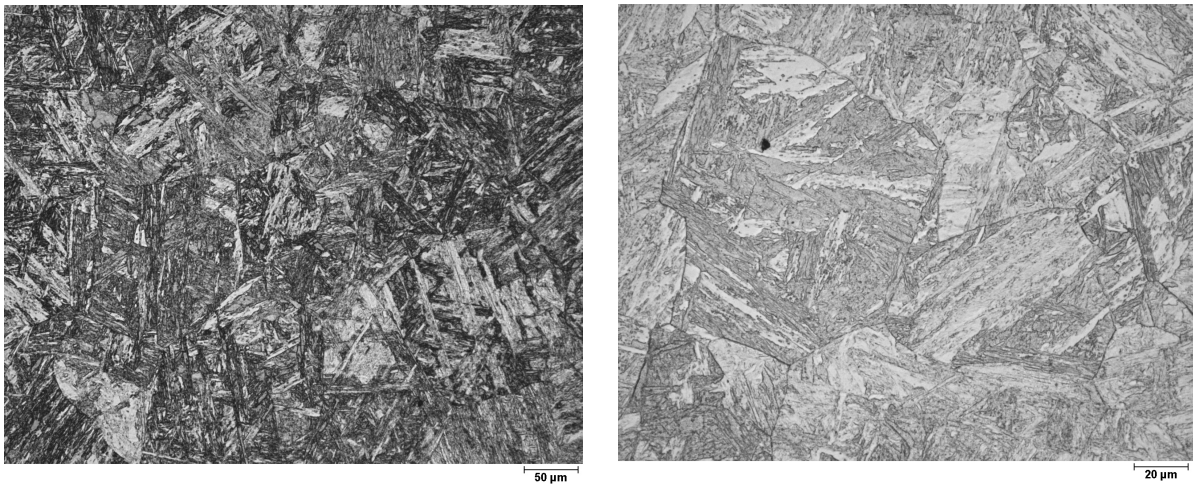

Fig. 3: Micrograph of the diffusion bond (weld line runs horizontally in the centre of the images) of sample no. 28 (which yielded the worst results) in two different degrees of magnifications.

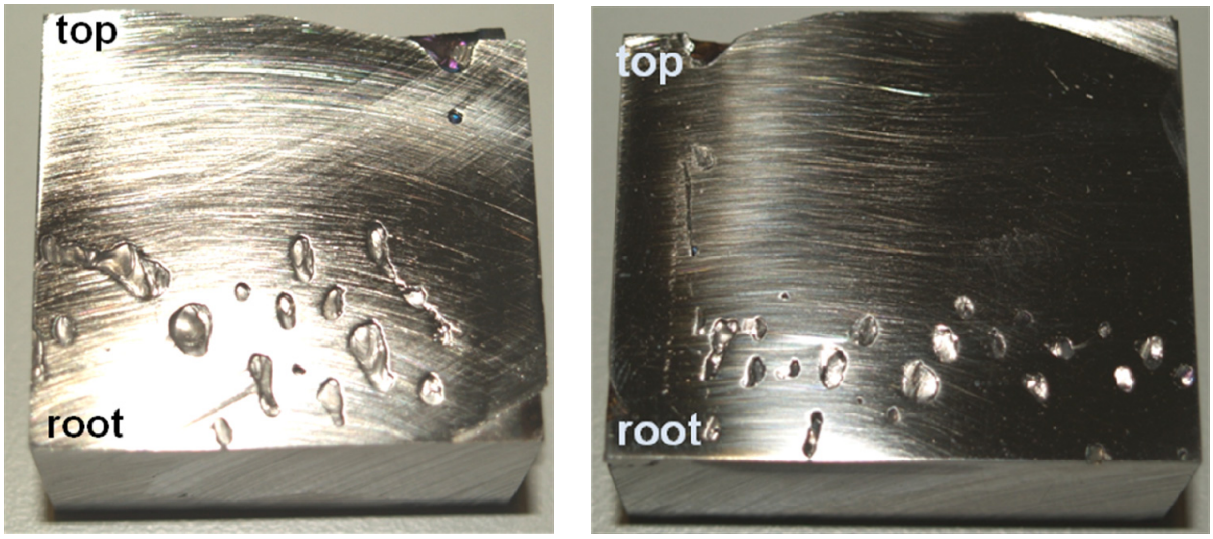

Fig. 4: Preheating the components to less than 500 °C (rough estimate) doesn't suppress bubble formation either. The left image shows the cross section through the centre along the weld line. The beam moved from left to right. Preheating the components to less than 400 °C leads also to bubble formation (right image).

Therefore, another test was performed by preheating the whole weld sample in a furnace to 400 °C before putting it in the weld chamber for welding. The intention was to further decrease the preheating temperature. However, as can be seen in Fig. 4, there was also no reducing effect on the severe bubble formation.

With these discouraging results the EB weld study on 40 mm plates was terminated.

Conclusions and Outlook

The investigations have shown that there is a limit for EB welding EUROFER. While EB welding leads to excellent results with thin plates (e.g. 5 mm), there are increasing problems with thicker plates (12 mm and more). For joining caps and first wall of a TBM, EB welding cannot be recommended due to the following reasons: (1) Without preheating, the welding zone suffers from softening due to delta-ferrite formation. (2) With preheating, there is a severe bubble formation in the fusion zone. Also, the joint fabrication of caps and first wall has to be fail save with respect to surface tolerances. With the observed small lateral extension of the EB welds it seems to be rather difficult to achieve. For completion of the EUROFER fabrication process data base, however, it would be necessary to perform a systematic EB

weld study for a determination of the limit of the welding depth. This will be the focus of the ongoing investigations.

Elementary diffusion weld parameters for EUROFER with respect to industrial production processes have been determined. In summary, it was elaborated that diffusion welding is not only sensitive to surface contamination but depends also strongly to the surface structure which results from milling. However, it could be demonstrated that two-step HIP diffusion welding can eliminate unfavourable surface fabrication defects and, therefore, might allow for more efficient milling processes. A fault-tolerant weld process, however, can only be achieved by welding at elevated temperatures like 1150 °C. Some of the results may be applied to the fabrication of parts with inner cooling channels (for example the first wall). This is especially true for surface fabrication, contamination and cleaning aspects discussed above. The final step within this study is to adopt the presented fabrication steps to an optimum first wall production cycle, with respect to efficiency, quality, redundancy, fault-tolerance, and operation safety. The first results are expected by mid of 2009.

Staff:

A. Baumgärtner
B. Dafferner
S. Heger
U. Jäntsch
M. Klimiankou
M. Rieth
R. Ziegler
H. Zimmermann

Literature:

[1] Rieth, M., *Specific welds for test blanket modules,* 13th Internat. Conf. on Fusion Reactor Materials (ICFRM-13), Nice, F, December 10-14, 2007.

[2] M. Rieth, B. Dafferner, S. Heger, H. Zimmermann, *Diffusion weld study for Test Blanket Module fabrication*, 25th Symposium on Fusion Technology, SOFT 2008, 15. - 19. September 2008, Rostock, Germany.

[3] M. Rieth, B. Dafferner, U. Jäntsch, H. Zimmermann, *Welding Techniques for Blanket Fabrication*, Annual Meeting on Nuclear Technology, Hamburg, Germany, May 27-29, 2008.

TTMS-005
Rules of Design, Fabricaton and Inspection

TW2-TTMS-005b D 4
Creep-fatigue Lifetime Prediction Rules for Irradiated EUROFER

The objectives of this task are the modification of the lifetime prediction model developed in TW2-TTMS-005a D4 for RAFM steels under creep fatigue conditions taking into account the irradiation influence and the verification of the modified model by applying it to EUROFER 97 in the post-irradiated state.

Within the reporting time period the irradiation induced hardening model developed and successfully applied to EUROFER 97 describing its behaviour observed in post irradiation examination (PIE) has been coupled to the deformation damage model resulting in a powerful model describing the constitutive behaviour even under irradiation conditions. This model has been applied to post irradiation low cycle fatigue tests performed on EUROFER 97 at 336°C (≈ irradiation temperature) within the ARBOR-1 irradiation programme. Thereby fairly good prediction of the pronounced cyclic softening and the lifetime could be obtained (s. Figure 1).

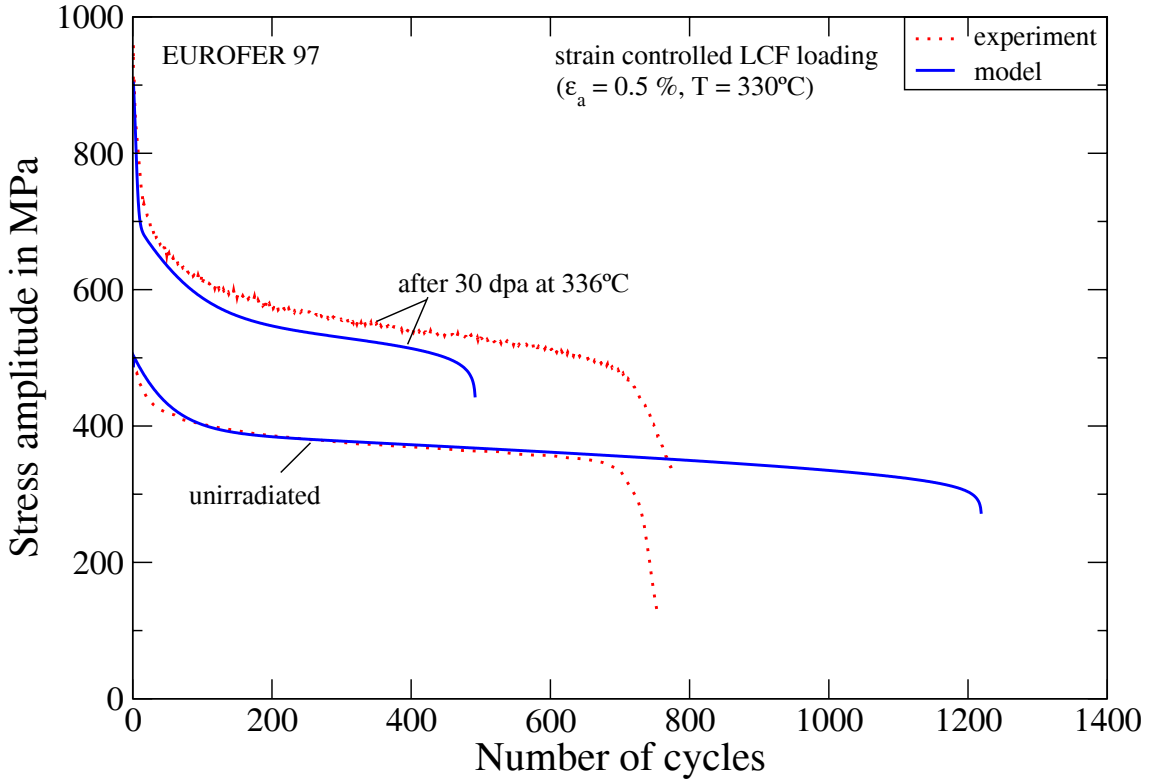

Fig. 1: Cyclic softening and lifetime behaviour of EUROFER 97 before and after irradiation as observed in low cycle fatigue tests and their prediction by the constitutive model developed for RAFM steels under irradiation conditions.

In addition the irradiation induced hardening model has been used to describe the observed healing in annealing experiments at 550°C on irradiated specimens whose strength achieve after 3 hours annealing nearly the level before irradiation. Thereby the decrease of the irradiation induced hardening with the annealing time could be well modelled determining the respective model parameters (s. Figure 2).

Currently, PIE among others low cycle fatigue tests on irradiated EUROFER 97 will be conducted within the SPICE and ARBOR-2 irradiation programmes providing valuable data for further verifications of the constitutive model developed.

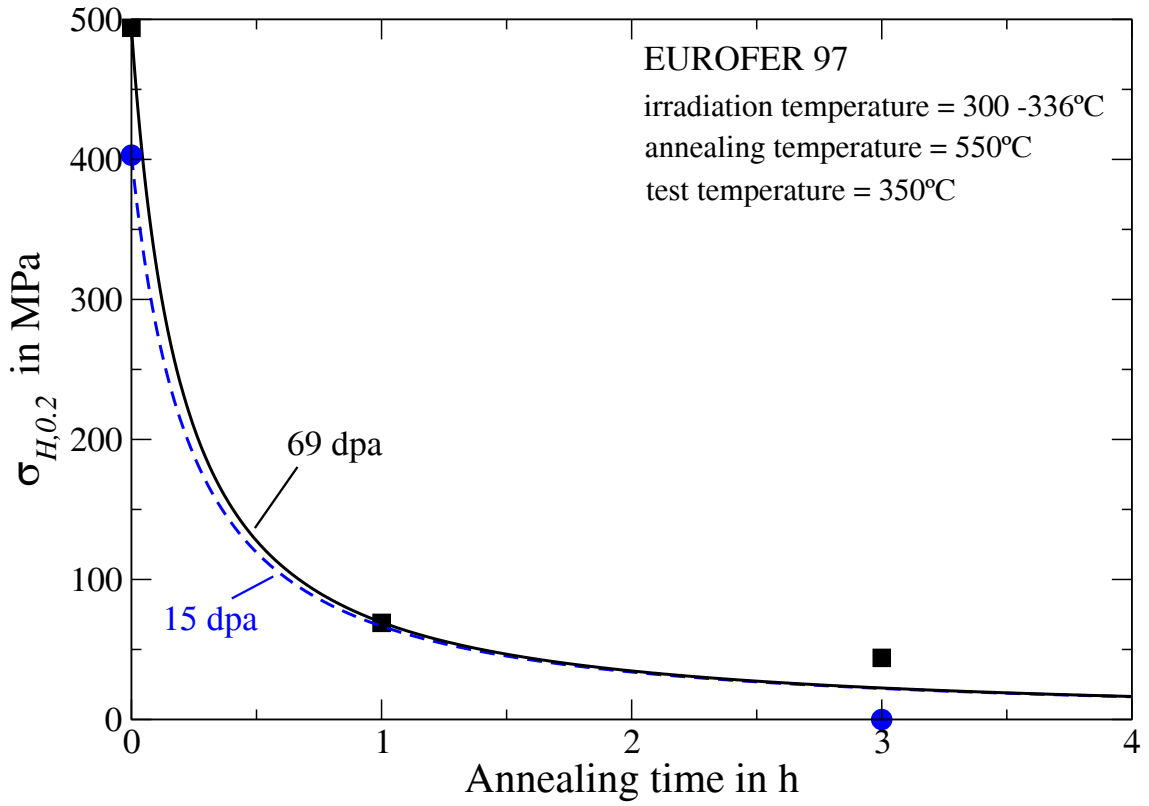

Fig. 2: Influence of annealing on irradiation induced hardening, comparison between experimental data (markers) and model description (lines).

Staff:

J. Aktaa

Literature:

[1] J. Aktaa and C. Petersen: “Modeling of the constitutive behaviour of RAFM steels under irradiation conditions”, MRS Fall Meeting, Boston, USA, Dec. 2008

TW5-TTMS-005 D 5
High Temperature Fracture Mechanical (creep-fatigue) Rules: Formulation and Implementation

The objectives are the development of the high temperature part of a design code for fusion reactor components built from EUROFER which includes reliable fracture mechanical rules for the assessment of detected defects under creep and creep-fatigue conditions.

Therefore the fracture mechanical rules of the R5 procedure (British Standards) have been adopted. The evaluation of the R5 procedure has been performed investigating different crack assessment procedures for high temperature application. Beside the R5, the extended R6, the BS7910-Partial safety factors, the A16 and the JNC procedures are considered. For application of the R5 procedure to assess cracks detected in components built from EUROFER 97 parameters of the creep crack growth relation are required. These parameters will be determined in fracture mechanical tests performed on EUROFER under TW5-TTMS-005 D6, which are however still in progress.

Within the reporting time period the finite element simulations started to verify the validity of appropriate relations estimating crack loading parameters C* and C(t) have been finished. Thereby, the crack loading parameters are calculated using the appropriate algorithm provided by the finite element code for one and two-dimensional cracks in several structures - among others TBM relevant structures - and compared with the values estimated by the R5 procedure.

A handbook for the application of R5 procedure on EUROFER 97 structures was created with a description of the necessary data and experiments which have to be performed to obtain reliable parameters for lifetime prediction. A final report summarizing the knowledge gathered has been written and will be published soon.

Staff:

F. Siska
J. Aktaa

TW5-TTMS-005 D 6
Define and Perform Accompanying Experiments to D 5 (e.g. creep crack growth at 550°C)'

Background and Objectives

For TBM's licensing, in order to establish design rules for the materials, joints and specific sub-components, a broad set of R&D activities have been launched within the WP 2002. These activities will continue with emphasis on implementation in DSCD (Demo structural design code) and verification and validation experiments. Additional rules for HT (high temperature) fatigue-creep interaction need to be formulated, in particular for fracture mechanics.

The low ductility of EUROFER (in particular after irradiation) gives very conservative limits for design against fast fracture and local flow localization. Some experiments are required in support of special design code activities that could lower very conservative assumptions in existing frameworks.

In addition, development of small scale test techniques in fracture mechanics will continue including transferability of the small size specimen tests to the behaviour of the TBM's sub-components.

The objective of this subtask is to perform long time creep crack growth experiments on EUROFER to determine the da/dt (crack velocity) - C* (C*-integral)- behaviour at the temperatures 500 °C and 550 °C. The results are needed for the determination of material parameters in HT fracture mechanical rules.

Status

Based on a replacement of the responsible technician, a new technician had to be trained on the project. Within this frame, a lot of tests had to be done again. Especially preliminary tests were repeated in order to determine the correct values of the increasing crack length during the crack propagation in the main experiments. For that purpose, the DC potential method is used. Fundament of this method is an increasing electrical resistance (increasing potential at a constant current) of a fracture mechanical specimen with an increasing crack length. To figure out the correct correlation between crack length and potential (measured in voltage), fatigue cracks were created stepwise and the length of the single steps were compared with the change of the potential during the steps.

By using the standard electronic set-up one could observe, that the method didn't work well at higher temperatures (> 500 °C). Mainly influenced by oxidation, it was a problem to figure out the right correlation between the crack growth and the change of the electrical potential during the tests. Thus, the set-up had to be optimised for the relevant temperature range. This was done by changing electronic devices (current source, amplifier), by changing the material for the conductors (nickel instead copper) and by changing the conduction of the conductors with the specimens (laser welded instead screwed). After these modifications the method worked well and the correlation between potential and crack length could be determined at 500 °C and 550°C as shown in Figs. 1 and 2.

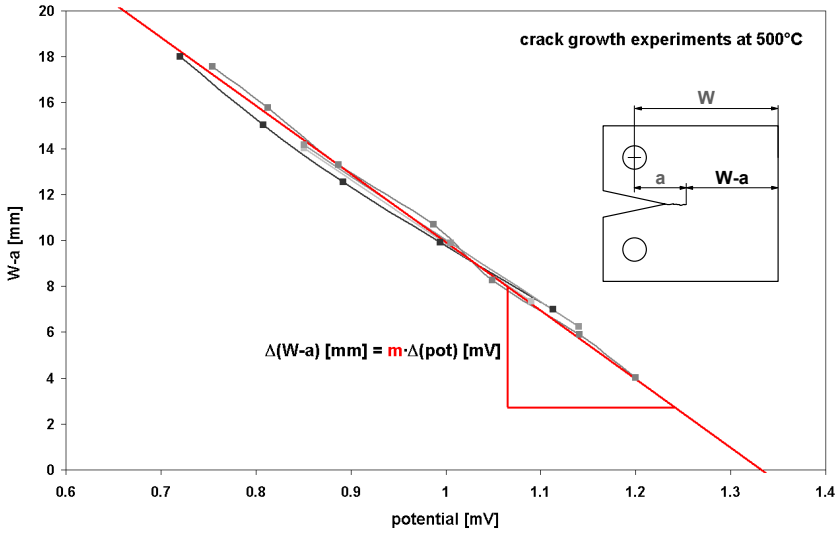

Fig. 1: Results from crack growth experiments at 500 °C to determine the crack growth-potential change-correlation.

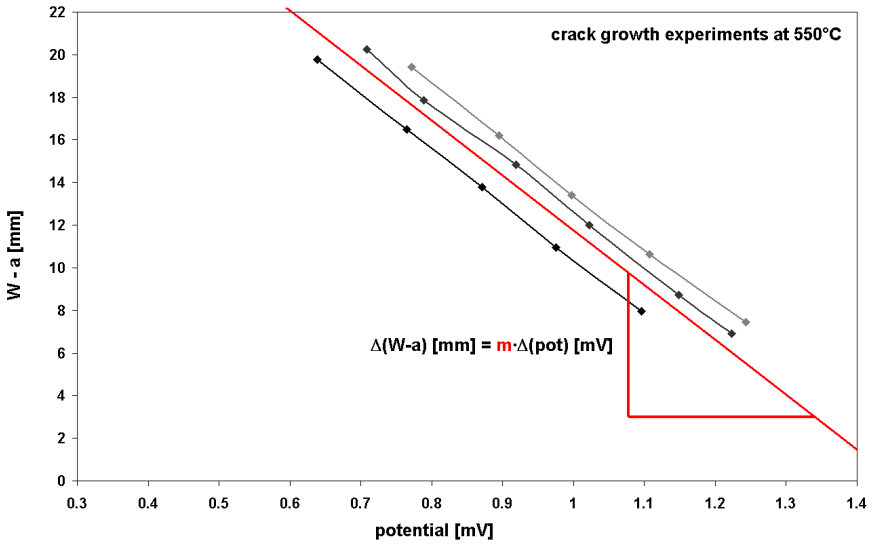

Fig. 2: Results from crack growth experiments at 550 °C to determine the crack growth-potential change-correlation.

Parallel to these tests, special clip gauges were developed and fabricated to measure the crack opening during the main experiments.

Conclusion and Outlook

The assembling of the experimental set-up has been finished. Preliminary tests with the set-up for the DC potential method were done in order to determine the correct correlation between voltage and crack length in the relevant temperature range. Currently, new specimens with incipient fatigue cracks were fabricated and after removing the side-notches, the tests to determine the suitable load cases for the long term experiments can start. After finishing these pre-tests, the main experiments will start.

Staff:

St. Knaak
M. Walter

TW6-TTMS-005 D 4
Experimental Verification and Validation of Newly Implemented HT Creep-fatigue Rules

Background and Objectives

For TBM's licensing, in order to establish design rules for the materials, joints and specific sub-components, a broad set of R&D activities have been launched within the FP VI. These activities will be continued with emphasis on implementation in SCD (Structural design code) and verification and validation experiments. Additional rules for HT (high temperature) fatigue-creep interaction need to be formulated, in particular for fracture mechanics and subsequently validated within experiments with increasing complexity in loading history and (mock-up) geometry.

The low ductility of EUROFER (in particular after irradiation) gives very conservative limits for design against fast fracture and local flow localization. Investigations are required to define improved fatigue rules that could lower very conservative assumptions in existing frameworks. Development and qualification of NDT (non destructive detection techniques) should get more attention and need to be launched. In particular, NDT will provide the information needed on the minimum detectable crack-size as function of location in the TBM, which is essential for any reliable crack analysis.

Development of small scale test techniques (SSTT) in fracture mechanics will be continued including transferability of the small size specimens tests to the behaviour of the TBM's sub-components.

Subtask:
The objectives are to evaluate the mechanical properties of EUROFER and EUROFER diffusion welded joints in the region of creep-fatigue performing suitable

- Uniaxial isothermal LCF-experiments with dwell time at 500/550 °C on EUROFER
- Uniaxial isothermal LCF-experiments with different total strain amplitudes at 500/550 °C on EUROFER diffusion welded joints
- Thermo-mechanical fatigue experiments in the temperature range 100-550 °C with dwell times on EUROFER.

Status

The LCF-experiments on mini-specimens with diffusion welded joints (at RT, 500 °C and 550° C) have been finished. In general one can see, that the specimens do not fail at the welded joints. Compared with not welded specimens, they also show the typical softening behaviour of RAFM-steels under LCF-conditions. However, it is observable that the maximum stress level is higher, whereas the single hystereses show lower plastic strain amplitudes. This could base on a marginal change of the micro structure during the welding process.

With the transition towards HCF-conditions, the material changes its behaviour and shows hardening in the beginning at RT tests. An explanation for this change could be that at low total strain amplitudes, the plastic strain amplitude at RT is also very low. From this it follows, that the plastic deformation at the beginning occurs locally and not homogeneously over the volume – in that case, the influence of the partial irreversible deformed welded joint zone on the integral stress-strain-behaviour should increase.

Nevertheless, the lifetimes of the specimens with diffusion welded joints are comparable with the lifetime of specimens without welded joints. They are even marginal higher in the relevant

range as one can see in the following diagrams (Fig. 1 and 2). Here, the lifetimes of diffusion welded mini-LCF-specimens, mini-LCF-specimens and additionally of standard specimens, tested at RT as well as 550 °C, are shown. Fig. 3 shows a comparison of the results of the experiments on specimens with welded joints at 500 °C, with the results of welded specimens tested at RT and 550 °C, respectively (standard specimens and mini specimens haven't been tested at 500 °C).

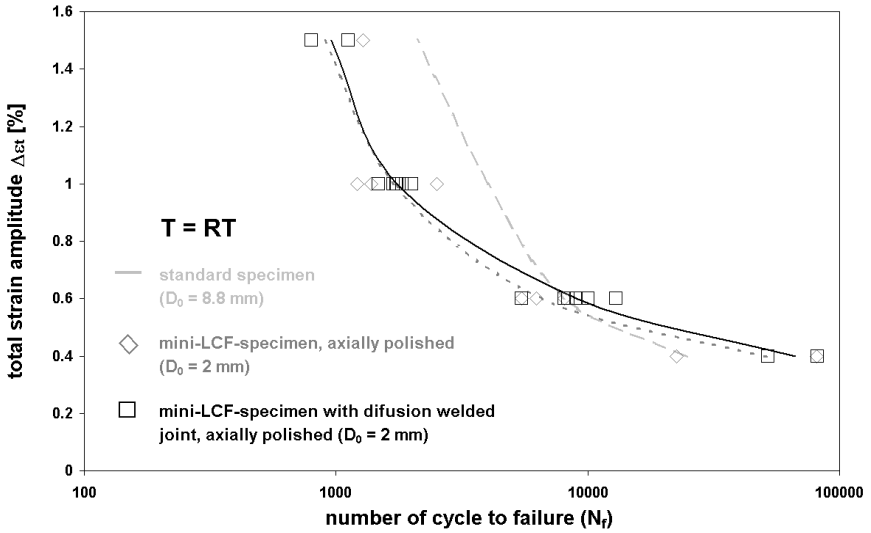

Fig. 1: Results of the RT LCF-tests on diffusion welded mini specimens, compared with the results of tests on mini specimens and standard specimens.

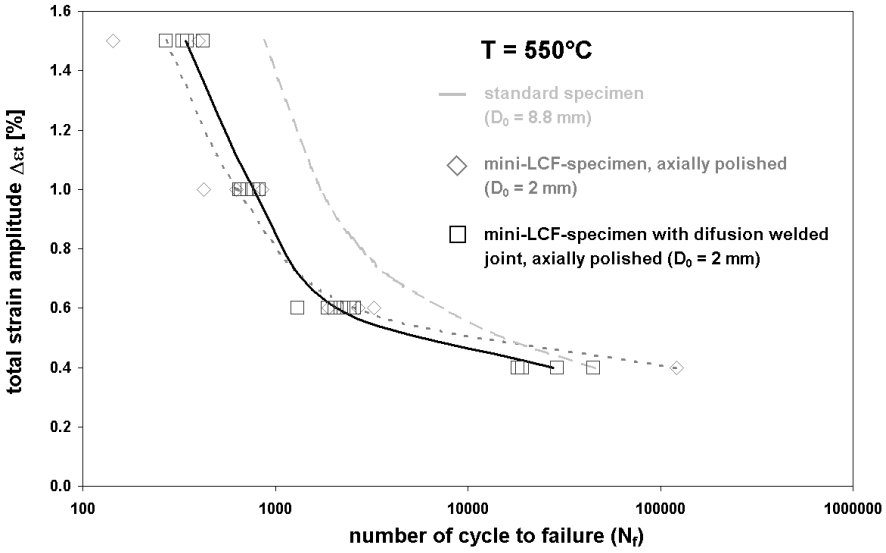

Fig. 2: Results of the 550 °C LCF-tests on diffusion welded mini specimens, compared with the results of tests on mini specimens and standard specimens.

The thermo-mechanical fatigue (TMF) experiments with dwell times (1 min, 3 min and 10 min) under tension, under compression and under tension and compression in the temperature range of 100-550 °C have also been finished. In general one can observe that at shorter dwell times, the specimens which were tested with dwell times under tension and dwell times under compression show higher lifetimes than specimens tested without dwell time. At higher dwell times, the lifetime of specimens which were tested with dwell times under tension is decreasing continuously, whereas the lifetime of specimens which were tested with dwell times under compression is decreasing clearly stronger. Specimens which were tested with dwell times under tension and compression show a continuously decrease of the lifetime with increasing dwell times (Fig. 4).

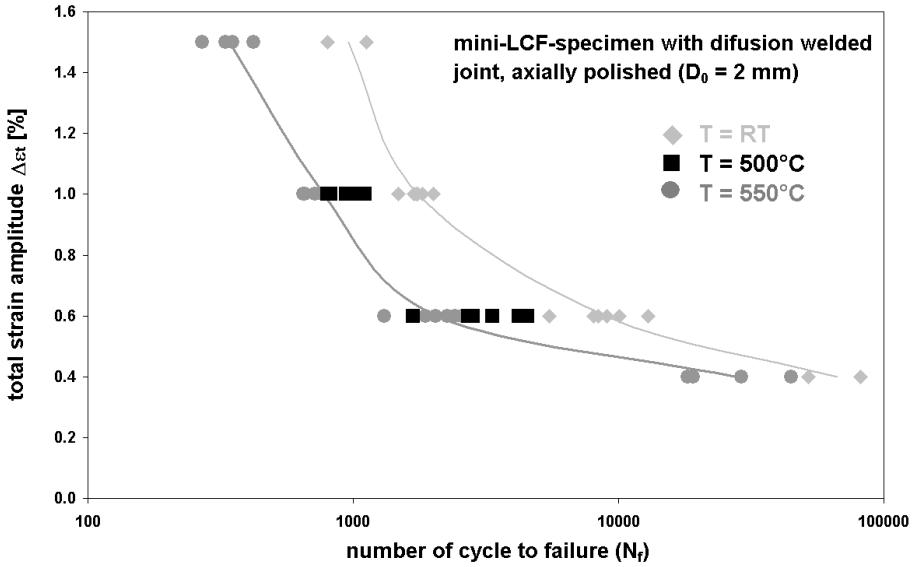

Fig. 3: Results of the 500 °C LCF-tests on diffusion welded mini specimens, compared with the results of tests at RT and 550 °C, respectively.

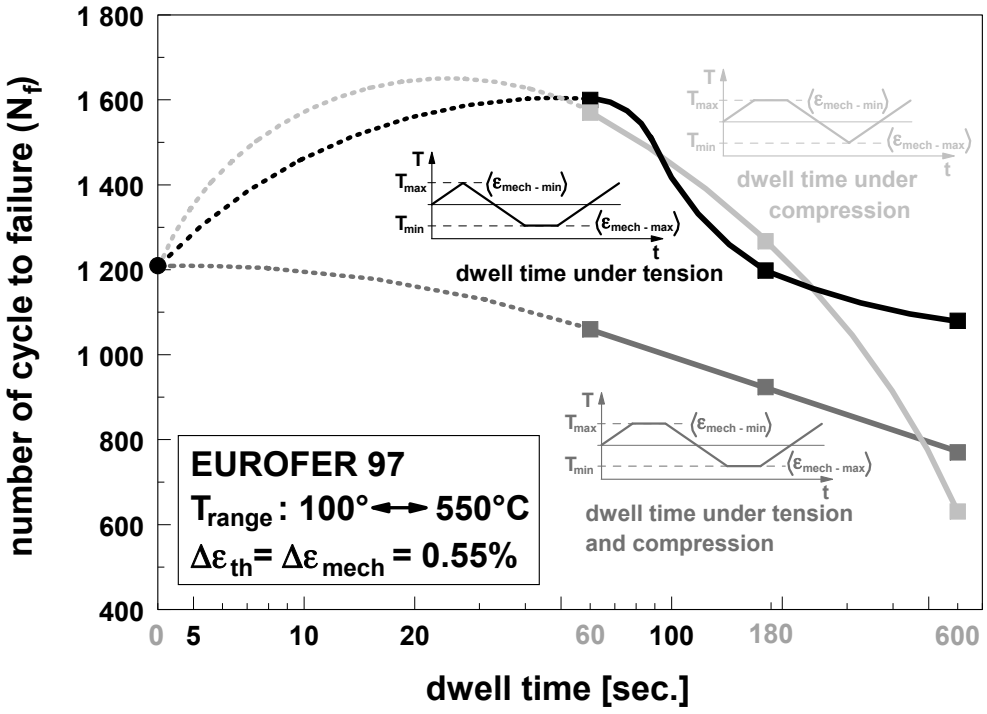

Fig. 4: Results of the TMF tests, illustrated in a number of cycles to failure-dwell time-diagram.

Although the material behaviour at longer dwell times is qualitatively comparable with the behaviour of the material at isothermal LCF-dwell time-tests (report 2007), more experiments are necessary to understand the background, especially of the results at short dwell times. Up to now, neither analyses of the stress amplitudes, nor analyses of comparable stress-strain-hystereses curves lead to comprehensible explanations.

The positions of the results from LCF dwell time tests, TMF dwell time tests and LCF tests on diffusion welded mini specimens relative to the design curve (ASME Code Case N47-29) are illustrated in the last diagram [Fig. 5]. It can be seen, that all results are beyond the design curve on the save side. But depending on the results of the TMF tests with longer dwell

times, there seems to be no possibility to modify the design code towards less conservative assumptions.

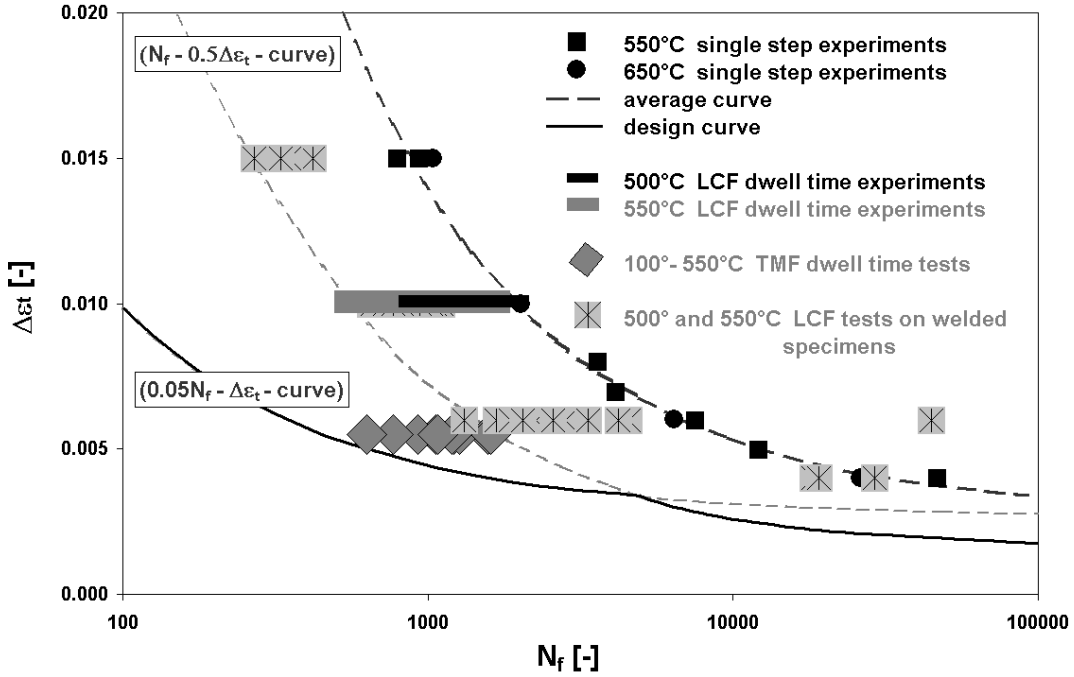

Fig. 5: Comparison of the results from LCF dwell time tests, TMF dwell time tests and LCF tests on diffusion welded mini specimens with the design curve (ASME Code Case N47-29).

Conclusion and Outlook

The experiments have been finished and compared with the design curve (ASME Code Case N47-29). It can be seen, that all results are inside the design space. The results from the LCF dwell time tests and LCF tests on diffusion welded mini specimens show that with respect to the design curve, there is more than enough distance to be on the safe side for calculations of constructions. In contrast to this, the results of the TMF tests with longer dwell times lie close to the curve. Here it is necessary to perform additional tests with dwell times up to hours.

Staff:

U. Bürkle
M. Klotz
M. Walter

TW6-TTMS-005 D 5
Qualification of NDT (non-destructive detection techniques) for Evaluation of Limits of Detectable Cracks

The objectives of this task are to find out an adequate NDT (non-destructive detection technique) for detecting cracks particularly in the welded areas of blanket components built from EUROFER 97 and to realise it with an automated NDT testing procedure.

In the EU Test Blanket Modules (TBMs) design, the low activation steel like EUROFER 97 will be used as structural material. The first wall and cooling plates with cooling channels will be HIP welded, and the stiff grids are expected to be welded by Electron beam (EB) or Tungsten Inert Gas (TIG). Welded structures can fail catastrophically if they contain cracks above a certain critical size for the load applied. Using the concepts of fracture mechanics, it is possible to determine the extent to which a pre-existing crack might propagate to an unacceptable level during service. For computation of fracture mechanics parameters like stress intensity factor, it is essential to know the exact location, configuration and the size of the cracks. Therefore, development of a non-destructive testing (NDT) method to detect the cracks in the welded area is one of the key issues in developing plasma-facing components (PFCs) for next generation fusion devices. Among the most widely used NDT techniques, Magnetic particle testing (MT), Liquid Penetrant testing (PT) and Eddy current testing (ET) can only detect the flaws on the surface of the specimen. In contrast, radiography (RT) and ultrasonic testing (UT) are the most frequently used methods of testing different test pieces for internal flaws. A detailed comparison between RT and UT yields the selection of ultrasonic testing technique that was chosen in the current work.

Within the reporting period the ultrasonic testing has been further evaluated performing tests on EUROFER 97 welds specimens of different geometries with artificial flaws of well known sizes and positions. On T-shaped TIG- and EB-specimens holes of 0.5 mm diameter could be detected by manual UT and angle probe. With automated immersion UT testing conducted at GE Inspection Technologies on diffusion bonded plate with internal cooling channel 0.4 mm small holes could be easily found. On the base of this evaluation, flaws of even 0.3 mm diameter are expected to be detectable with automated immersion UT.

Consequently, an automated ultrasonic testing facility was already ordered from GE Inspection Technologies, which includes a USIP 40 device, a KC-tank, and K-Scan software. The facility will be delivered in December 2008 and its capability to detect small flaws in welds of test blanket module shall be demonstrated within the next 6 months conducting suitable experiments on EUROFER 97 welded mock-ups.

Staff:

J. Aktaa
S. Knaak
Y. Zhong

TTMS-006
High Performance Steels

TW5-TTMS-006 D 5
Nano Composited Ferritic Steels for HT Application: Identification of Promising Candidate Alloy Compositions and Respective Fabrication Routes According to the Outcome of the 2004 Study. Production of Different Laboratory Batches (14%Cr)

The operation temperature of RAFM ODS steels like ODS-EUROFER for application as structural material in advanced blanket concepts like the Dual-Coolant Concept is limited to about 650°C. More advanced blanket concepts like the Advanced HCPB (Model C) or the use as backbone material in gas cooled divertors, require allowable operational temperatures of 700 to 750°C or even more. Reduced activation ferritic (RAF) ODS-steels could fulfil these requirements but are not commercially available at the moment and must be developed. Fe-(12-14)Cr-(2-3)W-(0.2-0.5)Ti-(0.2-0.5)Y_2O_3 being developed in USA and Japan for fission and fusion application seem to be promising and is presently also considered to form the basis for EU efforts.

Within this task, two master alloys containing 13-14% Cr and 1.0-1.2% W and varying Ti contents were ordered and inert gas atomised. These steel powders formed the basis for the production of different ODS steels with varying Y_2O_3 and Ti contents by mechanical alloying in a high-energy attritor mill. Hot-Isostatic-Pressing was applied to consolidate the MA powder. Powders and hipped samples of the different alloys were screened by appropriate methods like metallography, SEM, XRD, HRTEM, and chemical analyses. Tensile and charpy tests on miniaturised specimens are used for the mechanical characterisation of these alloys. The main goal of this task is the screening of composition, production parameters and heat treatments on microstructure and mechanical properties of RAF 13-14Cr1.1W(Ti, Y_2O_3) ODS steels.

In terms of continuing the general parameter studies on the 13Cr-1W-0.3Ti-0.3Y_2O_3 ferritic ODS-alloy several new variations and additions within the production process have been conducted. The influences on important mechanical properties were examined.

Figure 1a) and b) contain the ultimate tensile strengths R_m of the 13Cr-1W-0.3Ti-0.3Y_2O_3 alloy produced according to different parameter sets. The curves 2) and 3) show a version of the alloy manufactured with a mechanical alloying time of 21 hours while using 1200 rpm/800 rpm as a rotational speed interval. The following HIP parameters (p_{hip} =1000 bar, T_{hip} =1150 °C, t_{hip} =2 h) as well as the final heat treatments (30 min; 1050 °C) were kept identical. The only difference between both was the originally applied milling atmospheres during mechanical alloying: argon as well as hydrogen were used. As figure 1a) shows, both curves have nearly identical R_m levels, except at 400 °C, where the argon milled version demonstrates a little higher strength. Furthermore the curves 4) and 5) have been produced with a hydrogen milling atmosphere too, but the HIP temperatures as another significant manufacturing parameter were altered. Curve 4) displays R_m data with a lower HIP temperature of 1050 °C while curve 5) shows the according values for a HIP temperature of 950 °C. The final heat treatments were kept identical too. The difference within these HIP- temperatures does not seem to have a great influence on the ultimate tensile strengths too. Only at 400 °C the R_m level of curve 5) is a little lower than R_m of curves 2), 3) and 4). Generally the mentioned variation of the milling atmosphere as well as the reduction of the HIP temperatures with all other parameters kept identical do not lead to significant changes in R_m. In addition it can be stated that the very positive strength increases for the ferritic ODS-alloy compared to the non ODS-alloys FeCr13 (curve 1)) (basic powder hipped with p_{hip} =1000 bar, T_{hip} =1150 °C, t_{hip} =2 h) and EUROFER 97 (curve 6)) have been maintained in all versions of 13Cr-1W-0.3Ti-0.3Y_2O_3. Furthermore the general strength levels of the ferritic ODS-alloys (curve 7)) are

similar to ODS- EUROFER, except at room temperature where the ferritics show a higher strength.

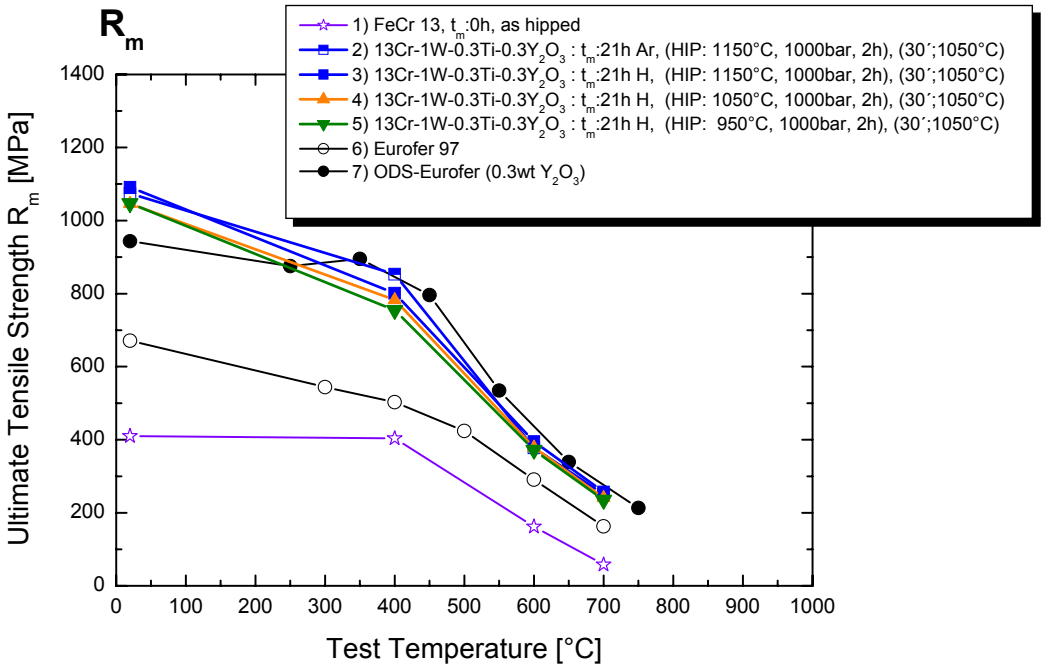

Fig. 1a): Comparison of ultimate tensile strengths of the ferritic ODS-alloy 13Cr-1W-0.3Ti-0.3Y_2O_3 produced with different mechanical alloying and HIP parameters to ODS- EUROFER as well as non ODS type materials FeCr13 and EUROFER 97 as reference alloys.

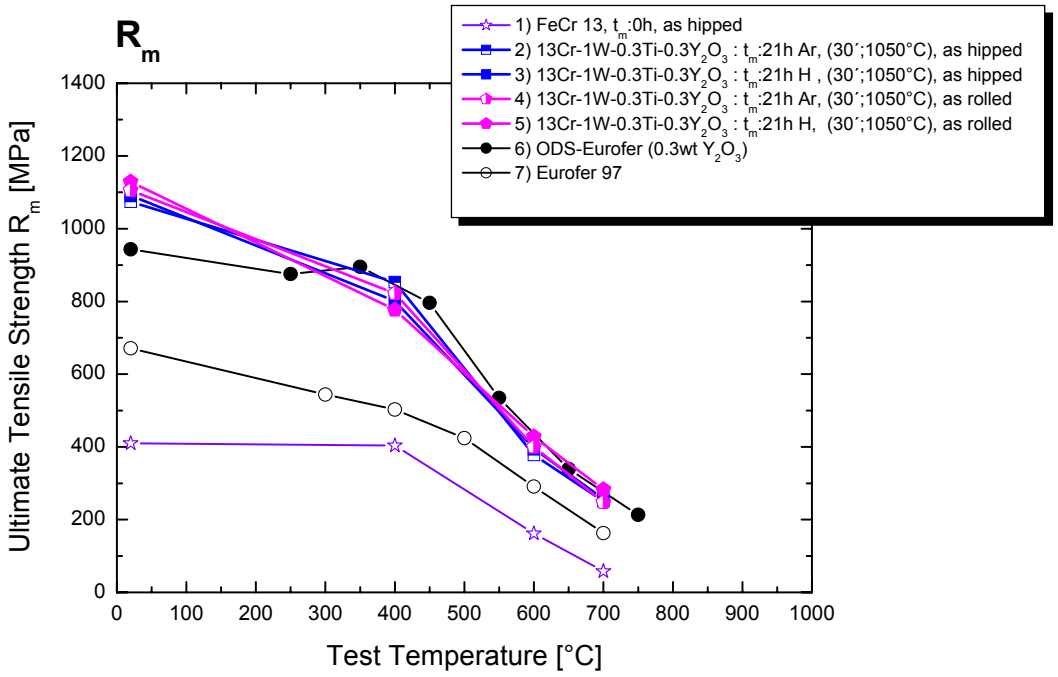

Fig. 1b): Comparison of ultimate tensile strengths of the ferritic ODS-alloy 13Cr-1W-0.3Ti-0.3Y2O3 produced with different mechanical alloying but equal HIP as well as rolling parameters to ODS-EUROFER and non ODS type materials FeCr13 and EUROFER 97 as reference alloys.

Figure 1b) contains another variation within the overall production process of the 13Cr-1W-0.3Ti-0.3Y_2O_3 ODS-alloy: rolling of the hipped ODS-cans at 800°C with a following heat treatment of (30 min; 1050 °C) each (curves 4) and 5)). The grain textures in the specimens of these as rolled alloy versions were orientated in rolling direction. The diagram also displays the already discussed as hipped versions with the different milling atmospheres. For the as rolled versions both atmospheres were applied too. As it can be seen in figure 1 b) the general ultimate strength levels do not demonstrate strong variations for the as hipped and as rolled versions with both milling atmospheres for the 13Cr-1W-0.3Ti-0.3Y_2O_3 ODS-alloy.

Only at room temperature the as rolled alloy types have a larger R_m value. For all other temperatures the rolling effect on R_m as well as the change in milling atmosphere seems to be limited as well compared to the as hipped versions (curves 2) and 3)). Generally R_m levels stay high for the ferritics compared to the reference alloys FeCr13 (curve 1)) and EUROFER 97 (curve 6)) for these changes in production. The higher strength at room temperature compared to ODS- EUROFER is equally visible.

In addition to these experiments three point bending tests have been executed for the ferritic ODS-alloy 13Cr-1W-0.3Ti-0.3Y_2O_3 ODS-alloy aiming in determining the fracture toughness of the alloy. Single etched notched specimens (SEB) were made in the same way, as described before: the only difference between the examined alloy types in the production process were again the applied milling atmospheres argon and hydrogen. After hipping the ODS-cans were also rolled and heat treated with same parameter sets as already mentioned. The notches and pre-cracks of the specimens were orientated perpendicular to the rolling direction. Load displacement curves were acquired parallel as figure 2 shows exemplary for a room temperature test:

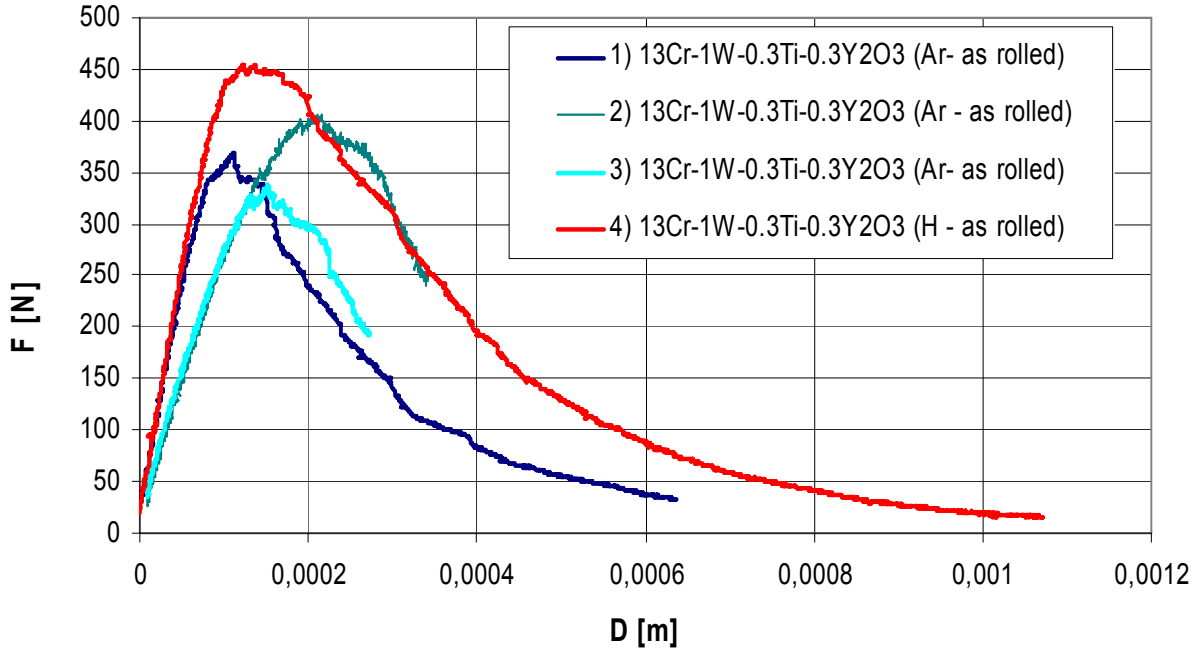

Fig. 2: Comparison of load displacement curves for the ferritic ODS-alloy 13Cr-0.3Ti-0.3Y2O3 with two configurations, Test Temperature T = 24 °C.

It can be seen that for T=24 °C the originally specimen produced with hydrogen (curve 4) exhibits the highest applied force (454 N) and a displacement of 0.00107 m. For the other specimens manufactured in argon a lot larger fluctuation of the force and displacement levels is clearly visible. Curve 2) has a maximum force around 400 N and a displacement of 0.00034 m, while curve 1) shows a maximum force around 367 N with a displacement of

0.00064 m. Curve 3) shows lower levels with F_{max} =336 N and lies in between those with v_{max}= 0,00027 m.

Using the information of those diagrams for all test temperatures the critical stress intensity factors K_{Jc} can be calculated.

Figure 3 a) and b) contain the critical stress intensity factors for specimens produced with hydrogen and argon including hipping, rolling and heat treating as discussed. The acquired results for the fracture toughness in 3a) lay in between 69 MPa√m at room temperature and 44 MPa√m at –150 °C. The values fluctuate strongly at –50 °C (83 MPa√m to 28 MPa√m). The DBTT can not be clearly seen and is around -50 °C<T<0 °C. Reasons for that need to be investigated but it is assumed that inhomogenities within the material cause this behaviour.

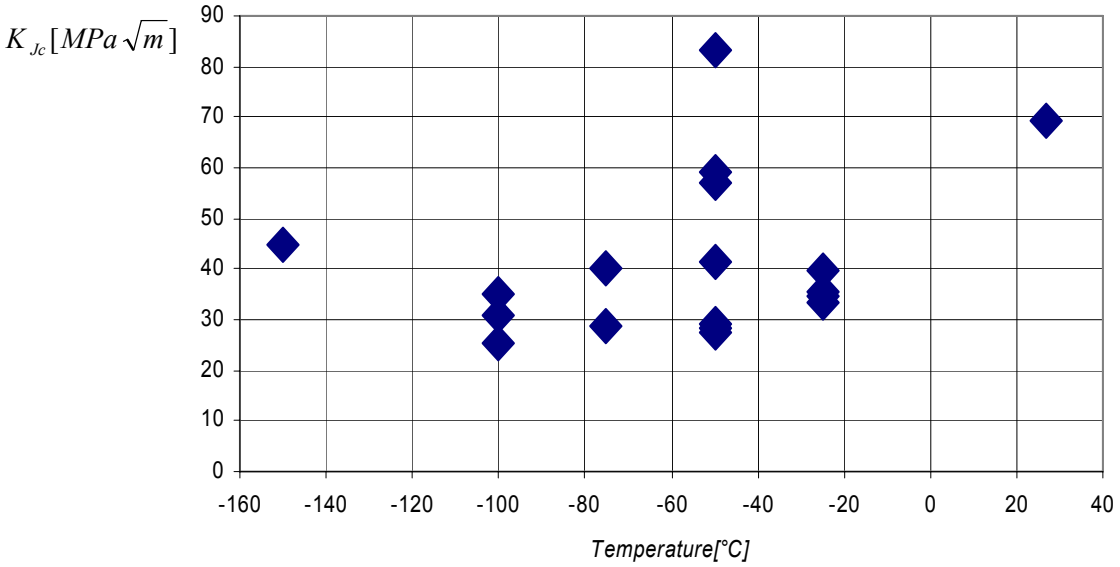

Fig. 3a): K_{Jc} factors for the ferritic ODS-alloy 13Cr-1W-0,3Y_2O_3-0,3Ti, manufactured with hydrogen as milling atmosphere.

Figure 3b) shows the critical stress intensity factors for the argon made specimens.

There the fluctuations for several tests within one temperature are not as large as in figure 3a). The values vary from 56 MPa√m for room temperature and 23 MPa√m for –150 °C. The DBTT temperature is around T=-25 °C. The K_{Jc} levels between the argon and hydrogen produced specimens are not very different.

Charpy impact tests with specimens made using hydrogen and argon in the as hipped and as rolled state show still a low ductility. In general the results for the ferritic ODS-alloy 13Cr-1W-0.3Ti-0.3Y_2O_3 are very promising but the introduction of hydrogen and rolling did not lead to an improvement of all mechanical properties. Therefore, in addition to the described optimizations, future steps will be undertaken to further purify the overall production process. This purification procedure shall lead to a higher fracture toughness as well as larger impact energies while equally the high strength levels shall be kept.

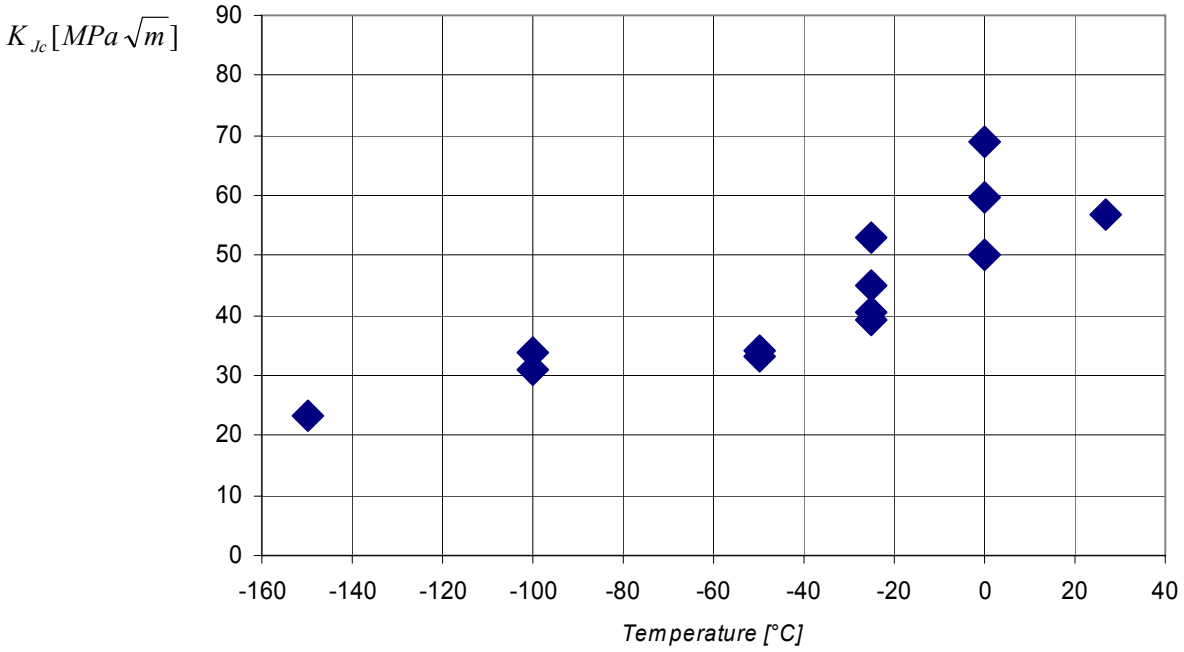

Fig. 3b): K_{Jc} factors for the ferritic ODS-alloy 13Cr-1W-0,3Y_2O_3-0,3Ti, manufactured with argon as milling atmosphere.

Staff:

C. Adelhelm
S. Baumgärtner
C. Eiselt
P. Graf
M. Klimenkov
T. Kaiser
R. Lindau
A. Möslang
U. Jäntsch
R. Ziegler
H. Zimmermann

Literature:

[1] Ch. Ch. Eiselt, R. Lindau, A. Möslang; First results and prospects on the characterization of the 13Cr-1W-0,3Ti-0,3Y2O3 RAF-ODS-Steel; Poster EUROMAT, Nürnberg, September 10th – September 14th, 2007

[2] Ch. Ch. Eiselt, M. Klimenkov, R. Lindau, A. Möslang; Characteristic results and prospects of the 13Cr1W0.3Ti0.3Y2O3 ODS-Steel; J.of. Nucl. Mat. (2007), Nizza, December 10th – September 14th, 2007

[3] Ch. Ch. Eiselt, M. Klimenkov, R. Lindau, A. Möslang; Characteristic results and prospects of the 13Cr1W0.3Ti0.3Y2O3 ODS-Steel; Poster ICFRM 13, Nizza, December 10th – September 14th, 2007

[4] Ch. Ch. Eiselt, M. Klimenkov, R. Lindau, A. Möslang, H.R.Z. Sandim, A.F. Padilha and D. Raabe; High resolution transmission electron microscopy and electron backscatter diffraction in nanoscaled ferritic and ferritic-martensitic oxide dispersion strengthened steels; EMRS Spring Meeting 2008, Strasbourg , May 26th – May 29th, Article in press

[5] Ch. Ch. Eiselt, M. Klimenkov, R. Lindau, A. Möslang; Ergebnisse zur Charakterisierung und Herstellung des ferritischen ODS-Stahls 13Cr-1W-0.3Ti-0.3Y2O3, KTG Tagung 2008, Hamburg, May 27th – May 29th, Konferenzproceedings

TTMS-007
Modellisation of Irradiation Effect

TW6-TTMS-007 D 10
Elaboration of a Critical Review of the Physical Metallurgy of EUROFER Alloying Elements and Impurities, Heat-treatment/Phases/Microstructure, Phase Stability, and Segregation

Overview

The general objective of this work was to support the modelling activities by providing general information about the metallurgy of the EUROFER steel. The aim was to illustrate the differences between an ideal single crystalline material (as usually considered in atomistic models) and a real multi-phase, polycrystalline, and contaminated material like the EUROFER steel. Therefore, this work reviews the effect of alloying elements and impurities on various material properties. It also describes the general effects of heat treatments on microstructure and phases. Furthermore, irradiation specifics and aging behaviour are discussed. Furthermore, the goal of the modelling efforts within the fusion programme is the numerical simulation of a real material like the EUROFER steel. Therefore, a critical review of all relevant modelling aspects would be a helpful source for the definition of future development trends.

Progress of the Critical Review

The review has been finished. Compared to the EUROFER assessment task TW5-TTMS-001 additional information about irradiation effects as well as a final chapter on precipitates and aging has been added. In the following an excerpt of this chapter is outlined.

Aging studies of F82H at 500-650 ºC as well as of JLF-1 at 375-600 ºC and other 9Cr steels with high amounts of tungsten demonstrated the propensity of these steels to form Laves phase (Fe2W), which lowers the impact toughness (see Fig. 1). The most striking difference to EUROFER 97 is the higher tungsten content of 2 percent (EUROFER has 1%). One of several design criterions of the EUROFER steel was a high resistance against thermal aging. But to date, the aging behaviour of EUROFER has not been determined for times exceeding 10,000 hours (e.g. [2]). Therefore, at FZK a preliminary analysis of selected long-term creep specimens has been performed. The screw head of one of these creep specimens has been used for TEM sample preparation (for details see Table 1 and Fig. 2).

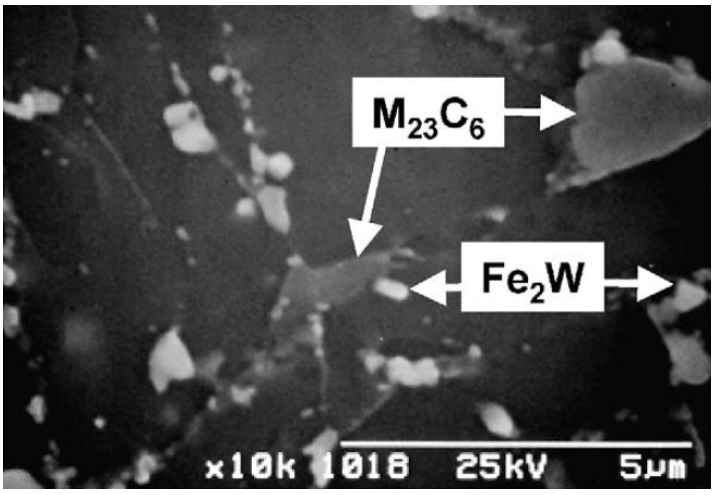

Fig. 1: SEM micrograph of a 9Cr3W3Co steel after aging for 10,300 h at 923 K (from [1]).

Table 1: Aging conditions for the screw head of a creep specimen fabricated of EUROFER97, Heat E83698 (14 mm plate).

Specimen	Heat Treatment prior to creep test	Test Temperature	Time to Rupture
ZSV2772	980 °C + 740 °C	600 °C	35,688 h

Fig. 2: EUROFER 97 creep specimen after 35,688 hours (4 years) at 600 °C. For the ageing study only the screw heads are used, since they are un-strained.

The TEM image of this aged specimen (4 years at 600 °C) in principle confirms the results obtained by the before mentioned studies (Fig. 3). There is an enhanced precipitation, mainly on lath and prior grain boundaries of the austenitic phase. At first glance, there are no large precipitates (like sigma or Laves phase) which would significantly reduce the mechanical properties. The majority of the recognizable precipitates are most probably of the chromium rich M23C6 type. Seemingly, there are also some MX carbo-nitrides due to the tantalum content.

But more detailed assessments will only be possible after the completion of the ongoing study. Anyway, considering all the available results, the EUROFER alloy can certainly be marked as a steel of high thermal aging resistance.

Conclusions

The report provides a comprising knowledge base on all relevant properties and characteristics of the EUROFER steel. The concept of reduced and low activation, physical metallurgy, structure and transformation, effect of heat treatments, certain aspects of the chemical composition, basic outline of irradiation defects as well as phase stability is compiled and may be used as input for the advanced modelling activities in this field.

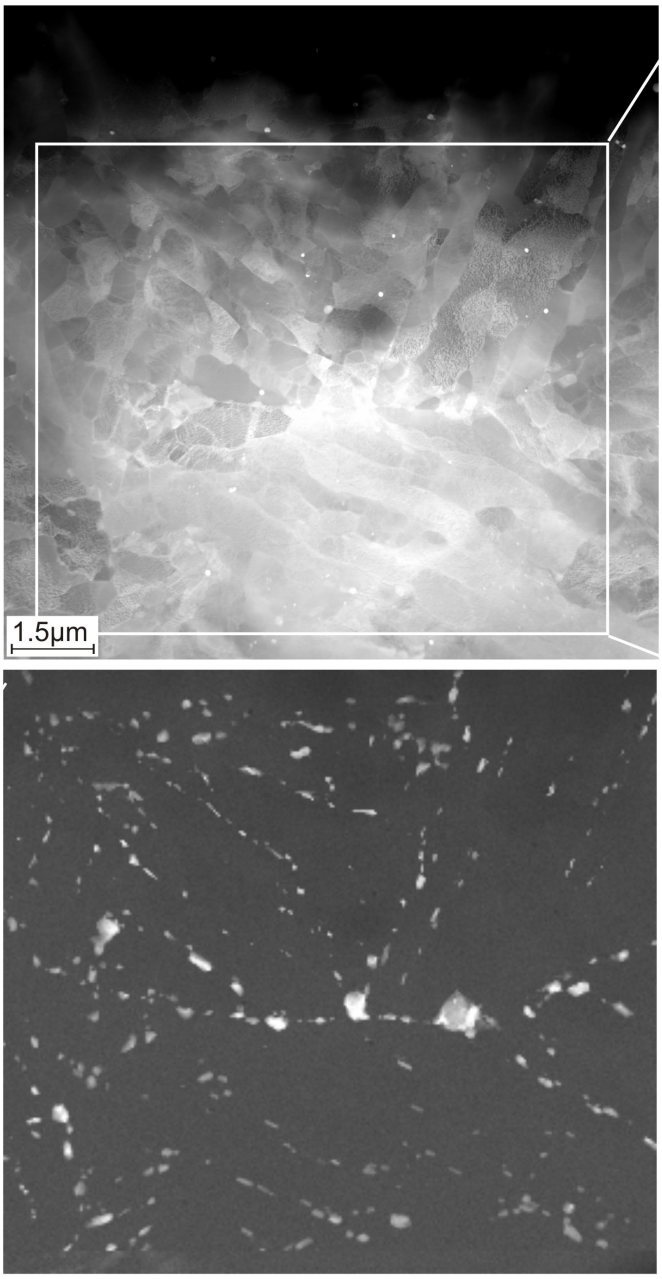

Fig. 3: TEM image of the micro structure (upper image) and the according element mapping image for Cr (lower image).

Staff:

B. Dafferner
S. Heger
U. Jäntsch
M. Klimiankou
E. Materna-Morris
A. Möslang
M. Rieth
H. Zimmermann

Literature:

[1] F. Abe, T. Horiuchi, M. Taneike, K. Sawada, Stabilization of martensitic microstruture in advanced 9Cr steel during creep at high temperature, Materials Science and Engineering A, 378 (2004) 299-303.

[2] P. Fernández, M. García-Mazarío, A. M. Lancha and J. Lapeña, Grain boundary microchemistry and metallurgical characterization of Eurofer'97 after simulated service condition, Proceedings of the 11th International Conference on Fusion Reactor Materials (ICFRM-11), Journal of Nuclear Materials, Volumes 329-333, Part 1, 1 August 2004, Pages 273-277.

Corrosion Resistance of Bare and Coated EUROFER in Liquid PbLi

Introduction

In a future fusion reactor of the He-cooled liquid lithium-lead blanket type (HCLL), reduced activation ferritic-martensitic steels (RAFM) are considered as structural materials, which are in direct contact with the liquid breeder Pb-17Li. The corrosion of the steels is one major effect which determines functionality and life time of such non-isothermal liquid metal system. At moderate temperatures of up to e.g. 480 °C various corrosion experiments in flowing Pb-15.7Li were performed in the past [1-4]. All examined steels (e.g. Manet, F82H-mod., Optifer and EUROFER) showed similar corrosion behaviour concerning activation energies and mechanism. The main focus of these test series performed in PICOLO loop, a non-isothermal liquid metal system was directed on evaluation of corrosion attack phenomena. Generally accepted is meanwhile that the corrosion of steels in such environment is ruled by dissolution mechanism. However, extrapolation is risky due to large uncertainties to other process regimes like higher temperatures in the hot zone, changed flow velocities or dependencies of processes correlated to other loop features like temperature gradients in the non-isothermal loop or transportation and precipitation mechanisms.

The positions where dissolution and precipitation takes place are mainly determined by the temperature dependence of the solubility of iron (and chromium) in the liquid breeder Pb-15.7Li. Hence, one has to face dissolution in the hot parts of the system and precipitation in the cold parts due to increasing Fe solubility by raising temperature, irrespective of the nature of the dissolution process, whether it is exothermic or endothermic. However, extrapolations to other system parameters e.g. higher temperatures are problematic and exhibit large uncertainties due to missing data and models. Thus long-term tests at 550 °C including the development of modeling tools were performed to build up a consistent data base for Pb-15.7Li corrosion and precipitation effects. A simple model, which calculates the mass transfer and the geometrical changes – mass loss due to corrosion attack - of structural components in liquid metal loops, was developed. This model was implemented in a computer code named MATLIM.

These new activities are initiated by changes in TBM requirements and TBM testing in ITER and analyzing the knowledge on interacting loop effects with corrosion and safe loop operation like transportation of corrosion products and their precipitation at cooler loop sections.

Both activities, experimental corrosion testing and modeling development, show that corrosion is a serious problem affecting safe system operation. One method to overcome or reduce corrosion issues is given by coating of RAFM-steels by corrosion resistant scales. In the past the advantage of Al based surface modification by the HDA process (Hot-Dip-Aluminizing) [5,6] was clearly shown. Due to technological restrictions of HDA process e.g. high input of Al into a low activation steel or inflexibility in coating complex geometries the development of novel coating technologies (ECA and ECX process) was successfully started. First ECA samples are under evaluation in Pb-15.7Li.

Corrosion testing

The samples for the corrosion testing were fabricated by machining from EUROFER plate material produced by Böhler Edelstahl GmbH, Austria (thickness 14 mm, badge no. E 83698, plate No. 14, lot No. 249). The machining process was followed by fine grinding and all samples showed a bright metallic surface with average roughness of about R_a = 0.5 µm and with peak roughness values exceeding R_z = 2.4 µm. The chemical composition of the EUROFER master alloy together with the other above mentioned RAFM steels is given in Table 1.

Table1: Chemical composition of RAFM steels.

Steel	C	Cr	Ni	Mn	W	V	Ta
EUROFER	0.11	8.82	0.02	0.47	1.09	0.20	0.13
MANET I	0.13	10.6	0.87	0.82	-	0.22	-
Optifer IVa	0.11	8.50	-	0.57	1.16	0.23	0.16
F82H-mod.	0.09	7.70	-	0.16	1.95	0.16	0.02

The austenitization conditions of the bare materials were 980 °C/27 min followed by cooling in air. Tempering was done at 760 °C for 90 min with subsequent air cooling. No additional thermal treatment was performed after machining of bare test samples. The fabricated samples were cleaned in an ultrasonic acetone bath and dried before mounting into PICOLO loop. The performed Auger surface analyses showed only a 10 nm thick oxide scale on the bare samples being a Fe-oxide with small amounts of Cr and Mn. The test samples were screwed together to a stack of 12 pieces with a total length of ca. 400 mm and inserted into the test section of PICOLO loop through the sample exchange vessel positioned in a glove box with purified inert gas atmosphere. Fig. 1 shows schematically the PICOLO loop with the main components.

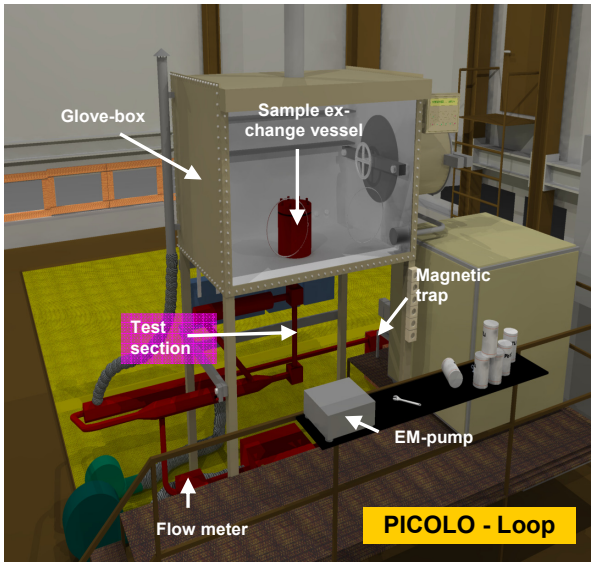

Fig. 1: PICOLO loop with indexed main components-

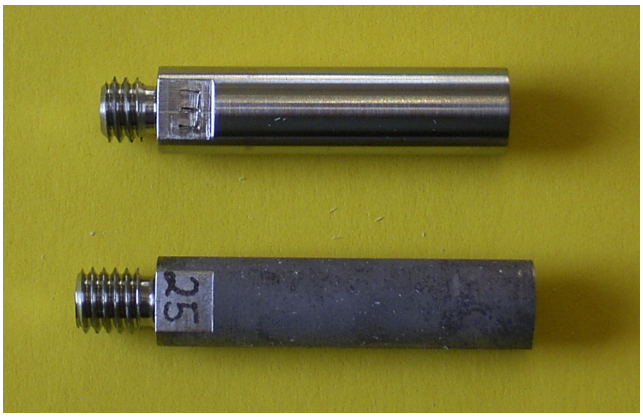

Fig. 2: Fresh test samples of bare EUROFER (top) and Al coated sample by ECA process after heat treatment.

For Al coating by the both processes, ECA and ECX, samples of the same batch were used. However, these samples had to undergo a heat treatment to form the protective surface scales. The selected values were the same as used for austenitization and tempering of bare EUROFER. First ECA coated samples were added to the screwed test stack. Fig. 2 shows a bare and ECA coated sample (20 µm deposited Al scale) after heat treatment.

The corrosion testing in the PICOLO loop was performed at a flow velocity of 0.22 m/s. The highest temperature in the loop was present along the tubular test section with ca. 550 °C. The coolest areas were the electromagnetic pump and magnetic trap devices with roughly 350 °C. A more detailed description with main data of PICOLO loop can be found in Ref. 7. The virgin test samples had a diameter of 8.0 mm and were fixed concentrically in the test section. The longest exposed sample was removed after nearly 12,000 h, whereas the smallest exposure time was ca. 500 h. Due to the distinct corrosion attack at 550 °C, a high amount of precipitates were present in the loop which caused a first plugging after about 3,000 h of operation. The blockage appeared in the magnetic trap section which is installed to collect precipitates and prevent the electromagnetic pump from damages. The replaced magnetic traps had in the following an average life time before plugging of around 3,000 to

4,000 h. After testing, the samples were analyzed by standard metallographic techniques and by applying SEM and EDX methods.

Corrosion attack

The corrosion testing of RAFM steels performed at 480 °C in PICOLO loop in earlier test campaigns showed that dissolution of e.g. Fe, Cr out of the steel matrix is the acting corrosion mechanism which leads to a corrosion rate at 480 °C of roughly 90 µm/year at 0.22 m/s. The evaluation of the new tests performed at 550 °C delivered the same corrosion mechanisms and showed also a homogeneous attack of the surfaces at longer exposure times as can be seen in the micrograph depicted in Fig. 3. In contrast to 480 °C testing the new corrosion testing performed under TW4 and TW6-TTMS-003 showed rather small incubation periods below 500 h. The first sample removed in this campaign after 500 exhibited only some small not attack surface fractions of about 5%.

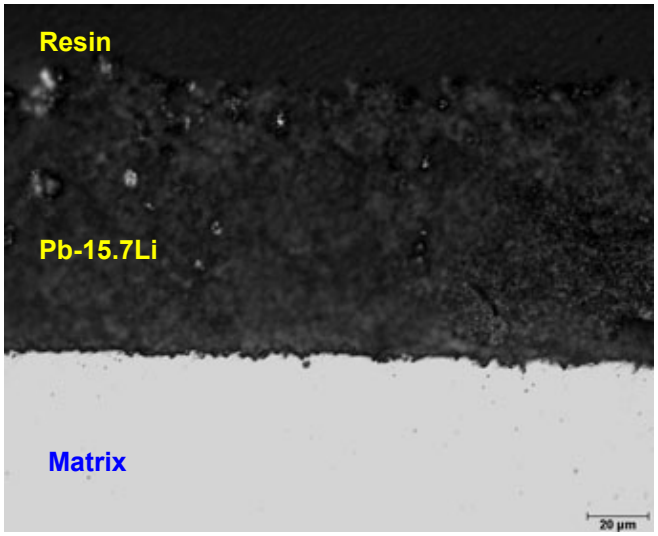

Fig. 3: Micrograph of EUROFER sample exposed to Pb-15.7Li for 10.000 h with adherent PbLi scale after removal from test section.

The corrosion rate = material loss of each sample was determined by measuring the diameters of each sample before and after exposure to the flowing Pb-17Li. The half difference of these diameters stands for the corrosion rate. Diameter measurements of fresh samples were done mechanically. Some specially prepared cuts of such samples were used as reference standards for calibration of the optical measurement process which is applied for determination of the diameter from the metallurgical cuts of Pb-17Li exposed samples. The cuts of all Pb-17Li exposed samples showed a symmetrical spherical attack within the resolution limits of about 5 µm of the used measurement process.

Extrapolations done by samples removed after short times (500 to 1,500 h) deliver rather high corrosion values of about 700 µm/year. This high rate seems to be an overestimation of the yearly loss e.g. due to high uncertainties in diameter determination and extrapolation from short exposure times to long operation times. For longer exposure times (2,500 to 12,000 h) smaller rates were evaluated.

Due to diameter changes by corrosion in the test section the flow velocity of v(t=0) = 0.22 m/s was reduced to nearby 0.18 m/s after about 12,000 h roughly 80% of the originally selected velocity. Thus measured corrosion values especially for long term exposure are too small and show a too optimistic behaviour if they are not normalized. Considering the reduced flow velocity during testing linear interpolation leads to a corrosion rate of about 400 µm/year materials take off with more emphasis to the values evaluated for the long term exposed samples. Both, measured and corrected values are presented in Fig. 4.

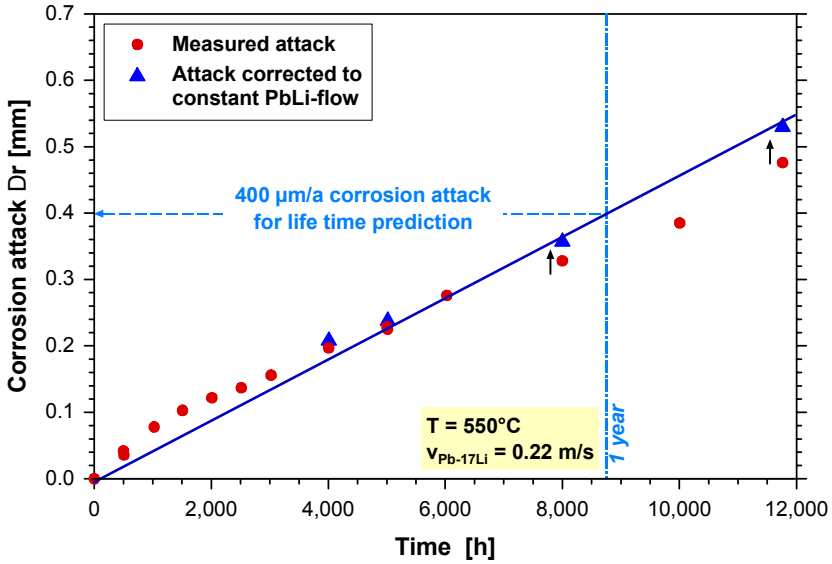

Fig. 4: Corrosion attack of EUROFER 97 at 550 °C test temperature vs. exposure time.

Development of modeling tools and validation of MATLIM code

In previous reports [7,8] the motivation and necessity for the development of modeling tools based on physical, chemical and thermo-hydraulic parameters was discussed for supporting PICOLO test evaluation and for understanding the ongoing processes in a complex system with interacting phenomena. In these reports the correlations for the mass transfer coefficient, the solubility and diffusivity are disused. In general three different types of physical properties and parameters are mainly present, which determine material behaviour in a liquid metal system. One group covers surely the properties of the wall materials. In the next second group material data have to be integrated like viscosity of the liquid metal, diffusivity and solubility of the solutes. The third group concerns the thermo-hydraulic data of the system like the flow velocity and the hydraulic diameter but also the temperature distribution along the system. Fig. 5 shows for PICOLO loop calculated dissolution rates in the test section in dependence of the flow velocity. It has to be noted that in the actual test regime of 22 cm/s fully turbulent conditions are present while below ca. 3 cm/s laminar flow dominates. This curve indicates the clear dependency of corrosion attack on flow velocity at constant temperature but illustrates also that materials take off never disappears.

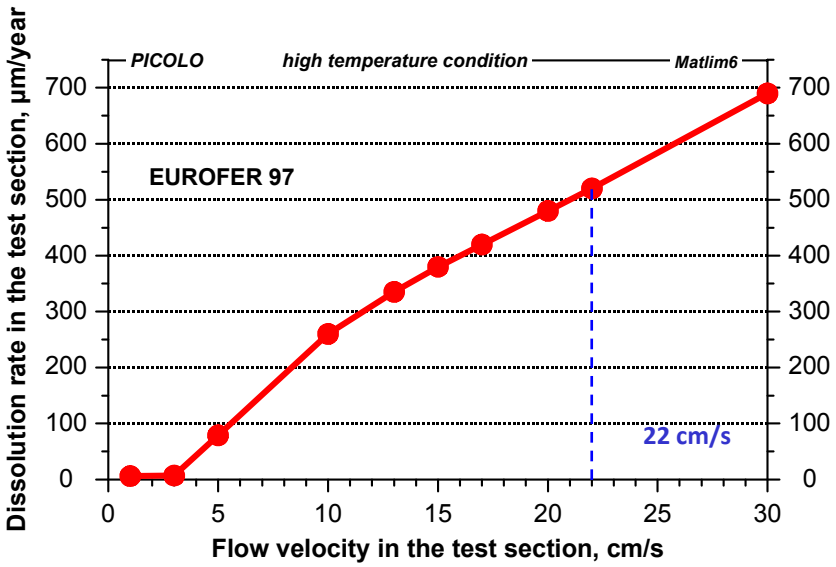

Fig. 5: Dependency of corrosion attack on flow velocity in PICOLO test section.

Fig. 6 shows a comparison of corrosion modeling by MATLIM vs. measured data without any correction for reduced flow velocity in the test section. Due to enlarging the gap between test section wall and concentrically mounted test sample by corrosion attack the flow velocity declined from v(t=0) = 22 cm/s to about 18 cm/s at test duration 12,000 h as illustrated by curve corresponding to the legend of axe on right side. This change in flow velocity generates no linear curve shape of calculated and measured corrosion values vs. time (legend on left side). The calculated removal of material fits well the measured attack and implies that material data were selected in good mode.

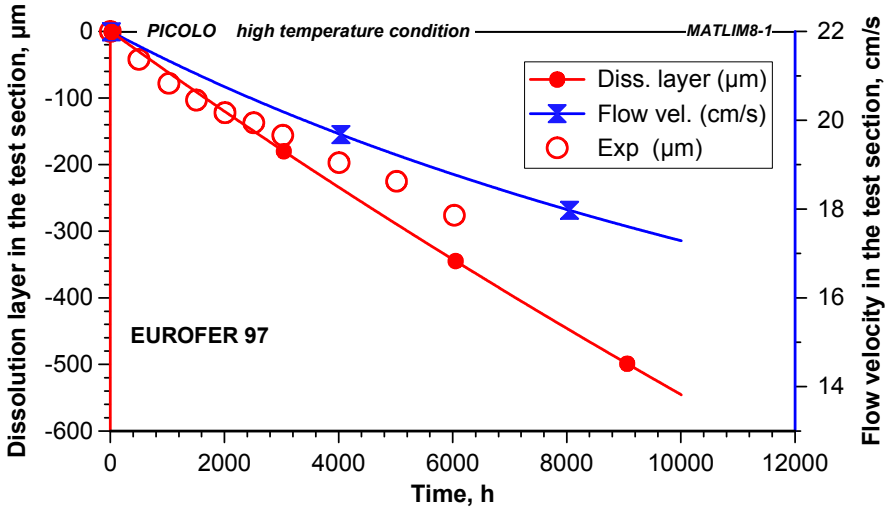

Fig. 6: Comparison of calculated and measured dissolution layers in PICOLO testing.

Coatings

The high corrosion rate at 550 °C led to dramatically increased corrosion attack and to an enormous amount of corrosion products which may be not sustainable in an ITER TBM system. Based on this feature, corrosion resistant barriers are in the focus of development, which also simultaneously act as T-permeation barriers. In previous period 2007 the work on development of an industrially relevant new Al coating process was reported. This process named **ECA** for **E**lectro-**C**hemical-**Al** deposition works with an organic based electrolyte. The Al deposition on the steel (EUROFER) is controllable by the process parameters. The main impact has coating time and current density on scale thickness. Due to the very homogeneous coating behaviour thin scales in the range 5 to 20 µm can be deposited which change only marginally the low activation behaviour of EUROFER. The performed metallurgical investigations showed that by adopted heat treatment the desired and from HDA [6] (Hot Dip Aluminisation) known protective surface scales can be formed. However, the qualification in corrosion testing – execution foreseen by an external partner under EDFA contract – is still delayed. Thus own corrosion testing in PICOLO loop was started in this report period. Cylindrically shaped test samples were exposed to Pb-15.7Li at flow velocity of 22 cm/s together with bare EUROFER. The first Al coated sample was removed after 1500 h exposure time. The metallurgical testing showed no evidence for corrosion attack. No reduction of diameter could be detected. Fig. 7 depicts the micrograph of this sample with intact surface scales. Surely, long term testing is still under execution to provide reliable data on the corrosion resistance of the generated Al-based scales by ECA and to improve process parameters with respect to TBM typical geometries.

The development of ECA and its successful application in EUROFER coating is a famous result towards industrially relevant barrier formation on Al base. ECA showed the potential to deposit thin and homogeneous Al scales on complex geometries. The electro-chemical behavior of the organic solvent restrict the deposition to Al or elements with smaller electro negativities e.g. Cu. Other elements which may also act as barrier material e.g. W can not be deposited from organic electrolytes. Thus investigations were started on a novel electrochemically based process named ECX working with novel electrolytes of type ionic liquids to increase the electrochemical potential towards higher values. EMIM-Cl was selected as ionic liquid for the first basic electrochemical development of suitable salt – electrolyte mixtures. For Al deposition by ECX systematical tests with varied salt concentration of AlCl in EMIM-Cl were electrochemically analyzed in voltametric studies concerning homogeneous scale formation. Fig. 8 depicts a homogeneous Al scale deposited on EUROFER from an electrolyte with a weight fraction of roughly 1 to 1 in Al salt vs. ionic liquid. ECX has also the feature of controllable scale deposition by process parameters like ECA. However, in contrast to ECA the improved ECX process can handle more reactive metals or elements with more unique properties. The path in development deals towards refractory elements like W, Ta to form corrosion resistant surface coatings for TBM.

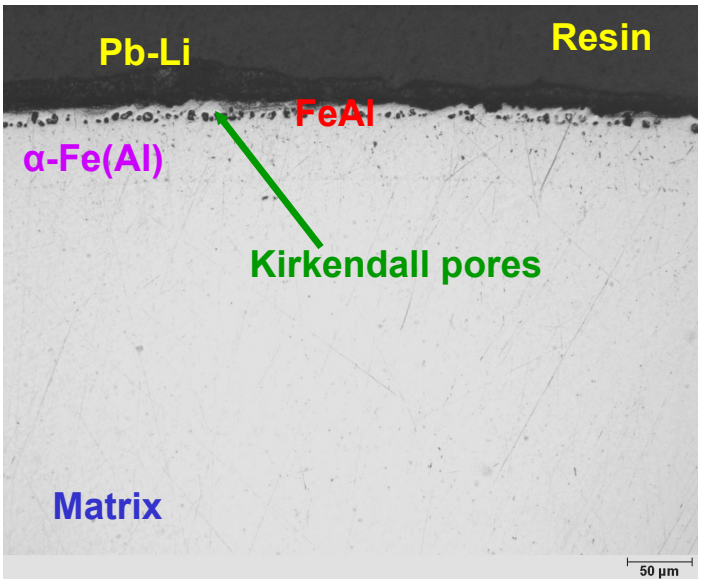

Fig. 7: Micrograph of ECA coated EUROFER exposed to Pb-15.7Li in PICOLO loop.

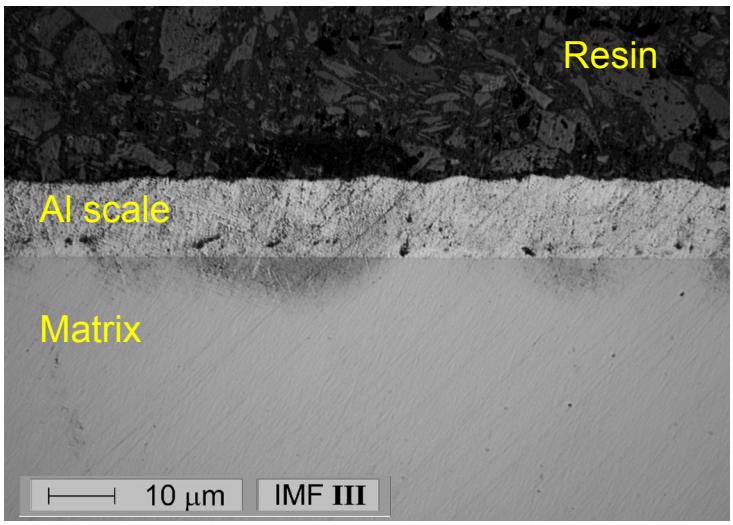

Fig. 8: ECX deposited Al scale on EUROFER.

Conclusions

The ECA process – a new electrochemically based process to fabricate corrosion and T-permeation barriers from organic solvents - was successfully developed and thin Al coatings were deposited. The performed metallurgical investigations showed that the protective surface scale sequence known from HAD process can be generated by correct heat treatment.

In contrast to HDA process ECA is highly industrially relevant and can be applied for coating of complex geometries. The performed first screening of compatibility with Pb-15.7Li showed promising results without visible attack in PICOLO testing at flow velocity of 22 cm/s. The initiated corrosion testing program will be extended to longer exposure times of at least 5000 h and in the future testing will be also performed at TBM relevant smaller flow velocities. Meanwhile, the ECA process was further developed towards application of novel ionic liquids instead of organic electrolytes. First homogenous Al scales with controllable scale thickness and high homogeneity could be deposited. The next steps for this ECX called process will be in the field of metallurgical characterization before entering into compatibility testing. An additional medium term goal in ECX development is the deposition of barriers from refractory metals (e.g. W) and multilayer coatings.

For the first time corrosion testing of EUROFER 97 was successfully performed at 550 °C conditions at a flow rate of 0.22 m/s and exposure times up to about 12,000 h and by combination of experimental and modeling work. A significant progress was realized especially in the change over from only mechanism-based tests to considering the whole loop behavior under corrosion, transport and precipitation view.

Both activities, corrosion testing and modeling / code development, reveal that a dramatically increase in corrosion rates takes place at a small increase of operation temperature from 480 to 550 °C by a factor of 5. The calculations performed by MATLIM code show for the analyzed scenarios 480 and 550 °C good agreement with the measured corrosion behaviour. MATLIM predicts also the high risk of precipitate formation at cooler loop sections leading to system blockages. Surely, the comparison of modeling and experiments indicated that additional system data have to be integrated into the modularly structured code and that experimental data e.g. on Fe content of Pb-15.7Li vs. loop operation time have to be provided to increase the accuracy of corrosion attack predictions. The next absolutely necessary step is the validation of MATLIM code at smaller flow velocities. In the meantime experimental testing was started at flow velocities of ca. 10 cm/s as intermediate step towards TBM characteristic Pb-15.7Li velocities near 1 cm/s. Both calculated and measured values will be required to understand and validate the processes going on in future TBM tests in ITER. These tests will also integrate ECA / ECX coated EUROFER components.

Staff:

M. Heck
N. Holstein
J. Konys
W. Krauss
J. Lorenz
J. Novotny
A. Skrypnik
O. Wedemeyer

Literature:

[1] H.U. Borgstedt, G. Drechsler, G. Frees, Z. Peric, J. Nucl. Mater. 155-157 (1988), 728 – 731.

[2] H. Glasbrenner, J. Konys, H. D. Röhrig, K. Stein-Fechner, Z. Voss; Corrosion of ferritic-martensitic steels in the eutectic Pb-17Li, J. Nucl. Mater. 283-287, (2000), 1332.

[3] G. Benamati, C. Fazio, I. Ricapito; Mechanical and corrosion behavior of EUROFER 97 steel exposed to Pb-17Li, J. Nucl. Mater. 307 - 311, (2002), 1391.

[4] J. Konys, W. Krauss, Z. Voss, O. Wedemeyer, Corrosion behavior of EUROFER steel in flowing eutectic Pb–17Li alloy, J. Nuc. Mater. Vol. 329-333, Part 2, (2004), 1379-1383.

[5] H. Glasbrenner, J. Konys, G. Reimann, K. Stein, O. Wedemeyer, The formation of aluminide coatings on MANET stainless steel as tritium permeation barrier by using a new test facility, Proc. 19th SOFT, Lisbon, Portugal, (1996), pp. 1423–1426.

[6] J. Konys, W. Krauss, Z. Voss, O. Wedemeyer, Comparison of corrosion behavior of bare and hot-dip coated EUROFER steel in flowing Pb–17Li, J. Nucl. Mat. 367–370 (2007) 1144–1149

[7] W. Krauss, J. Konys, H. Steiner, J. Novotny, Z. Voss, O. Wedemeyer, Development of modeling tools to describe the corrosion behavior of uncoated EUROFER in flowing Pb-17Li and their validation by performing of corrosion tests at T up to 550°C, FZKA report 7295, March 2007

[8] H. Steiner, W. Krauss, J. Konys; Calculation of dissolution/desposition rates in flowing eutectic Pb-17Li with the MATLIM code, J. Nucl. Mat., In Press, December 2008

[9] J. Konys, W. Krauss, H. Steiner; Validation of Modeling Tools to Describe the Corrosion/Precipitation Behavior of EUROFER Steel in Flowing Pb-17Li, TOFE-18, San Fransisco, CA, 28.9.-2.10.2008

[10] J. Konys, W. Krauss, J. Novotny, H. Steiner, Z. Voss, O. Wedemeyer; Compatibility behavior of EUROFER steel in flowing Pb–17Li; J. Nucl. Mat., In Press, December 2008

Materials Development
Advanced Materials

TTMA-002
Divertor and Plasma Facing Materials

TW6-TTMA-002 D 6
Fundamental Studies on Mechanical Properties of W-alloys

Introduction

Present helium cooled DEMO divertor designs make use of the high temperature strength and good heat conductivity of refractory materials. In such outlines, structural parts of W-1%La_2O_3 (WL10), for example, are used for operation temperatures between 600 and 1300 °C. Here the lower temperature is limited due to the transition to a steel part while the upper temperature limit is defined by the onset of recrystallization and/or loss of strength, respectively. Other important criterions for structural divertor applications are creep strength (55 MPa for time to rupture of minimum 20,000 hours at 1200 °C) and thermal conductivity (100 W/mK at 1200 °C. As can be seen in the available data plotted in Fig. 1 and 2, creep strength as well as thermal conductivity is already satisfied by certain WL10 materials.

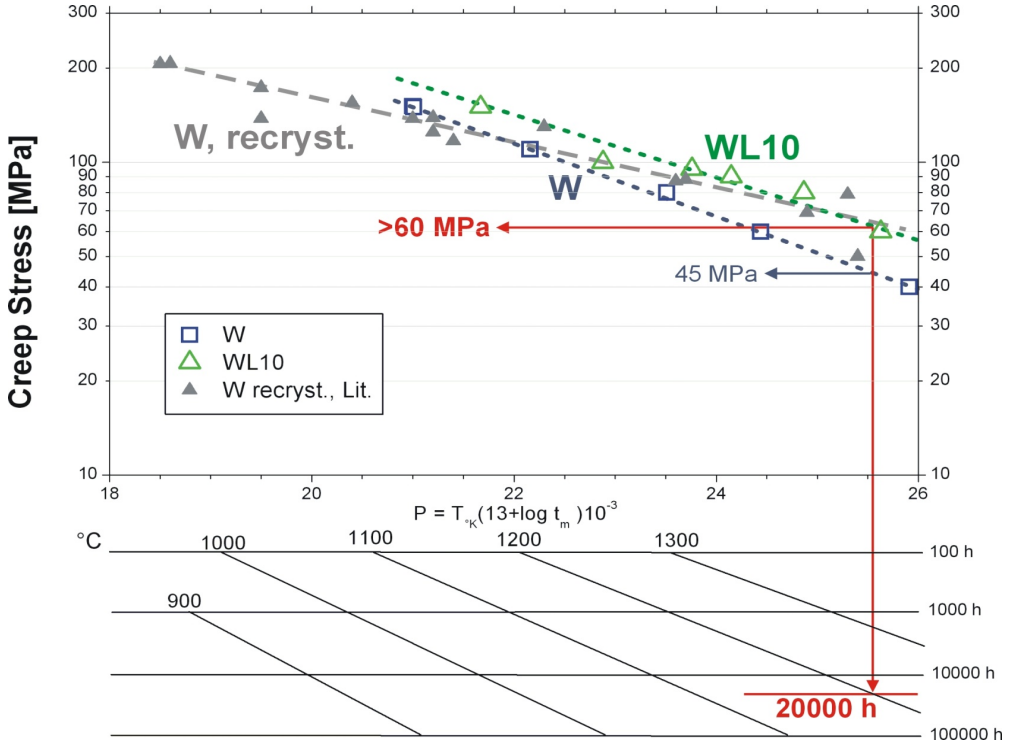

Fig. 1: Creep strength prediction (Larson-Miller plot for times-to-rupture).

The design is based on an operation time of about 20,000 hours. Hence, this would be the minimum recrystallization time of a structural material. Figure 3 shows results for a 10 mm rod of pure tungsten. It can be clearly seen that this material recrystallizes easily at 1300 °C. Within other studies at the same temperature with WL10, recrystallization was not observed even after nearly 2000 hours. Anyway, the available data is not sufficient and, therefore, recrystallization is still an open question.

The most critical issue of tungsten based alloys in connection with structural applications, however, is the required ductile-to-brittle transition temperature (DBTT) of less than 600 °C after irradiation (measured by EU standard mini-Charpy tests). A comprising study has been performed to characterize different tungsten materials with respect to their applicability for structural divertor parts.

Fabrication and testing Charpy specimens has been performed according to the EU standards DIN EN ISO 148-1 and 14556:2006-10. That is, small size specimens (27 mm x 3 mm x 4 mm, 1mm notch depth, 22 mm span) have been used for instrumented Charpy tests. The specimens were fabricated by electrical discharge machining (EDM). For investigating the influence of machining, the notches of some specimens were fabricated by a diamond wire saw. The notch orientation was R-C in the case of rod materials and T-S as well as L-S in the case of the plates. Notches were all fabricated perpendicular to the rolling direction. This is important and has to be kept in mind for the evaluation of the Charpy results, since this orientation is the most favourable for energy and DBTT values.

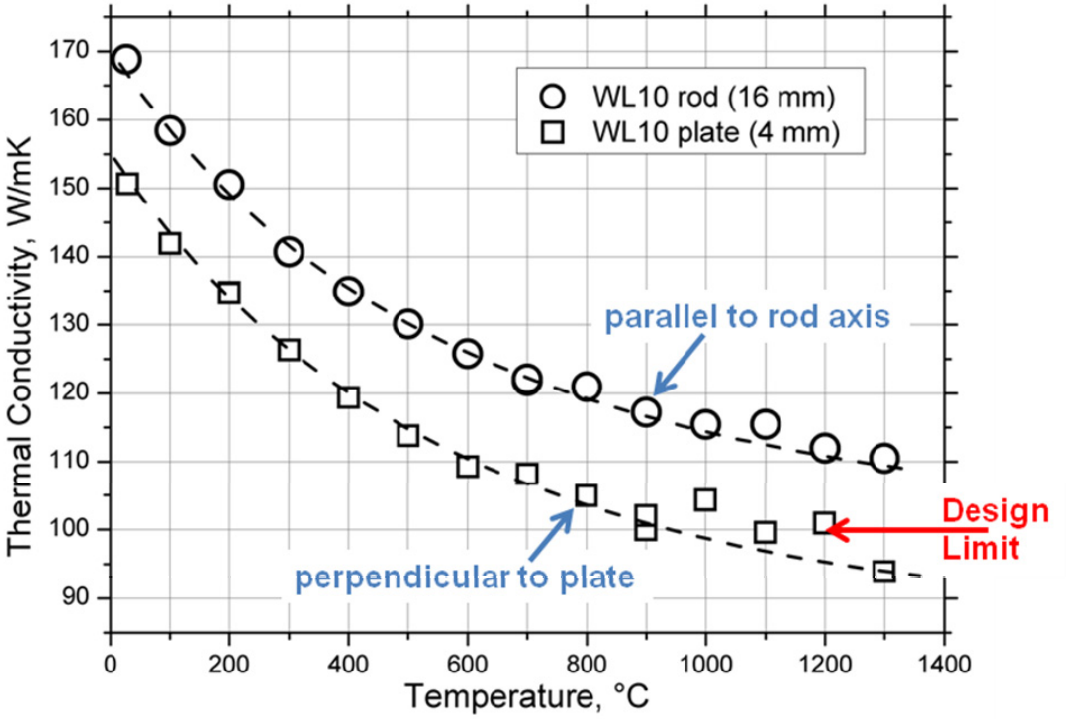

Fig. 2: Thermal conductivity determined by laser flash analysis.

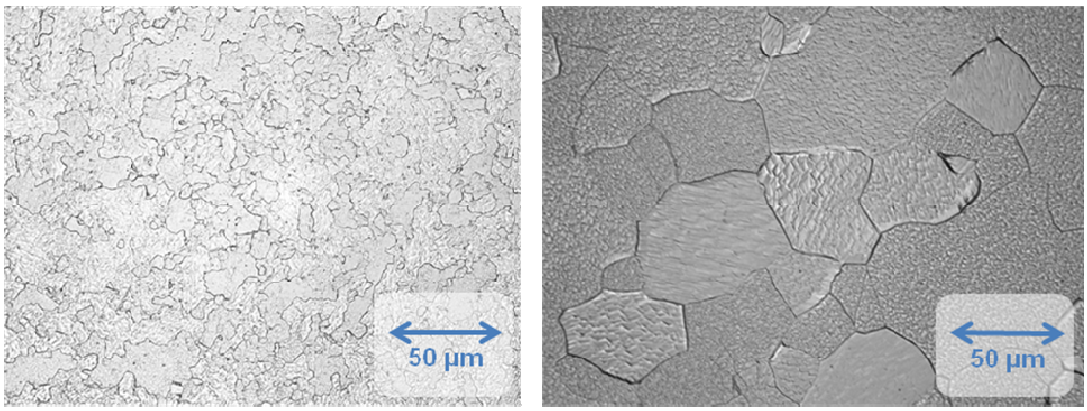

Fig. 3: Microstructure of a 10 mm W rod before (left image) and after aging at 1300 °C for 343 hours (right diagram).

Materials, Study and Results

Five different tungsten rod materials were provided by PLANSEE: pure W, WL10 in two different levels of deformation, potassium (0.005%) doped tungsten (WVM), and WL10 with 1% Re. Plates of pure W, WL10, and WVM were also used for the investigation. Finally, molybdenum-Ti-Zr (TZM) rod and plate material was used as reference. The microstructures are illustrated in Fig. 4.

By comparing the Charpy test results of the tungsten materials with those of TZM (see Fig. 5) it is obvious that only TZM shows the usual embrittlement behaviour which is typical for most body-centred cubic structured metals. That is, (1) there is a clear transition from brittle (at lower temperatures) to ductile (at higher temperatures) fracture, and (2) there is an extended regime of ductile fracture (the so-called upper shelf). In the case of TZM DBTT lies between 200 °C (fully brittle) and 400 °C (fully ductile fracture) and the upper shelf energy varies around 9 and 10 J.

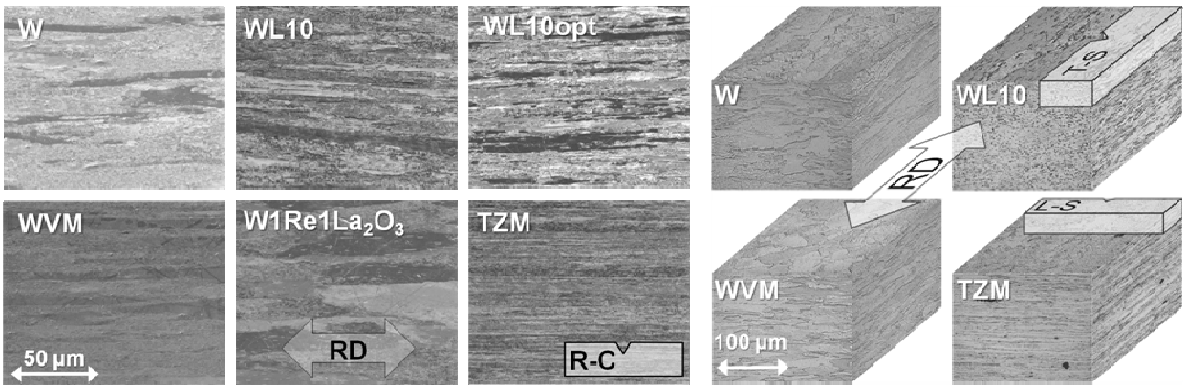

Fig. 4: Micro-structure of the rod materials and of the plate materials. Rolling direction (RD) and specimen orientations are indicated.

The tungsten materials don't show this single transition. Only specimens of pure tungsten and WVM show an upper shelf starting at 1000 °C and 900 °C. All other rod materials do not fracture fully ductile within the whole test temperature range. However, all tested materials tend to brittle fracture at temperatures below 600 °C. But above that temperature, the specimens show fractures which (partly) propagate along the rod axis, that is, parallel to the specimen's long side and perpendicular to the notch. This is called delamination or cleavage.

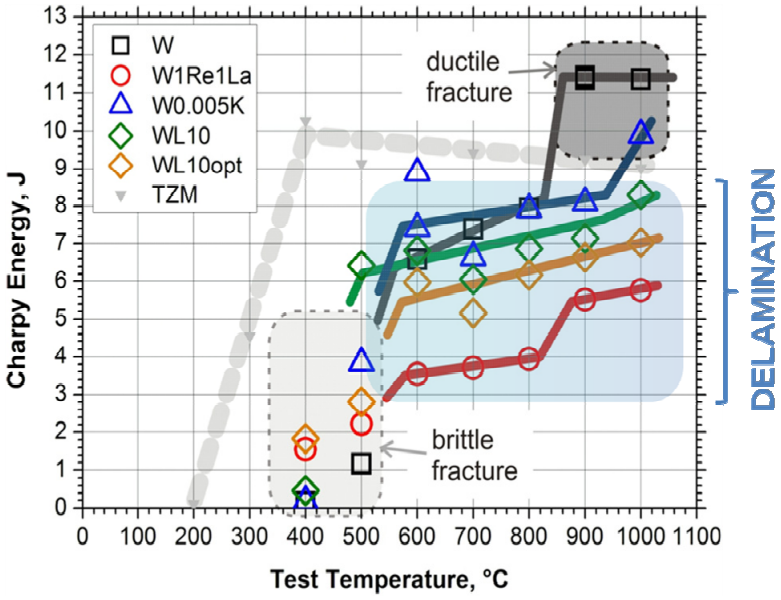

Fig. 5: Charpy test results of the rod materials.

In summary, there are three types of fractures (brittle, delamination, and ductile) which are obviously linked by a brittle-to-delamination transition and a delamination-to-ductile transition. The brittle-to-delamination transition temperature (defined in analogy to DBTT) varies around 500±50 °C for all tungsten materials while the delamination-to-ductile transition temperature is about 900 °C for tungsten and about 1000 °C for WVM. The other materials (WL10, WL10opt, and W1Re1La$_2$O$_3$) show slightly increasing energies with temperature but they do not show a further transition.

The results presented in Fig. 6 confirm that at 800 °C there is no difference (at a certain point in the delamination regime) between an un-notched Charpy specimen and a sample with a notch fabricated by EDM. However, the un-notched tungsten specimens show the usual fracture behaviour with a sharp DBTT at 450 °C. Figure 4 demonstrates also the influence of

different notch fabrication methods: Compared to EDM, sawed notches lead to an improvement of the delamination-to-ductile transition by about 100 °C. Also, delamination takes place at higher energies by about 1 J. This coincides also with the result of the un-notched specimen at 700 °C. The brittle-to-delamination transition, however, is not influenced by the fabrication process.

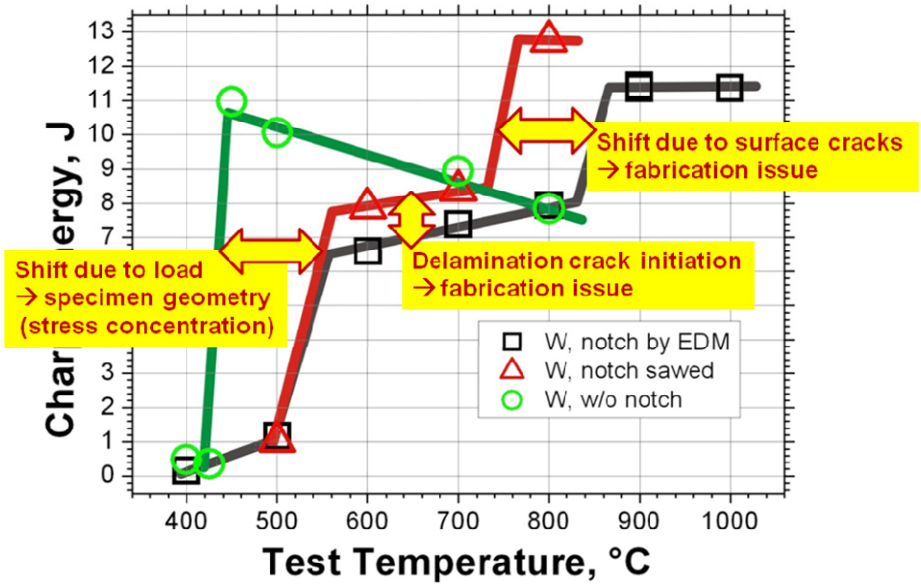

Fig. 6: Comparative study on the notch fabrication effect on the Charpy properties.

Conclusions

The known benefits of lanthanum-oxide particles in tungsten are (1) an improvement of the processability, (2) the suppression of recrystallization, and (3) a slight creep strengthening. On the other hand, as is clearly confirmed by the present study, the already insufficient fracture characteristic of pure tungsten is further deteriorated by the addition of lanthanum oxide (also by potassium, but to a lesser degree).

The study reveals furthermore that all considered tungsten rod materials fracture brittle below about 600 °C. Earlier studies on commercial weld electrode materials revealed brittle transition temperatures of more than 900 °C. Compared to that, the presently tested tungsten rod materials from PLANSEE confirm an improvement with respect to ductile fracture. Anyway, it could also be demonstrated that (rolled) plate materials in general perform worse than (rolled) rod materials. This can be certainly attributed to the different microstructures which develop during material production.

Finally, the following conclusions may be drawn from the various results with the investigated materials:

- Un-notched pure tungsten rod specimens have a common DBTT of 450 °C, fracture fully ductile at 450 °C, and show no delamination.
- Tungsten rod specimens with sawed notches fracture fully ductile at 800 °C (transition temperature from delamination-to-ductile fracture of 750 °C).
- Tungsten rod specimens with electro discharge machined notches fracture fully ductile at 900 °C (transition temperature from delamination-to-ductile fracture of 850 °C).
- WVM rod specimens are fully ductile at 1000 °C (delamination-to-ductile transition at 950 °C).

- WL10, WL10opt, W1Re1La_2O_3 rod materials do not fracture fully ductile up to 1000 °C.
- All tungsten rod materials show brittle fractures below 600 °C.
- All plate materials (including TZM) exhibit sever delamination. The brittle-to-delamination transition is 150 °C for TZM and 450 °C for pure tungsten plates.

The impact on further material development and fabrication may be summarized as follows:

- The micro-structure has a significant influence on the transition to ductile fracture (rod micro-structure is more favourable than that of rolled plates).
- Oxide particles as well as potassium doping obviously promote delamination (probably by weakening the grain boundary cohesion). On the other hand, they also stabilize the grain boundaries and therefore suppress re-crystallization.
- Optimum fracture behaviour can possibly reached only by avoiding machining and by aligning the grains along the contour of the according part.

Staff:

S. Baumgärtner
B. Dafferner
S. Heger
U. Jäntsch
M. Klimiankou
A. Möslang
P. Lukits
M. Rieth
M. Rohde
R. Ziegler
H. Zimmermann

Literature:

[1] M. Rieth, A. Hoffmann, B. Dafferner, S. Heger, Impact Bending Tests on Selected Tungsten Materials, 1st International Conference on New Materials for Extreme Environments, June 2-4, 2008, San Sebastián, Spain.

[2] M. Rieth, A. Hoffmann, B. Dafferner, S. Heger, E. Materna-Morris, H. Sandim, H. Zimmermann, Mechanical properties of different refractory materials for nuclear fusion applications, Materials Science and Engineering, Sept. 1-4, Nürnberg, Germany.

[3] M. Rieth, A. Hoffmann, Fracture behavior of tungsten materials depending on microstructure and surface fabrication, 18th Topical Meeting on the Technology of Fusion Energy (TOFE-18), San Francisco, Calif., September 28 - October 2, 2008.

[4] M. Rieth, A. Hoffmann, M. Rohde, Tungsten as Structural Material for Power Plant High Heat Flux Components, Int. High Heat Flux Components Workshop, San Diego, Calif., December 10 - 12, 2008.

[5] M. Rieth, A. Hoffmann, B. Dafferner, S. Heger, U. Jäntsch, M. Klimenkov, P. Lukits, M. Rohde, H. Zimmermann, TUNGSTEN as Structural DEMO Divertor Material, Jahrestagung Kerntechnik 2009, 12.-14. Mai, Dresden, Germany, submitted.

[6] M. Rieth, A. Hoffmann, Influence of microstructure and surface fabrication on impact bending properties of tungsten materials, 17th PLANSEE SEMINAR, 25-29 May 2009, Reutte, Austria, submitted.

TW5-TTMA-002 D 6
Mechanical Testing of Irradiated W Tungsten Samples

High temperature alloys (such as tungsten) are assumed to be primary materials candidates for structural application in the divertor. However, these materials suffer from irradiation-inducted embrittlement at “low” temperatures. The DBTT strongly depends on the irradiation dose and probably depends on the material processing. Tungsten furthermore is also considered as a plasma facing material, i.e. as a first wall coating for Demo-related blankets and as armour material for gas-cooled divertors. Appropriate techniques for mechanical characterisation are to be investigated.

Specimens of WL10 (Tungsten and 1% of La_2O_3) are included in an irradiation experiment called Furioso in the OSIRIS reactor at Saclay. KLST-type bend bar specimens and mini tensile specimens (flat bar, T19-type) are to be irradiated at temperatures of 600 and 1000°C up to 5 dpa - equivalent in steel. Tensile and KLST-specimens are foreseen for PIE in the Fusion Materials Laboratory (FML) of FZK after end of irradiation. 56 KLST- and a to be defined number of tensile specimens will be transported to the FML. Specimens are 3 x 4 x 27 mm³ Charpy-specimens [KLST] and 5 x 1 x 19 mm³ flat bar mini tensile specimens [T19] with a centre area of 1.5 x 1.0 mm², cf. Fig. 1.

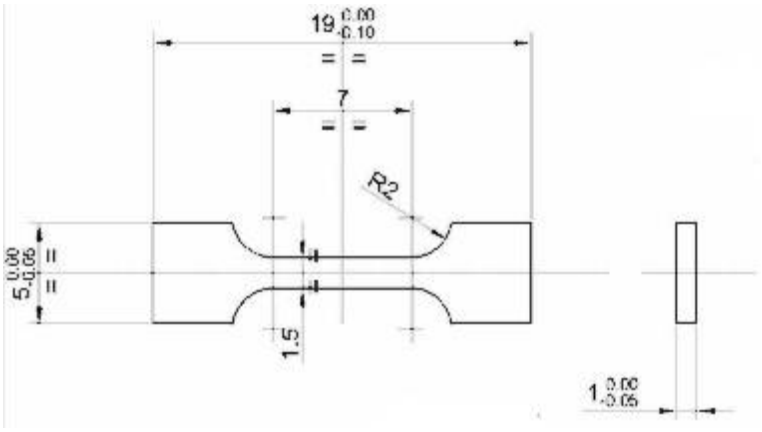

Fig. 1: Tensile specimen (T 19-type), drawing by CEA.

The Furioso irradiation campaign originally was planned to take place in 2005 (TW5-TTMA-002 Del. 3). Actually, the irradiation is expected to be finished in December 2008. After cooling down, sorting and packaging, the specimens can be transported to the FML in spring 2009.

The specimens will be tested at different elevated temperatures to define the ductile-to-brittle-transition and the irradiation effect on it. Fractographic analysis of the tested specimens will be done by light microscopy and by SEM, including three-dimensional stereographic analysis.

As soon as specimens are available, unirradiated reference tests will be performed. The PIE will be finished 12 months after availability of specimens.

The Charpy specimens will be tested with an instrumented pendulum to define the transition region, the transition temperature, the upper- and lower shelf energy for every irradiation parameter. For every specimen, the force-versus-deflection-curve is recorded, impact energy and dynamic yield stress are derived. The pendulum’s energy and impact speed can be varied if necessary.

Tensile tests will be performed accompanying to the impact tests as well as at irradiation temperature to give a full dataset of tensile results. A universal testing machine with vacuum-furnace (up to 1200°C) is used for force- and strain-controlled tensile tests.

In addition, non-destructive testing by indentation can be done on both specimen types before or after they are tested in the pendulum or in the tensile machine. This method was presented in TW4-TTMA-002 Del. 3 (report 2005). It allows the determination of the complete

tensile and cyclic material behaviour from multi-stage indentation tests. Meanwhile, this method had been successfully applied to different tungsten-alloys and to irradiated structure materials, it offers useful additional information about the material's characteristics at room temperature.

Future activities

Transport and PIE of specimens:

- Transport from OSIRIS reactor (France) to FML
- Decontamination of the specimens
- Sorting of specimens
- Adaptation of testing machines
- Mechanical testing and microscopy to determine irradiation effects on mechanical properties and microstructure.

Staff:

S. Lautensack
H.-C. Schneider
I. Sacksteder

PM Production and PIM of Tungsten and Tungsten Alloys

Objectives of the task

A He-cooled divertor design for future fusion power plants has been developed at FZK [1]. For application as functional and structural materials, tungsten and tungsten alloys, respectively, are presently considered. The design criteria for a He-cooled divertor structure in particular are low ductile-brittle transition temperature (DBTT), high strength, and adequate ductility. The advantages of tungsten lie in its high melting point, high thermal conductivity, low thermal expansion, and low activation. But on the other hand its disadvantages are high hardness and brittleness. This mismatch can be potentially minimized by a new kind of material developed by means of a new Powder Injection Moulding (PIM) process of tungsten and/or tungsten alloys which has been launched at FZK. Commonly known commercial PIM has a large potential for mass production of near-net-shape parts with high precision. In addition, material properties gained by the new W-PIM process like ductility and tensile strength are suggestible.

State of the art PIM R&D

At FZK first successful experiences with W-PIM were made in the last few years. In detail, a tungsten feedstock with 55 vol.-% powder was developed. By the following process steps including injection moulding, sintering, and hot isostatic pressing (HIP) W components were manufactured [2] reaching a final density of up to approximately 98 %TD.

Currently, questions arose upon the need for new powders and also a new sintering and HIP route. This leads to the new R&D work programme which is divided into two different routes: a) Powder Metallurgy (PM) to understand the fundamental material properties and b) application of the current knowledge gained from PM on the PIM process for manufacturing divertor components. The PIM process route comprises powder preparation, feedstock (powder and binder) formulation, injection moulding process, debinding, sintering, and HIP. The key steps in PM such as powder mixing, pressing, sintering and hot isostatic pressing have been studied; the first results shall be discussed below.

Results

Powder properties

More than 10 different tungsten powders are analysed concerning particle size distribution, BET-surface, microstructure and density. From these two tungsten powders show the best properties and are promising for the next working steps. The results are summarized in Table 1.

Table1: Powder particle size distribution and BET-surfaces of applied tungsten powders

Particle size [µm FSSS]	D10 [µm]	D50 [µm]	D90 [µm]	BET [m²/g]
0.7	0.14	0.47	1.25	1.27
1.70	0.55	1.80	4.91	0.43

Fig. 1 shows particle distribution of the two applied tungsten powders with a grain size of 0.7 µm (HC70) and 1.70 µm (HC170), respectively. In Fig. 2 SEM images are presented.

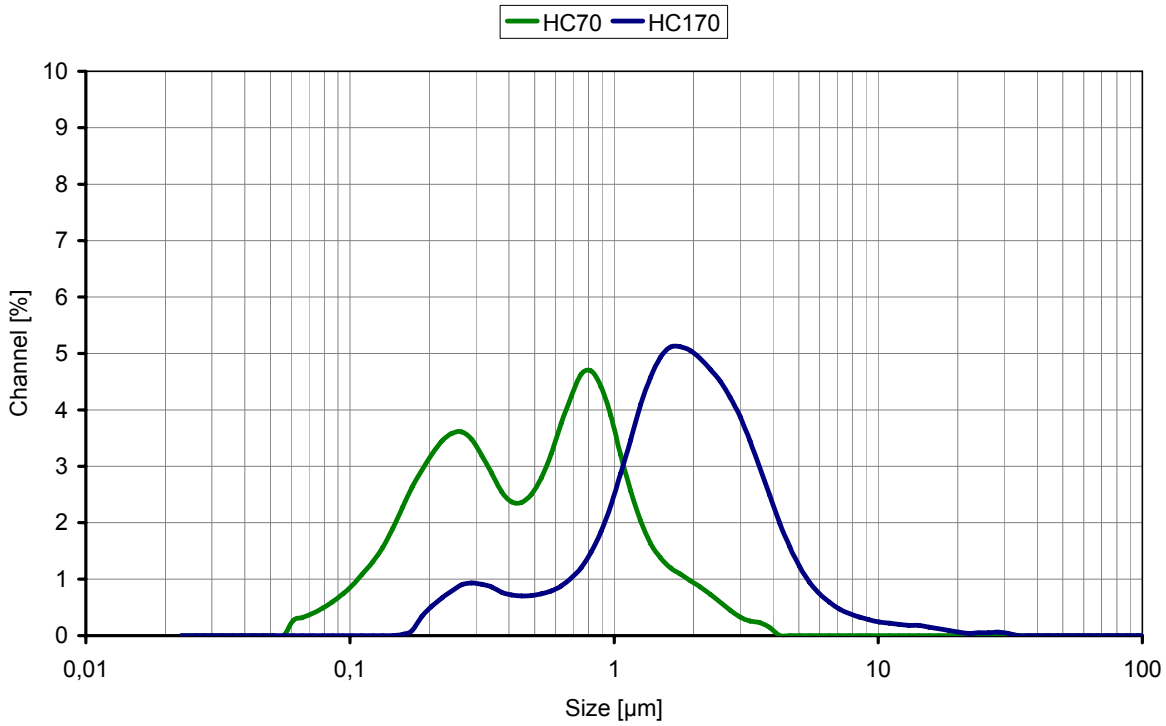

Fig. 1: powder particle distribution of applied tungsten powders.

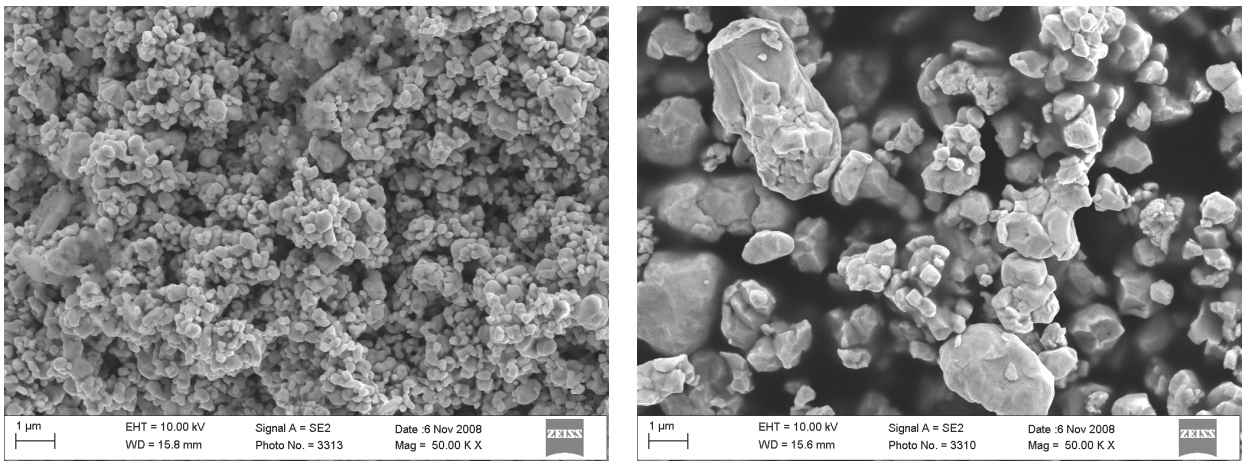

Fig. 2: SEM images of applied tungsten powders, left: HC70, right HC170.

Powder Metallurgy

Three different tungsten powder samples are compounded: 1) 100wt.-% HC70, 2) 100wt.-% HC170, 3) 30wt.-% HC70 + 70wt.-% HC170. The samples are mixed and pressed. By applying a suitable pre-sintering cycle (at T = 1600°C, t = 2h under N_2:H_2 = 95:5) and HIP cycle (at T = 1500°C, t = 3h under a pressure of p > 2500bar in Argon atmosphere) the samples are compacted.

The microstructure after (pre-) sintering and hot isostatic pressing (Fig. 3) shows for the two W powders of different grain size a grain size decrease and residual porosity after HIP (Fig. 3, right).

It was also observed that powder with a smaller grain size is advantageous with respect to higher sintering activity.

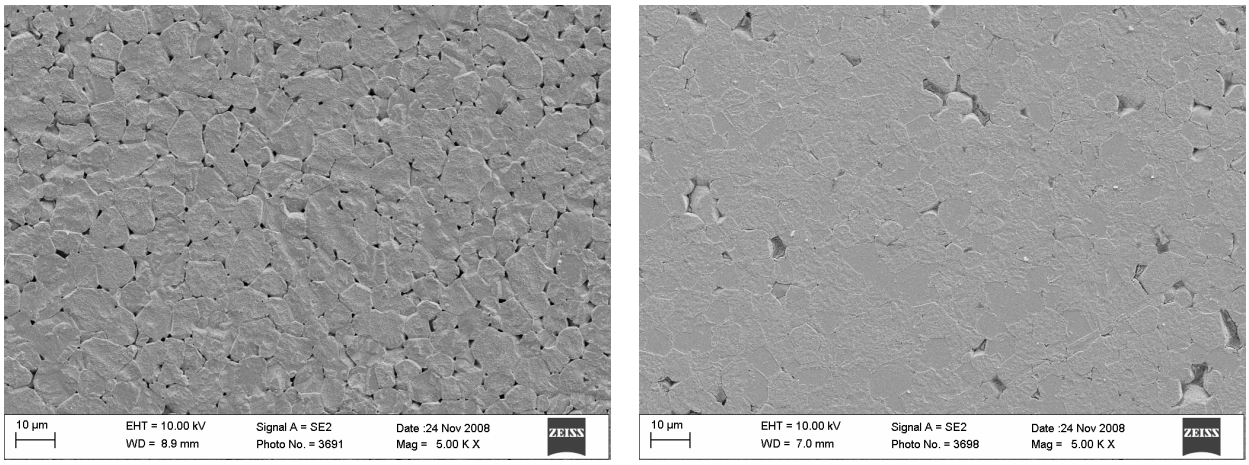

Fig. 3: Microstructure of pre-sintered + HIPed tungsten samples prepared by PM: left 100wt.-% HC70, right 30wt.-% HC70 + 70wt.-% HC170.

Powder Injection Moulding

The knowledge gained from the PM test runs is taken as a basis for the further PIM development route. Present work is focussing on feedstock development (different W-powder contents and powder-binder combinations are mixed and kneaded). First PIM and sintering trials have been performed successfully. Now, work is continuing on providing an optimal feedstock and on studying the properties of the new PIM products.

Conclusions and outlook

The first W-PM experiments for studying the material properties have been successfully carried out.

An injection-moulding tool for PIM manufacturing of fusion relevant components such as the hexagonal tile and the thimble will be designed.

The feedstock for tungsten and tungsten alloys will be developed and optimized. Further R&D on optimal thermal processing (sinter and sinter-HIP combination) as well as on the investigation of mechanical properties of new PIM parts will be performed with high priority.

Staff:

S. Antusch
P. Holzer
T. Müller
P. Norajitra
C. Odemer
M. Offermann
V. Piotter
K. Plewa
H.-J. Ritzhaupt-Kleissl
R. Vouriot

Literature:

[1] P. Norajitra, R. Giniyatulin, T. Ihli, G. Janeschitz, W. Krauss, R. Kruessmann, V. Kuznetsov, I. Mazul, V. Widak, I. Ovchinnikov, R. Ruprecht, B. Zeep, He-cooled divertor development for DEMO, Fusion Engineering and Design 82 (2007) 2740-2744.

[2] B. Zeep, P. Norajitra, V. Piotter, R. Ruprecht, J. Hausselt, Net shaping of tungsten components by micro powder injection moulding, Fusion Engineering and Design 82 (2007) 2660-2665.

TW6-TTMA-002 D 8
Production of Small Laboratory Scale Batches of Improved Materials for Characterization

Objectives of the Task

At FZK an enhanced powder injection moulding (PIM) process for refractory alloys is currently under development and can be used for fabrication of all geometries of divertor components. PIM of steels is well-known in industrial manufacturing as it exhibits large economic potential for production of tungsten divertor components in case of large scale series. The W-PIM approach directly yields tungsten products or components without any finishing work being required. For this a purpose a new moulding tool with all features necessary for producing divertor shape parts has to be developed and manufactured.

Nevertheless, this new technology still has to prove its suitability in terms of material properties like ductility and tensile strength: As already known, commercially available refractory alloys show a rather high DBTT and would never meet the current design criteria for a He-cooled divertor. Therefore, ductility is still the most critical property and has to be improved in pallel to the process development.

State of the Art when R+D Work Commenced

For future fusion power plants a high amount of complex shaped tungsten components have to be fabricated. For this purpose, powder injection moulding (PIM) as an established near net shaping technology has been adapted on tungsten. The process is favourably used for large-scale production and achieves high economic efficiency. The processing technology of PIM is based on a four-step sequence including mixing of a metal powder / binder feedstock, shaping by injection moulding, debindering, and sintering of the final product.

As part of the entire process development the goal of this particular project was to create a special process chain for fine-structured tungsten components to provide laboratory scale batches of samples for characterization.

To develop a suitable feedstock, the binder composition, solid load and powder particle properties have been varied and the resulting viscosities were compared. Due to the relatively high density of tungsten feedstocks (~11g/cm³) the green stability is especially an issue in powder injection moulding. Thus tensile test bars have been replicated and tested in the green state.

Further on injection moulded samples have been debindered and sintered. For final densification, a suitable HIP-process has been developed by which densities up to 98% were reached. Metallographic analysis concerning grain growth and density of sintered as well as sintered and HIPed tungsten samples have been produced. Whereas Charpy tests revealed a poor ductility only tensile strength tests of sintered specimen showed a reduced tensile strength but increased elongation at break compared to specimen made by less cost-effective methods.

Besides pure tungsten, a wide range of tungsten alloys are of industrial interest for e.g. thermal shielding, microelectronics, automotive and military applications. Accordingly feedstock development has been extended on the tungsten alloys W1La, W-Ni-Fe and WCu.

All trials described above were carried out with sample geometries typically used for macroscopic or microscopic PIM process experiments. Therefore, the results gained allow conclusions on the general material behaviour only but exhibit no definite inferences on specific properties of future Divertor-Components. For such a purpose and due to the large impact of sample geometry on the capabilities of PIM parts further progress can only be obtained by

investigating samples of Divertor-Components shape. Thus, design and construction of a novel injection moulding tool specially tailored for producing tungsten Divertor components presently stands in the foreground.

Results

Following the considerations explained above the development of MicroPIM with tungsten materials lasts on two main topics, i.e. the material progress as exemplified by new tungsten alloys and the process development with the goal of producing parts with near Divertor-Component designs.

Concerning the first topic main progress is documented as a contribution titled “PM production and PIM of tungsten and tungsten alloys” in this volume. Therefore, the focus of this report lies on the process enhancement including the development of a new tool to produce samples with a Divertor-Component shape.

Work started with a specification for the new tool comprising the following features as the most important ones:

- Suitability for high-filled W-feedstocks with severe abrasive behaviour,
- Changeable mould inserts, parting plates and ejection units to produce different kinds of Divertor-Components,
- Electrical heating up to 180°C to secure appropriate mold filling and cooling system using water as media,
- Possibility to apply variothermal process conduct,
- Possibility for venting of the cavity,
- Runner and gate system optimized for Divertor-Components
- Ejection system tailored to demold parts without critical distortions.

Up to now a few meetings have been held with skilled tool makers to discuss and find solutions so that the above mentioned demands can be met. Concept and design of the new tool is stepwise developed and supported by simulation calculations. As the detailed design is not completely finished yet and is still in an optimization phase a description of the innovative features of the new tool shall be reserved for later reports.

Tool construction will follow the design phase immediately so that moulding trials can begin as soon as possible.

Conclusions and Outlook

As explained above the most important currently running development step is to design and construct an injection moulding tool for replicating components with divertor relevant geometries such as e.g. the hexagonal tiles which are directly facing the plasma zone. The tool concept will allow an easy changing of the core cavities so that an adjustment to future part designs can be realized without major efforts.

Comprehensive simulation investigations have already been started and will continue to determine the most appropriate tool design incl. runner and gate system, demoulding procedure etc. for the aspired application.

After finishing construction and commissioning of the tool first moulding trials with – at that time – new developed W feedstocks will be carried out. For the debinding, sintering and densification procedures new parameter sets have to be developed based on the experiences gained within the previous investigations: Corresponding performance tests to determine the

material and geometrical properties of the molded parts will e.g. be carried out in an appropriate high heat flux test facility.

Staff:

S. Antusch
V. Piotter
K. Plewa
M. Rieth
H.-J. Ritzhaupt-Kleissl

Electrochemical Machining (ECM) of Tungsten and Tungsten Alloys

Introduction

The helium cooled divertor concept is projected to remove heat loads of up to 15 MW/m² in fusion power plants. This divertor design (Fig. 1) is based on a modular arrangement of cooling fingers [1,2], which have to be fabricated from heat-resistant material like tungsten alloys to fulfill the requirements. Due to the extreme physical and mechanical properties and the required structures shaping of W is a challenging task. At least in the range of micro-structural shaping all state-of-the-art methods are highly cost intensive, not adapted to line fabrication or introduce micro-structural defects into W-alloys.

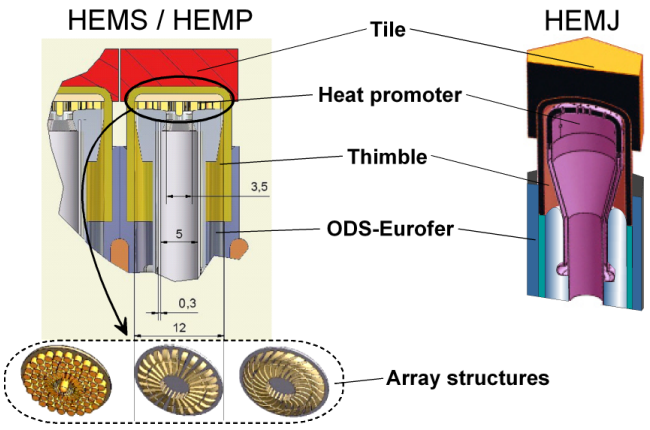

Fig. 1: Design variants HEMS / HEMP and HEMJ (Jet-design). The W arrays are integrated into the thimble made of WL10 (W+1%La2O3). Shaped array variants are: pin, straight slot and curved slot arrays with groove dimensions of approx. 1.5 x 0.3 mm (H x W).

The innovative ECM technology can produce low costs, high precision and defect free surfaces by anodic dissolution in iron-alloys, because during ECM any mechanical forces and stresses take not place [3,4]. Due to strong technological and chemical restrictions, the usual standard ECM processes have up to yet no industrial application in tungsten, and tests for shaping tungsten probes under well-engineered industrial ECM-conditions failed by effects e.g. passivation of surfaces, as a result of the unique physical, chemical and electrochemical properties of tungsten. Basic physico / electro-chemically investigations showed by development of adapted electrolytes that these drawbacks can be overcome. The aim of this work package is to implement a new ECM technology for W alloys and to evaluate process parameters for micro-structural shaping of fusion relevant components.

Electrochemical tungsten investigations

ECM is an electro-chemically assisted soft working dissolution process with region selective characteristic. This process is used in shaping hardened steels but failed in industrial W shaping due to formation of passivation scales. To apply ECM to W-alloys a multi step programme was set up starting with basic physico-chemical analyses and investigating in further steps systematically variations of process parameters on region selective dissolution of W-alloys.

The investigations were concerning the following areas

- The general electrochemical behaviour of refractory metals (with focus on tungsten) in common industrial electrolyte solutions and the evaluation of known electrochemical and chemical data in view of applicability.
- The electrochemical behaviour in dependence of several diversified chemical, physical and electrochemical parameters directing to an adopted ECM electrolyte development.
- Development of methods and processes (e.g. M-ECM or C-ECM) based on the new electrolytes and fixing of the necessary parameters.
- Development of new equipment or variation of facilities adapted to the obtained results in view of a transfer in technical scales.

Electrochemicals fundamentals

Tungsten is, given by its pure parameters, in theory less stable than iron in typical ECM etching solutions, but in praxis, W forms after first initial dissolution reactions passivating oxide layers of few micrometers thickness [5,6,7] and the W scales become totally insoluble in acidic and neutral solutions. Especially commercial and well-engineered electrolytes for the electrochemical etching of steel cannot remove and dissolve the insulating passive-layers from tungsten.

A systematic electrochemical investigation programme was necessary to clarify first the passivation features, the electrochemical behaviour in dependence of different chemical parameters and the possible troubleshooting. Fig.°2 shows potentiodynamic studies for the development of the new **T**wo-**C**omponent **E**CM **E**lectrolyte (TCEE) type with variations of the pH-value. A drastic increase of dissolution currents (over four decades) was stated.

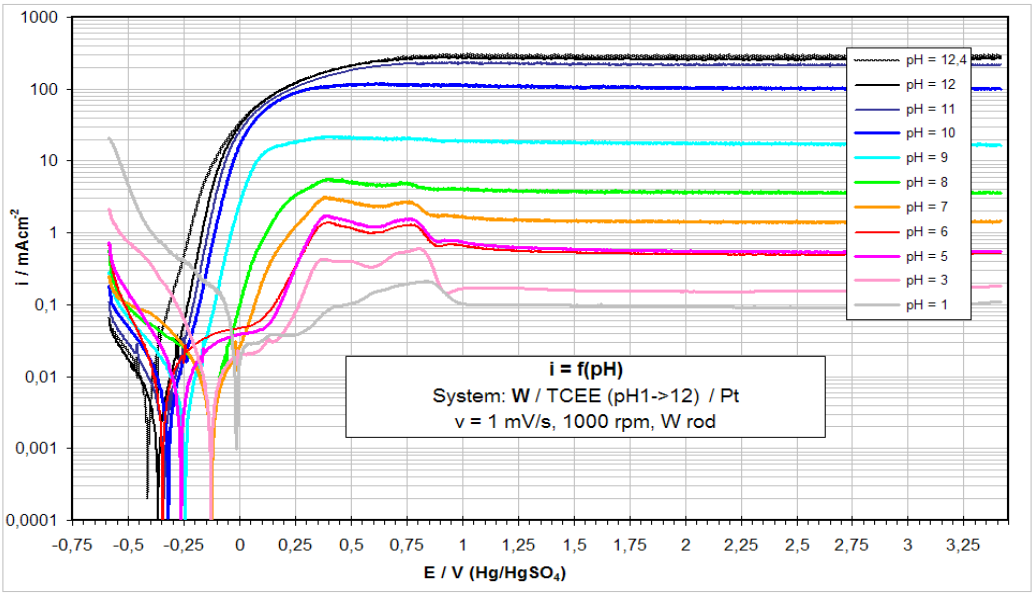

Fig. 2: Electrochemical behavior of tungsten in electrolytes of different pH-values, visualized by potentiodynamic measurement with a scan-rate of 1 mV/s.

ECM process variants for structuring

Additionally, the realization of tungsten-ECM has to correspond with some unavoidable necessities, e.g. the compatibility between chemical and technical environment and the minimal design requirements. It pointed the technical conditions for the optimization of directed removal, to enable a shaping process with the intention to generate structure devices of more than one millimeter deepness.

As ECM-process variants M-ECM and C-ECM were specified. The prefixes **M** and **C** are standing for **M**ask or **C**athode, indicating the most important shaping tool. The M-ECM branch belongs to the lithographic structuring methods [7], where an insulating mask is deposited on the work piece and structured afterwards, allowing dissolution of the metal only in the un-coated surface fractions. In

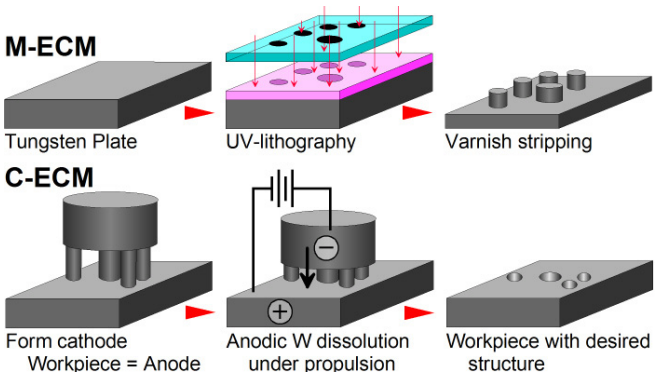

Fig. 3: Sequence scheme of the two ECM principles: M-ECM and C-ECM.

contrast to M-ECM the C-ECM process works with a negatively shaped tool (Cathode) which is imaged into the work piece. By this method mainly the distance between anode and cathode controls the material take off neglecting other parameters e.g. current type. Fig. 3 illustrates the two ECM process branches M-ECM and C-ECM inclusively of the main process steps.

The M-ECM process

The M-ECM is based on anodic dissolution of a partly covered metal, were the insulating mask prevents etching, therefore at strongly defined positions. This mask is processed by lithographic techniques, so that high flexibility is given in desired design variants down to the micrometer scale. Main parameters in the M-ECM are only the current densities and the chemical conditions. The electric conductivity in the whole electrolyte should be sufficient high and the distance cathode–anode can be varied in a wide range without impact on the structuring accuracy.

The main structuring element, by which region-selectivity is achieved, is the mask, so it has to be resistant against the electrolyte in the whole pH regime of this ECM-type. The masks used were made of layers of Novolak, Polyimide, and SU-8. Novolak and Polyimide show good adhesion and films with homogeneous thickness can be fabricated. SU-8 coatings are more difficult in processing due to lack in adhesion especially on polished surfaces. All films can be structured by standard processing methods (light) or laser ablation [7].

In ECM of W structures metal removal with large aspect ratios perpendicular to the surface is desired and a horizontal dissolution has to be avoided resulting in underetching of the mask. This underetching effect is beyond other parameters also correlated to anisotropic grain structure. Due to raw material processing of W-alloys, they are fabricated by PM technology with subsequent forging or rolling steps, W raw materials exhibit strong anisotropic grain structures. These anisotropic grain orientations support W-removal parallel to mechanical raw material processing by M-ECM etching.

From the two types of future divertor alloys - pure W and WL10 (W-1%La_2O_3) specimens were machined from rods and plates, covered by Novolak (insulating mask material) and irradiated with UV-light. The masked specimens were contacted as anodes and processed under inert gas atmosphere. All tests showed that the dissolution started at the free W surface areas with high accuracy and imaged the mask figure into the W-bulk if erosion depth is very low. Strong dependencies on grain orientation appear if etching depth is more than 0.1 mm. Specimens fabricated from rolled plates with grain orientation perpendicular to the processing orientation in ECM exhibit a type of fully isotropic dissolution with the result, that minor good quality is obtained of the desired structures. In contrast, discs cut from rod material consisting of fiber like arranged grains, orientated perpendicular to the surface, provides a highly anisotropic removal into the depth of W-bulk. Using constant DC currents up to 400 mA/cm^2, structure depths up to 0.8 mm were achieved without significant loss in accuracy i.e. under etching of the mask.

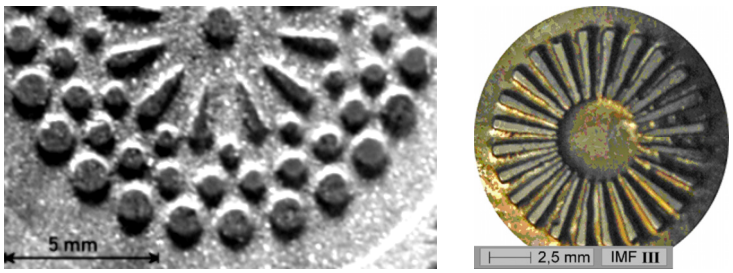

Fig. 4: Structured probe of WL10 with constant DC.

Structuring of the WL10 alloy is principally possible using similar process parameters as evaluated for pure W (Fig. 4). However, lanthanum oxide is insoluble in the TCEE and forms after a certain time precipitates of not-adhesive La_2O_3-powders on the remaining electrode surface, which can removed by adopted technical conditions.

The M-ECM development showed that with increasing structure depth e.g. beyond 1 mm and aspect ratios above 10 the accuracy decreases due to under etching mostly also correlated to dissolution of the mask. The higher stability of improved masks e.g. fabricated from SU-8 will help. Additionally was found that with rising depths, the weak insulating effects of grain boundaries lose influence and assist lateral etching. Selection of optimal parameter sets is more challenging working in pure DC mode. Some increase of better structure constancy is obtained by switching over to pulsed C current. Beyond physical parameters a high influence of variations of the raw material quality (sometimes in the same rod piece) became evident.

One important advantage of this M-ECM is the simplicity of the method due to working with unstructured electrodes and the well proven lithographic masking techniques. Thus M-ECM has a high potential for an application in mass production processes. However, processing depth seems to be limited in micro-structuring to the 1 mm range.

The C-ECM process

This is the process variant known from electrochemical steel shaping, where a cathode formed as a negative mold is propelled into the unmasked anodic work piece during a synchronic current supported dissolution [4], imaging the mould in to the piece. For all performed C-ECM W structuring tests the same electrolyte was applied as in M-ECM shaping. The development in C-ECM for W structuring started with the shaping of “simple” structures e.g. single and multiple grooves or crosses. The used currents were in the range of about 1 to 10 A.

Compared to M-ECM deep structures (more than 2 mm) can be realized much easier by C-ECM coupled with the propelled tools. In the test series removal rates up to about 10 µm/min were obtained – about a factor 10 more than in M-ECM. The investigations showed that the distance cathode-anode is a main parameter in C-ECM to achieve region-selectivity. Only, if distances in the low µm-range are chosen a provoked dissolution is obtained of selected areas. In the other case a scattering of the electric field will favor a not region-selective erosion of surfaces. This fact claims a distance control during etching of anode to cathode or at least in the first improvement step a adjustable feed motion of the tool. Of course several other process parameters were identified to have more or less impact on geometries of etched structures. Such parameters are e.g. the electrolyte pressure and electrolyte flow in the gap between work piece and tool, type of DC current and pulse to pause times of current. Due to these challenging requirements in process control C-ECM needs both an adequate technical equipment and accurate parameter adaptation to the structures to be machined.

In a first Lab equipment a moveable electrode system was integrated to evaluate the impact of tool to work piece distance. Fig. 5 shows the type of working tool and its copying into a W-disc at a distance of roughly 50 µm between tool and work piece. All four eroded gaps show similar geometries and small edge rounding – an indication that feed motion of the electrode was adapted to the erosion rate at appropriate levels. This test delivered two very important results. The first is that W can be structured by C-ECM in general. The second one illustrates that small distances have to be guaranteed during the whole processing to achieve true geometries. Surely, beyond these highlighting results the performed tests also showed which required additional steps have to be undertaken to come down in the structure dimensions from roughly 1 mm groves to 50 µm gaps.

These basic C-ECM tests confirmed that also in W structuring the working tool is not consumable and can be used for line production of complex shaped and deep structured geometries. All collected results in this prescreening C-ECM testing were used to design an improved lab facility, which has more mechanical stability, better motion control of the electrode and additionally the feature of forced electrolyte flow in the gap between tool and work piece. This designed set up was meanwhile successfully installed and went into first commissioning

test. The next tests performed with this new equipment will focus on smaller gap distances to increase further the accuracy of geometries and to reduce edge rounding.

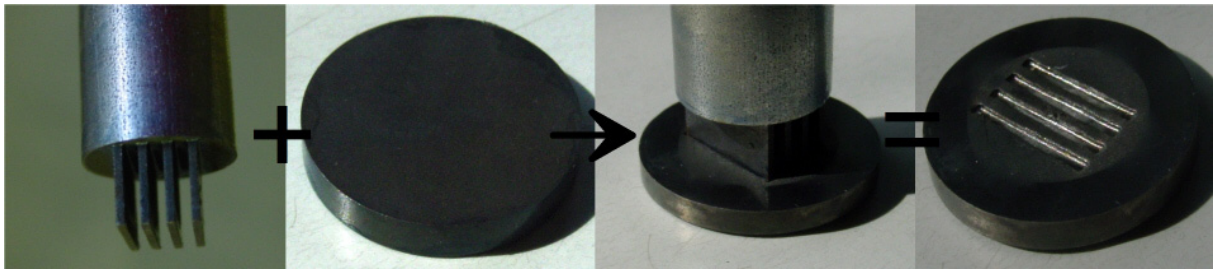

Fig. 5: A slot array with diameter 12 mm processed is depicted on the right side.

Looking forward to non-mechanically based impacts on structuring the physico-chemical features will dominate process improvement. The W-dissolution in both M-ECM and C-ECM are based on an elementary two-step reaction with different features (electrochemical oxidation to insoluble WO_3 without chemical influence; chemical hydroxylation to soluble product without electrochemical influence: E-C-mechanism). A support should be achieved by giving each kind of reaction adopted conditions for a sufficient time. In electric terms this means nothing other then pulsed currents, with an interval for anodic current, and a current-less interval for the chemical reaction. Because, no time constants are available for tungsten in TCEE, the next task steps will include the investigation of pulse profiles. Some principle tests performed in a basic set indicate that the dependence frequency vs. accuracy vigorous.

Conclusions

The general result of these investigations is, that W alloys can be well-defined structured by ECM methods with specially adopted electrolytes. Two ECM based structuring lines were elaborated and successfully tested in shaping of W parts for the first time in a lab. Both ECM lines guarantee a soft shaping of the brittle and hard W-alloys without introducing the risky microcracks as e.g. EDM (spark) erosion or rough milling. M-ECM is a low cost method to structure W with small aspect ratios. C-ECM shows clear advantages in deep structuring and for high aspect ratios. A set of parameters was elaborated for further process improvement and a new test rig was built up. The obtained results show that a variation of the electric regime, e.g. pulse sequences is the right path for process optimization. This is the main (midterm) objective in the current research program on ECM of tungsten to increase accuracy of parts fabricated from the bulk. Additional activates are also under execution to apply ECM as surface finishing method e. g. in micro-crack elimination from mechanically pre-shaped components. The general and future aim of whole development is to make ECM technology available for industrial fabrication of all W components in a future fusion system as innovative and reliable process with a transfer step of collaboration with industries.

Staff:

N. Holstein
J. Konys
W. Krauss
J. Lorenz

Literature:

[1] P. Norajitra et al., Development of a helium-cooled divertor concept: design-related requirements on materials and fabrication technology, J. Nucl. Mat. 329–333 (2004) 1594–1598

[2] P. Norajitra, R. Giniyatulin, N. Holstein, T. Ihli, W. Krauss et al.; Status of He-cooled divertor development for DEMO, Fus. Eng. Design; 75–79 (2005) 307–311

[3] W. Krauss, N. Holstein, J. Konys, Development and fabrication aspects regarding tungsten components for a He cooled divertor, Fus. Eng. Design, 75-79, (2005) 775-778.

[4] W. Krauss, N. Holstein, J. Konys, I. Mazul, Investigation of the impact of fabrication methods on the micro-structure features of W-components of a He-cooled divertor, Fus. Eng. Design, Vol. 81, 1-7, (2006), pp. 259-264.

[5] M. Köhler, Ätzverfahren für die Mikrotechnik, p.113, Wiley-VCH Weinheim, 1998.

[6] W. König, F. Klocke, Elektrochemisches Abtragen (ECM), Fertigungsverfahren, Vol. 3, Springer, (1997), pp. 91-121.

[7] J. Amberg, M. Guttmann, N. Holstein, M. Moneke, W. Pfleging, K. Seemann, Section UV-Lithography in FZKA Bericht 6804, Forschungszentrum Karlsruhe, (2003), p. 16.

[8] N. Holstein, W. Krauss, J. Konys; Structuring of tungsten by pulsed ECM processes for He-cooled divertor application; Fus. Eng. Design, 83 (2008) 1512–1516

Materials Development
Nuclear Data

EFDA/07-1704-1626 (TW6-TTMN-001B)
Nuclear Data: EFF/EAF Data File Upgrade, Processing and Benchmark Analyses

Overall objective: The European Fusion File (EFF) and Activation File (EAF) projects aim at developing a qualified nuclear data base and validated computational tools for nuclear calculations of fusion reactors. The related Task TTMN-001B of the EFDA technology work programme was devoted to the evaluation, processing, application, and benchmarking of required nuclear cross section and uncertainty data as well as to the development of computational tools for uncertainty calculations. The FZK contribution to Task TTMN-001B was on the evaluation of EFF-3 data, the qualification of new and updated EFF data evaluations through computational benchmark analyses including sensitivity/uncertainty analyses, and the development of advanced computational schemes for sensitivity calculations based on the Monte Carlo technique.

Deliverable 3
Improvement of the methods and tools for Monte Carlo based sensitivity/uncertainty calculations for application in ITER and TBM

The objective of Deliverable 3 was to further improve the computational tools for the calculation of sensitivities and uncertainties of neutron fluxes and nuclear responses on the basis of the Monte Carlo technique. To this end, algorithms were developed and implemented in the MCSEN code, a local update to the MCNP Monte Carlo transport code, that allow the efficient calculation of sensitivities in the same way as the corresponding transport calculation.

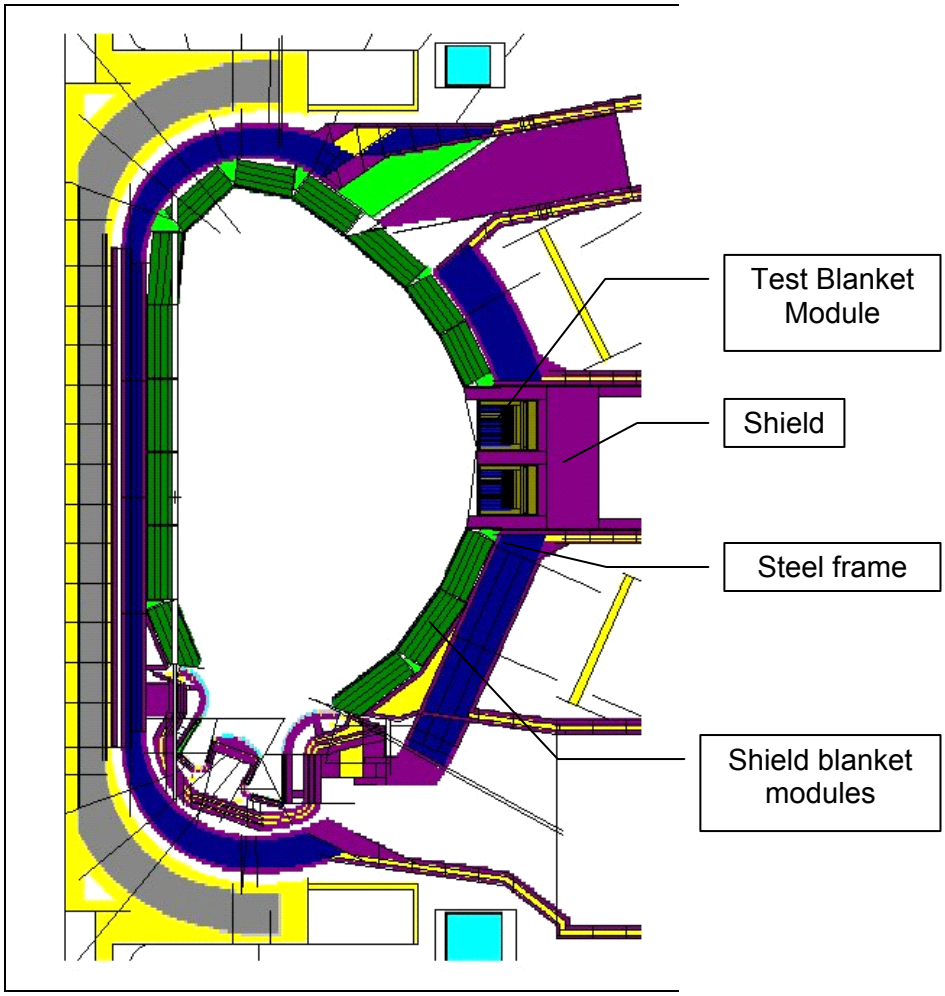

Fig. 1: MCNP model (vertical cut) of ITER 20° torus sector with integrated HCPB test blanket modules.

In a previous work on sensitivity and uncertainty analyses of tritium production in the Helium Cooled Pebble Bed (HCPB) Test Blanket Module (TBM), the processing of many materials has shown to be cumbersome and lengthy. Therefore, the upgrade to be implemented into MCSEN was to allow a more efficient calculation of the sensitivities for applications where a specific nuclide is contained in many materials in different reactor components. The logical program flow has to be optimized in such a way that only one single run is required to calculate the sensitivity of a nuclear response to the nuclear cross-section of a specified nuclide contained in any material which is present in the problem geometry. The improved feature is to be verified by means of test applications to the TBM in ITER, using the standard 3D MCNP model (20 degree torus sector of ITER) with integrated TBM of the HCPB type (see Fig. 1 and 2), and the comparison with previous sensitivity results obtained with the non optimized MCSEN version of 2006.

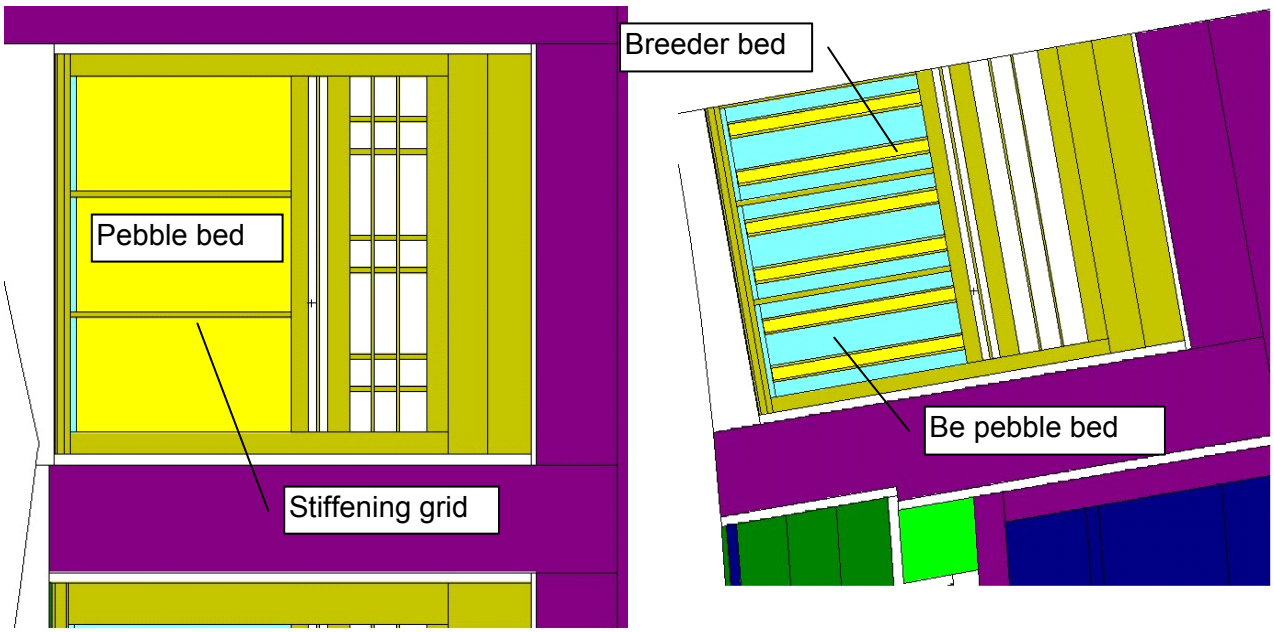

Fig. 2: Vertical (left) and horizontal (right) cross-sections of the MCNP model at the level of the test blanket port.

The main change introduced in the new, upgraded version of MCSEN was to introduce the concept of a “sensitivity isotope”, whose atomic abundance in each material is given in a vector. At each event, the code checks the occurrence of the desired “sensitivity isotope” using this vector. It allows to combine contributions of the “sensitivity isotope” contained in a material mixture (e.g. ^{16}O in water-steel is contained in water and, as an impurity, in steel) or to select only specific materials by assigning different nuclear data libraries (e.g. ^{16}O in TBM and ^{16}O in the rest of ITER are using different data-sets). The new feature does not override the older ones, but adds new capabilities to MCSEN, namely to allow calculations of sensitivities for the “sensitivity isotope” in a given cell, in a given material or in all materials.

After successful basic testing of the upgraded code and the new feature, a test application has been performed on the tritium production in the HCPB TBM of ITER. Sensitivities were calculated with the track length (flux in cell) estimator using MCSEN and the 175-group VITAMIN-J group structure. The nuclear responses were calculated in 6 coarse energy groups: 0.1eV, 1keV, 100 keV, 1 MeV, 10 MeV, 20 MeV. Generally, FENDL-2 nuclear data libraries have been used except for the TBM materials, where JEFF3.1 and EFF2.4 data have been chosen. Based on the results obtained previously, we focused our investigations on sensitivities to the cross sections of the most important isotopes ^{9}Be, ^{16}O, ^{56}Fe, and ^{1}H. For these isotopes, the co-variance data have been extracted from EFF3, JENDL3.3, EFF3, and ENDF/B-V, respectively.

As for the total relative sensitivities, all the results obtained with the new feature coincide with the previous results precisely within the statistical uncertainty of the MCNP runs. Only very minor differences are present in the case of ^{16}O and in the case of ^{1}H. Possible reasons may lie in the different post-processing procedures and, in the case of ^{16}O, in the two separate MCNP runs needed to add contributions from the TBM itself and from the rest of the assembly.

The sensitivity profiles (see e.g. ^{16}O in Fig. 3) agree very well with the previous results. As could be expected, the minor differences occur when one isotope appears in several materials. In the new procedure, the true correlation between events is taken into account, e.g. for ^{9}Be in the first wall of the TBM and in the beryllium pebble bed. For all practical purposes the sensitivity profiles are identical.

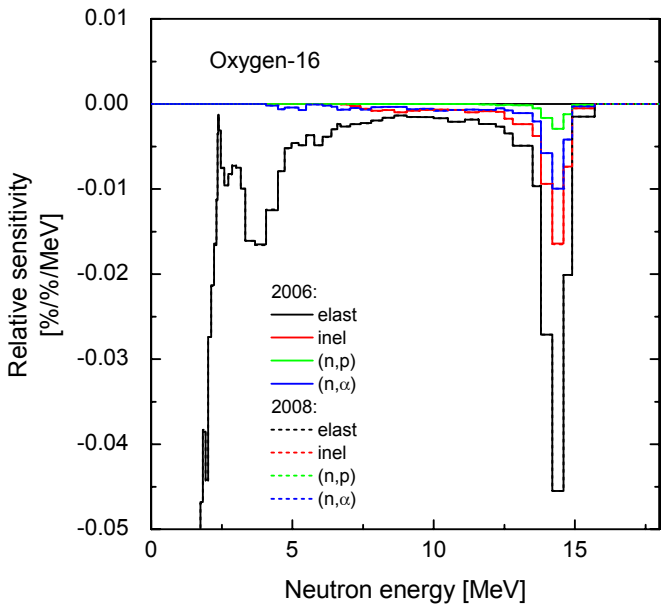

Fig. 3: Relative sensitivity profiles for O16 cross sections; comparison between previous (2006) and new (2008) results.

The performance gain using the new option could be significant in terms of computing time. In the case of, e.g., ^{56}Fe, the new option requires one MCSEN job compared to 6 jobs with the previous option. The speed-up is about 3.2, for other isotopes the factor is in the same range depending on the number of materials the isotope is part of. In any case, the time-consuming and error-prone post-processing of several different outputs for the same sensitivity isotope could be eliminated. It can be concluded that for all practical purposes the new option does not introduce any significant changes but could speed up and facilitate significantly complex sensitivity and uncertainty calculations in fusion systems.

Deliverable 4
Evaluation of ^{52}Cr Neutron Cross Sections up to 150 MeV for the EFF-3 data library

According to the priority list elaborated in 2003 to satisfy, in particular, the data needs of the IFMIF project, the objective of the 2008 work programme was to provide a complete general purpose data evaluation of the reaction system n + ^{52}Cr up to 150 MeV for the EFF-3 nuclear data library. Accordingly, a complete data evaluation of nuclear cross-sections for general purpose applications was performed for n + ^{52}Cr nuclear data in the energy range 0.001 up to 150 MeV.

The evaluation procedure adopted for the task makes use of the well established system elaborated at FZK. Optical model calculations are performed by ECIS to generate transmission coefficients for subsequent nuclear model calculations and to prepare cross sections for total, elastic and non-elastic scattering, as well as for collective excitations. Nuclear model calculations were performed with the GNASH code using level densities, nuclear masses and other data from the RIPL-2 reference library. All cross sections and distributions obtained by the GNASH calculations are written automatically to ENDF-6 formatted data files ready to be used by standard processing codes.

Optical model calculations

In the optical model calculations the emission of neutrons, protons, deuterons, tritons, helions (^{3}He) and alphas have been considered using local (neutrons, protons) as well as global OMPs (other particles). In the case of tritons and helions, newly developed global OMPs have been used.

Both the total and the elastic scattering cross section from ECIS have a very complex resonance structure below 5 MeV. In this region, the new evaluation of the elastic cross section is in good agreement with ENDF/B-VII data. In the case of inelastic scattering cross sections, direct contributions from several excited states have been obtained from ECIS, other levels are treated by equilibrium inelastic scattering. The total inelastic scattering cross section is well measured below 20 MeV, providing a distinct resonance structure. This of course cannot be reproduced by optical model calculations for the individual levels; therefore the total inelastic scattering cross section lacks this structure. Nevertheless, the trend of the excitation curves agrees well with the experimental data (Fig. 4).

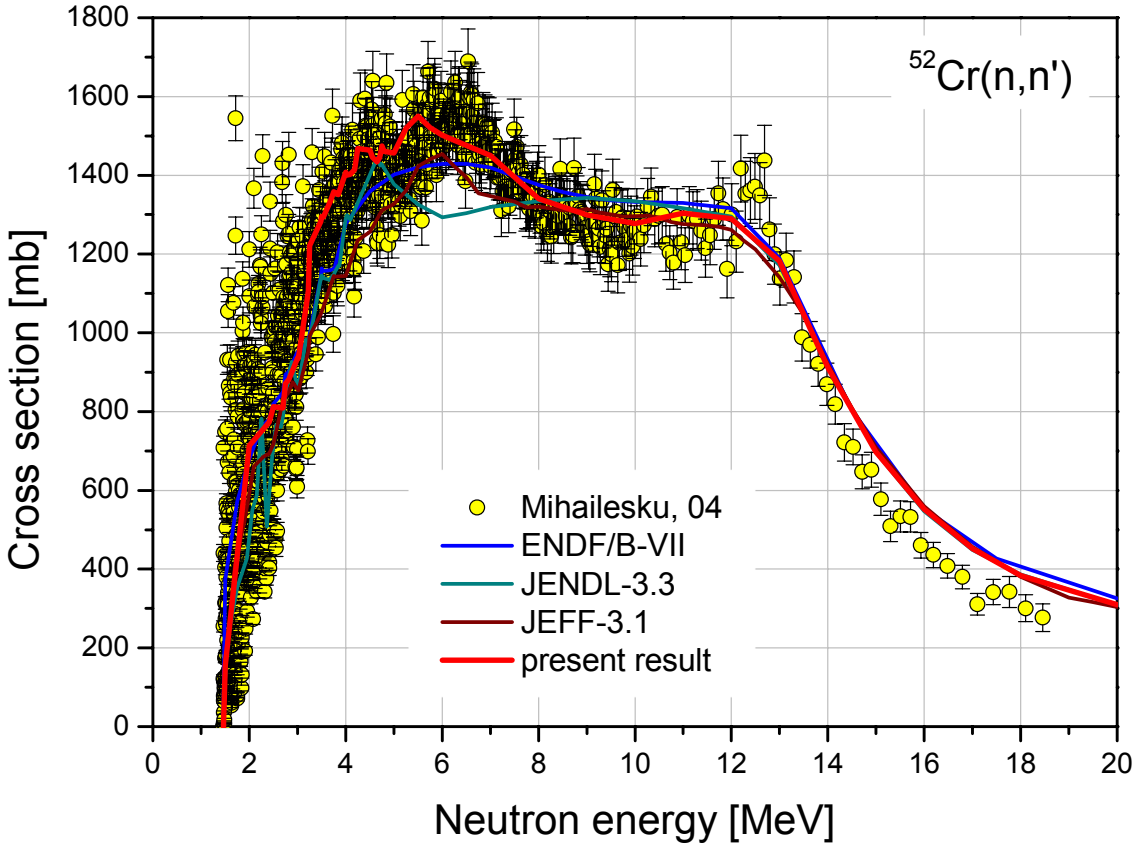

Fig. 4: Evaluated total inelastic cross section (MT=4) in comparison with other evaluations and experimental data.

Nuclear model calculations

Nuclear reaction cross sections and particle emission spectra were calculated with the GNASH code. This code has been extensively used for nuclear data evaluations over the past three decades. To treat the excitation of collective states with different multi-polarities, which are responsible for the well known humps in the high energy tails of the energy emission spectra, a model by Kalbach was applied. Besides RIPL-2 data for level densities and masses, additional data was extracted where needed from the Table of Isotopes and the built-in mass table of GNASH.

Exclusive nuclear reaction channels below 20 MeV have been calculated (see e.g. Fig. 5) and stored into the final evaluated data file separately; above 20 MeV, the lumped cross section (MT5) was adopted. In the case where experimental data was available above 20 MeV and the GNASH results were significantly different, available evaluations from EAF (in the case of (n,2n)) and JEFF3.1 (for (n,γ)) was adopted in the final evaluation.

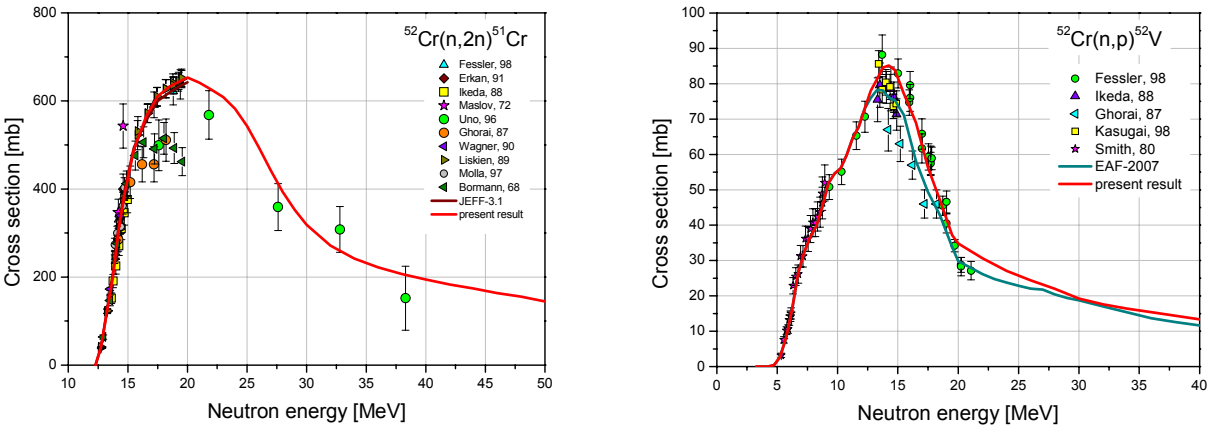

Fig. 5: Evaluated cross sections (left: (n,2n), right: (n,p)) in comparison with JEFF3.1 evaluation and experimental data.

Similar to the storage of cross sections, also particle emission spectra are treated differently for the exclusive channels below 20 MeV and for the lumped cross section above this energy. The energy distributions obtained by GNASH generally agree better with experimental data than the JEFF3.1 evaluation. Also double-differential data has been calculated using Kalbach systematics. All outgoing particle emission spectra have been provided, including recoil spectra for radiation damage estimations.

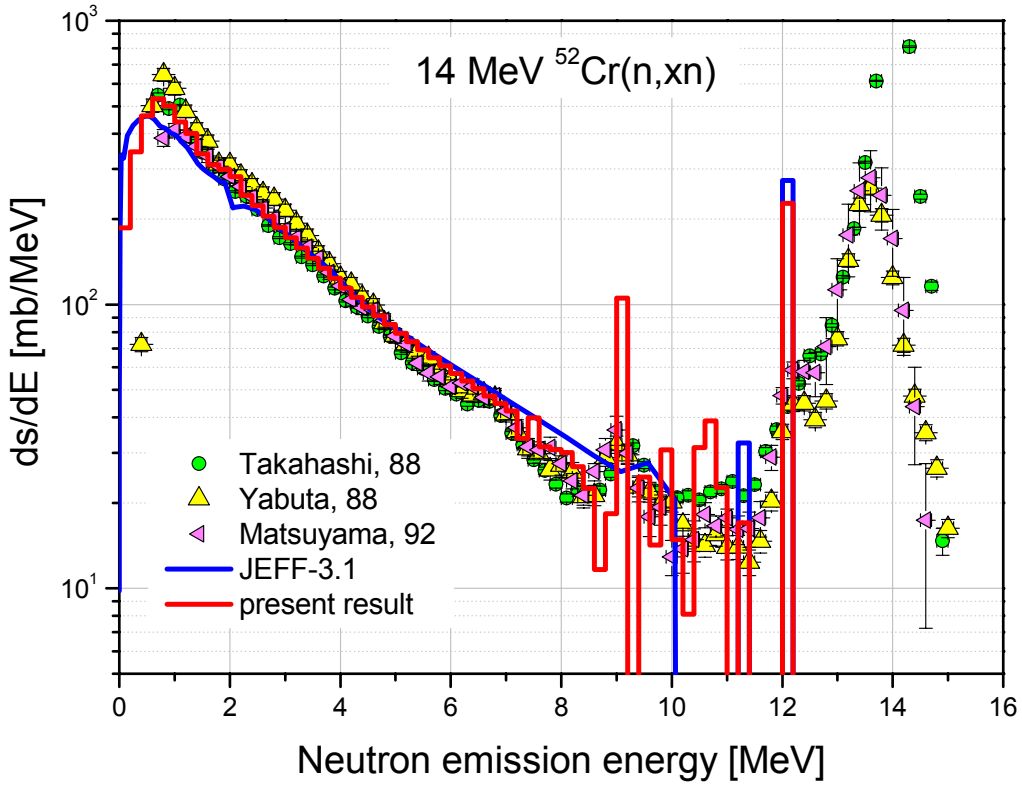

Fig. 6: Evaluated neutron emission spectra at 14 MeV in comparison with JEFF3.1 evaluation and experimental data.

A complete general purpose data file in ENDF-6 format was finally prepared covering the entire energy range from thermal energies up to 150 MeV. The data file was verified with standard ENDF-6 format checkers. ENDF/B-VII data were adopted for MF=2, MT=151 (resonance parameters) and MF=3, MT=102 were taken from JEFF-3.1. The newly evaluated data are in good agreement with measurements available for the ^{52}Cr cross sections and particle emission spectra.

Deliverable 5
Benchmark analyses of Mn and Ta cross sections with MCNP for revised/updated EFF-3 data evaluations

The objective of sub-task TW6-TTMN-001B, D5, was to test and validate the revised/updated EFF-3 data evaluations of Mn and Ta isotopes by means of benchmark analyses and thereby provide feed-back to the evaluators. The benchmark analyses include cross-checks with other available evaluations on suitable integral benchmark experiments using MCNP calculations.

Nuclear data libraries and benchmark experiments

The recent EFF evaluation for Ta-181 at FZK up to 150 MeV, complemented with covariance data and adjusted to experimental partial cross-sections, is a candidate evaluation for the JEFF-3.2T library. Two other independent evaluations have been considered in the benchmark analyses, namely ENDF/B-VI and JENDL-3.3. In the case of Mn-55, the recent evaluation of FZK has been compared to ENDF/B-VI.8 and JENDL-3.3 (adopted in FENDL2.1 and JEFF3.1).

Two integral benchmark experiments on Tantalum were found in the SINBAD database and used in the benchmark analyses. One was performed at the Lawrence Livermore National Laboratory (LLNL) in 1986 on two Ta spherical shells with a central 14 MeV neutron source (D-T source). The shell thicknesses amounted to 3.4 and 10.2 cm corresponding to 1 and 3 mean free paths for 14 MeV neutrons, respectively. Time-of-flight spectra were recorded at a distance of 10 m from the centre of the Ta shell. Another experiment on a tantalum sphere with a diameter of 24.2 cm and a central Am-Be neutron source was carried out in the Lewis Research Center (LRC). The neutron leakage spectrum was measured by proton recoil scintillator detector from 0.5 MeV to 12 MeV. Since neutron emission from a spontaneously decaying Am-Be source is isotropic, the neutron leakage has no angular dependence.

Only one integral benchmark experiment with 14 MeV neutrons was found for Mn. It was conducted at the OKTAVIAN facility of the University of Osaka on a spherical shell with a thickness of 30.5 cm corresponding to 3.4 mean free paths for 14 MeV neutrons. Neutron and photon leakage spectra were measured using the time-of-flight and the pulse height unfolding technique, respectively.

Benchmark results

The benchmark analyses have been performed using detailed 3D geometry models of the experiments in the MCNP5 calculations. In the case of the two Ta-experiments, it could be observed that both ENDF/B-VI and JENDL-3.3 calculations disagree with the measurements up to 50-70%, whereas FZK'06 agrees within 10-20% (shown as C/E values in Fig. 7). The candidate JEFF-3.2T evaluation (FZK'06 with adjustment to experimental data) performs slightly better for the D-T source (LLNL experiment) but underestimates systematically the transport of neutrons in the case of the Am-Be source (LRC experiment), see Fig. 7.

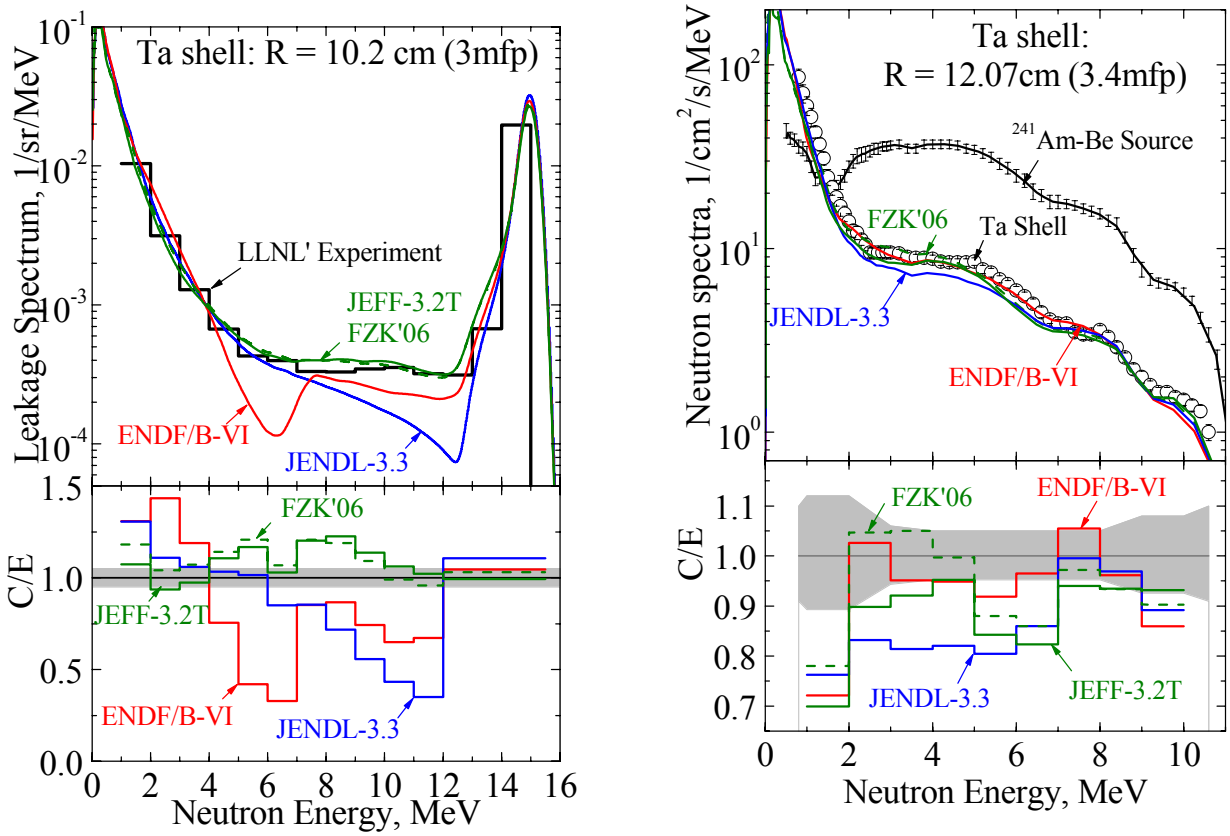

Fig. 7: Comparison of measured and calculated neutron leakage spectra from Ta spherical shells: D-T source (LLNL) left, Am-Be source (LRC) right.

For the Mn spherical shell experiment, neutron as well as photon leakage spectra have been calculated and compared to experimental data (C/E values). The neutron leakage yields C/E values in a range of around 24 % above and below unity in the case of ENDV/B-VI and JENDL-3.3, and 31% in the case of FZK'07 (see Fig. 8 left). It is noted, that the neutron emission spectra at 14 MeV from those libraries deviate grossly, and also the emission below 0.5 MeV is discrepant. In the latter case it is difficult to judge on the validity since no experimental data is available in this energy range.

As for the photon leakage spectra, the FZK'07 result is underestimating the flux below 4 MeV by a factor of 3, whereas the other libraries perform significantly better. This may be attributed to the similar behaviour seen in the energy differential cross section of (n,xγ), where both ENDF/B-VI and JENDL-3.3 are reproducing the experimental data very well (except in the range 0.2 to 0.6 MeV) in contrast to FZK'07.

Benchmark analyses were conducted on the new JEFF-3.2T data evaluations for Ta-181 using the 14 MeV neutron benchmark experiment of the Lawrence Livermore National Laboratory (LLNL) on two Ta spherical shells with shell thicknesses of 3.4 and 10.2 cm, and an integral experiment of the Lewis Research Centre (LRC) on a 9 cm thick Ta shell with a central Am-Be source. Neutron emission spectra were checked against measured data for 14.1, 7.94 and 5.2 MeV incident neutron energies. It was found that the new JEFF-3.2T evaluation, provided by FZK in the frame of the 2005 EFDA work programme, can reproduce the neutron emission spectra at 14. 1 and 7.94 MeV and can predict the transport of T-D neutrons through bulk Ta assemblies up to 3 mean free paths. At 5.2 MeV incident neutron energy, discrepancies have been found in the neutron emission spectrum which might be attributed to the Ta(n,n') reaction and also shows up in the neutron leakage spectrum of the LRC spherical shell driven by an Am-Be source.

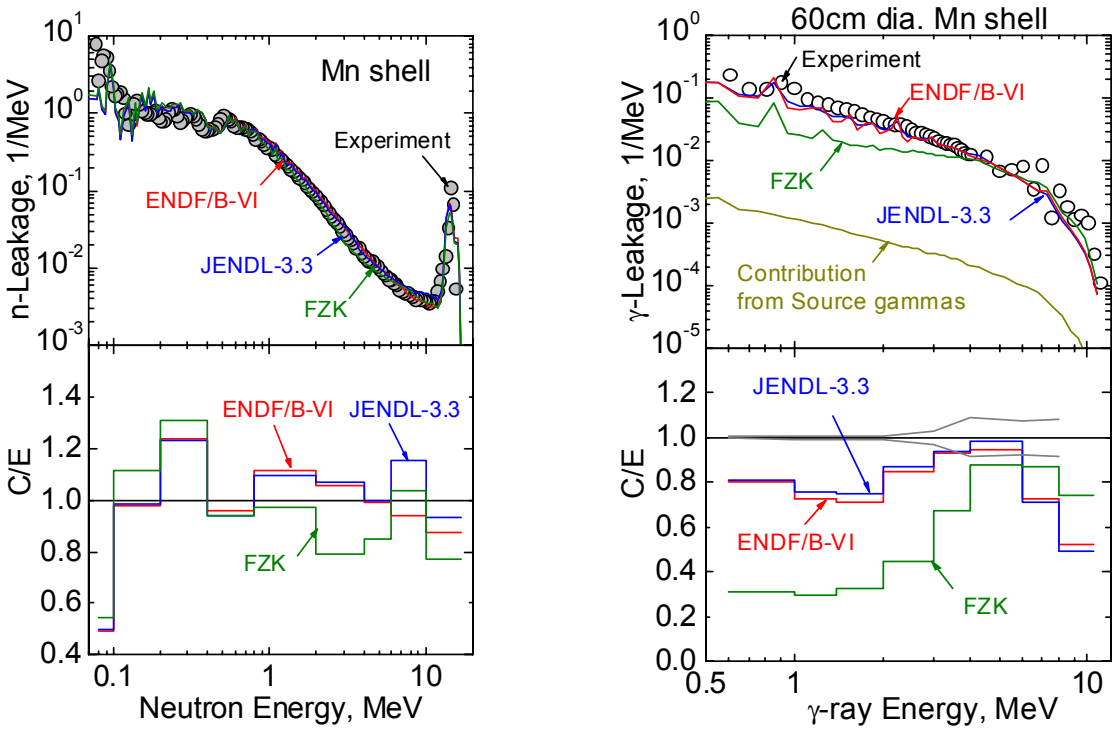

Fig. 8: Comparison of measured and calculated neutron (left) and photon (right) leakage spectra for a Mn sphere with 30 cm radial thickness with central 14 MeV neutron source.

The Manganese benchmark analyses were conducted on the new JEFF-3.2T data evaluation provided by FZK in the frame of the 2006 EFDA work programme. The Mn spherical shell experiment conducted at the OKTAVIAN facility (14 MeV neutron generator) was used for the benchmark analyses providing measured data for both the neutron and photon leakage spectra. The new JEFF-3.2T evaluation was shown to reproduce the measured neutron leakage spectra with the same accuracy as the recent ENDF/B-VII and JENDL-3.3 Mn-55 data evaluations. As for the photon leakage spectra, the JEFF-3.2T evaluation was found to be in worse agreement with the experimental results. The same trend was observed in analysing the energy differential cross sections. Thus the JEFF-3.2T photon production data need to be revised for Mn-55 prior to the inclusion in JEFF-3.2.

Summary

Benchmark analyses were conducted on the new JEFF-3.2T data evaluations for Ta-181 using the 14 MeV neutron benchmark experiment of the Lawrence Livermore National Laboratory (LLNL) on two Ta spherical shells with shell thicknesses of 3.4 and 10.2 cm, and an integral experiment of the Lewis Research Centre (LRC) on a 9 cm thick Ta shell with a central Am-Be source. Neutron emission spectra were checked against measured data for 14.1, 7.94 and 5.2 MeV incident neutron energies. It was found that the new JEFF-3.2T evaluation, provided by FZK in the frame of the 2005 EFDA work programme, can reproduce the neutron emission spectra at 14. 1 and 7.94 MeV and can predict the transport of T-D neutrons through bulk Ta assemblies up to 3 mean free paths. At 5.2 MeV incident neutron energy, discrepancies have been found in the neutron emission spectrum which might be attributed to the Ta(n,n') reaction and also shows up in the neutron leakage spectrum of the LRC spherical shell driven by a Am-Be source.

The Manganese benchmark analyses were conducted on the new JEFF-3.2T data evaluation provided by FZK in the frame of the 2006 EFDA work programme. The Mn spherical shell experiment conducted at the OKTAVIAN facility (14 MeV neutron generator) was used for the benchmark analyses providing measured data for both the neutron and photon leakage spectra. The new JEFF-3.2T evaluation was shown to reproduce the measured neutron

leakage spectra with the same accuracy as the recent ENDF/B-VII and JENDL-3.3 Mn-55 data evaluations. As for the photon leakage spectra, the JEFF-3.2T evaluation was found to be in worse agreement with the experimental results. The same trend was observed in analysing the energy differential cross sections. Thus, the JEFF-3.2T photon production data need to be revised for Mn-55 prior to the inclusion in JEFF-3.2.

Staff:

U. Fischer
D. Leichtle
S. Herber
R. Perel (Hebrew University of Jerusalem)
P. Pereslavtsev
S. P. Simakov

EFDA/07-1704-1631 (TW6-TTMN-002B)
Nuclear Data: Benchmark Experiments to Validate EFF/EAF Data

Overall objective: The overall objective of Task TW6-TTMN-002B was to provide the experimental data base required for the validation of the nuclear data libraries EFF (European Fusion File) and EAF (European Activation File) developed in the frame of Task TW6-TTMN-001B of the EU Fusion Technology Programme. According to the programme orientation on ITER (TBM) and IFMIF, the focus was on activities devoted to the experimental validation of TBM design calculations by means of a neutronics mock-up experiment and cross-section validation experiments relevant for IFMIF.

Deliverable 2
Measurements of the tritium production and neutron and gamma spectra in the neutronics HCLL TBM mock-up by a second experimental team

Background

A dedicated neutronics experiment [1 - 3] had been previously performed on a mock-up of the Helium-Cooled Pebble Bed (HCPB) Test Blanket Module (TBM) with the objective to validate the capability of the neutronics codes and nuclear data to predict nuclear responses, such as the tritium production rate (TPR), with qualified uncertainties. In the frame of TW6-TTMN-002B, a follow-up experiment on a mock-up of the Helium-Cooled Lithium-Lead (HCLL) TBM is being performed [4]. Fig. 1 shows schematic views of the HCLL mock-up prepared at ENEA Frascati with LiPb bricks.

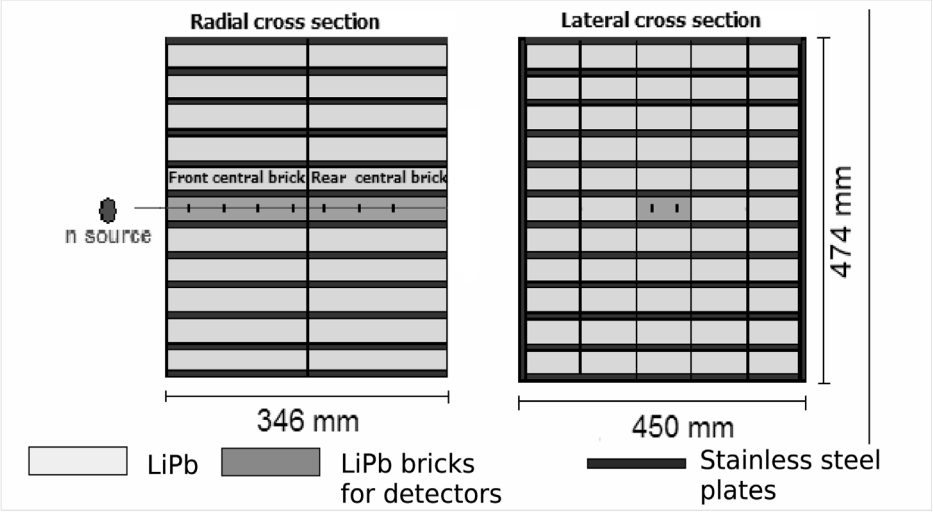

Fig. 1: Experimental LiPb assembly (2D schematic views).

Experiment

Like in the neutronics experiment on a HCPB mock-up, the TPR will be first measured at the Frascati Neutron Generator (FNG) laboratory of ENEA Frascati. Afterwards, the HCLL mock-up will be shipped to the TU Dresden neutron laboratory for measurements of the fast neutron and γ-ray flux spectra.

The TPR will be measured with two methods:

1. A procedure involving pellet detectors made of Li_2CO_3 which will be processed with liquid scintillation counting techniques.

2. A combination of LiF thermoluminescence detectors (TLD) with natural isotopic composition of Li and enriched in ^{7}Li (99.99%).

In preparation of this experiment, the TPR measurement method with LiF-TLD has been successfully tested in a LiAl-Pb assembly constructed at the TUD neutron laboratory [5]. The TPR value is obtained from the dose deposited in the LiF thermo-luminescence detector (TLD) which is mostly due to the tritons and α-particles emitted in the tritium producing reactions. A combination of LiF-TLDs of natural lithium composition and depleted in ^{6}Li is used to eliminate contributions from γ-rays etc. in each measurement position. This method is considered more sensitive than the TPR measurement technique with the Li_2CO_3 pellet detectors and allows for faster detector processing after irradiation.

The irradiation with 14 MeV neutrons from FNG for TPR measurements was in progress at the

time of writing of this report. The fast neutron spectra measurements at TUD are scheduled for Spring 2009.

Staff:

J. Henniger (TU Dresden)
A. Klix
M. Sommer (TU Dresden)

Literature:

[1] K. Seidel, P. Batistoni, U. Fischer, et.al., “Measurement and analysis of neutron and gamma-ray flux spectra in a neutronics mock-up of the HCPB Test Blanket Module”, Fus.Eng.Des. 82 (2007) 2212-2216

[2] D. Leichtle, U. Fischer, I. Kodeli, et.al., “Sensitivity and uncertainty analyses of the tritium production in the HCPB breeder blanket mock-up experiment”, Fus.Eng.Des. 82 (2007) 2406-2412

[3] P. Batistoni, M. Angelone, L. Bettinali, et.al., “Neutronics experiment on a helium cooled pebble bed (HCPB) breeder blanket mock-up”, Fus.Eng.Des. 82 (2007) 2095-2104

[4] P. Batistoni, “Status of TBM neutronics experiment”, EFFDOC-987, OECD/NEA Data Bank, OECD/NEA (2006)

[5] A. Klix, H. Freiesleben, J. Henniger, et.al., “Blanket mock-up experiment with a LiAlPb assembly irradiated with 14 MeV neutrons in preparation of the HCLL-TBM neutronics experiment”, Fus.Eng.Des. 83 (2008) 1813-1817

Deliverable 4
Monte Carlo based transport and sensitivity/uncertainty pre-analysis of neutron flux spectra and tritium production measurements in the neutronics HCLL TBM mock-up

The objective of Deliverable 4 is the computational pre-analysis of the HCLL mock-up experiment [6] using Monte Carlo techniques for transport and sensitivity/uncertainty calculations. To this end, the MCSEN code will be employed for the Monte Carlo sensitivity calculations of neutron fluxes and tritium production on nuclear cross-sections. Available covariance data will be used to obtain nuclear response uncertainties related to nuclear data uncertainties.

The HCLL mock-up consists of alternating layers of LiPb (in the form of solid bricks) and Eurofer-97 plates (simulation the cooling plates). In order to obtain neutron flux spectra inside the mock-up as close as possible to those occurring in the TBM in ITER, two thin layers and a reflector of Polyethylene (PE) are introduced inside the mock-up and behind it, simulating

the effect of neutron reflecting materials surrounding the TBM module in ITER. The TPR will be measured using Li_2CO_3 pellets located at various depths in the two central LiPb bricks along the mock-up radial axis. Several other measurement techniques are being developed and will be used to measure the TPR as well.

The computational analyses were performed with the objective to optimise the HCLL mock-up in such a way that the essential nuclear features of the HCLL TBM in ITER can be represented in the experiment. To this end, Monte Carlo calculations were performed with the MCNP5 code and nuclear cross-section data from the FENDL-2.1 nuclear data library for both the HCLL TBM in ITER and the TBM mock-up. Neutron flux spectra were calculated for two representative positions near the front and the back of the assembly (centered at 5.3 and 30.4 cm distance from the front surface, respectively). Tritium production distributions were compared at 7 radial positions (2.8 cm to 28 cm depth), cf. Fig. 2.

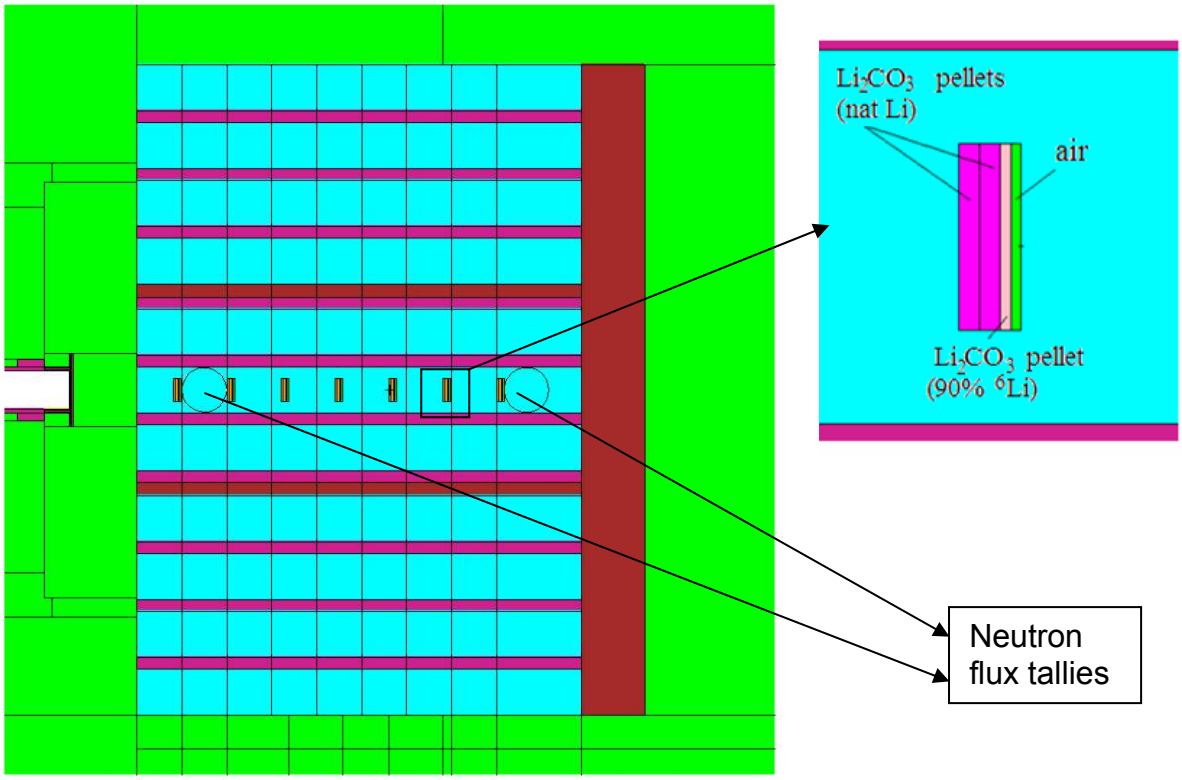

Fig. 2: MCNP model (vertical cut) of the HCLL mock-up assembly; enlarged view of the Li2CO3 pellet stack.

For the bare “look-alike” HCLL mock-up assembly, the neutron spectra were shown to be significantly harder than in the real HCLL TBM in ITER. This is mainly due to the fact that the TBM in ITER is surrounded by shield modules made of a steel/water mixture thus resulting in a comparatively soft spectrum impinging onto the TBM. The bare HCLL mock-up assembly, on the other hand, does not contain any neutron moderator. In addition, it does not contain a strong neutron absorber since the lithium of the Pb-Li alloy is not enriched in ^{6}Li. Together with the high neutron scattering power of lead this results, first of all, in a rather high neutron leakage out of the mock-up assembly and, second, in a rather hard neutron spectrum. The tritium generation in the mock-up therefore mainly takes place in the high energy range above 0.1 MeV, while in the TBM, a significant amount of tritium is produced in the low energy range. A better agreement could be achieved applying additional PE shields, both at the back of the mock-up assembly and as thin horizontal layers in the centre of the block. This modification softens the neutron flux spectra, mainly in the rear part of the assembly, and enhances the contribution of tritium production from ^{6}Li. The neutron flux spectrum then could be closely adapted to the ITER TBM results, as shown in Fig. 3.

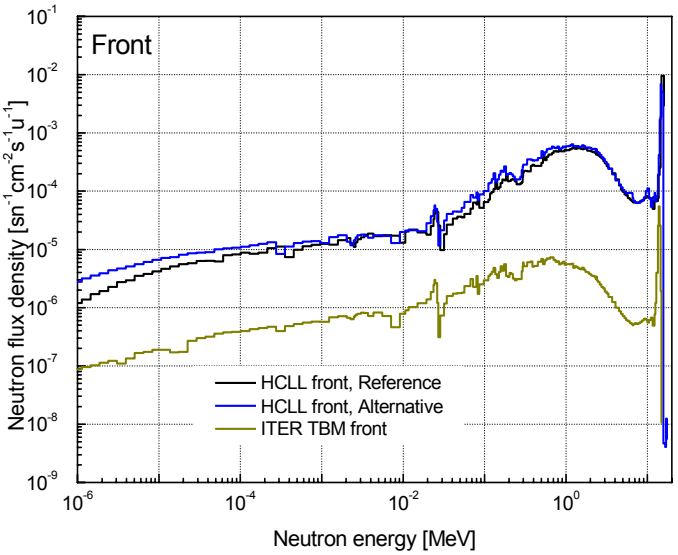

Fig. 3: Neutron flux spectra in the HCLL mock-up (front position) compared to ITER TBM; the alternative HCLL results were obtained using a massive PE shield.

The tritium production rates have been calculated for the series of Li_2CO_3 pellets, both with natural lithium ("Li-nat") and enriched in Li^6 ("Li-6"). The total tritium production rates in the Li-nat pellets are decreasing from the front to the back of the mock-up by a factor of 6 (from 126 Bq/g to 26 Bq/g). In the front position, the contribution by ^{6}Li is only 33%, but already at a depth of 7 cm this share increases to 63% due to the moderation of the high energy neutron flux. In the case of Li-6 pellets, the total tritium production varies only by a factor of 2 (from 458 Bq/g to 239 Bq/g), since the contribution of ^{7}Li, i.e. via fast neutrons, is negligible already at the front of the mock-up (1.8%).

Fig. 4 shows cumulative normalized tritium production (in Li-nat pellets) for the mock-up configuration with two PE layers inside and a PE reflector attached to the back of the assembly. It can be observed that the moderation power of the HCLL mock-up assembly is still weak as compared to the ITER TBM configuration. The ^{7}Li contribution is significant in the first two positions of the mock-up assembly; only at larger depths the agreement of the spectral tritium production with the ITER TBM configuration is satisfying. However, due to the additional use of pellets enriched in ^{6}Li, the specific tritium production response at the given location could be tailored properly, see fig. 5.

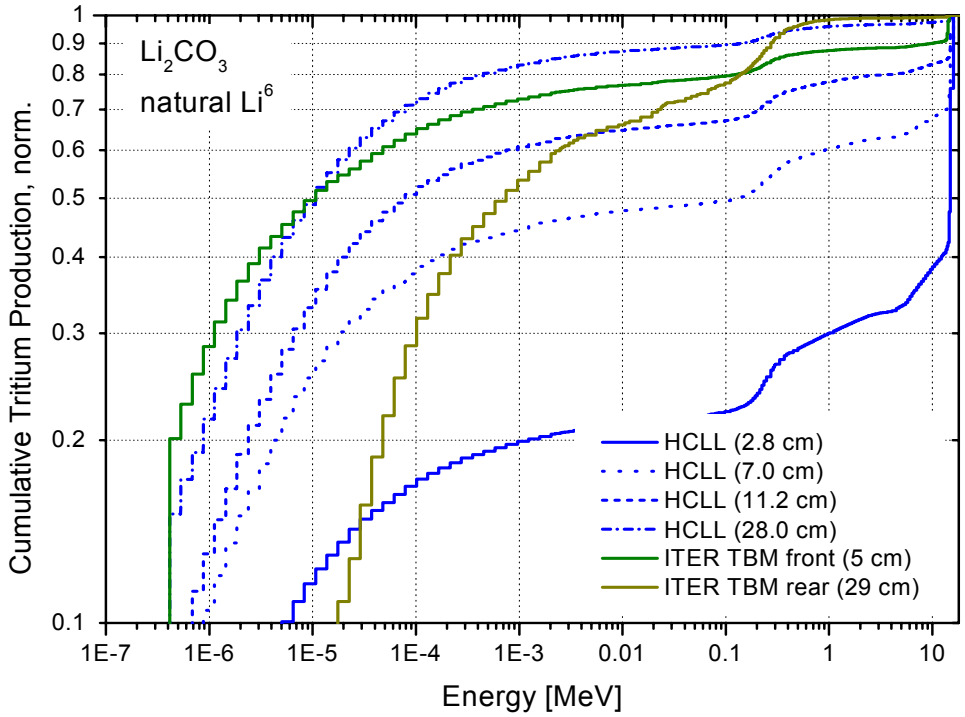

Fig. 4: Cumulative tritium production (norm.) in Li2CO3 pellets (natural lithium) at different depths of the HCLL mock-up compared to ITER TBM.

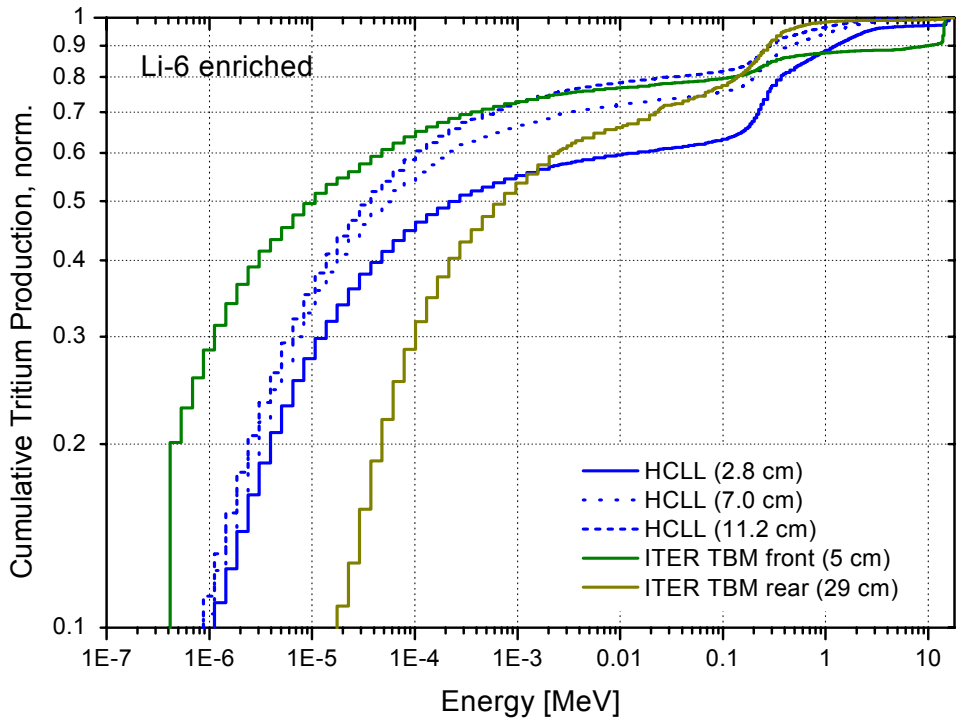

Fig. 5: Cumulative tritium production (norm.) in Li2CO3 pellets (enriched in 6Li) at different depths of the HCLL mock-up, as compared to the ITER TBM.

Staff:

U. Fischer
D. Leichtle
A. Klix

Literature:

[6] P. Batistoni, M. Angelone, U. Fischer, D. Leichtle, A. Klix, et al., Design optimisation and measuring techniques for the neutronics experiment on a HCLL-TBM mock-up, Proc. Symposium of Fusion Technology, 15-19 Sept. 2008, Rostock, Germany

Deliverable 7
Analyses of the validation experiments for Bi cross-sections up to 35 MeV in a quasi-monoenergetic neutron spectrum

The objective of this subtask was to perform a computational pre-analyses for the optimization of the set-up for the Bi activation experiments in a quasi-monoenergetic neutron spectrum ranging up to 35 MeV [7] and, after completion of the experiment, to perform the computational post-analysis to check the relevant activation cross-section data and, in case of discrepancies, identify the cross-sections causing the deviations.

Pre-calculations were performed with the MCNPX code and LA-150h cross section data for the Li(p,xn) reaction to predict the intensity and the spectral shape of the quasi mono-energetic neutron source employing a thin lithium target and a carbon proton beam stopper. The comparison of calculations with available experimental data has shown that MCNPX together with the LA-150h library predicts satisfactorily the energy-angular distributions of the neutrons emitted from the Li/C target. As an example, Fig. 6 demonstrates such a comparison with measurements performed at the CYRIC facility in Japan [8].

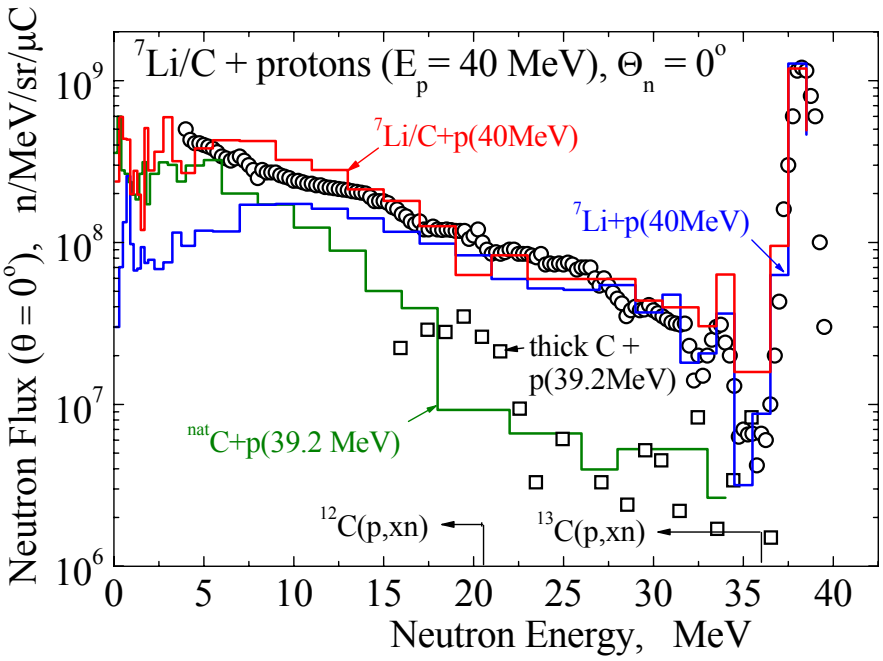

Fig. 6: Spectrum of neutrons emitted from the Li/C target at an incident proton energy of 40 MeV. Points – measurements [8], curves – MCNPX/LA150h calculations.

The activation of Bi samples was performed at the isochronous cyclotron U120M at NRI/Rez [7] in the frame of the EFDA task TW6-TTMN-002B, D6. The neutron target consisted of a thin ^{7}Li foil backed by a carbon beam stopper, cooled by flowing water. The measurements have been performed at incident proton energies of 22.1, 27.1, 32.1 and 36.5 MeV, producing neutron spectra having peaks at the energies 19.6, 24.3, 29.6 and 34.3 MeV, respectively. The Bi foils were located at 4.8 and 8.8 cm distance from the target and were activated during 17-20 hours. The samples were analysed off-line by the gamma-spectroscopy technique employing two calibrated HPGe detectors with an energy resolution of 1.8 keV at 1.3 MeV. The unstable, decaying isotopes were identified on the basis of the half-lives $T_{1/2}$ and the γ-ray energies and intensities. The measurement period of decaying gammas ranged from minutes to 100 days.

The Li/C source neutron spectra calculated at the locations of the Bi sample indicated that mono-energetic peaks account for 30-50% of the total flux, the rest being the low energy neutrons from the Li breakdown reaction and re-scattering on the target assembly. To assess the contribution of all neutrons to the ^{209}Bi(n,xn) activation reaction, we used the FISPACT-2007 inventory code and the EAF-2007 activation cross section library [9]. The results of the activation calculations were compared with the measured specific activities for ^{207}Bi, ^{206}Bi and ^{205}Bi isotopes produced by the (n,3n), (n4n) and (n,5n) reactions on the target nucleus ^{209}Bi. The comparison is showing satisfactory agreement at incident neutron energies around 20 MeV, but increasing discrepancies at higher energies. These results indicate the need for updating the ^{209}Bi(n,xn) reaction cross sections in the EAF-2007 library.

Staff:

U. Fischer
S. P. Simakov

Literature:

[7] P. Bém, V. Burjan, U. Fischer, M. Götz, M. Honusek, V. Kroha, J. Novák, S.P. Simakov, E. Šimečková, The NPI Cyclotron-based Fast neutron Facility, Int. Conf. on Nuclear Data for Sci. and Techn. (ND-2007), Nice 2007; EDP Sciences 2008, p. 555-558

[8] Y. Uwamino et al., NIM A389 (1997) 463.

[9] R.A. Forrest, J. Kopecky, J-Ch. Sublet, The European Activation File: EAF-2007 neutron-induced cross section library, Report UKAEA FUS 535, Culham, 2007

Deliverable 8
Integral activation experiment with Erbium in a fusion peak neutron field

The activation induced by neutrons in the materials of fusion power plant reactors represents a central safety-related topic from the viewpoint of licensing, maintenance, decommissioning, and accident management. The activity of the materials is mainly produced by neutrons of the fusion peak energy range, where the number of reaction channels is a maximum, and by thermal neutrons because for some reactions the cross section is large in this energy region [10].

Erbium oxide was suggested as an electrically insulating coating for liquid metal breeder blankets and tritium barriers [11]. As such, it would be employed near the first wall as well as in rear areas of the blanket and hence would be exposed to intense fluxes of fast and slow neutrons.

In the present work, samples of pure Er were irradiated with D-T neutrons, and the measured γ-activities were analysed with the European Activation System EASY-2007 [12] with the objective to validate the relevant cross sections contained in the activation file EAF-2007. The investigation was focused on activation by fast neutrons; the fluence of the slow neutrons could not be determined with sufficient accuracy enough such as to draw conclusions from the C/E (calculation/experiment) ratios obtained.

Experiment

In order to determine the time slot after irradiation when activity measurements should be done, a calculation with FISPACT of the EASY-2007 package was carried out. Erbium was assumed to be irradiated with 14 MeV neutrons at power plant conditions, at a flux corresponding to a power density of 1.0 MW/m^2 for a period of one year. The results obtained for the contact dose rate as a function of the decay time after irradiation are shown in Fig. 7.

Up to the recycling limit of the material, the dose rate is dominated by the activities of ^{161}Er, ^{165}Er, ^{168}Tm and ^{166m}Ho. The recycling limit as recommended by ICRP [13] is reached after approximately 300 years, although the contact dose rate from 10 to 300 years is only about 50% above this limit. The cooling time required to reach the hands-on limit is determined by ^{166m}Ho and it is reached after approximately 14,000 years.

Two irradiations have been done to investigate the major γ-ray activities: A short irradiation with γ-ray spectra taken at decay times in the range of minutes up to one hour and a longer irradiation with γ-ray spectra taken at decay times from 17 to 65 hours after the irradiation.

The irradiation of the samples was performed with the D-T neutron generator of Technische Universität Dresden. The mean neutron energy of the fusion peak was 14.78 MeV; the full width of the peak at half maximum was 0.30 MeV. The tritium target was a rotating disk loaded with approximately 1.85*10^{12} Bq (50 Ci) tritium and bombarded with a deuterium ion beam with an energy of 300 keV and a current of 4 mA.

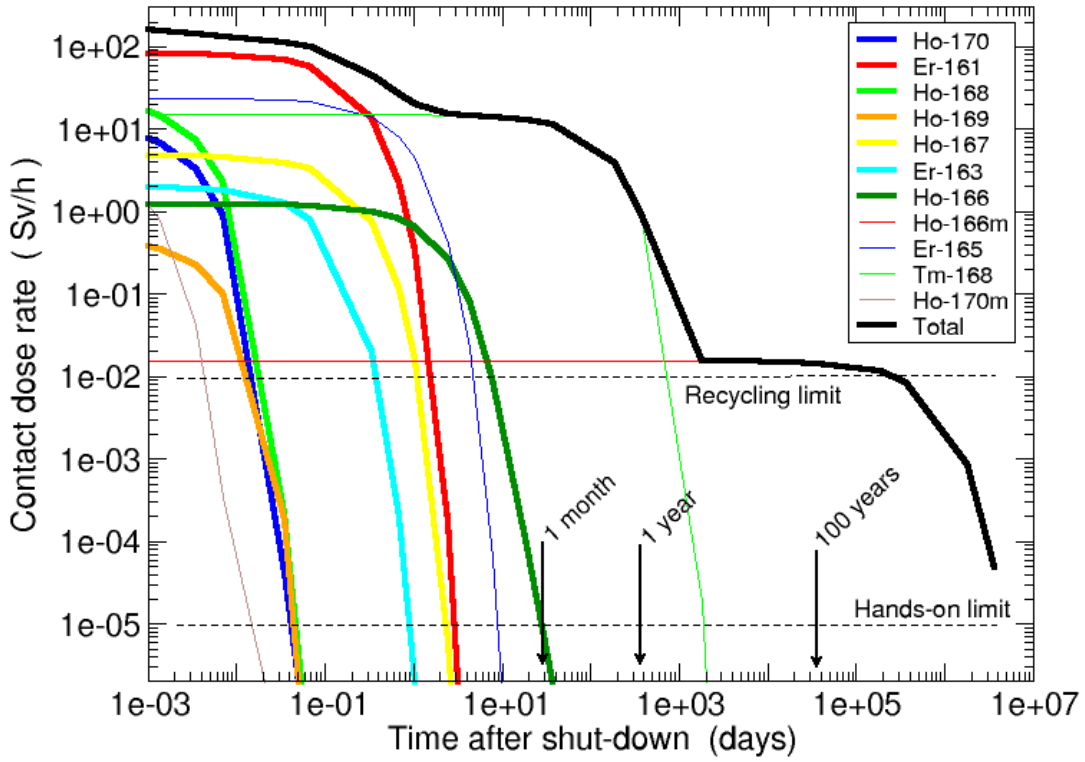

Fig. 7: Contact dose rate calculated for the different radio-nuclides after irradiation of Er with fusion peak neutrons of 1.0 MW/m2 power density for one year as a function of the decay time. Calculation with EASY-2007 (FISPACT and EAF-2007 data).

The sample material had a purity of 99.95%. The two samples were discs with a thickness of 0.62 mm, a diameter of 25 mm and a mass of 2.8828 g and 2.8981 g for the short and long irradiation, respectively.

The time profile of the neutron source strength was monitored with a ^{238}U fission chamber and a silicon semiconductor detector for the associated α-particle of the D-T neutron source reaction in case of the short irradiation. For the long irradiation, only the fission chamber was used since the radiation damage to the semiconductor would have been too high. The absolute fluence at the position of the sample was determined by simultaneous activation of niobium foils and evaluating the activity induced by the ^{93}Nb(n,2n)^{92m}Nb reaction. The cross section of this reaction was considered to be constant in the range of 14–15 MeV with a value of 463 mb and an uncertainty of 4%. The long irradiation time was 8.54 h with a total neutron fluence of $7.17 \cdot 10^{13}$ cm^{-2}. The short irradiation time was 1300 s with a total neutron fluence of $1.52 \cdot 10^{12}$ cm^{-2}.

After the irradiations, γ-ray spectra were taken with a high-purity Ge-spectrometer. The γ-activities identified by energy and half-life were used to determine the nuclide activities using γ-yield data from EAF-2007. The attenuation of the neutron and γ-ray fluxes in the sample as well as the geometry factors (source-sample and sample-detector) were determined by 3D Monte Carlo calculations.

Results and conclusions

The experiments were analysed with the version EASY-2007 of the European Activation System. The results are presented in Table 1.

Table 1: Results obtained for the activity of radionuclides; nuclides identified, their half-life and the γ-rays (Eγ) with yield data (Yγ) used to determine the activity, the neutron reaction producing the nuclide, the ratio of calculated-to-experimental activity (C/E) and the uncertainty of both experimental (ΔE/E) and calculated (ΔC/C) activities. Half-lifes and branching are taken from JEFF-3.1.1. Irradiation times were 1300 s for all measurements except Ho-166 which was measured after an irradiation time of 8.54 h. Note that the yield of the pathways depends on the irradiation time.

Nuclide	Half-life	Eγ (keV)	Yγ	C/E	ΔE/E (%)	ΔC/C (%)	Pathway	(%)
^{161}Er	3.21 h	826.6 592.6 211.2	0.641 0.037 0.122	1.08	8.4	7	^{162}Er (n,2n)	100.0
^{167}Ho	3.10 h	346.5 321.3 237.9	0.573 0.241 0.052	0.95	5.6	26	^{167}Er (n,p) ^{168}Er (n,d)	84.7 13.9
^{168}Ho (^{168m}Ho)	2.99 min (2.2 min, branching to ^{168}Ho 0.995)	821.1 815.9 741.3	0.340 0.182 0.364	0.97	7.5	14	^{168}Er (n,p)	100.0
^{170}Ho (^{170m}Ho)	2.78 min (43 s, branching to ^{170}Er 1.000)	931.8	0.349	0.64	18.7	63	^{170}Er (n,p)	100.0
^{163}Er	1.25 h	1113.5	4.9e-4	0.77	9.4	15	^{164}Er (n,2n)	100.0
^{169}Ho	4.7 min	852.9 788.4	0.071 0.134	0.89	23.5	179	^{170}Er (n,d)	100.0
^{166}Ho (^{166m}Ho)	1.12 d (1200 yr, branching to ^{166}Er 1.000)	1662.4 1581.9 1379.4	1.16e-3 1.81e-3 9.30e-3	0.90	6.0	59	^{166}Er (n,p) ^{167}Er (n,d)	93.1 6.7

The uncertainty of the calculated activity (ΔC/C) includes both cross section and half-life-errors as estimated by EASY-2007. The uncertainty of the experimental value (ΔE/E) takes into ac-count possible errors of the γ-activity measurements (statistical uncertainty of the γ-ray counting, the uncertainty of the efficiency determination of the spectrometer including the geometry factor), of the sample mass, of the γ-yield data, and of the neutron flux monitoring.

It may be stated that for four of the dominant activities in the decay time range up to several days of Er irradiated with fusion peak neutrons, the EASY-2007 data result in calculated predictions within 10% or better of the activities obtained experimentally. The ^{163}Er activities are underestimated by the calculation, the C/E ratio was 0.77 in this experiment. The ^{170}Ho production is considerably underestimated by the calculation, and the estimate of the experimental error is significantly smaller than that of the calculation. The estimated calculation error of 179% for the ^{169}Ho production is rather large, however, the C/E ratio is 0.89% in the present experiment. Therefore, the EAF database for the ^{170}Er(n,d)^{169}Ho reaction should be improved in view of the error estimate produced by the EASY calculation despite the relatively large experimental error.

As the experimental uncertainties (ΔE/E in Table 1) in many cases are smaller than the uncer-tainties of the calculation (ΔC/C in the table), the present measurements could contribute to further improve the EASY data base.

It may be concluded that the recycling limit of Er irradiated with fusion peak neutrons at power plant conditions will be reached at decay times smaller than approximately 300 years.

Staff:

H. Freiesleben (Tu Dresden)
A. Klix
K. Schomburg (TU Dresden)
K. Seidel (TU Dresden)
S. Unholzer (TU Dresden)

Literature:

[10] R.A. Forrest, J. Kopecky, M. Pillon, A. Klix, S.P. Simakov, J-Ch Sublet, P. Bem, M. Honusek and E. Simeckova, Validation of EASY-2007 using integral measurements, Report Culham Science Centre, UKAEA FUS 547, 2008.

[11] D. Levchuk, S. Levchuk, H. Maier, H. Bolt, A. Suzuki, Erbium oxide as a new promising tritium permeation barrier, J. Nucl. Mat. 367-370 (2007), pp. 1033-1037

[12] R.A. Forrest, The European Activation System: EASY-2007 overview, Report Culham Science Centre, UKAEA FUS 533, 2007.

[13] ICRP recommendations, ICRP publication 60, Annals of the ICRP 21

Materials Development
IFMIF

International Fusion Materials Irradiation Facility (IFMIF) Test Cell

In the reporting period the IFMIF activities were specifically characterized by several design revisions, specifically regarding the Test Cell architecture. In addition, substantial progress has been achieved regarding the fast installation of a large, 1:1 scale Helium loop, the HELOKA-LP facility, at FZK.

The main activities and achievements in the IFMIF test facilities field may be summarized as follows:

Target and Test Cell (TTC)

The reference IFMIF TTC design summarized in the CDR report has been reviewed and evaluated during the reporting period. For the purpose of precise and flexible positioning of test modules against the back-plate, a revised design of TTC has been developed. After the evaluations of the conceptual design works and intensive international discussion, a referential table for the TTC design has been released.

For the purpose of providing variable operation environments, flexible accessibility for RH and precise/reliable positioning for test modules, an improved TTC conceptual design (MTC) has been introduced and developed in the reporting period. The MTC merges the advantages of the previous concepts, avoids critical drawbacks of the previous designs, respects the list of requirements, and provides flexibility in critical details. The sketch of MTC design is illustrated in Fig. 1.

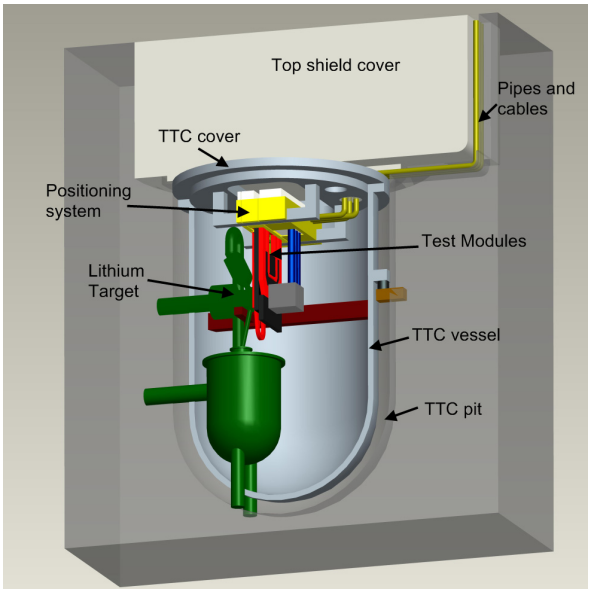

Fig. 1: The sketch of the MTC design.

Compared to the reference design, the following main changes have been addressed in the new design:

1. A closed, actively cooled, removable, circular-shaped TTC-vessel is introduced instead of using a welded stainless steel-liner covering the inner surface of the rectangular Target and test cell. Comparing to the fixed rectangle-shaped liner-on-concrete test cell in the reference design, this design has advantages on achieving variable inner environment from vacuum to atmospheric pressure, laying active cooling channels, distributing thermal stresses, etc. Additionally, the TTC vessel is designed to be located in a concrete pit with gaps to the concrete wall to allow the access to the vessel can from outside for inspection. The movable design of the vessel also provides flexible adjustment for accurate positioning of the in-cell components against the beam line.
2. The functions of irradiation shielding, leakage tightness sealing, and test module positioning are separated to independent blocks to allow optimizing these functions independently. In MTC design:
   a. an actively-cooled single-piece of shielding plug TMs is adopted without pipes/cables connected to test modules,
   b. separated test cell cover is applied for leakage tightness sealing to allow variable inner environments of TTC, and

c. test modules are independently installed at different positioning blocks which can be moved at the direction of beam line for precise and reliable positioning against the backplate.

3. Test modules are connected outside of the TTC vessel through a flexible quick-coupling system to allow the RH access to backplate or lithium target without disconnecting test

High Flux Test Module (HFTM)

The progress regarding the HFTM was focused on the design optimization, through experiments in the helium loop ITHEX, thermohydraulic calculations, the design of the Na/NaK filling station and the test of the brazing technique. The upgrade of ITHEX facility for new experiments was also finalized.

Design of HFTM container

This task includes the technological aspects, as brazing and welding techniques, the NaK filling procedures, extended thermohydraulic calculations, and design considerations. Result obtained in the different fields may give rise to improvements in the conceptual design of the HFTM that are accordingly implemented in the design.

- Test Modules: A major progress is that the reflector positions can now be used as additional irradiation volume. Although big flux gradients cannot be avoided in these reflector positions, its irradiation volume is now equipped with additional rigs, that can be cooled and heated as the rigs in the reference volume behind the beam footprint.
- High flux container: The design has been reconsidered. Individual flow control is now possible for all rigs in the target and reflector position. In addition thermal induced secondary stresses have been minimized. Several other design improvements have been done.

The design of the container was revised in order to introduce a number of new requirements and general design improvements. The main points which were addressed are:

- Individual flow control to adjust the needed mass flow and inlet temperature for the individual compartments of the container separately.
- Allow controlling the mass flow into the lateral zones of the container (reflectors) and its relation to the mass flow into the main irradiation zones (inner compartments).
- Usage of lateral area of the container for additional irradiation programs.
- Improve the general design strategy of the container for improving reliability and reducing risk of failures. Separate the thin walled and extensively neutron heated irradiation container (inner zone with reflector zone) from the support frame.
- Allow for thermal deformations of the inner irradiation zones without causing high thermal stress levels by bearing it in the support frame and by introducing some flexibility in the hydraulic connections.
- Include the Helium supply lines into the support frame to hold its temperature at a relatively low and almost constant value during the irradiation campaigns.
- Increase the safety in terms of internal pressure loads in the container by slightly increasing the wall thickness (by ~0.5 mm).
- Design the container in a way that plastic deformations won't take place. These could be critical as the behavior of the materials under IFMIF conditions is not sufficiently known. Reducing thermal stress levels by design and introducing some freedom for swelling deformations is considered reasonable.

The design of the HFTM was improved in several steps with the current status of the design being shown in Fig. 2.

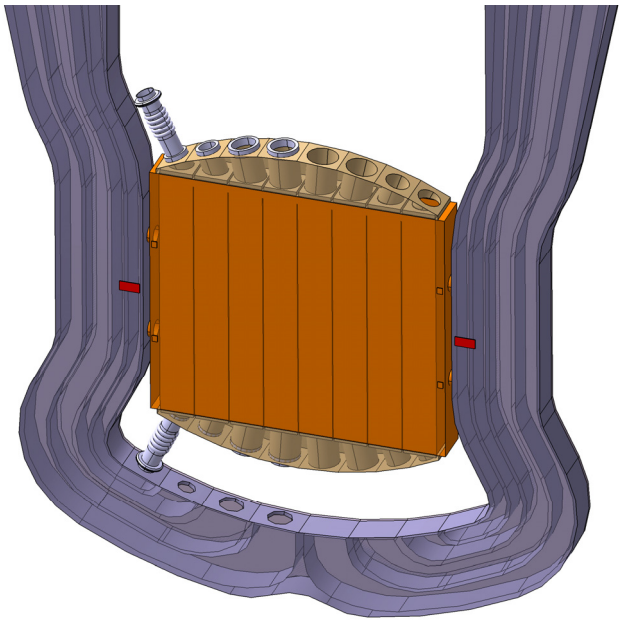

Fig. 2: Revised draft baseline design of the HFTM container.

In the revised baseline design of the HFTM container the following solutions are introduced considering the list of requirements and improvements given before:

- Introduction of a symmetric „horse shoe“ shaped support and feed structure.
- Cut free lateral reflectors; decouple the massive reflectors from the fragile inner container zone.
- Usage of Rig-like reflectors, resulting in an 8x3 modular design of the inner part of the HFTM. Additional irradiation volume (e.g. for tungsten specimen) is available and mechanical advantages (reduced thermal stress) is reached.
- Introduction of individual feed lines per compartment to control mass flow.
- Flexible mounting of the mechanically separated container zone, the vertical position of the irradiation container in the support frame is fixed in the mid-beam level by specific bearing elements.
- The irradiation container can be decoupled from the support structure for replacement and exchange of specimen.

The support frame can be fabricated by milling the flow channels into a massive body and welding the cover plate on it. Internal flow channels are closed by transparent welding (e-beam or laser). The inner part of the irradiation container is fabricated by EDM technique, while the upper and lower connector parts for the hydraulic piping will be welded to the irradiation zone. While the flow channels at the lower (cold) side of the container are separated, the different compartments are hydraulically connected on the upper, the hot side.

CFD analyses

The analyses performed with the STAR-CD CFD code in the frame of the HFTM development were concentrated on two main tasks:

A) Pre-experiment calculations for the HFTM-SR single rig experiment: Temperature fields of the structure were simulated, as input for the following FEM calculation.

B) The effect of modification of several design properties and analysis assumptions were assessed in parametrical studies, to provide useful guidance for the further optimization of the whole HFTM in the later stage.

Manufacturing technology

A liquid metal filling of the irradiation volume is foreseen to guarantee a homogenous heat transfer between the specimen stack and the capsule wall. To assess systematically the capability to fill narrow gaps (as between the specimen, or between specimen and the capsule walls), a dedicated experiment was prepared. For this experiment, channels with gap widths

of 0.05, 0.1, 0.2 and 0.4mm, each of the length 120mm have been machined in a block of stainless steel. These channels are fed with liquid metal from a common manifold, into which the liquid metal is pressed by a screw driven cylinder. This setup mimics the situation of the specimen stack in the capsule, where the liquid metal must flow in a multitude of gaps between the specimens, each with different flow resistance. It can therefore be estimated by experiment (a) which pressure will be needed for the liquid metal filling procedure, and (b) which is the biggest gap size which will not be filled with liquid metal, and which will have to be considered as thermal resistance for calculations of the specimen stack temperature. For this experiment, the screw driven filling apparatus and the flow gaps have been manufactured, and the necessary glove box to handle the liquid metal has been prepared.

Tests in Helium loop ITHEX

In 2008, the experimental work concentrated on the development and testing of the deformation instrumentation for the HFTM single rig experiment and the following HFTM mockups. Additionally, flow experiments were performed in the ITHEX-F mockup.

The HFTM-SR single rig experiment shall be conducted in the ITHEX helium loop. The test section consists of a single 1:1 IFMIF HFTM rig containing a capsule, which is housed in a compartment to form cooling channels as found in a HFTM compartment for three rigs. Progress was achieved on the following issues:

- Electronic setup has been improved to a noise level for nanometer resolution
- Typical reproducibility has been determined as 2-3µm
- Measurement spot size reduced to 6mm, installation height needed is about 600µm
- An application tool for installation in the insulation gap, and an in situ calibration procedure were devised.
- Several measurements of the axial pressure profile along the sidewalls of a flat channel mock-up were performed with helium and nitrogen gas at inlet pressure levels of 0.15 and 0.3 MPa.

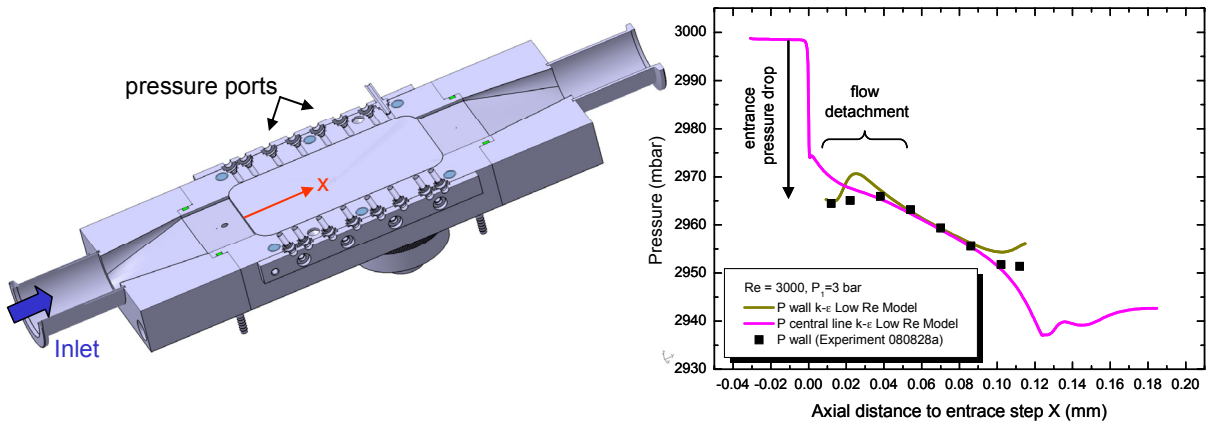

Fig. 3: Left: ITHEX-F minichannel (top cover cut away) showing the change of the channel cross sections along the flow path and the positions of the pressure ports.
Right: Comparison of CFD calculations of the pressure field with experimental values.

- First comparisons with CFD calculations were also performed und showed good agreement. The results for the experiment and two CFD calculations using different turbulence models are shown in Fig. 3. The large pressure drop over the entrance step can be very well predicted by the chosen turbulence model. Such a situation is

very similar to the entrance nozzle of the HFTM. Also the slope of the pressure drop in the minichannel is also predicted with satisfactory precision.

Staff:

F. Arbeiter
Y. Cheng
B. Dolensky
D. Eilert
U. Fischer
J. Freund
S. Gordeev
V. Heinzel
T. Heupel
T. Ihli
Ch. Klein
K.-H. Lang
D. Leichtle
M. Lux
G. Messemer
M. Mittwollen
A. Möslang
N. Scheel
S. Simakov
R. Stieglitz
E. Stratmanns
K. Tian
S. Vielhaber
P. Vladimirov

Literature:

[1] F. Arbeiter, S. Gordeev, V. Heinzel, T. Ihli, D. Leichtle, A. Möslang and V. Slobotchouk, Features and optimization approaches of the entrance section cooling gas flow of the IFMIF High Flux Test Module, Fusion Engineering and Design, In Press, Corrected Proof, Available online 3 September 2008.

[2] D. Leichtle, F. Arbeiter, B. Dolensky, U. Fischer, S. Gordeev, V. Heinzel, T. Ihli, K.-H. Lang, A. Moeslang, S.P. Simakov, V. Slobodchuk, E. Stratmanns, IFMIF High Flux Test Module - recent Progress in Design and Manufacturing, Fusion Engineering and Design, Volume 83, Issues 10-12, December 2008, Pages 1484-1489.

[3] F. Arbeiter, C. Klein, T. Ihli, Prospective Testing and Design Validation Program for the IFMIF High-Flux Test Module within the EVEDA Phase, presented at 25th Symposium on Fusion Technology (SOFT), 15-19 September 2008, Rostock, Germany.

Helium Gas Loop (HELOKA-LP): Procurement and Installation

In the scope of the development of the International Fusion Materials Irradiation Facility (IFMIF) test facilities, mainly the high flux test module, the procurement of a specific helium loop test facility was decided. Therefore, this task aims at the procurement, installation and commissioning of a helium loop suitable for testing of large scale components, supporting the engineering design of the High Flux Test Module (HFTM) during the EVEDA period, and allowing a design validation of a 1:1 HFTM mockup under realistic operation conditions.

The detailed planning of the process, the piping system and the control system of the facility was performed by the contractor, Kraftanlagen Heidelberg (Fig. 1). In 2008, all major components, including an auxiliary hall to place among others the helium compressor (Fig. 2) and piping elements have been installed on the FZK building site, and the gas loop piping system was closed. The process control system (switch cabinets and software) was produced, factory tested, and delivered to FZK. Start of operation is scheduled for March 2009.

The major components of the loop have been selected as follows:

Helium compressor	Kaeser type FSD 571, 355kW, 9bar
Gas heater	OhmEx type STR0025, 300kW
Refrigerating machine	McQuay, 743kW
Automation system	Siemens SIMATIC S7-417 F

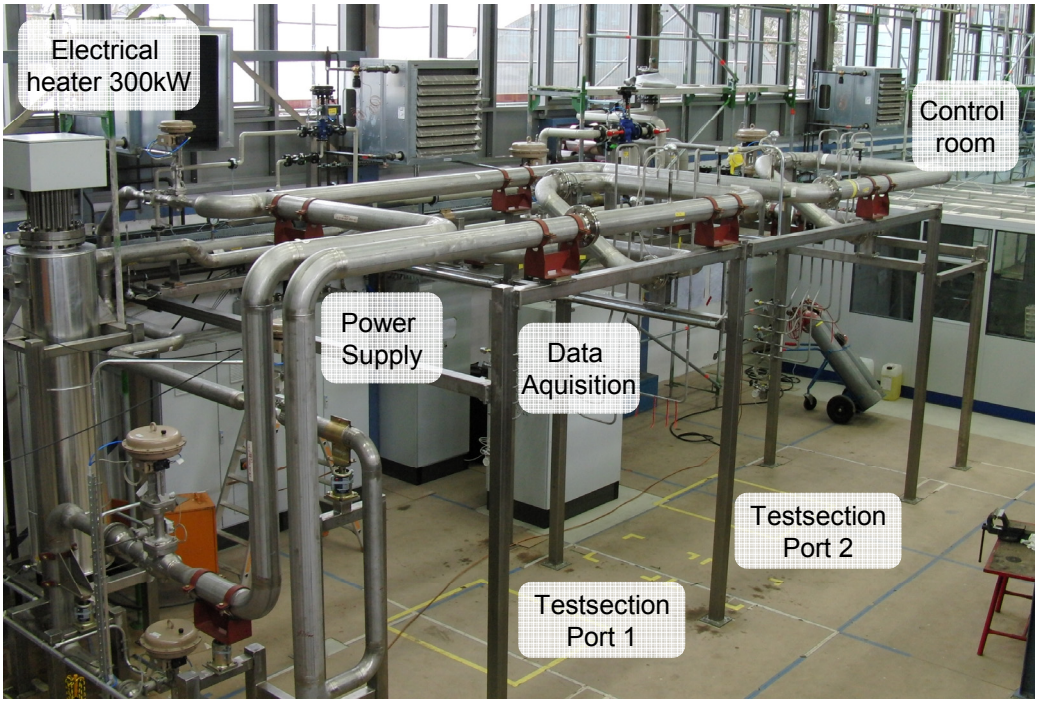

Fig. 1: Piping system and components of the HELOKA-LP facility with piping and support structure.

.

Fig. 2: Installation in new auxiliary hall (building 508).

Staff:

O. Albrecht
F. Arbeiter
J. Freund
T. Ihli
Ch. Klein
G. Messemer
E. Stratmanns
K. Zinn

International Fusion Materials Irradiation Facility - Engineering Validation Engineering Design Activities (IFMIF - EVEDA)

Study of the Effect of Tungsten Plates on Material Irradiation Conditions in the Medium Flux Test Module (MFTM)

Introduction

Besides irradiation of structural materials to high dose in the high flux test module, in-situ creep-fatigue and tritium release experiments are foreseen in the medium flux test module of IFMIF. IFMIF is designed to mimic fusion irradiation conditions of structural materials as close as possible.

Materials and geometry of MFTM can be selected to change neutron energy and flux within some range for adjustment of irradiations conditions for specific materials. For example, tungsten neutron-spectrum-shifter-plates before and after creep-fatigue machine were proposed to adjust recoil spectra in creep-fatigue samples. For lithium based ceramics tritium to dpa production ratio is of the most importance and should be fitted.

However, it is difficult to fulfill all these conditions for all materials at the same time. Therefore priorities for these experiments should be considered based on feasibility as well as on their relevance.

It should be noted that the *in-situ* creep-fatigue machine (CFM) has only 3 samples. Although the *in-situ* experiments provide more realistic estimate of the fatigue lifetime then the post irradiation experiments, hardly the DEMO design will be based on the very limited in-situ database. On the other hand, in the present concept of HCPB beryllium serves as neutron multiplier and tritium contamination of 300 tons of Be pebbles poses a severe safety problem. Li-based ceramics are used for the efficient tritium breeding.

The aim of this study is to investigate what irradiation conditions are required for each experiment foreseen to be performed in MFTM and what experiments could be performed in parallel. Consequences for the MFTM design and choice of material for irradiation are discussed.

Method

The d-Li neutron source and neutron transport were simulated by Monte Carlo code MCDeLicious, which is an extension to MCNP-4C with the capability of simulating the generation of neutrons, γ-rays and other d-Li reaction products on the basis of the evaluated Li(d,xn) reaction cross section data (Task TW4-TTMI-003, deliverable D9). Neutron cross sections from general purpose high-energy libraries were used for the transport and nuclear response calculations.

To represent the IFMIF test cell for the Monte Carlo calculations a comprehensive three dimensional model has been developed in the frame of Task TW4-TTMI-003 D5a. It reflects the latest IFMIF design modifications and describes in detail the geometry and material specifications of the IFMIF test cell: the deuteron beam pipe, the lithium loop, the vertical test assemblies accommodating the high, medium and low flux test modules, as well as the cover, walls and floor of the test cell.

Since d-Li IFMIF neutron source generates a neutron spectrum extending up to 55 MeV, the activation and transmutation calculations require cross sections exceeding the traditional limit of 20 MeV. For this reason the Intermediate Energy Activation File IEAF-2001 has been used which includes neutron reaction cross sections up to 150 MeV (validated in the frame of Task

TW4-TTMN-002, D5). The inventory codes ALARA and FISPACT were used to assess the tritium and helium production.

Results

Previous studies have shown that recoil spectrum inside the creep-fatigue samples can be made very close to that expected for fusion by positioning tungsten neutron-spectrum-shifter-plates. Several schemes of their placement were considered. It appears that the variants with one or two plates behind the CFTM provide the best fit of DEMO recoil spectra.

Tritium and helium production in lithium based ceramics depends crucially on the thermal neutron spectrum. This part of the spectrum can be effectively increased using the same tungsten plates as well as carbon moderator blocks. The results of calculations shows (see Figure 1) that

- increase of C-moderator size result in moderate increase of gas production;
- more pronounced increase of gas production can be achieved by using tungsten neutron-spectrum-shifter-plates placed before CFM;
- although the gas production rates in TRM are significantly lower than those in DEMO, the ratio of tritium to helium production in TRM (0.98 appm T/appm He) is very similar to that in DEMO (0.9 appm T/appm He).

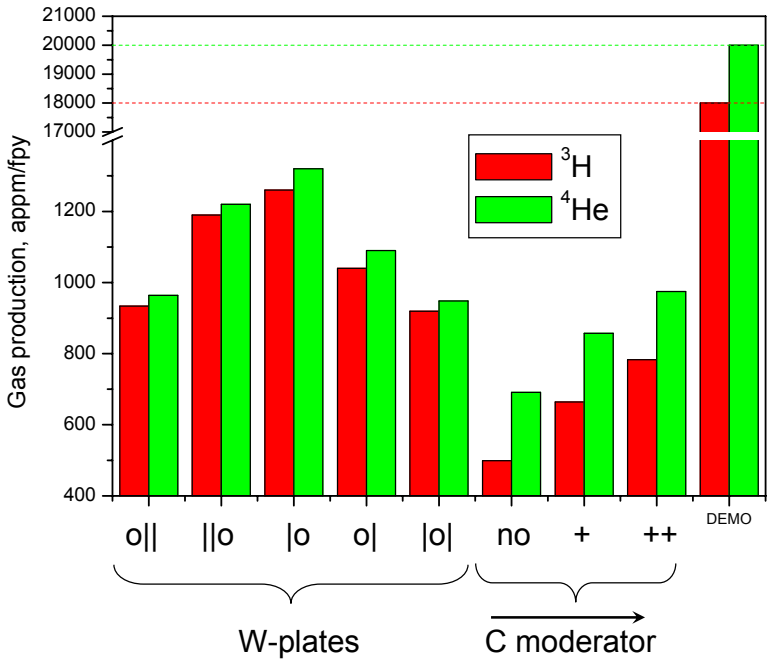

Fig. 1: Tritium and helium production rates in Li_4SiO_4 irradiated in TRM of IFMIF. Symbols show the tungsten plate positioning relative to CFM: o|| and ||o - both plates behind or before, |o and o| - one plate behind or before and |o| - one plate before and one behind CFM. Other symbols are related to carbon moderator: “no” – without C-moderator, “+” – with C-moderator, “++” – increased size of the C-moderator.

Gas production in beryllium seems to be independent of the thermal neutron spectrum. As can be seen from the Figure 2 carbon-moderator does affect neither gas production nor damage in beryllium. Helium production rate is essentially the same as that expected for DEMO, while damage production in Be inside TRM is somewhat lower (10 dpa/fpy vs 17 dpa/fpy for DEMO).

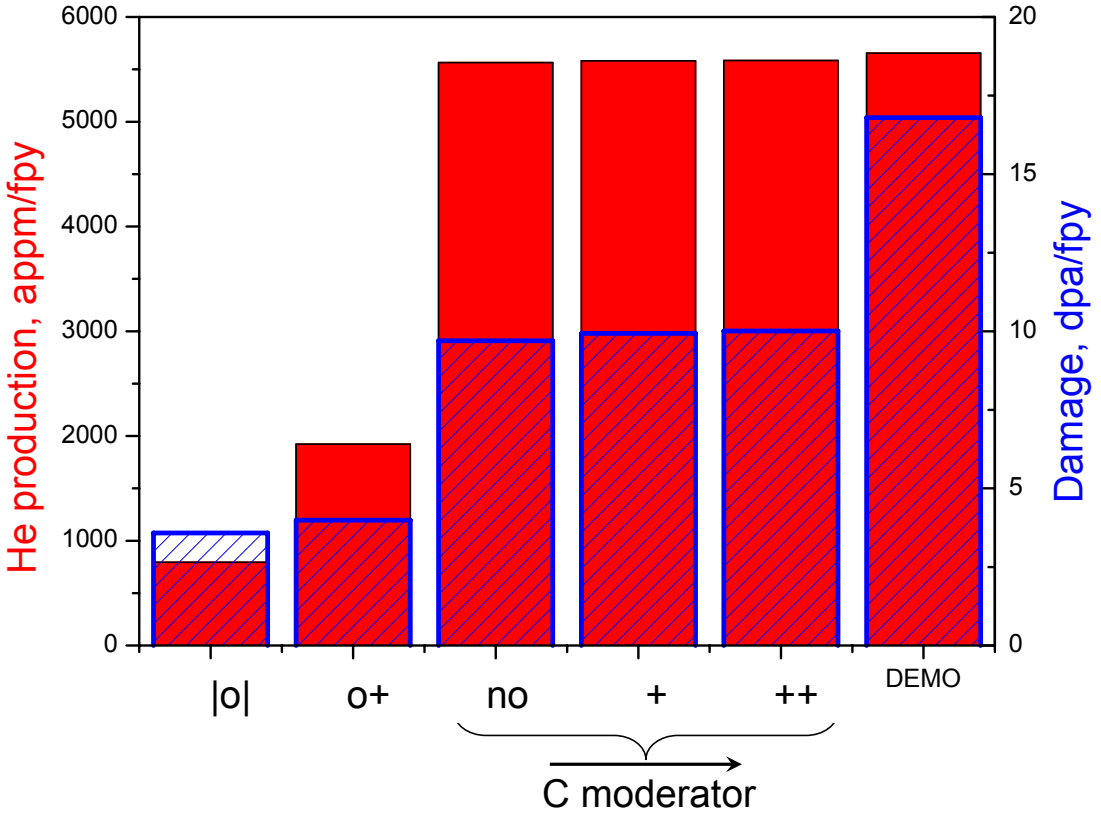

Fig. 2: Helium and displacement damage rates in Be irradiated in TRM of IFMIF. Symbols have the same meanings as in Figure 1.

Conclusions

Some conclusions relevant for the IFMIF MFTM design can be drawn based on the results of this study.

- Irradiation of Li-ceramics can be performed together with in-situ creep-fatigue experiments.
- W-plate and extended C-moderator are necessary for the increase of gas production in Li-ceramics to the fusion relevant level.
- To increase gas production in Be to fusion relevant values it is necessary to remove temporary CFTM and W spectral shifter and move TRM upstream.
- Additional carbon moderator/reflector does not increase significantly tritium production in Be and can be removed if tritium release from Li-based ceramics is of second priority.
- These contradictions can be solved by setting priorities for material irradiation matrix for TRM, which should be done inside the international IFMIF users' community.

Staff:

U. Fischer
A. Möslang
S. Simakov
P. Vladimirov

Literature:

[1] V. Heinzel, F. Arbeiter, B. Dolensky, U. Fischer, S. Gordeev, K.H. Lang, D. Leichtle, Möslang A., St. Simakov, E. Stratmanns, S. Slobodtchouk and P. Vladimirov, *IFMIF high flux test module and test cell—Design and design validation*, Fus. Eng. Design 82 (2007) 2444-2450

[2] P. Vladimirov, A. Möslang, U. Fischer, S. Simakov, *Material Irradiation Conditions for the IFMIF medium Flux Test Module*, J. Nucl. Mater. 367-370 (2007) 1574-1579

[3] P. V. Vladimirov, A. Möslang, P. Marmy, *Material Responses in IFMIF Creep-fatigue Testing Machine*, Fus. Eng. Design 83(10-12) (2008) 1548-1552

[4] P. Vladimirov, S. Bouffard, *Displacement damage and transmutations in metals under neutron and proton irradiation*, Eds.: J. L. Boutard, S. Dudarev and G. Martin, Fusion and Generation IV Fission Power Reactors: Behaviour of Materials Subjected to Fast Neutron Irradiation, Compt. rend. Phys. 9 (2008) 303-322

Fuel Cycle
Vacuum Pumping

TW5-TTFF-VP 58
Upgrade of TIMO

Background and objectives

Following successful completion of the testing of the 50% scale ITER model pump, a full scale ITER torus prototype torus cryopump (PTC) is being designed and constructed for testing in the TIMO facility. Certain features of the TIMO infrastructure need to be upgraded to accommodate the larger ITER-scale pump, and the scope of this task is to provide for the supply and installation of these features so as to have a replication of ITER conditions in many aspects for the new, bigger sized pumps in the same way as it was provided for the 50% scale model pump. The fully upgraded facility is called TIMO-2. In the reporting period, the enhancement activities towards TIMO-2 were continued and the work in most subsystems could be completed [1].

Upgrade of the TIMO regeneration vacuum pump station

To adapt the TIMO facility to the requirements concerning the regeneration pump down time (10 Pa cross-over pressure in 150 s) for the ITER PTC, a new forevacuum pump train (type WOD 18000, Pfeiffer Vacuum) was delivered, installed and tested. The new pump station, which was especially designed for pumping hydrogen includes a 2000 m³/h roots pump backed by a 250 m³/h two-stage rotary vane pump (see Fig. 1).

Fig. 1: The new regeneration vacuum pump station of TIMO-2.

New cryotransfer line for TIMO-2

The future programme for TIMO-2 foresees a full testing of the PTC prototype and conformity testing for a few of the serial torus and cryostat cryopumps. In order to be more versatile and to come up with minimised turnover times for pump exchange operations, it was decided to replace the existing rigid cryotransfer line (between the cold valve box and the pump) by a flexible cryoline. This also allowed checking manufacturability of such a line according to the latest revised ITER design requests, especially 25 bar design pressure and flexible cryojumpers (Johnston coupling connections).

The new TIMO-2 transfer line includes two parts as shown in Fig. 2. The fixed part of the new transfer line (see Fig. 2, left) will be connected to the TIMO valve box, where the various gaseous helium flows at different temperature levels between 4.5 K and 470 K are controlled. Following the ITER cryojumper concept, the second part of the new line is a flexible corrugated cryotransfer line (see Fig. 2, right) with allocated Johnston couplings at the end of these flexible parts. To be able to qualify and test the cryoline within a closed cryogenic cooling loop without an installed cryopump, a bypass system is integrated.

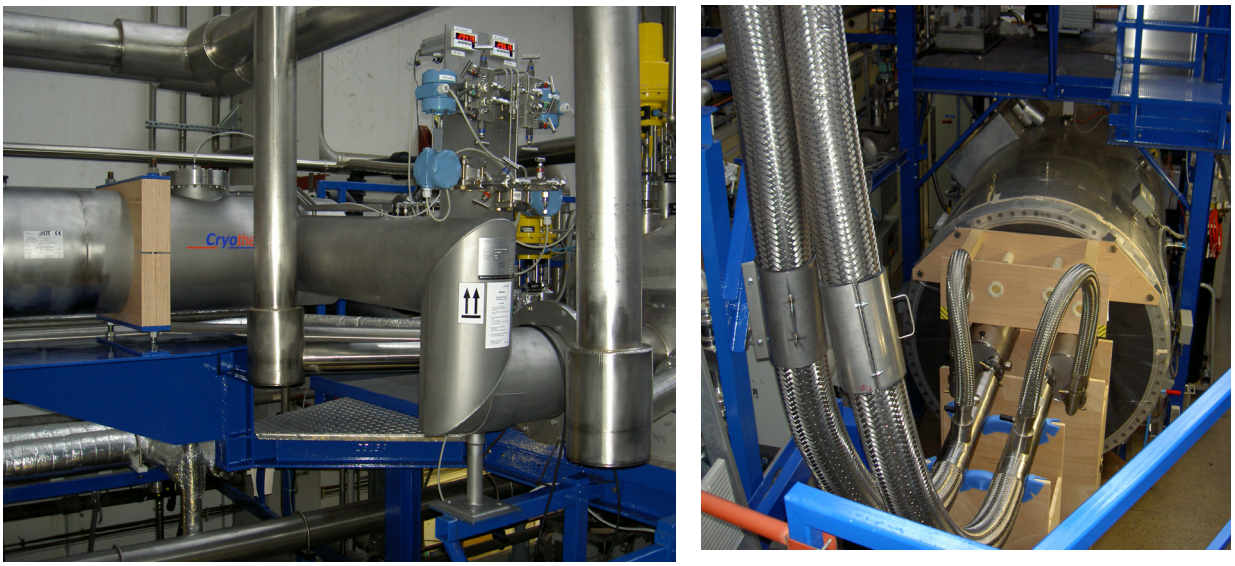

Fig. 2: The new TIMO-2 transfer line with fixed part (left) connected to the TIMO valve box and the flexible part (right) with Johnston coupling for the connection of the cryogenic supply with PTC pump flange.

The design of this ITER relevant cryoline was prepared at FZK, and an order for the manufacturing was placed to the company NEXANS, Hannover. The NEXANS company, which is specialized for manufacturing flexible corrugated cryotransfer line produced together with the sub supplier CRYOTHERM, Kirchheim (Sieg) which has more experience in the field of rigid lines.

The new TIMO transfer line was delivered in September 2008. Following the assembly and installation of the line in TIMO the acceptance tests were started. Caused by problems with the isolation vacuum which had to be worked on, the tests are still ongoing.

New TIMO-2 PLC and data acquisition system

The new PLC at TIMO-2 on the basis of the Siemens PC-S7 together with the WIN CC visualization system, and the new data acquisition and storage system were prepared, installed and commissioned. Fig. 3 is showing a typical WINCC operation screen. In a first test stage, reception testing was done as a stand-alone system. The second part of the tests could be done in conjunction with the cryoline acceptance tests, as, at that point of time, the cryogenic circuits were closed.

During these tests all operational functions were checked, and if necessary optimised. This included the correct data collection with the data acquisition during the tests, and the communication between the involved PLC systems of the TIMO-2 facility and the connected cryoplant at the Institute.

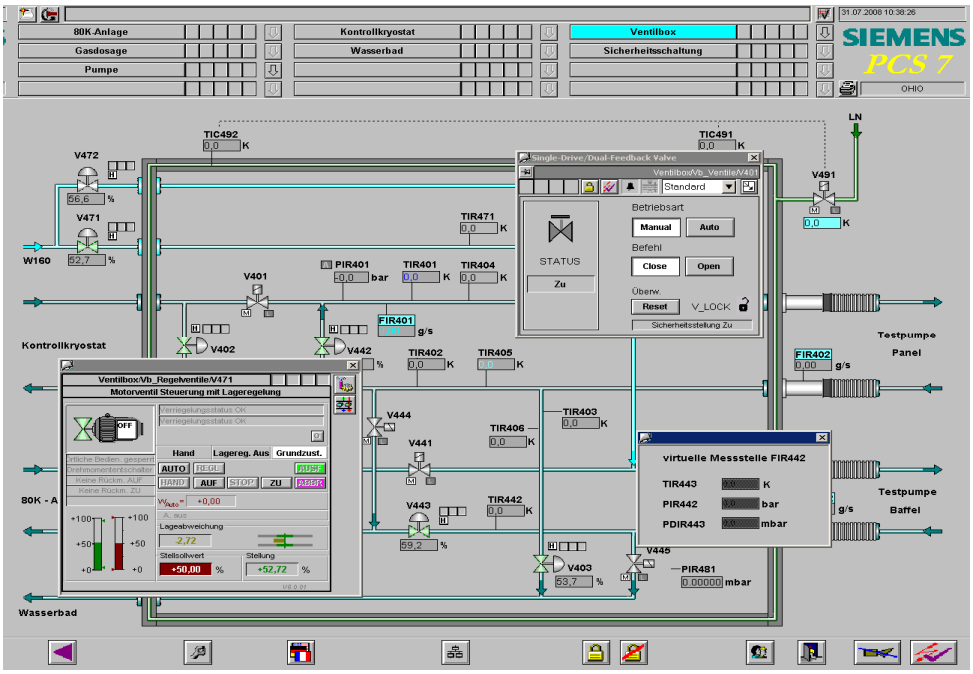

Fig. 3: PLC PCS7 operation screen for the cryogenic valve box.

New mass flow controller for the TIMO-2 gas metering system

In order to replicate ITER conditions, the major requirement of the gas metering system was to provide identical gas flow rates. This means 150 (Pa·m³)/s /4 (ITER nominal throughput distributed to 4 pumps pumping) = 22,000 sccm.

The available metering device at TIMO consisted of four parallel flow meters for the maximum ranges 10 sccm, 100 sccm, 1,000 sccm and 10,000 sccm (nitrogen equivalent) together with a flow controller. With this cascade it was possible to perform pumping tests with the model pump (approx. 3 times less charcoal coated surface) under ITER relevant conditions in terms of surface related gas flows. As part of the upgrade programme, the available flow was extended to 50,000 sccm. The new set-up is shown in Fig. 4.

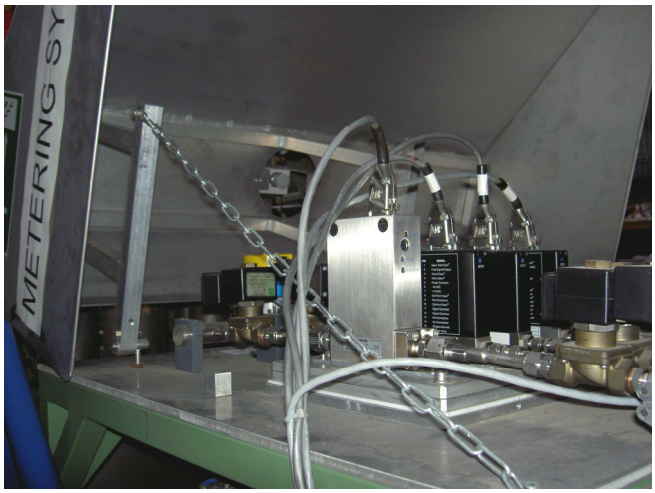

Fig. 4: Extended metering system for gas flows up to 50,000 sccm.

Conclusions

The TIMO upgrade has progressed according to plan and will be ready in time for the foreseen experimental campaigns to be conducted in TIMO-2.

Staff:

Chr. Day
H. Haas
H. Jensen
Th. Johann
R. Müller
P. Pfeil
H. Strobel
H. Stump
J. Weinhold

Literature:

[1] H. Haas, Chr. Day, M. Dremel, V. Hauer, G. Piazza, Preparing the test facility TIMO-2 for the operational tests with the ITER torus cryopumps, 22nd Int. Cryogenic Engineering Conference, July 2008, Seoul, Korea.

EFDA/07-1704-1567 (TW6-TTFF-VP 79)
Definition of Detailed TIMO-2 Test Programme for the ITER Prototype Torus Cryopump

Background and objectives

EU has to supply the torus and cryostat cryogenic pumps. As pilot project, a full-scale torus cryopump (PTC) is being manufactured by European industry. After delivery to FZK site, it will be installed in the TIMO-2-facility at FZK and acceptance tested. A parametric test programme is then required in order to validate the design with respect to the ITER requirements and to check the operational limits of the cryopump. Due to the EU schedule which is optimised to deliver the production cryopump, so as to meet the ITER schedule for first plasma, the production pumps design optimisation will overlap with the prototype test programme. Consequently, a carefully planned, prioritised programme and detailed test procedures are required to ensure that all design relevant data is available for the production pump design. This planning is the scope of the present task.

Experimental plan

The following experimental plan has been elaborated for the first stage of experiments with the PTC in TIMO-2 [1].

Final acceptance tests in TIMO-2:

In the course of final acceptance the PTC shall be installed in TIMO-2 and subjected to the following test programme (The TIMO-2 facility will simulate both the ITER outer flange boundary and vacuum).

1. After evacuation of TIMO-2 with the PTC installed, the PTC will be operated at ambient temperature over 10 times at full valve stroke (500 mm) and also at 25%, 50%, 75% settings. The valve control must position the valve disk accurately (±1 mm) within a maximum duration of 10 s. The position will be continuously monitored and recorded.
2. Repetition of the He leak test programme at ambient temperature. All pump volumes will be leak tested with acceptance levels for each individual volume of 10-10 Pam3/s and 10-9 Pam3/s for the integral pump volume. However, the acceptance leak rate for the valve head is only 10-3 Pam3/s.
3. Raise temperature of the 4.35 K loop to 470 K with warm He gas and repeat leak test of this circuit.
4. Cool down to nominal operational temperature (4.35K or 80K or 300K as appropriate) and repeat the valve operation and leak test programme.
5. Warm-up to ambient and repeat the valve operation and leak test programme.
6. Functional tests of the pressure and temperature sensors and read-out devices shall be performed during the previously performed cool-down and warm-up tests.

In addition, pressure drop and mass flow rate characterization measurements shall be carried out during the previously performed cool-down of the 4.35K, 80K and ambient circuits as well as for the 4.35K loop at 470K. At least two measurements of pressure drop and corresponding mass flow rate for each circuit must be provided.

Detailed test campaigns:

After acceptance testing a series of tests will be performed in TIMO-2 comprising the following categories given below. It should be noted that tests can be performed at 4.5K instead of 4.35K if the lower temperature is not absolutely required for the specific test and expected

results. As the design of the serial torus cryopump has to be frozen as soon as possible, the test campaigns are grouped in a first stage (urgent test with validative input to the procurement arrangement for the ITER serial pumps) and a second stage with complementary tests.

First stage:

1. Fatigue testing of the valve actuator and bellows arrangement. Repetition of opening and closing (at maximum stroke) cycling test programme (plus leak testing of the leak tightness of the large valve) of the valve actuator and bellows arrangement up to 30000 cycles at the representative operating temperature of the bellows arrangements. This test programme will be as specified for a very limited number of cycles for the PTC acceptance programme at the manufacturer's premises.
2. Capacity tests for He (pure) and 1 He-containing mixture at varied throughputs. During the campaign, capacity tests with pure He as well as ITER typical exhaust gas mixtures and gas throughputs of 5500 sccm, 10000 sccm and 27000 sccm are foreseen. Each test needs a minimum of 1 day.
3. Full replication of the ITER staggered operation pattern: Multi-cycle tests with complete 100K regeneration cycles (incl. check of temperature distribution). For preparation of this complex test performance, the TIMO-2 PLC must be programmed/optimized for the complete automatic operation.
4. Confirmation of the high temperature regeneration concept. Tests with Ar and water-like impurities will be performed. These tests include for each impurity a pump test with the ITER relevant gas mixture and two He capacity tests to control the influence of the pumped gas on the pump performance.

Second stage:

5. Parametric cryogenic characterization of the pump (heat loads, pressure losses). During these tests of cooling circuits, the 4.35K, 80K and 470K supply of the pump will be performed at different mass flows to check the resulting pressure drops (200 g/s and 100 g/s for 4.35K; 40 g/s and 20 g/s for 80K). Following these tests, different regeneration and reactivation operations with the accompanying mass flows for the pump cooling loops will be performed. To determine the heat loads and the pressure loses under ITER relevant conditions, tests will be performed using the ITER typical exhaust gas mixtures D_2-base/He including helium (10%) and 3% impurities (CO, CH_4, CO_2 ,O_2).
6. Parametric pump tests as a function of varied gas type, throughput and valve position. The results shall be cross-checked with extrapolated model pump data. Each tests campaign for one gas needs one week test duration.
7. Assessment of different cryopanels/cryo-supply temperatures.
8. Capacity tests for He-containing mixtures at varied throughputs.
9. Check of the pumping performance with impurities. The aim of these tests is to analyse the influence of the different impurities on the pumping behaviour.
10. Comparison of regenerations with closed/open valve to simulate ITER conditions in terms of volume/heat load. Pumping test and/or capacity tests will be performed followed by two different regeneration procedures to check the influence on the pump performance of the gas released during the regeneration and the influence of the volume available to buffer this released gas amount. The case of regeneration at open valve replicates more closely the ITER conditions with regard to the volume available for the released gas; the case of regeneration at closed valve replicates more closely the ITER conditions with regard to heat loads.

11. Confirmation of impurity release behaviour. To clarify the behaviour of impurity during regeneration release, a relatively complex sequence of different tests is needed.
12. Check of the operation limits (maximum acceptable throughputs, disruption mitigation events). The point of thermal breakdown will be assessed when the operation temperatures, which rise with increasing throughput, have reached an unacceptable level so that the pumping effect vanishes.
13. Transient tests to characterise dynamic pump response. These tests are aimed at characterising the throughput control function of the inlet valve to ameliorate the effect of rapid throughput changes.
14. Cryostat cryopump simulation tests.

Based on this plan, as next step the necessary operational procedures for TIMO-2 will be described and a prioritised and risk minimized time plan for the tests (acceptance and parametric) and all holding and witness points will be elaborated.

Staff:

Chr. Day
H. Haas

Literature:

[1] H. Haas, Chr. Day, M. Dremel, V. Hauer, G. Piazza, Preparing the test facility TIMO-2 for the operational tests with the ITER torus cryopumps, 22nd Int. Cryogenic Engineering Conference, July 2008, Seoul, Korea.

EFDA/07-1704-1546 (TW6-TTFF-VP 73)
Supply of CATIA Manufacturing Drawings for the ITER Prototype Torus Cryopump

Extended Summary

This task complements the Article 7 contract for manufacturing the full-size prototype torus cryopump (PTC).

As input to the PTC contract, the manufacturer was supplied with a comprehensive set of ~ 150 detailed drawings (down to the single part level) in CATIAV5 R12. The contract asked the manufacturer to verify the presented design, develop the design to meet this specification and prior to manufacture to complete the design of items not covered by the manufacturing drawings as well as to finalize the drawings with his welding procedures. Some of the mentioned areas were for example the compensator and bellows arrangement design and the 80 K system. The manufacturer placed an engineering service contract to a subcontractor to cover all design works to be done within the PTC contract. The contract specification requested 4 formats for interchange of the final drawings: The original CATIAV5 R12, STEP for 3D, dwg for 2D, and pdf for all.

This present task aimed to provide the design drawings elaborated under the manufacturing contract in CATIA V5 R17, the currently agreed drawings format for ITER and F4E. Due to various reasons, the design could not be completed.

The last design of the PTC manufacturer (before he stopped his further contractual activities) was been sent to FZK and transformed in CATIAV5 R17 format there. All in all, this package comprised 265 CATPART and CATPRODUCT files as well as 161 CAT Drawings. This is a complete record of the last version of the design achieved under the stopped PTC manufacturing task. Fig. 1 is illustrating the (incomplete) PTC design at that stage, from which it will be continued under a new F4E Grant.

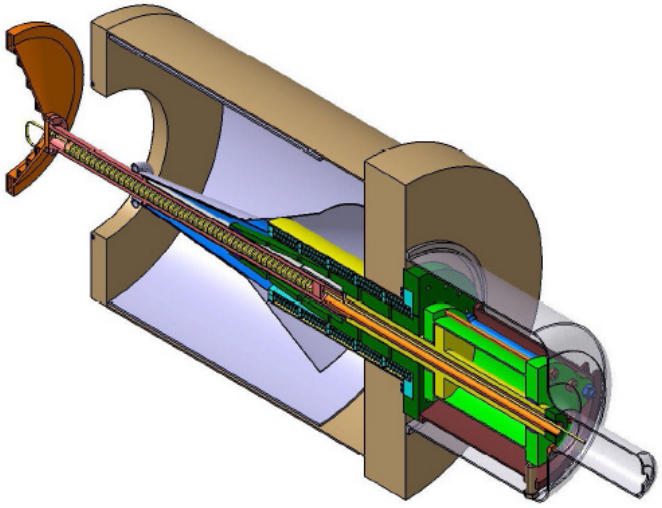

Fig. 1: Design of the PTC.

Staff:

Chr. Day
H. Jensen
R. Simon

TW5-TTFF-VP 57
ITERVAC Validation Test

Background and objectives

The ITERVAC code is being used for the optimisation of the ITER vacuum pumping systems which are at most locations characterised by very high throughputs and therefore being operated in transitional flow regime around Knudsen numbers of unity (cf the parallel task TW6-TTFF-VP68 for assessment of the divertor system). Thus, the standard vacuum formulae for molecular or laminar flow and Monte Carlo codes are not applicable [1].

Because of the importance which is given to the calculation results of ITERVAC, the code must be extensively benchmarked. A theoretical benchmarking was done in the field of laminar and purely molecular flow, however, it has been found that literature data for (intermediate) transitional flow range, which is of major importance for the ITER conditions, are scarce and even not existing for geometries as complex as for the ITER vacuum pumping ducts. In order to validate proposed design modifications, such as to increase the conductance of the path from the divertor to the torus exhaust cryopumps, which have to be made while respecting other functions of the design (e. g. shielding, structural strength of the cassette), an experimental confirmation of the modelling results is required. The TRANSFLOW facility was built up and is now under routine operation to provide a broad and relevant range of well defined experimental data which can be used to benchmark the code.

Experimental results for the test channels

All measurements are performed in the TRANSFLOW test rig which has been set up under this task. The test channels for the experiments were four long channels with a circular, square shaped, triangular and a trapezoidal cross section and one short channel with the same trapezoidal cross section as the long channel. The long channels have a length of 1277 mm each, and the short channel is 157 mm long. They all have identical hydraulic diameter of about 16 mm.

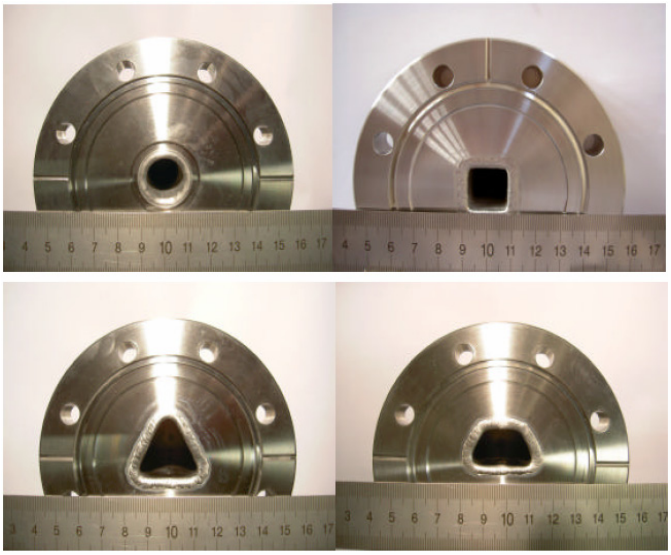

Fig. 1: Investigated test channel cross-sections.

The inner surface of the channels has no special treatment. On both ends flanges DN 63 CF are welded, which are used for the installation of the test channels between the small adapter flanges of the dosing and the pump dome (see Figs. 1 and 2).

The experiments with all channels were performed at constant gas flow rates between 0.02 and 110 sccm. The flow rate of 0.02 sccm was the lowest stably achievable, the highest flow rate was chosen to have several measurement points in the hydrodynamic flow regime. The test gas in all experiments was nitrogen at ambient temperature.

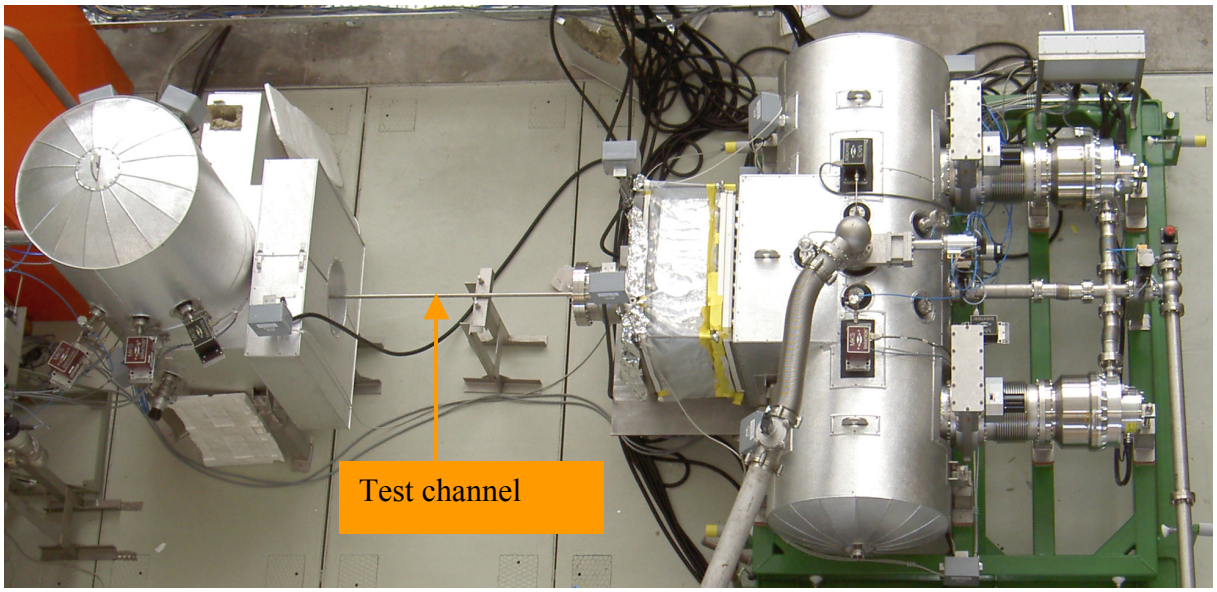

Fig. 2: Circular test channel installed in TRANSFLOW [2, 3].

At a measurement, the flow rate, the temperature and the pressure in the dosing dome and in the pumping dome are recorded. The flow rate and pressures were corrected by use of calibration tables. The pressures were additionally corrected with respect to thermal transpiration. From the pressures inside the dosing and the pump dome and the flow rates the integral conductances were calculated as shown in Fig. 3. These values do include the conductances of the adapter flanges themselves. However, they are much larger compared to the conductance of the test channels so that their influence is negligibly low, especially for the long channels.

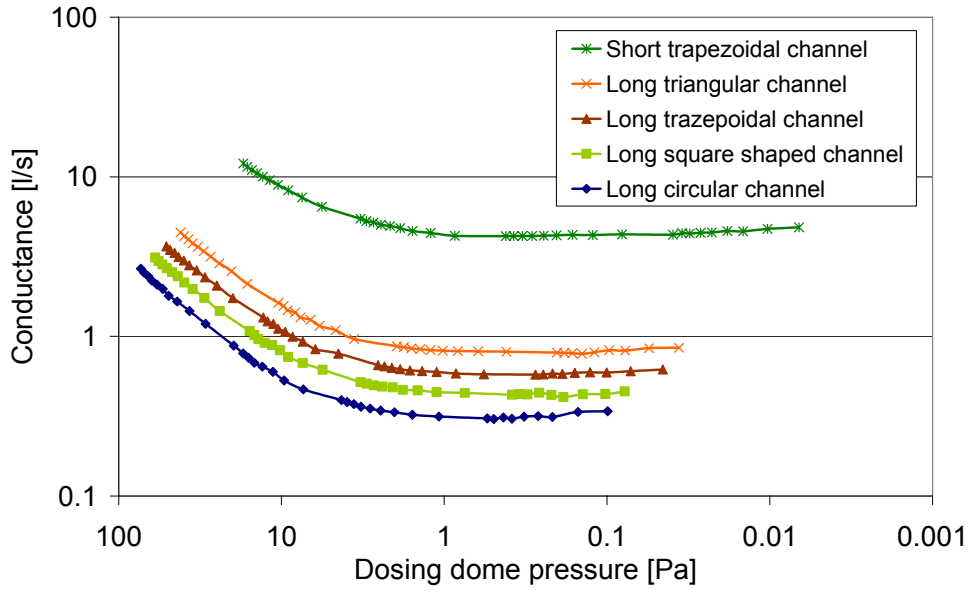

Fig. 3: Calculated conductance of all channels.

Comparison with theory and simulation

The resulting conductances were compared not only with the results of ITERVAC simulations but also with numerical calculations. For the latter, a fruitful collaboration with the University of Thessaly in Volos, Greece has been established, who are leading experts in that field [2]. The Boltzmann kinetic equations were used to calculate the mass flow rates at given pres-

sure difference for long channels. This approach is not feasible for short channels, which require the use of the Direct Simulation Monte Carlo method. These results are available for short circular ducts, but unfortunately not for a trapezoidal cross-section.

The agreement found between experiment and calculation or simulation was very similar for all four long channels. Fig. 4 exemplifies the results for the long square and trapezoidal channel. As an average over the full experimental range, the relative differences between kinetic calculation and experiment are between 4 and 6% and between 4 and 8% between experiment and ITERVAC simulation. However, over a wide range, especially around Kn numbers of unity, the deviations are below 2%. In all cases, no systematic errors were seen. The found differences are inside the total uncertainties, which include the uncertainties from the measurements and kinetic calculations or ITERVAC simulations. The largest uncertainty contribution comes from the determination of the hydraulic diameter, which is used as a key parameter in the calculations and simulations. The dependence of the conductance upon the hydraulic diameter is given by a power law in the diameter with an exponent between 3 and 4, depending on the flow regime).

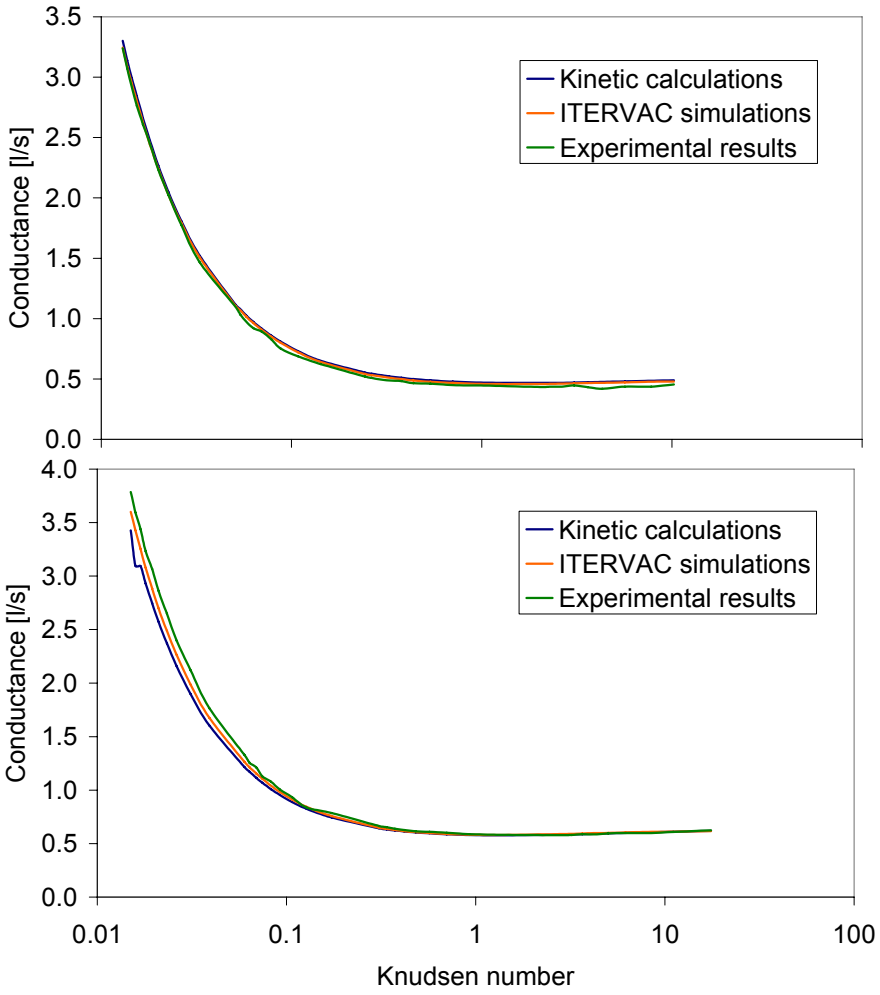

Fig. 4: Channel conductance as a function of the Knudsen number; experimental results, calculations from kinetic theory [3] and ITERVAC simulations for the long square shaped channel *(top)* and the long trapezoidal channel *(bottom)*.

Fig. 5 illustrates the simulation and experimental results for the short trapezoidal channel. Here, the whole set-up has been considered for the ITERVAC simulation, to make sure that the influence of the adapter flanges on the measured conductance is properly included. In average there results a deviation of 9%. As shown in the figure, this deviation may refer to a systematic difference. But a single test channel is not sufficient to underline such a statement.

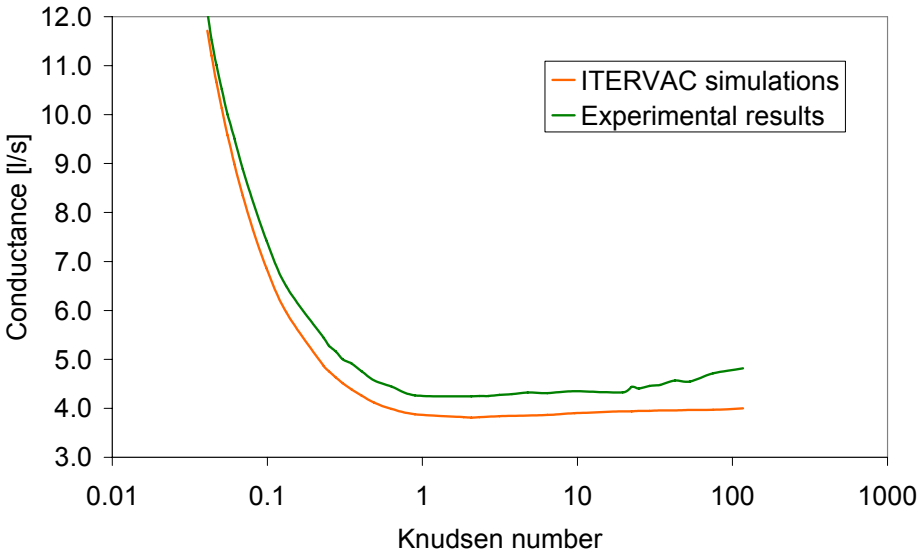

Fig. 5: Conductance of the short trapezoidal channel set-up (i.e. including the adapter flanges) as a function of the Knudsen number; experimental results and ITERVAC simulations for the short trapezoidal channel.

Conclusions

The measurements campaign with the four long test channels (circular, square shaped, triangular, trapezoidal cross section) and one short channel with a trapezoidal cross section is completed. For all long channels, the found agreement between the measurements and the simulations as well as the calculations is very satisfactory so that ITERVAC is considered to be fully validated in this region. The experiment with the one short channel, however, shows larger and systematic deviations. As the ITER torus vacuum system includes several short channels with a length to hydraulic diameter rate below ten, it is strictly recommended to continue the validation work for short channels. New measurements are proposed with three short channels with a length to hydraulic diameter rate of 1, 5 and 10, respectively. If supported, the collaboration with the EURATOM/Hellenic Republic Association in University of Volos on calculations of vacuum flows through circular and non-circular cross-sections based on solutions of the Boltzmann kinetic equations or Direct Simulation Monte-Carlo (DSMC) method will also be continued.

Staff:

Chr. Day
V. Hauer
H. Jensen
S. Pantazis (Guest scientist, University Thessaly, Volos, Greece)
P. Pfeil
H. Stump
St. Varoutis (Guest scientist, University Thessaly, Volos, Greece)
J. Weinhold

Literature:

[1] Chr. Day, V. Hauer, G. Class, D. Valougeorgis, M. Wykes, Development of a simulation code for ITER vacuum flows, IAEA Fusion Energy Conference, Chengdu, China, Oct 2006.

[2] S. Varoutis, S. Naris, V. Hauer, Chr. Day, D. Valougeorgis, Computational and experimental study of gas flows through long channels of various cross sections in the whole range of the Knudsen number, accepted for publication in: Journal of Vacuum Science and Technology A.

[3] S. Varoutis, S. Naris, V. Hauer, Chr. Day, D. Valougeorgis, A study of flows in triangular and trapezoidal channels under low, medium and high vacuum conditions, European Vacuum Conference, Sept. 2008, Balatonalmadi, Hungary.

EFDA/06-1498 (TW6-TTFF-VP 68)
Conductance Modelling of ITER Divertor and Torus Pumping Duct

Background and objectives

The simulation of the ITER torus vacuum system was started in 2004/2005 under the EFDA Task TW4-TTFF-VP 47. At that time, the results revealed a strong conductance limitation of the reference pumping duct. The calculated pressure profile of the duct identified the divertor pumping slots as the bottlenecks. This was one of the reasons for ITER to re-design the divertor.

The scope of this present task is to estimate the conductance of the re-designed ITER divertor and torus pumping ducts. The aim is to give a hint to the improvements which can be expected from a more open divertor design as well as to give a more detailed picture of the flow distribution inside the ITER torus vacuum system. This shall be achieved by intense use of the ITERVAC code [1].

ITERVAC full network model

Within this task, a comprehensive and very detailed model of the ITER torus vacuum system was built up for the first time. Only the maximum throughput for one gas species at isothermal conditions can be calculated, determined by the conductance of the individual elements. So, the calculated maximum throughputs can be larger than the real fuelling flow rate into the torus.

The ITERVAC full network model (see Fig. 1) is based on the ITER design as of June 2007. The model can be logically separated into the divertor ring, the pumping ports and additional channels simulating the gas back streaming to plasma.

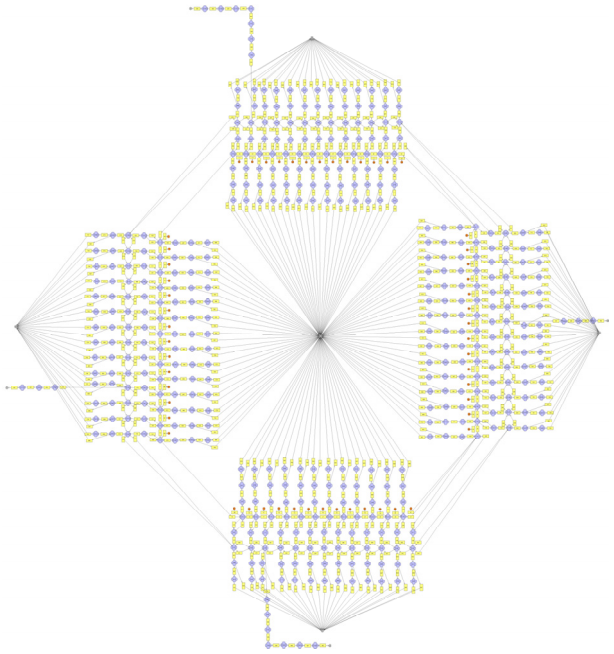

Fig. 1: ITERVAC model of the full ITER torus vacuum system (divertor design 2007).

In the ITERVAC models 4 symbols are used:

Dark orange circles are gas sources which are simulating the gas flow from the divertor cassette domes into the lower parts of the cassettes. The total neutral pressure inside the divertor cassette domes is one input parameter and the interface towards the plasma side.

Grey circles are representing the pumps. Pumps are the torus cryopumps and, acting as virtual pumps, the plasma at plasma burn operation. In ITERVAC, pumps are characterised with the properties: pressure, inlet cross section and pumping speed. The design values are used for the torus cryopumps. The total inlet cross section of the plasma pumps is chosen to 680 m². The pumping speed of the plasma is assumed to be very large (above 20,000 m³/s), which is limited by ITERVAC in relation to the small opening inside the divertor dome and target plates supports and between the cassettes to the black hole pumping speed for the plasma pumps.

Yellow rectangles symbolise the different channels. The sections of the torus vacuum system are logically split into channels with constant shapes, cross sections and length.

The channel symbols in the models are linked with linking nodes. Linking nodes define the locations inside the model where the results have to be calculated. After a simulation the pressure and mass flow for every node is known.

This simulation model was intensively tested and simulations were performed with a setup for deuterium at 420 K [2]. Fig. 2 shows the simulated maximum throughput to torus pumps and plasma for divertor pressures between 1 and 10 Pa. The backflow to the plasma reaches the same level as the throughput to the torus pumps at 5 Pa and is about 30% above the throughput to the torus pumps at 10 Pa divertor pressure.

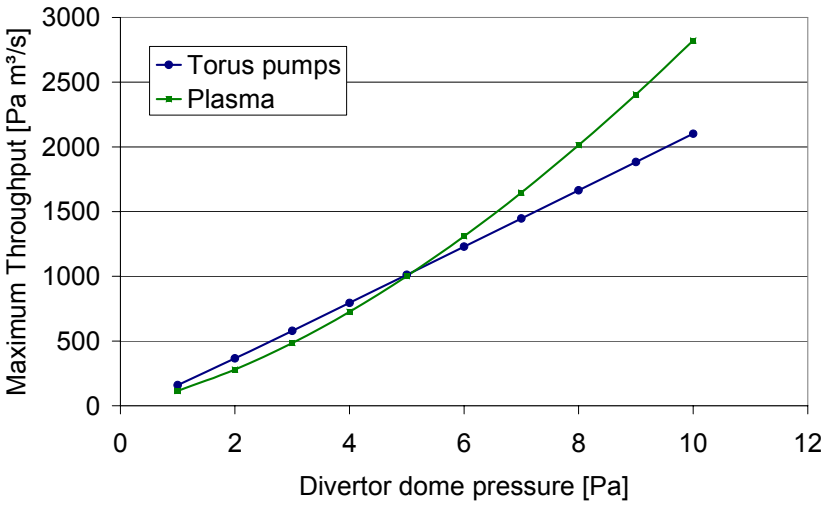

Fig. 2: Maximum throughputs to torus pumps and plasma (backstreaming).

The full network model was updated in 2008 due to ongoing changes in the design of the ITER torus vacuum system. The updated model (see Fig. 3) includes more channels to simulate the toroidal conductances inside the divertor cassettes as well as the different connections to the plasma. The gaps between the divertor cassettes were increased from 10 to 20 mm. The strike point data and therefore the length of the connection channels to the plasma were also changed. The updated model is also set up for deuterium at 420 K.

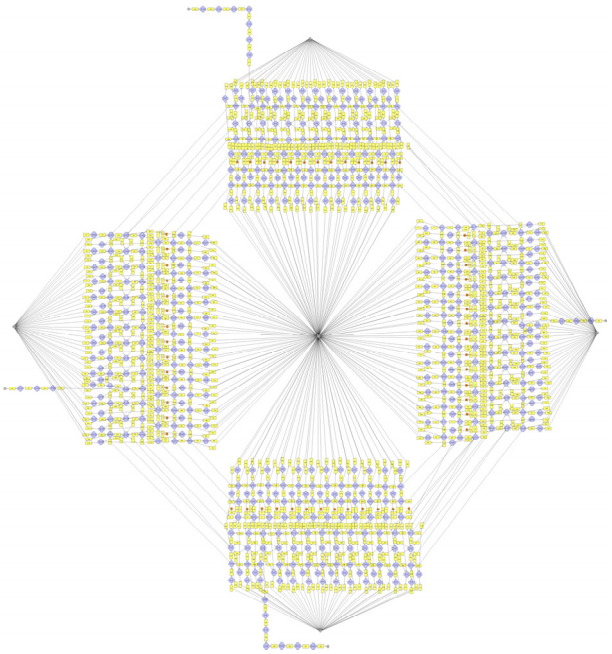

Fig. 3: Updated ITERVAC model of the full ITER torus vacuum system at 2008.

Status and outlook

A variation of the gas species and torus pumping speeds is planned to become part of the further simulation process. The pressure inside the divertor dome will be varied between 1 and 10 Pa for the burn phase and between 10^{-4} and 1 Pa for the dwell pumping. The simulation of dwell pumping needs a change of the model: the pumps simulating the plasma have to be replaced by gas sources. The inclusion of 4 additional pumping ducts is another option that will be prepared for simulating the dwell pumping with 8 torus pumps.

Staff:

Chr. Day
V. Hauer

Literature:

[1] Chr. Day, V. Hauer, G. Class, D. Valougeorgis, M. Wykes, Development of a simulation code for ITER vacuum flows, IAEA Fusion Energy Conference, Chengdu, China, Oct 2006.

[2] V. Hauer, Chr. Day, Conductance modelling of ITER vacuum systems, SOFT, Sept. 2008, Rostock, Germany.

EFDA/07-1704-1566 (TW6-TTFF-VP 78)
ITER Torus Cryopump Mechanical and Thermal EM Load Study

Background and objectives

The eight torus cryopumps for ITER are connected to the torus lower ports within the port cells. The pumps will be subject to electromagnetic loads (EM) due to their close proximity to the torus. The mechanical (forces, torques) and thermal effects (heat loads) of the EM loads need to be analysed in order to confirm the design and to ensure sufficient margin on the cryopumps and cryogen supplies, and mechanical loading on the cryo-array supports.

Initial assumptions

After classification of all principle cases, the first stage of this task identified the following four worst cases with regard to the EM forces on the torus cryopumps:

1. Among all studied events (Disruption I,II,III and vertical displacement event (VDE) type II and III), the fast downward (FD) VDE III with linear current quench (linear 36 ms current decay) will produce the most loaded conditions for the cryopump.
2. But the VDE III event is 100 times less probable than VDE II. So the VDE II has to define cyclic loads on the torus cryopump: The maximum cyclic loads take place at the fast downward VDE II with 36 ms linear current quench.
3. Under fast discharge, the most loaded conditions are associated with the TF coils,
4. and the PF4 and PF5 coils.

Previous work on electromagnetic loads under FD VDE conditions resulting on the cryopumps has been performed in 2001, based on a conceptual pump model. Also, the calculation of the pump loads was decoupled from the vacuum vessel for simplification purposes. The maximum radial force and toroidal moment was found to be –26 N and 62 Nm, which was considered as uncritical at that time. However, as the cryopump design has progressed since 2001 (now with the design of the prototype torus cryopump) and the ITER load cases have been revised, the analysis needs to be repeated, now based on a less simplified cryopump model.

Calculational approach

For the calculations, the torus cryopump and vacuum vessel lower port system (CATIA model transmitted from ITER, Nov 2007) and the CATIA model of the ITER torus cryopump (reflecting the design status as achieved under Task TW4-TTFF-VP41, final report March 2007) were first carefully checked to identify all valid electromagnetic flow paths.

After clarification of all input parameters, a complete model of the lower port region with the cryopump port was built in the TYPHOON code, see Fig. 1. The whole calculation model describes a 40-degrees sector of the ITER machine. The sector includes:

- double walled vacuum vessel (VV) with ports and ribs,
- divertor inboard and outboard rails,
- blanket triangular support,
- upper and equatorial port plugs,
- cryopump,
- plasma, CS, PF and TF coils.

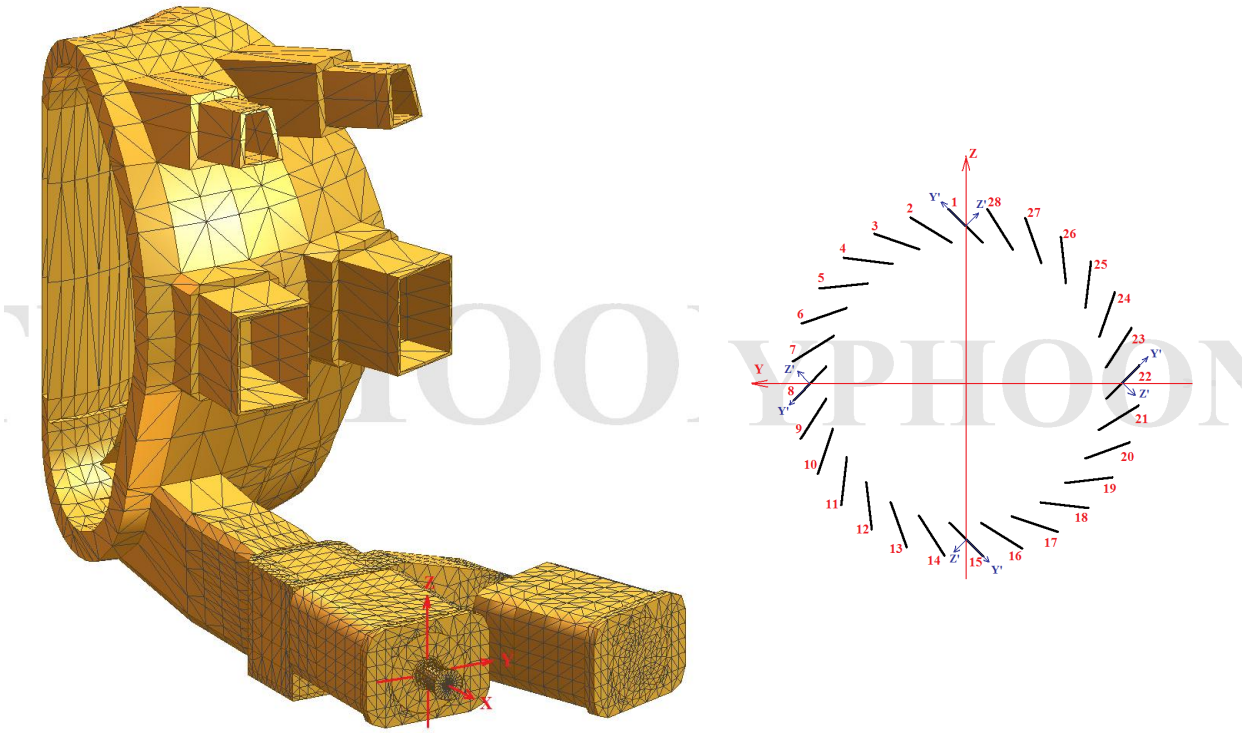

Fig. 1: Full 40° sector calculation model of vacuum vessel and cryopump. The local coordinate system associated with the cryopump is shown as well as the chosen coordinate system for the cryopanels.

For each event the total EM loads (forces, moments and AC losses) have been calculated separately for the following cryopump components and sub-assemblies:

- the whole cryopump assembly,
- the cryopump housing assembly,
- the whole 80K assembly including carrier tubes,
- the 80K louvers assembly separately,
- the 4K panels assembly,
- all 4K panels individually,
- the cryopump valve assembly (the case with fully opened valve is taken as worst case).

Modelling results

The calculations have shown that the forces keep growing after the plasma current is zero. Consequently, the calculations were continued beyond disruption time, which was time consumptive and needed significant CPU time. Due to the complexity of the detailed model, the computing time for each 10 ms was of the order of 24 h. The calculation time could have been reduced by going to a more simplified model and/or by decoupling the pump from the vacuum vessel. The latter approach means to calculate the currents only for the vacuum vessel and then to apply them on the cryopumps in a separate step afterwards. However, to provide most reliable results, we have decided against the simplification and in favour of the full and detailed modelling.

The calculation results for various sub-assemblies are summarized in the two tables below. On top of that, each individual cryopanel was treated separately for FD VDE III and FD VDE II conditions; the results are summarized in the third Table below, indicating that panels # 4, 6 and 25 are showing the highest loads.

Table 1: Maximal (among all examined loading events) EM loads acting on the cryopump components. The loads are given in the local coordinate system associated with the cryopump.

	F_x (N)	F_y (N)	F_z (N)	M_x (N·m)	M_y (N·m)	M_z (N·m)
Housing assembly	-297 (VDE-III)	1.00 (VDE-III)	412 (VDE-III)	-1.13 (VDE-II)	347 (VDE-II)	2.5 (VDE-II)
80K assembly including louvers and radiation shield	18.2 (VDE-II)	0.195 (VDE-II)	1.98 (VDE-II)	-0.408 (VDE-II)	23.5 (VDE-II)	0.446 (VDE-II)
80K louvers assembly	1.04 (VDE-II)	-0.272 (PFCFD)	0.479 (VDE-II)	0.022 (VDE-III)	3.94 (VDE-II)	-0.057 (VDE-III)
4K panels assembly	1.02 (VDE-II)	-0.134 (VDE-III)	-0.674 (VDE-III)	-0.114 (VDE-III)	-2.20 (VDE-III)	0.334 (VDE-III)
Valve assembly	10.3 (VDE-III)	0.109 (VDE-II)	12.8 (VDE-III)	-0.022 (VDE-II)	4.28 (VDE-II)	-0.071 (VDE-II)
Whole cryopump assembly	-296 (VDE-III)	1.06 (VDE-III)	426 (VDE-III)	-1.61 (VDE-II)	374 (VDE-II)	3.02 (VDE-II)

Table 2: Maximal (among all examined loading events) AC losses dissipated in conducting structures of the torus cryopump. The losses are presented as: a) the maximal values of losses power $P_{\max}$; b) estimates of total energy E^*_{tot} dissi pated during the event.

	$P_{\max}$ (W)	E^*_{tot} (J)
Housing assembly	167 (VDE-II)	169 (PFCFD)
80K assembly including louvers and radiation shield	26.3 (VDE-II)	25.4 (PFCFD)
80K louvers assembly	1.36 (VDE-II)	1.21 (PFCFD)
4K panels assembly	1.22 (VDE-II)	1.24 (PFCFD)
Valve assembly	3.51 (VDE-II)	3.47 (PFCFD)
The whole cryopump assembly	198 (VDE-II)	200 (PFCFD)

Table 3: Maximal (among all examined loading events) EM loads acting on the cryopanels (number given in brackets). The loads are given in the local coordinate system of the cryopanel.

	F_x (mN)	F_y (mN)	F_z (mN)	M_x (mN·m)	M_y (mN·m)	M_z (mN·m)
FD VDE III	19 (#4)	-190 (#4)	-241 (#25)	6.5 (#1)	-14.4 (#6)	2.4 (#4)
FD VDE II	20 (#6)	-201 (#6)	-221 (#23, #25)	5.7 (#1)	-12.4 (#6)	2.5 (#6)

The calculations clearly show that the EM mechanical loads (forces and torques) for the whole cryopump assembly are well below the gravity loads. Also the EM loads on the hous-

ing assembly are negligible against the acting loads due to the valve closing, for which the housing has been designed for. The calculated mechanical loads on the 4K and 80K assembly are of small order and can therefore be coped with in the existing cryopump design. This also holds for the local forces and moments on the individual cryopanels. A similar situation is resulting for the stored energies. The worst case here is found for the 4K panel assembly, where the calculated loads are of the order of a few % of the smallest nominal heat loads of the torus cryopump (under dwell).

In summary, no critical cases were identified. The task is closed.

Staff:

A. Antipenkov
A. Belov (STC, Efremov Institute)
Chr. Day
E. Gapionuk (STC, Efremov Institute)
V. Kukhtin (STC, Efremov Institute)
H. Strobel
S. Sychevsky (STC, Efremov Institute)

TW6-TTFF-VP 53
Tritium Test of Ferrofluidic Cartridge Seals for Roots Roughing Pump

Background and objectives

In accordance with the ITER vacuum requirements and the results achieved in the previous tasks, the ITER forevacuum pumping system shall provide a unit pumping speed at its inlet of at least 1 m^3/s [1]. The best pump type to meet this goal is a Roots pump. A tailor-made tritium compatible pump of 250 m^3/h was tested at FZK on helium in frame of the previous R&D Task TW3-TTF/VP12.

To make a catalogue pump tritium compatible the following main modifications are needed: a stainless steel housing; metal stationary seals; and in both directions tight rotary shaft seals between the process and lubricant chambers. For the latter issue, a ferrofluidic rotary feedthrough is proposed. The testing of one of such seals was the scope of this task.

Test facility FACT

The tritium test of a ferrofluidic rotary feedthrough completes the investigation programme of this seal [2]. The test unit consists of two compartments, separated by the ferrofluidic test cartridge. The tritium leak through the cartridge is continuously monitored by an ionisation chamber under rotation of the shaft at 1500 rpm and at pressure differences of 500 mbar. A dedicated test facility was set up, the test facility FACT (Ferrofluidic Advanced Cartridge Tritium experiment) which is located in an existing glove box in the Tritium Laboratory, as described in the previous report, see Fig. 1.

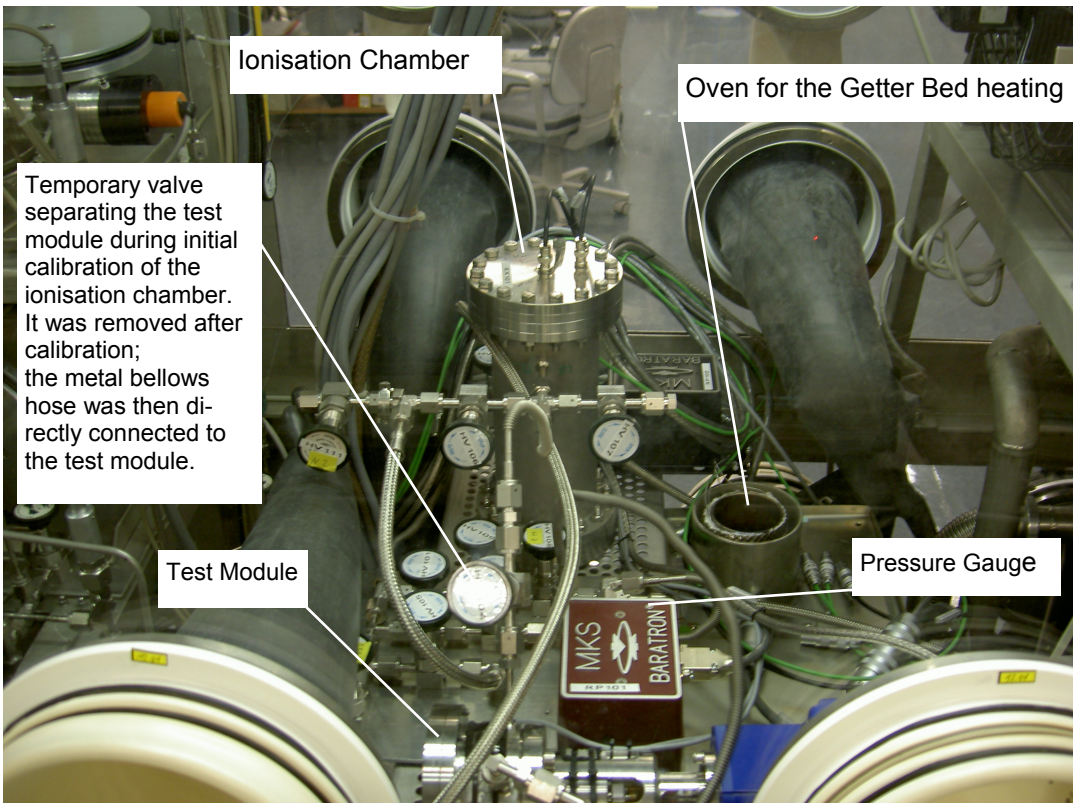

Fig. 1: FACT set-up inside the glove box.

Experimental results

During the measurements, the temperatures of the bearings and the tritium were found to be stable at 36/37°C and 42/43°C, correspondingly (depending on the glove box temperature fluctuation). The pressures in the tritium compartment (denoted ´chamber A´) and the ionisation chamber were stable at 882/890 mbar and 396/398 mbar, correspondingly (depending on the temperature).

The leak rate through the ferroseal was evaluated on the tritium concentration rise in the ionisation chamber and on the pressure loss in the tritium compartment. The results during the two first weeks are shown in Fig. 2 and agree rather well. The found leak rate was of the order of $1 \cdot 10^{-7}$ Pa·m^3/s at 500 mbar pressure difference ($2 \cdot 10^{-7}$ Pa·m^3/s at ΔP = 1 bar). The helium leak rate in this seal was formerly measured as $2 \cdot 10^{-8}$ Pa·m^3/s at 150 mbar pressure difference, i.e. $1.3 \cdot 10^{-7}$ Pa·m^3/s at ΔP = 1 bar. With account of the rather rough evaluation in the case of tritium, such an agreement can be considered as satisfactory.

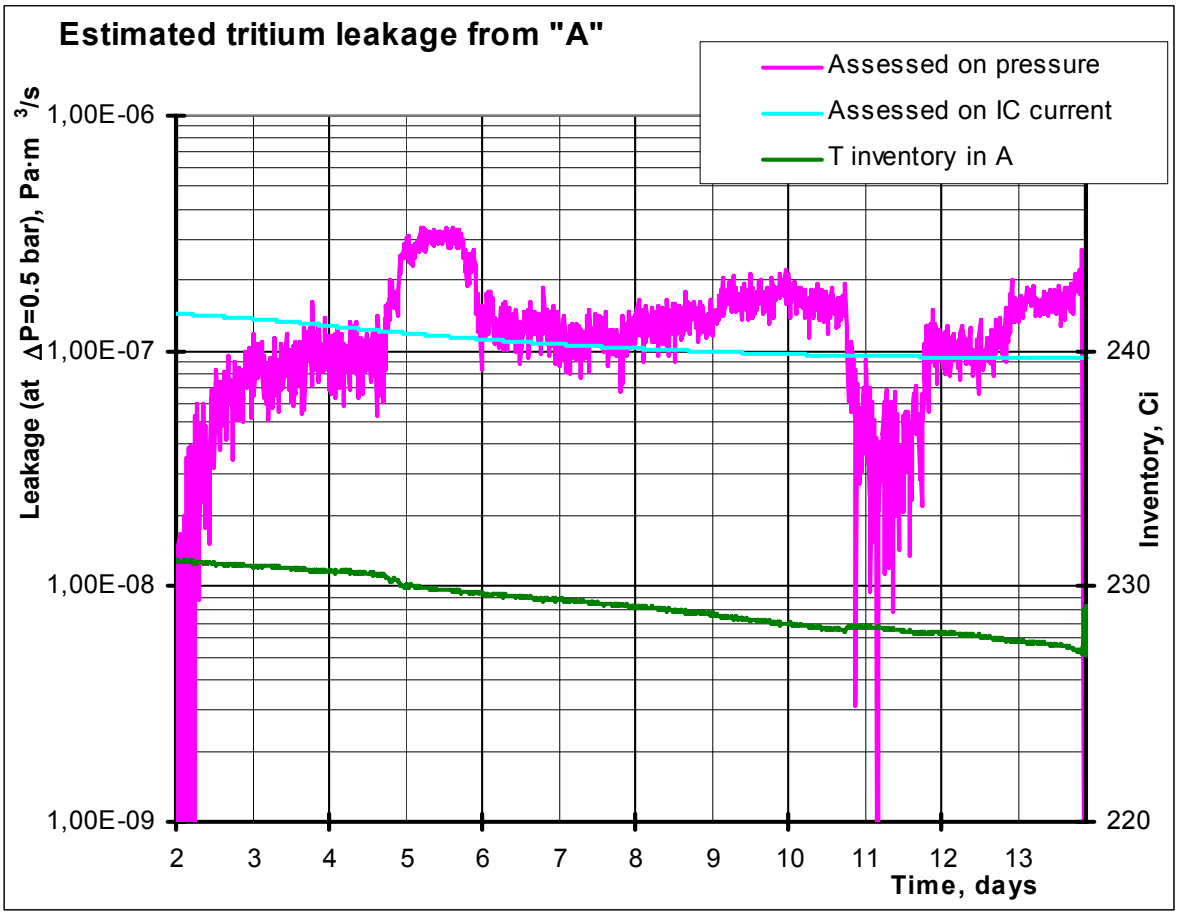

Fig. 2: Tritium leakage through the ferroseal, estimated on the tritium concentration rise in the ionisation chamber (blue curve) and on the pressure rise (pink curve).

The experiment had to be interrupted after two weeks from the start because of an activity increase in the glove box. After two following weeks being in stand-by (that means the constant tritium pressure of 900 mbar in the compartment “A” and nitrogen pressure of 400 mbar in the other compartment) the motor was started for one full day. The start torque was significantly higher that at the beginning of the experiment: at the beginning the rotation speed of >1400rpm has been achieved within few seconds, now within several seconds of running the speed was on the level of 500rpm. In about one hour the speed has achieved its nominal value.

After one month stand-by (two month total tritium exposure) the motor could not start. Even by hand through the glove it was impossible to overcome the start torque. After helping with a lever the motor was able to start and achieved 1200rpm within two hours. At this moment the ferroseal was broken through, the pressure in the compartment A dropped down to 60 mbar above the pressure in the compartment B. After evacuation of the ionisation chamber the stationary seal could stand just 480 mbar (before tritium exposure the seal, both stationary and rotating, withstood ΔP = 1 bar; within the two first weeks of the tritium experiment it withstood ΔP = 0.9 bar at stationary rotor). It was then running for five hours, but the achieved frequency of 1100 rpm was significantly below the normal value of >1400 rpm. There has obviously been some permanent degradation in the seal. The fact that it was running constantly over the full day, once initiated, indicates however that any mechanical damage can be excluded as a reason for the malfunction.

After another month stand-by without tritium fill (three months of tritium experiment, two months net tritium exposure) the tritium side of the seal was filled with some 100 mbar of nitrogen. Then again, it was tried to start the device. Similarly, as before, manual force was needed to initiate the rotation. The nitrogen pressure was stepwise increased and at 650 mbar a similar breakthrough appeared (under rotation at 1100 rpm), the seal was not able anymore to hold any pressure difference larger than Δp = 200 mbar in both directions. On the next day at stationary rotor we made attempts to increase the pressure difference and again the seal could maximal hold Δp = 200 mbar. Based on this event, the tests were not continued.

Conclusions

In consultancy with the ferrofluid manufacturer it was confirmed that the used ester-based ferrofluid is obviously not suitable for tritium application. It was chosen due to its capability to withstand high pressure differences. The change towards higher viscosity was explained by polymerisation in the presence of hydrogen. In additional tests it was demonstrated that similar degradation, although less severe, was already generated by deuterium, so the deterioration is not tritium specific, but probably accelerated by tritium (isotope exchange).

The next candidate ferrofluid would be a synthetic hydrocarbon-based liquid, which is at least known to be compatible with hydrogen.

Staff:

A. Antipenkov
Chr. Day
L. Dörr
Chr. Caldwell-Nichols
U. Besserer
H.-D. Adami

Literature:

[1] Chr. Day, D. Murdoch, The ITER vacuum systems, J. Phys. Conf. Series 114 (2008) 012013.

[2] A. Antipenkov, Chr. Day, H.D. Adami, Tritium test of a ferrofluidic rotary seal, Fusion Science and Technology 54 (2008) 35-38.

EFDA/07-1704-1568 (TW6-TTFF-LD 71)
Risk Analysis Tool for ITER Operations from Vacuum Leaks

First steps towards risk analysis

The main purpose of this work is to develop a methodology and tools for the analysis of risks posed from leakage from different parts of the vacuum systems so that areas requiring further attention can be readily identified. Therefore, it is foreseen to analyse both, the probability of a failure and the impact of the resulting leak.

For the first step in that direction, the divertor-water cooling system as a manageable subsystem was chosen. As agreed with ITER, the commercial risk analysis programme BlockSim® 7 was used to identify components or sub-systems with an exceptional impact of their failure rate to the reliability of the entire system. With the basic approach that every component will work far below its life cycle, for every single functional block representing a subsystem a static probability instead of a time depending behaviour was chosen. For this principle exercise, the reliability values were just arbitrary numbers to allow principle conclusions, and have not yet cross-checked with any fusion component failure data base. The underlying design (Fig. 1) and the developed (simplified) BlockSim®-diagram (Fig. 2) are shown below.

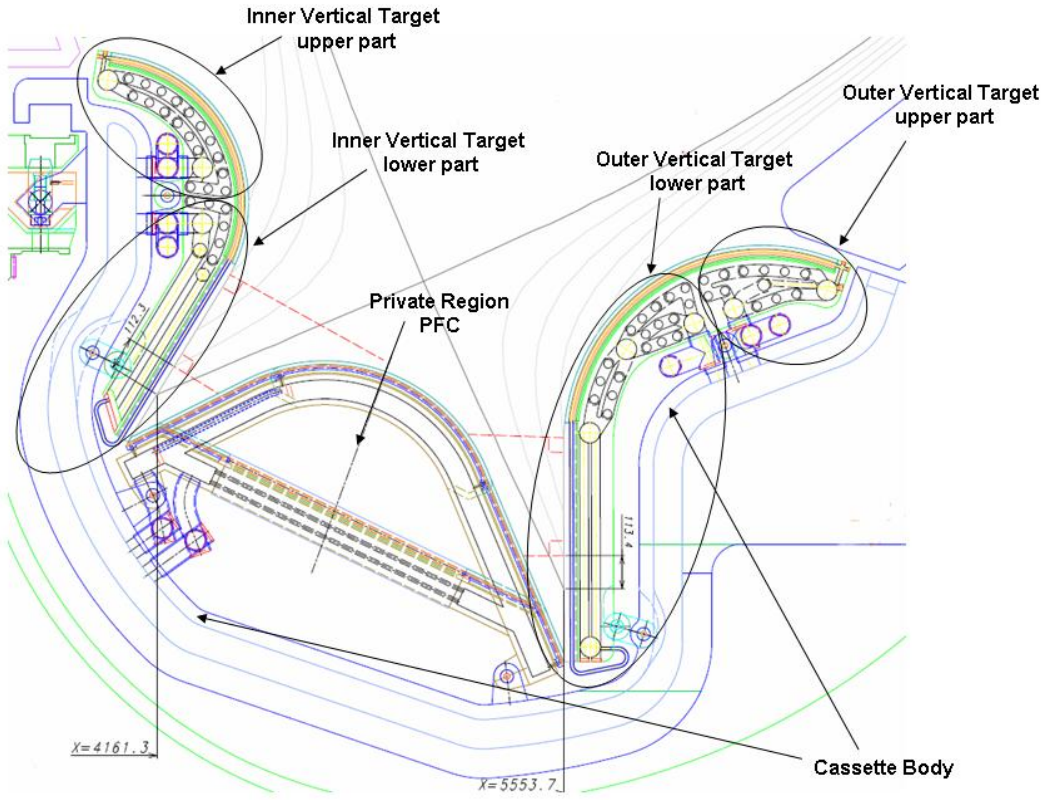

Fig. 1: Divertor cassette split up to 6 regions for a first simple analysis.

When for all blocks a reliability of 0.99 was assumed, the overall reliability of the whole system was calculated with 0.9415. The next step was to (arbitrarily) reduce the reliability piece by piece of every single block to 0.5 and to re-do the calculation of the corresponding system reliability. Table 1 shows the corresponding analysis results. Column 2 lists the found values of the divertor model with component reliabilities of 0.99 except of the designated component with only 0.5. These results indicate the impact of the single reliability drop on the whole system as shown in column 3. The impact class denotes the influence of the single reliability R of one component to the overall reliability of the entire system. This is only a relative number

for qualitative intercomparison and has a similar meaning as the criticality value in standard FMECA.

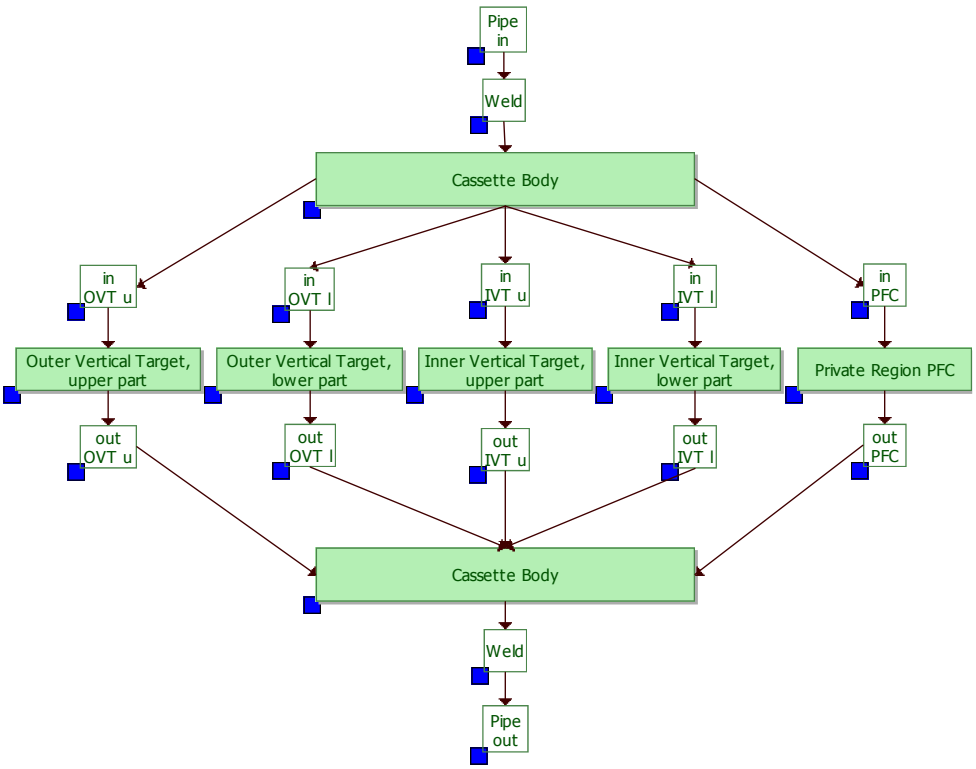

Fig. 2: Resulting BlockSim®-model.

Obviously there are only two classes of components, one to which we allocated an impact of 1, that means the component reliability defines the new resulting system reliability, and one with an impact of nearly 0, that means the component has no significant influence to the reliability of the entire system. By systematic analysis it was found that only the formation of the components defines their impact class: parallelly arranged units do not show significant influence (as the system function from leakage point of view is fulfilled in a redundant way) whereas serially arranged components do affect the system very much.

The attempt of enhancing the diversity of impact classes by increasing the complexity of the BlockSim®-model did not improve the significance of the results.

Software suitability

With these intermediate results general doubts in the methodology of BlockSim® related to our special application have arisen. BlockSim® shows an increasing overall reliability with more parallel arranged components, an obvious result from the point of view of safeguarding the system by installation of more backup systems. On the other hand our angle of view is another one. We will focus on the probability and the impact of a failure and the resulting vacuum leak instead of the focus on the reliability of the water cooling system with regard to its cooling function.

With this assumption, more parallel arranged components should cause a higher risk for a leak failure scenario instead of higher system reliability. So there is the question if BlockSim® is the right tool for our approach at all. If BlockSim® will prove to be the right tool for future work is still open and further investigations concerning potentially more appropriate instruments are needed.

Table 1: Reliability analysis of the simple divertor model. The whole system reliability with all blocks at R=0.99 is 0.9415.

component name	*individual component* ***R=0.5*** *all the rest R=0.99*	***impact class***
pipe (in)	0.4755	1
weld (in)	0.4755	1
pipe (out)	0.4755	1
weld (out)	0.4755	1
outer vertical target (upper part, in)	0.9415	0
outer vertical target (upper part, out)	0.9415	0
outer vertical target (lower part, in)	0.9415	0
outer vertical target (lower part, out)	0.9415	0
inner vertical target (upper part, in)	0.9415	0
inner vertical target (upper part, out)	0.9415	0
inner vertical target (lower part, in)	0.9415	0
inner vertical target (lower part, out)	0,9415	0
private region PFC (in)	0.9415	0
private region PFC (out)	0.9415	0
cassette body (in)	0.4755	1
cassette body (out)	0.4755	1
outer vertical target (upper part)	0.9415	0
outer vertical target (lower part)	0.9415	0
inner vertical target (upper part)	0.9415	0
inner vertical target (lower part)	0.9415	0
private region PFC	0.9415	0

Outlook

The work summarised above depicts the first step of the development of a flexible tool for analysis of risks to ITER operations due to any kind of leakage from different systems. BlockSim® as a commercial programme for reliability analysis was tested but the suitability as a basic tool for this development is questioned [1,2].

With the obtained experiences, the next step will swap the angle of view from the potentially leaking system to the vacuum itself. Within this approach the risks for the cryostat vacuum by the various potential leak sources will be analysed.

Staff:

A. Antipenkov
Chr. Day
St. Hanke

Literature:

[1] Chr. Day, A. Antipenkov, How to predict availability and reliability of a complex vacuum system?, 2nd Workshop on the operation of large vacuum systems, Warrington, UK, March 2008

[2] St. Hanke, Chr. Day, Risk analysis assessment for ITER in-vessel water leaks, SOFT, Sept. 2008, Rostock, Germany.

EFDA/07-1704-1547 (TW6-TTFF-VP 72)
Study of the Effects of ITER off-normal and Mitigation Events on Torus and Cryostat Cryopumps

Background and objectives

The ITER torus and cryostat cryopumps will be sensitive to off-normal events in other components which hence may affect reliability, maintainability, integrity and safety. Studies so far have tended to look at the effects on systems as a whole and have been focused on finding areas which are pivotal to safety. The specific components of torus and cryostat cryopumps will now be studied to determine the effects of many postulated events on these components. This task will cover the implications of damage to or reduced performance of the cryopumps themselves and to the interfacing systems. Greater understanding of the operational margins for the pump shall also be obtained.

The ITER safety philosophy

The ITER safety analysis approach comprises any off-normal event with a potential to initiate a sequence leading to some hazardous outcome and differentiates between accidents and incidents. An event is considered to be safety relevant when it relates to mobilization spreading and release of radioactive materials. These events are to be analysed to demonstrate that these potential consequences are minimised, preferably eliminated but at all times kept below the prescribed limits, by physical processes and by features of the ITER design. And in any case, the consequences must be below the (dose) limits defined in the General Safety Objectives. Any specific failure consequence which is not associated with a release is not covered, although it may be very essential and associated to long down-times. These non-safety related events, such as operational events with effects on neighbouring systems, had also to be identified for the torus and cryostat cryopumps.

The categorisation of an event as either an incident or an accident is done mainly according to its likelihood, however both event categories are within design basis, i.e. they have been taken into account and implemented in the ITER design base. There is a third event category comprising accident events that are extremely unlikely to occur (frequency below 10^{-6}/year) by themselves or because they involve two completely independent failures each of low likelihood. These Beyond Design Base Accidents are hypothetical events, which have not been taken into account in the design. Nevertheless analysis of these events has been done.

The initiating event itself (Postulated Initiating Event PIE), does not directly cause harm, but requires other failures to occur before a sequence of events could end up realising a hazard. When a PIE occurs, such as the burst of a cooling pipe, the sequence of events that could follow may include aggravating failures, each of which may be a consequential failure, such as further damage caused by the plasma disruption as steam rushes into the plasma chamber, or an independent failure, such as loss of power supplies, reducing the capability of active systems to cope with the event.

ITER has mainly used two independent methods to identify accident sequences, namely a deterministic approach and the so-called PIT approach (Postulated Impact Tables).

The deterministic approach identified 28 ´Reference events´ (and 12 hypothetical events). Four reference events have been introduced in recent discussions with the regulator in 2007; the other 24 have already been described in a deterministic way in the 2001 Generic Site safety Report GSSR.

There is another list of events, the so-called list of 13 bounding events (7 for tokamak, 3 for tritium plant, 1 for hot cell, and 2 during maintenance), which originated from a different, non-deterministic analysis approach. This alternative approach is based on PIE-PIT and com-

bines the bottom-up component level FMEA (Failure Mode and Effect Analysis) approach with the top-down global event tree approach. The PIEs are the events for which deterministic analyses will have to demonstrate the plant capacity in mitigating and, in every case, in withstanding the accident consequences below established safety limits.

The 13 bounding events have been defined on the basis of all in all 93 PIEs that have been treated inside ITER IO according to the PIT approach. These comprise 74 for the ITER tokamak, 14 for the tritium plant and 5 for the hot cells. This means, also in this approach, the cryogenic pumping systems were not (yet) separately considered (whereas the roughing pumps have been, as part of the tritium plant study). With the PIE-PIT approach the deterministically selected reference events could be successfully confirmed. One additional scenario could be identified. All other bounding events are covered by the reference events list.

Safety events affecting torus and cryostat pumping

The next step aimed to identify these events which are of relevance for torus and cryostat pumping. In view of this scope, the PIE-PIT approach resulting in the 93 events is especially helpful. It immediately identifies the relevant cases for torus and cryostat pumping, because vacuum vessel and cryostat have been thoroughly assessed for safety events.

In a very recent study, a FMEA study for the vacuum pumping systems was performed by EU DA. This study was based on the 1998-2001 ITER baseline, which is to a large extent superseded. However, from the safety point of view, the main conclusions of that study are still believed to hold. The authors have identified three PIEs leading to safety relevant disturbance resulting in personnel exposure and environmental release, which however are already enveloped by the reference ITER safety cases.

Finally, besides VV and cryostat, there are additional systems interfacing to the torus and cryostat pumping systems. The major system boundaries are the roughing system which carries the exhaust gases of the cryopumps to the tritium plant, and the cryoplant and cryodistribution system which supplies the cryopanels and shields inside the cryopumps. The FMEA on the roughing system did not produce separate PIEs. The FMEA on cryogenic systems pointed out that no elementary failures initiate safety relevant events in terms of mobilization spreading and release of radioactive materials, so that no PIEs have been set in the FMEA Tables. Of course there exist failure modes for the distribution system, but they result only in an operational inconvenience or interruption of the process, not a public dose hazard. Many are mitigated by redundancies within the system or safety measures. Since that FMEA study, the cryoplant and cryodistribution system has undergone significant changes. However, these changes are believed not to have introduced additional safety issues, so that the generic results still hold. It must be noted that the studies on the cryogenic systems were focussed to check if there are direct safety concerns from faults initiating inside the system and did not deal with possible repercussions in case the accident initiates in other systems such as the cryopumps.

There is one (potential) safety event in the cryodistribution system which is not described in the existing ITER safety documentation: Potential tritium permeation into the coolant helium circuits during high temperature regeneration of the cryopumps at 470 K.

After a detailed study of all relevant events, the cases for the torus cryopump system can be qualitatively grouped as follows (the brackets give the event denominators as used in the ITER safety documentation).

1. Air ingress in the vacuum vessel (VVA2, VNG, hypothetical events 2 and 9),
2. Gas ingress in the vacuum vessel, other than air (service gas nitrogen/helium/neon) (VNG, TVP1/2),

3. Cooling water ingress in the vacuum vessel (all LW, LF, LD, LN cases, hypothetical event 3),
4. Fuelling failure in the vacuum vessel (TPI4),
5. Cryogenic coolant release (break/leak) from the cryopumps (including the case that NB sees torus pumps and vice versa) (VVC, VNC, LPP1),
6. Tritium permeation (TVP6).

And the corresponding cases for the cryostat cryopumps are:

1. Air ingress in the cryostat (VCA),
2. Helium ingress in the cryostat (VCG),
3. Cooling water ingress in the cryostat (LFC1, LWC),
4. Helium and cooling water ingress (hypothetical event 12),
5. Cryogenic coolant release from the cryopumps (MCJ1, VCC, VCH).

Conclusions

After checking the underlying event specifications and including the found non-safety related off-normal events, we concluded with the following central questions.

1. How does the torus pumping system behave under increased gas inflow conditions and what are the consequences to the boundary systems (cryodistribution, forepumping)?
   a. Air from a leak,
   b. Other gas (helium) from a cryogenic break,
   c. Increased fuelling flows,
   d. Disruption mitigation flows: the ability of the pumps to handle the additional transient and steady state gas loads arising from disruption mitigation by massive gas injection.
2. How does the torus pumping system behave under water ingress conditions from different cooled sources ?
3. What are the consequences of a loss of cryopump cryogenic coolant?
   a. To the cryopump itself, if the cryopump volume is closed,
   b. To the vessel,
   c. To the cryosystem.
4. How does the cryostat cryopumping system behave under off-normal ingress of gas (air, helium) or water?
5. What is the consequence of off-normal tritium permeation (tritium at high partial pressure present in the cryopump under high temperature regeneration)?
6. Which cryopump failure conditions have the potential to result in increased hydrogen inventories (administrative limit for tritium, oxy-hydrogen explosion limit for all isotopomers)?
7. What happens with respect to the gasloads on the (remaining) pumping torus cryopumps, if one pump fails to pump?

Within the next stage of this task, it is suggested to assess the operational margins for the above mentioned cases. The details are listed in the following Table, which is currently under review at ITER IO.

Table 1: Resulting key areas of concern from this study and suggested approaches for their assessment.

Key area	***Approach for assessment***
Ability of the cryopumps to handle additional gas loads (inflows as a result to an accident in cryostat or vacuum vessel, within disruption mitigation or from cryogen breaks inside).	Already under nominal pumping conditions, the cryopumps are operated in transitional flow regime. This provides a pumping speed higher than the reference speed according to molecular flow regime. Under increasing gas loads, the cryopump will go further towards viscous operation and, at some point, face a thermal breakdown with consequences to the cryoplant and cryodistribution system (heat loads, pressure drops) [1]. There is no deterministic tool available to predict how the cryopump behaves under these conditions (speeds, capacities, dynamic responses, losing pumping capability, heat load increases). Hence, a two-fold approach will be taken. As first step seen in a longer term development, a theoretical code for description of the cryopump behaviour under transitional flow conditions will be initiated, based on Direct Simulation Monte Carlo. In parallel, the operational window of the cryopumps will be extrapolated from the existing TIMO-data base.
Consequences of severe water ingress conditions on the cryopumps.	The cryosorbent will become saturated with water vapor. The capacity limits will be extrapolated from existing sorption data for the ITER reference charcoal at FZK. In addition, estimates will be given on necessary regeneration conditions to restore full functionality.
Assessment of tritium permeation	An analytic study of the results of tritium permeation under off-normal conditions (475 K regeneration) will be made. Depending on the results, recommendations will be given so as to ameliorate this issue.
Pump drop-out	ITERVAC Study of the resulting distribution of gasloads on the remaining pumps.
Small gas leaks	In the case of small air leaks, the cryogenic situation may be kept and the leaks therefore be unnoticed for a long time, thereby building up high inventories. From that point of view, it may involve a higher risk than a big leak. The operational boundaries will be assessed and recommendations to manage this risk will be given.

Staff:

Chr. Day
X. Luo

Literature:

[1] Chr. Day, V. Hauer, X. Luo, R. Pearce, M. Wykes, G. Piazza, Implications of increased gas throughputs at ITER on the torus exhaust pumping system, IAEA Fusion Energy Conf, Oct. 2008, Geneva, Switzerland

EFDA/07-1704-1618 (TW6-TTFF-VP 75-1)
DNB Cryopump Initial Design Study

Objectives

The Diagnostic Neutral Beam (DNB) for ITER is shorter and will have different requirements than the Heating Neutral Beam (HNB). This task is an initial design study on the cryopump system for the DNB and aims to provide a base design reflecting the operation scenarios foreseen, the space envelope and an assessment of the resulting heat loads as input parameters for cryogenic valvebox and cryoplant design.

Conceptual design development

Together with the main parties involved in the DNB (i.e. ITER IO (Vacuum Group and NBI group), F4E and the Indian DA), a comprehensive list of input data was agreed upon. The maximum possible pumping size, the position of the cryopump in the beam line vessel as well as the needed pumping speed, and the possible maximum pumping times for protium have been derived from that. The positioning of the beam line components was investigated and has been finally fixed and agreed. The resulting beam line geometry has been used to investigate the detailed performance of the proposed cryopump system and to optimize the vacuum conditions.

In case of the gas dynamics in the DNB, the main result of the design review was that the same 3 m long neutralizer with a 4 channel structure as for HNB will be used [1]. This reduces the needed gas flow for the neutralization of the ion beam, improves the vacuum conditions along the beam line and increases the operation times. Also the distance between the neutralizer and the RID has not been reduced (contrary to former design suggestions) so that a good access for pumping in between the components was ensured. It has been further outlined that the pressure between the neutralizer and the accelerator is less critical than for HNB and can reach values up to 0.04 Pa. The final set-up of the DNB components is illustrated in Fig. 1.

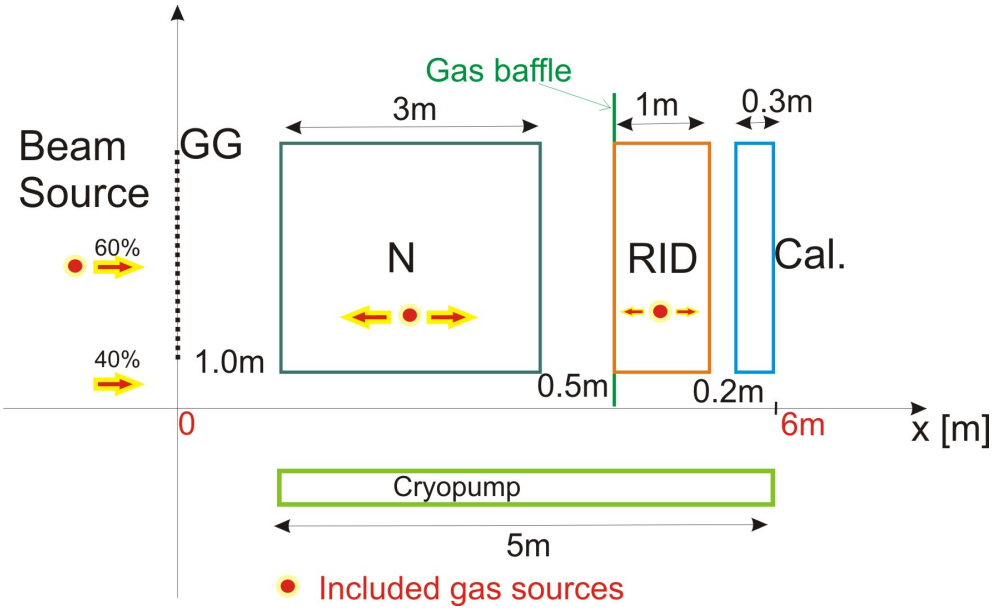

Fig. 1: Geometry of the beam line as used for the gas profile calculations.

As final result of the conceptual design work, it could be demonstrated that the same modular design as developed for the HNB (under task TW6-THHN-NBD1) can be used for the DNB as well, only the number of modules has to be adapted to the shorter DNB beamline [2]

(5 modules). Consequently, the design of the DNB followed the same steps as described for the HNB under TW6-THHN-NBD1 in this Annual report.

Benchmark of the Monte Carlo based method for thermal radiation calculation.

For this new open structured NBI cryopump design FZK developed a new method for the determination of the heat loads by thermal radiation, which starts from the analytical formulae and calculates the accurate viewing factors from the 3D Monte Carlo models (MOVAK3D) which are anyway existing from the detailed vacuum design process. One sub-task was to validate the FZK approach by an independent benchmark of the obtained radiation results. For that purpose, the CATIA models were explained and given to IST Portugal who were re-calculating thermal radiation with ESARAD, a verified code which is very routinely used in aerospace applications. The found agreement was excellent. The calculated values are summarised in Table 1. There is an additional significant heat load Q_{el} coming from electrons which are backscattered from the beamline components. This is still an unknown quantity.

Table 1: Heat loads for the ITER diagnostic neutral beam cryopump in the case of unshielded beamline components at 373 K and a beamline vessel temperature of 300 K. The shielding temperature is assumed to be between 80 K (in) and 90 K (out), and the panel circuits are between 4.4 and 6.7 K.

Mode	***Radiations Shields***	***Panels***
Stand by	7.2 kW	160 W
Pulse operation	7.27 kW + Q_{el}(shields)	223 W + Q_{el}(panels)

This extensive method was used because of the complex surface arrangement in the cryopump design, see Fig. 2. Compared to the former designs the heat load by 300 K radiation from the beam line plays an important role. Therefore the appropriate coating of the surfaces is essential to derive finally with the minimized heat load on the 5.5 K panel circuits.

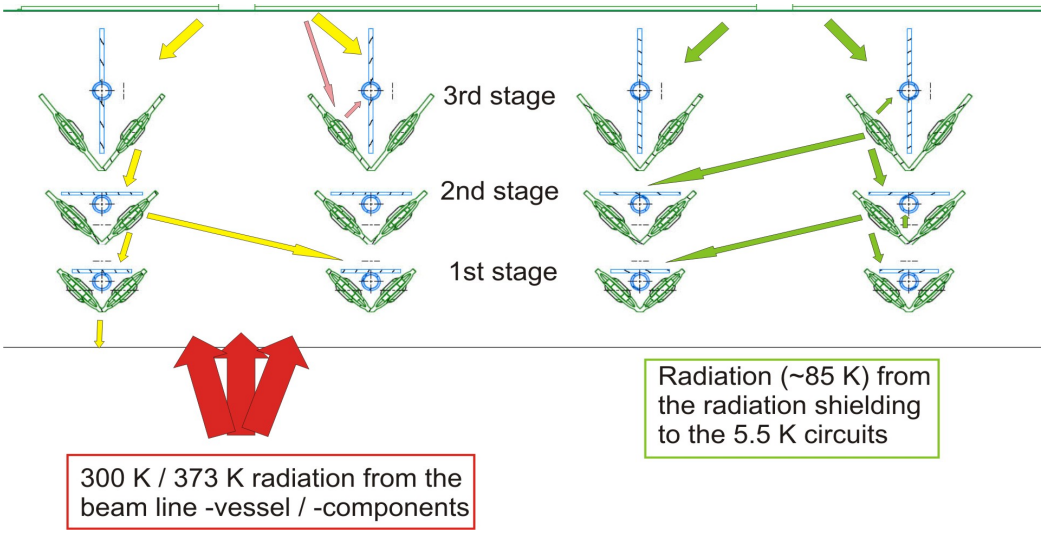

Fig. 2: Scheme of the final DNB cryopump concept (shown is one module; blue are the 5.5 K cryopanels, green are the radiation shields). The two dominant radiation heat loads to the 5.5 K circuits are the reflected 300 K and 373 K radiation (yellow arrows) and the directly radiated 85 K radiation from the shielding (green arrows).

Final status and future work

Finally, FZK provided a CATIA5 model of the initial cryopump design for the ITER Diagnostic Neutral Beam. Thus, the scope of this task has been fully achieved and the task is now closed. But it does not yet contain all design or manufacturing details, which have to be provided in a follow-up task.

In summary, each cryopump half is 5 m long, 2.76 m high, and 0.5 m deep. It provides for a protium pumping speed of 3000 m³/s at a capture coefficient of 30%. The pressure between accelerator and neutralizer has been calculated as 0.012 Pa. The difference between this value and the maximum acceptable one of 0.04 Pa determines the maximum pumping time in protium operation, because protium accumulation leads to a slight, but noticeable pumping speed decrease (which means pressure increase). This effect limits the maximum pumping time to 3000 s under continuous operation and to 4800 s under pulsed mode.

Staff:

M. Dremel
St. Hanke
V. Hauer
X. Luo
R. Simon
H. Strobel

Literature:

[1] X. Luo, M. Dremel, Chr. Day, ProVac3D and application to the neutral beam injection system of ITER, 26th Int. Symp. Rarefied Gas Dynamics, July 2008, Kyoto, Japan.

[2] M. Dremel, Chr. Day, St. Hanke, X. Luo, Cryopump design development for the ITER Neutral beam injectors, 25th SOFT, Sept. 2008, Rostock, Germany.

Fuel Cycle
Tritium Plant

TW4-TTFD-TR 41
Experimental Investigation of Undesired Side-reactions in PERMCAT

TW4-TTFD-TR 43
Comparison of Batch and Continuous Operation Modes for the Impurity Processing Stage of the Tokamak Exhaust Processing System

Introduction to CAPER and Tokamak Exhaust Processing (TEP)

The CAPER process developed at TLK has been chosen as a reference design for the TEP systems in ITER (design from 2001). It comprises 3 stages (Fig. 1) to achieve very high Decontamination Factors (DF). The first stage includes a front-end permeator to remove the major part of the tritium present in the molecular form. The second stage comprises a combination of a catalytic reactor and a permeator so as to recover tritium bound in molecules. The third stage called PERMCAT (combined permeator / catalytic reactor) operated in the counter current swamping techniques allows recovering the remaining tritium down to a very low residual activity. The EFDA tasks reported here cover the second stage but mainly focus on the last one.

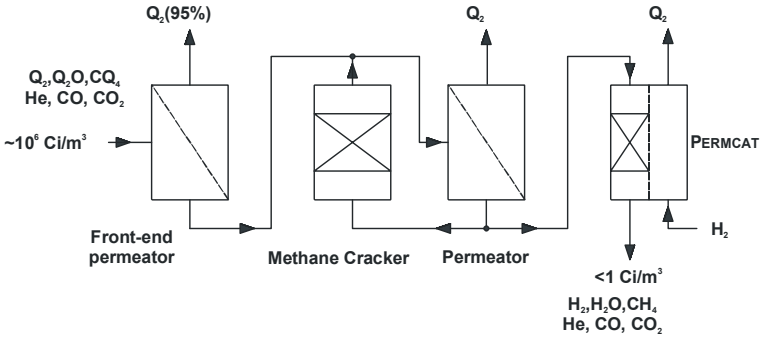

Fig. 1: The 3 stages of the CAPER process.

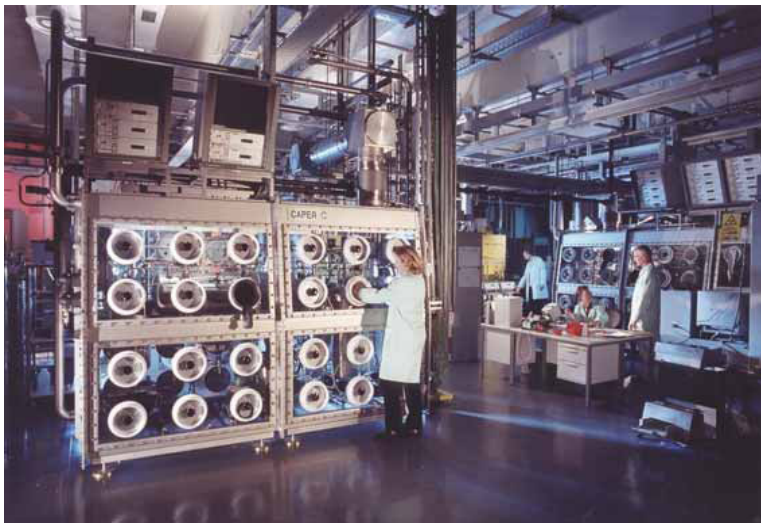

Fig. 2: The CAPER facility at TLK (Permcat).

The CAPER facility (Fig. 2) has been constructed at the Tritium Laboratory Karlsruhe (TLK) to study at the technical scale the combination of physico-chemical processes engaged in the TEP systems of fusion machines. The facility is also an essential and central system at TLK since all the primary gaseous waste arising from other experiments at TLK have to be processed with CAPER for the tritium recovery.

Improvement to the mechanical design of PERMCAT reactor

Background

The design of PERMCAT reactors has to provide technical solutions to avoid or compensate mechanical constraints during operation. Beside the thermal expansion at the nominal operating temperature of 400°C, the significant lattice parameter increase of the Pd/Ag membrane due to hydrogen absorption at room temperature (off normal event) can have severe consequences on the PERMCAT reactor integrity. This has been unfortunately observed with

the failure of the first technical PERMCAT reactor based on a parallel arrangement of single-tube units

Different alternatives have been studied in order to simplify the design and improve the robustness of PERMCAT reactor. All PERMCAT reactors are produced in collaboration with the main workshop of FZK.

Corrugated PERMCAT (single-tube unit) in CAPER

The PERMCAT reactor operated since November 2006 in the CAPER facility includes special corrugated Pd/Ag membranes produced in collaboration with the company BEST-Swagelock [1]. It has been chosen among different designs according to its promising processing capability, especially when the amount of tritium bound in molecules is significant. The rather short length of such PERMCAT unit is turned into advantage using 2 single-tube units in line, which allows integrating in between a monitoring system (ionisation chamber) at the mid-pathway for a better control and understanding of the process in a whole.

This upgraded reactor has been validated throughout a comprehensive gas processing tests campaign in CAPER using relevant tritiated gaseous mixtures covering a wide range for gas composition and activity. According to this campaign, one can admit that the upgraded PERMCAT design has successfully passed the endurance test phase, which was in fact the last step of the study concerning the improvement of the PERMCAT mechanical design. Very high detritiation factors have been measured with this reactor even on gas mixtures above the specifications, thus confirming that PERMCAT can easily cope with activities and impurity concentrations far above the design values.

However, it has been noticed during the last part of the experiment focusing on side reaction with carbon oxides (cf. next chapter) that the reactor showed some limitations when significant amounts of water vapour are present in the process. It was decided to transfer this PERMCAT into the RBX (Repair) box of TLK, to remove the outer jacket, and to change the internal configuration so as to ensure a sufficient heat all over the process. After this modification, the reactor appears totally compatible with high level of water vapour, which is vital for the next experiments planned for the near future.

New technical-scale PERMCAT (multi-tube unit in a single catalyst bed)

The process of larger throughputs asks for a technical (i.e. multi-tube) PERMCAT reactor.

The production of the new reactor involving a battery of 13 Pd/Ag membranes inserted in a single common catalyst bed has been recently completed in collaboration with the main workshop of FZK.

Even if it uses finger-type membranes (together with capillary tubes), it is considered as an upgraded design. The first technical PERMCAT reactor was a straightforward parallel arrangement of finger-type single-tube units so that the failure of one tube spoils the entire reactor. In contrast, for the next reactor, if one membrane fails, one can rely on the others to keep the efficiency of the reactor at a reasonable level.

This reactor has been designed to enable the exchange of the capillary tube set (Fig. 3) in order to study the influence of the

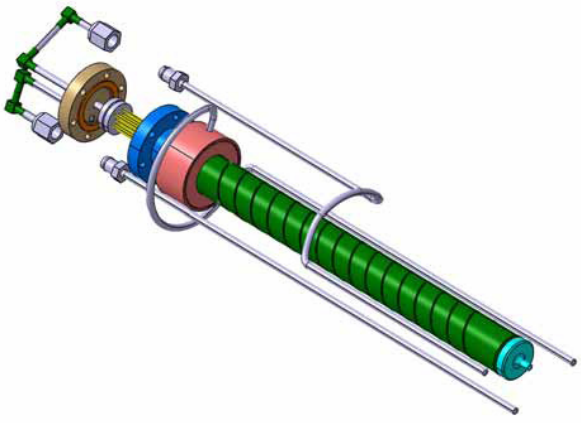

Fig. 3: New technical scale PERMCAT.

capillaries diameter, since previous experiments revealed a significant influence of this parameter. An experimental campaign has been started to point out the optimal for the capillaries diameter using isotope exchanges between H_2O and D_2.

Experimental investigation of undesired side-reactions in PERMCAT (TR 41)

Background

The following reactions are taking place simultaneously in the PERMCAT reactor:

1.	Isotope exchange reactions	$CQ_4 + 2\ H_2 \leftrightarrow CH_4 + 2\ Q_2$
2.	Isotope exchange reactions	$Q_2O + H_2 \leftrightarrow H_2O + Q_2$
3.	Inverse Water Gas Shift reaction	$CO_2 + Q_2 \leftrightarrow Q_2O + CO$
4.	Methanation reaction	$CO + 3\ Q_2 \leftrightarrow CQ_4 + Q_2O$
5.	Methanation reaction	$CO_2 + 4\ Q_2 \leftrightarrow CQ_4 + 2\ Q_2O$

The PERMCAT process relies on catalyzed isotope exchange reactions to recover tritium from hydrocarbons or water (reaction 1 and 2). However, different unwanted side reactions occur (3 to 5) as well. The occurrence and importance of these reactions depend not only on the gas composition, but also significantly on the catalyst material. A nickel based catalyst has been chosen because it has shown the best compromise in case of a complex gas mixture containing all these species.

In fact, the presence of carbon oxides (CO and CO_2) might be the most significant limitation for the PERMCAT process because side reactions take place. The main concern for the reactions (3) to (5) is the Q_2 consumption either with CO or CO_2 and the resulting production of water and hydrocarbon. In fact Q_2 is chemically locked in molecules instead of participating to the detritiation process via permeation and isotope exchange reactions. In addition, the production of water could lead to severe problems of condensation.

Experimental campaign and main results

The significance of these effects, and possible counter measures have been studied in details with the PERMCAT reactor of the CAPER facility. Relevant gaseous mixtures containing different amount of carbon oxides have been produced and processed with different parameters.

As an example, the Figure 4 shows a typical PERMCAT record plotting the evolution with time of impurity & purge flow rates and purge pressure (left y-axis, log scale) together with ionisation chamber signals and humidity at the PERMCAT outlet (right y-axis). The gas mixture originally contains 4% Q_2 @ 5.8 kCi/m^3 in He, and CO_2 up to 2% has been added during the run. Between the purge of the PERMCAT at the beginning and the end, the experiment can be separated into 3 main parts, consisting of different concentrations of CO_2 clearly mentioned on the figure.

The last part is used as reference to see the how PERMCAT is working without CO_2. The humidity (violet) and activity (yellow) at the impurity outlet are very close to the ones measured during the purge. With addition of 1% CO_2, the humidity at the impurity outlet already shows a constant high level corresponding to the saturation of the sensor, thus reflecting potential for water condensation in the system. However the detritiation efficiency is only weakly affected. Dilution with helium downstream of the PERMCAT is necessary to avoid water condensation while processing the mixture with 2% CO_2. Both humidity and activity at the outlet are relatively but artificially low (factor 4 for dilution).

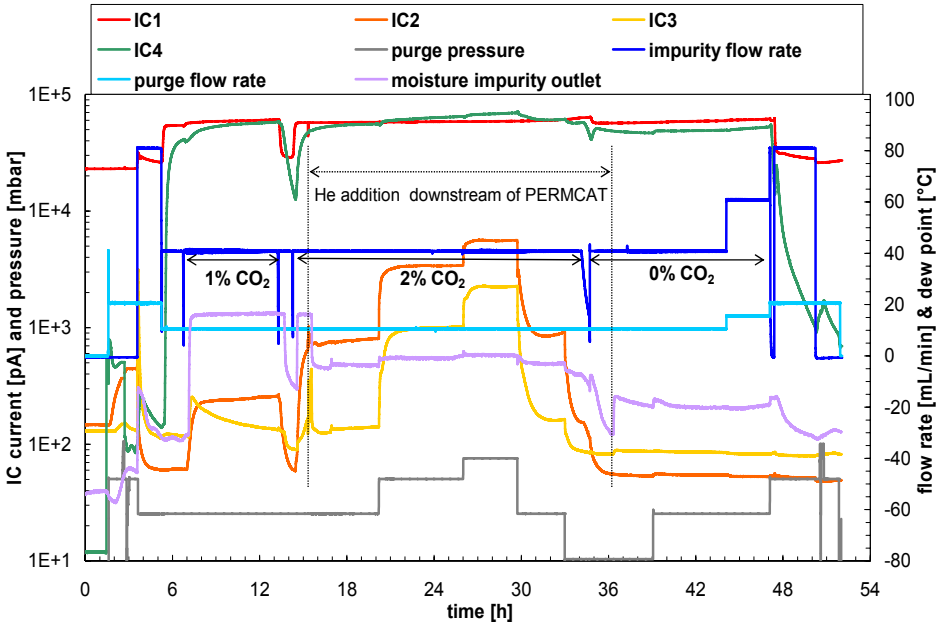

Fig. 4: PERMCAT run with different CO2 concentration and effect of purge pressure.

The influence of H_2 purge pressure (in grey) on the detritiation performance is studied. Different H_2 pressures are imposed and the ionisation chamber signals (yellow and orange) reflect change in the detritiation performances. In fact, the lower pressure gives the best results for detritiation and humidity. It has been confirmed with other experiments that a low purge pressure is very effective to minimise the effects of side reactions, since methanation reactions (4 and 5) cannot proceed even with high amounts of carbon oxides in the mixture.

Comparison of batch and continuous operation modes for the Impurity Processing stage of the Tokamak Exhaust Processing system (TR 43)

Background

The second stage of the CAPER process uses heterogeneously catalyzed reactions to split tritiated molecules and permeation of hydrogen isotopes through a Pd/Ag membrane. A loop combining these processes can be basically operated in two different modes. In the straightforward batch mode the loop is filled with the gas to be detritiated, it is cycled and processed for a certain period of time until the tritium level is sufficiently lowered, and then the loop is emptied for the next batch. In the continuous mode, the gas to be detritiated is continuously fed into the loop at a flow rate much lower than the loop circulation flow rate; the amount of gas in the loop is kept constant by a continuous withdrawal of gas.

While the batch mode is the nominal operation mode at TLK since the priority is given to high decontamination factors with minor time constraint, the continuous mode has been chosen as reference for ITER, motivated by an easier control and a reduced tritium inventory.

Experimental campaign and results

A comprehensive experimental campaign has been carried out to point out the advantages and drawbacks of each mode in terms of performance (decontamination factor at a given throughput) and operation. The experimental results cover a three year long campaign with more than 40 data taking days (time for gas preparation not counted). In total more than 15 g of tritium have been processed and recovered afterwards.

Whatever the operation mode, the performances strongly depends on the permeation. During the process of hydrocarbons at high partial pressures, coking of the permeator resulting

from hydrocarbons decomposition onto the surface of the permeator occurs. This seriously affects the overall efficiency of the process since the permeation is reduced. Therefore regular regeneration of the permeator cannot be avoided, also for ITER operation. To get reliable results, this procedure has been performed before each experiment.

The Figure 5 shows the comparison of the performances under different operation modes. The batch mode shows by far the highest decontamination factors of this study, but the total throughput (amount of gas processed per time) is limited. However, at the same throughput, the decontamination factors measured with the continuous mode are at least two orders of magnitude lower. So, the batch mode is preferred with regards to performances, while the continuous mode is more convenient to operate.

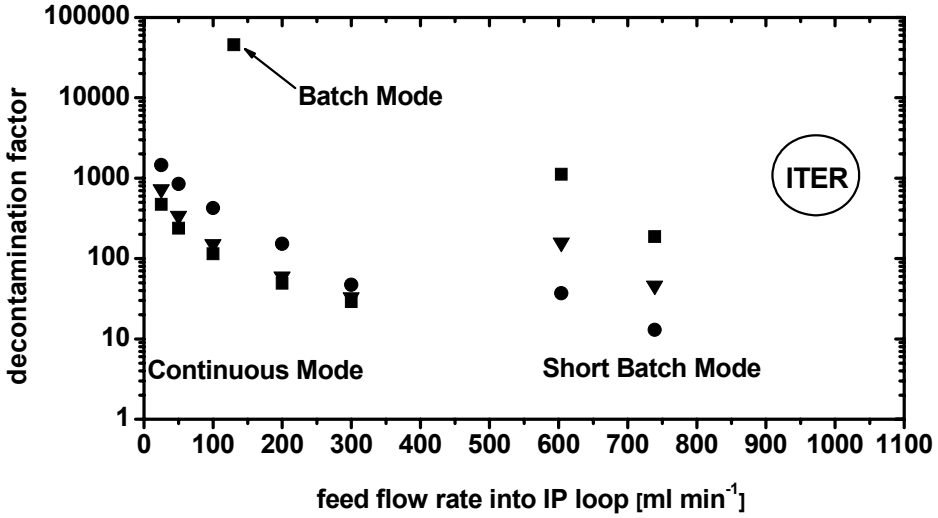

Fig. 5: Comparison of performance for different operations of the 2nd loop (square: CQ_4, circle: Q_2, triangle: overall).

Using a compromise between batch and continuous operation, the so-called short batch mode enables reaching sufficiently high decontamination factors at relatively high throughputs. Another advantage of the short batch mode is its lower fault liability against coking of the permeator membrane in presence of carbon containing gases. Therefore it has been suggested to adopt the short batch mode for ITER operation. With the 2nd loop of CAPER operated in this short batch mode, DF at about half of the ITER throughput have been measured, although the size of the both main components (methane cracker and permeator) are only 1/5 of the values from ITER design DDD 2001.

General conclusion and perspectives

The CAPER facility has been operated at the Tritium Laboratory Karlsruhe (TLK) for more than one decade to support and optimise the TEP design in ITER. The significant amount of experimental results accumulated throughout intensive experimental campaigns carried out and covering all 3 stages of the process constitute a comprehensive and unique database for the design of the process at the ITER scale. The study and optimisation of the last stage is still going on given the complexity and the high potentials of the PERMCAT process.

Beside the pure R&D activities, the CAPER facility is regularly involved and used to support other experiments at TLK. The activities cover naturally the tritium recovery from “waste” gas produced during any experiments working with tritium, but also the preparation of certified tritiated gas mixtures. In view of its future increasing role in the infrastructure, several modifications have been integrated to enhance the overall availability and reliability of CAPER. Several new by-pass lines have been installed for flexibility and redundancy. Several old, defect or unused components [2] have been removed from the glove boxes, either sent as

waste or kept as spare parts. Modifications towards very highly tritiated water processing with PERMCAT are ongoing. These actions in a whole are very valuable to reinforce the know-how at TLK for the modifications of existing facilities handling tritium.

TEP related R&D activities will focus next year on PERMCAT technology, focussing on 2 major experimental campaigns:

- Experimental demonstration of the potential for PERMCAT to detritiate very active water using the current PERMCAT (single-tube) in CAPER,
- Experimental demonstration at the technical scale of the PERMCAT versatility [3] for its use in the fuel cycle and blankets systems using the new multi-tube PERMCAT.

Staff:

B. Bornschein
D. Demange
K. Guenther
T.L. Le
P. Schuster
F. Scheel
K.H. Simon
S. Welte
R. Wagner

Literature:

[1] D. Demange et al. "Tritium processing tests for the validation of upgraded PERMCAT mechanical design" Fus. Sci. Technol. 54 (2008) 14.

[2] C. Cadwell-Nichols et al. "Post service examination of a tritium permeator and a turbomolecular pump from the CAPER facility at the Tritium Laboratory Karlsruhe" Fus. Sci. Technol. 54 (2008) 599.

[3] D. Demange et al. "The PERMCAT process for the decontamination of highly tritiated gaseous mixtures and liquid water produced during cleaning phases of fusion machines" to be published in Fus. Eng. Des.

TW4-TTFD-TR 44
Inactive Tests of Selected SDS Control Loop Performance under Typical ITER Operating Conditions

This task was redefined to assess the accuracy to which gas mixtures could be produced using thermal mass flow controllers. Existing components and loops of the CAPER facility were used to perform these tests using inactive gases, namely protium, deuterium and helium. After individual calibrations of the thermal mass flow controllers, pairs of gases were delivered simultaneously to a buffer volume using predefined flow rate profiles. The actual pressure profiles produced were compared with estimated pressure profiles using the calibration data. As the calibration of mass flow controllers is non-linear for light gases due to the transition between laminar-turbulent flow in the thermal mass flow controllers, variable calibration coefficients were used and they produced the best results, though still at the limit of estimated accuracy for the experimental system and analysis used.

Recommendations on the use of thermal mass flow meters in ITER applications have been made, together with recommendations for consideration to be made of other devices which may be more appropriate to the environmental conditions of many proposed ITER applications.

Staff:

C.J. Caldwell-Nichols

TW6-TTFD-TR 64
Endurance Tests of Water Detritiation System

The Water Detritiation System (WDS) and the Vent Detritiation Systems (VDS) are the only systems in ITER which have direct interface with the environment after processing tritiated streams. Moreover the WDS is in direct combination with the ITER Isotope Separation System (ISS) which should process tritiated streams in a fluctuation mode in view of flow rates and composition.

An evaluation of time behavior of the critical components, such as the catalyst/packing mixture of the LPCE columns and the SPM electrolyte of the electrolysis unit is compulsory in order to implement an appropriate management and maintenance scheme in the ITER WDS.

The so-called TRENTA facility for water detritiation which consists of a Combined Electrolysis Catalytic Exchange (CECE) process employing a LPCE column has been commissioned with tritium at the Tritium Laboratory Karlsruhe (TLK). The TRENTA CECE is in operation on long term basis for process performance studies and endurance tests of critical components needed for the design of ITER WDS.

The maximum tritium activity in the tritiated water which is allowed be processed within the TRENTA facility at TLK is 10 Ci/kg. In order to extend the endurance tests with catalyst under similar conditions as envisaged in ITER, an experimental rig is in operation at ICIT Rm. Valcea with tritiated water of 100 Ci/kg. The experimental program on both experimental rigs is carried out in cooperation.

The experimental activities at ICSI Rm. Valcea have been completed and the experimental data for the catalyst showed that the differences in the values of the key parameters measured at the beginning of the experiment and after 9 months of operation are in the range of measurement errors and there is no clear indication that at this level of tritium concentration the catalyst was damaged.

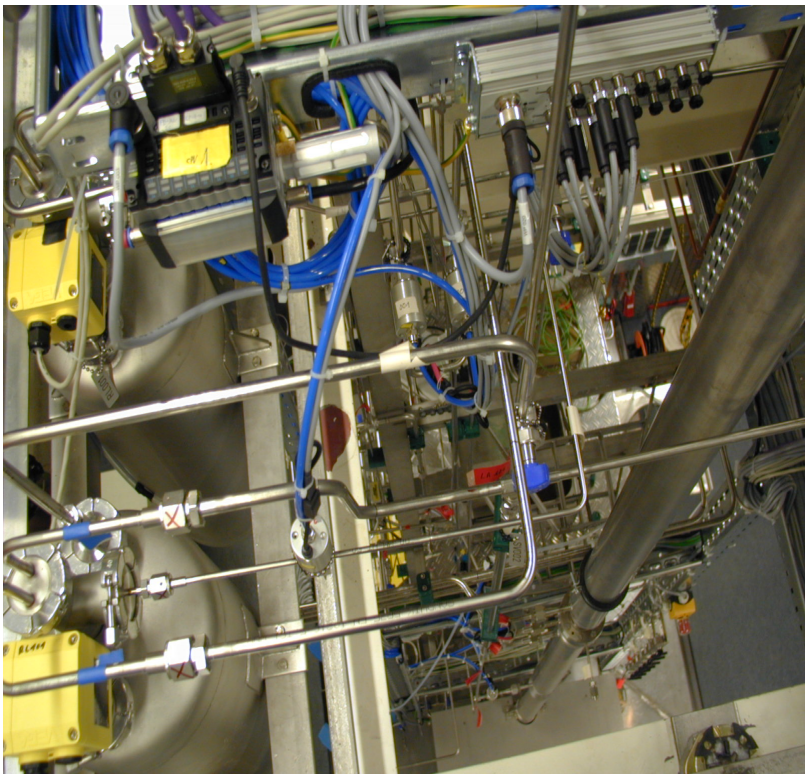

Fig. 1: The LPCE column of CECE process.

The main activities at TLK in 2008 on the CECE process of TRENTA facility, shown in Figure 1, have been focused on:

- Running the CECE process of TRENTA facility with increased concentration of tritium
- Evaluation of separation performances of mixture catalyst/packing under various operation conditions, i.e. temperature and ratio gas to liquid
- Measuring the chemical quality of the water inside the LPCE column in order to identify the composition degradation of the catalyst, if any.

The experimental results from the 2008 runs of the LPCE column showed a good separation of the mixture catalyst/packing, which are in agreement with the separation measured on the 2 m LPCE column which was used as a prequalification of the mixture before installation of the 8 m LPCE column.

Staff:

R. Michling
S. Welte
W. Wurster
I. Cristescu

TW6-TTFD-TR 56
Isotope Separation Tests for Evaluation of Column Packing Options

Minimization of tritium inventory in the ITER ISS can be achieved both by operation of the columns at appropriate loadings and by using a packing or combinations of packing with low tritium inventory and high separation performances. Therefore, two types of packing, namely Helipack-C and Sulzer EX have been tested on the Cryogenic Distillation (CD) column of the TRENTA ISS test loop in TLK (FZK).

In order to validate key aspects of the ITER Isotope Separation System (ISS) design and in view of tritium inventory minimization, a single column CD system with a condensing power approximately half of ITER columns has been used within TRENTA facility. A test program involving the CD system has been carried out and the results concerning the liquid hold-up and separation performances of two types of packing, Helipack-C and Sulzer EX shown in Figure 1, have been evaluated.

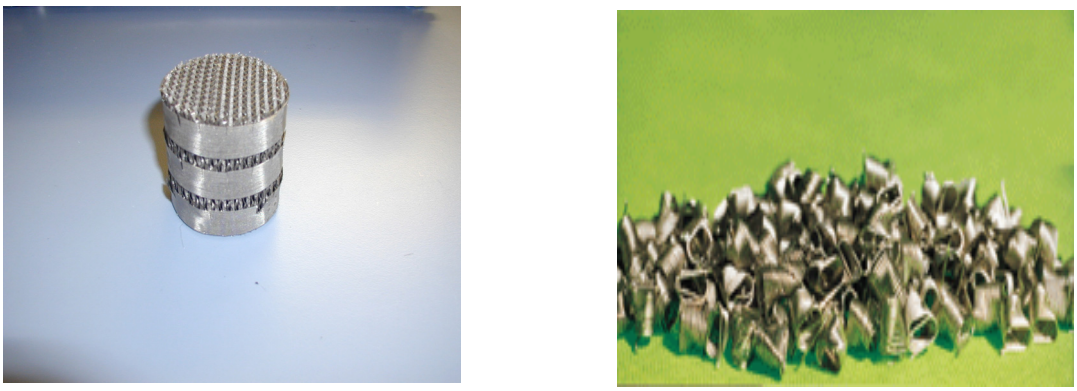

Fig. 1: The Sulzer EX and Helipack–C packings.

For determination of the liquid hold-up on the packing, the amount of hydrogen retained in the main components of the CD column was subtracted from the total amount of hydrogen fed into the CD column. The main components with retained hydrogen are:

- Boiler: The amount was calculated considering the liquid level in the boiler and the specific volume of liquid at the saturation pressure. Corrections have been made based on the liquid composition which was measured with the quadrupole spectrometer
- The amount of liquid contained in the batch liquid hydrogen flow measurement
- Condenser: The amount of liquid hydrogen on the vertical tubes of the condenser has been calculated based on Nusselt theory of a liquid hydrogen film.
- The amount of liquid hydrogen in the collector beneath the CD condenser
- Liquid hydrogen in the radio frequency liquid hydrogen flow measurement.

A dedicated software based on TRIMO model was used in order to calculate the HETP of the Helipack C packing.

The experiments for measuring the liquid hold-up and the separation performances of the Sulzer EX have been carried following the same procedures as during the Helipack-C characterization. The amount of gas required to cool down and to get liquid in the lower part of the column was higher compared with the Helipack C packing; between 1.5 -2.0 times higher. Several attempts to cool down the entire column and to get a stable liquid hydrogen in the boiler of the columns have been made but without success. Due to the fact that the amount of gas required to be fed in the CD column equipped with Sulzer EX was far higher compared with the Helipack-C and due to the hydrodynamic instabilities during the cooling

down of the column, the activities for characterization of this packing, as a potential candidate for ITER CD columns, have been canceled.

Preliminary conclusions and recommendations

The hold-up of the Helipack C packing measured on the CD dedicated process at TLK showed to be higher than the reference hold-up in the DDD's 2001, respectively 0.005 moles/cm^3.

A new type of packing, Sulzer CY, is proposed to be investigated.

After the comparison of these two packings, Helipack C and Sulzer CY, the packing which will provide the lowest hold-up for the column of the ITER ISS will be selected for detailed investigations. During the investigations of the selected packing, the influence of the isotopic composition on the liquid hold-up should be considered as a first priority. Tests with various mixtures hydrogen-deuterium shall be carried out and the extrapolation, if possible, to the liquid hold-up for tritium shall be made.

Staff:

R. Michling
S. Welte
W. Wurster
I. Cristescu

TW6-TTFD-TR 63
Testing of Isotope Separation System (ISS) with the WDS

The Water Detritiation System (WDS) and Isotope Separation System (ISS), based on cryogenic distillation (CD), will operate in such a way that WDS will be a final barrier for the processed protium waste gas stream discharged from ISS. The concern over tritium release into the environment during pulsed operation of the Torus and the proof of the compliance with the limiting values for tritium needs to be addressed very carefully. To investigate the capability of the WDS to achieve the goal, the influence of the additional discharge stream from ISS (basically hydrogen) and its feeding location into the WDS, the separation performance of the Liquid Phase Catalytic Exchange process has to be investigated and accurately mathematically modeled.

In order to develop the experimental data base needed for design of ITER WDS and ISS, the following modes of operation have been considered during the design of the WDS-ISS combination:

- Operation of the LPCE column with composition fluctuation in the stream returned from the CD column
- Operating of the CD column with composition and flow rate fluctuations in the feeding stream
- Operation in different dynamic modes in order to validate and bench mark the TRIMO code

To support the research activities an experimental facility called TRENTA based on the combination of Combined Electrolysis Catalytic Exchange (CECE) and Cryogenic Distillation (CD) has been installed at the Tritium Laboratory Karlsruhe. The main issue of the experimental program on the TRENTA facility at TLK is to investigate the combined WDS-ISS process during isotopic and thermal transitory regimes. Therefore, a detailed investigation of the control system and separation performances of the CECE process when working as a final barrier of the top product of the CD column to be discharged into the environment is under investigation.

In support of the above program the following activities have been carried out in 2008:

- The detailed design of the heat exchangers to be installed within the cryogenic distillation cold box with the aim to allow for feeding and processing of various streams of the CD column.
- The detail design of the valve box where the components which shall work at room temperature are accommodated
- The manufacturing of the heat exchangers is 80% completed
- The installation of the components within the valve box and glove box is almost completed as is shown in Figure 1.

Staff:

S. Welte
R. Michling
R. Wagner
W. Wurster
I. Cristescu

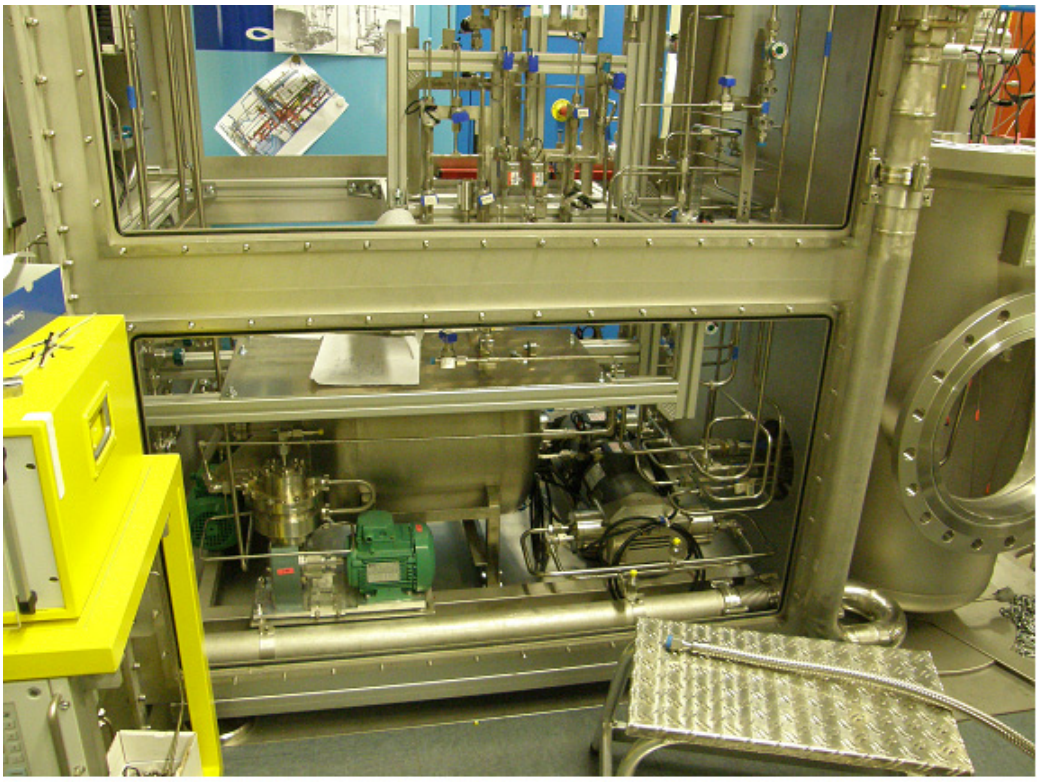

Fig. 1: Installation of the components within the valve box.

EFDA/06-1510 (TW6-TTFD-TPI 55)
Update of ITER ISS-WDS Process Design -1

The objective of this task is to update the designs of the ITER ISS and WDS as documented in the 2001 FDR (Final Design Report). The activities performed during 2008 have been focused on the evaluation of the impact of the new requirements from ITER IO as a result of design integration activities. The following issues have been considered as a reference for the activities carried out:

- Plasma operation (helium, protium, deuterium and DT) taking into account fluctuations between burn and dwell phases and due to cryopump partial regeneration schedules;
- Overnight shifts when full regeneration of cryopumps is carried out;
- Tritium recovery from PFC's and vessel wall conditioning;
- Long term maintenance outages when the WDS will remain in operation but no "high tritium" streams to the ISS are present;
- Special operations such as tritium inventory determinations.

The update of ITER ISS-WDS design was developed on the basis that the ISS and the WDS will be integrated by routing the top product stream from the ISS to a feed point near the bottom end of the WDS Liquid Phase Catalytic Exchange (LPCE) Column. In this respect the evaluation of the optimum position of the feed points, hydrogen stream from ISS and the combined "low tritium" feed stream which includes the WDS electrolyser Q_2 stream and the NBI regeneration gas and (possibly) pellet injector propellant, has been established.

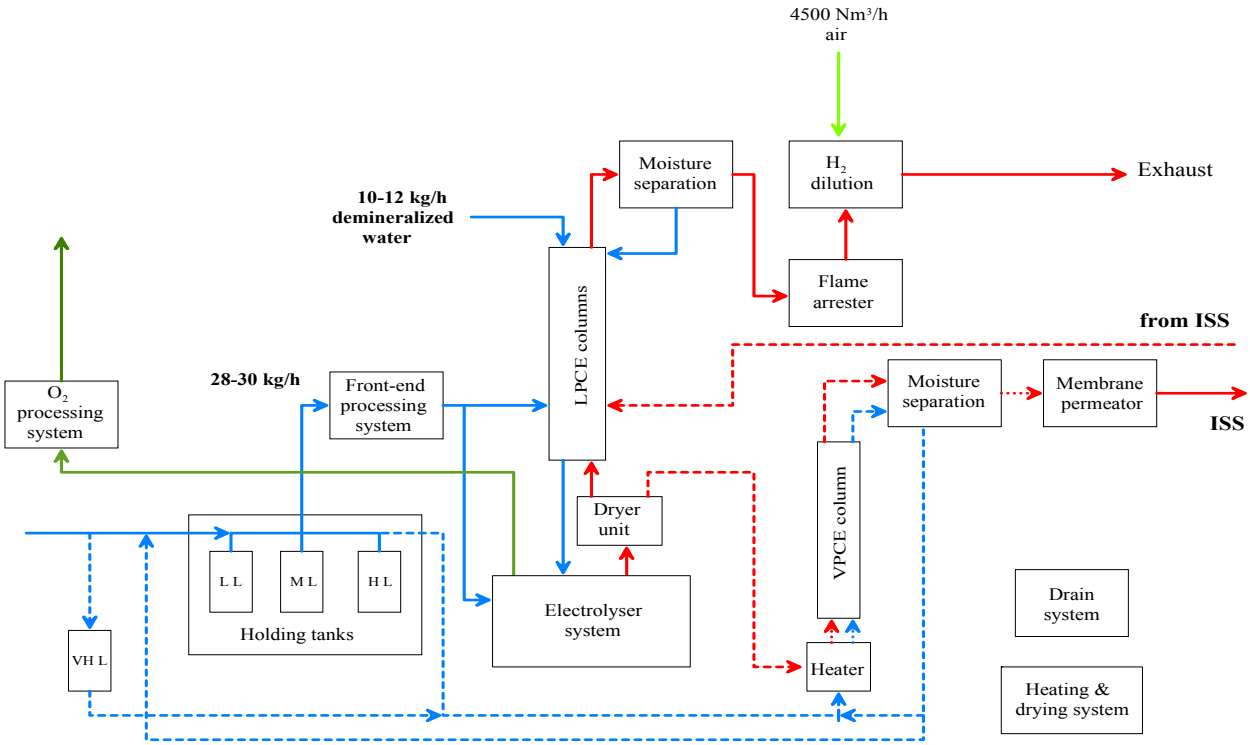

Fig. 1: New configuration of WDS-ISS

The main achievements are:

1. Detailed investigation of the WDS-ISS configuration which allows for reduction of the tritium activity in water to be fed in the CECE process. The new configuration, Fig. 1,

allows also to process the highly tritiated water which shall be produced during high temperature regeneration of the cryopumps.

2. Detailed investigation of the cryogenic distillation cascade; A cascade of three cryogenic distillation columns instead of four columns was found to be feasible for the new approach of the combination between the WDS and ISS. In addition a three cryogenic distillation columns cascade allows producing the deuterium and tritium required for the Torus by only two products:
   - A deuterium stream of high quality: protium <0.5% and tritium <0.02%, which will allow feeding both the NBI and gas fuelling systems.
   - A tritium product of quality higher than 90% which mixed with deuterium of high quality allows feeding Torus with various mixtures.
3. The ISS SRD has been produced and handed over to ITER IO.
4. The 3-D layout and room by room components allocation inside the WDS-ISS room for the ITER Tritium Plant have been developed and provided to ITER IO in view of design integration activities.
5. Technical support for development of WDS SRD has been provided to ITER IO.

Staff:

I. Cristescu
W. Wurster
A. Lazar (ICSI-Rm. Valcea – Romania)

EFDA/06-1514 (TW6-TTFD-TR 65)
Development and Customization of CATIA V5 for Tritium Plant Systems

The Computer Aided Three Dimensional Interactive Application (CATIA) is a multi-platform commercial software suite intended for computer aided design, engineering and manufacturing of mechanical, electrical and fluid systems. The wide range of applications (P&ID, HVAC diagrams, piping design, tubing design, HVAC design and equipment arrangement) provides the ability for a upstream design process from functional 2-D to a 3-D detailed design including a consistent and structured data base containing all necessary information for system components.

The Project Resource Management (PRM) system and the standard parts catalogue required for customisation of the CATIA data base and the design tools for tritium plants were developed within the previous task TW5-TTFD-TPI 51. However, a facilitation of the design work on the ITER Fuel Cycle systems layout within the ITER Tritium Building required a further development of the CATIA PRM. This development includes an implementation of the numbering systems (for example the ITER numbering system), design methods reflecting the plant breakdown structure and using ENOVIA remote participation. Another important task was the implementation of ISOGEN software for the production of piping isometric drawings necessary for manufacturing. Since ISOGEN is not included in the CATIA package, such implementation requires customisation of E&S PRM in order to allow for seamless integration of additional tools into the CAD system.

Testing of the CATIA E&S PRM together with the development of design methods was performed within the existing TLK project “Tritium Purification and Circulation Loop for Beta-Source” (IL). This project was chosen as the pilot since it represents the most complicated system designed and manufactured in TLK at present.

On the basis of presented flow diagram and process description, a P&I diagram was developed inside CATIA PRM. Necessary valves, pressure and flow rate sensors providing the process control and safety conditions were added. The pipes diameters (numbers of pipes are not shown in the figure for readability) were chosen to minimize the tritium inventory in the system. An ITER-like numbering system developed for the experiment was applied to the diagrams and CATIA data base for further 3-D design. In total, the system consists of 8 pumps, 56 valves, 28 pressure sensors, 3 flow rate meters and controllers and 9 temperature sensors. Following the TLK operational conditions and space limitations, a decision was made to arrange the system within the existing glove box of the Isotope Separation System (ISS) in TLK. The space available for IL arrangement was rather limited.

As first step, the existing frame inside the glove box was modelled in CATIA v.5 standard. Then, the rough estimation of required plain surface was made and a draft support structure was designed taking into account the existing frame.

As second step, the system equipments, valves and instruments using the standard parts catalogue were placed on the support structure taking into account the requirements of piping length minimization. Necessary modification of the support structure was done within this step.

As third step, the elements were connected by CATIA runs. Necessary joint elements like VCR glands, nuts and gaskets or CF flanges were implemented to the design from the catalogue. The element positions were adjusted during this process for optimal pass of the runs and final modification of the support structure was performed. The resulting 3-D model of the system is presented in the figure 1.

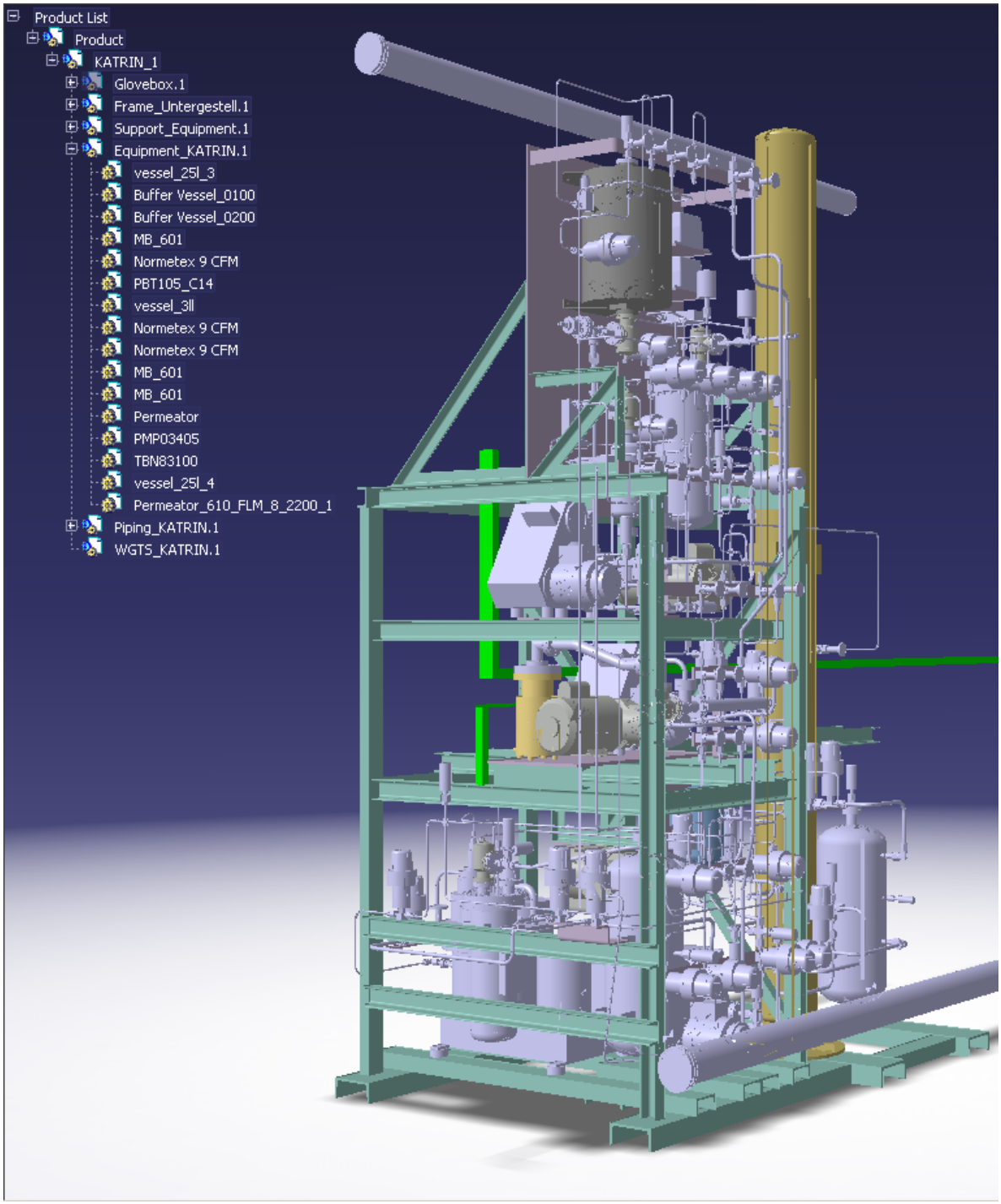

Fig. 1: 3-D model of the Tritium Purification and Circulation Loop.

The manufacturing of the system requires isometric drawings of pipes. The CATIA v.5 E&S does not have a part which allows the production of such drawings. For this reason, the ISOGEN software package was introduced into the CAD system. This package gives a possibility for production of the isometric working drawings of pipelines containing all necessary information directly from the CATIA v.5 3D model.

Staff:

B. Bornschein
O. Kazachenko
R. Wagner

EFDA/ 06-1512 (TW6-TTFD-TR 66)
Design Study on ITER HVAC/LAC, Depression Systems, ADS/VDS and Safety Tritium Monitoring – 1

A Design Review (DR) was launched by the ITER Organisation (IO) in order to consider the status of the design and where necessary to develop revised concepts for key features of the reference ITER design. This work was carried out under the coordination of a number of Working Groups. The objective of this task was to develop/update/revise the features of the design concept which was identified for the EU PT to be addressed as its contribution to the work of WG7, as agreed between the ITER Director and the EU PT.

The generic Tokamak Complex (TC) confinement system (HVAC, sub-atmospheric pressure control, Safety Tritium Monitoring, ADS/VDS) concept was analyzed in detail and found to be unworkable, particularly considering the failure rate of SIC systems and site-specific requirements such as fire regulations. In a concerted effort, the ITER IO, the JA-PT and the EU-PT developed and detailed a new TC confinement concept.

The ITER Detritiation System is considered as a Safety Important Component because it provides tritium confinement during normal operations and incident/accident events, and needs to be available and operational all the time. The new design of the Detritiation System also contains 6 modules based on Wet Scrubber Columns. The availability of space in the building of the ITER tritium plant is limited. Four sections of Wet Scrubber columns of 2.5 m height each are foreseen to be located in two lines which are connected through gas and liquid lines.

With the support of the Fusion Centre Moscow, a detailed description of principal operation, a list of equipments and a preliminary draft Block Diagram of an ITER Detritiation System module (see figure 1) based on Wet Scrubber columns, was developed.

An ITER Detritation System module based on Wet Scrubber columns consists of:

1. Sections of the wet scrubber column (SWS1). These sections are filled with a structured packing material and have a water distributor on the top of structured packing and a packing support at the bottom.
2. Air humidifier (MXH1). This unit is of the same design as the sections of SWS1 and is filled with the same packing material.
3. Buffer vessel (BV3) for tritiated water to be re-circulated through MXH1
4. Water dosing pumps (PL1 and PL2) to re-circulate water through MXH1
5. Purification units for demineralized water (RPU1 and RPU2), which includes filters, ion exchange resins, activated charcoal reactors (and possibly a reverse osmosis reactor and ultraviolet lamps)
6. Buffer vessel for purified demineralized water (BV1)
7. Flow controller for demineralized water feed stream (FC)
8. Condenser (SC1)
9. Air compressor (PC1)
10. Air compressor (PC2)
11. Buffer vessel for detritiated air (BV2)

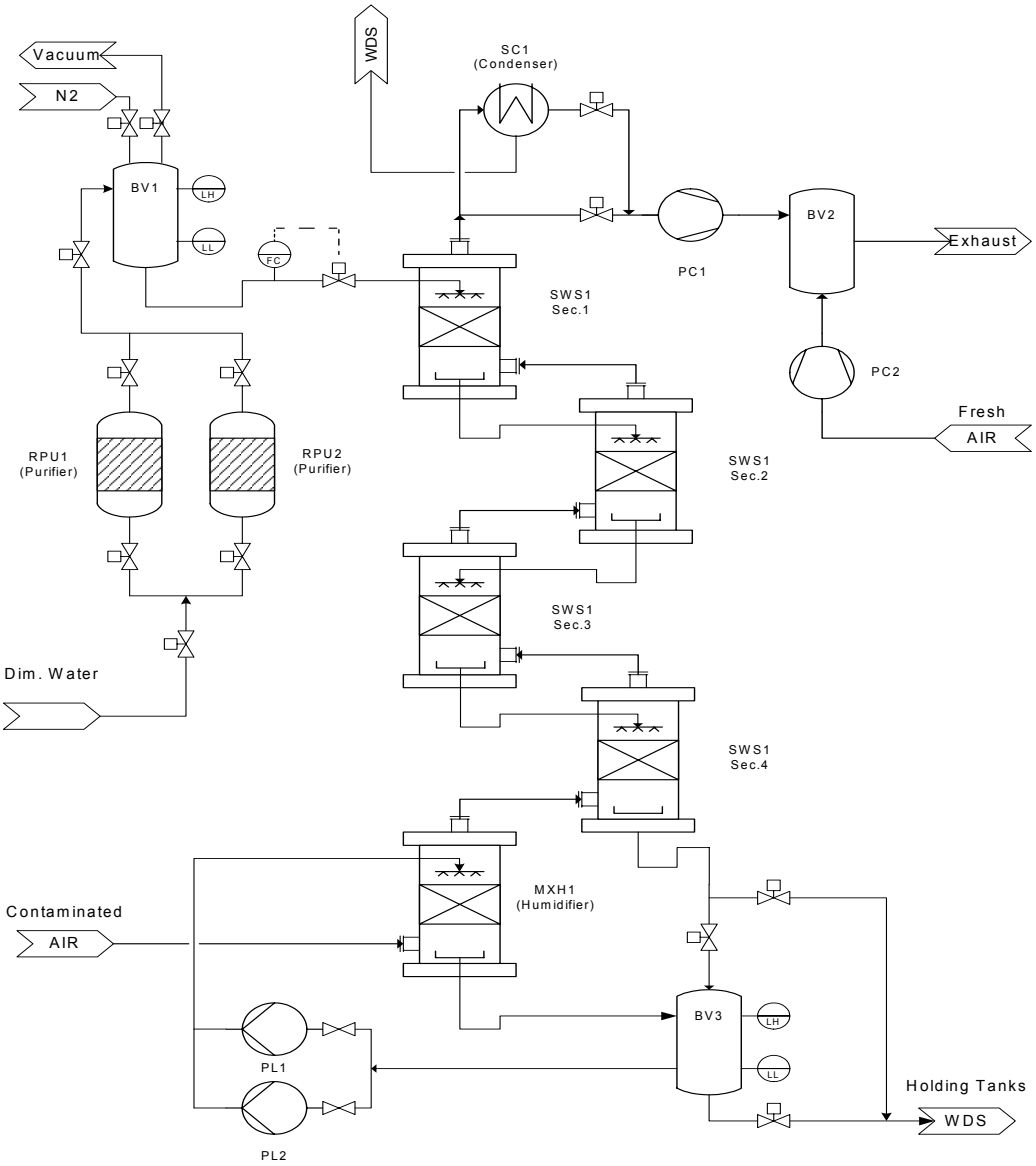

Fig. 1: Preliminary Block Diagram of an ITER Detritiation System module based on WS Column.

The conceptual mechanical layout of the wet scrubber modules was developed addressing the location of the major equipment, the routing of all major pipe lines and the position of the major valves nozzles/fittings. The work included the development of schematic drawings including process flow diagrams, P&ID diagrams and the creation of 3D CATIA models for the location in the ITER Tritium Plant building.

Staff:

L. Dörr
M. L. Subbotin (Fusion Centre Moscow)

EFDA/07-1704-1550 (TW6-TTFD-TR 69)
ITER Design Review 2008 WG7 (Tritium) – FZK input (TLK part)

The Tritium Plant of ITER will be a complex chemical plant for handling, processing and safe confinement of tritium in support of machine operation. A Design Review (DR) was launched by the ITER Organisation (IO) in order to consider the status of the design and where necessary to develop revised concepts for key features of the reference ITER design. The work carried out by FZK tritium group (Tritium Laboratory Karlsruhe (TLK)) is an input to the EU PT contribution to the overall programme developed by the Tritium Working Group (WG7) and comprises the Tokamak Complex Confinement, layout of the Tritium Plant building, TEP, tritium tracking, selection of hydride material, storage bed design and tritium manual.

The generic Tokamak Complex (TC) confinement system (HVAC, sub-atmospheric pressure control, Safety Tritium Monitoring, ADS/VDS) concept was analyzed in detail and found to be unworkable, particularly considering the failure rate of SIC systems and site specific requirements such as fire regulations. In a concerted effort, the ITER IO, the JA-PT and the EU-PT developed and detailed a new TC confinement concept. FZK contributed to the effort by providing work force on systems design and layout, interfaces to building and auxiliaries within the Design Review.

Through an approved Design Change Request (DCR) of ITER, the Tritium Plant building had to be redesigned, particularly in view of fire zoning, fire sectors, tritium inventory segregation and the new confinement concept. TLK contributed mainly to the effort on the issue and provided work force to develop a new Tritium Plant building layout using the customized CATIA V5 tool for design. Space requirements for the systems located in the Tritium Building also were considered. The main focus was put on the needs for the EU procurement packages WDS and ISS.

Only when the torus cryo-pumps are regenerated at elevated temperatures, species like tritiated water or tritiated hydrocarbons will be released, leading, for example, to water vapour pressures above the dew point at ambient temperature. This issue was addressed in view of the interface to TEP and process options proposed. For many years TLK developed the technical CAPER facility, which was considered as reference process for the ITER tokamak exhaust process. The US-PT is now responsible for the procurement package of TEP. Work was focused on the interface between the cryo-pumps and TEP with the main work to update the US on the current status. A further focus was on the interface between TEP and ISS. TEP and pumping systems were discussed in a common meeting between FZK and US in October 2007. A lot of process details based on the TLK developments were discussed during the review process for TEP and in-depth information was exchanged in particular about the PERMCAT reactor developed at TLK.

The distribution of tritium within the main material balance area is of severe concern. The TRIMO code and other specific models will be employed or developed to analyze the potential design improvements of ITER tritium systems and to determine the accuracy or uncertainties of tritium tracking. The main work force was directed on tritium inventories in the different subsystems with a focus on tritium assessment for licensing. TRIMO was then used intensively to study design modifications, particularly to examine the ISS.

In experiments at TLK with a 1:1 ITER getter bed, zirconium-cobalt as the current hydride reference material was disqualified, and instead uranium is proposed to be employed. To support the ITER IO in its decision, work force was provided to discuss all aspects and experiences gained during the operation of the 1:1 ITER getter bed at TLK. The main requirements for the hydrogen storage bed were a strict physical limitation of the tritium storage capacity (at the time of design 100 g), a high supply flow rate of hydrogen isotopes, in-situ calorimetry capabilities with an accuracy of 1 g, i.e. 1% at a level of 100 g of tritium, and a fully tritium compatible design. At present, zirconium-cobalt (ZrCo) is used in the prototype 1:1

ITER getter bed as hydride material. Within wide-ranging experiments, the storage bed was characterized not only in view of supply, storage and accountancy performance, but also in view of the possible isotopic effects during rapid delivery and static isotopic effects. Alarming disproportionation was noticed during testing. Disproportionation is a degradation of the gettering ability of ZrCo.

The experiments at TLK with a 1:1 ITER getter bed showed potential for improvement in the design of such a bed. To support the ITER IO in its effort on a new bed design, work force was provided to support the design of a new 1:1 ITER getter bed with a maximum tritium capacity of 70 g (70 g limitation because of new safety limitations from ITER site Caderache). A prototype storage bed of full scale was designed and manufactured at Forschungszentrum Karlsruhe with a capacity of 100 g tritium and a target supply rate of up to 200 Pam^3s^{-1}. The bed was filled with ZrCo powder and intensively tested in the test rig at TLK. The test rig is equipped with a PVT vessel with a volume of 0.5 m^3, a compressor for the hydrogen transfer of PBT 105-C18 (Thales Engineering & Consulting S.A.) type, pressurized air supply for the active cooling loop operations, two vacuum trains, and sampling manifold for the measurements of the isotope composition of the supply stream. The design of the getter bed allows for in-bed tritium inventory accountancy by flowing gas calorimetry. A Helium stream of up to 40 l/s is circulated through the “U”-shaped tube installed inside the ZrCo container. The Helium circulation is provided by two compressors of MB 158E (Metal Bellows) type and is controlled by flow and pressure controllers. Temperature of the inlet and outlet helium is measured with Pt100 thermometers. The experience from the operation of ZrCo getter bed including loading/deloading operation, calorimetric loop performance and active gas cooling of the bed for fast absorption operation as well as the implications of hydride material characteristics on the SDS system configuration and design were discussed in meetings to support ITER IO in his final decision for the selection of the getter material.

Besides the Project Requirements (PR) and the System Requirements Document (SRD) as top level ITER documents, background documentation for design requirements and guidelines are essential. To further detail the Tritium Manual as one of these background documents, input was provided to update the Tritium Manual. A draft version of the Tritium Manual was posted on IDM. It consists of 2 volumes, one on the properties of tritium and the other on engineering standards for tritium systems. A 3rd volume on tritium safety aspects is in preparation. A revised version of the 1st volume will soon be posted on IDM. Several areas of the 2nd Volume require further input when the designs of certain processes and systems are agreed, such as Water Detritiation, Air Detritiation and Ventilation. The contents of the updated ITER Vacuum Handbook will be fully referred to as these will be the vacuum standards for all ITER systems. The contents of the Tritium Manual have to be approved by the Domestic Agencies as the agreed ITER standards for tritium systems which have to be followed in any future work.

Staff:

U. Besserer
C. Caldwell-Nichols
I. Cristescu
D. Demange
L. Dörr
R. Wagner

Safety Analysis and Environmental Impact

EFDA/07-1704-1592 (TW6-TSS-SEA 4.5a)
Experiments and Calculations for Demonstration of Inert Gas Injection Feasibility

Objectives

As part of the overall strategy for hydrogen/dust explosion management in ITER, an approach to control hydrogen and dust explosions may be based on oxygen limitation inside the vacuum vessel (VV) instead of an administrative limitation of dust. Nitrogen injection into the VV and hydrogen recombination in the suppression tank (ST) are considered as a possible mitigation method to prevent hydrogen and dust explosion in both vessels. To provide a technical basis for the design of such a system the following topics were investigated at FZK in 2008:

- Model development for numerical simulation of dust mobilization and transport in complex 3d geometries (GASFLOW code),
- Measurement of limiting oxygen concentrations for suppression of combined hydrogen/tungsten dust explosion (DUSTEX facility),
- Model development for simulation of limiting oxygen experiments with hydrogen/graphite dust mixtures (DET3D code),
- Analysis of the ITER "wet by-pass" accident scenario including nitrogen injection in the VV and recombiners in the ST (GASFLOW code).

The last three topics are deliverables for the given EFDA task, the work on the first topic is done exclusively within the national (Helmholtz) work programme. The results obtained in 2008 for the four topics will be summarized in the following sections.

Modelling of dust mobilization (Z. Xu, J.R. Travis)

The model for dust re-suspension in GASFLOW is based on the force balance for a single particle resting on a solid surface. A free-particle peak-up velocity can be determined from the force balance, which however does not take into account stochastic processes. Therefore, an empirical probability density function approach was developed and benchmarked on the SOFIA coal dust experiments. In these experiments [1], coal dust samples with different mean particle diameters (56 - 200 µm) were exposed to steady-state nitrogen flows with different bulk velocities (5 - 35 m/s) and the re-suspension rates were measured.

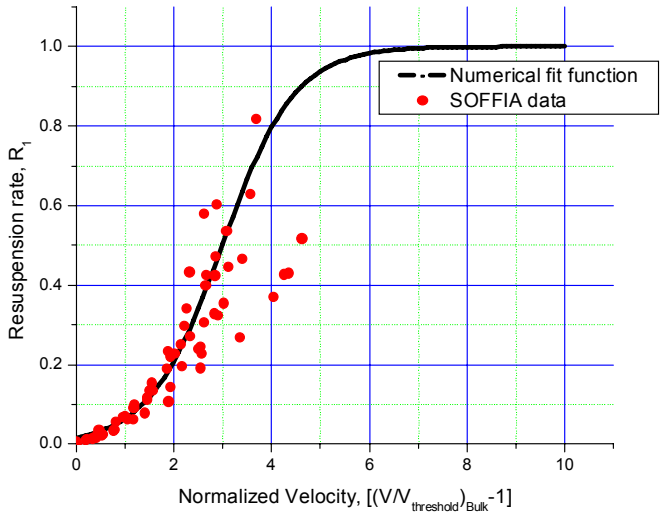

Fig. 1: Comparison of all SOFIA data with probability function derived, in a non-dimensional plot.

The statistical model developed can reproduce the experimental data in quite a satisfactory way. Fig. 1 shows a normalized plot for all experimental data and the probability function derived. Fig. 2 gives a detailed comparison between test data and the new GASFLOW model for coal dust particles with 60 µm diameter.

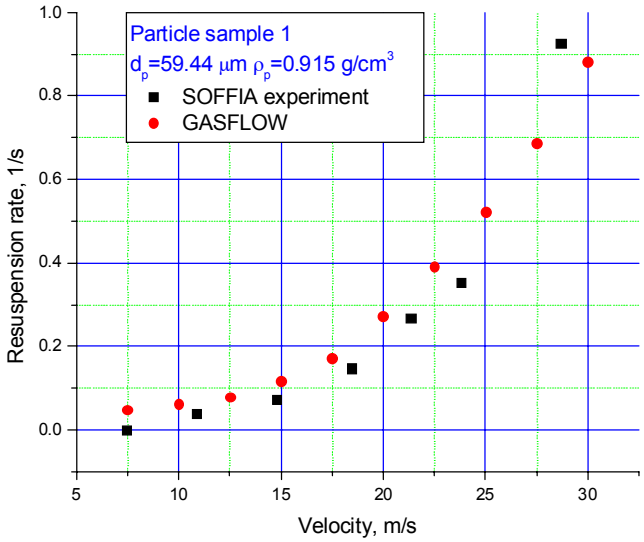

Fig. 2: Comparison of measured [1] and calculated re-suspension rates with coal dust particles of 60 µm diameter.

Additional experimental re-suspension data are highly needed to further validate this model for ITER typical dust materials (C, Be, W) and particle size distributions (0.1 - 10 µm). Also the effect of flow turbulence on the re-suspension will be addressed in future work.

Limiting oxygen concentrations for hydrogen/tungsten dust explosions (A. Denkevits, B. Oechsler)

Small scale experiments have been performed in the DUSTEX facility to measure the maximum oxygen concentration where no fast hydrogen/W-combustion is possible. This value is an important design parameter for a nitrogen injection system which can suppress H_2/W-dust explosions. In a first test series, W/H_2 mixtures were investigated in a wide range of W-dust concentration (200 - 8000 gW/m^3) at normal air oxygen concentration (21 %) to determine the optimum W-dust concentration with respect to peak explosion pressure and maximum pressure rise rate. The 0.5 µm W-dust used can be ignited with a weak electrical spark for hydrogen concentrations above 7 %. Fig. 3a shows peak pressures measured for this hydrogen concentration. Comparison with the pure H_2-tests shows that the dust contribution to the total pressure is very significant for low H_2 content and decreases with increasing initial H_2 concentration.

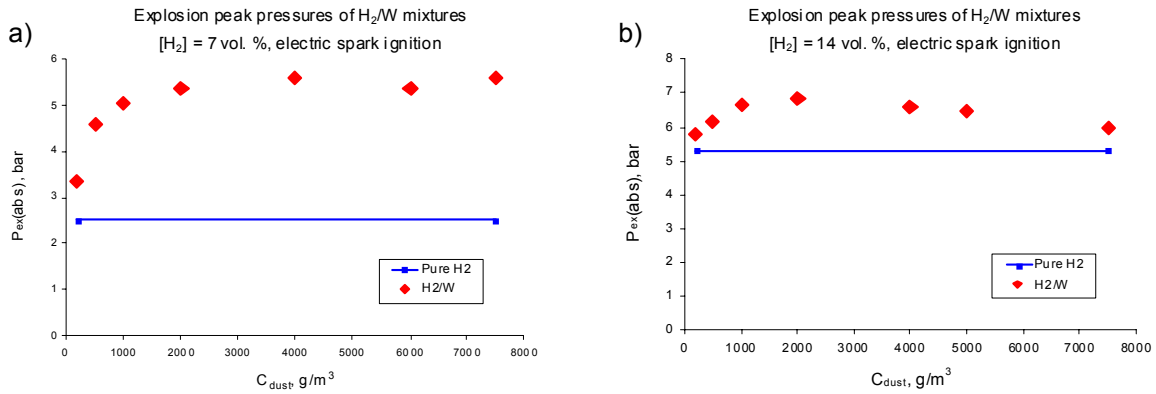

Fig. 3: Measured explosion peak pressures of 0.5 µm tungsten dust with a) 7 % H_2, and b) 14 % H_2 in air.

Experiments were performed with 7, 10, 14 and 18 vol.% H_2 in air and various tungsten contents. In nearly all cases, 2000 gW/m^3 provided the highest explosion pressures, therefore this dust concentration was selected for the limiting oxygen concentration measurements.

In the second test series, the initial oxygen concentration in the pre-explosion atmosphere was reduced from 21 vol.% O_2 down to 10 vol%. The hydrogen concentration again was varied from 7 to 18 vol.% as in the first test series. Fig. 4 shows the results for 7 vol.% hydrogen in the pre-explosion atmosphere.

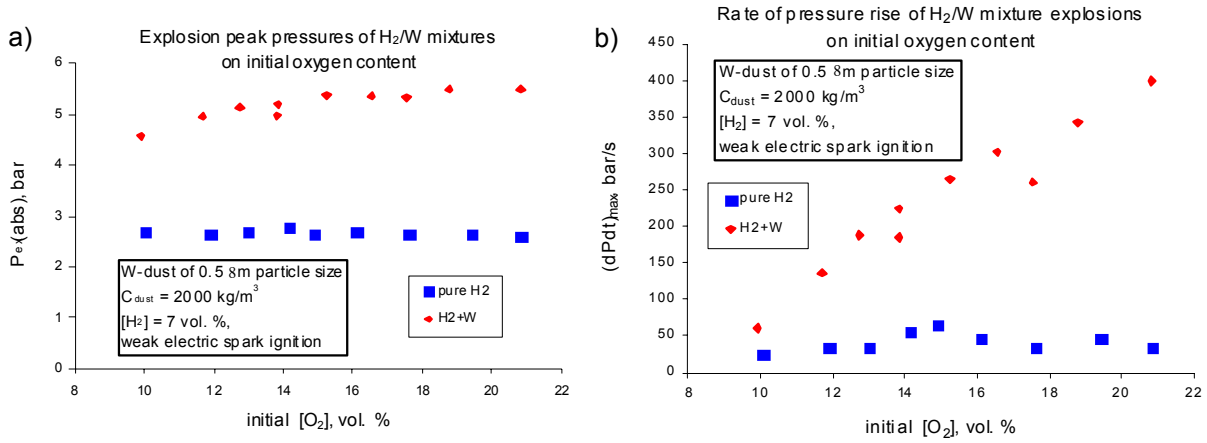

Fig. 4: Measured peak explosion pressures and pressure rise rates of 0.5 µm W / H_2 - air mixtures versus initial oxygen content. Hydrogen concentration 7 vol.%.

The peak pressures measured decrease only slightly with decreasing O_2 content (Fig. 4a), however the maximum pressure rise rate decreases significantly (Fig. 4b), which is related to the lower temperatures and reaction rates with less oxygen available. Extrapolation of the pressure rise rates to O_2 concentration below 10 % indicates a limiting oxygen concentration (LOC) near 8 vol.% O_2. Measurements at lower O_2 concentrations were not possible with the current DUSTEX design.

Similar observations were made for higher H_2 concentrations, indicating a LOC between 8 and 10 vol.% O_2. After modification of the DUSTEX facility, additional W/H_2 experiments will be made at lower O_2 concentrations to determine the LOC more precisely.

Numerical simulation of combined hydrogen/graphite dust explosion experiments (R. Redlinger)

The limiting oxygen concentration (LOC) experiments performed in DUSTEX with hybrid hydrogen/graphite-dust mixtures showed three different combustion regimes which should be reproduced with a numerical model:

- Two-stage regime for low hydrogen content (e.g. 11 vol.% H_2)
- Transient regime for medium H_2 content (e.g. 13 vol.% H_2)
- One-stage regime for high H_2 content (e.g. 16 vol.% H_2)

The DET3D code was extended and used for simulation of the hybrid H_2/C-dust explosion experiments. DET3D solves the 3d Euler equations of gas dynamics using an explicit finite difference scheme. The code also models heat exchange between the burned gas and the surrounding solid structure. A continuum approach is used to model dust, i.e. dust particles are not resolved in the computational grid, but treated like a "gas" component. Gas and dust have the same temperature and velocity. The reaction model treats a hydrogen-oxygen and a graphite-oxygen reaction in parallel with a fixed rate constant for each reaction ($d[H_2]/dt = -K_{H2}$, $d[C]/dt = -K_c$). The K-values are adapted to DUSTEX experiments with pure H_2-air and graphite-air mixtures respectively. Oxygen is consumed in the calculation only to the extent measured in the tests, i.e. the residual O_2 amount is an input to the simulation.

Fig. 5 shows that this model can well reproduce the three different reaction regimes observed for H_2 / graphite dust reactions in air (21 vol.% O_2).

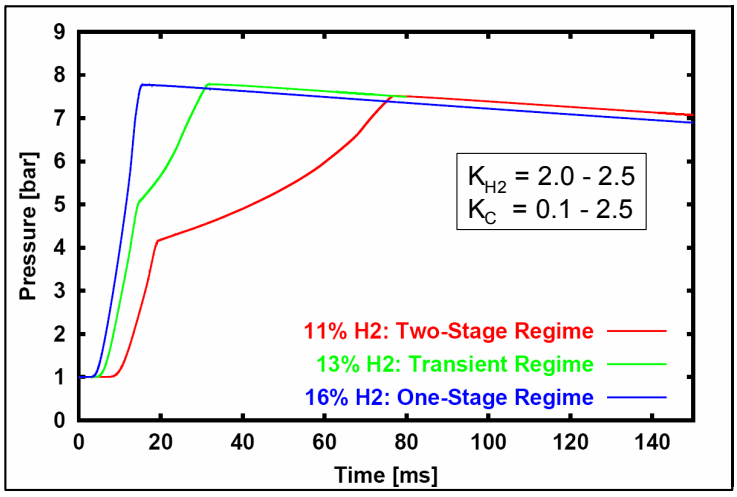

Fig. 5: DET3D simulation of combined H_2 / graphite dust reactions in air (graphite density 150 g/m^3, average particle size 4 µm, initial pressure 1 bar, initial temperature 300 K, mesh size 5.6 mm, total number of cells 27.000).

The hydrogen reaction rate constant K_{H2} was determined from pure H_2 tests in DUSTEX, it shows only a weak temperature dependence. The K_c value of 0.1 was taken from graphite-air tests in DUSTEX and adjusted to hydrogen-graphite experiments. With increasing H_2 concentration the dust reacts in an increasingly hotter atmosphere of residual O_2, steam and N_2, which causes the significant increase of K_c with H_2 concentration. At 16 % H_2, hydrogen and dust react on the same timescale in a one-stage reaction. At 11 % H_2, hydrogen reacts first, followed by the much slower graphite dust combustion.

The DET3D model was used to predict peak overpressures as a function of oxygen concentration in the initial pre-explosion atmosphere. Fig. 6a shows that the experiments for 11 % H_2 can be well reproduced with the reaction constants from pure H_2 and pure graphite tests (K_{H2} = 2, K_c = 0.1). For higher initial hydrogen concentrations, K_c needs to be increased due to the higher gas temperature from the H_2 reaction. A value of K_c = 2.5 allows to model the experiments with 16 % H_2 very well, K_{H2} = 2.5 was taken from the 16 % H_2 test (Fig. 6b).

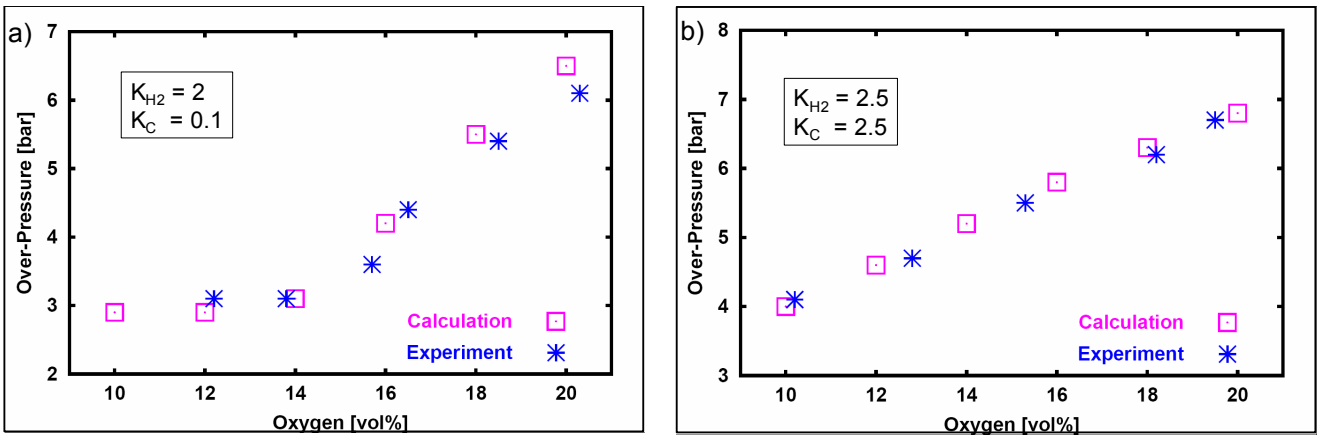

Fig. 6: Comparison of calculated and measured peak pressures in hybrid hydrogen / graphite dust explosions, 150 g/m^3 dust concentration with a) 11 % H_2 and b) 16 % H_2.

In summary it was found that the K-values for the chemical reaction in the combined fuel system (H_2 and graphite) are consistent with the K-values found for the single fuel systems. The K-values are independent of the oxygen concentration in the investigated range of H_2, O_2, and graphite dust concentrations. These results indicate that the relatively simple model of two parallel global reactions has large potential for further successful refinements and predictions for other H_2/dust systems. An analogous study of H_2 / tungsten dust explosions will be performed next. In a further modelling step, the empirically found rate constants should be connected to a microscopic gas-particle reaction model.

Analysis of nitrogen injection and recombiner installation in the suppression tank (J. Xiao, J.R. Travis)

In the ITER "wet by-pass" accident scenario, detonable H_2 / air mixtures can form in the suppression tank. The ITER project has therefore proposed nitrogen injection in the VV and installation of catalytic recombiners in the ST as possible mitigation measures. The full accident scenario was analysed with the FZK code GASFLOW. New ITER-specific models were developed, tested and implemented in GASFLOW, concerning the critical air inflow at the break, the isotropic steam expansion into the VV, the gas behaviour in the suppression pool, and hydrogen production by steam oxidation of hot Be dust on the divertor.

Fig. 7 shows an iso-view of the ITER sub-systems and a vertical cut of the GASFLOW geometry model for ITER. The GASFLOW model rearranged the relevant sub-systems slightly in space but kept the respective volumes at the correct values.

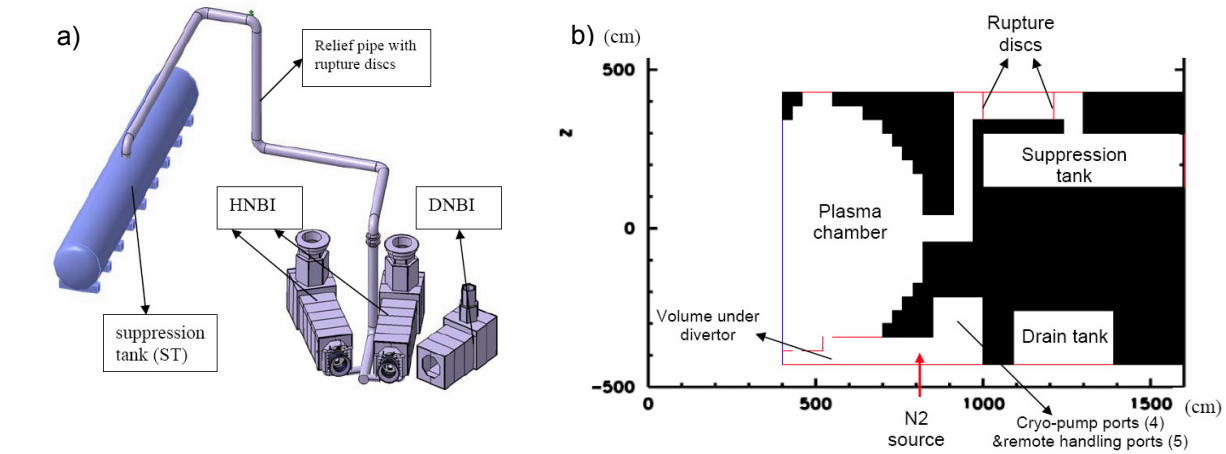

Fig. 7: Iso-view of ITER sub-volumes (a) and vertical cut of GASFLOW geometry model (b).

Fig. 8 depicts the location of two catalytic recombiners of the type PAR FR90/1-1500 in the suppression tank. The recombiners contain catalytic surfaces where hydrogen and oxygen react to form steam. The hot exhaust gases (steam, rest O_2 and N_2) provide a buoyant flow which causes a passive start and action of the recombiner device. In the study 1, 2 and 4 recombiners were modelled.

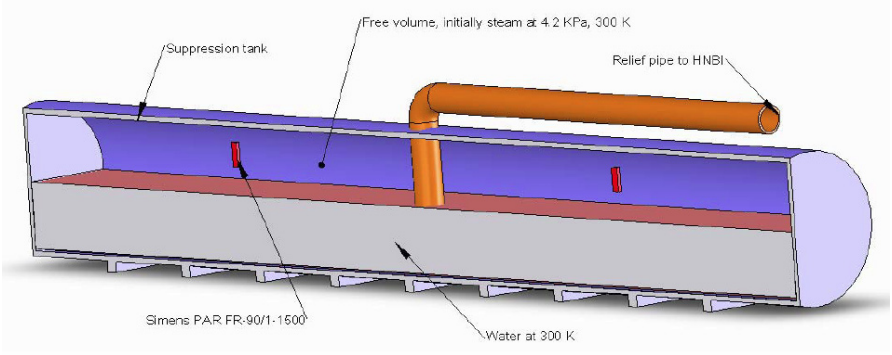

Fig. 8: Location of two catalytic recombiners in the suppression tank (ST).

The atmosphere developing in the ST was analyzed with respect to the possible hydrogen combustion modes. Detonations are clearly excluded by N_2 injection and by combinations of N_2 with recombiners. A long-term possibility for fast deflagrations still remains if only N_2 injection is used as mitigation method. The addition of recombiners shortens the time span for fast deflagrations significantly. Fig. 9 shows the computed mass of hydrogen in the ST which

could sustain a fast deflagration for the 5 cases - without any mitigation, - with N_2 injection only, and - with additional recombiners (3 scenarios). The analysis also showed that in all 5 cases a long-term possibility for slow deflagrations still remains. Ignition of the ST atmosphere, e.g. by hot recombiner surfaces, must be avoided. The related pressure increase may endanger the ST integrity and may lead to reverse water flow from the ST to the VV.

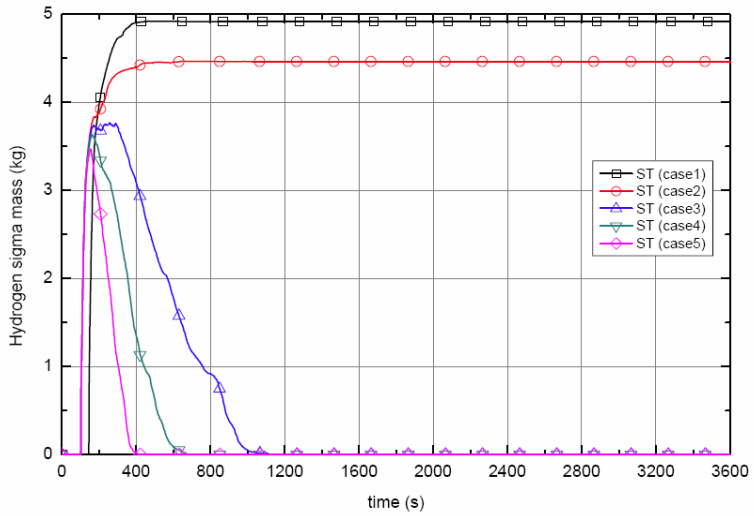

Fig. 9: Computed mass of hydrogen in the suppression tank which could support a fast deflagration. Recombiners reduce the time span for potential fast deflagration in proportion with increasing number of catalytic recombiners. (Case1= wet bypass scenario without mitigation, case 2= nitrogen injection in VV, case 3= nitrogen injection with 1 recombiner, case 4= N_2 with 2 recombiners, case 5= N_2 with 4 recombiners).

Staff:

W. Breitung
A. Denkevits
B. Oechsler
R. Redlinger
J. Xiao
Z. Xu
G. Stern, ProScience GmbH, Ettlingen, Germany
A. Veser, ProScience GmbH, Ettlingen, Germany
J.R. Travis, Dubois-Pitzer-Travis, Offenbach, Germany

Literature:

[1] Parozzi, F., Resuspension of multi-layered dust deposits, Chemical Engineering Transactions, p 269-274, Volume 10, 2006, Proceedings of Advanced Atmospheric Aerosol Symposium (aaas), Milan, Italy, 12-15 November 2006

EFDA/07-1704-1575 (TW6-TSS-SEA 5.4)
Magnet Busbar Arc - Development of an ITER-representative Model and Supporting Validation Experiments

D 3 - Final report on VACARC experimental results
D 4 - Draft final report on numerical busbar arc modeling with MAGS
D 5 - Final report on numerical busbar arc modeling with MAGS
D 6 - Report on feasibility of a large scale experiment

High power arcs at the ITER magnet coils current leads (so-called busbars) with their considerable power release are a possible threat to the ITER cryostat wall and other safety relevant components within their range. Such very improbable events may be looked at during licensing. Presently, no suitable numerical models with reasonable accuracy are available. Model development turned out to be difficult due to limited knowledge of arc propagation and destruction behaviour. This was the reason to set up a campaign of model experiments of high current arcs propagating along insulated conductors.

The experimental contribution to busbar arcs at FZK started with the MOVARC experiments in the frame of EFDA task TW3-TSS-SEA5.4. MOVARC represented a very small stage of arc experiments to learn about arc behaviour in principle and the feasibility of this kind of experiments. The next step to investigate busbar arcs are the VACARC experiments. The VACARC results are not intended for direct extrapolation to ITER scale but will be used for supporting model development and model validation. In addition, VACARC also provides experimental experience for possible full scale experiments. The VACARC setup is based on an available plasma spray device which had been taken out of service several years ago (Fig. 1). The VACARC vessel is designed for vacuum conditions which represent a more realistic simulation of the ITER cryostat conditions than the 1 bar argon atmosphere of MOVARC. VACARC was completed and brought into service in spring 2006, and was used since then for more than a hundred busbar arc experiments. After several device improvement steps, in 2008 finally arc powers up to 175kW and arc currents up to 1700A could be achieved. The most important findings from the VACARC experiments are:

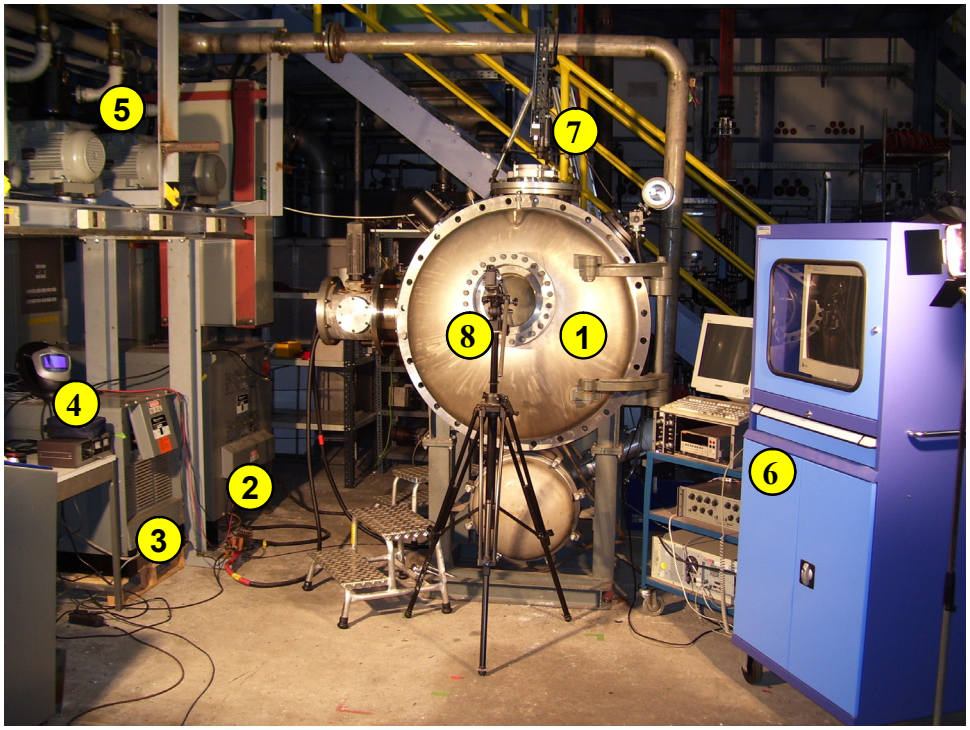

Fig. 1: VACARC setup: 1. Vacuum vessel, 2. 120kW power converter, 3. 20kW power converter, 4. control unit for power converters, 5. vacuum pumps, 6. data acquisition devices, 7. high-speed camera, 8. video camcorder.

- Pressure is important for arc stability and reproducibility. Vacuum conditions and pumping on the vessel brings the reproducibility required for numerical modeling.
- Magnetic self-induced forces determine the burning direction of the arc. From that, one can conclude that an external field will have considerable impact, too.
- The strong busbar insulation has a considerable impact on the arc shape, power and propagation velocity: Remaining insulation forms a nozzle that results in a long, jet-like arc column. Arc propagation velocity and arc total power are enhanced, however the power is less localized at the opposite ground side spot. Figs. 2 -4 show the impact of epoxy reinforcing the insulation. The strong insulation also excludes that there is a fast propagating insulation cut (former called "forward") mode. The arc always destroys the complete cross section of the model busbar ("backward" mode).

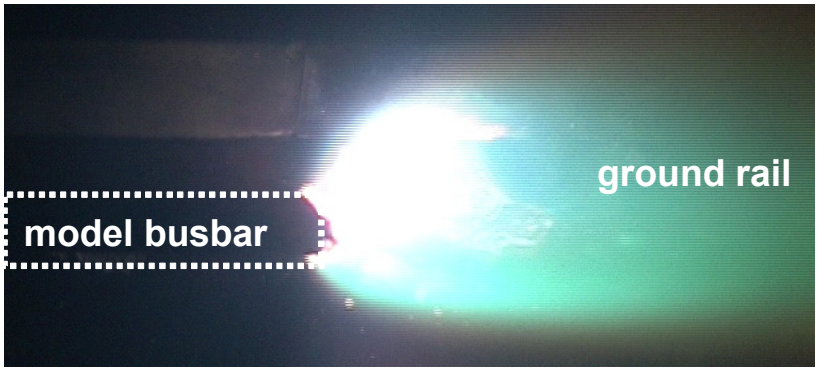

Fig. 2: VACARC experiment RB0303: 1014A, 45kW, arc velocity 0.37cm/s, burning time ~30s. Without resin reinforcement, the short arc burns quite straightly towards the ground rail. The arc spot on the ground rail is clearly visible.

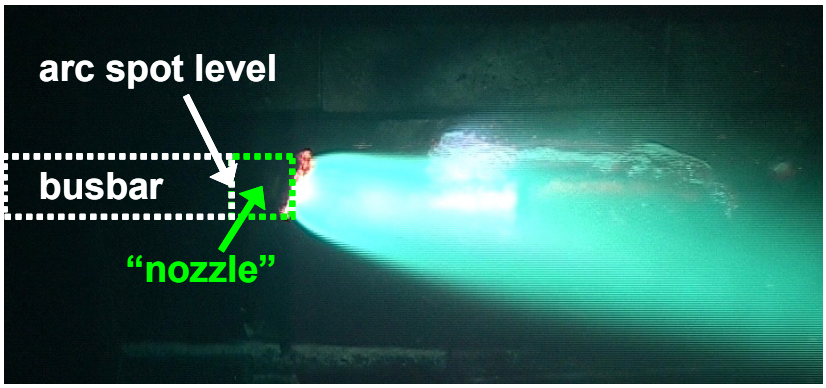

Fig. 3: VACARC experiment RB0508: 959A, 102kW, arc velocity 0.68cm/s, burning time ~20s. The resin reinforced insulation is more stable and a remaining nozzle-like part of it restrains and shapes the arc column. This has several consequences as compared to RB0303 with similar current shown in Fig. 2. The arc now burns in a long jet parallel to the model conductor. The ground rail arc spot expands and appears diffuse and the arc length and power increase significantly. The arc propagates faster (although more busbar material must be burned) due to the enhanced local voltage (power) in the restricted "nozzle" part of the column.

- More realistic model conductors with 65% void containing stranded wire copper cores instead of solid rods were used. The principal arc behaviour was similar, the arcs were somewhat faster, which could rather be attributed to an enhanced nozzle effect than directly to the lower copper mass.
- Inline arcing simulating a busbar quench with subsequent melting failure and arcing is possible (Fig. 5). These arcs show a high stability even without the guiding nozzle effect of a strong insulation.

Fig. 4: Damage after RB0303 (left) and RB0508 (right): Although the total power during RB0508 was more than twice the total power during RB0303 (while the burning time was only 30% shorter), the damage to the ground rail is somewhat weaker. The jet-like arc column distributes the power away from the ground rail and expands the structure side spot there which reduces structure damage. One objective of the experiments was to find out about such special behavior of busbar arcs and its relevance for safety questions.

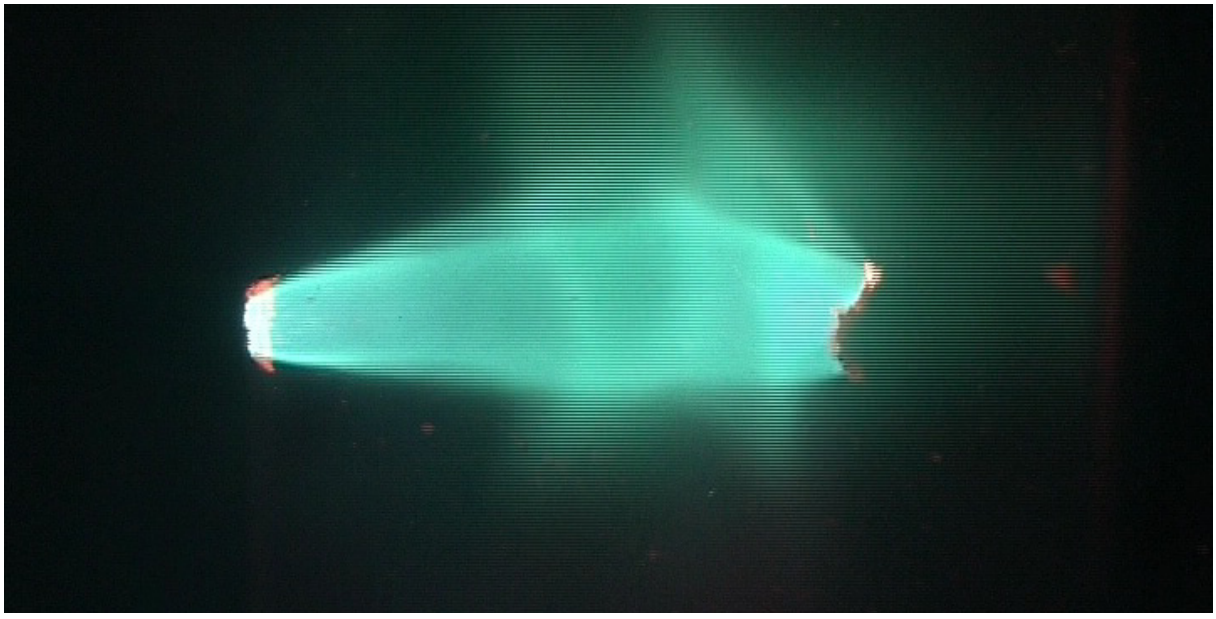

Fig. 5: Snapshot of an inline arc in VACARC (RC0302, 600A, 30-60kW). The arc length is about 14cm after 23s. The arc was ignited in a small gap between the ends of the two conductors facing each other. Arcs of this configuration can become quite long even at low currents and without a guiding insulation nozzle.

In parallel to the VACARC experiments, a modeling effort with the MAGS code was started. The busbar arc model was programmed in a new MAGS module called BUSARC which makes use of the available MAGS capabilities of providing a structure and performing a thermal and electrical analysis of it. BUSARC uses a phenomenological model which is closely oriented to the available VACARC experiments. So far, BUSARC calculations show a satisfactory coincidence with the measured arc propagation velocities. In future steps, the calculation model will be compared to VACARC experiments at more realistic conditions. For application to ITER, validation experiments and an extrapolation to ITER scale are foreseen.

The possibility to investigate long and powerful arcs is limited by the capabilities of the power converter and the available space in the VACARC vessel. The feasibility of performing larger scale experiments was investigated. The former STAR cryostat ($20m^3$) seems to be a reasonable option to host the next stage of experiments which will be called LONGARC. Presently, LONGARC is under construction. It is scheduled to go into service in 2009 still with the present VACARC power converter. From the decommissioning of MZFR, a former experimental nuclear reactor, three plasma cutting power converters may become available. These

devices would provide voltages up to 250V (at 900A) which are required to investigate longer arcs in the future.

Staff:

D. Klimenko
V. Pasler

Doses to the Public and Validation of UFOTRI

Objectives

The objective of this task is to demonstrate the validation level of the computer codes used and to calculate, on request by EFDA, in a consistent way doses to the public for given source terms, for realistic meteorological and site conditions, for ITER (European site) and for fusion power plants. This work is focused mainly on the validation of UFOTRI in the frame of the EMRAS (Environmental Modelling for RAdiation Safety) international benchmark project including a comparison of concentration and dose criteria for the ingestion pathways.

Work performed

The activities on testing and validation of UFOTRI in the frame of the EMRAS activity and providing support to the ITER team in the licensing procedure are completed.

The Tritium Working Group of the EMRAS project aims on improving models of OBT formation and translocation in plants, animals and fish. Up to now seven different scenarios were examined. FZK contributed with the UFOTRI code to the soybean and the hypothetical scenario. The soybean scenario is based on experimental data collected at the Korean Atomic Energy Research Institute. Commercially available soybean was sown in May 2001 in 6 plastic pots (41cm x 33cm x 23cm high). Tritium exposure was carried out six times at different growth stages: July 2, July 13, July 30, August 9, August 24, and September 17. The pots were inserted into a glove box for the tritium exposure and the experiments were conducted under natural solar conditions, which resulted in high temperatures within the glove box. The surface of the soil was covered with vinyl paper so that uptake was only through the foliage. After exposure, the pots were placed in an open field among other soybean plants. UFOTRI performed well in the scenarios being the only model which provides simulation results within one order of magnitude around the measurements for all the 6 different exposure conditions.

The objective of the hypothetical scenario is to analyse the consequences of an acute atmospheric release of tritium, by considering various pathways in terms of activity in biosphere compartments and products, as well as the contribution of the various forms of tritium (HT, HTO and OBT) to the total exposure. The basic assumption is that 10 g of tritium is released over a period of 1 hr and the calculation period is 1 year. Results of the first predictions differed considerably and it was not possible to find consensus on why model results diverged. Therefore, a new revised scenario was prepared to resolve the differences between the models. It is important to note, that UFOTRI and the French code used also for the licensing of ITER in France performed in a similar way. This strengthened the confidence in both codes to be further applied in the licensing procedure. One drawback, however, was the fact that within this exercise not all discrepancies between the various contributing simulation models could be explained. The still existing huge variety in some of the results demonstrated the need for further refinement of the codes and will not raise confidence as some of these codes are used operationally in their home country.

No further calculations were performed to support the licensing calculations of the French colleagues.

Further work

Work on dose assessment for ITER is completed. No further work is expected in this area.

Staff:

I. Hasemann
F. Fischer
W. Raskob

Literature:

[1] Raskob, W.: Test and validation studies performed with UFOTRI and NORMTRI. TW5-TSS/SEP2 - deliverable 4. Wissenschaftliche Berichte, FZKA-7281 (März 2007)

DEMO Conceptual Studies

TRP-001
PPCS He-cooled Divertor Concepts

TW6-TRP-001 D 2
Manufacturing of Medium Scale Mock-ups - First Tests

Introduction

A helium-cooled divertor [1] has been developed at the FZK since several years. The design goal is to withstand an extremely high heat flux (HHF) of at least 10 MW/m^2 expected in DEMO. The reference jet concept uses small W finger modules favourable for stress reduction. It relies on impingement cooling with high pressure helium jets (10 MPa, 600°C). Subsequent R&D activities towards DEMO comprise, among others, development and tests of 1-finger and 9-finger cooling finger modules (Fig. 1) which build up bigger parts, e.g. target plates. For experimental verification of the design, a combined helium loop & Electron beam facility (60 kW, 27 keV) (Fig. 2) [2] suitable for HHF tests was built at the Efremov Institute, St. Petersburg, Russia. Technological studies on manufacturing of the W finger mock-ups (MUs) [3] were performed.

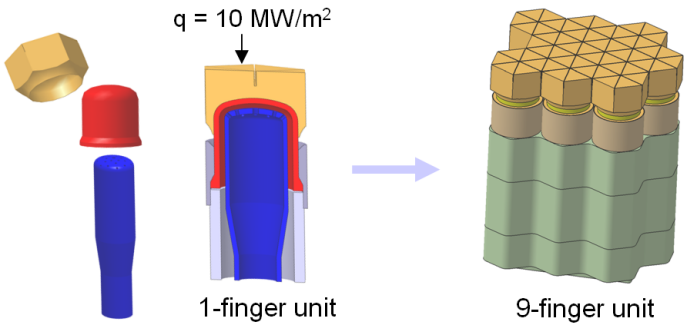

Fig. 1: He-cooled modular divertor designs HEMJ.

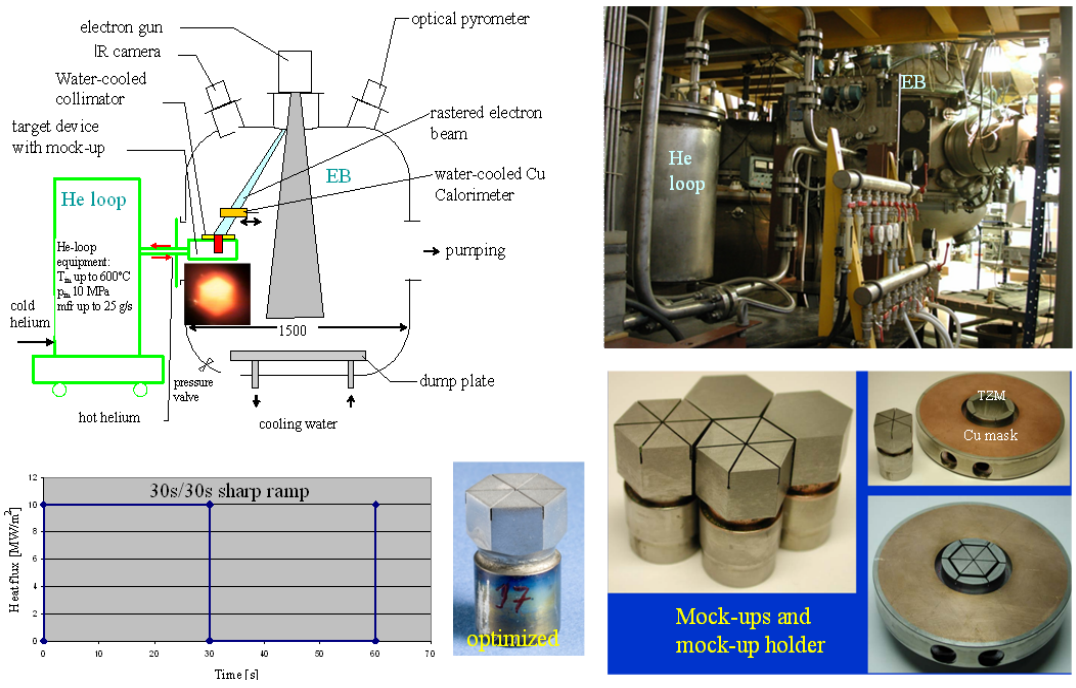

Fig. 2: Combined He loop and TSEFEY test facility at Efremov.

Two experiment series for 1-finger modules were successfully performed in 2006 and 2007 [4, 5]. The results of HHF tests till now confirmed the divertor design performance. Nevertheless, based on the knowledge gained from experiments, still iterative improvement on manufacturing and design is being done in order to ensure the reliable and faultless function of the divertor cooling fingers. In the following, manufacturing and HHF tests of third 1-finger test

series as well as manufacturing and thermohydraulic tests of a 9-finger module shall be reported.

Third HHF test series on 1-finger modules 2007/2008

The definition of 1-finger tungsten modules for the third HHF test series is illustrated in Fig. 3. The third HHF test series [6, 7] contained ten mock-ups with castellated W tiles. Fig. 4 shows the set of mock-ups before testing, except the mock-ups #18 and 22 which were subjected to the tests for the second time. They differ in tile design, tile material used, brazing filler metal, and type of machining (EDM vs. turning). A new type of brazing filler CuNi44 (brazing temperature Tbr = 1300°C) was applied to three mock-ups (#24, 26, and 32) for W tile and WL10 thimble joining; mock-up #26 was defective after brazing and therefore not available for testing. For the rest of the mock-ups, tile and thimble are brazed together with STEMET 1311® (Tbr = 1050°C). WL10 thimble/Eurofer steel joint is exclusively brazed with 71KHCP (Co-based, Tbr = 1050°C) filler metal.

The following test conditions were applied in the 3rd test series: a) He mass flow rate was raised within the range of up to 13 g/s in order to keep the temperature at the tile/thimble brazing layer below Tbr of 1050°C, b) the He inlet temperature was within the range of 450 – 550°C, c) the Heat flux was varied from 8 to 12 MW/m^2, and d) besides standard ‚sharp ramp' (30 s - on, 30 s – off) some tests were partially performed with ‚soft ramp' (20s – up, 20s – on, 20s – down, 20s – pause).

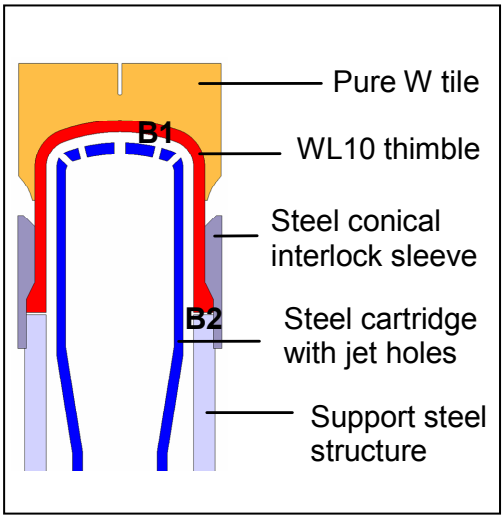

Materials	
W tile	▪ Plansee W grade (MUs #21-22) ▪ Russian W grade (remaining MUs)
W thimble	Plansee WL10 (W–1%La_2O_3)
Support structure	Eurofer
Joining methods	
W/W (B1)	Brazing with - nickel-based filler metal STEMET 1311®, T_{br} = 1050°C - CuNi44, T_{br} = 1300°C
W/Steel (B2)	Conical lock brazed with cobalt-based filler metal 71KHCP; T_{br} = 1050°C

Fig. 3: Definition of 1-finger tungsten modules for the third HHF test series.

Clear progress was achieved in this test series. Eleven testing experiments were performed with 1-finger mock-ups, two mock-ups were tested for the second time and 9 mock-ups were tested once. Six HHF tested mock-ups (#18, 22, 25, 27, 28, and 31) (Fig. 5) are still available for further tests. Decreasing the He inlet temperature allowed to check the functionality of mock-ups at the absorbed heat flux up to 12 MW/m^2 even with a 1050°C tile/thimble 'low' temperature brazing. EDM mock-ups (#21, #22) show good performance, but no significant difference was found with regularly turned/machined mock-ups at performed testing conditions (q up to ~11 MW/m^2, cycle number up to ~200). Mock-ups fabricated by improved machining (mechanical grinding and electrochemical grinding) show very stable performance at cyclic absorbed heat flux up to 11 MW/m^2 during more then 100 cycles. First tests with horizontal orientation of the tile material structure do not show differences in function stability of the mock-up (in comparison with vertical structure) at the used testing conditions. This type of material orientation could be used for further investigation. The mock-ups were tested at soft and sharp loading ramps. No difference in results was detected. Next tests could be performed with sharp ramp if the testing time is limited. First tests of the mock-ups with

tile/thimble high (1300°C) temperature brazing have shown delaminating of the tile from the thimble (or cracking of the brazing interface). This means that careful investigation with the samples of such brazing have to be done prior to mock-ups brazing and testing.

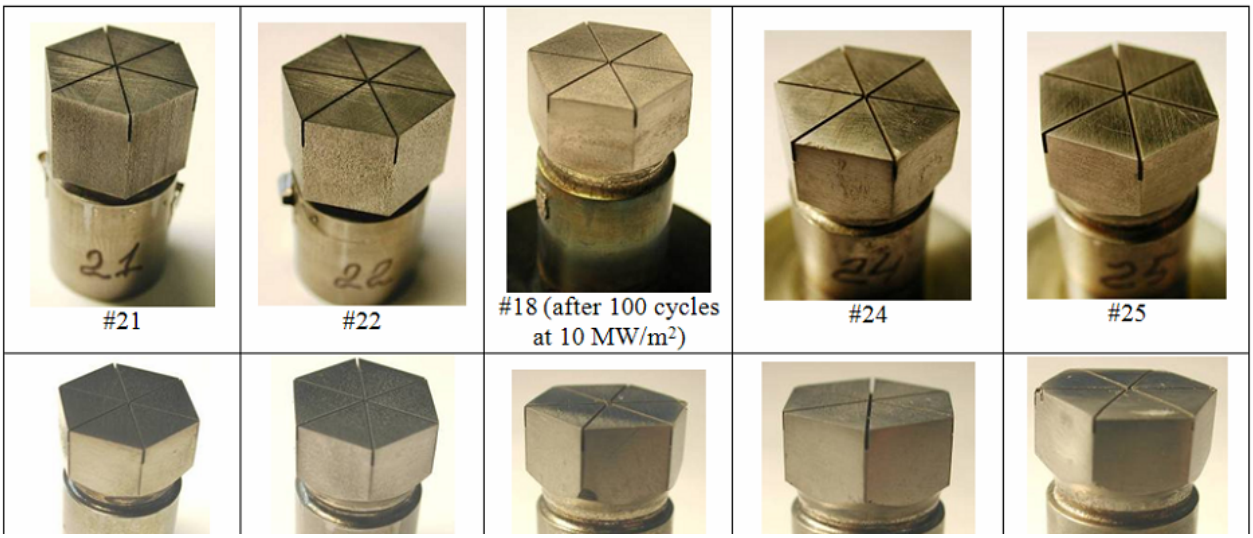

Mock-up #	Tile design	Tile material/ grain orientation	Tile/thimble braz-ing	Thimble/ conic sleeve joining	Type of improved turning (tile & thimble)
21	Efremov H_{castel}=4	Rod (Plansee, Ø25)/ vertical	1311 (1050 °C)	Brazing (71KHCP) 1050°C	EDM
22 *(1st & 2nd tests)*					
18 *(2nd test)*	FZK H_{castel}=2.7				regular
24		Rod (Russian, Ø30)/ vertical	CuNi44 (1300°C)		
25			1311 (1050°C)		
(26)*			CuNi44 (1300°C)		
27			1311 (1050°C)		
28			1311 (1050°C)		
29		Rolled plate (Russian, 24 mm thickness)/ horizontal	1311 (1050°C)		numerical
31	mod. FZK $H_{cas-tel}$=2.3 H_{tile} = 11.3 mm instead of 12 mm		1311 (1050°C)		
32			CuNi44 (1300°C)		

* Defective after brazing, non-testable

Fig. 4: Fabricated 1-finger tungsten modules for the third HHF test series.

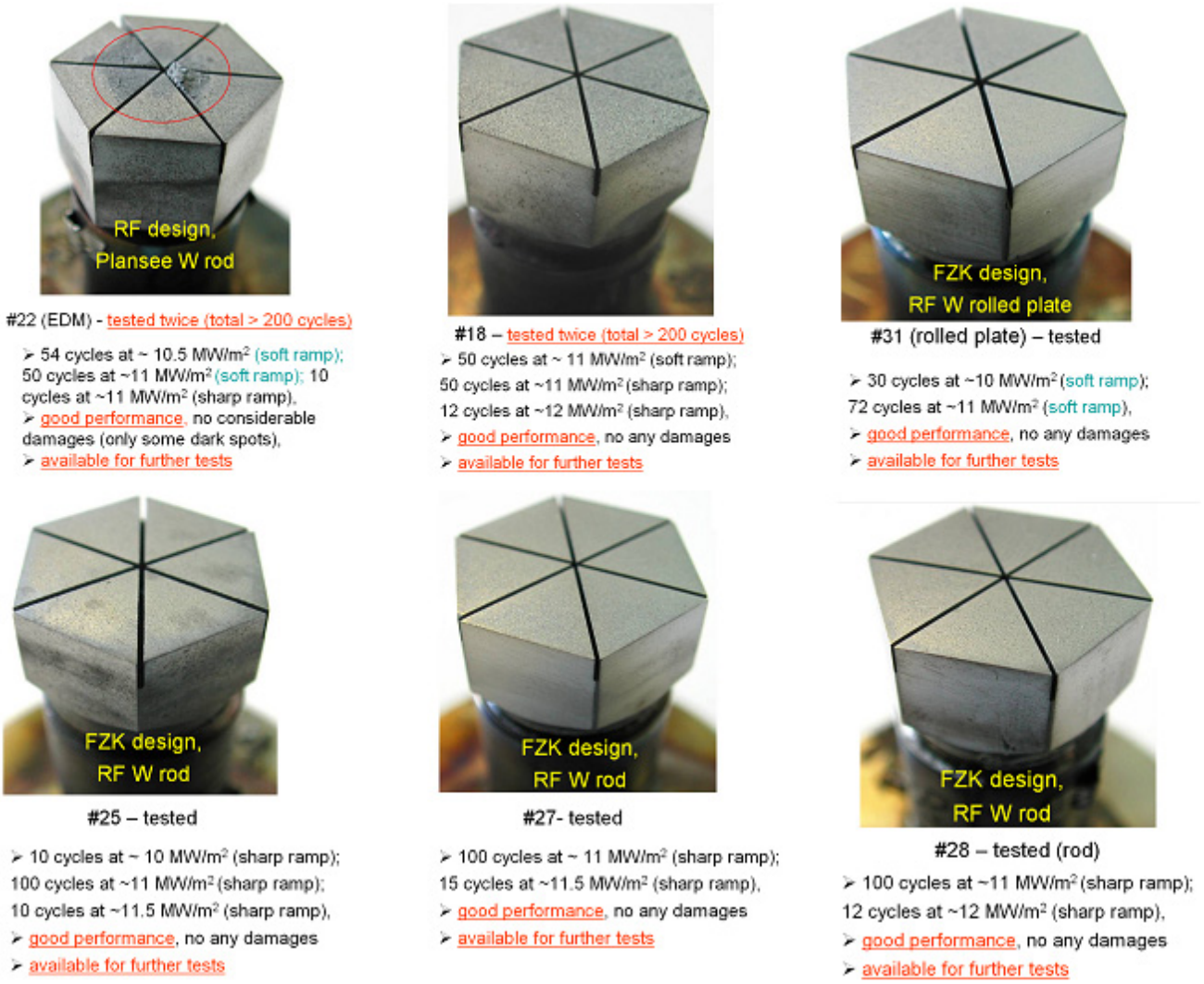

Fig. 5: HHF tested mock-ups which are still intact and available for further HHF tests.

Manufacturing and thermohydraulic tests of 9-finger steel mock-up

Prior to the HHF tests of 9-finger modules (Fig. 1) technological study on mock-up manufacturing [7] was done by means of a steel mock-up. The 9-finger design was adapted to meet the available manufacturing possibilities at Efremov, e.g. manual TIG welding, laser welding, EDM, and 3D machining. The 9-finger steel mock-up was successfully fabricated, assembled, (Fig. 6) and mounted to the helium loop (Fig. 7).

For the thermohydraulic tests the following conditions were chosen: 1) Helium 600°C, 10 MPa, 2) mass flow rate variable within a range of 20 – 100 g/s by means of gas puffing, where 3 sizes of throttle were applied, 3) measurement of He parameters and mass flow pulses within a time period of about 50 s, and 4) measurement of surface temperature by means of an infrared (IR) camera. Goal of the first gas-flow tests (without heat flux at the surface) is the examination of: A) uniformity of flow distribution in the fingers (via surface temperature distribution), B) change of outer dimension under the testing conditions (~ 600°C and 10 MPa He), and C) the gas flow parameters.

Three series of gas-puffing experiments were performed with three different Flow Rate Throttles (4, 5 and 8 mm). Examination of the flow distribution in the fingers via surface temperature distribution shows a very uniform distribution (Fig. 8). The pressure loss equivalent for the DEMO reference case (9 x 6.8 g/s = 61.2 g/s) amounts to about 0.17 MPa which lies in

the range predicted. Only a slight increase of the height at central finger of about 0.2 mm was observed (possibly due to the banding of the upper plate).

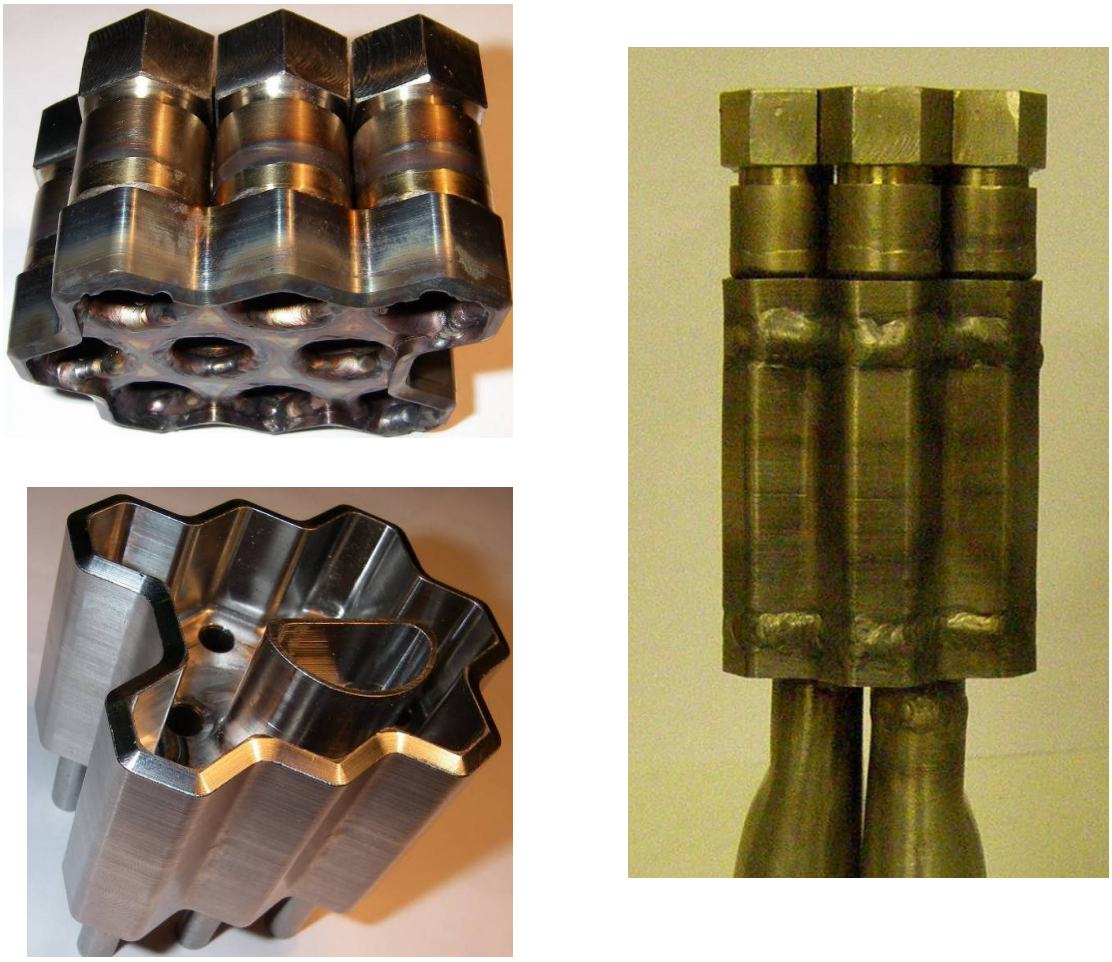

Fig. 6: Final assembly and TIG welding of the 9-finger module parts.

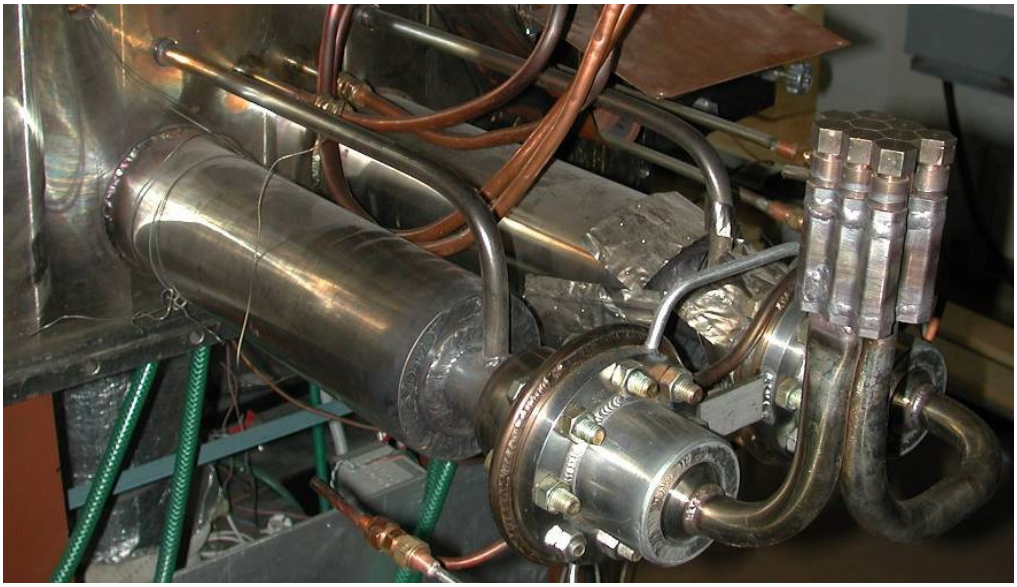

Fig. 7: 9-finger steel mock-up integrated into the helium loop for thermohydraulic tests.

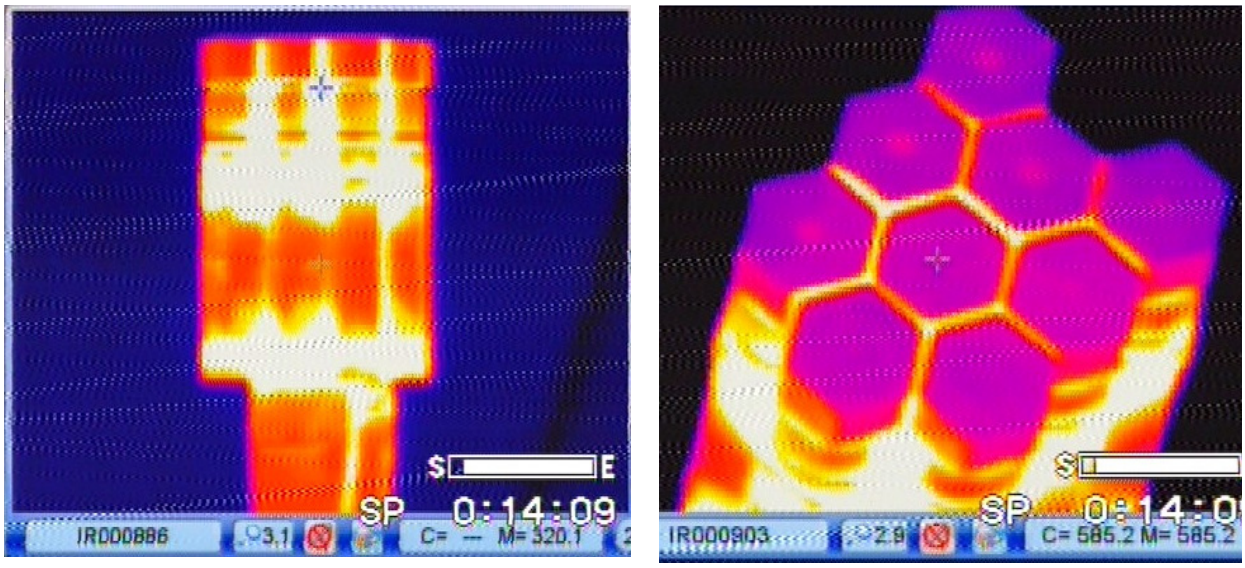

Fig. 8. An IR image of the 9-finger module during the tests at THe ~ 600°C.

Conclusions and outlook

The current step of work is aimed at the HHF tests of divertor 1-finger mock-ups to demonstrate their producibility and performances, and at technological study on fabrication, integration and tests of a 9-finger module. The tests were performed in a combined electron beam and He loop facility at Efremov. The first two high-heat-flux test series using 1-finger mock-ups already confirmed the feasibility and the performance of the current divertor design. Stable performance of the mock-ups was achieved in this third test series, which was probably due to the improved machining, e.g. mechanical grinding and ECM grinding. One of the uncertainties still lies in unpredictable material and no absolute reproducibility of the manufacturing quality. Non-destructive testing is regarded as an indispensable measure for the verification/qualification of the raw material and mock-ups. Principle fabrication technology of 9-finger mock-up has been demonstrated with a steel 9-finger mock-up. Thermo-hydraulics tests were successfully performed using tank-to-tank gas-puffing in pulse-mode (600°C, 10 MPa, mfr ~20-100 g/s) showing uniform temperature distribution on the top surface.

Work on qualification of W mock-ups exposed to high heat fluxes (Ref. 7) has been launched. The evaluation results of 1 finger mock-up tests will be a basis for completion of the 9-finger mock-ups and their following HHF tests. The next HHF 1-finger test series will focus on: a) reaching the breakthrough of 10 MW/m² and 1000 cycles by continuing testing the mock-ups from the last test series, b) Examination of new mock-ups machined with sophisticated technology in FZK (Ref. 10) and Efremov. Future HHF tests on 9-finger modules will be performed with real W mock-ups. Non-destructive testing is also regarded as an indispensable measure for mock-up verification/qualification. ‘High’ temperature brazing (e.g. CuNi44 filler metal, T_{br} = 1300°C) will be investigated. Further design optimisation is also required in particular for the W-steel joint region with a large mismatch.

Staff:

S. Antusch
N. Holstein
W. Krauss
R. Kruessmann
G. Messemer
P. Norajitra
V. Piotter
J. Reiser
M. Rieth
H.-J. Ritzhaupt-Kleissl
V. Widak
K. Zinn

Literature:

[1] P. Norajitra et al., He-cooled divertor development for DEMO, Fusion Eng. Design 82 (2007) 2740–2744.

[2] I. Ovchinnikov et al., Experimental study of DEMO helium cooled divertor target mock-ups to estimate their thermal and pumping efficiencies, Fusion Engineering and Design 73 (2005) 181–186.

[3] R. Giniyatulin et al., Study of technological and material aspects of He-cooled divertor for DEMO reactor, 23rd SOFT, Venice, Italy, 20.–24.9.2004.

[4] P. Norajitra et al., He-cooled divertor development: Technological studies and HHF experiments for design verification, Proceedings of the 21st IAEA Fusion Energy Conference, Chengdu, 16-21 October 2006, ISBN 92-0-100907-0 / ISSN 0074-1884.

[5] P. Norajitra et al., Helium-cooled divertor for DEMO: Manufacture and high heat flux tests of tungsten-based mock-ups, proceedings of the ICFRM-13, Nice, France, 10 –14.12.2007, to be published in Journal of Nuclear Materials (2008).

[6] P. Norajitra et al., Current status of He-cooled divertor development for DEMO, 25th SOFT, Rostock, Germany, 15.–19.9.2008.

[7] P. Norajitra et al., He-cooled divertor development towards DEMO, TOFE-18, San Fransisco, USA, 28.9.-2.10.2008.

TRP-002
DEMO Physics Studies

TW6-TRP-002 D 3
Development of an Improved Treatment of Plasma Radiation for Medium- and High-Z Impurities

Introduction

The aim of this task is to extend the assessment of operation of a DEMO-sized tokamak at high core radiation using the then current integrated 2D edge and 1.5 D core plasma model which had been developed in the EFDA Task TW5-TRP-002 [1] by including the effect of seed impurities on the SOL/divertor region, thus introducing an additional coupling between core and edge, and to assess longer pulse operation. The task uses a 2D plasma edge code (B2-EIRENE) and a 1.5D core transport code (ICPS), which allows the radiation fraction in tokamak reactor scenarios to be analyzed and characterized in terms of edge and core plasma parameters, in particular to quantify the core impurity contamination associated with a given level of radiation. The task is carried out with the integrated modeling.

Plasma Modelling

A number of simulations of DEMO long pulse operation in ELMy H-mode without impurity seeding have been performed, leading to an initial definition of the operating window and initial evaluation of the pulse length for these conditions without impurity seeding. These are summarised elsewhere in this Annual Report [2].

The status of mutually consistent core-edge simulations of impurity-seeded DEMO plasmas, unchanged since the previous Annual Report as explained in the next section, can be briefly summarised as follows. The implications of impurity-seeding on long-pulse operation of DEMO were investigated using the reference model of [1], i.e. with neoclassical transport of particles in the absence of an anomalous pinch. Four different impurities were modelled ranging from medium-low to medium-high Z (neon to xenon). The additional heating power, which could also be used to drive current, was held fixed at 50 MW, while the fuelling was adjusted so as to obtain a fusion power of 3 GW, resulting in an essentially ignited plasma (Q=60). Power deposition profiles were either peaked near the mid-radius (at 0.4 minor radius) or far off-axis (at 0.7 minor radius). The effect of a modest decrease of plasma current from the nominal 21 MA to 18 MA was also investigated. The gas puffing and impurity seeding were adjusted so as to operate at 70% of the edge-based pressure limit at a peak power load of 5 MW/m^2.For the same fusion power, the normalized beta increases from 2.6 to a moderately optimistic value of 3.1. Whereas the ratio of density to Greenwald limit increases from 1.1 to 1.3, the density remains at 0.7 of the edge-based density limit.

Those calculations had not yet taken into account the lower confinement in the absence of momentum input from neutral beams, which has since become a feature of observed experimental results and which will be included in future calculations. With this caveat, the burn duration, assuming 100 Vs available for burn at 21 MA, was then found to be approximately 3000s in the absence of impurity seeding and current drive, and is reduced to 1800 s by neon seeding (the decrease is less for higher Z impurities). Reduction of the plasma current to 18 MA extends the burn duration with neon seeding to 4000s in the absence of current drive, 10000 s with near-axis current drive, and 25000 s with off-axis current drive. Increasing the Z of the seed impurity to xenon then yields a burn duration of ~50000 s at these conditions.

Perspectives

The task has followed the Task TW5-TRP-002, D 2. The present task has been ongoing since September 2006, as has a parallel task [3].

In the course of the work on neon seeding of ITER, described in [2], it became apparent that 2D edge modelling of the impurity seeded operation is crucial to obtain the correct boundary conditions for the core. This modelling was undertaken for ITER conditions. It was shown that it is necessary to use the comprehensive nonlinear neutral model, which is the present state of the art. However, this leads to very long run times. Such simulations for DEMO resulted in impracticable run times in the absence of parallel processing of EIRENE. This year, the developers of the EIRENE code and the ITER team have implemented parallel processing, leading to significant gains in computational time.

DEMO 2D modelling of the edge was then started with this improved configuration and several DEMO runs are now underway. Comprehensive results from these runs are not yet available. It is hoped that extrapolation of the scaling for impurity-seeded operation determined from ITER simulations (see [2]), benchmarked and modified by analysis of the relatively small number of DEMO runs under way when they become available, will lead to a consistent scenario for DEMO., and then allow the coupled 1D core plasma simulations (similar to those described in [2]) required to complete these tasks.

Every effort will be made to complete the two EFDA tasks, including 2D modelling of the DEMO divertor and edge plasma with impurity seeding and subsequent 1D modelling of the DEMO core, in 2009.

Staff:

H. D. Pacher (INRS-EMT, Varennes, Québec, Canada)
G. W. Pacher (Hydro-Québec, Varennes, Québec, Canada)
A. S. Kukushkin (ITER Organization)
G. Janeschitz,
I. Landman
S. Pestchanyi - with the collaboration of G. Pereverzev (IPP Garching)

Literature:

[1] Pacher H.D., Pacher G.W., "Task TW5-TRP-002.D2 DEMO Physics Studies, D2 Analysis of total radiation in tokamak reactor scenarios", Annual Report 2006 (Systems Studies Section)

[2] Pacher H.D., Pacher G.W., "Divertor and Core Plasma Modelling for ITER", this Annual Report

[3] Pacher H.D., Pacher G.W., "Task TW6-TRP-012, D1b, Optimisation of fusion power plants for H2 production, D 1b - Optimisation of a ‘start-up’ scenario where the power is less than 100MW", this Annual Report

TRP-005
Neutronic Analysis, Model Generation and Neutronic Design Analyses

TW6-TRP-005 D 1a
Model Generation and Neutronic Design Analyses for the European DEMO Conceptual Study

Task TW6-TRP-005 (“Neutronic Analysis”) of the European DEMO Conceptual Study, performed under the EFDA 2006 Technology Work programme, was devoted to neutronics and activation analyses for the DEMO reactor model, employing different blanket concepts for the tritium breeding and the power production, in particular the Helium Cooled Lithium Lead (HCLL) and the Helium Cooled Pebble Bed (HCPB) blanket.

The objective of task deliverable 1a, provided by Forschungzentrum Karlsruhe, was (i) to perform the shielding analyses required to determine the dimensions of the shielding system and to define the radial build of DEMO, (ii) to develop, on the basis of the elaborated engineering CAD model, a generic three-dimensional neutronics model of DEMO, suitable for integration of blanket modules of different types, (iii) further, to develop neutronics DEMO models for the HCLL and HCPB variants, and perform the required nuclear analyses. In particular, it was requested to prove, by means of three-dimensional Monte Carlo calculations, the capability of the elaborated HCLL and HCPB DEMO reactor models to achieve tritium self-sufficiency within a specified margin.

The work performed consists of four parts, starting from pre-analyses for the reactor shield dimensioning. Then, a generic CAD DEMO model suitable for the integration of blanket modules of the HCLL (Helium Cooled Lithium Lead) and HCPB (Helium Cooled Pebble Bed) types have been set up. This in turn was converted to the MCNP geometry model by applying the McCad interface program developed at FZK. After successful integration of the blanket geometry models into the generic DEMO model, several nuclear analyses have been performed to verify and optimise the nuclear performance of the two DEMO variants in terms of the shielding efficiency and the tritium breeding capability.

Shielding pre-analysis

Besides design constraints and the overall tritium breeding performance of the blanket, two main radiation design limits have to be considered for the general shielding assessment of the DEMO tokamak: First, the re-weldability of life-time components made of steel such as the vacuum vessel, and, second, the sufficient protection of the super-conducting toroidal field (TF) coils. The pre-analyses for the DEMO reactor study were performed on the basis of a provisional set of reactor parameters obtained by employing physics and technology assumptions similar to those of plant model AB (with HCLL-type blanket) of the European Power Plant Conceptual Study (PPCS).

As the tritium breeding performance was shown to be sufficient for the blanket dimensions assumed of 50 cm and 80 cm at inboard and outboard, respectively, the present work focused on the assessment of the minimum shield thickness at the inboard side to protect the TF coils. As an example, the neutron flux profile given for the start-up radial build up (40 cm shield, 40 cm vacuum vessel) is shown in Fig. 1. From the analyses it could be deduced that radial thicknesses of 30 and 35 cm for the shield and the vacuum vessel, respectively, can be applied for the DEMO inboard side.

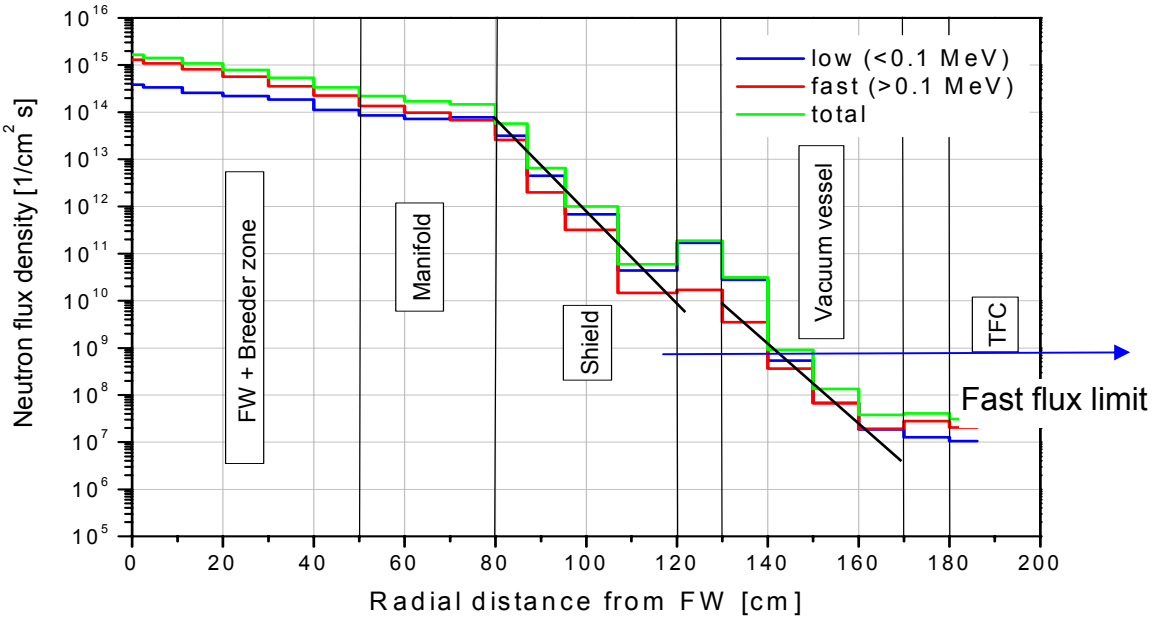

Fig. 1: Radial profile of the neutron flux density across the inboard mid-plane of the HCLL power reactor.

Supplementary analyses have been conducted to investigate the shielding performance of an integrated vacuum vessel (50 cm thickness) and shield (15 cm). This kind of component, as proposed by EFDA, would greatly facilitate the attachment scheme of the blanket modules. The nuclear analyses show that the neutron flux at the TF coils complies with the radiation limits. However, as the helium production at the front of the vacuum vessel amounts to 0.1 appm/fpy, its lifetime with respect to re-weldability is limited to 10 years; the intermediate shield in any case has to be designed as a replaceable component.

DEMO reactor model generation

Based on the provisional DEMO data and the results of the pre-analysis for the radial build, a generic CAD model of a 22.5° torus sector was designed at EFDA, CSU Garching, using CATIA V5. Before converting this CAD model to MCNP geometry data using the McCad interface programme, the generic model needs to be adapted to the requirements for its use in Monte Carlo simulations. To this end, a certain set of boundary surfaces have to be assured, geometry errors, like gaps and overlaps, have to be repaired and simplifications and detail suppression, if suitable for the neutronics calculations, have to be introduced. This remodelling step is performed in an iterative way with the McCad conversion process. After the final conversion and error check step the geometry is completed by voids, which are not contained in the CAD model.

Fig. 2 shows the generic neutronics CAD model of DEMO prepared at FZK with CATIA V5 after a few iteration steps with McCad for checking, and as far as necessary, correcting the suitability for neutroncis analyses and geometry errors.

For the integration of blanket modules into the generic DEMO model described above, a poloidal segmentation of the generic blanket boxes with 7 outboard and 6 inboard modules was introduced. In toroidal direction, a 11.25° sector was assumed with a segmentation of 1 and ½ blanket modules both at the inboard and outboard side. Both the HCLL and the HCPB blanket, based on the concepts developed in the PPCS study by CEA and FZK, respectively, were then, after the McCad conversion, integrated into the generic DEMO model (see Fig. 3 showing vertical cross sections of the torus sector with integrated blanket modules).

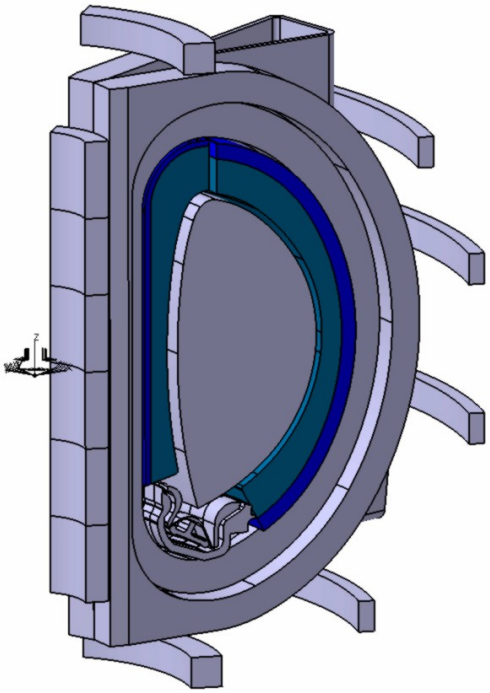

Fig. 2: Generic DEMO torus sector model (22.5°) prepared at FZK with CATIA V5 for neutronics analyses.

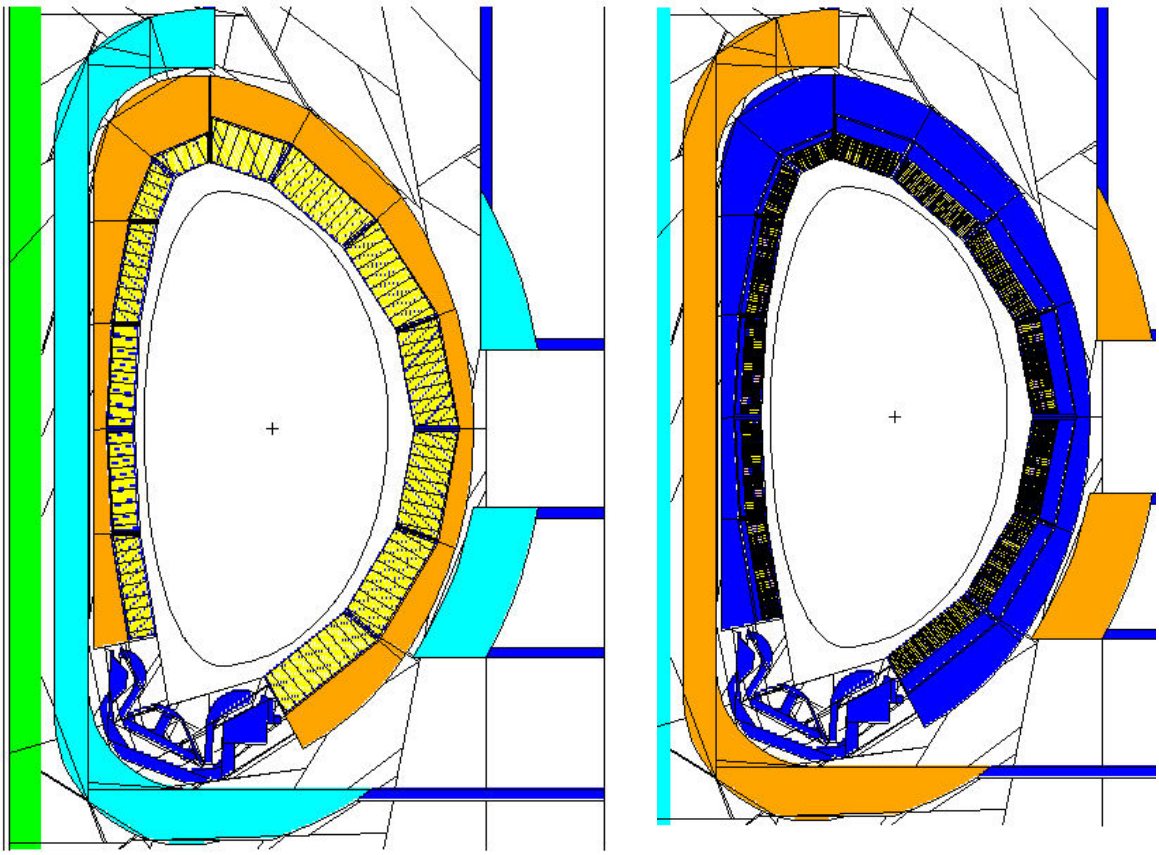

Fig. 3: Converted MCNP model of DEMO (11,25° torus sector) with integrated HCLL (left) and HCPB (right) blanket modules.

Nuclear performance analyses for the HCPB and HCLL variants

The main objective of the nuclear analyses have been, first, to asses the tritium breeding performance of the HCPB and HCLL variants of DEMO, and, in particular, to prove that within a specified margin tritium self-sufficiency can be achieved for the reactor configuration with the parameters and radial build derived from the pre-analyses, and, second, to provide the nuclear power production data which are required for assessing the balance of power for the DEMO plant. The analyses have been performed using the MCNP5 code with FENDL2 nuclear data and the geometry model explained above.

Assuming a standard Li^6-enrichment of 40 at% for the HCPB, and 90% for the HCLL blanket, the global Tritium Breeding Ratio (TBR) amounts to 1.08 and 1.09 for the two variants, respectively. In the case of the HCPB blanket, the TBR could be easily increased by enhancing the Li^6-enrichment and, in addition, by extending the breeding zone at the outboard side. However, it has been accepted that a TBR of 1.08 to 1.10 is sufficient to guarantee tritum self-sufficiency for the system including the effects of Lithium burn-up, presence of ports, tritium loss in the fuel cycle and uncertainties of the calculation.

The nuclear power generation was calculated for the complete DEMO reactor assuming a fusion power of 2385 MW. On this basis, the total nuclear power amounts to 2530 MW and 2225 MW for the HCPB and HCLL variants resulting in energy multiplication factors of 1.33 and 1.18, respectively.

Summary and Conclusions

Nuclear design analyses were performed for the European DEMO Conceptual Study, applying a novel methodological approach. A central element of the approach was using the new geometry conversion tool McCad which allows the automatic generation of a Monte Carlo geometry model from available CAD geometry data. Starting from neutronics pre-analyses to define the radial reactor build, a generic neutronics CAD model of the DEMO reactor was constructed. This generic model served as basis for the generation of DEMO reactor models employing the HCLL and HCPB blankets for the tritium breeding and the power production. Available engineering CAD models of single HCLL and HCPB blanket modules were modified to comply with the neutronics requirements and integrated into the generic neutronics CAD model. The resulting HCLL and HCPB reactor models were converted to the MCNP geometry representation by the McCad software. The nuclear analyses performed on the basis of MCNP Monte Carlo calculations showed that both DEMO reactor variants can satisfy the requirements for a sufficient shielding and Tritium breeding performance.

Staff:

U. Fischer
P. Pereslavstev
D. Große
S. Stickel
H. Tsige-Tamirat
V. Weber

Literature:

[1] U. Fischer, D. Grosse, P. Pereslavtsev, S. Stickel, H. Tsige-Tamirat, V. Weber: Neutronics Design Analyses of Fusion Power Reactors Based on a Novel Integral Approach, 25th Symp. Fusion Technology, Rostock, Germany, 15-19 September, 2008, to appear in Fusion Engineering and Design

EFDA/06-1454 (TW6-TRP-007)
DEMO Conceptual Design – FZK Contribution -
Design Conflicts arising between different Tasks for DEMO Conceptual Studies for In-vessel Integration

Objectives

The DEMO engineering design aspects (Electro-Magnetics, Tritium production, Neutronics, Structural Mechanics, Maintenance, etc.) are all closely related. The design constraints imposed considering separately all these aspects often generate the herein called “design conflicts”.

For instance, the Tritium Breeding Ratio (TBR) is influenced: i) by neutron irradiation that produces nuclear reactions in the breeder and the neutron multiplier host inside the blanket; ii) by the type of structural material (the isotopic composition has an impact on neutron absorption); iii) by the number and size of the openings on the blanket volume (openings like those for H&CD system, that is mandatory to heat and control the plasma cannot be covered with breeding blankets). These needs (TBR and ports) are in conflict thus in the future development of DEMO design a solution of compromise has to be found.

The recent conceptual studies at FZK on the current European DEMO reactor (in-vessel integration) focused on these relevant issues arising from the coupling between different tasks. These conflicts have been identified, described, and, when possible, a solution has been suggested.

Design conflicts arising from H&CD systems integration

The main functions of the H&CD systems are to heat the plasma to a burning steady state, but also to control the safety factor profile and the current profile in order to improve the confinement performance and the stability of the plasma.

The impact of H&CD systems on MMS design is quite important. In order to save as much as possible the volume dedicated to breeding blankets removed by the opening of the equatorial ports, and thus saving the total TBR of the reactor, MMS have to be cut around the ports as close as possible; two concepts are foreseen (Figure 1 and 2):

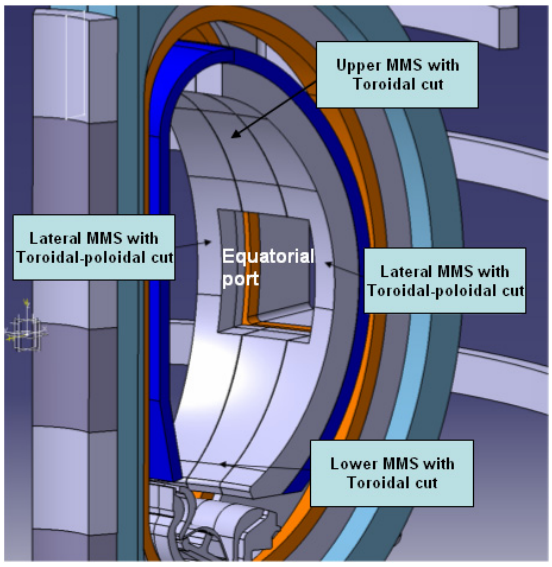

Fig. 1: Solution of MMS cut toroidally and poloidally around an equatorial port.

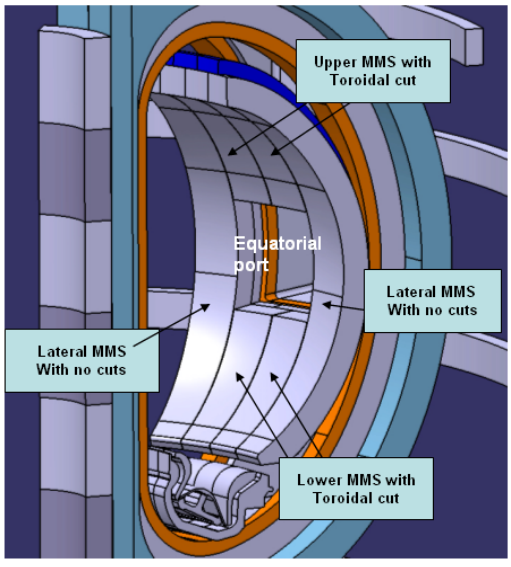

Fig. 2: Solution of MMS cut only toroidally around an equatorial ports.

1) MMS cut poloidally and toroidally (Figure 1). These MMS will be easier to mount and dismount. The drawbacks of this solution could be a revision of the fluid-dynamics design of the Helium channels inside the MF due to the smaller cross section in the poloidal mid region of the MMS, and the feasibility of the MMS itself from the structural and manufacturing point of view.

2) MMS cut only in toroidal direction (Figure 2). The advantages of these MMS are an easier design of the blanket modules and an easier Fluid Dynamic design for the Helium channels in the MF. One drawback can be the revision of the maintenance procedures for the MMS and the dedicated RH tools; another disadvantage can be the connection of the pipes for the helium cooling system of the lower small MMS. These concepts are independent from the DEMO concept adopted for the shields (“hot shield” or “cold shield”).

For the HCPB DEMO some neutronic calculations provided a value of 1.16 for the total TBR; the removal of some breeding blankets in correspondence of the equatorial ports has an impact on the TBR itself and can easily reduce it below the lower limit threshold of 1.10.

Design conflicts arising from divertor integration

The same issues described for H&CD systems are found for the Divertor integration. To allow the divertor extraction some of the MMS have to be cut in the lower part. In this case the impact on the MMS design is lower (easier design modifications), and also the TBR reduction is not so significant (the breeding volume removed for divertor is much less than that removed for H&CD systems ports) (Figure 3).

An issue that is typical of the divertor integration concerns the shift of the plasma. The last EFDA design (July 2007) considers a divertor that is under-dimensioned for a DEMO reactor. The substitution of this divertor with a more DEMO relevant divertor imposes a shift of the X-point thus a shift of the whole plasma region and a recalculation of the magnets currents and position is required.

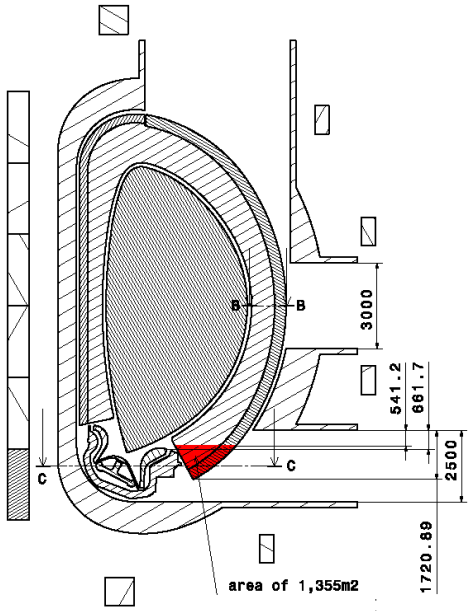

Fig. 3: MMS cut in the lower region to allow divertor extraction.

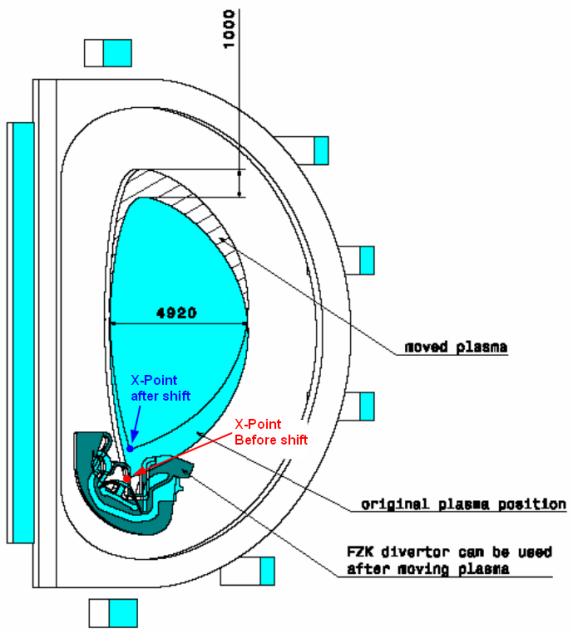

Fig. 4: Divertor comparison between EFDA2007 and FZK2007 by overlapping and plasma shift.

Design conflicts arising from Blanket modules integration

The size of the MMS is limited by some constraints: the size of the blanket modules and the overall weight of the MMS itself. The dimensions of the upper ports should be a consequence of the MMS size. In the last DEMO EFDA design the upper ports is not large enough to allow a vertical extraction of the MMS. Either the upper port dimensions should be revised or the maintenance procedure for MMS extraction.

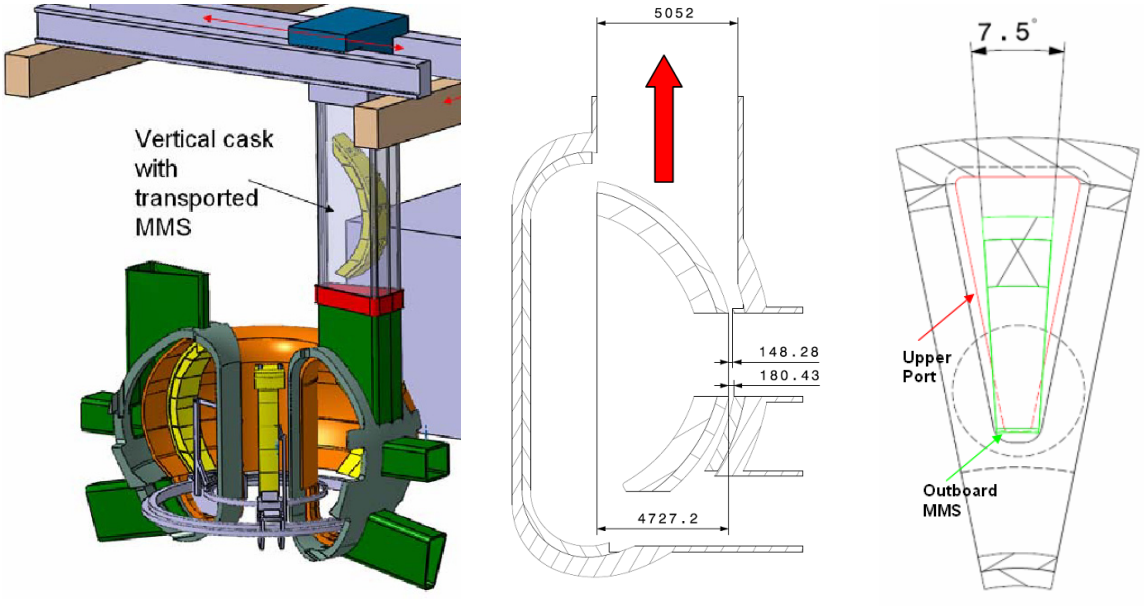

Fig. 5: DEMO HRS, MMS extraction from the upper port. 3D outlook (left), radial-poloidal cross section (middle), and sector top view (right).

Design conflicts between structural materials and attachments

The DEMO concept foreseeing MMS hold by flexible bending bars in front of the shield (Cold Shield Concept, Figure 6) gives rise to some issues related to the attachments structural materials. The operating temperature window for RAFM steels imposes lower (300-350°C) and upper (500-550°C) limits which are difficult to respect in the operating conditions before the shield.

The neutron irradiation doses and the consequent DPA produced inside structural materials (for permanent and non-permanent components), are incompatible (if RAFM steels are considered) with the temperature at which the neutron irradiation takes place (below 300-350 °C): this produce a shift of the DBTT and embrittlement issues (Figure 7).

On the other side, neutron irradiation produces a high Neutron Power Density that heats up all the attachments structures, imposing temperatures too high (if they are not actively cooled) for the materials that are currently developed (creep issues, Figure 7).

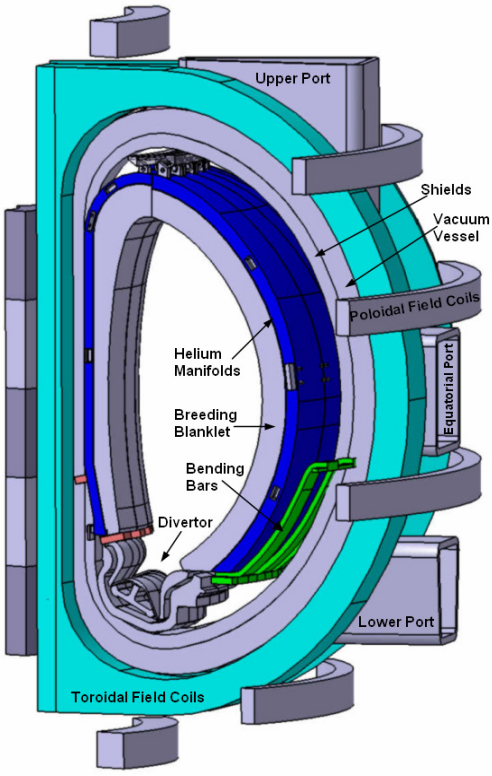

Fig. 6: DEMO outlook, cold shield concept with attachments.

At the current status of materials development an active cooling system for attachments has thus to be foreseen and integrated (Figure 8).

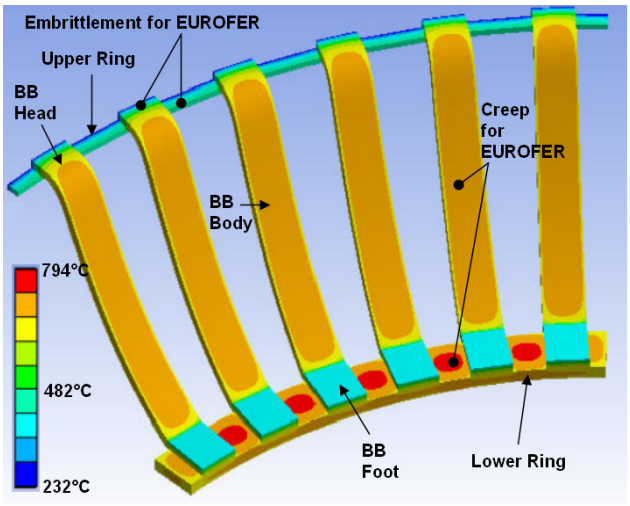

Fig. 7: Flexible bending bars. Temperature field and material issues.

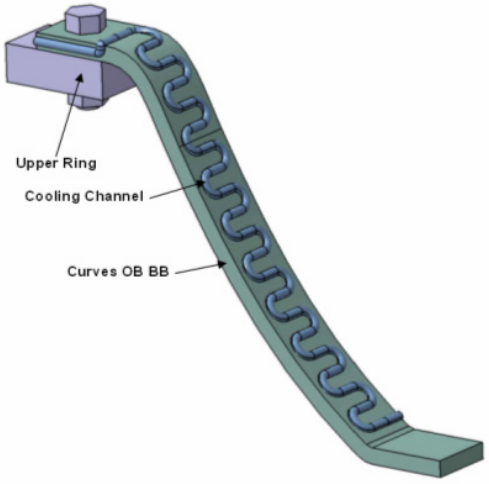

Fig. 8: Proposal of an active cooling system for bending bars.

Staff:

A. Abou-Sena
F. Cismondi
T. Ihli
E. Magnani
P. Pereslavtsev
R. Roccella
N. Scheel
D. Nagy (HAS, KFKI-Research Institute, Budapest, Hungary)

TRP-012
Optimisation of a Fusion Power Plant for the Production of Hydrogen

TW6-TRP-012 D 1b
Optimisation of a 'Start-up' Scenario where the Power is less than 100 MW

Introduction

The aim of this task is to optimise the "start-up" of a DEMO-sized tokamak including the L- to H-mode transition with auxiliary power below 100 MW. The task is carried out using the integrated modelling based on a 2D plasma edge code (B2-EIRENE) and a 1.5D core transport code (ICPS), as described in more detail in [1] and [2]. The present task has been active since autumn 2006.

Initial Plasma Modelling

The geometric parameters chosen for the DEMO modelling task are similar to those of ITER as developed in the Conceptual Design Activity (1991) (B=5.7T, R=8.1m, a=2.8m, κ=1.7, δ=0.36).

The ICPS model for core plasma transport in the related work described in [1] and references and appendices therein is a time-dependent model. For the work described in previous annual reports, accelerator algorithms had been introduced to obtain more rapid convergence to quasi-steady-state conditions. Removal of these algorithms, as required for the present task, has been completed, and testing will commence soon.

Work on this task had to be suspended, initially to instead pursue the investigation of ITER operating windows in the framework of the ITER design review, but particularly to improve the edge model in the presence of heavier impurities. The improved model had been developed for ITER conditions [2] and must be adapted for DEMO parameters. This task therefore required the implementation of parallel processing of EIRENE, since the convergence under DEMO conditions otherwise is too slow. The implementation has been completed recently by the EIRENE developers and the ITER team. The ongoing work on impurity radition, and the status of these developments in relation to DEMO, is described elsewhere in the Annual Report [3].

Perspectives

When the improved SOL/divertor impurity model will be available, the ramp-up of plasma current from ~5 MA onwards and the concurrent ramp-up of density and auxiliary power will be optimised using the ICPS model in Astra so as to obtain an L- to H-mode transition with an auxiliary power below 100 MW. Simplified boundary conditions will be used while the plasma is in the limiter configuration and the full integrated model for core and edge will be used after transition to the diverted geometry.

Staff:

H. D. Pacher (INRS-EMT, Varennes, Québec, Canada)
G. W. Pacher (Hydro-Québec, Varennes, Québec, Canada)
A. S. Kukushkin (ITER Organization)
G. Janeschitz,
I. Landman
S. Pestchanyi - with the collaboration of G. Pereverzev (IPP Garching)

Literature:

[1] Pacher H.D., Pacher G.W., in collaboration with ITER IT Garching, FZ Karlsruhe, Max-Planck-Institut für Plasmaphysik Garching, EFDA CSU Garching, "Divertor and core plasma modelling for ITER - Final Report June 2008", INRS Energie, Mat. et Télécom. Report, INRS-EMT-043-0608, June, 2008

[2] Pacher H.D., Pacher G.W., "Divertor and Core Plasma Modelling for ITER", this Annual Report

[3] Pacher H.D., Pacher G.W., "Task TW6-TRP-002.D3 DEMO Physics Studies, D3 - Development of an improved treatment of plasma radiation for medium- and high-Z impurities", this Annual Report

TW6-TRP-012 D 2
Assessment of the Impact of a Fusion Power Plant for H_2 Production on Internal Components

Objectives

Studies carried out in the EU on fusion power plants have focused so far on electricity production. Another important alternative is the production of hydrogen in view of a hydrogen economy (e.g. heating and transportation). The objectives of the present study are the optimization of the design of a fusion plant for the production of hydrogen rather than electricity – a Hydrogen Production Fusion Power Plant (HPFPP).

The scope of the work performed under this DEMO technology subtask comprises the following more or less independent aspects: 1) The impact on the design of internal components of an HPFPP, including possible alternative blanket layouts. 2) Cooling fluid(s), in particular the possible use of CO_2 rather than He. 3) The impact of pulsed operation on the design of the mechanical structures.

Design of Internal Components

Breeding blankets are key components of fusion power plants and determine to a large degree their attractiveness. Regardless of other aspects, the key parameter to judge the attractiveness of a blanket concept is the prognoses of the achievable outlet temperature. The outlet temperature determines the choice of the most appropriate cycle for energy production and its efficiency. Therefore it also determines the most decisive value of a power plant, namely the cost of electricity. The blanket outlet temperature determines the possible processes for hydrogen production from fusion power and it also determines the thermal-to-hydrogen conversion efficiency to be expected. The blanket outlet temperature is an indicator to assess the impact of a HPFPP on the design of internal components.

An overview of applicable hydrogen production processes is given and their requirements on process temperature are specified. The presented processes were selected considering conceivable technical feasibility and sufficient efficiency. Thermo-chemical water splitting is the conversion of water into hydrogen and oxygen by a series of thermally driven chemical reactions (Figure 1). Currently the leading alternatives for thermo-chemical hydrogen production are the Westinghouse Hybrid Sulphur Process (WSP) and the Sulphur-Iodine Process (SI).

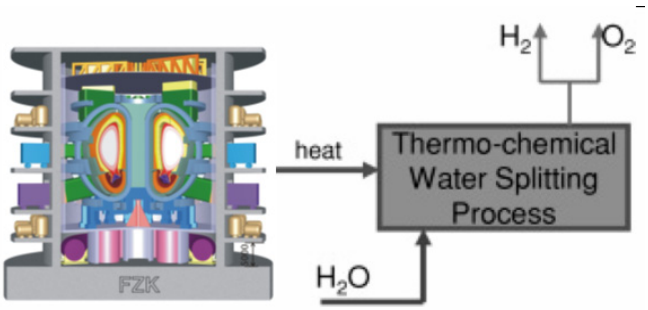

Fig. 1: Schematic of thermo-chemical water-splitting process for hydrogen production coupled with a fusion reactor.

Of particular interest for the presented study is the process in which High Temperature Steam Electrolysis (HTSE) is coupled with an Advanced Gas cooled fission Reactor (AGR). The HTSE average process temperature is 900°C, whereas the reactor exit temperature and the SCO_2 cycle turbine inlet temperature are: 550°C to 700°C. The 900°C at the HTSE unit, which is higher than the reactor exit temperature, is achieved with recuperative and electrical heating. With direct coupling between the power conversion cycle (supercritical CO_2 recompression Brayton cycle) and the reactor it should be possible to achieve 39% to 48% of net hydrogen production energy efficiency in the temperature range between 500 and 600°C.

Therefore it can be stated that the HTSE process seems to be the best solution for a typical fusion reactor where the exit temperature is limited due to technological requirements or limitations (Figure 3).

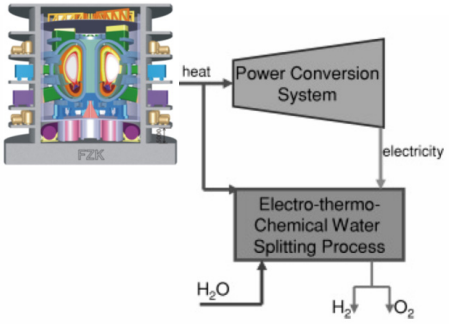

Fig. 2: Schematic of High Temperature Steam Electrolysis (HTSE) process for hydrogen production coupled with a fusion reactor.

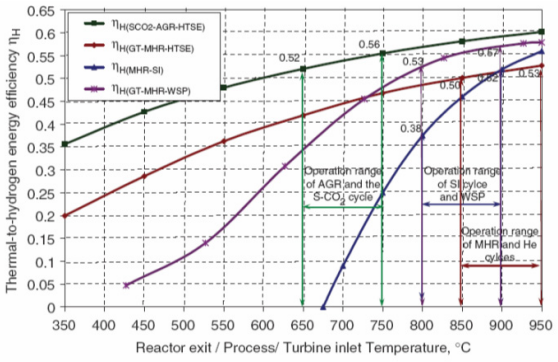

Fig. 3: Thermal-to-Hydrogen production efficiency vs. reactor exit temperature.

Cooling Fluids: CO_2 – Helium Comparison

Helium is the current choice of coolant for DEMO. The decision to use it in large power plants will probably not only rest on thermodynamic considerations; for instance, a satisfactory solution of the practical problem of sealing the system at the high pressures is required. Experience with sealing high-pressure carbon dioxide in gas-cooled reactors has shown that leakage is substantial, and helium, being a lighter gas, will be even more difficult to contain.

Moreover, the required pumping power for the coolant is of high relevance since it directly reduces the achievable output power.

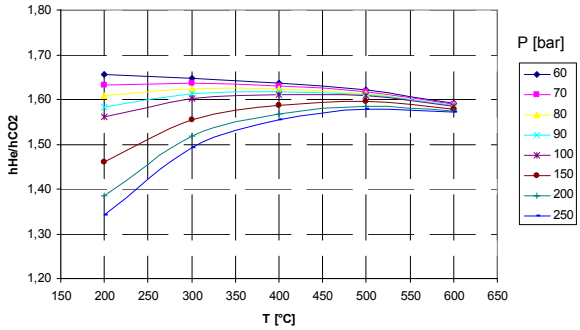

Fig. 4: Heat transfer coefficient ratio for helium and CO_2.

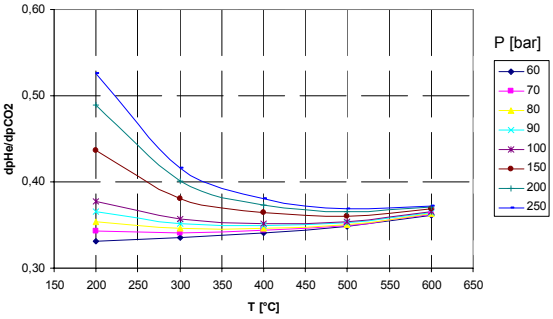

Fig. 5: Pressure losses ratio for helium and CO_2.

In Figure 4 it can be seen that the ratio hHe/hCO_2 is always above unity, meaning that the heat transfer coefficient for He assuming the same thermodynamic conditions (p, T) and the same pressure loss is higher than the one for CO_2. For lower pressure this effect is pronounced. At about 80 bar the influence of the temperature nearly diminishes. The influence of the pressure decreases with higher temperature.

In Figure 5 all values of the dp-ratio are below unity, meaning that the pressure loss for He is lower than the one for CO_2. The effect is pronounced for low pressures. Again, as could be expected at about 80 bar, the influence of the temperature is low. For higher temperatures a nearly constant value for all pressures of about 37% is determined.

Figure 6 shows the maximal value of 190% for high pressure and low temperature. Meaning that under this conditions the pumping power for He is higher than the one for CO_2. At 300°C

and 60 bar (the lowest investigated pressure) the pumping power for He is only 80% of the pumping power required for CO_2. For DEMO the pressure of the cooling fluid is set to 80 bar.

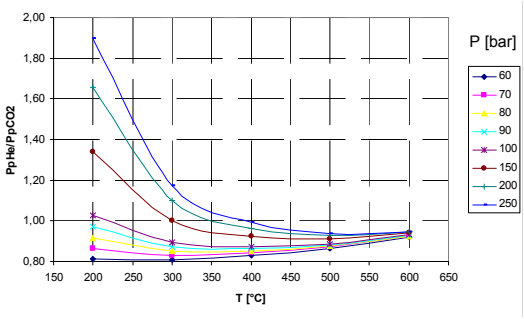

Fig. 6: Pumping power ratio for helium and CO_2.

For this pressure of the medium the ratio $PpHe/PpCO_2$ is below unity for the investigated temperature range. This means that in terms of pumping power the use of He is advantageous! The investigation exhibits lower pumping power for CO_2 only for higher pressures and lower temperatures. In addition to this it must also be observed that CO_2 is affected by neutron activation instead of helium that is not sensitive to neutron irradiation. All this leads to the conclusion that for current blanket designs operating in the temperature range between 300°C and 500°C at 80 bar substitution of He by CO_2 does not seem to be advantageous. The only advantage of CO_2 can be seen in Figure 3, namely the higher efficiency reached by a HTSE coupled with a CO_2 AGR. The option of an indirect coupling He-CO_2-HTSE could be analyzed.

Impact of Pulsed Operations on the Design of the Mechanical Structure

Steady-state electricity production is an essential requirement of a fusion reactor and it has generally been assumed that the most cost-effective approach to this goal involves steady-state plasma operations. The (cost) disadvantages associated with pulsed plasma operations may be acceptable if certain physics challenges involved in achieving steady-state are proved to be more difficult or more expensive to resolve than assumed. Therefore, more detailed comparisons between steady-state and pulsed Tokamak operations, including physics as well as technological aspects, have to deliver essential input for future DEMO studies.

Regarding technology aspects these comparisons need to include the transient operations of the internal components. Only limited information is available, but former work in the frame of the DEMO studies and also the US PULSAR study can serve as starting point.

An estimation of cyclic temperatures and cyclic thermo-mechanical loads faced by the most relevant reactor components needs to be provided. Appropriate stress estimations need to be performed.

Prospective life time analyses are required considering the expected number of cycles. The pulse length is a function of burn time and dwell time; an agreement about a representative pulsed scenario is necessary, nevertheless a first attempt that seems reasonable to make the pulsed reactor competitive with a steady one is shown in Figure 7.

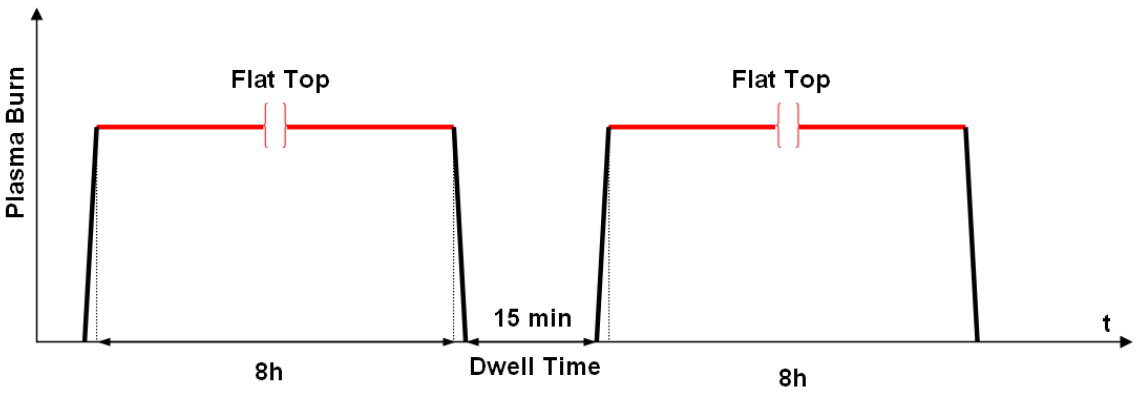

Fig. 7: Reasonable scenario for the pulses of a pulsed DEMO reactor.

Following this scenario some calculations have been performed in order to estimate the temperature variation inside the main in-vessel structural components.

The results show that if an active cooling of 300°C is maintained in the Blanket/Manifolds during the dwell time, the ΔT inside the structural materials is important (~200°) (see Figures 8 and 9), and the effects on thermo-mechanical stress (σ) and deformations (ε) are not negligible. To reduce the large ΔT and the consequent Δσ inside structural materials, during the dwell time phase the active cooling should be stopped or bypassed.

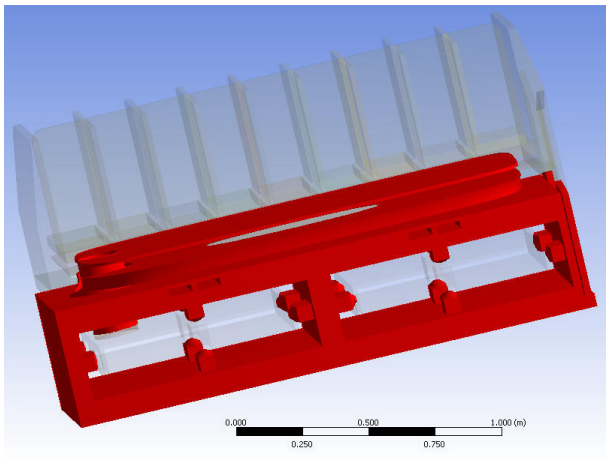

Fig. 8: Isothermal field between 400 and 500°C for blanket and manifold at inboard mid-plane at the end of the flat top.

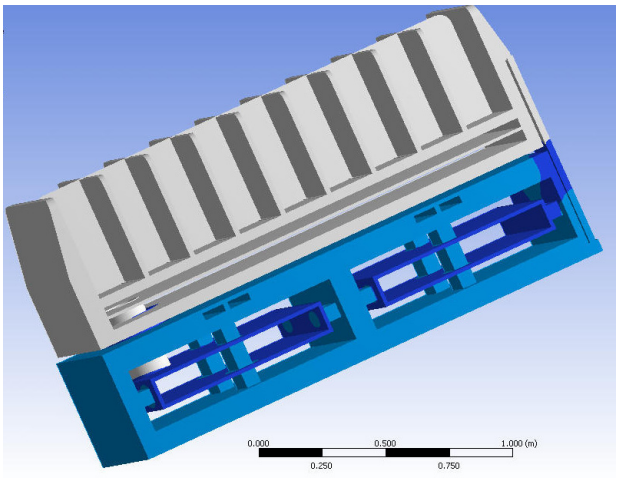

Fig. 9: Isothermal field at 300°C for blanket and manifold at inboard mid-plane after 15 minutes of dwell time.

A permanent component inside a pulsed reactor faces about 21900 pulses; a non-permanent component operating during 5 FPY about 5500. The minimum number of cycles to be tolerated by the structural materials can be determined if data about cyclic thermo-mechanical fatigue are available for the structural materials taken into account. EUROFER, ODS-EUROFER, Tungsten Alloys, Vanadium Alloys, Silicon Carbide are the reference structural materials for the DEMO concepts. EUROFER is the most advanced and some relevant data exist. The other structural materials are under development and few data exist.

The pulse shape of a pulsed reactor produces a creep-fatigue coupled effect in structural materials that is still not completely investigated by materials tests for evident reasons of experimental time (hold time of 8h for 20000 cycles!). Nevertheless this effect is relevant and shortens the components lifetime much faster than the simple cycling without hold time (compare figures 10 and 11).

Stress-strain estimations on the most loaded components will impose a limit on the number of cycles that the components can face; vice versa the restriction imposed on the permissible stress by a fixed number of cycles can affect the design of the components.

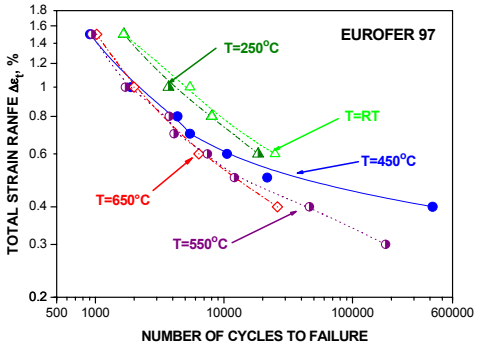

Fig. 10: Total strain vs. number of cycles to failure for un-irradiated EUROFER97 at different temperatures [1].

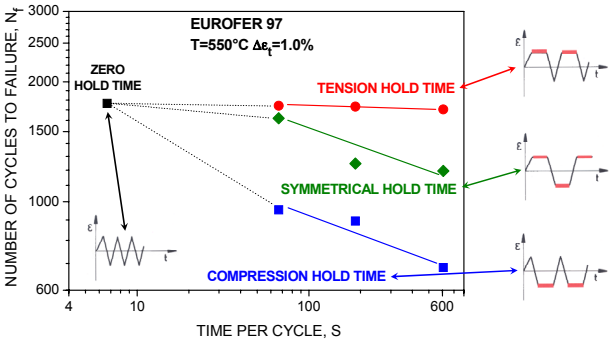

Fig. 11: Number of cycles to failure for un-irradiated EUROFER97 vs. time per cycle for different hold time modes [1].

In addition to this, both thermal and thermo-mechanical fatigues are affected by neutron irradiation. In general the effects in Low Cycle Fatigue (LCF) of a 300 °C neutron irradiation are significant. The effects are illustrated in Figure 12 using irradiated and un-irradiated Eurofer-97 plate specimens (they hold for other product forms as well). The LCF life is reduced at higher strain range and enhanced at lower strain range.

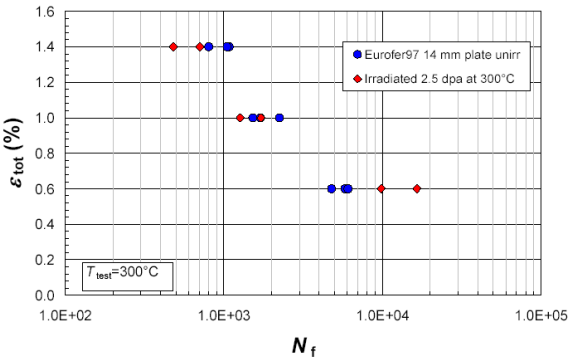

Fig. 12: Total strain vs. number of cycles to failure for irradiated and un-irradiated EUROFER97 at 300°C [2].

Nowadays materials data at DEMO doses (70-80 dpa) are not available and data for thermal and thermo-mechanical fatigue are not enough to make general assumptions.

The necessary materials data have to be collected as far as the current state of material development allows.

If the relevant data are not available, meaningful assumptions have to be established for an estimation of the feasibility of the different DEMO concepts.

Staff:

F. Cismondi
D. Filsinger
T. Ihli
E. Magnani

JET Technology

JW5-FT-5.20
Shutdown Dose Rate at JET Tokamak – Code Benchmark

The objective of Task JW5-FT-5.20 was to validate the computational methods for shutdown dose rate calculations through the comparison with dose rates measured in a dedicated benchmark experiment on JET. The dose measurements were performed by the experimental team of ENEA Frascati during the 2005 – 2007 JET campaigns at different cooling times using a Thermo Luminescence Detector (TLD) for a position in the upper irradiation end (IE) inside the vacuum vessel and a Geiger-Mueller (GM) detector for a position outside the vessel [1]. The task of FZK was to analyse the experiments by means of calculations employing the rigorous 2-step (R2S) approach, developed previously for Monte Carlo based calculations of shut-down dose rates in 3D geometry [2]. In parallel, the experiments were analysed by ENEA Frascati using the direct one-step (D1S) approach [3] for the shut-down dose rate calculations.

Satisfactory agreement of the calculations and the TLD dose measurements was obtained for the upper IE inside the vessel although the D1S results were systematically higher and the R2S results systematically lower than the measurements see Fig. 1.

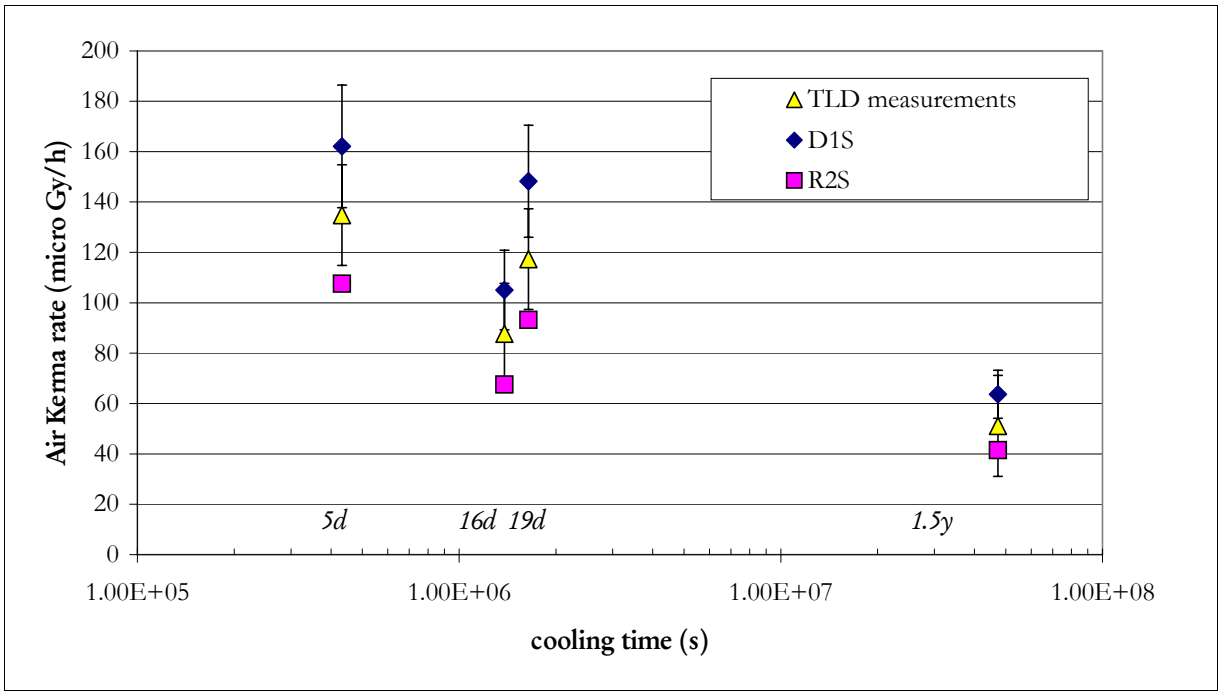

Fig. 1: Calculated and measured dose rates for the position in the upper irradiation end inside the vessel as function of the cooling time.

The GM measurements in the ex-vessel position, on the other hand, were significantly underestimated by both the R2S and D1S calculations, see Fig. 2. The R2S and D1S calculation results, however, agree in general within 20% except for very short (1d: R2S/D1S = 0.7) and very long cooling times (1.5 y: R2S/D1S = 1.6). This indicates that the complex surrounding of the detector is still insufficiently represented in the model. Such deficiencies may result in large underestimations of the induced activation and the gamma decay source. To minimize the resulting inaccuracies, a dedicated follow-up experiment will be performed on JET in two steps comprising neutron flux measurements during operation and dose measurements after shut-down at the same detector location.

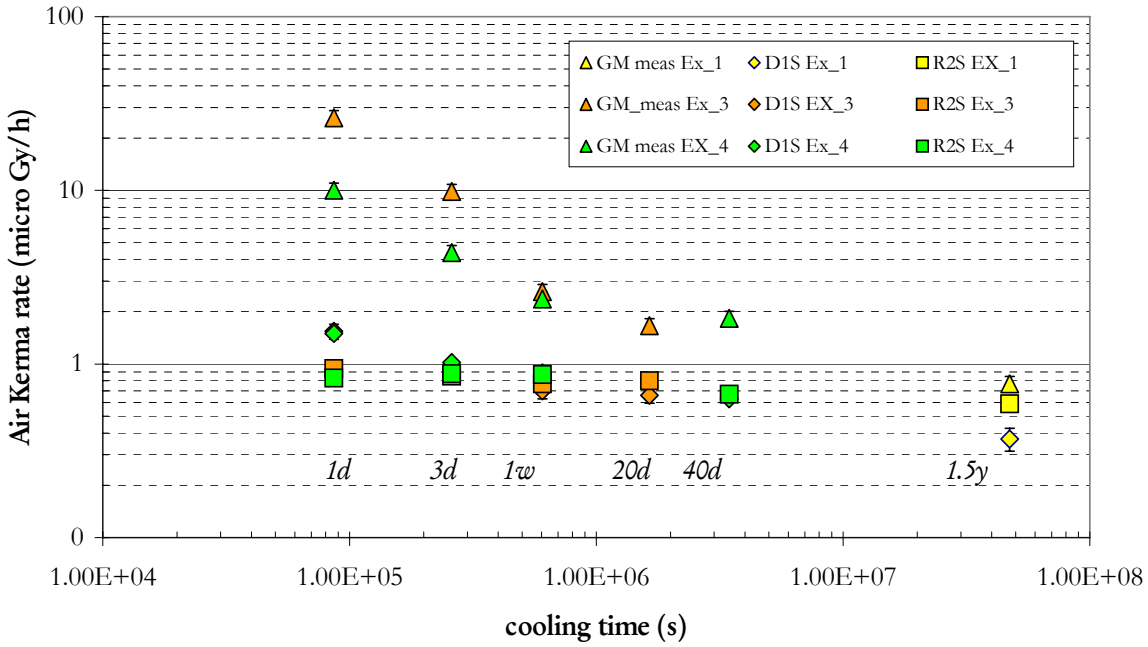

Fig. 2: Calculated and measured dose rates for the ex-vessel position as function of the cooling time.

Staff:

U. Fischer
P. Pereslavtsev
M. Angelone (ENEA Frascati)
L. Petrizzi (ENEA Frascati)
R. Villari (ENEA Frascati)

Literature:

[1] R. Villari, M. Angelone, P.Batistoni, U. Fischer, P. Pereslavtsev , L. Petrizzi, S. Popovichev et al, Validation of shutdown dose rate Monte Carlo calculations through a benchmark experiment at JET, Fus. Eng. and Des. 83 (2008), 1742-1746.

[2] Y. Chen, U. Fischer, “Rigorous MCNP based shutdown dose rate calculations: Computational scheme, verification calculatins and applications to ITER”, Fus. Eng. Des. 63-64 (2002), 107-114.

[3] H. Iida, D. Valenza, R. Plenteda, R. T. Santoro AND J. Dietz, Radiation Shielding for ITER to allow for Hands-on Maintenance inside the Cryostat, J. of Nuc. Sci. and Tech., Supplement 1. (March 2000) 235-242

JW2-FT-2.4 / JW5-FT-2.24
Tritium Inventories of Spent Cryopanels and Waste Conditioning / Characterisation of ITER relevant Cryosorption Panels after Tritium Operation at JET

Background and objectives

An ITER-relevant cryosorption pump (PCP) has been manufactured, installed and operated at the Active Gas Handling System (AGHS) of JET. Under the previous task JW1-FT-6.1, the pump has been fully characterized, firstly for direct operation of the tokamak, secondly in parametric test campaigns. This present task aims to assess the tritium retained on the ITER cryopanel after operating under these representative conditions. It will provide data for the composition of gas evolved following regeneration over a range of temperatures and determine the amount of tritium retained on the cryopanels. Furthermore, additional pumping speed tests will be made to check that the original pumping performance can be fully restored.

Experimental results

For the final original tests of the PCP (under task JW1-FT-6.1), the cryopanels have been pre-loaded with a methane/ethane/propane mixture.

The PCP has then been regenerated to 300 K, and the gas been collected and processed. According expectation, a certain part of tritium retained on the pump has been released. It was processed in the Ni catalyst bed and the permeator of the AGHS impurity processing system. Altogether there was 3.2 bar·l of gas containing 30 TBq of T_2.

However, as the bound tritium is anticipated to be incorporated into tritiated hydrocarbons, which were the pumped gas species of the final test campaigns, the predominant fraction is still sorbed. A preliminary accountancy balance of the tritium fractions pumped out and seen by the PCP and released during the various regenerations performed in the past yields a residual overall tritium inventory of the PCP of about 420 TBq (1.18 g) (to compare with 900 TBq if all hydrocarbons would be completely tritiated). Based on that value, the 300 K regeneration achieved a release of ~ 7%. Composition analysis of the hydrogen isotopes was made which yielded H/D/T=88/4/8%; no carbon could be identified and the helium content of the released gas was 26%.

In a further step, the PCP was regenerated at 473 K and released further 0.35 bar·l. The composition analysis of the hydrogen isotopes in the released gas yielded H/D/T=90/4/6%, which is very much the same as it was for the ambient regeneration. This underlines that all hydrogen was already released at the regeneration steps at 100 K and 300 K, according expectation. But 38% carbons could be identified in the 473 K regeneration gas. It is understood that the main release within this high temperature regeneration were the hydrocarbons.

After that, pumping speed tests with hydrogen, deuterium and helium were made. Fig. 1 is comparing the measured experimental curve for deuterium with the measurements 4 years ago (before pumping test with tritium and hydrocarbons). This very good agreement was found for all three gases, which clearly shows that there was no permanent degradation whatsoever.

In summary, the cryosorption pumping concept was demonstrated to be reliably working also for tritium and tritiated gases, and allowing for good inventory control. The task is now closed.

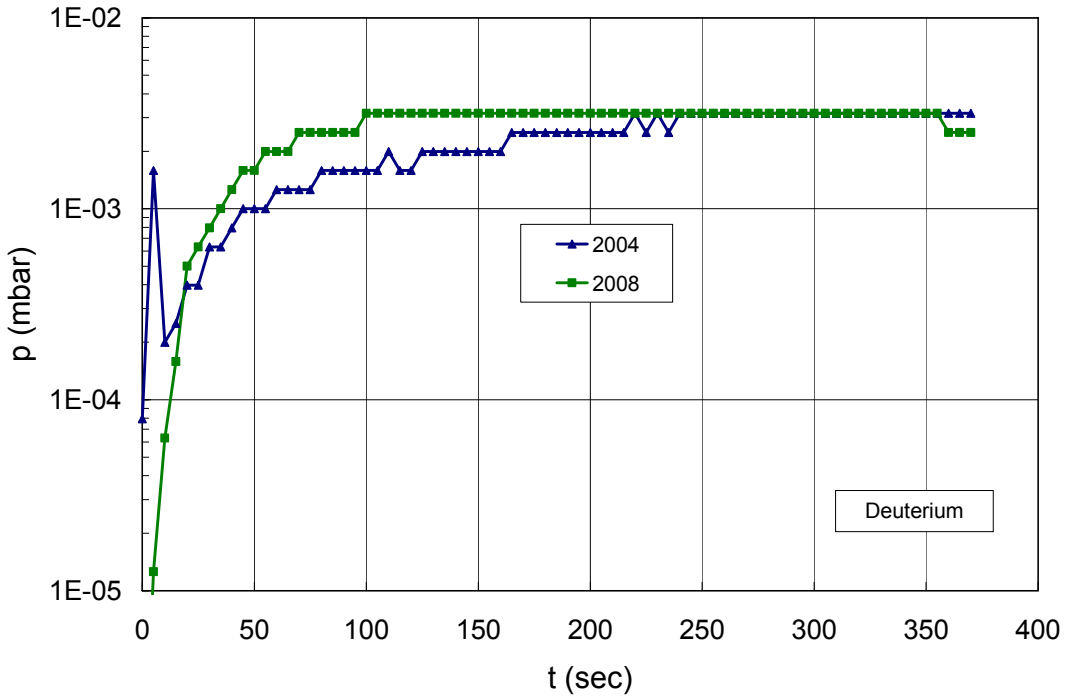

Fig. 1: Comparison of pumping speed curves for deuterium prior and after the PCP experimental phase.

Staff:

Chr. Day
P. Camp (UKAEA)
S. Grünhagen (UKAEA)
S. Knipe (UKAEA)
R. Stagg (UKAEA)

Heating Systems Technology Project

EFDA/06-1502 (TW6-THHN-NBD1)
Design Activities for the first ITER HNB Injector

Objectives

The change in 2006 from a circular to a rectangular shaped beam line vessel lead to a total change of the available base geometry of the ITER HNB cryopumps. An additional consequence was that the pumping surface had to be reduced by 20% due to space limitations. Moreover, the new vessel geometry leads to a less uniform distribution of the cryopump pumping speed of the beam line, which makes the cryopump design more difficult. Finally, new experimental investigations have shown that the needed gas density between the accelerator and the neutralizer must be further decreased (towards 0.02 Pa), and a completely revised density profile was requested. The engineering design of a cryopump fully adapted to all needs was the main task in 2008.

Stepwise design development

For the ITER heating neutral beam injectors a cryopump has been developed which covers all actual requirements given by the injector. To achieve this, the following stepwise approach has been taken:

1. Set-up of the initial data base of interfaces: Assumptions, base geometry, size and position of the cryopump in the given beam line vessel were agreed and frozen. The resulting space envelopes for the cryopumps are shown in Fig. 1.

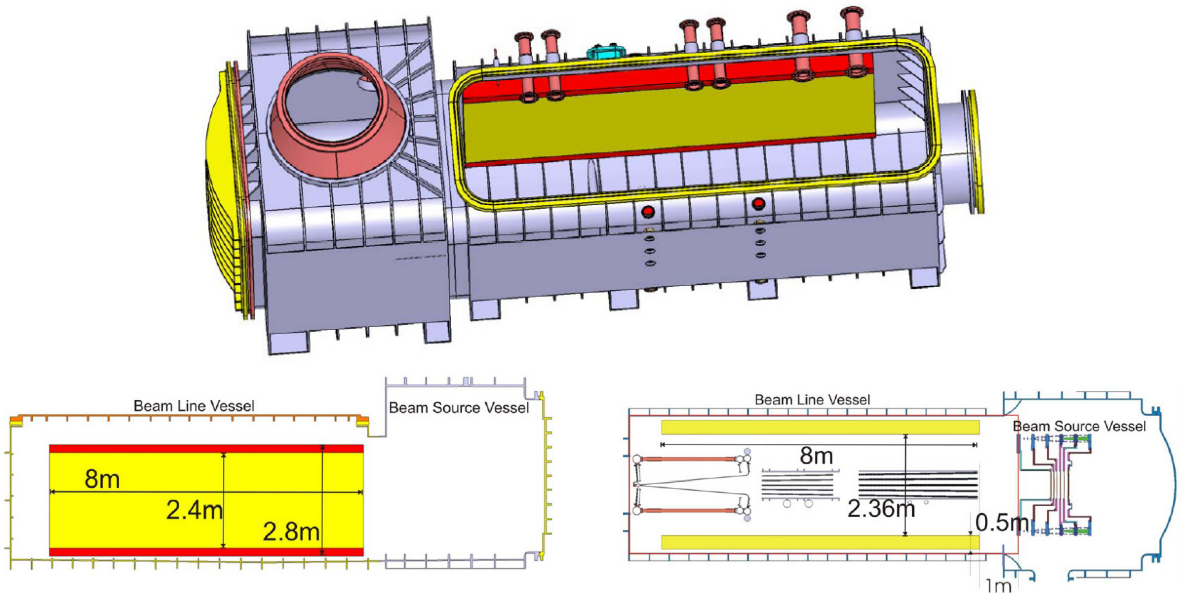

Fig.1: Available geometric envelope for the HNB cryopumps.

2. Calculation of the gas distribution profiles: The density distribution profiles in the beam line were calculated for different capture probabilities of the cryopumps and different configurations of the beam line, carried out by the use of different vacuum codes (such as ITERVAC and ProVac3D from FZK or the Monte Carlo Gas Flow code developed by KIAE especially for the ITER HNB.

The most important result of the investigations was the need of a cryopump with a gas capture probability 50% higher than a classical cryopump (that means equipped with a chevron baffle as radiation shield). Consequently, detailed investigations on the development of a new cryopump design were made. Various designs have been elaborated and their properties (pumping speed, heat loads, etc.) have been compared to find the best solution. After a

final review discussion held with ITER IO and F4E, the agreed result was the cryopump concept illustrated in Fig. 1, which provides for a gas capture coefficient of 0.33 for deuterium and 0.3 for protium. The whole pump per HNB will have two identical halves, each of them comprising eight of the modules shown in Fig. 2.

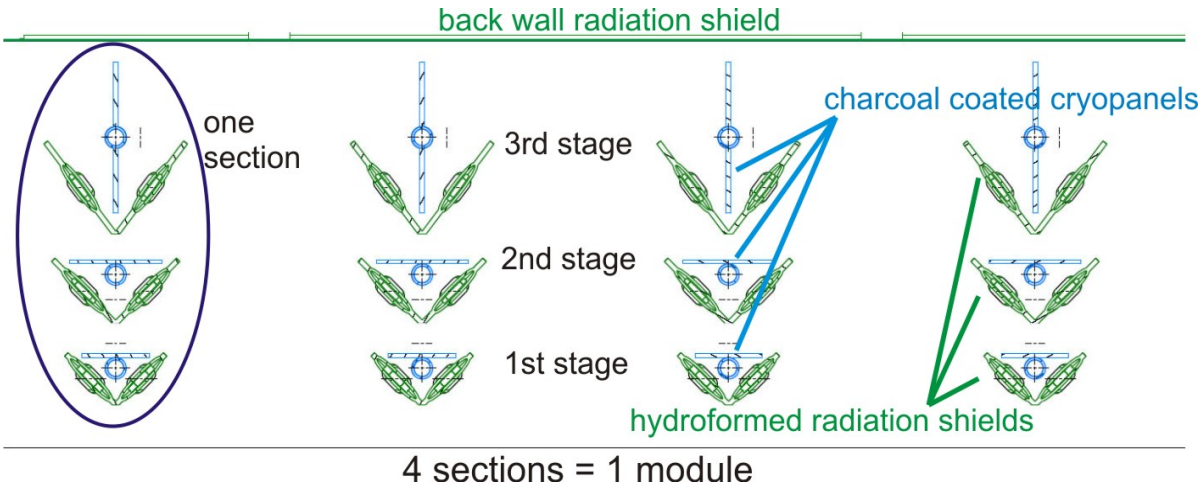

Fig. 2: Revised cryopump concept with optimised capture coefficient.

3. Vacuum technological detailed design: To come up with an optimised cryopump design (increased pumping speeds), extensive and detailed Monte Carlo simulation work was performed [1, 2]. One versatile Monte Carlo model was set up in ProVac3D to calculate density profiles (see the parallel task TW5-THHN-MONRF) [3]. In this design stage, further detailed calculations have been done to assess the influence of introduced gas baffles in the beam line. It could be shown that a gas baffle fixed to the neutralizer end is unavoidable.

4. Heat load and cryogenic detailed design: Another 3-dimensional Monte Carlo model was set up in MOVAK3D for the determination of the heat loads to the shielding (supplied with 80 K at the inlet and allowed to have 90 K at the outlet) and the panel circuits (between 4.6 and 6.7 K). In Table 1 the heat loads for the two main operation scenarios are listed. For the stand-by operation of the beam line, only radiation and solid heat conduction are contributing. For the pulsed operation, additional heat loads by the pumped gas must be taken into account.

Table 1: Heat loads for the ITER heating neutral beam cryopump in the case of unshielded beamline components (worst case).

Mode	***Radiations Shields***	***Panels***
Stand by	11.5 kW	254 W
Pulse operation	11.7 kW	465 W(H_2) and 354 W(D_2)

The cryogenic design was then completed with the calculation of the needed cryogenic mass flows and to identify the input parameters for the cryoplant design.

5. Complete 3D design of the cryopump in CATIAV5: This model was consistently checked and revised following the results of thermomechanical FEM analysis with ANSYS and thermohydraulic analysis. The latter can be reliably done for the panel circuits as their flow cross-section is circular for which there exist approved formulae. Contrary is the situation for the shielding circuit with line-welded hydroformed panels and spot welded backshields, for which there do not exist any reliably pressure loss data. Thus, the pressure drops for the radiation shields can currently not be predicted.

Finally, a complete set of detailed design drawings was elaborated. The width of each module is 1 m with a depth of 0.4 m. A 3D view on the pumping sections is given in Fig. 3.

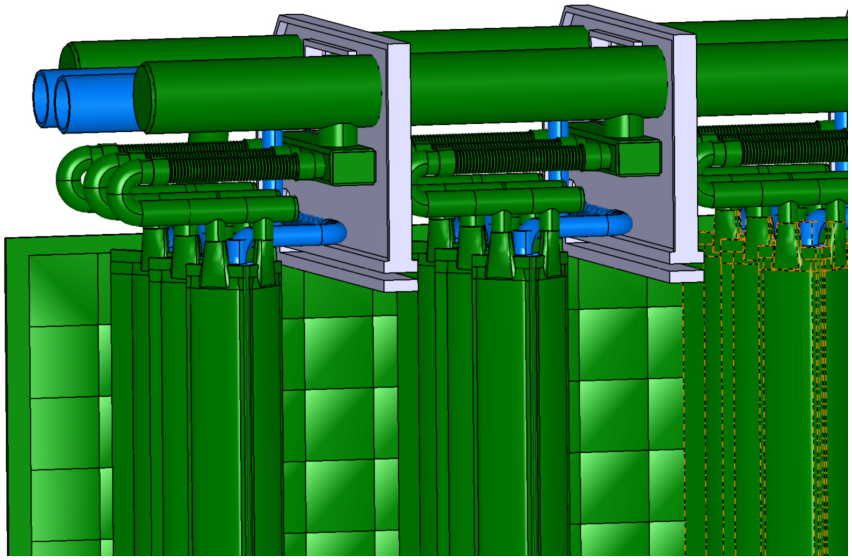

Fig. 3: Manifolds of the radiation shielding (green) and the cryopanels (blue).

The total weight (for both cryopump halves together) of the shield system is 8.6 tons, and the panel system is weighing 1.6 tons. Due to the size, it was necessary to perform extensive transient warm-up and cool-down calculations to check thermal stresses. In many cases, sub-models had to be used as the mesh of the full system was not detailed enough to provide the required resolution (an example is illustrated in Fig. 4).

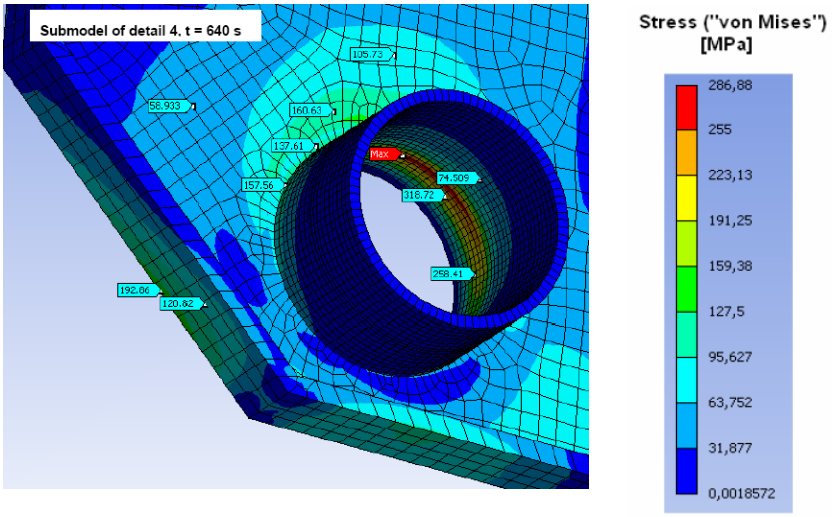

Fig. 4: Stress analysis at the critical transition from the cryogenic pipe to the support frame after 640 s. The maximum values of 320 MPa are acceptable if 316L material is used.

The full CATIA design package including details of support structures and thermal anchors has been delivered to F4E in June 2008. The final report also included manufacturing issues and a procurement plan.

Final status and future work

The scope of this task has been fully achieved and the task is now closed. But there are a series of open issues which remain to be addressed in the future, for example:

- The connection to the feeding cryolines must be designed, once their location is known.
- Installation routines and support design may have to be harmonized and refined.

- Consider the real temperature of the gas coming from the different sources.
- Include the real beamline surface temperature in the heat load calculations, once the cooling procedures of the beamline components are fixed.
- Provide data for pressure drops through hydroformed components.
- Re-iterate pressure drops and cryogenic flow rates with the cryoplant designers.

In summary, the pumping area of the entire system is 36.8 m². It provides an overall pumping speed of 4800 m³/s for protium and 3750 m³/s for deuterium. It must be noted that, due to the strong density profiles inside and the correspondingly very different pumped gas loads, the pumping speed is not uniform across the projected pumping surface, but adapted to the various gas source flows and their location. The critical pressure between accelerator and neutralizer has been calculated as 0.015 Pa. The difference between this value and the maximum acceptable one of 0.02 Pa determines the maximum pumping time in protium operation, because protium accumulation leads to a slight, but noticeable pumping speed decrease (which means pressure increase). This effect limits the maximum pumping time in protium operation to 3000 s. For deuterium operation, the pumping speed is constant and the maximum pumping time is given by oxy-hydrogen explosion hazards. This leads to maximum pumping times in deuterium operation of 7 h.

Staff:

Chr. Day
M. Dremel
St. Hanke
V. Hauer
X. Luo
R. Simon
H. Strobel

Literature:

[1] M. Dremel et al., Cryopump design for the ITER Heating Neutral Beam injector, IAEA Fusion Energy Conference, Oct. 2008, Geneva, Switzerland.

[2] M. Dremel, Chr. Day, St. Hanke, X. Luo, Cryopump design development for the ITER Neutral beam injectors, 25th SOFT, Sept. 2008, Rostock, Germany.

[3] X. Luo, M. Dremel, Chr. Day, ProVac3D and application to the neutral beam injection system of ITER, 26th Int. Symp. Rarefied Gas Dynamics, July 2008, Kyoto, Japan.

EFDA/05-1352 (TW5-THHN-MONRF)
Monitoring the EU/RF Collaborative Tasks on the First ITER NB Injector and the ITER NB Test Facility

Background and objectives

The central work of this task is related to the tools for gas flow and density calculations for the Neutral Beam Test Facility (NBTF) and the ITER Neutral Beam Injector (NBI). In that area, the Kurchatov Institute of the Russian Federation (KIAE) is performing flow calculations using the MC-GF (Monte Carlo - Gas Flow) code, developed in KIAE for ITER NBI and similar devices.

The collaborative task was organised in a structured way between KIAEA and FZK. In the first stage, FZK has defined the input parameters for the KIAE calculations from the cryopump point of view, which acts as the dominant gas sink, having a strong influence on the gas profile along the entire beam line and, thus, on the re-ionisation processes and the efficiency of the machine. In the following stage, KIAEA was asked to adapt the MC-GF model to the present design of the ITER NB and NBTF and to carry out calculations of gas flow and density profiles in the NB line components. And in the final stage, the calculation results had to be cross-checked and assessed by FZK.

In order to have a well defined cross check process, FZK decided to develop its own code named as ProVac3D – **3D** density (pressure) **Pro**files in **Vac**uum systems. The main objective was to provide a versatile tool to investigate the gas flows and densities in a complex vacuum system with distributed gas sources and gas sinks (pumps).

Main ideas and features

Generally speaking, ProVac3D is an extension of the more common Test Particle Monte Carlo simulation (TPMC) approach. However, ProVac3D can simulate not only the transmission probability in free molecular flow regime, but also the gas density distributions based on the same basic hypothesis as used in the MC-GF code — the density in one cell is proportional to the accumulation of flight times of every molecules in this cell and inversely proportional to the cell volume.

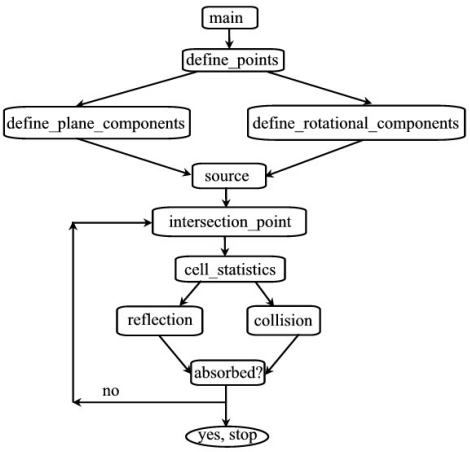

Fig. 1: ProVac3D program flow chart and its modular structure.

Fig. 1 shows the modular structure of ProVac3D, which is written with FORTRAN 90. In module ***main*** one only gives the dimensions and physical parameters of the vacuum system. They are used to define corresponding points in the module ***define_points***. These points are then used to define many different components in modules ***define_plane_components*** and ***define_rotational_components***, such as triangle, parallelogram, circle, ellipse, ring, square with hole, hexagon with hole, octagon with hole, cylinder, elliptical cylinder, wedge, cone, crown, 3-way cross, 4-way cross, 5-way cross, 6-way cross, etc. One can combine different components and build up a complex vacuum system. The test particle is generated in the module ***source***. Its trajectories are tracked down in module ***intersection_point,*** which is followed by module ***reflection***, where diffuse reflection, specular reflection or penetration with a certain probability can be treated. The module ***cell_statistics*** is newly developed, where the density profile is regis-

tered by means of accumulating the flight times of the simulated molecules. The module ***collision*** in Fig. 1 is only shown for information, as it was not needed for benchmarking the MC-GF code which does not consider molecule-molecule interaction.

Other than for MC-GF, which is a special code that contains the NBI specific system geometry features deeply in its kernel, ProVac3D has a general structure and offers maximum versatility for broader application to arbitrarily complex vacuum systems.

Assumptions made for the NBI model

The basis of our simulation model is shown in Fig. 2. The dimensions of each component have been taken from the detailed and actual CATIAv5 drawings of the ITER database and are given in order of length*height*width. The simulation region is from x= -0.9 m to x=10 m. Because the goal is to simulate neutral gas flows, the beam source (BS) chamber and the accelerator is not included in our model, but the BS duct from x= -0.9 m to x=0 m is included. The main gas source is the deuterium (about 18 Pa m3/s) coming from two vertical injection tubes inside the neutraliser and flowing in opposite directions. Each two of four neutraliser channels share one vertical injection tube. They are not placed at the center of the neutraliser, but shifted away from the beam source, at relative position of 0.72 of the full length of the neutraliser. The gas injection is almost homogeneous along the tubes and the deuterium gas flows in two directions as indicated by arrows in Fig. 2. The second gas source (about 3.6 Pa m3/s) is the non-ionized deuterium coming from the BS duct (10%) and peripheral electrostatic screen (90%). The third gas source is the RID where the dumped ions lead to a relatively small gas flux of 0.38 Pa m3/s. It is assumed coming from the vertical central line of RID. The temperature of source gas is at 20 °C, but the normalization is made at T=0 °C. The sophisticated cryopumps are simplified by two vertical cryopanels at a mean temperature of T=90 K with an effective capture factor c=0.34. This value has been demonstrated in normal TPMC calculations for the full detailed design of the cryopump. The transparency of the calorimeter is t=0.1. The thermal accommodation of all components is assumed to be a=0.2, except for the cryopanel with a=0.5.

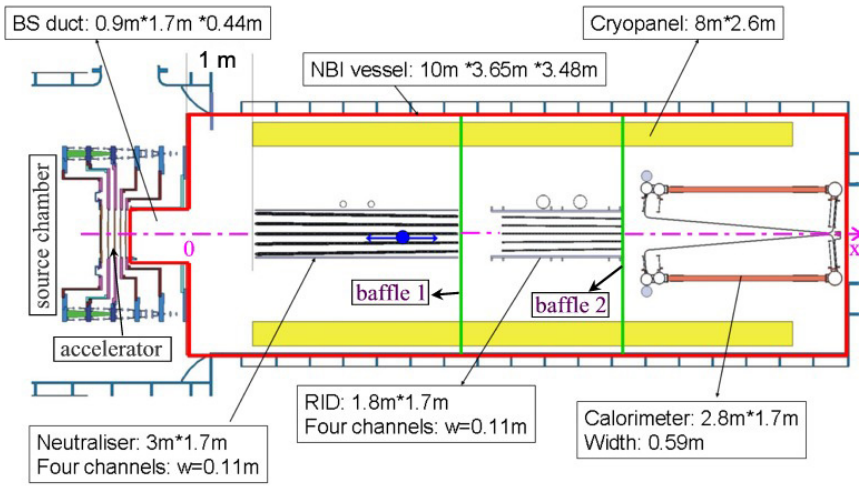

Fig. 2: Sketch of NBI. x denotes the system longitudinal direction and x=0 is the ground grid position of the accelerator.

Main results in free molecular flow regime

Axial density profiles

Here, two design cases of the system (with one or two baffles at different positions) have been concerned. Fig. 3 shows the ProVac3D results, where the two most favorite baffle cases are plotted. The position of the first baffle is at the end of the neutraliser in both cases, but the position of the second baffle is at the end and start of the RID in Case 1 and Case 2, respectively. During the variation of the baffle locations, it was found that MC-GF did significantly underestimate the strong effect of the distance between the two gas baffles on the resulting profile. In Fig. 4 a comparison between the two codes, MC-GF and ProVac3D, is depicted for Case 1. The number of particle density bump between the gas baffles is more pronouncing when these two baffles get closer. This effect is revealed for the first time by ProVac3D.

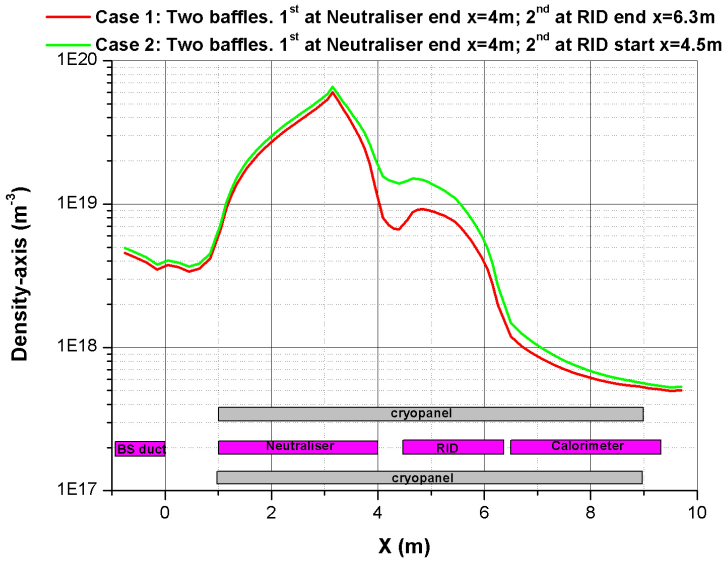

Fig. 3: Total axial number of particle density profile resulting from the integral gas flow $Q = Q_N+Q_{BS}+Q_{RID}$ = (18+3.6+0.38) Pa·m^3/s = 21.98 Pa·m^3/s for two cases of baffle location. The positions of the main components (not in scale) are indicated for better understanding.

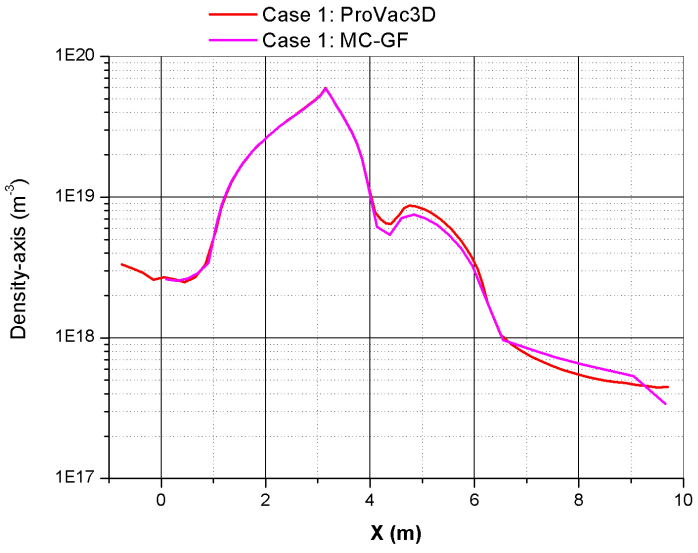

Fig. 4: Comparison of ProVac3D and MC-GF for baffle location case 1. Only one gas source (Q_N = 18 Pa·m^3/s) has been considered.

Density profiles in front of the cryopanels

This region is interesting from general vacuum point of view because the density profile here not only determines the local pumping speeds but also the heat load coming from the molecules via gaseous heat conduction. Actually, for cryogenic pump design it is always an iteration process to optimize the pumping speed with minimum heat load (radiation, gas conduction, solid conduction). Unfortunately, the MC-GF model cannot separate the front cryopanel region. The ability to derive the local densities in front of the cryopanel with ProVac3D is a unique approach to very correctly consider this heat load. The simulated result of the number of particle density profile is shown in Fig. 6. We can also see a density bump between two baffles caused by the limited pumping speed of this region. The width of this bump is corresponding to the distance between two baffles and the peak is higher when the distance is shorter. From pure cryopump design point of view, case 1 is clearly to prefer, because not only the pressure in the region close to the beam source is lower, but also the region bet-ween two baffles is not heavily loaded.

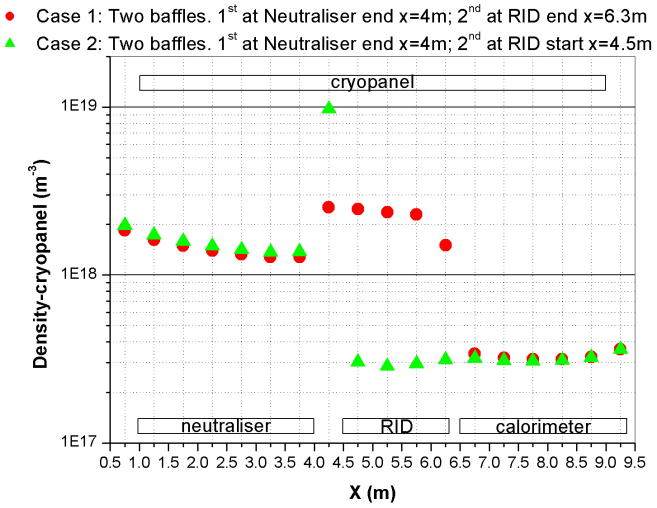

Fig. 6: Number of particle density profile in front of the cryopanel resulting from the integral gas flow Q = Q_N+Q_{BS}+Q_{RID} = (18+3.6+0.38) Pa·m^3/s = 21.98 Pa·m^3/s. The positions of main components (not in scale) are indicated for better understanding.

Hit numbers

Within the Monte Carlo approach, the relative numbers of gas molecules cryogenically adsorbed can be easily calculated by means of a particle balance ratio. For the calculations above, the found value of 0.3 is an excellent calculational confirmation of the cryopump capture coefficient and perfectly illustrates the overall consistency of the ProVac3D calculations.

More results can be found in [1-3].

Outlook and future work

This task has been completed. It has been shown that the MC-GF code developed at KIAE is normally working well, but has some deficiencies and limitations if it comes to systems with stronger density gradients, as typically caused by distributed pumping of multiple gas sources. The MC-GF feature to contain the NBI system geometry at a very deep level in the code is regarded as drawback from a general application point of view. This was the main reason to develop another, much more versatile software, namely ProVac3D. In direct comparison between the two codes, it was found that the new ProVac3D code can predict the full system very properly.

In the next step, it is therefore planned to expand the existing ProVac3D software and to include the collision between gas molecules by considering appropriate interaction between the probe molecule and the gas background. A first feasibility check of such a development is being performed under task TW6-TTFF-VP72 [4].

Staff:

M. Dremel
X. Luo

Literature:

[1] X. Luo, M. Dremel, Chr. Day, ProVac3D and application to the neutral beam injection system of ITER, 26th Int. Symp. Rarefied Gas Dynamics, July 2008, Kyoto, Japan.

[2] M. Dremel et al., Cryopump design for the ITER Heating Neutral Beam injector, IAEA Fusion Energy Conference, Oct. 2008, Geneva, Switzerland.

[3] M. Dremel, Chr. Day, St. Hanke, X. Luo, Cryopump design development for the ITER Neutral beam injectors, 25th SOFT, Sept. 2008, Rostock, Germany.

[4] Chr. Day et al., Implications of increased gas throughputs at ITER on the torus exhaust pumping system, IAEA Fusion Energy Conference, Oct. 2008, Geneva, Switzerland.

EFDA/07-1704-1583 (TW6-THHE-CCGDS5)
European Development of a Gyrotron for ITER: Design and Analysis, and Support to the Industrial Contracts

D 1: Design of an improved RF optical system for the refurbished gyrotron and support to the experiments on the FZK pre-prototype (FZK)

Note: This task ended in March 2008. The work was carried out in support of the prototype experiment at CRPP (Task CCGT1). It is expected that the topic reported here will be included in a new task (CCGDS6), retroactively starting from October / November 2008. The remaining gap in mid 2008 is not covered by EFDA tasks.

Introduction

The development of a 2 MW, CW, 170 GHz coaxial cavity gyrotron for ITER, in cooperation with European research institutions (CRPP, Lausanne; TEKES, Helsinki; NTUA, Athens) and European tube industry (Thales Electron Devices (TED), France), is supported by experimental work using an additional short-pulse gyrotron at FZK. This so-called pre-prototype was initially designed for 1.5 MW output power only, due to magnetic field limitations. It serves mainly as a flexible tool for investigations on issues possibly appearing in the prototype experiments at CRPP.

Main topics of these investigations at FZK during 2008 were:

- Suppression of unwanted low frequency parasitic oscillations
- Investigations on parasitic high frequency oscillations in the beam tunnel
- High power pulses and performance demonstration at nominal operating point
- Investigations on mode converter improvements

The development of a new launcher synthesis code, creating launchers with arbitrary wall deformations, is also aiming at improving the mode converter and particularly the launcher design.

Status at the beginning of 2008

In the last report, detailed investigations on low frequency (LF) oscillations around 260 MHz in the pre-prototype were shown, with the intermediate solution of modifying the electron gun or using a different electron gun from the former 165 GHz gyrotron. While the latter was a very successful, modifications to the new electron gun for suppressing the LF oscillations are still to be investigated.

In the experiments, 1.3 MW rf power were reached, limited by the appearance of an additional parasitic high frequency oscillation around 160 GHz. The gyrotron was operated at a reduced magnetic field, compared to the nominal field of the industrial prototype at CRPP Lausanne, because of limitations of the FZK magnet.

The first mode converter design, optimized for a well concentrated rf output beam at the output window, but not for maximum Gaussian content, was considered insufficient, and investigations on methods to improve this design were started.

Suppression of unwanted low frequency parasitic oscillations

In the first experiments in 2008, the pre-prototype was equipped with the former “165 GHz” electron gun. This actually removed any problem with LF parasitic oscillations. However,

since the emitter of this electron gun was reaching the end of its lifetime, additional experiments with the original new electron gun were undertaken. Modification on the inner rod of the gyrotron increased the starting current of the LF parasitic oscillation, but did not remove it completely. The LF instability can be removed by external absorbers in the electron gun region, so they don't deteriorate the experiment. Further experiments are planned.

Investigations on parasitic high frequency oscillations in the beam tunnel

At high power levels, output power and efficiency in the experiment were lower than simulated, while at the same time an additional frequency of 160 GHz appeared (Fig. 1). It is assumed that this effect is caused by a parasitic oscillation in the beam tunnel, similar to what appeared in the 140 GHz W7-X gyrotron.

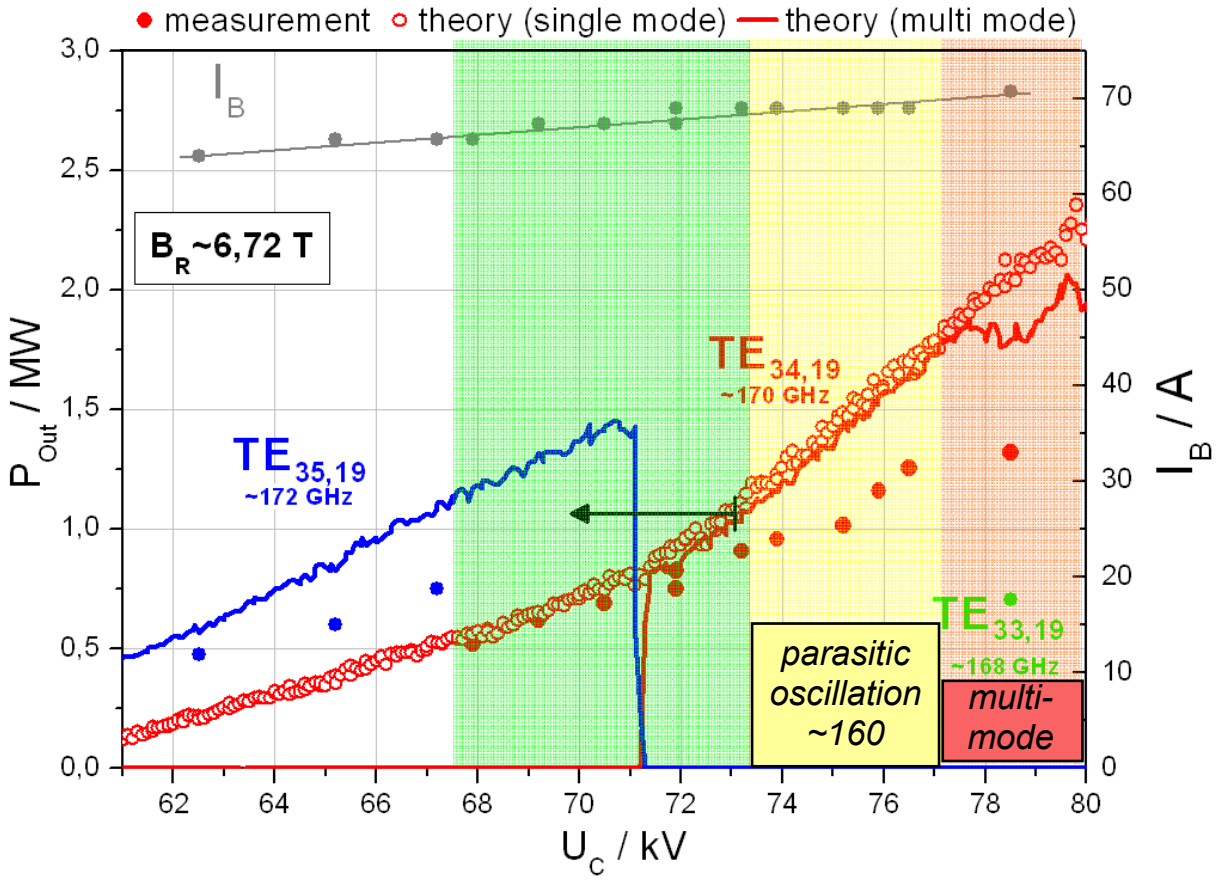

Fig. 1: Experimental results – output power in different modes - demonstrating the deviation of the experimental output power (filled circles) from the simulation (open circles and lines). The upper limit of the mode's stability region is correctly reproduced in the simulation.

In a first attempt, the beam tunnel was replaced by a full stainless steel conical tunnel with a smooth inner surface, in order to test the influence of the high taper angle of the wall on the oscillations. This could not prevent the oscillations at all, which may be an indication that it is necessary to break the cylindrical symmetry in the beam tunnel. In the running experiment, the original beam tunnel, consisting of stacked copper rings and damping ceramics, was modified by milling slots into the cylindrical copper rings (Fig. 2). In the mean time it became possible to predict the parasitic oscillations approximately. Since, in these simulations, the parasitics appeared as a gyro-backward wave in a symmetrical $TE_{0,n}$ mode, supported by the cylindrical copper rings, it is expected that an irregular distortion in the cylindrical symmetry of the rings will also remove these oscillations.

The experiment is currently running (see next section). Additional experiments are planned using a full ceramic SiC beam tunnel without metallic components (Fig. 2).

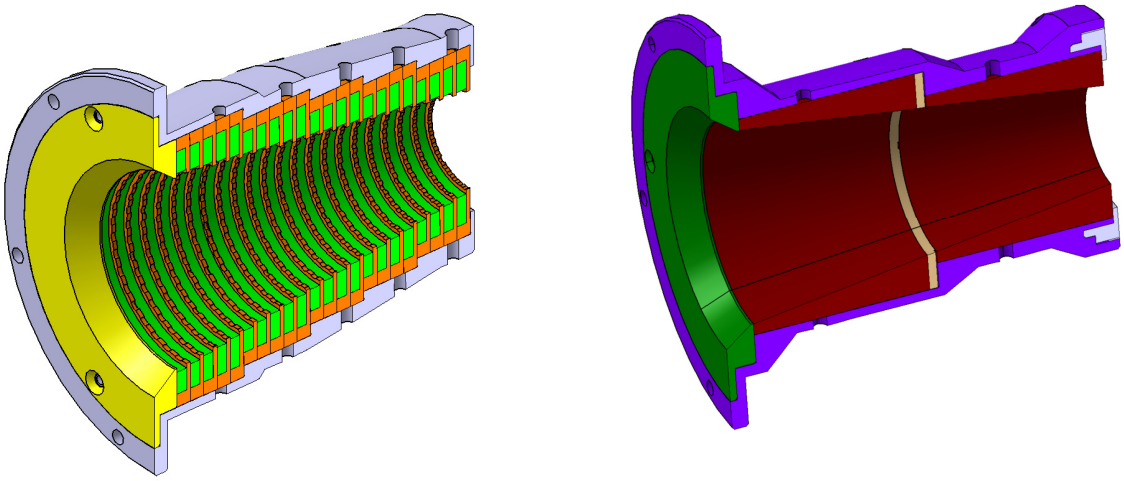

Fig. 2: Left: Original beam tunnel, consisting of stacked copper (orange) and ceramic (green) rings. The copper rings are modified by irregular slots of 0.5 mm depth. Right: Full ceramic SiC (brown) beam tunnel. An experiment with a similarly shaped tunnel made from stainless steel failed.

High power pulses and performance demonstration at nominal operating point

The pre-prototype was optimized for operation at a magnetic field of B = 6.7 T, because this is the highest field strength that can be reached by the FZK magnet. For this reason, the expected output power was only 1.5 MW at 30 % efficiency (without DPC), in contrast to the prototype at CRPP, which operates at 6.87 T and should provide 2 MW. The highest power reached at 6.7 T was 1.36 MW at 26 % efficiency, in 2 ms pulses. This is a quite respectable result, in spite of the existing problems with high frequency parasitic oscillations.

However, the problems with the prototype gyrotron are demanding short-pulse experiments that are better comparable to the prototype experiments at CRPP. Therefore an activity was started to equip the FZK superconducting (SC) magnet with an additional normal conducting (NC) coil inside its warm bore hole in order to increase the maximum magnetic field. First, a separate normally conducting coil was produced and tested successfully: The magnetic field at the cavity region now reaches 6.87 T (in pulses up to 1 s), without quenching of the SC magnet. In parallel, the preparation of an entire test bed for operating the industrial prototype gyrotron at FZK was started, as a backup solution if the SC magnet at CRPP is rejected.

Since this test proved that increasing the magnetic field is possible, a second NC coil was produced by winding it directly on the pre-prototype gyrotron. Because of lack of space – the pre-prototype has a larger diameter than the prototype – this was the only possibility to employ such a NC coil in the short-pulse experiment. At the same time, the electron gun's anode of the pre-prototype had to be modified to be usable at the higher magnetic field. This "nominal field experiment" is already installed and currently running. It now aims at demonstrating 2 MW short-pulse operation, with an efficiency around 30 % (without DPC) and without parasitic oscillations. Thereby, both the beam tunnel and the electron gun design would be verified for usage in the long-pulse experiment of the industrial prototype gyrotron.

Investigations on mode converter improvements

The existing quasi-optical mode converter, which was designed at FZK and installed in both the pre-prototype and the prototype gyrotron, is known to be insufficient, because the rf output beam has only 77 % Gaussian content, while the stray radiation level inside the tube is at the inacceptably high level of 8 %. Several ways to improve this mode converter were investigated in parallel because of the urgent need for a solution:

- The quasi-optical system was thoroughly tested with FZK's low power vector network analyser. The result is that a possible cause for the bad performance could be a shift of the second mirror of around 0.3 mm, or a sub-optimal design of the third, phase correcting mirror. This mirror was re-designed, however, even the optimum result would be 88 % Gaussian content, far from the desired 95 %.
- An independent quasi-optical system design was ordered at IAP, Russia. The system designed by IAP has > 95 % Gaussian content in the rf beam simulated and should be delivered in December, to be tested both at low and high power in 2009.
- A new launcher synthesis code TWL_DO, suited to solve the scalar diffraction integral equation, was developed for launchers using arbitrary wall deformations. This overcomes the problems of the established launcher design methods using periodic wall deformations in a cross section – it turned out that the latter design method is not suitable for typical operating modes of coaxial gyrotrons, which typically are chosen with a relative caustic radius of 1/3, in contrast to the caustic radius in conventional gyrotrons of 1/2. The coaxial modes can not be described by an integer number of reflections at the waveguide walls per cycle any more, making periodic wall deformations ineffective for launcher design. With the new code, a launcher and corresponding complete quasi-optical system was designed providing 97 % Gaussian content in simulation (Figs. 3 and 4).

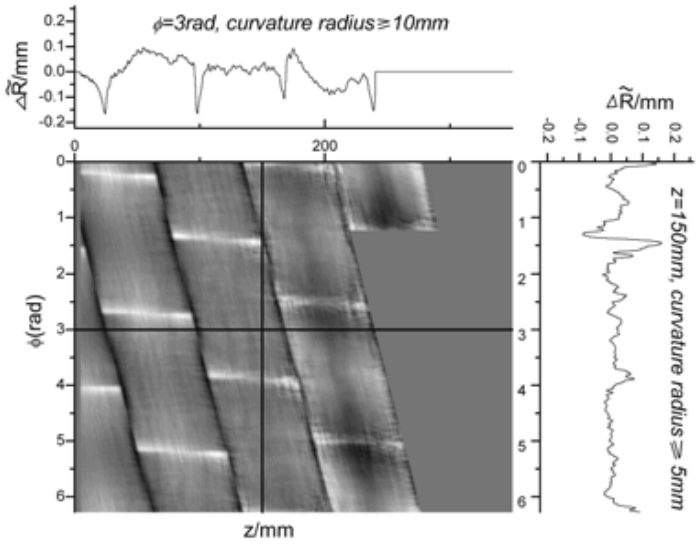

Fig. 3: Unrolled wall profile of the new launcher with arbitrary wall deformations.

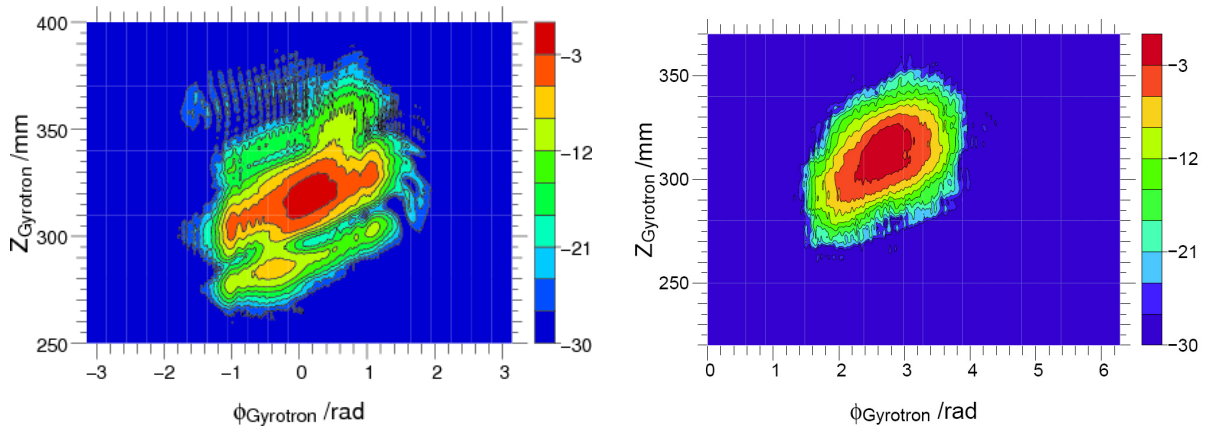

Fig. 4: Left: Output rf field of the original launcher (with helical 1st and 3rd order periodic wall deformations), Right: Output rf field of the new launcher, indicating 97 % Gaussian content already after the launcher.

Even though all three attempts can be considered successful up to now, none has been tested yet experimentally. The new launcher with arbitrary wall deformation is being built and will be tested in early 2009 both in cold and high power tests. The IAP system will also be tested afterwards.

Staff:

A. Arnold
G. Dammertz
J. Flamm (Uni K'he)
G. Gantenbein
S. Illy
J. Jin
S. Kern
R. Lang
W. Leonhardt
Li, Guolin
D. Mellein
B. Piosczyk
O. Prinz (Uni K'he)
T. Rzesnicki
A. Samartsev
M. Schmid
W. Spiess
J. Szczesny
M. Thumm

Literature:

[1] Albajar, F., Alberti, S., Bonicelli, T., Dumbrajs, O., Fasel, D., Gantenbein, G., Goodman, T., Henderson, M., Hogge, J.-P., Cirant, C., Kern, S., Illy, S., Piosczyk, P., Porte, L., Rzesnicki, T., Saibene, G., Santinelli, M., Thumm, M., Tran, M.Q., Review of the European Programme for the Development of the Gyrotron for ITER, 15th Joint Workshop on Electron Cyclotron Emission and Electron Cyclotron Resonance Heating, Yosemite National Park, Calif., March 10-13, 2008

[2] Illy, S. Particle-in-cell simulation tools for design and optimization of high power CW gyrotron oscillators, 7th School of Fusion Physics and Technology, Volos, GR, April 14-19, 2008

[3] Jin, J., Thumm, M., Piosczyk, B., Rzesnicki, T., Improved launcher/mode converter for coaxial cavity ITER gyrotron, 35th IEEE Internat.Conf.on Plasma Science (ICOPS), Karlsruhe, June 15-19, 2008

[4] Jin, J., Thumm, M., Piosczyk, B., Flamm, J., Prinz, O., Rzesnicki, T., Improved quasi-optical launcher for coaxial cavity ITER gyrotron, Internat.Conf.on Infrared, Millimeter and Terahertz Waves (IRMMW-THz), Pasadena, Calif., September 15-19, 2008

[5] Kern, S., Rzesnicki, T., Dumbrajs, O., Flamm, J., Gantenbein, G., Illy, S., Jin, J., Piosczyk, B., Prinz, O., Thumm, M., Recent improvements on the 170 GHz,1,5 MW coaxial cavity gyrotron at FZK, 35th IEEE Internat.Conf.on Plasma Science (ICOPS), Karlsruhe, June 15-19, 2008

[6] Kern, S., Rzesnicki, T., Gantenbein, G., Illy, S., Jin, J., Piosczyk, B., Thumm, M., Dumbrajs, O., Flamm, J., Prinz, O., Status of experiments on the EU 2MW coaxial cavity ITER gyrotron pre-prototype at FZK, 15th Joint Workshop on Electron Cyclotron Emission and Electron Cyclotron Resonance Heating, Yosemite National Park, Calif., March 10-13, 2008

[7] Piosczyk, B., Development of multi-megawatt gyrotrons at FZK. Present status and goals, 7th School of Fusion Physics and Technology, Volos, GR, April 14-19, 2008

[8] Piosczyk, B., High power gyrotrons for EC H&CD applications in fusion plasmas - basic design, status and goals, 7th School of Fusion Physics and Technology, Volos, GR, April 14-19, 2008

[9] Piosczyk, B., Alberti, S., Albajar, F., Avramidis, K., Benin, P., Bonicelli, T., Cirant, S., Dumbrajs, O., Fasel, D., Flamm, J., Gantenbein, G., Goodman, T., Hogge, J.P., Illy, S., Jawla, S., Jin, J., Kern, S., Lievin, C., Pagonakis, I., Prinz, O., Rzesnicki, T., Thumm, M., Tran, M.Q., Status of the European 2 MW, 170 GHz coaxial

cavity gyrotron for ITER, 7th Internat.Workshop Strong Microwaves: Sources and Applications, Nizhny Novgorod, Russia, July 27 - August 2, 2008

[10] Rzesnicki, T., Piosczyk, B., Flamm, J., Jin, J., Kern, S., Prinz, O., Thumm, M., *170 GHz, 2 MW coaxial cavity gyrotron - experimental investigations on the pre- prototype tube*, 9th IEEE Internat.Vacuum Electronics Conf. (IVEC 2008), Monterey, Calif., April 22-24, 2008

[11] Rzesnicki, T., Kern, S., Piosczyk, B., Flamm, J., Jin, J., Prinz, O., Thumm, M., *A prototype of a 2 MW, 170 GHz coaxial cavity gyrotron for ITER. A close perspective*, 1st ITG Internat.Vacuum Electronics Workshop, Bad Honnef, November 10-11, 2008

[12] Rzesnicki, T., Piosczyk, B., Flamm, J., Jin, J., Kern, S., Prinz, O., Thumm, M., *Experimental investigation on the pre-prototype of the 170 GHz, 2 MW coaxial cavity gyrotron for ITER*, 22nd IAEA Fusion Energy Conf., Geneve, CH, October 13-18, 2008

[13] Rzesnicki, T., Piosczyk, B., Flamm, J., Jin, J., Kern, S., Prinz, O., Thumm, M., Recent experimental results on the 170 GHz, *2 MW coaxial cavity pre-prototype gyrotron for ITER*, Internat.Conf.on Infrared, Millimeter and Terahertz Waves (IRMMW-THz), Pasadena, Calif., September 15-19, 2008

[14] Thumm, M., *Megawatt microwave power*, Seminar on Recent Advances in High Power Microwave Research and Applications, Melbourne, AUS, January 29-31, 2008

[15] Thumm, M., Alberti, S., Albajar, F., Avramidis, K., Benin, P., Bonicelli, T., Cirant, S., Dumbrajs, O., Fasel, D., Flamm, J., Gantenbein, G., Goodman, T., Hogge, J.P., Illy, S., Jawla, S., Jin, J., Kern, S., Lievin, C., Pagonakis, I., Piosczyk, B., Prinz, O., Rzesnicki, T., Tran, M.Q., *Progess of the European 2 MW, 170 GHz coaxial cavity gyrotron for ITER*, Workshop on RF-Heating Technology of Fusion Plasmas 2008, San Diego, Calif., September 10-12, 2008

EFDA/07-1704-1583 (TW6-THHE-CCGDS5)
European Development of a Gyrotron for ITER: Design and Analysis, and Support to the Industrial Contracts

D 2a: Preliminary design of a 170 GHz, 1 MW, CW cylindrical cavity gyrotron as fall-back solution

Note: This task ended in March 2008, and the investigations were stopped. It is expected that this work will be continued within the frame of the new F4E grant CCGDS6.

Introduction

In cooperation with European research institutions (CRPP, Lausanne; TEKES; Helsinki, NTUA; Athens) and European tube industry (Thales Electron Devices (TED), France), the development of a 2 MW, CW, 170 GHz coaxial cavity gyrotron for ITER is going on. Tests of the coaxial prototype tubes are performed under Task TW6-THHE-CCGT1. In parallel, a 1 MW, 170 GHz conventional gyrotron with a conventional cavity is under design as fallback solution within the same cooperation. This report describes the related results achieved until March 2008 and a few additional results on a proposed experiment.

Definition of the main specifications of the 170 GHz, 1 MW, cylindrical cavity gyrotron

Starting point and technical constraints

The starting point was set by the technical constraints as defined by TED and applied to the W7-X gyrotron. Main goals of the design were:

- 1 MW calculated output power at the rf window at peak wall losses of about 2 kW/cm^2 in the cavity (realistic wall losses, twice the wall losses calculated for ideal copper at room temperature) and at reasonable overall efficiency (> 30 % without depressed collector). This calculation has to include losses in the cavity, losses caused by after cavity interaction and between cavity and window. The total losses are estimated as 15% of the generated power.
- 1.3 MW stably generated calculated power in single-mode operation, as a safety margin. At this power level higher wall losses are allowed.
- Current density at the emitter below 3 A/cm^2. Higher current density and lower cathode voltage, respectively, may increase the interaction efficiency slightly, but it was decided not to deviate too much from the W7-X gyrotron parameters.
- Relative caustic radius m/$\chi_{m,p}$ close to 0.5 to ensure feasibility of the quasi-optical mode converter in a way similar to the W7-X system.

Selection of the operating mode and optimization of the cavity, taking into account the mode competition, wall loading, suitability of the mode for quasi-optical conversion etc.

First considerations on modes led to a pre-selection of 5 possible modes that can fulfill the given constraints: $TE_{32,09}$, $TE_{33,09}$, $TE_{33,10}$, $TE_{34,09}$ and $TE_{34,10}$. Several cavity designs for $TE_{32,09}$, $TE_{33,09}$ and $TE_{34,10}$ were checked. While for the modes $TE_{32,09}$ and $TE_{33,09}$ designs were found that almost completely fulfill the conditions given above, the $TE_{34,10}$ mode appears unstable at high powers in the calculations done by FZK. It was decided to use the $TE_{32,09}$ mode as the first candidate, with $TE_{33,09}$ as backup solution (Table 1 and Fig. 1). All three modes have been successfully checked for their suitability for quasi-optical mode conversion.

Table 1: Nominal operating parameters for the $TE_{32,09}$ mode in the FZK cavity proposal.

Magnetic field B_r (T)	6.76
Beam voltage U_b (kV)	79.0
Beam current I_b (A)	40.0
Beam radius r_b (mm)	9.5
Electron velocity ratio α	1.3
Output power at rf window (MW)	1.0
Overall efficiency without depressed collector (%)	31.6
Peak wall losses (kW/cm^2)	2.2
Operating frequency (GHz)	170.04
Selfconsistent quality factor Q	1514

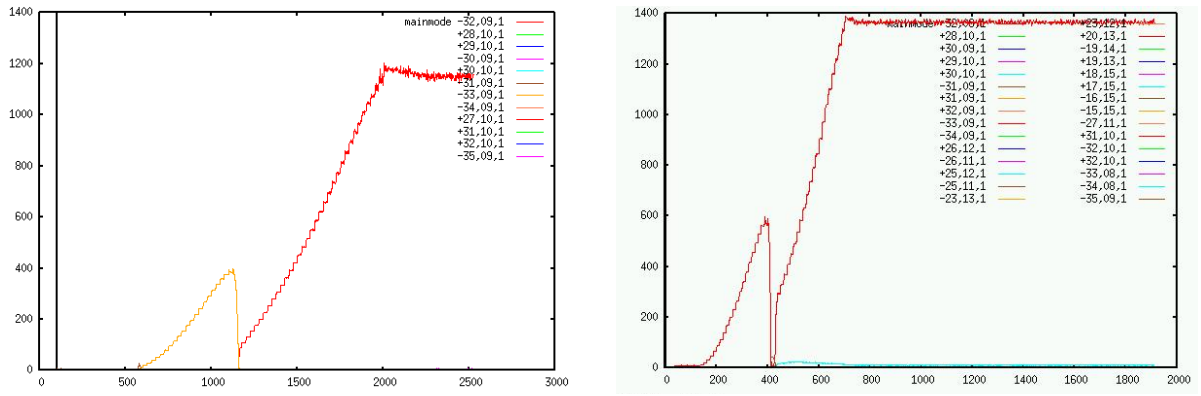

Fig. 1: Startup calculation for the TE32,09 mode yielding >1 MW at 40 A beam current (left) and >1.3 MW at 45 A beam current (right). The acceleration voltage rises to 79 kV during the first 2000 ns, other parameters as in Table 1.

The final verification of the cavity design for the $TE_{32,09}$ mode still has to be done, by calculating a broader range of stability regions. This includes designing of the nonlinear uptaper and minimization of unwanted mode conversion.

Support for defining the specifications of the magnetic field

The magnetic field strength in the cavity should be around 6.76 T. It is expected that field shapes as generated by the ASG magnet at CRPP Lausanne can be used, but other configurations are still possible.

As the next step, the final requirements for the field shape have to be fixed in the frame of the gun and collector design. If possible, fields as generated by the ASG magnet are to be preferred.

Preliminary design of the quasi-optical RF output system (launcher and mirrors)

Several modes between $TE_{32,09}$ and $TE_{34,10}$ have been investigated. For all of them, quasi-optical mode converters would be feasible, but the preferred mode $TE_{32,09}$ seems to have superior properties in terms of launcher length and Gaussian mode content of the output beam, which confirms this choice.

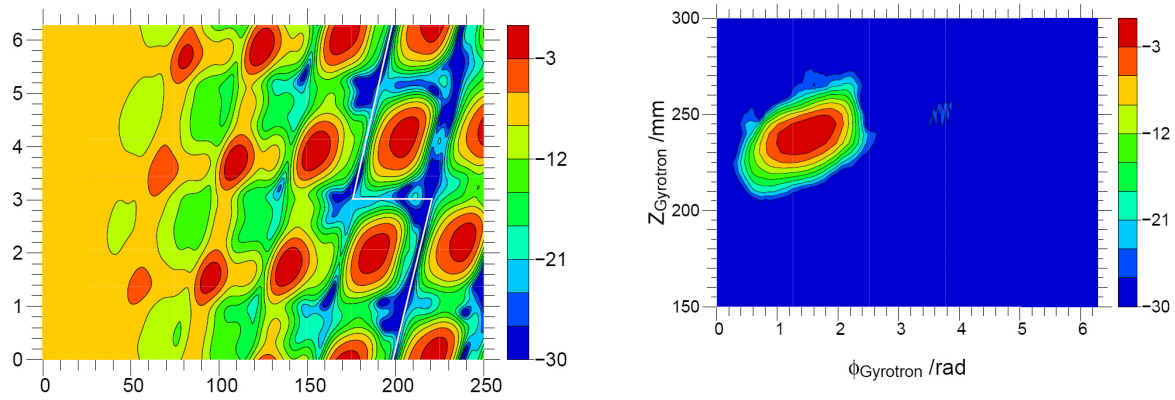

Fig. 2: Wall currents on the unrolled launcher wall for TE32,09 mode (left) and radiated field on a cylinder with 100mm radius, indicating high Gaussian content (right).

The design of an optimized launcher and mirror system for the mode chosen finally is still to be done. The detailed design also has to consider the shape of the electron beam after leaving the cavity and the geometry of the superconducting magnet; i.e.,,the final work must be done in interaction with the collector and magnet design.

Support to the preliminary design of the electron gun

First calculations done by CRPP under D2.b have been verified.

In the next step,, the electron gun design work at CRPP will be supported. This includes on the one hand the verification of the gun design and on the other hand simulations of startup and beam neutralisation parameters.

Preliminary design of the collector

A new collector design activity has not been started yet. It is expected that the collector for the 170 GHz gyrotron can be practically identical to the collector of the 140 GHz W7-X gyrotron, especially including the lower stainless steel part. This allows, in particular, radial electron beam sweeping, which should be employed like for the 140 GHz tube in order to make use of the improved temperature distribution at higher sweeping frequencies gained by this technique.

The usability of the 140 GHz collector design must be verified, under consideration of preferred magnetic field shapes. Modifications of the design for higher safety margin or other advantages have to be investigated.

Proposed additional experiment: 174 GHz operation of the W7-X gyrotron

As a possible alternative solution, theoretical studies on high frequency operation of the existing 140 GHz, 1 MW CW W7-X gyrotron were done. The build-in rf window of this gyrotron has its next reflexion factor minimum at 175 GHz, which opens a chance for efficient operation of this gyrotron in that frequency region. The $TE_{-34,10}$ mode was determined to be the most suitable operating mode at 173.9 GHz. Note that this mode was excluded from the study above because it did not prove stable 1.3 MW operation. However, since the proposed experiment would be done with an existing gyrotron, it is acceptable to release this safety margin, which was introduced to increase the design safety for a newly built gyrotron.

After stable mode operation at 1 MW output power was established theoretically, with some modified parameters of the electron gun, the existing quasi-optical mode converter was

checked at 173.9 GHz. Even though this device surely is not optimum for producing a perfect Gaussian beam for this mode, it will work well enough to make the experiment possible.

To perform the experiment, the new magnet ordered at FZK is required. Delivery is expected in Spring 2009, so that a 1 MW 173.9 GHz experiment as quick demonstrator for an ITER-like 1 MW CW gyrotron would probably be feasible. At the same time, this would demonstrate the first powerful two-frequency gyrotron, as requested by recent publications about the ECRH on ITER.

Staff:

E. Borie (University of Karlsruhe)
G. Gantenbein
S. Illy
S. Kern
B. Piosczyk
O. Prinz (University of Karlsruhe)
M. Thumm

Literature:

[1] Albajar, F., Alberti, S., Bonicelli, T., Dumbrajs, O., Fasel, D., Gantenbein, G., Goodman, T., Henderson, M., Hogge, J.-P., Cirant, C., Kern, S., Illy, S., Piosczyk, P., Porte, L., Rzesnicki, T., Saibene, G., Santinelli, M., Thumm, M., Tran, M.Q., *Review of the European Programme for the Development of the Gyrotron for ITER*, 15th Joint Workshop on Electron Cyclotron Emission and Electron Cyclotron Resonance Heating, Yosemite National Park, Calif., March 10-13, 2008

[2] Avramides, K.A., Vomvoridis, J.L., Kern, S., Pagonakis, I.G., *Electron-beam modeling in gyrotron interaction simulations*, 35th IEEE Internat.Conf.on Plasma Science (ICOPS), Karlsruhe, June 15-19, 2008

[3] Avramides, K.A., Dumbrajs, O., Kern, S., Pagonakis, I.Gr., Vomvoridis, J.L., *Mode Selection for a 170 GHz, 1 MW Gyrotron*, 7th School of Fusion Physics and Technology, Volos, GR, April 14-19, 2008

[4] Avramides, K.A., Dumbrajs, O., Kern, S., Pagonakis, I.Gr., Vomvoridis, J.L., *Mode Selection for a 170 GHz, 1 MW Gyrotron*, 35th European Physical Society (EPS) Conference on Plasma Physics 9-13 June 2008, Hersonissos, Crete, Greece

[5] Kern, S., Avramides, K.A., Beringer, M.H., Dumbrajs, O., Liu, Y.H., *Gyrotron mode competition calculations: investigations on the choice of numerical parameters*, Internat.Conf.on Infrared, Millimeter and Terahertz Waves (IRMMW-THz), Pasadena, Calif., September 15-19, 2008

[6] Kern, S., Borie, E., Illy, S., Prinz, O., Thumm, M., *Theoretical study of 174 GHz operation of the W7-X 1 MW, 140 GHz gyrotron*, Internat.Conf.on Infrared, Millimeter and Terahertz Waves (IRMMW-THz), Pasadena, Calif., September 15-19, 2008

[7] Pagonakis, I.G., Hogge, J.P., Alberti, S., Avramides, K.A., Piosczyk, B., *Preliminary numerical study of the beam neutralization effect in the EU 170 GHz, 2 MW coaxial gyrotron*, 35th IEEE Internat.Conf.on Plasma Science (ICOPS), Karlsruhe, June 15-19, 2008

[8] Piosczyk, *B., Development of multi-megawatt gyrotrons at FZK. Present status and goals*, 7th School of Fusion Physics and Technology, Volos, GR, April 14-19, 2008

[9] Piosczyk, B., High power gyrotrons for EC H&CD applications in fusion plasmas - basic design, status and goals, 7th School of Fusion Physics and Technology, Volos, GR, April 14-19, 2008

[10] Thumm, M., *Megawatt microwave power*, Seminar on Recent Advances in High Power Microwave Research and Applications, Melbourne, AUS, January 29-31, 2008

Physics

ECR Heating and Current Drive – Step-Tunable Gyrotron Development

Introduction

In recent years electron cyclotron resonance heating and current drive (ECRH and ECCD) has been established as a successful instrument in magnetically confined fusion plasmas. : With output power in the MW range, 100 – 200 GHz output frequency, and pulse lengths from several seconds up to continuous wave, gyrotrons are the unique devices which meet the extraordinary requirements of this application. Due to its excellent coupling to the plasma and the very good localisation of the absorbed RF power, ECRH is applied in present day machines and is also foreseen in large forthcoming fusion projects: It will be the main heating system for the stellarator W7-X which is currently under construction, and it will play a major role in the ITER tokamak. In particular, advanced tokamaks are operated in a plasma regime where MHD instabilities which may limit the perfomance are present. To a large extent, plasma stability in a tokamak is influenced by the distribution of the internal plasma currents, which can be manipulated by the injection of RF waves. The location of the RF wave absorption is dependent on the resonance condition $\omega - k_z v_z = \omega_c$ (ω: angular frequency of the RF wave, k_z: z-component of the wave number, v_z: electron velocity along z-axis). Thus, by changing the wave frequency ω, the absorption can be moved to any radial position where the local cyclotron frequency of the electrons ω_c holds for the expression above.

Industrial gyrotrons in the relevant frequency range with an output power of about 1 MW are usually designed for a fixed frequency. Frequency tunable gyrotrons, however, are not a standard product since these broadband tubes require additional optimization of major gyrotron components like the electron beam forming optics, cavity, quasi-optical mode converter and output window.

For experiments on plasma stabilisation at ASDEX Upgrade (IPP Garching) with advanced ECRH and ECCD, multi-frequency tunable (105 – 143 GHz) 1-MW long-pulse gyrotrons are highly needed.

Quasi-optical mode converter

The quasi-optical mode converter transfers the cavity mode into a Gaussian beam which fits through the window aperture. It consists of a dimpled-wall waveguide antenna, the so-called launcher, and a set of three beam-forming mirrors. For the multi-mode gyrotron the mode converter has to be optimized to convert all the nine modes between $TE_{17,6}$ and $TE_{23,8}$ with different properties into a Gaussian beam which does not change its properties from mode to mode. The optimization to achieve these properties can be split in two tasks. First, the launcher's inner waveguide wall is optimized to a Gaussian output pattern and a minimum of stray radiation. Second, the mirrors are designed for maximum power transmission through the window aperture by optimizing the diameter and position of the waist of the Gaussian beam for all modes.

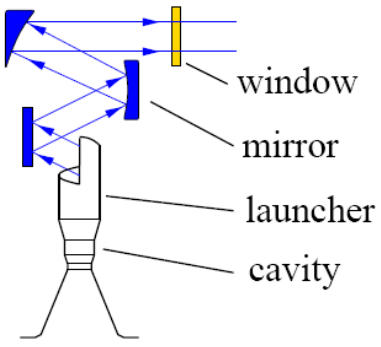

Fig. 1: Basic elements and principle of quasi-optical system.

In the past year the design of a second generation mode converter was completed and a prototype version was manufactured and characterised in a low-power test set-up. The results are presented below.

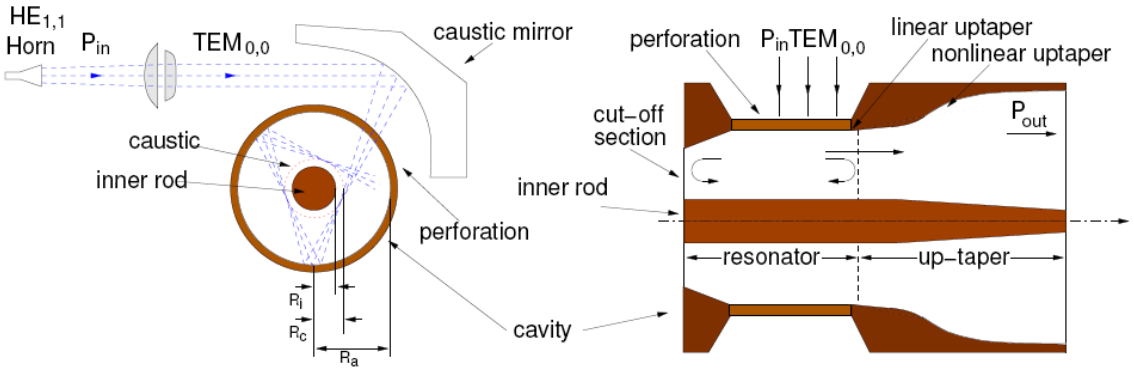

Fig. 2: Mode generator for broadband excitation of different cavity modes.

A mode generator has been optimized to produce the nine modes in the frequency range 105 – 143 GHz with a minimum content of wrong modes. This device uses a free-space fundamental Gaussian beam which is transmitted through the translucent wall of a coaxial cavity with high quality factor, and is focussed to the caustic radius of the mode to be excited. A coaxial inner rod supports the selection of the desired mode and reduces the quality factor of competing modes. The inner diameter is increased with a nonlinear uptaper to avoid mode conversion; the launcher is directly mounted to the uptaper. The key components of the device are given in Figure 2.

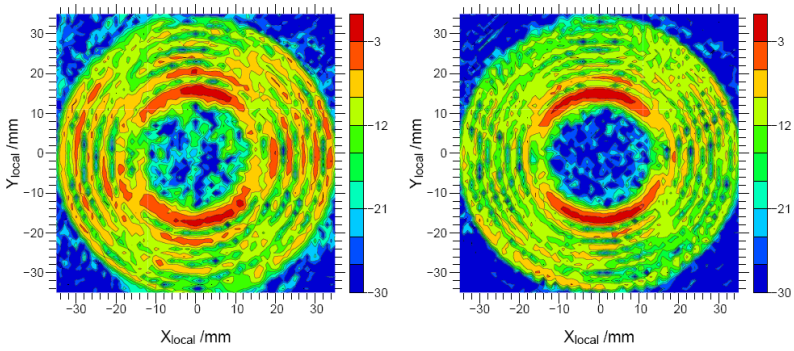

Fig. 3: Output pattern of the mode generator for the $TE_{17,6}$ mode at 104.829 GHz (left) and the $TE_{22,8}$ mode at 139.929 GHz (right).

The output pattern of the mode generator has been measured for nine modes from $TE_{17,6}$ at 104.829 GHz up to $TE_{22,8}$ at 139.929 GHz, using a pick-up antenna fed by a vector network analyzer and an x-y scanner moving the antenna within the relevant measurement area. As an example, Fig. 3 shows the measured output pattern (power) of the $TE_{17,6}$ mode and $TE_{22,8}$ mode. The analysis of this measurement yields a counter rotating mode content of 2.5 % and 1.5 %, respectively.

Extensive experiments have been performed to characterize the output pattern of the launcher and the optical system at different positions for all modes under consideration, to analyze the fundamental Gaussian mode content and to compare with numerical simulations.

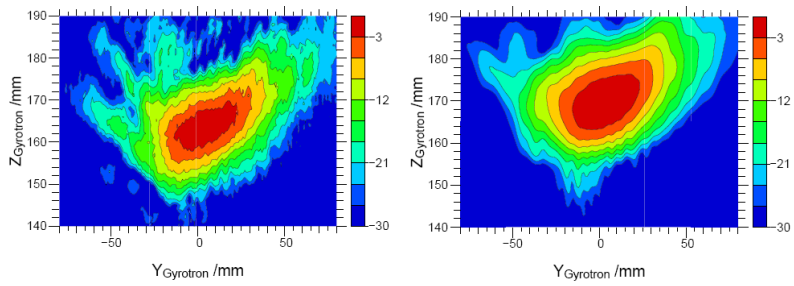

Fig. 4: Radiation pattern of the $TE_{22,8}$ mode at the launcher: measurement (left) and simulation (right).

Figure 4 shows a cut through the beam after leaving the launcher and before being reflected at the first focusing mirror for the $TE_{22,8}$ mode. From this plot a good agreement of the experiment and the simulation can be seen.

The output beam pattern in the window plane is given in Figure 5. Here, the experi-

mental data and the numerical simulation for the modes $TE_{17,6}$ and $TE_{22,8}$ are compared. For both modes, there is very good agreement between experiment and simulation, which is also documented in Table 1 where the Gaussian content calculated from the measurements is given and compared to numerical simulations.

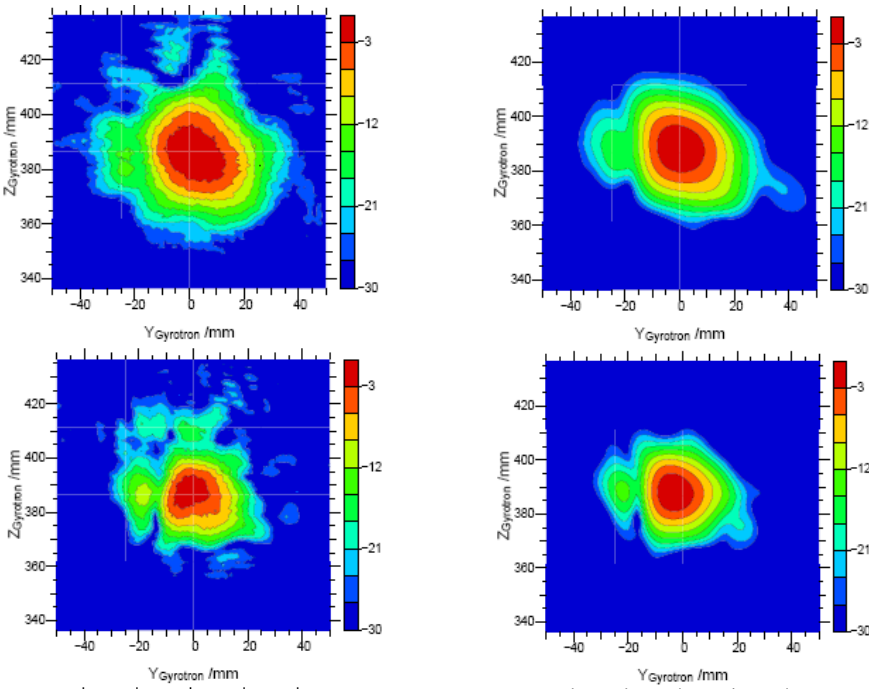

Fig. 5: Radiation pattern at the window plane: measurement (left) and simulation (right) for the $TE_{17,6}$ mode (top) and the $TE_{22,8}$ mode (bottom).

A high power version of this system has been ordered and will be installed and tested in the gyrotron in the next future.

Further optimization of the quasi-optical system, yielding a Gauss content of more than 93 % for all modes, has been started.

Table 1: Gaussian content of different modes.

Frequency [GHz]	Mode	Gaussian Content (Measurement)	Gaussian Content (Simulation)
108.398	$TE_{18,6}$	0.896	0.929
124.185	$TE_{20,7}$	0.894	0.934
127.680	$TE_{21,7}$	0.877	0.917
136.305	$TE_{21,8}$	0.894	0.930
139.927	$TE_{22,8}$	0.875	0.933
143.342	$TE_{23,8}$	0.852	0.915

CVD-diamond Brewster window

Efficient gyrotron operation in a large number of operating modes at different frequencies is only possible if a broadband synthetic diamond Brewster window fabricated by chemical vapor deposition (CVD) is used. Due to the large Brewster angle of 67.2° deg, the diameter of the disk has to be rather large, too, in order to have sufficient aperture for the RF beam. One disk with a thickness of 1.7 mm and a diameter of 140 mm was produced by Element Six and already delivered. This disk can be used for the elliptic shape of a Brewster window with an effective aperture of 50 mm.

Because of the elliptic shape, the stresses during the brazing procedure are different from those for circular disks. These stresses were calculated to be increased by a factor of 1.3. To investigate whether a diamond disk will sustain these stresses, brazing tests are being performed at Thales Electron Devices with a quartz disk and a small diamond disk, where the stresses are increased compared to the circular one. In case of successful brazing, the 140 mm diamond disk will be brazed with copper cuffs, allowing edge cooling of the disk.

In 2008, FEM calculations were performed to validate the new brazing tool.

Fast step-tunable magnet

A fast, step-tunable magnet, offering the possibility to change the magnetic field in the range 4.15 – 5.67 T, has been ordered. This magnet will provide the unique possibility to change the gyrotron frequency from 105 GHz to 143 GHz in steps of approximately 3 GHz within 0.5 s every 10 s. The maximum field will be 7.2 T ,making it suitable also for the investigation of 170 GHz gyrotrons for the ITER ECRH system.

In 2008, the assembling of the coil system has been finished and first cold tests in a test cryostat are foreseen at the end of 2008.

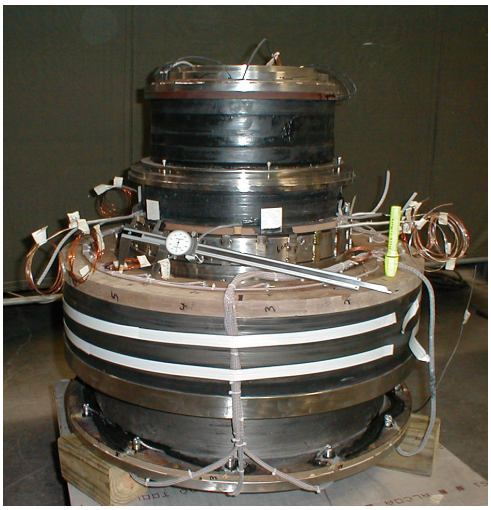

Fig. 6: Assembled coil system of the fast tunable magnet.

Staff:

A. Arnold
G. Dammertz
J. Flamm (Uni Karlsruhe)
G. Gantenbein
R. Heidinger
S. Illy
S. Kern
W. Leonhardt
G. Li
D. Mellein
B. Piosczyk
O. Prinz
A. Samartsev
M. Schmid
W. Spieß
D. Strauss
J. Szczesny
M. Thumm

Literature:

[1] Prinz, O.; Gantenbein, G.; Thumm, M. Advanced quasi-optical mode converter for a multi-frequency gyrotron. 9th IEEE Internat.Vacuum Electronics Conf. (IVEC 2008), Monterey, Calif., April 22-24, 2008 Book of Abstracts S.64-65

[2] Prinz, O.; Arnold, A.; Flamm, F.; Gantenbein, G.; Thumm, M. Recent development of the step-tunable gyrotron at FZK. 35th IEEE Internat.Conf.on Plasma Science (ICOPS), Karlsruhe, June 15-19, 2008 IEEE Conference Records - Abstracts S.202

[3] Stober, J.; Grünwald, G.; Leuterer, F.; Manini, A.; Monaco, F.; Münich, M.; Neu, R.; Schütz, H.; Wagner, D.; Zohm, H.; Franke, T.; Thumm, M.; Gantenbein, G.; Heidinger, R.; Meier, A.; Kasparek, W.; Lechte, C.; Litvak, A.; Denisov, G.G.; Chirkov, A.V.; Tai, E.M.; Popov, L.G.; Nichiporenko, V.O.; Myasnikov, V.E.; Solyanova, E.A.; Malygin, S.A.; Meo, F.; Woskov, P. On the way to a multi-frequency ECRH system for ASDEX upgrade. 15th Joint Workshop on Electron Cyclotron Emission and Electron Cyclotron Resonance Heating, Yosemite National Park, Calif., March 10-13, 2008 Book of Abstracts TECH/GYRO-III-1

[4] Wagner, D.; Grünwald, G.; Leuterer, F.; Manini, A.; Monaco, F.; Münich, M.; Schütz, H.; Stober, J.; Zohm, H.; Franke, T.; Thumm, M.; Gantenbein, G.; Heidinger, R.; Meier, A.; Kasparek, W.; Lechte, C.; Litvak, A.; Denisov, G.G.; Chirkov, A.V.; Tai, E.M.; Popov, L.G.; Nichiporenko, V.; Myasnikov, V.E.; Solyanova, E.A.; Malygin, S.A.; Meo, F.; Woskov, P. Status of the new multi-frequency ECRH system for ASDEX upgrade. Nuclear Fusion, 48(2008) S.054006/1-6

Design Studies towards a 170 GHz 4 MW Coaxial Gyrotron

(supported by the European Community under the EURATOM FUSION Training Scheme project EC-TECH, contract No. 042636 (FU06))

Design studies towards a 170 GHz 4 MW coaxial cavity gyrotron

In a long term view, it is of highest interest to develop gyrotrons with higher unit power for fusion applications. The next step after the 2 MW coaxial cavity gyrotron has been started with a detailed design study for a 170 GHz 4 MW coaxial cavity gyrotron. The study is the main topic of a Ph.D. thesis work, supported by the European Community under the EURATOM FUSION Training Scheme project EC-TECH, contract No. 042636 (FU06). It aims at proving the physical and technical feasibility of such a gyrotron. Table 1 summarizes major design parameters.

Table 1: Design requirements for a 170 GHz 4 MW CW, coaxial cavity gyrotron.

Operating frequency f_0	170 GHz
RF output power P_{out}	4 MW
Total interaction efficiency η_{tot}	> 35 % (without depressed collector)
Peak ohmic wall loading (realistic) ρ_{wall}	< 2 kW/cm²
Loading coaxial insert (realistic) ρ_{coax}	< 0.2 kW/cm²
Emitter current density j_{beam}	< 5 A/cm²

After extensive cavity design studies and mode competition calculations, two suitable operating modes were chosen that can provide the desired output power in single-mode operation while keeping the technical limits as given in Tab. 1: TE-44,26 and TE-52,31. Figure 1 shows two typical start-up simulations for these modes.

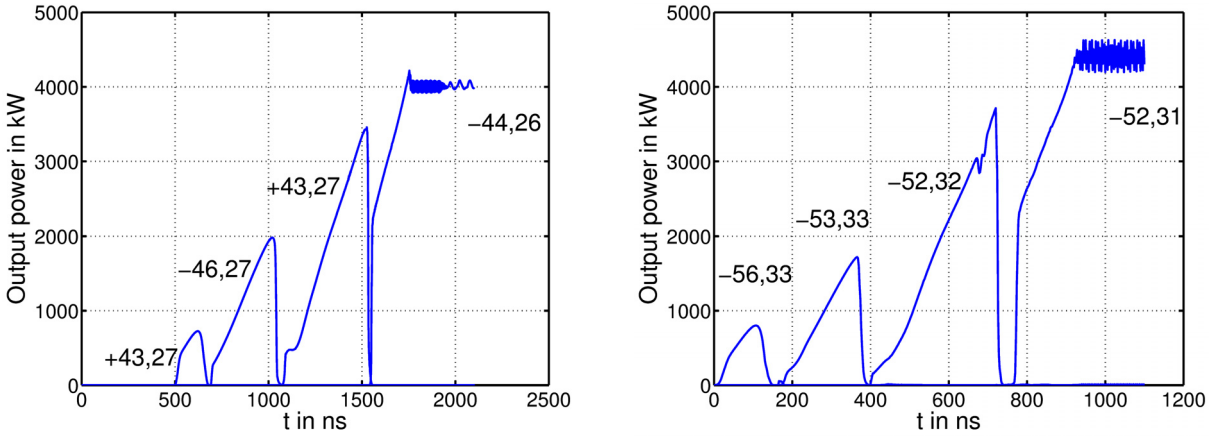

Fig. 1: Startup simulations for the two chosen design modes. Both can provide the desired rf output power.

After that, a detailed design of the electron gun for both operating modes was undertaken. The design was carefully optimized through parameter studies, as shown in Fig. 2. The next steps will be the verification of the rf performance using the simulated parameters of the realistic electron guns, and design of a suitable single-stage depressed collector. It is planned to verify the technical feasibility of the final design during a visiting period at Thales Electron Devices (TED) in 2009 / 2010.

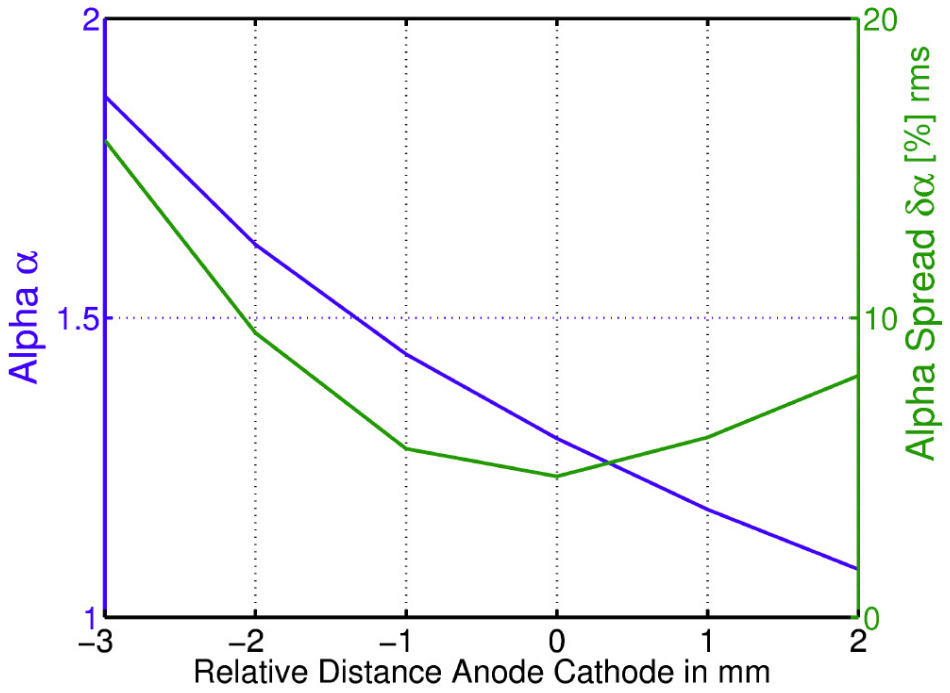

Fig. 2: Influence of the anode-cathode distance on the velocity ratio alpha and its spread.

Staff:

M.H. Beringer
S. Illy
S. Kern
Y.-h. Liu
M. Thumm

Literature:

[1] Beringer, M.H., Kern, S., Liu, Y.H., Thumm, M., *Towards a 4 MW 170 GHz coaxial gyrotron resonator design*, Internat. Conf. on Infrared, Millimeter and Terahertz Waves (IRMMW-THz), Pasadena, Calif., September 15-19, 2008

[2] Beringer, M.H., Kern, S., Illy, S., Thumm, M., *Towards a 4MW 170 GHz coaxial gyrotron resonator and gun design*, 1st ITG Internat. Vacuum Electronics Workshop, Bad Honnef, November 10-11, 2008

[3] Kern, S., Avramides, K.A., Beringer, M.H., Dumbrajs, O., Liu, Y.H., *Gyrotron mode competition calculations: investigations on the choice of numerical parameters*, Internat. Conf. on Infrared, Millimeter and Terahertz Waves (IRMMW-THz), Pasadena, Calif., September 15-19, 2008

Microwave Heating for Wendelstein 7-X

Introduction

In the recent years, electron cyclotron resonance systems have been established as a standard method for localised heating (ECRH) or current drive (ECCD) in fusion relevant plasmas. Thus, ECRH will be the basic day-one heating system for the stellarator W7-X, which is currently under construction at IPP Greifswald. In the first stage, W7-X will be equipped with a 10 MW ECRH system operating at 140 GHz in continuous wave (CW). The complete ECRH-system will be provided by FZK, which in 1998 established, together with EU partners, the 'Projekt Mikrowellenheizung für W7-X' (PMW). The project responsibility covers the design, development, construction, installation and integrated tests of all components required for stationary plasma heating on site at IPP Greifswald. PMW also coordinates the contributions from Institut für Plasmaforschung (IPF) of the University of Stuttgart , which is responsible for the microwave transmission system and part of the HV-system, and those from the team at IPP Greifswald, which is responsible for the in-vessel components and for the in-house auxiliary systems. PMW benefits also from the collaboration with Centre de Recherche de Physique des Plasmas (CRPP) Lausanne, Commissariat à l´Energie Atomique (CEA) in Cadarache and Thales Electron Devices (TED) in Vélizy.

A contract between CRPP Lausanne, FZK Karlsruhe and TED, Vélizy, had been settled to develop and build the continuously operating series gyrotrons. The first step of this collaboration was the development of a prototype gyrotron for W7-X with an output power of 1 MW for CW operation at 140 GHz. This step has been finished successfully.

Seven series gyrotrons have been ordered from the industrial company TED. First operation and long pulse conditioning of these gyrotrons will take place at the test stand at FZK, where pulses up to 180 s at full power are possible (factory acceptance test, FAT). 30 minutes shots at full power are possible at IPP (site acceptance test, SAT). Including the pre-prototype tube, the prototype tube and the 140 GHz tube delivered by CPI, ten gyrotrons will be available for W7-X. To operate these gyrotrons, in addition to the Oxford Instruments and ACCEL magnets, eight superconducting magnetic systems have been ordered from Cryomagnetics Inc., Oak Ridge, USA.

The project made progress in 2008 and is now in a highly advanced state. Most of the components of the transmission system, HV-systems and in-vessel-components have been ordered, manufactured, delivered and are ready for operation at IPP Greifswald. A part of the existing ECRH system is already used to test new concepts and components for ECRH. Some delay arose in the project during the last 1-2 years due to unexpected difficulties in the production of the series gyrotrons.

Series Gyrotrons

The first series gyrotron SN1 had been tested successfully at FZK and IPP in 2005. It fulfilled all the specifications; during the acceptance test no specific limitations were observed. In order to preserve the warranty, this gyrotron has been sealed, and the two prototype gyrotrons are routinely used for experiments.

The following series gyrotrons showed a different behaviour with respect to parasitic oscillations excited in the beam tunnel region. These oscillations result in an excessive heating of the beam tunnel components, in particular of the absorbing ceramic rings. Two gyrotrons that were re-opened after test operation showed significant damages due to overheating at the ceramic rings and the brazing of the rings. This in general limited the pulse length in high power operation to a few ms.

In a first attempt to improve the situation, the manufacturer installed ceramic rings with a better brazing (SN2a, SN3a) in the series gyrotrons SN2 and SN3 that had been re-opened, and changed the sequence of the ceramic rings with different inner diameter (SN5). However, both measures did not improve the situation significantly.

Therefore, FZK in 2008 started first design work to overcome this issue and to come to a more robust beam tunnel which suppresses the excitation of parasitic oscillations more efficiently. In order to validate a new beam tunnel design as much as possible, it is planned to perform tests with a coaxial cavity gyrotron and a frequency step tunable gyrotron with a structurally modified beam tunnel which represents only a small change in the existing design (see Fig. 1). In the experiments, a beam tunnel design as close as possible to that of W7-X will be used, final approval of the progress will be demonstrated in one of the series gyrotrons.

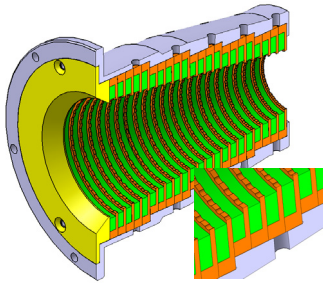

Fig. 1: New beam tunnel design with corrugated copper rings.

In the following we will report on the experimental results obtained with the series gyrotrons SN2a, SN3a and SN5, all equipped with the original beam tunnel.

In 2008, FATs were ontinued with the repaired serial gyrotron SN2a at IPP Greifswald. 830 kW were achieved with the tube at 3 min, and 704 kW at 25 min. However, during conditioning of the tube, the pressure level in the tube increased and complicated further progress. The controls of the vacuum system of the gyrotron did not show a leakage. The acceptance tests of the tube had to be stopped after a crack of the output window had occured during operation, without any alarm message from the interlock system. The gyrotron was sent back to the manufacturer for opening and detailed failure analysis. The diamond window disk also was investigated by experts from IMF I at FZK. The results of the analysis showed a partial destruction of the beam tunnel, a vacuum leak at the relief window (sapphire window), as well as pollution and corrosion at different parts of the gyrotron. Heavy corrosion was found at the brazing of the diamond window and in the cooling circuit of the window assembly. The inner (vacuum) side of the diamond disk showed a copper layer which increases the RF losses by a factor of 10. The absorbing layer supports the assumption of a failure due to thermal overheating.

The (repaired) serial gyrotron SN3a has been tested at FZK in short pulse (~ ms) and long pulse (up to 30 min) operation with power levels of up to 800 kW and 500 kW, respectively. The output beam pattern has been measured and analysed. The beam parameters are very close to those obtained in the first version of the gyrotron, showing a stable and reliable quasi-optical output system. Some output beam parameters of the TED gyrotrons measured so far are given in Table1. Parasitic oscillations at a lower frequency (120 – 130 GHz) were observed which are supposed to be excited in the beam tunnel region and limit the performance of the gyrotron. After conditioning of the gyrotron, it was possible to operate the tube with a maximum power of about 720 kW for 3 min and 500 kW for 30 min, the specified 900 kW output power could not be reached. Long-pulse tests of that tube have been performed with a dummy load provided by CNR, Milano.

Acceptance tests of the serial gyrotron SN5 have been started at FZK. This tube has been equipped with a beam tunnel with a small modification of the inner contour which should decrease the excitation of parasitic oscillations. In short pulse operation, the gyrotron delivered up to 950 kW. However, parasitic oscillations were still limiting the performance of the tube. Regardless of the beam tunnel issue, the parameter optimisation of this gyrotron had to be stopped as the RF output beam was sifted out of the centre of the window thus causing frequent arcing and raising the risk of a failure of the diamond disk. Moreover, spurious oscillations at a lower frequency (120 – 130 GHz) were observed.

Table 1: Gaussian output beam parameters of the series TED gyrotrons calculated from measured patterns.

Gyrotron	w_{0x}; w_{0y}	z_{0x}; z_{0y}	Beam center offset at window Δx; Δy	φ_{hor}; θ_{vert} [mrad]	TEM_{00} [%]
Maquette	19.3; 17.4	-82.8; 61.2	0.0; 4.9	8.1; -23.8	95
Prototype	18.6; 21.3	202; 71	18.2; 16.4	3.5; -1.7	97
TED SN1	17.7; 21.6	126.9; 126.0	-7.0; 8.0	12; -2	95
TED SN2	20.2; 22.5	103.5; 39.8	10.0; 9.0	7; 7	97
TED SN 2a	18.7; 22.2	127.0; 30.0	3.4; 11.9	8.5; 6.7	95
TED SN3	17.5; 20.6	130; 90	5.4; 9.0	0.1; 13	97
TED SN3a	17.6; 20.5	24; 77	6.0; 3.0	-1; 17	96
TED SN 4	18.1; 18.5	105; 51	-1; 2	-4.; 5.	97

Transmission Line

The transmission line consists of single-beam waveguide (SBWG) and multi-beam waveguide (MBWG) elements. For each gyrotron, a beam conditioning assembly of five single-beam mirrors is used. Two of these mirrors match the gyrotron output to a Gaussian beam with the correct beam parameters, two others are used to set the appropriate polarization needed for optimum absorption of the radiation in the plasma. The fifth mirror directs the beam to a plane mirror array, i.e., the beam combining optics, situated at the input plane of a multi-beam wave guide. This MBWG is designed to transmit up to seven beams (five 140 GHz beams, one 70 GHz beam plus an additional spare channel) from the gyrotron area (entrance plane) to the stellarator hall (exit plane). At the output plane of the MBWG, a mirror array re-separates the beams and distributes them via CVD-diamond vacuum barrier windows to individually movable antennas (launchers) in the torus. To transmit the power of all gyrotrons, two symmetrically arranged MBWGs are used.

In 2008, the manufacturing of the transmission system near the torus was mostly completed. This comprises the reflectors type M13 and M14, which test-wise have been already installed in the two "towers" finally to be installed in front of W7-X in order to provide microwave shielding and a stable basis for the optics. The fabrication of these towers was completed, including the installation of control systems for reflectors and launchers, support structures, and granite absorbing plates. A photograph is shown in Fig. 2. Present work concentrates on the shielding structures on top of the towers, the interfaces to the stellarator ports, absorbing screens and the transmission diagnostics in conjunction with grating couplers integrated into the surfaces of the mirrors.

Fig. 2: „ECRH tower“ for shielding and installation of the mirrors near to W7-X.

For the gyrotrons commissioned in 2008, thermographical beam profiles were recorded, and subsequently, phase retrieval to provide a basis for the design of the matching optics was performed. For two of the repaired tubes, the matching optics fabricated before could be used after the repair; for one gyrotron, the

beam parameters had changed somewhat, therefore a re-machining of the matching mirror surfaces (M1 and M2) was necessary. Diagnostic boxes with newly developed multi-mode horns for power monitoring were manufactured after passing the hot test in Greifswald. These diagnostic boxes receive a probe beam, which is diffracted from a holographic grating on the first matching mirror; an internal power splitter couples the sample power to a Bolometer (overall power detector) as well as into a high-quality Gaussian beam receiver measuring the power in the nominal mode.

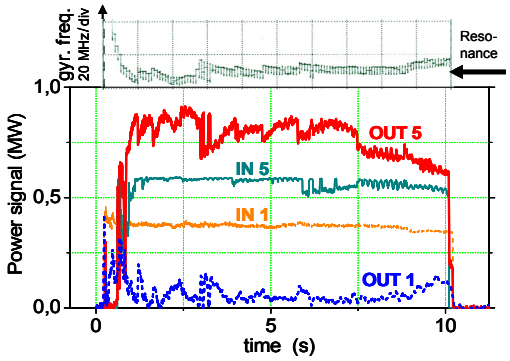

Fig. 3: A 10-s power combination experiment. IN1 and IN5: Power of gyrotrons B1 and B5; OUT1 and OUT5: output power from the diplexer coupled to the loads. Residual power in OUT1 is mainly caused by spontaneous frequency jumps of the B1 gyrotron and an increase of the B1 frequency during the end of the pulse. On top of the figure, the frequency of gyrotron B1 is displayed relative to the resonance of the diplexer.

As in the past years, the ECRH system could be used for the testing of special components. Among others, a new test campaign now was dedicated to the investigation of the high-power diplexer, which is developed for use as a combiner for the power of two gyrotrons, as well as a fast directional switch (FADIS) between two outputs. After successful demonstration of fast switching using the steep transmission slope of the device and a tiny frequency-shift keying initiated by modulation of the acceleration voltage of the gyrotron in 2007, a power combination experiment was performed in 2008**.** For the test, two gyrotrons (B1 and B5) were coupled to the inputs. The resonance of the FADIS was adjusted such that B1 was transmitted through the resonant channel, B5 was non-resonant, leading to a power combination with an efficiency of better than 90 % in the common output (OUT 5), see Fig. 3. The efficiency is mainly limited by fluctuations of the gyrotron frequency, which will be an issue to work on in the future; the pulse length of 10 seconds was limited by the max. temperature of the un-cooled Al mirrors.

Due to frequent problems with the existing CW loads, some work was dedicated to the development of a new load. This load consists of a long (> 20 m) waveguide made from stainless steel, where the power is coupled as a Gaussian beam. By appropriate down-tapering, the absorption of the waveguide is matched to the eventual power loss along the guide. A first test with thermal imaging of the waveguide wall shows the expected beat structure of TE_{11} and TM_{11}, which are excited by the input beam. However, the simple mock-up system using standard water tubes with welded connections suffered from strong arcing. In a second attempt, electro-polished tubes with flanged connections will be used.

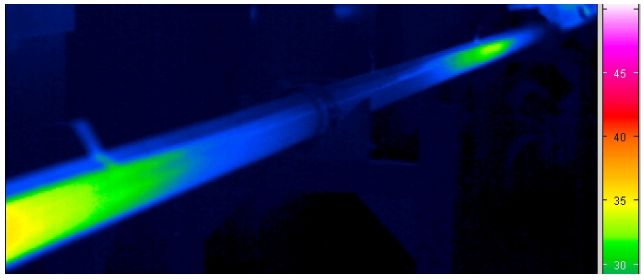

Fig. 4: Thermal image of the wall of a mock-up of the "long absorber load" showing the beat structure of the TE11 and TM11 waveguide modes excited from the input beam.

HV-systems

For the operation of gyrotrons with depressed collector, a precisely controlled beam acceleration voltage is necessary, which is supplied by the body-voltage modulator. The gyrotron beam current is controlled by the cathode heater supply, which is on cathode potential (about -55 kV). In case of arcing inside the gyrotron, a thyratron crowbar protects the tubes from being damaged.

All ten body-voltage modulators and the protection units are now ready for operation. An additional protection unit was integrated to allow the exact location of the source of a fault in case of malfunction of the gyrotron. The prototype modulator was upgraded to meet the same specifications as the series systems. At present, some final optimization concerning the system diagnostics in case of a gyrotron fault is implemented. Fig. 5 shows a complete modulator/crowbar system installed in the gyrotron hall in Greifswald.

Fig. 5: Complete modulator/crowbar system installed in the gyrotron hall in Greifswald.

In-vessel-components

The assembly of the four ECRH plug-in antennas is going on. Each antenna consists of three front steering mirrors, which are movable in both, the toroidal and poloidal direction (see Figure 6 for a complete antenna). This gives a maximum flexibility for the different heating and current drive scenarios, which are foreseen for W7-X.

Fig. 6: Assembled ECRH plug-in antenna.

The beam position and the absorbed power will be measured by a pick-up horn array, which is integrated into the heat shield tiles opposite of the antennas. A first prototype of the waveguide bundle with 16 circular copper tubes with an outer diameter of 4 mm and an inner diameter of 2 mm was manufactured and is ready for a test assembly in an original W7-X vacuum vessel module.

In total, 120 waveguides will cross the vacuum air interface in four B-type ports. The B-port flanges have been redesigned due to a change note concerning the water supply of the port protection cooling. Now, additional intermediate flanges allow both, the water supply and the microwave connection from the port side. The manufacturing of these intermediate flanges has started recently.

Staff:

IHM / FZK	IPF (University of Stuttgart)	IPP (Greifswald/Garching)
A. Arnold	P. Brand	B. Berndt
K. Baumann	C. Lechte	H. Braune
G. Dammertz	W. Kasparek	V. Erckmann (PMW)
G. Gantenbein	H. Kumric	F. Hollmann
R. Heidinger (IMF I)	M. Krämer	L. Jonitz
S. Illy	R. Munk	H. Laqua
S. Kern	F. Müller	G. Michel
M. Kupper	B. Plaum	M. Nitz (Diplomand)
W. Leonhardt	S. Prets	F. Noke
R. Lang	P. Salzmann	F. Purps
D. Mellein	K.H. Schlüter	T. Schulz
S. Miksch	D. Wimmer	P. Uhren
B. Piosczyk		M. Weißgerber
H. O. Prinz		
A. Samartsev		
M. Schmid		
W. Spiess		
J. Szczesny		
M. Thumm		
J. Weggen		

Literature:

[1] Erckmann, V.; Brand, P.; Braune, H.; Gantenbein, G.; Kasparek, W.; Laqua, H.P.; Marushchenko, N.B.; Michel, G.; Petelin, M.I.; Shchegolkov, D.Yu.; Thumm, M.; Turkin, Y. ; W7-X ECRH Teams at IPP, FZK and IPF Steady state ECRH for next step magnetic fusion devices. 25th Symp.on Fusion Technology (SOFT 2008), Rostock, September 15-19, 2008

[2] Erckmann, V.; Braune, H.; Laqua, H.P.; Marushchenko, N.B.; Michel, G.; Turkin, Y.; Weissgerber, M.; Gantenbein, G.; Thumm, M.; Brand, P.; Kasparek, W.; Lechte, C. ; W7-X ECRH Teams at IPP, FZK and IPF The 10 MW, CW, ECRH-plant for W7-X: status and high power performance. 15th Joint Workshop on Electron Cyclotron Emission and Electron Cyclotron Resonance Heating, Yosemite National Park, Calif., March 10-13, 2008 Book of Abstracts TECH/GYRO-II-2

[3] Gantenbein, G.; Braune, H.; Dammertz, G.; Erckmann, V.; Illy, S.; Kern, S.; Kasparek, W.; Laqua, H.P.; Lechte, C.; Legrand, F.; Leonhardt, W.; Lievin, C.; Michel, G.; Piosczyk, B.; Prinz, O.; Schmid, M.; Thumm, M. 1 MW 140 Ghz gyrotron development for W7-X at FZK. 1st ITG Internat.Vacuum Electronics Workshop, Bad Honnef, November 10-11, 2008

[4] Gantenbein, G.; Braune, H.; Dammertz, G.; Erckmann, V.; Illy, S.; Kern, S.; Kasparek, W.; Laqua, H.P.; Lechte, C.; Legrand, F.; Leonhardt, W.; Lievin, C.; Michel, G.; Piosczyk, B.; Prinz, O.; Schmid, M.; Thumm, M. Experimental results of series gyrotrons for the stellarator W7-X. 22nd IAEA Fusion Energy Conf., Geneve, CH, October 13-18, 2008 Book of Abstracts S.115

[5] Gantenbein, G.; Braune, H.; Dammertz, G.; Erckmann, V.; Illy, S.; Kern, S.; Kasparek, W.; Laqua, H.P.; Lechte, C.; Legrand, F.; Leonhardt, W.; Lievin, C.; Michel, G.; Piosczyk, B.; Prinz, O.; Schmid, M.; Thumm, M. Recent results in high power gyrotron development for W7-X at FZK. 35th IEEE Internat.Conf.on Plasma Science (ICOPS), Karlsruhe, June 15-19, 2008 IEEE Conference Records - Abstracts S.201

[6] Gantenbein, G.; Dammertz, G.; Illy, S.; Leonhardt, W.; Piosczyk, B.; Schmid, M.; Thumm, M.; Braune, H.; Erckmann, V.; Michel, G.; Kasparek, W.; Legrand, F.; Lievin, C.; Prinz, O.; Thumm, M. The W7-X 140 GHz, 1MW gyrotron - status and recent results. 15th Joint Workshop on Electron Cyclotron Emission and Electron Cyclotron Resonance Heating, Yosemite National Park, Calif., March 10-13, 2008 Book of Abstracts PII-TECH/GYRO-5

[7] Schmid, M.; Dammertz, G.; Gantenbein, G.; Hrabal, D.; Illy, S.; Kern, S.; Kasparek, W.; Leonhardt, W.; Müller, G.; Piosczyk, B.; Thumm, M. The gyrotron test facility and its power supplies at the Forschungszentrum Karlsruhe. 1st ITG Internat.Vacuum Electronics Workshop, Bad Honnef, November 10-11, 2008

[8] Thumm, M.; Braune, H.; Dammertz, G.; Erckmann, V.; Gantenbein, G.; Illy, S.; Kern, S.; Kasparek, W.; Laqua, H.P.; Lechte, C.; Legrand, F.; Leonhardt, W.; Lievin, C.; Michel, G.; Piosczyk, B.; Prinz, O.; Schmid, M. 1 MW, 140 GHz series gyrotrons for the W7-X stellarator. 7th Internat.Workshop on Strong Microwaves: Sources and Applications, Nizhny Novgorod, Russia, July 27 - August 2, 2008 Book of Abstracts S.27

[9] Thumm, M.; Dammertz, G.; Gantenbein, G.; Illy, S.; Kern, S.; Leonhardt, W.; Neffe, G.; Piosczyk, B.; Schmid, M.; Braune, H.; Erckmann, V.; Hollmann, F.; Jonitz, L.; Laqua, H.P.; Michel, G.; Noke, F.; Purps, F.; Schulz, T.; Weissgerber, M.; Brand, P.; Grünert, M.; Kasparek, W.; Kumric, H.; Lechte, C.; Plaum, B. 10 MW, 0.14 THz, CW gyrotron and optical transmission system for millimeter wave heating of plasmas in the stellarator W7-X. Terahertz Science and Technology, 1(2008) Nr.2, S.73-99

[10] Thumm, M.; Dammertz, G.; Gantenbein, G.; Illy, S.; Leonhardt, W.; Neffe, G.; Piosczyk, B.; Schmid, M.; Braune, H.; Erckmann, V.; Laqua, H.P.; Michel, G.; Weissgerber, M.; Brand, P.; Kasparek, W.; Lechte, C. 10 MW, 140 GHz, CW millimeter wave heating system for the stellarator W7-X. Development of Physics and Technology of Stellarators/Heliotrons en route to DEMO : 18th Internat.Toki, Conf., Toki City, J, December 9-12, 2008

[11] Thumm, M.; Brand, P.; Braune, H.; Dammertz, G.; Erckmann, V.; Gantenbein, G.; Illy, S.; Kasparek, W.; Laqua, H.P.; Lechte, C.; Leonhardt, W.; Michel, G.; Neffe, G.; Piosczyk, B.; Schmid, M.; Weissgerber, M. Progress in the 10-MW 140 GHz ECH system for the stellarator W7-X. IEEE Transactions on Plasma Science, 38(2008) S.341-55 DOI:10.1109/TPS.2008.917950

[12] Thumm, M.; Brand, P.; Braune, H.; Erckmann, V.; Gantenbein, G.; Illy, S.; Kasparek, W.; Laqua, H.P.; Lechte, C.; Marushchenko, N.B.; Michel, G.; Piosczyk, B.; Schmid, M.; Turkin, Y.; Weissgerber, M. ; W7-X ECRH Teams at IPP, IPF and FZK Progress of the 10-MW 140-GHz ECH system for the stellarator W7-X. Workshop on RF-Heating Technology for Fusion Plasmas 2008, San Diego, Calif., September 10-12, 2008

Underlying Technology

Underlying Technology

Operation of the Fusion Materials Laboratory FML)

The Fusion Materials Laboratory provides the infrastructure for the performance of tasks defined in the EFDA and F4E workprogrammes related to the characterisation and testing of irradiated and non-irradiated materials. Methods such as optical and electron microscopy, tritium adsorption and desorption, He pycnometry and Hg porosimetry, crush load, micro hardness, creep, charpy impact, tensile, LCF and instrumented indentation tests as well as long-time annealing tests are applied. The work includes Post Irradiation Examinations (PIE) of Reduced Activation Ferritic Martensitic (RAFM) steels (reference material for DEMO and ITER-TBMs) and investigations on materials relevant for the HCPB blanket (ceramic breeder materials, beryllium).

PIE on selected samples from the HFR IB and HFR IIB experiments were performed. For this purpose tensile tests and LCF tests were performed and tested specimens' small cuts for light optical, scanning and transmission electron microscopy were prepared and examined. Broken halves of charpy specimens were prepared for instrumented indentation and served for identifying material parameters and Vickers hardness. The aim of the investigations was to study the irradiation effects on the mechanical and structural properties of these materials and to investigate the possibilities of a post-irradiation heat-treatment in order to reduce irradiation defects.

The investigation of blanket materials was continued with the characterisation of materials. Lithium orthosilicate pebbles were investigated by light optical microscopy and their porosity and deformation hardness were determined. Different batches of materials were characterised with respect to the influence of parameters of the fabrication process on the mechanical and structural properties. Tritium adsorption/desorption tests were done on beryllium and beryllium titanium alloys and on BeO-doped beryllium.

Adsorption and desorption experiments were also done with unirradiated beryllium titanium pebbles. Furthermore different beryllium titanium alloys were characterized by light optical microscopy and porosity measurements and creep tests were done.

Detailed results and consecutive analysis of the measurements are reported in the respective chapters of this report.

For the PIE the following equipment was used:

Charpy impact, LCF and tensile testing devices
Indentation device for instrumented ball-indentation and Vickers hardness-test
Light optical, scanning electron and transmission electron microscopes with analysis of chemical elements
Desorption device with high temperature furnace for tritium and helium release measurements
He-pycnometer and Hg-porosimeter
Sphere crush and creep testing apparatus

In the frame of our upgrading programme, a new 200 kV high resolution transmission electron microscope for investigation of radioactive material down to atomic scale was installed. Furthermore, a new remotely operated light optical microscope was installed and came into operation.

Future activities:

Continuation of measurements as referred to above:

- PIE of the HFR II B irradiation phase, 15 dpa
- PIE of the BOR 60 irradiation campaign, 15 – 30 dpa
- PIE of the OSIRIS FURIOSO high temperature irradiation, WL10-tungsten, 5 dpa
- Development of a device for instrumented indentation at elevated temperatures
- Characterization of new batches of ceramic breeder materials and beryllium
- Installation of a gamma-ray spectrometer to study the activation of RAFM steels

Staff:

P. Barié
J. Ehrmann
A. Erbe
M. Gilpert
M. Holzer
H. Jackisch
S. Lautensack
G. Mangei
W. Nägele
H. Ries
M. Rietschel
R. Rolli
G. Rösch
I. Sacksteder
R. Schmidt
H.-C. Schneider
H. Steinle

Literature:

[1] N. Huber, E. Tyulyukovskiy, H.-C. Schneider, R. Rolli, M. Weick, “An indentation system for determination of viscoplastic stress-strain behaviour of small metal volumes before and after irradiation“, Journal of Nuclear Materials, 377 (2008), pages 352 - 358

[2] J. Reimann, R.A. Pieritz, C. Ferrero, M. di Michiel, R. Rolli, “X-ray tomography investigations on pebble bed structures”, Fusion Engineering ans Design (2008), in press

[3] Gaganidze, E.; Dafferner, B.; Ries, H.; Rolli, R.; Schneider, H.C., Aktaa, J.: “Irradiation programme HFR phase IIb – SPICE. Impact testing on up to 16.3 dpa irradiated RAFM steels”. Final report for task TW2-TTMS 001b-D05. Wissenschaftliche Berichte, FZKA-7371 (April 2008)

[4] Schneider, H.-C.; Sacksteder, I.; Materna-Morris, E.: “Tensile behaviour of 15 dpa irradiated steel, determined by instrumented indentation. Jahrestagung Kerntechnik 2008, Hamburg

[5] Sacksteder, I.; Schneider, H.-C.; Materna-Morris, E.: “Characterisation of irradiated materials by microindentation testing. Materials Science and Engineering 2008, Nürnberg

Goal Oriented Training Programme

WP08-GOT-EUROBREED (FU07-CT-2008-00047)
Goal Oriented Training Programme "Breeding Blanket Developments for Fusion Reactors"

Objective

The overall objective of the training programme WP08-GOT-EUROBREED is helping to provide the necessary broad expert basis to successfully conduct the European breeding blanket development programme along with ITER and the developments beyond ITER, i.e., for a fusion power reactor, comprising the development of the optimum breeder and neutron multiplier materials, the design of specific breeder blanket components for future fusion reactors, and testing the breeding blanket in ITER. The training programme will proceed along, and enhance, already existing projects in the framework of the European Breeder Blanket Programme, and support activities in the associations. Existing experimental facilities like Helium loops, irradiation facilities and laboratories will be utilised in the training programme and as well new projects related to the other main topics.

The associations participating in the network have a large competence in the topics mentioned above, as the long term participation in the development of the European Breeding blankets demonstrates. In particular, FZK and CEA are the leading associations for the development of the Helium Cooled Pebble Bed (HCPB) and the Helium Cooled Lithium Lead (HCLL), the two blanket concepts supported by the European Union as candidate for the DEMO blanket and selected for the testing in ITER.

The network is integrating almost the complete breeder blanket development programme including development of breeder materials, characterisation and modelling of properties (e.g. thermo-mechanics and tritium release), test of these materials in out-of-pile and in-pile experiments, integration of them in ITER, and also some aspects for the integration in the future DEMO reactor. Thus, the broad range of competences required in the European breeder development in the future is addressed, and the proposed project will provide a significant and necessary improvement in the expert basis required.

The work is broken down into 8 work packages as follows:

Work Package Id	Leader Org.	Other Org.	Description
WP1	FZK	CEA	Design, procurement and test of solid breeder units
WP2	FZK	NRG	Pebble bed development and testing for the EU solid breeder blanket
WP3	CEA	FZK, ENEA, CIEMAT	Neutronics and radiation protection shielding design of the HCLL reactor
WP4	CEA	FZK, HAS	TBM integration in Port Plug with engineering design and interfaces management
WP5	HAS	FZK,CEA,CIEMAT	Measurement techniques development for breeder blankets
WP6	NRG	CEA, NRG	Pebble bed nuclear performance testing
WP7	CIEMAT	CEA,NRG	Tritium transport predictive modelling tool for Breeding Blanket design analyses and system modelling
WP8	AEUL	FZK,UKAEA	Properties and diffusion of tritium accumulated in fusion reactor materials

Forschungszentrum Karlsruhe is participating to this network assuming the role of network Coordinator and leading 2 of the 8 proposed Work Packages (WP). The coordination of the network is achieved by means of a Programme Coordinator (L.V. Boccaccini), a Secretary (D. Radloff) and a Financial Manager (M. Henn). WP-1 and WP-2 have T. Ihli and R. Knitter, respectively, as Personal Supervisors (PS).

Results in 2008: Start of the Grant and Kick-off Meeting

The Grand started officially on 1st September 2008. The Kick-off-meeting, with the presence of the EFDA Responsible Officer J-L. Boutard, was held on 3rd - 4th November, 2008 in Karlsruhe.

Status of the work

The procedures for the recruitment of the 2 trainees in FZK have been started in 2008. The due date for starting the WPs is September 2009.

Staff:

L.V. Boccaccini
U. Fischer
T. Ihli
R. Knitter
M. Henn
D. Radloff

WP08-GOT-TRI-TOFFY (FU07-CT-2008-00047)
Goal Oriented Training Programme “Tritium Technologies for the Fusion Fuel Cycle”

The overall objective of the project is to support EU activities in the Deuterium-Tritium Fuel Cycle area for ITER by the training of six Early-Stage Researchers. The training programme is developed along existing projects in the framework of the European procurement package for the ITER Fuel Cycle with the main focus on water detritiation (WDS) and isotope separation (ISS) systems, detritiation processes, gas analysis and tritium measurements (see overview table: List of Work Packages). The participating Associations are: FZK, CEA, ENEA, HAS/MTA ATOMKI, MEdC/ICIT and UKAEA.

Overview Table: List of Work Packages

No.	Title	Partners involved
1	Combined operation of WDS and ISS	FZK (ICIT, UKAEA)
2	Detritiation of waste	CEA (FZK, UKAEA)
3	Technologies for tritium recovery and trapping	ENEA (FZK, UKAEA)
4	Calorimeter with large sample volume	MTA ATOMKI (FZK, UKAEA)
5	Experimental Pilot Plant for Tritium and Deuterium Separation	ICIT (FZK, UKAEA)
6	Participation in JET operation	UKAEA (FZK)

The project was only started in late 2008. Hence, so far only a kick-off meeting was held and the process of recruitment of trainees was initiated. The selection of trainees is up to the employing network partner. It has been agreed that approval should be obtained by any network partner hosting the trainee for a substantial time. Employment of the TRI-TOFFY trainees shall start no later than September 1, 2009; if possible earlier.

Programme Coordinator:

L. Dörr

Appendix I: FZK Departments Contributing to the Fusion Programme

FZK Department	FZK Institut/Abteilung	Director	Ext.
Institute for Materials Research	Institut für Materialforschung (IMF)	I. Prof. Dr.K.-H. Zum Gahr	3897
		II. Prof. Dr. O. Kraft	4815
		III. Prof. Dr. H. Haußelt	2518
Institute for Pulsed Power and Microwave Technology	Institut für Hochleistungsimpuls- und Mikrowellentechnik (IHM)	Prof. Dr. M. Thumm	2440
Institute for Nuclear and Energy Technology	Institut für Kern- und Energietechnik (IKET)	Prof. Dr. T. Schulenberg	3450
Institute for Reactor Safety	Institut für Reaktorsicherheit (IRS)	Dr. J. Knebel (Acting Head)	2550/ 5510
Institute for Technical Physics	Institut für Technische Physik (ITP)	Prof. Dr. M. Noe	3500
- Tritium Laboratory Karlsruhe	- Tritiumlabor Karlsruhe (TLK)	Dr. L. Dörr	4546
Institute for Data Processing and Electronics	Institut für Prozessdatenverarbeitung und Elektronik (IPE)	Prof. Dr. H. Gemmeke	5635

Appendix II: Fusion Programme Management Staff

Head of the Research Unit	Dr.K. Hesch (Acting Head)	ext. 5460 e-mail: klaus.hesch@fusion.fzk.de
Secretariat:	Mrs. M. Lettow-Rattu	ext. 5461 e-mail: mira.lettow-rattu@fusion.fzk.de
	Mrs. Eva-Maria Wünschel	ext. 2435 e-mail: eva-maria.wuenschel@fusion.fzk.de
Program Budget, Administration, Reports, EU-Affairs	BW. M. Henn	ext. 5547 e-mail: michael.henn@fusion.fzk.de
	Mrs. I. Pleli	ext. 8292 e-mail: ingrid.pleli@fusion.fzk.de
Blanket and Divertor Development, HELOKA, IFMIF, Public Relations	Dr. D. Radloff	ext. 8750 e-mail: dirk.radloff@fusion.fzk.de
Fuel Cycle, Structural Materials, Superconducting Magnets, CAD-Office	DI. S. Gross	ext. 5468 e-mail: sigurd.gross@fusion.fzk.de
Plasma Heating Technology, Safety Studies, Neutronics, Physics	Dr. K. Hesch	ext. 5460 e-mail: klaus.hesch@fusion.fzk.de
Quality Management Resource Loaded Planning, Document Management	Dr. J. Gafert	ext. 2923 e-mail: juergen.gafert@fusion.fzk.de
	DI. P. Freiner	ext. 4194 e-mail: peter.freiner@fusion.fzk.de
	Dr. M. Ionescu-Bujor	ext. 8325 e-mail: mihaela.ionescu-bujor@fusion.fzk.de

Address: **Forschungszentrum Karlsruhe GmbH**
Nuclear Fusion Programme Management

Post Office Box 3640, D - 76021 Karlsruhe / Germany

Telephone No: **07247-82- Extensions .....**

Telefax No: **07247-82-5467**

world wide web: **http://www.fzk.de/fusion**

Appendix III: Glossary

AC	Alternating Current
ADC	Analog to Digital Converter
ADS	Atomosphere Detritiation System
ADS 2, ADS 3, ADS 4	Boron doped EUROFER 97
AEU	Ancillary Equipment Unit
AGHS	Active Gas Handling System
ALARA	Analytic and Laplacian Adaptive Radioactivity Analysis Code
ALTAIR	Fast Reactor Irradiation from CEA in BOR 60
ARBOR-1	Fast Reactor Irradiation from FZK in BOR 60
ARBOR-2	Fast Reactor Irradiation from FZK and CEA in BOR 60
ASDEX	Axial-Symmetrisches Divertor-EXperiment
ASG	ASG Superconductors, Italy (former Ansaldo Superconduttori)
BB	Bending Bars
BET	Specific surface (Brunauer, Emmet, Teller)
BOR 60	Fast Reactor at SSC RF RIAR, Dimitrovgrad, Russia
BU	Breeding Unit
C/E	Calculation/Experiment
CAD	Computer Aided Design
CATIA	Computer Aided Three Dimensional Interactive Application
CD	Cryogenic Distillation
CDR	Contract Dose Rate
CEA	Commissariat à l'Énergie Atomique, Saclay (France)
CECE	Combined Electrolysis Catalytic Exchange
C-ECM	Cathode guided ECM
CFC	Carbon Fibre Composite
CFD	Computational Fluid Dynamic
CFTM	Creep Fatigue Test Module
CICC	Cable in Conduit Conductor
CIEMAT	Centro de Investigaciones Energeticas Medioambientales y Tecnologicas
CNR	Consiglio Nazionale delle Ricerche, Milano, Italy
CRPP	Centre de Recherces en Physique des Plasmas, Lausanne, Switzerland
CS	Central Solenoïd
CSU	Centra Support Unit, department of EFDA
CuLTKa	Current Lead Test Facility Karlsruhe

CW	Continuous Wave
D	Diameter
D1S	Direct one-step method for shut-down dose rate calculations
DA	Domestic Agency
DBTT	Ductile-to-Brittle Transition Temperature
DC	Direct Current
DD	Deuterium Deuterium Fusion Process
DEMO	Demonstration Power Station
DNB	Diagnostic Neutral Beam
dpa	Displacement per atom
DPC	Depressed Collection, Energy Recovery Device for Electron Beams
DT	Deuterium Tritium Fusion Process
EAF	European Activation File
EASY	European Activation System
EB	Electron Beam
ECA	Electro-Chemical Aluminium Deposition
ECCD	Electron Cyclotron Current Drive
ECIS	Optical Model Code
ECM	Electrochemical Maching
ECRH	Electron Cyclotron Resonance Heating
EDM	Electric Discharge Manufacturing
EDX	Energy Dispersive X-ray Analysis
EFDA	European Fusion Development Agreement
EFF	European Fusion File (by EU)
ELM	Edge Localized Mode
EM	Electro Magnetic
EMRAS	Environmental Modelling for Radiation Safety
ENDF/B	Evaluated Nuclear Data File (neutron data)
ENDF-6	Evaluated Nuclear Data File Format
ENEA	Italian National Agency for New Technologies, Energy and the Enviroment
ESRAY	FZK Ray Tracing Code for Electron Gun Designs
EUROFER	European RAF/M Steel
EVEDA	Engineering Validation Engineering Design Activities
F4E	Fusion for Energy
F82H	Japanese low activation steel (8Cr2WVTa)
F82H mod.	Japanese RAF/M Steel

FEM	Finite Element Method
FENDL	Fusion Evaluated Nuclear Data Library
FISPACT	Fusion Inventory Code
FMEA	Failure Model and Effect Analysis
FMECA	Failure Mode Effect and Criticality Analysis
FML	Fusion Materials Laboratory
FNG	Frascati Neutron Generator
FPD	FPD - Full Power Days
FPY	Full Power Years
FSSS	Fisher Sub Sieve Size
FW	First Wall
FZJ	Forschungszentrum Jülich
FZK	Forschungszentrum Karlsruhe
GNASH	Nuclear Model Code
GSSR	Generic Site Safety Report
H&CD	Heat & Current Drive
HAS	Hungarian Academy of Sciences
HAZ	Heat Affected Zone
HCLL	Helium Cooled Lithium Lead
HCPB	Helium Cooled Pebble Bed
He	Helium
HEBLO	HElium BLOwer (Helium facility at FZK)
HELOKA	Helium Loop Karlsruhe
HEMJ	Helium-cooled Divertor Concept with Multiple Jet Cooling
HEMP	Helium-cooled Pins
HEMS	Helium-cooled Slots
HETRA	HEat TRAnsfer Experiment
HFR	High Flux Reactor
HFTM	High Flux Test Module
HHF	High Heat Flux
HIP	Hot Isostatic Press
HNB	Heating Neutral Beam
HPFPP	Hydrogen Production Fusion Power Plant
HPGe	High Purity Germanium (detector)
HRS	Hot Ring Shield
HRTEM	High Resolution Transmission Electron Microscope

HT	Tritiated Gas
HT	High Temperature
HTO	Tritiated Water Vapour
HTS	High Temperature Superconducting
HV	High Voltage
IAEA	International Atomic Energy Agency
IAP	Institute of Applied Physics, Nizhny Novgorod, Russia
ICP-OES	Inductively Coupled Plasma – Optical Emission Spectrometry
ICRP	Internation Commission on Radiological PRotection
IFMIF	International Fusion Materials Irradiation Facility
IPE	Institute of Data Processing and Electronics
IPF	Max-Planck Institute for Plasma Physics, Garching
IPP	Institut für Plasmaforschung, Universität Stuttgart
ISS	Isotope Separation System
ITER	International Thermonuclear Experimental Reactor
ITERVAC	Code for Vacuum Gas Flows
JEFF	Joint European Fission Fusion File
JENDL	Japanese Evaluated Nuclear Data Library (by JA)
JET	Joint European Torus
JLF-1	Japanese low activation steel (9Cr2WVTa)
KIAE	Kurchatov Institute, Moscow
KLST	Kleinlast Impact Specimen
LCF	Low Cycle Fatigue
LF	Low Frequency, within the report: frequency below 1 GHz
LOFA	Loss of flow accident
LPCE	Liquid Phase Catalytic Exchange
LSE	Low Shelf Energy
MA	Mechanical Alloying
MAGS	Magnet Safety (Software module)
MBWG	Multi-beam Waveguide
MC	Monte Carlo
McCad	Interface programme for the conversion of CAD to MCNP geometry data
MCNP	Monte Carlo code for neutron and photon transport simulations
MCNPX	Monte Carlo Code for Neutral and Charged Particle Transport Simulations
MCSEN	Monte Carlo Sensitivity Code based on MCNP
M-ECM	Mask-leaded ECM

MEKKA	Magneto-Hydrodynamic Experiments in NaK Karlsruhe
MF	Manifold
MFTM	Medium Flux Test Module
MHD	Magneto Hydrodynamic
MMS	Multi Module Segments
MU	Mock-up
NB	Neutral Beam
NBI	Neutral Beam Injector
NBTF	Neutral Beam Test Facility
NC	Normal Conducting
NRG	Nuclear Research and Consultancy Group, National Nuclear Research Institute of the Netherlands, located in Petten
NTUA	The National Technical University of Athens, Greece
OCTAVIAN	14 MeV Neutron Source Facility at Osaka University, JA
ODS	Oxygen Dispersion Strengthened
ODS-EUROFER 97	Oxide Dispersed Strengthened EUROFER 97 with 0,5 % Y_2O_3
OMP	Optical Model Potential
OPT	Organically Bound Tritium
OPTIFER	German RAF/M Steel
OSi	Lithium Ortho9silicate
PCP	Prototype Cryosorption Pump
PF	Poloïdal Field
PFC	Plasma Facing Components
PHTS	Primary Heat Transfer System
PICOLO	Pb-Li Corrosion Loop
PIE	Post Irradiation Examination
PIM	Powder Injection Molding
PIT	Postulated Impact Tables
PLC	Programmable Logic Control
PM	Powder Metallurgy
PMW	Projekt Mikrowellenheizung for W7X
Pp	Peak to peak
PPCS	Power Plant Conceptual Study
PTC	Prototype Torus Cryopump
PWHT	Post Weld Heat Treatment
QD	Quench Detection
QDS	Quench Detection System

QDU	Quench Detector Unit
QRAM	Quench Event Record Buffer (Quench-RAM)
R2S	Rigorous two-step method for shut-down dose rate calculations
RACC	Roebel-cables Assembled from Coated Conductors
RAF	Reduced Activation Ferritic
RAFM	Reduced Activation Ferritic Martensitic
RD	Rolling Direction
REM	Raster Electron Microscope
RF, rf	Radio Frequency, within this report above 1 GHz
RGA	Residual Gas Analyser
RH	Remote Handling
RID	Residual Ion Dump
SBWG	Single-beam Waveguide
SC	Superconducting
sccm	cubic centimetre per minute at standard conditions (0°C, 101325 Pa)
SELFT	FZK Gyrotron Interaction and Cavity Design Code
SEM	Scanning Electron Microscopy
SiC	Silicon Carbide
SINBAD	Radiation Shielding and Dosimetry Experiments Database
SOL	Scrape-off Layer
SPICE	Sample Holder for Irradiation of Miniaturised Steel Specimens Simultaneously at Different Temperatures
SSC RF RIAR	State Scientific Centre of Russian Federation Research Institute of Atomic Reactors
SSP	Separatrix Strike Position
TBM	Test Blanket Module
TBR	Tritium Breeding Ratio
TCEE	Two Component ECM Electrolyte
TD	Theoretical Density
TED	Thales Electron Devices, Velizé, France
TEKES	Teknologian ja Innovatioden Kehittaemiskeskus, Helsinki, Finland
TEM	Transmission Electron Microscopy
TEP	Tokamak Exhaust Processing
TF	Toroidal field
TIG	Tungsten Inert Gas
TIMO	Test Facility for ITER Model Pump
TLD	Thermo Luminescence Detector
TLK	Tritium Laboratory Karlsruhe

TOSKA	Torusspulen Testanordnung Karlsruhe
TPMC	Test Particle Monte Carlo
TRIMO	Tritium Inventory Modelling
TRP	Tritium Production Rate
TSEFEY	Electron-beam Testing Facility
TTC	Target and Test Cell
TUD	Technical University of Dresden
TZM	Molybdenum, stabilized by small amounts of titanium and zirconium
UFOTRI	Unfallfolgenmodel Tritium
USE	Upper Shelf Energy
VDE	Vertical Displacement Event
VDS	Vent Detritiation System
VV	Vacuum Vessel
W	Tungsten
W-7X	Wendelstein 7-X stellarator project, Greifswald, Germany
WDS	Water Detritiation System
WL10	Tungsten Lanthanum Oxide
XRD	X-ray Diffraction
Y_2O_3	Yttrium Oxide